A Combined Experimental and Theoretical Study into the Excited States of Luminescent Platinum Complexes

FREEMAN, GEMMA,RACHEL

A Combined Experimental and Theoretical Study into the Excited States of Luminescent Platinum Complexes

Gemma Rachel Freeman

A thesis submitted in partial fulfilment of the requirements for the degree of Ph.D.

Department of Chemistry

June 2014

Abstract

Luminescent transition metal complexes have attracted much attention in recent years due to their potential as phosphors in organic light-emitting devices, their use in sensory systems and their applications in bioimaging. It is often desirable to predict the photophysical properties of such compounds to allow tailored design, accentuating certain characteristics. This combined experimental and theoretical study of the excited states of platinum complexes outlines synthesis, photophysical measurements and theoretical consideration of some such compounds, giving insight into the theoretical techniques applied.

Reproduction of absorption spectra is described for a series of previously reported Pt(II) complexes, using different basis sets, functionals and solvent models, the techniques then applied to a novel set of related Pt(IV) complexes. Understanding of these parameters was then used for more complicated modelling of the emissive process in thiolate-substituted derivatives of Pt(dpyb)Cl. These were studied experimentally and theoretically, showing a change in excitation character upon coordination of the thiolate ligand. TD-DFT showed the importance of modelling solvent for the prediction of the correct excitation character, alongside a consideration of techniques and mathematical parameters for the correct calculation of emission energies.

Bis-imine, bis-ketimine and bis-oxime ligands have been synthesised by Schiff base condensation chemistry and their corresponding N^C^N-coordinated Pt(II) complexes prepared. A wide range in quantum yields was observed and attributed to varying rates of non-radiative decay. Consideration of the S_0 and T_1 geometries by DFT and their distortion relative to one another showed the origin of this decay. Methyl-substituted benzenes were investigated for similar properties. Those derivatives for which the calculations predict significant distortion do show emission properties typical of triplet state distortion. However, due to "triplet instabilities", TDA geometries appear to be more reliable than those calculated by DFT, showing better consistency with the experimental trends.

Techniques described above were also applied to other classes of Pt(II) complexes. The rate of radiative decay was considered for these compounds by taking into account both the orbital overlap and the degree to which the metal atom was involved in the excitation.

Declaration

The work described herein was undertaken in the Department of Chemistry at Durham University between October 2009 and July 2013. The work presented is my own, except where otherwise stated. No part of it has previously been submitted for a degree at this or any other university.

Statement of copyright

Acknowledgements

Working in the department over the last few years has been a really fun experience. While the chemistry has been interesting, there are also many people who have made the day to day work much more enjoyable and ultimately possible to whom I would like to say 'thank you'. Firstly I would like to thank my supervisor Prof. Gareth Williams for his help, guidance, support and encouragement throughout my studies; particularly for long chemistry discussions which have been one of the most enjoyable aspects of this project. In addition, I would like to thank my co-supervisor Prof. David Tozer, and Dr Michael Peach for his continued patience in teaching me how to perform DFT calculations. Thank you to Durham University and to the EPSRC for financial support.

Members of the Williams group, both past and present, have been a great source of support, and friendship; thank you to Victoria, Lisa, Louise, Pierpaolo, Mickaële, Raminder, Fabian, Jonathan, Will and all of the 4th year project and summer students, not forgetting the other members of CG1, with their crazy antics and sarcasm. Thank you also to all the friends who have made tea breaks, lunch and Friday pub trips so much fun; especially Massey, Louis, Delley, Ricardo, Geri, Casey, Emma and Andrew.

It goes without saying that much of this work could not have been achieved without the help of other people. Thank you to Dr Aileen Congreve for help with HPLC and encouragement throughout; to Drs Hazel Sparkes and Dmitry Yufit for crystal structure determinations; Dr Massimo Cocchi for OLED fabrication; and to Andreas Köhn for RI-CC2 calculations. I would also like to thank Dr Alan Kenwright, Catherine Heffernan, Ian McKeag and Dr Juan Aguilar for high resolution NMR spectroscopy; Dr Jackie Moseley, David Parker and Peter Stokes, for mass spectrometry; Judith Magee for elemental analysis; and everyone working in stores and the workshops.

Finally, a big thank you to my family and friends outside of chemistry; Sarah for late night games of 'chemistry spot the difference'; and particularly to Mum and Dad, for support and encouragement throughout.

Table of Contents

List of abbreviations

acac	acetylacetonate
ASAP	atmospheric solids analysis probe mass spectrometry
aug-cc-pVDZ	augmented correlation-consistent polarised, valence-only, double-zeta basis set
ax	axial
b.p.	boiling point
B3LYP	Becke, 3-parameter, Lee-Yang-Parr hybrid exchange-correlation energy functional
bpy	2,2′-bipyridine
CAM-B3LYP	Coulomb attenuation method, Becke, 3-parameter, Lee-Yang-Parr range-separated hybrid exchange-correlation energy functional
cpu	central processing unit
cc-pVDZ	correlation-consistent polarised, valence-only, double-zeta basis set
cc-pVTZ	correlation-consistent polarised, valence-only, triple-zeta basis set
CPCM	conductor-like polarizable continuum model
CTC	carbon tetrachloride
DCM	dichloromethane
DFT	density functional theory
DMAE	dimethylaminoethanol
DME	1,2-dimethoxyethane
DMSO	dimethylsulfoxide
dpyb	1,3-di(2-pyridyl)benzene
ECP	effective core potential

EML	emissive layer
EPA	diethyl ether-isopentane-ethanol in 2:2:1 v/v ratio
EPR	electron paramagnetic resonance
eq	equatorial
ES	electrospray ionisation
f	oscillator strength
FC	Franck-Condon
GGA	generalised gradient approximation
HF	Hartree-Fock
HOMO	highest occupied molecular orbital
HPLC	high-performance liquid chromatography
HRMS	high resolution mass spectrometry
IC	internal conversion
ILCT	intraligand charge-transfer
ISC	intersystem crossing
ITO	indium tin oxide
LANL2DZ	Los Alamos National Laboratory 2-double-zeta basis set
LC	ligand centred
LLCT	ligand-to-ligand charge transfer
LMCT	ligand-to-metal charge transfer
LUMO	lowest unoccupied molecular orbital
m.p.	melting point
MC	metal centred
MLCT	metal-to-ligand charge transfer
MP	methylcyclohexane and isopentane in a 3:1 v/v ratio
NMR	nuclear magnetic resonance

OLED	organic light emitting device
PC	bisphenol-A-polycarbonate
PBE0	Perdew, Burke and Ernzerhof hybrid exchange-correlation energy functional
PCM	polarizable continuum model
ppyH	2-phenylpyridine
RHF	restricted Hartree-Fock
RI-CC2	resolution of the identity - approximate second order coupled cluster
RMSD	root-mean-square displacement
S_0	singlet ground state
SCF	self consistent field
sh	shoulder
S_n	n^{th} singlet excited state
SOC	spin-orbit coupling
TAZ	3-phenyl-4-(1′-naphthyl)-5-phenyl-1,2,4-triazole
TCTA	tris(4-carbazoyl-9-ylphenyl)amine
TDA	Tamm-Dancoff approximation
TD-DFT	time dependent density functional theory
T_n	n^{th} triplet excited state
THF	tetrahydrofuran
TPD	*N*,*N*′-bis(3-methylphenyl)-*N*,*N*′-diphenylbenzidine
tpy	2,2′:6′,2″-terpyridine
UHF	unrestricted Hartree-Fock
UV	ultra violet
v/v	the volume ratio of two or more solutions
WOLED	white organic light emitting device

1

Introduction

Luminescent transition metal complexes have attracted much attention in recent years due to their potential application in a diverse range of areas. Various groups have exploited their photophysical properties in organic light emitting devices (OLEDs),[1–4] white light OLEDs (WOLEDs),[5–7] for bioimaging applications[8–11] and in small molecule sensory systems.[12–16]

The incorporation of a metal atom into a compound drastically increases the efficiency of phosphorescent emission. This is desirable for production of low energy display screens and white lighting applications, enabling energy conservation. It has been found that the wavelength of emission can also be systematically tuned. This is achieved by alteration of ligand substituents, allowing for specific colour design and work towards WOLEDs to be undertaken.[17]

Phosphorescent emitters have longer lifetimes of emission (on the order of microseconds) than traditional, metal-free, fluorescent compounds. This is advantageous in bioimaging, allowing a time-gated approach so that autofluorescence from the cell has time to decay before images are viewed.[18]

Luminescent systems have also been designed where emission properties are altered in the presence of oxygen or small cations to act as sensory systems. Emission properties of devices can be monitored to assess whether a given

analyte is present and if so in what order of concentration.[19–22]

This literature review will briefly consider different electronic excitations that can take place and the difference between them. Factors that determine the luminescent properties of a compound will then be discussed along with strategies for promoting luminescence in transition metal complexes. The discussion will be broadly divided in to two: the first half predominantly considering the luminescent properties of terdentate platinum(II) complexes and the second, theoretical methods for predicting the absorption and emission properties of such complexes.

1.1 What is luminescence?

Photoluminescence is the emission of radiation subsequent to excitation of an atom or molecule through the absorption of radiation. Luminescence is an inefficient process in the majority of molecules since excited species can also return to the ground state by non-radiative decay pathways that normally predominate. In this second process, energy is lost by thermal dissipation to the molecule's surroundings, often via kinetic motion of the bonds. Luminescent decay of the excited state can be broadly divided into two categories: fluorescence and phosphorescence.

Fluorescence is the emission of light from an excited state whose spin multiplicity is the same as that of the ground state (usually singlets). Once absorption of light has occurred and an electron has been promoted in a molecule, intersystem crossing (ISC) can occur, changing the spin multiplicity to the triplet excited state. Relaxation of the molecule from the triplet state through a radiative transition (phosphorescence) is a spin-forbidden process with rate constants as low as 0.1-100 s^{-1} for purely organic molecules. Incorporation of high spin-orbit coupling (SOC) metals (such as platinum or iridium) into a molecule relaxes the spin selection rule, and allows relaxation through phosphorescent radiation from the triplet excited state, T_n, to the ground state, S_0. Radiative decay through this pathway is still significantly slower than fluorescence, leading to longer emission lifetimes (on the order of microseconds)

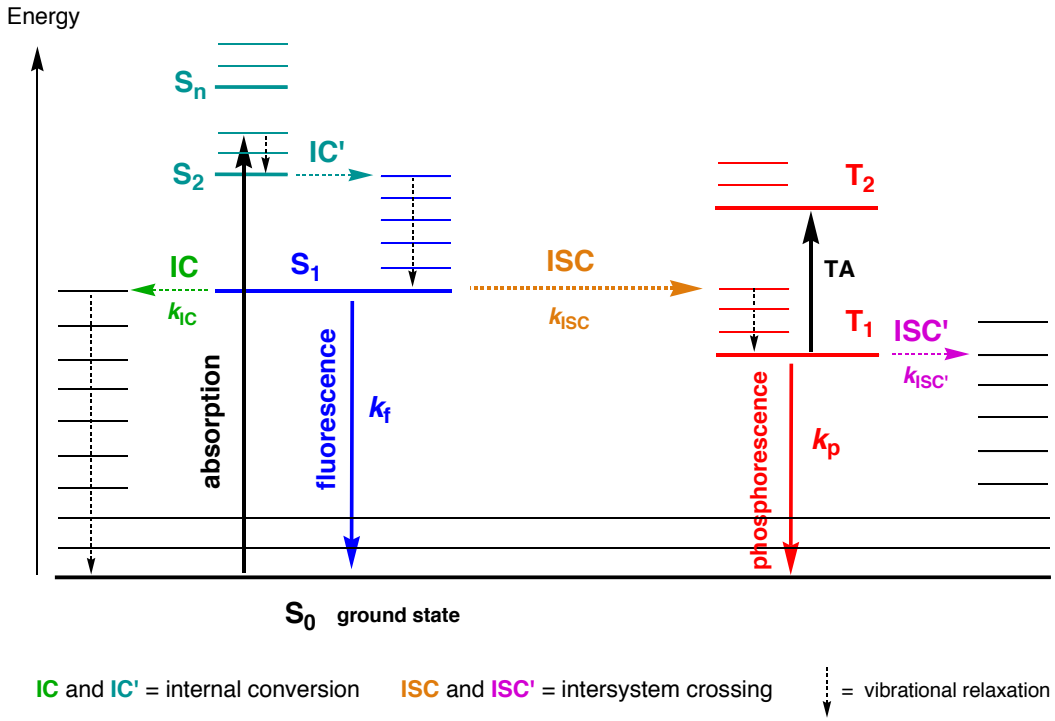

Figure 1.1: A Jablonski diagram to illustrate possible electronic transitions taking place.

in phosphorescence. These processes are illustrated in the Jablonski diagram shown in Figure 1.1.

1.1.1 What determines efficiency of emission?

The efficiency of a compound's luminescence is measured by its quantum yield, Φ_{lum}. This is determined by the relative rate constants for radiative (k_r, the sum of k_f and k_p) and non-radiative (k_{nr}) decay (assuming that the emitting state is formed with unitary efficiency upon absorption of light), according to Equation 1.1 (where n_E is the number of photons emitted and n_A is the number absorbed).

$$\Phi_{lum} = \frac{n_E}{n_A} = \frac{k_r}{k_r + k_{nr}} \tag{1.1}$$

Unlike many purely organic molecules, for complexes with small ligands and metals that have high spin-orbit coupling constants (such as platinum), ISC will be much faster than the rate of emission from the singlet excited state. This means that any observed emission normally emanates from the triplet excited state, namely phosphorescence. The exception to this rule is if the excited state is isolated away from the metal centre.[23]

1.1.2 Electronic transitions

In organometallic compounds, the emissive state (which is usually the lowest energy excited state) can generally be described as one of four states. These are: metal centred (MC) d-d states, metal-to-ligand charge transfer (MLCT), ligand-to-metal charge transfer (LMCT) and ligand centred transitions (LC). These are illustrated schematically in Figure 1.2. Though broadly classed into these states, if they are similar in energy, mixing of the states can occur and emission may be the result of a combination of transitions. The nature of the transition will greatly affect the emission observed and therefore design in this area can contribute to tuning of emission properties. For this reason, many groups employ the use of density functional theory (DFT) calculations to predict the character of the transitions.

1.1.3 Strategies for promoting luminescence

According to Equation 1.1, promotion of luminescence will involve either an increase in the rate of radiative decay (k_r), or a decrease in the rate of non-radiative decay (k_{nr}). In phosphorescent metal complexes, the metal character of the excited state becomes important in determining the efficiency of emission. The rate constant for radiative decay should be highest for excited states composed of a high degree of metal character.

Non-radiative decay of the excited states of platinum(II) complexes can be best understood in terms of a simplified potential energy surface diagram (Figure 1.3). The potential energy surface of the d-d excited state is displaced relative to the ground state in these complexes, since they have a strong preference for the square planar geometry in the ground state. This is due to ligand

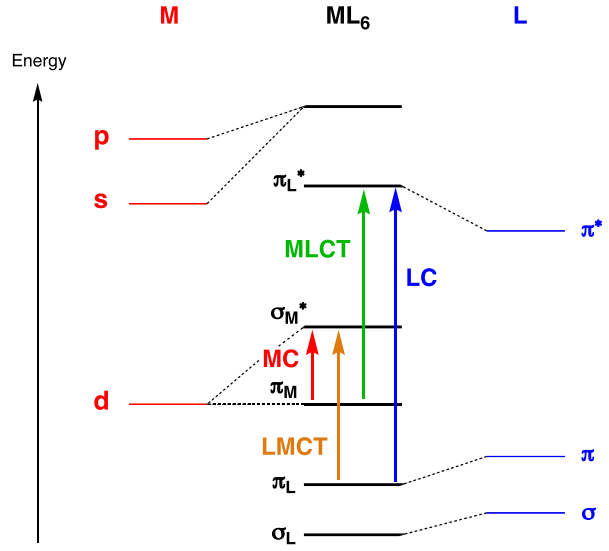

Figure 1.2: An energy level diagram to illustrate the various possible excited states of complexes.

field stabilisation and means that the unoccupied $d_{x^2-y^2}$ orbital will be very strongly anti-bonding in character. Population of this d-d state will therefore lengthen the platinum-ligand bond, distorting the complex and resulting in non-radiative decay. Though the d-π^* and π-π^* state may be lower in energy than the d-d, excited molecules (excitation shown along the red arrow of Figure 1.3) can cross over at the isoenergetic point to the d-d excited state and decay non-radiatively, following the blue arrow pathway.

There are two possible strategies then to reduce the rate of non-radiative decay: first to ensure that the lowest lying excited state is not a MC d-d state, second to increase the gap between the lowest lying excited state and the d-d excited state.

1.2 Luminescent platinum(II) complexes of aromatic terdentate pincer ligands

1.2.1 N^N^N-coordinated ligands

First synthesised by Morgan *et al.* in 1934,[24] the N^N^N-coordinated terpyridyl complex of platinum (Figure 1.4) was investigated with respect to its

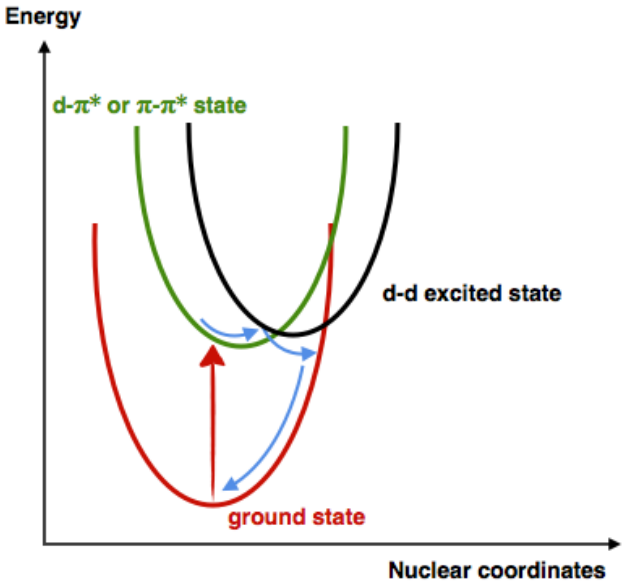

Figure 1.3: Potential energy surface diagram to show deactivation by d-d states for a D_{2d} distorted Pt(II) complex.

coordination properties. Derivatives of this complex were later studied by Lippard who altered the ancillary ligand to incorporate biological moieties. These were used to form DNA intercalators in an attempt to utilise electron microscopy to follow the platinum at base-specific sites by sequencing polynucleotides attached to the molecule.[25] The photophysical properties of the complex were not investigated until the 1990s when it was found that, contrary to expectation, luminescence at room temperature was not observed. While non-radiative decay by distortion was reduced by a rigid, terdentate ligand (preventing the D_{2d} distortions illustrated in Figure 1.3), the coordination angle of the N^N^N ligand around platinum is smaller than would be most favourable (180° for N−Pt−N).[26] This strain lowers the ligand field splitting energy, such that the strongly-antibonding $d_{x^2-y^2}$ orbital lies at a similar energy to the ligand π^*. This means that promotion from the excited state to this orbital can occur at ambient temperature, followed by ISC and non-radiative decay back to the ground state. It is obvious, then, that for room temperature luminescence to be possible for such structures, either the ligand field strength must be increased, raising the antibonding $d_{x^2-y^2}$ orbital

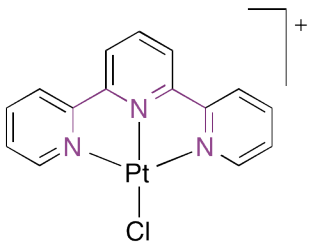

Figure 1.4: Terpyridyl platinum(II) complex

so that it can no longer be populated, or the radiative excited state lowered to an extent where population of $d_{x^2-y^2}$ is no longer possible.

McMillin *et al.* showed that substitution of the proton at the 4 position of the central pyridine ring (by either an electron withdrawing or electron donating group) produced compounds that were luminescent at room temperature. This was achieved by increasing the gap between the excited radiative decay state and the deactivating, state as illustrated in Figure 1.5.[27] Electron donating groups (such as NMe_2, $\Phi_{lum} = 0.08$ in DCM) stabilised the MLCT state in relation to the deactivating d-d states, due to conjugated systems formed between the lone pairs of the electron-rich substituents and the terpyridine ligand. A new π-π^* state is then formed with ILCT, increasing the gap between the emissive and non-radiative states. Electron withdrawing groups (such as CN, $\Phi_{lum} = 0.005$ in DCM) lowered the MLCT state further than the d-d state, increasing the energy gap and making the deactivating d-d state more difficult to populate.

Other studies have shown that 6-membered chelating ring systems (Figure 1.6) relieve ring strain in the system compared to their 5-membered chelate ring counterparts. This gives a bite angle for the ligand closer to 180° which in turn gives a stronger ligand field, promoting the deactivating d-d states to a higher, less thermally accessible energy and reducing non-radiative decay. Garner *et al.* showed phosphorescence from N^N^N-coordinated Pt(II) complexes modified in this way, with quantum yields of up to 4% in solution, at ambient temperature.[28] It should nonetheless be noted that electronic factors

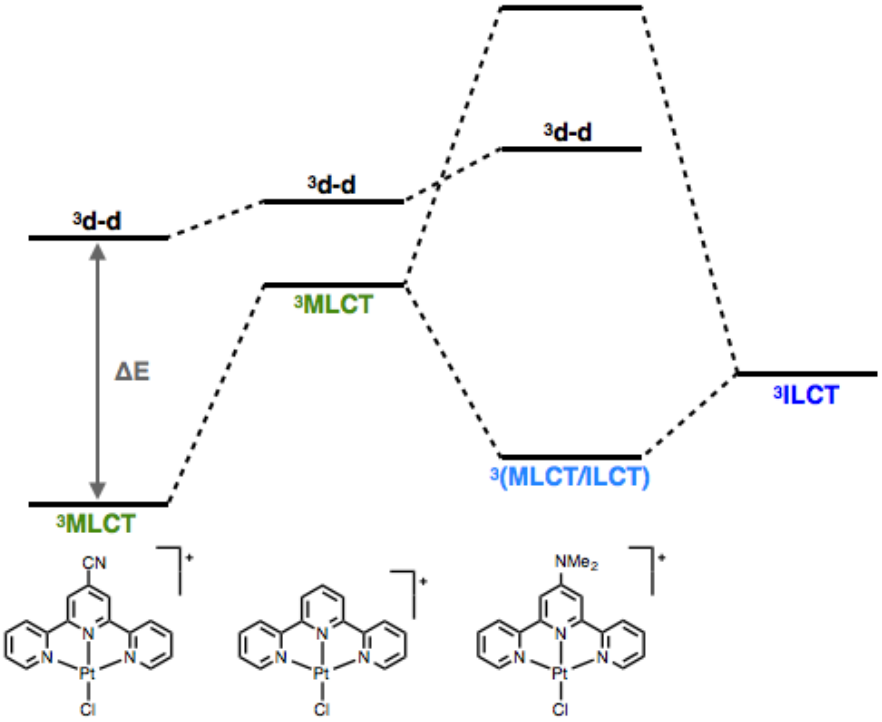

Figure 1.5: Molecular orbital diagram for the proposed excited state energies for 4-substituted N^N^N Pt(II) complexes for both electron withdrawing and electron donating substituents.[27]

are still important since the related azaindole-based complex is non-emissive at room temperature, despite having a computationally predicted N−Pt−N angle of 179°.

Substitution of the chloride ancillary ligand by a stronger field ligand has also been shown to increase ligand field splitting, increasing the energy of the d-d states and reducing the likelihood of their population. Several groups have replaced the chloride by ligands such as cyanides or acetylides.[30–32] For example, substitution of the chloride in the complex shown in Figure 1.6 for an acetylide increased the quantum yield of luminescence from 3.6 to 4.2%.[29]

The combined effect of substituting the 4-position of the central pyridine ring and also the chloride for a stronger field ligand was nicely illustrated by Sun and coworkers (Figure 1.7).[33] In this example, substitution of the pyridine

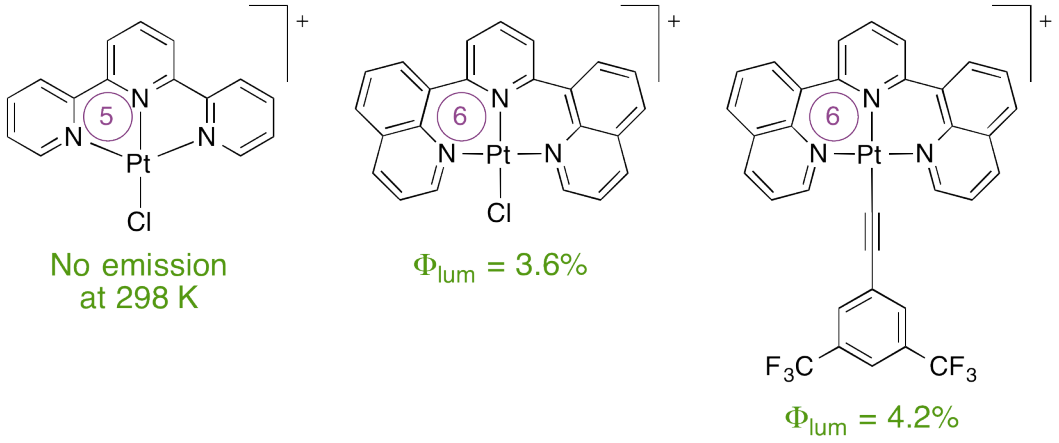

Figure 1.6: Three N^N^N-coordinated Pt(II) complexes and their quantum yields in DCM solution at room temperature.[26;28;29]

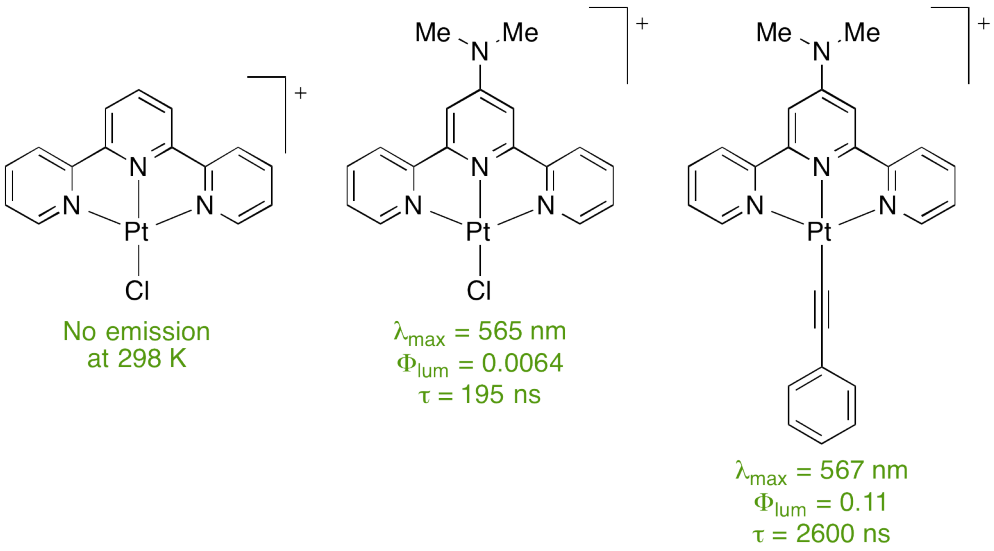

Figure 1.7: N^N^N-coordinated Pt(II) complexes reported by Sun and coworkers and their quantum yields, lifetimes and emission maxima in MeCN solution at room temperature.[33]

central ring with an NMe_2 group gave a complex which was weakly emissive at room temperature ($\Phi_{lum} = 0.0064$), then metathesis of the chloride for an acetylide increased the quantum yield by over two orders of magnitude ($\Phi_{lum} = 0.11$)

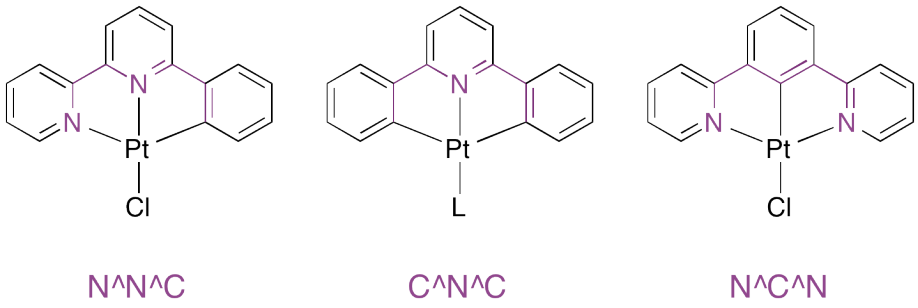

Figure 1.8: Structures of the parent terdentate cyclometallated Pt(II) complexes.

1.2.2 Ligands with aromatic amines and a cyclometallated carbon atom

Replacement of one or more of the nitrogen atoms in the terpyridine ligand by a cyclometallating carbon atom has a profound effect on the luminescent properties of the compound. While $[Pt(tpy)Cl]^+$ emits no light at room temperature, Pt(dpyb)Cl (Figure 1.8) is intensely luminescent and shows $\Phi_{lum} = 0.60$ (in DCM solution at room temperature). The carbon anion is a strong σ donor to the metal. Synergy with the π-accepting ability of the pyridyl rings means that such ligands create a very strong ligand field, raising the energy of the deactivating d-d states. While there are many examples of N^C^N and N^N^C-coordinated complexes, C^N^C analogues are still relatively rare, perhaps due to the unfavourable *trans* effect of two mutually *trans* cyclometallated rings.

N^N^C-coordinated complexes

Constable *et al.* first showed in 1990 that 6-phenyl-2,2′-bipyridine could be made to cyclometallate to platinum to give the parent N^N^C-coordinated complex shown in Figure 1.8.[34;35] In contrast to the N^N^N parent complex, the N^N^C shows room temperature luminescence ($\lambda_{max} = 565$ nm, $\Phi_{lum} = 0.025$ in DCM solution at 298 K).[36] The blue shift of the complex's emission with increased polarity of solvent ($\Delta\lambda_{max}$ from dichloromethane to acetoni-

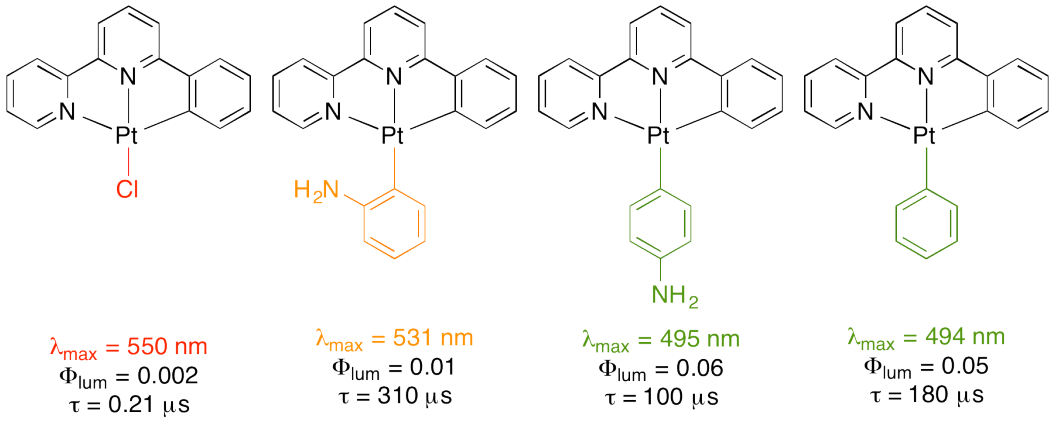

Figure 1.9: Structures and emission properties of N^N^C-coordinated Pt(II) complexes with different ancillary ligands. Measurements taken in degassed acetonitrile solution at 298 K.[37]

trile = 15 nm) suggests that radiative character was due mainly to the MLCT state. A reduction in the emission lifetime was observed with increasing concentration, indicative of self quenching by the complex. This is unsurprising since the planar structure of the molecule allows close packing and overlap of the delocalised electrons.

As for the N^N^N-coordinated complex, Yip *et al.* reported that metathesis of the ancillary ligand allowed subtle tuning of the emission properties of the complex and that a stronger field ligand gave an increase in quantum yield of luminescence (Figure 1.9).[37] Lu *et al.* later synthesised an extensive library of organometallic N^N^C-Pt(II) complexes, illustrating the control that is possible over the emission properties of this type of complex.[38] They systematically altered the ancillary ligand, along with substituents, on both the pyridyl and phenyl rings; electron withdrawing groups gave a blue shift in emission while electron-rich substituents caused emission to move into the red (Figure 1.10).

Fillaut *et al.* more recently showed that even subtle changes to the ancillary ligand can have a profound effect on the emission properties observed. They showed that addition of cyanide to their N^N^C-coordinated complex (which showed no luminescence in solution at room temperature) increased the efficiency of emission due to the introduction of a MLCT/L′LCT excita-

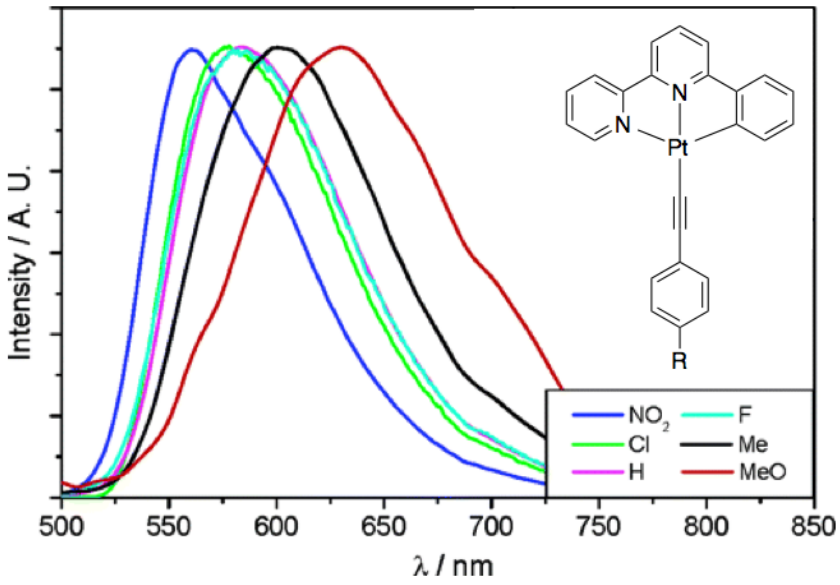

Figure 1.10: Normalised emission spectra for the N^N^C-Pt(II) complex with various R substituents shown. Spectra were taken at 298 K in DCM solution.[38]

tion in the cyanide rich form (determined by TD-DFT studies). This gave a highly selective sensor for CN^- as illustrated in Figure 1.11.[16]

Photophysical properties of the N^N^C complexes are also significantly influenced by the identity of the metallated aryl ring, a pattern exemplified between the compounds shown in Figure 1.12.[38] More recently, Huo and coworkers showed a small increase in emission efficiency by increasing the size of one of the 5-membered chelate rings to a 6-membered ring.[39] It can be seen from these results that the luminescence of these systems is vastly improved from that of the N^N^N complexes. Emission spectra for the N^N^C complexes are usually broad and origninate mainly from the MLCT state, though other states can be introduced by alteration of the ligands. Wavelengths of emission have been successfully altered by systematic introduction of substituents on the N^N^C and ancillary ligands. Room temperature quantum yields vary greatly though most are moderate and in the region of 0.1 or below.

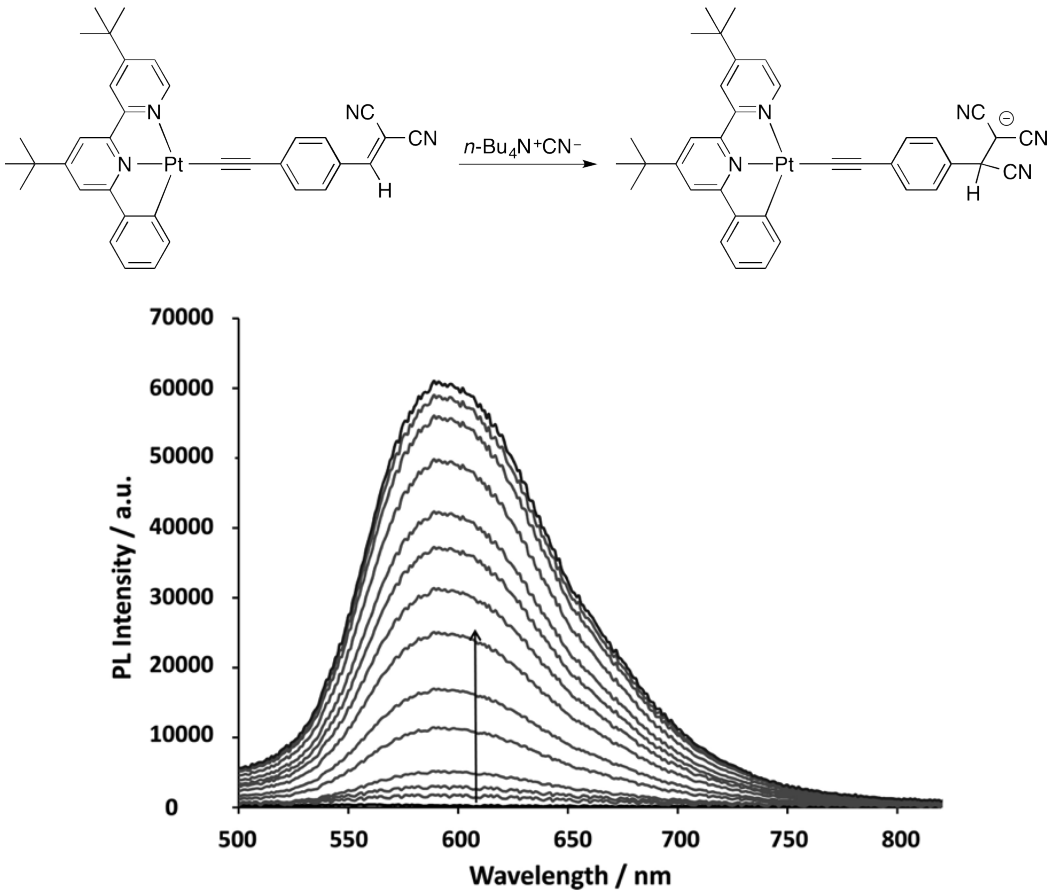

Figure 1.11: N^N^C complex before and after reaction with CN^- (top) and changes in photoluminescence intensity of the complex ($2.0\times\ 10^{-5}$ M in DCM) with addition of cyanide ($<2.4\times10^{-5}$ M n-Bu_4NCN).[16]

C^N^C-coordinated complexes

Given the vast improvement in room temperature luminescence observed upon the introduction of a single coordinating carbon into the complexes, it could be assumed that incorporation of a second such carbon atom would again improve luminescence properties. Complexes of this type (C^N^C-coordinating) were first synthesised and studied by Von Zelewsky and coworkers in 1988;[40] a simplified route to their formation was since reported by Cave *et al.* in 2000.[41] Photophysical study of these complexes showed that they were not luminescent in DCM solution at room temperature, though they

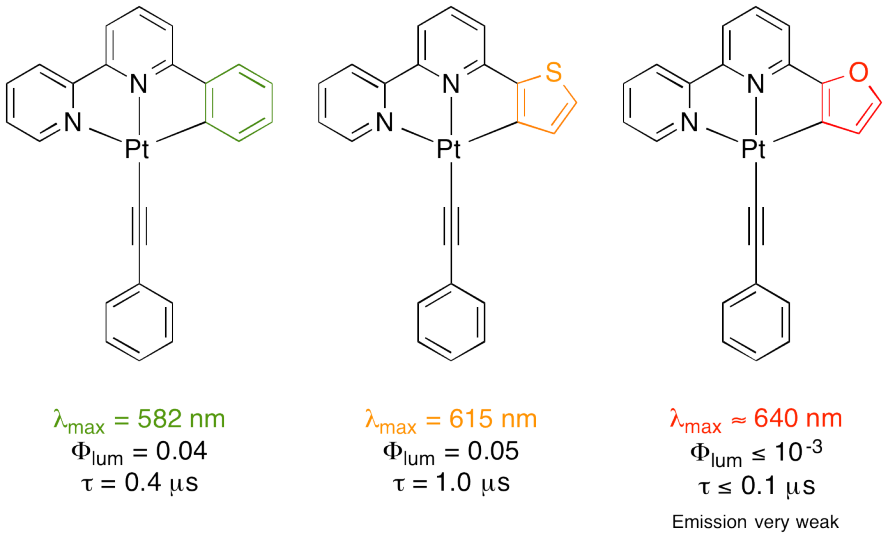

Figure 1.12: Structures and emission properties of N^N^C-coordinated Pt(II) complexes with altered carbon-coordinating rings. Measurements taken in degassed DCM solution at 298 K.[38]

did show emission of light in the solid state and in alcohols at 77 K.[42] By studying the crystal structures of a variety of compounds based around the C^N^C ligand coordinated to platinum, the group found that this series of molecules have a tendency to interact with one another through a variety of π stacking interactions. Other such complexes (for example [Pt(N^N^C)Cl]) show π stacking between pairs of the aromatic terdentate ligands, combined with metal-metal platinum interactions.[43;44]

In the last ten years a variety of C^N^C-coordinated Pt(II) complexes have been reported but few have shown any room temperature luminescence in solution.[45–49] The carbon-platinum bonds are elongated in these compounds where the cyclometallating carbons are *trans* to one another compared to those compounds where they are either *cis* or there is only one such carbon.[45;50] This is thought to be due to the unfavourable nature of having two cyclometallating carbons *trans* to one another.

N^C^N-coordinated complexes

The N^C^N-coordinated complex shown in Figure 1.8 was first reported by Cárdenas *et al.* in a study comparing the different reactions of the ligand 1,3-di(2-pyridyl)-benzene with platinum and palladium.[51] Reaction with K_2PtCl_4 gave the structure shown while reaction with $Pd(OAc)_2$ produced a dimeric complex with four acetate groups bridging two doubly metallated ligands. Williams *et al.* studied the photophysical properties of the platinum complex, reporting unusually high quantum yields of luminescence, the parent compound showing a quantum yield of 0.60 in DCM solution at room temperature.[52]

Alteration of substituents at the position *para* to the platinum of the benzene ring can be used to tune wavelength of emission. Many cyclometallated complexes of this form have been reported, one series of which, illustrating the range of energies possible, is shown in Figure 1.13.[53] Electron donating aryl substituents caused a red shift in the emission while electron deficient substituents gave a blue shift. A combination of electrochemical and density functional theory (DFT) studies suggested that the HOMO was located on this part of the complex while the LUMO (which was unaffected by these substituents) was located on the pyridyl rings (Figure 1.14). The energy of the HOMO can therefore be altered without affecting that of the LUMO.[53]

Tuning of emission energy can also be achieved by substitution at the 4-position of the pyridyl rings. This alters the energy of the LUMO which can be destabilised by the introduction of electron donating alkyl groups to give a blue shift.[54]

To date very little work has focused on the effect of relieving ring strain of the N^C^N-coordinated complexes through increase in the size of the chelate ring. Yoshida *et al.* fused a nickel porphyrin with an N^C^N-coordinated platinum complex (in both the +2 and +4 oxidation state) incorporating 6-membered chelate rings. Crystal structures were obtained of the different complexes, the Pt(II) compound showing relief of ring strain with a N−Pt−N angle of

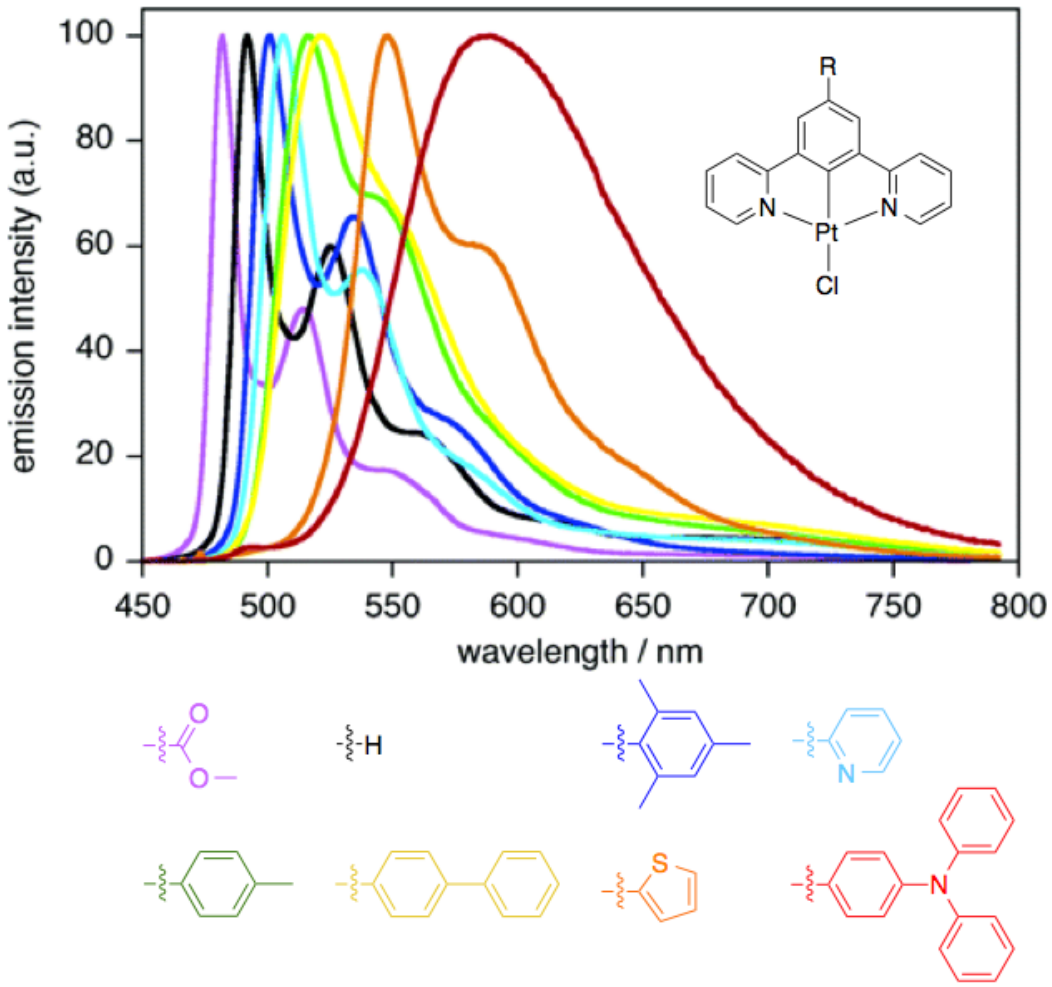

Figure 1.13: Normalised emission spectra of the eight complexes shown, in DCM at 298 K.[53]

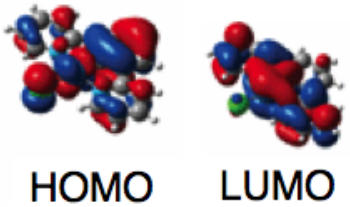

Figure 1.14: Frontier orbitals for the Pt(II) complex of 1,3-di(2-pyridyl)-benzene. Calculations performed with B3LYP with a CPCM for DCM.[53]

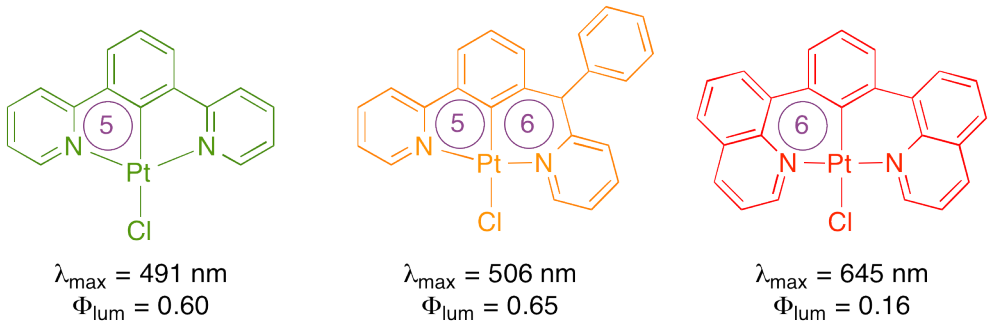

Figure 1.15: Geometries and photophysical properties of three N^C^N-coordinated Pt(II) complexes (in DCM at 298 K) showing their chelate ring size.[28;52;57]

176.5°[55] (compared to 161.1(2)° for Pt(dpyb)Cl).[51]

Williams and coworkers showed that augmentation of the 5-membered chelate ring of the N^C^N-coordinated complex to a 6-membered ring had a profound effect on the emissive properties of the complex (Figure 1.15, right).[28] In contrast to the N^N^N complex, emission efficiency was dramatically reduced (from Φ = 60 to 1.6%, in DCM solution at room temperature) as was its emission energy (λ_{max} = 491 to 645 nm). The group optimised the ground state geometry using DFT to investigate the effect of increasing chelate ring size on the compound. The calculations showed a relief of ring strain and a N−Pt−N angle of 178.5° which was subsequently reinforced by the crystal structure of a close derivative, for which the angle was 177.8(2)°.[56] The reduction in quantum yield was attributed to the radiative transition being less allowed, rather than to any detrimental effect on the rate of non-radiative decay.

Vezzu *et al.* synthesised a series of N^C^N complexes with one 5 and one 6-membered chelate ring, one example of which is shown in Figure 1.15.[57] In this example, a small increase in quantum yield was observed (compared to Pt(dpyb)Cl), despite the shift in λ_{max} to a lower energy (by 600 cm^{-1}). Crystal structures obtained by X-ray diffraction showed that the increase in one of the chelate rings (from 5 to 6-membered) resulted in a near linear N−Pt−N angle (172.93(8)°).

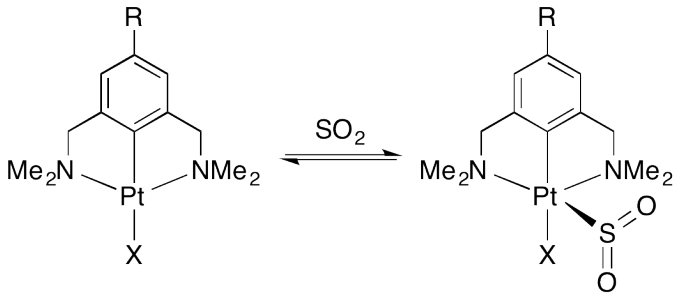

Figure 1.16: Reversible binding of SO_2 to a Pt(II) complex with an amine-based pincer ligand ligand.[61]

As for the other compounds discussed, substitution of the chloride ancillary ligand of the N^C^N-coordinated complexes has, in some cases, been shown to moderately increase the quantum yield of emission both in the solid state (with an NCS ligand)[58] and in solution (with an acetylide ligand).[59;60]

1.3 N^C^N-coordinated ligands of non-aromatic amines

Many examples of N^C^N-coordinated platinum complexes have also been reported incorporating non-aromatic amine ligands. Studies by Terheijden *et al.* showed the ability of one such saturated complex to bind sulfur dioxide in both solution and the solid sate[61] in a reversible process which was accompanied by a change from colourless to orange. Crystallographic characterisation of the SO_2 adduct (for X = Br) showed η^1-binding of the small molecule to the platinum, giving a square-pyramidal geometry (Figure 1.16).

A series of similar complexes with various substituents at the 4-position of the benzene ring (R in Figure 1.16) were later reported. This allowed for tuning of the response to SO_2.[62;63] Crystal structures of the compound shown in Figure 1.16 (R = OH, X = Cl) were also obtained by Albrecht *et al.* in both the bound and unbound states.[64] These studies showed hydrogen bonding between chlorine and −OH groups which was unaltered by the presence of SO_2. Solid-state exposure of the complex to SO_2 showed conversion to the adduct in just one minute.

Similar saturated-amine ligands have since been used to form platinum complexes for luminescence studies by Connick and coworkers.[65–68] The colourless compounds displayed strong UV absorption, attributed to MLCT transitions. Energies of absorption decreased with increasing electron density on the metal upon substitution of the ancillary ligand (Figure 1.17). Although the complexes showed no emission at room temperature, they displayed broad, low energy emission at 77 K (Figure 1.18) which was attributed to ^{3}MC excited states.

Various related complexes with substitution of the aromatic ring (Figure 1.19) have also been made by reaction of an aldehyde group at the 4-position of the benzene ring on the pre-formed complex.[69] These compounds have been studied for their non-linear optical properties since they show a large change in dipole moment upon excitation. Three of the complexes showed room temperature fluorescence: the NMe_2 (λ_{max} = 432 nm), CN (λ_{max} = 466 nm) and NO_2 (λ_{max} = 677 nm) substituted derivatives. Fluorescence, rather than phosphorescence, was assigned due to the short lifetimes of emission observed ($\sim$200 ps in DCM solution) and the extended conjugation of the ligand. Each of these three showed a strong positive solvatochromic response, indicative of the charge transfer nature of the excitation.

There are some examples in the literature of imine-based complexes of Pt(II) (Figure 1.20, left).[70] In contrast to the complexes of saturated amine ligands, these compounds showed phosphorescence at room temperature, although quantum yields were quite low (0.13-0.18%). Energies of emission were $\sim$575 nm with little change for different substituents. Song and coworkers have recently synthesised a series of related compounds[71] (Figure 1.20, right) which showed significantly elevated quantum yields ($\Phi_{lum} < 15\%$ in DCM solution). The addition of the aromatic ring results in delocalisation over the whole ligand, making the compound much more like Pt(dpyb)Cl.

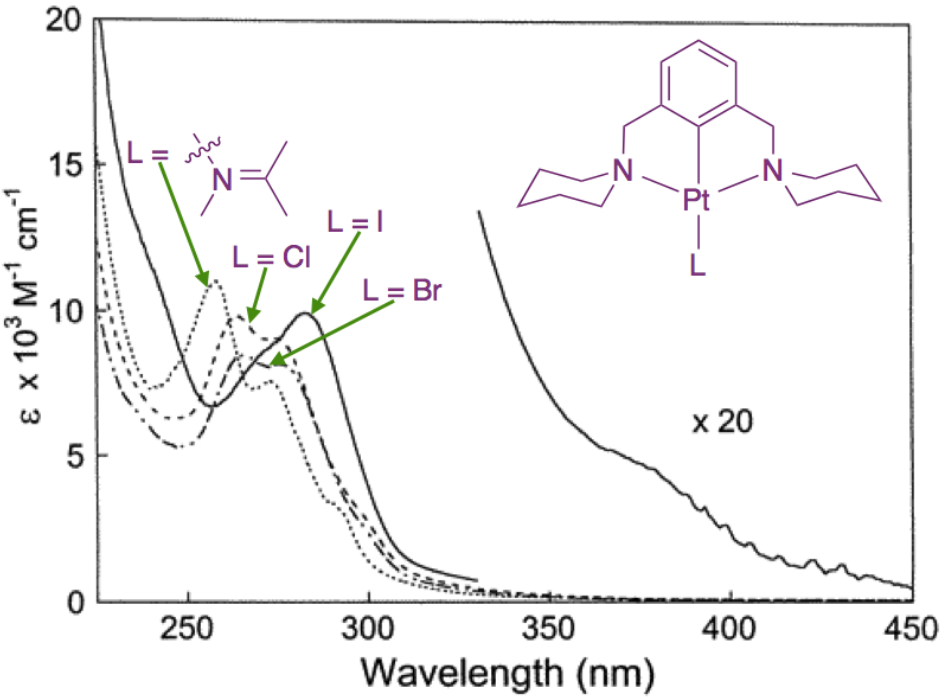

Figure 1.17: UV-vis absorption spectra of the compounds shown at 298 K in methanol.[65]

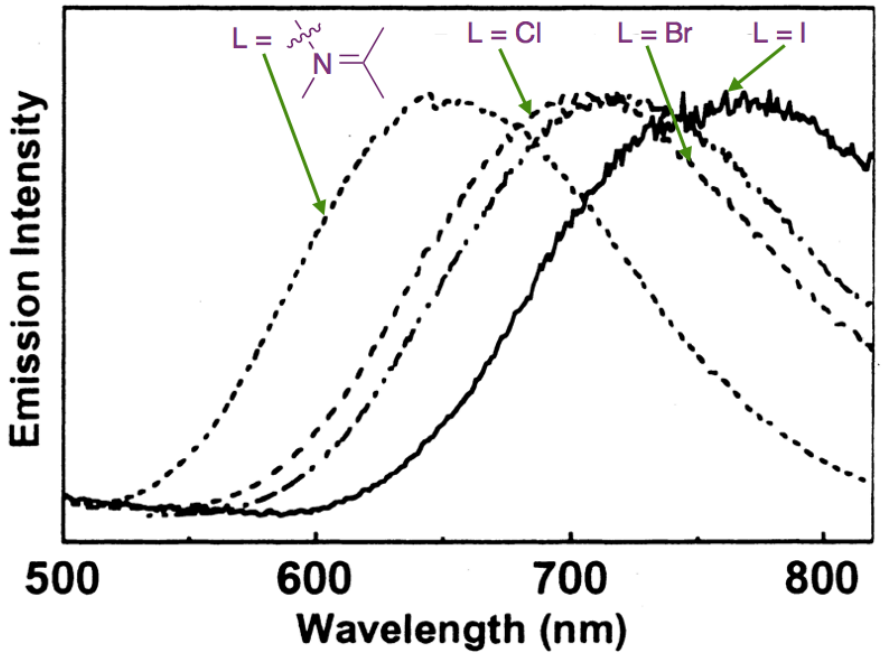

Figure 1.18: Normalised emission spectra at 77 K in 3:1 ethanol/methanol glass for the compounds shown (L corresponds to the ligand shown in Figure 1.17).[65]

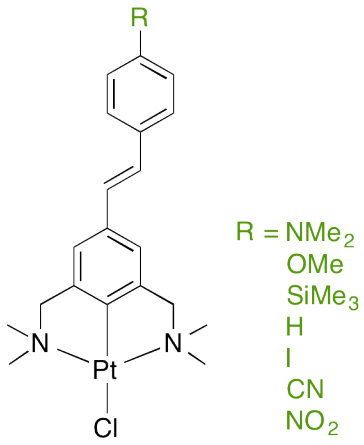

Figure 1.19: Structure of the Pt(II) amine complexes.[69]

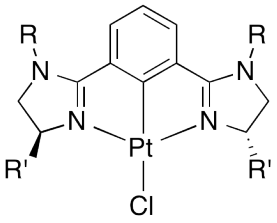

R' = *i*-Pr R = *p*-Tol
R' = *i*-Pr R = *p*-Anisyl
R' = CH_2Ph R = *p*-Anisyl
R' = CH_2Ph R = *p*-Anisyl

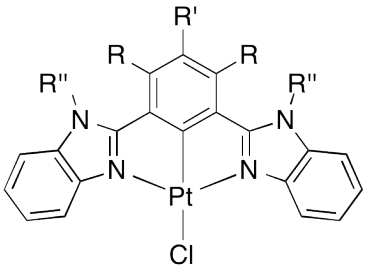

R = H R' = F R'' = Ph
R = H R' = *n*-BuO R'' = *n*-Bul
R = H R' = *n*-BuO R'' = *p*-Anisyl
R = H R' = *n*-Octoxy R'' = *n*-Octy
R = Me R' = H R'' = Ph

Figure 1.20: Structure of the Pt(II) imine complexes.[70;71]

1.4 Other luminescent Pt(II) complexes

Thus far only complexes incorporating a terdentate ligand coordinated to Pt(II) have been discussed. A search of the literature shows a plethora of other luminescent Pt(II) complexes, often formed from one bidentate, cyclometallating ligand (such as 2-phenylpyridine) and one other co-ligand such as β-diketonate,[72–75] acetylide,[76–78] carbene,[79;80] 2-picolinate[81;82] or 8-hydroxy quinoline.[83] An example of each is shown in Figure 1.21. In these examples, the TD-DFT studies, combined with observed photophysical behaviour of the compounds, show that excitations are usually centred on the cyclometallating ligand with only a small contribution from the co-ligand (though there are some exceptions to this).[82;84;85] This is illustrated by the orbital plots calculated for Pt(ppy)(acac) by Brooks *et al.* (Figure 1.22).

1.4.1 Increasing ligand rigidity

Mdleleni *et al.* reported that Pt(ppy)(ppyH)Cl is only weakly emissive in a solution of toluene at room temperature (Figure 1.23).[86] The local coordination sphere of this complex (two pyridine rings, one cyclometallated carbon and a chloride ligand) is the same as that of the brightly emissive NCN complex shown in Figure 1.13 (where R = H). Despite this, the emission efficiency of the two complexes varies significantly; while the energy of emission is similar between the two, the lifetime was an order of magnitude shorter for the less rigid complex (τ_{deg} = 641 ns in toluene for bidentate, 7200 ns for terdentate in DCM).[52;86] The increased rigidity of the terdentate ligand compared to the bidentate prevents distortion from local D_{4h} to D_{2d} symmetry in the excited state. This process has been described by many groups as a route for non-radiative decay.[87;88] Comparison of the room temperature solution state emission spectra show the ratio of the 0−0 band compared to the 0−1 band is higher for the terdentate ligand than the bidentate, providing further evidence for more excited state distortion in the latter (see Section 1.7).

Tetradentate ligands for platinum(II) complexes have received increasing interest in recent years.[89–91] The advantageous increase in rigidity from bidentate to

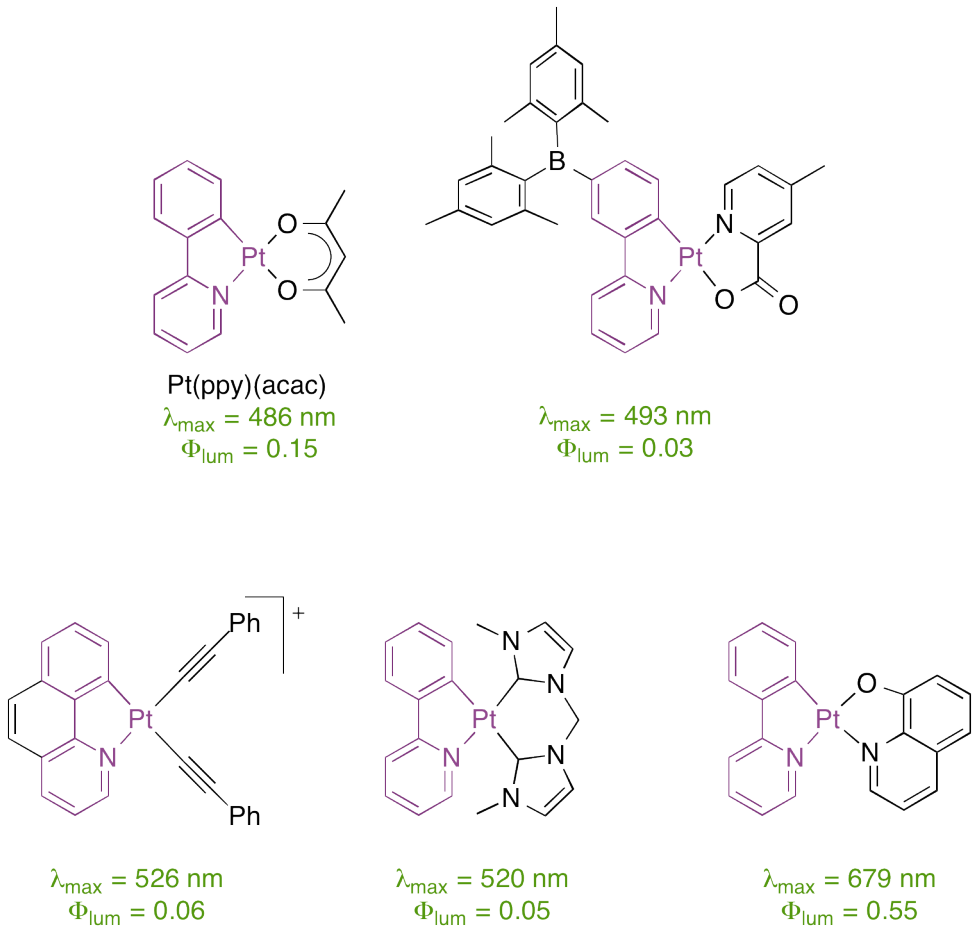

Figure 1.21: Examples of a β-diketonate (top left),[73] 2-picolinate (top right),[82] acetylide (bottom left),[76] carbene (bottom middle)[79] and 8-hydroxylquinoline[83] Pt(II) complex, showing λ_{max} of emission and Φ_{lum} at 298 K in DCM solution.

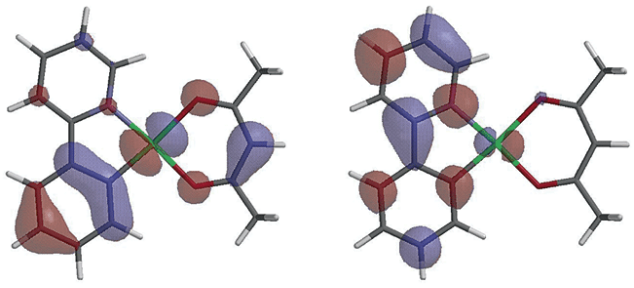

Figure 1.22: HOMO (left) and LUMO (right) orbital plots for Pt(ppy)(acac), calculated by DFT with B3LYP.[73]

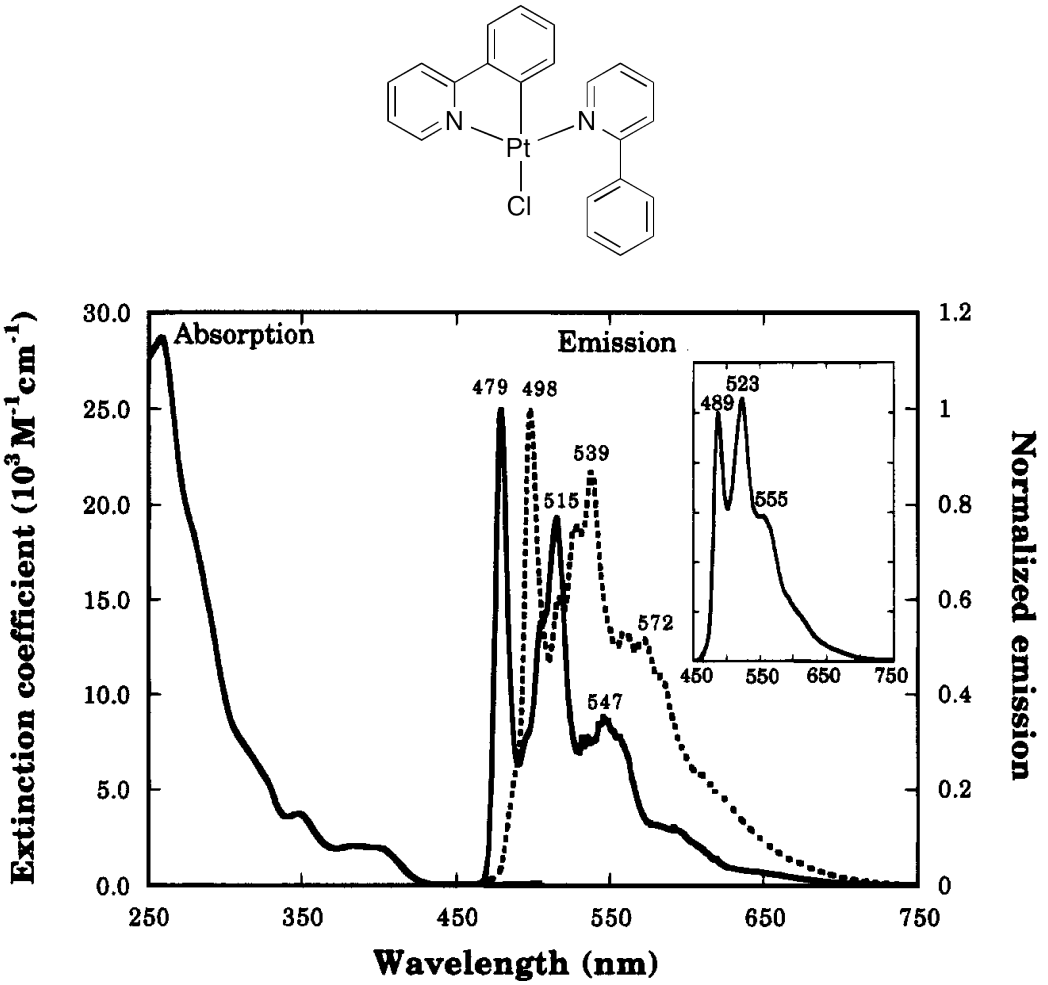

Figure 1.23: Structure and spectra of the complex studied by Mdleleni et al. Left: room temperature UV-vis absorption spectrum in DCM. Right 77 K emission spectra in toluene (solid line) and in the solid state (dashed line). Inset: Emission spectrum in toluene at 298 K.[86]

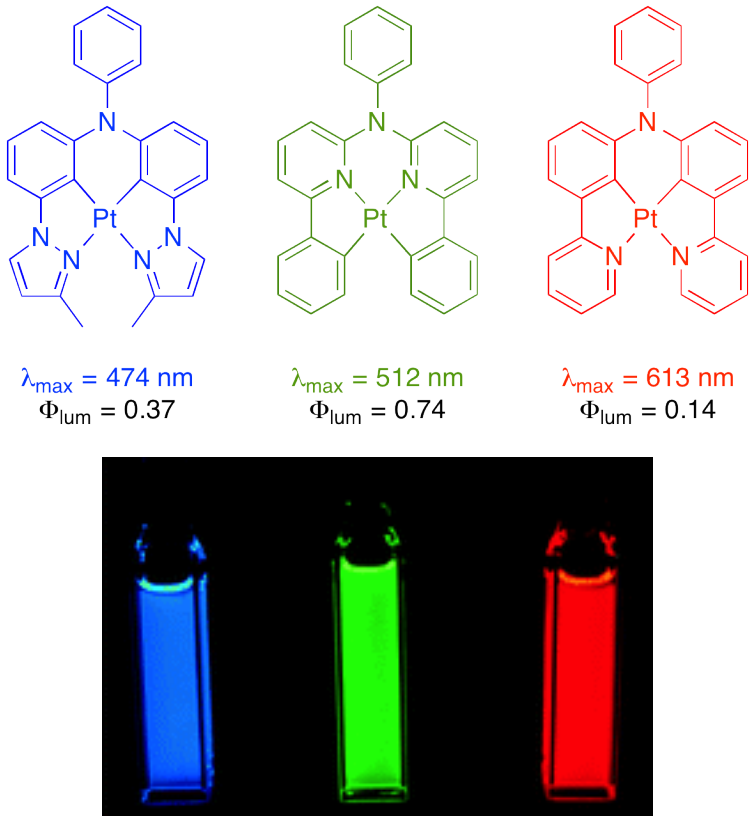

Figure 1.24: Structures and emission properties of three tetradentate platinum(II) complexes made by Huo and coworkers. Spectra and quantum yields measured in a solution of 2-methyltetraydrofuran at room temperature.[94]

terdentate ligands (*vide supra*) can potentially be increased further with such a ligand, increasing thermal stability and reducing the rate of non-radiative decay.[92] For example, *cis*-Pt(ppy)$_2$ exhibits D_{2d} distortion in the excited state leading to non-radiative decay and almost no room temperature emission.[93] Huo and coworkers showed that by linking together the two bidentate ligating units, thus increasing rigidity, the quantum yield of luminescence could be significantly improved (Figure 1.24).[94]

Turner *et al.* have since shown the synthesis and properties of some tetradentate Pt(II) complexes with oxygen linkers, increasing the chelate ring size (one example shown in Figure 1.25).[95] Despite the strained geometry adopted by the complex (illustrated in the crystal structure), quantum yields obtained

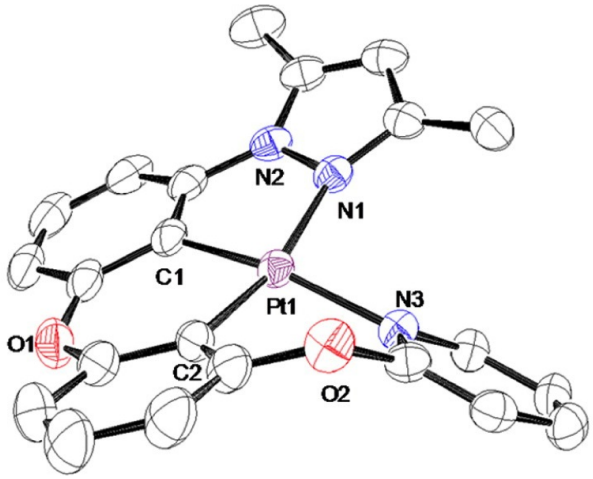

Figure 1.25: Crystal structure of a tetradentate Pt(II) complex determined by Turner et al.[95] *Hydrogen atoms omitted for clarity.*

for the series of complexes were high (Φ_{lum} = 0.39-0.64 in DCM solution at room temperature). The group found that these compounds were particularly efficient in a doped PMMA film, achieving quantum yields as high as 0.97 in OLED devices.

1.5 DFT and TD-DFT calculations

It is often desirable to predict the emissive properties of a given complex or series of complexes prior to synthesis in order to tailor the design of the compound towards particular properties. Many groups employ the use of density functional theory (DFT)[96–98] and its time-dependent derivative (TD-DFT)[99] in order to predict energies of absorption and emission of these compounds (or to rationalise their photophysical behaviour). This is done routinely in the literature with various degrees of success. $S_0 \rightarrow S_n$ excitations are formally allowed and an oscillator strength for the excitation is usually calculated, giving some indication as to the intensity of each absorptive process. It is often also important to rationalise the efficiency of emission of a complex. This is more rarely attempted since spin-orbit coupling (SOC) from the heavy metal atom (which allows the formally forbidden phosphorescence and ISC to occur) is usually omitted from such calculations due to the complexity of its inclusion.

As we have seen through experimental studies, even with inclusion of SOC, emission efficiency is complex; both k_r and Σk_{nr} must be considered, each comprised of many different factors.

1.6 TD-DFT calculation of excitation energies

The calculation of excitation energies by TD-DFT, both for absorption and emission of compounds, is desirable since it can help inform researchers on which compounds to make for their application of choice as well as providing reassurance that the correct transition is being described by the calculation. There are various ways different researchers calculate these quantities, often dependant on the time and computing power available. There are many examples of each in the literature and so only a few examples in each case will be discussed alongside the general principle.

In their review, Adamo and Jacquemin have outlined different methods that are commonly used for calculation of $S_0 \rightarrow S_1$ excitation energies; these are illustrated in Figure 1.26.[100;101] The same principles can generally be applied in the calculation of triplet excitation energies. Optimisation of the ground state geometry followed by TD-DFT calculation ($E^{vert-abso}$) represents the absorptive process, in this example for the $S_0 \rightarrow S_1$ excitation. The same calculation at the S_1 excited state geometry, $E^{vert-fluo}$ corresponds to fluorescence (or for triplet excitations at the triplet-optimised geometry, phosphorescence, $E^{vert-phos}$). Optimisation of the triplet geometry followed by TD-DFT excitation calculations (equvalent to $E^{vert-phos}$) is frequently used in the literature[39;102;103] and is the closest estimation to the actual process taking place. Calculations of the $S_0 \rightarrow T_1$ excitation at the triplet geometry can though sometimes produce excitation energies which are unexpectedly low in energy (or even imaginary, *vide infra*). The difference between the two minima, E^{adia} is the adiabatic energy. This method is occasionally used by groups to calculate phosphorescent emission ($T_1 \rightarrow S_0$)[104] but will generally calculate excitation energies which are too high since it considers only the difference in the two minima.

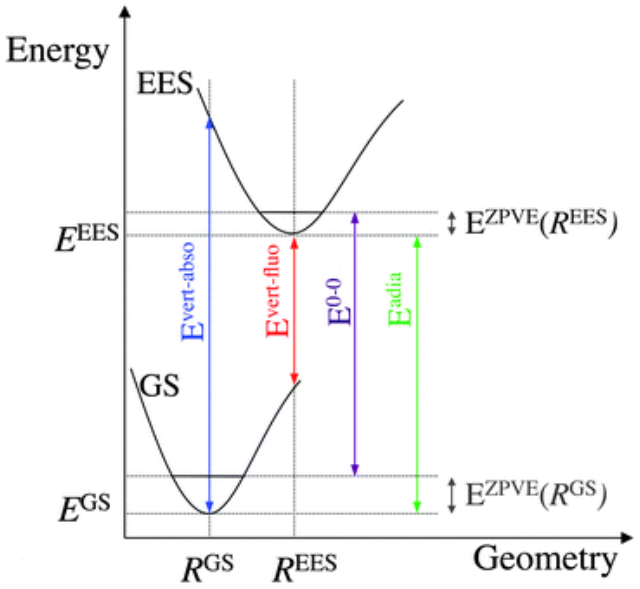

Figure 1.26: Potential energy curve diagram representing two singlet states and possible methods for calculating excitation energies.[100]

For triplet emission, $S_0 \rightarrow T_1$ excitations calculated at the S_0 geometry ($E^{vert-abso}$) will necessarily be too high in energy. This is common practice however[105–107] since it saves on computational time, requiring only one geometry optimisation for prediction of both absorptive and emissive properties. Similarly, triplet geometries are often optimised from the compound's crystal structure (or optimised ground state) geometry.[108;109] It should be noted that once symmetrical, a geometry cannot break its symmetry during the calculation and this practice can lead to the optimisation of false global minima. Excitation energies calculated at the crystal structure geometry itself are also commonplace.[110–112] These values should be approached with caution since the geometry obtained is the result of intermolecular interactions not considered in the calculation.

1.6.1 Triplet instabilities

The phenomenon of unexpectedly low excitation energies, sometimes calculated with TD-DFT, for $S_0 \rightarrow T_1$ excitations has recently been discussed in small molecule systems and ascribed to "triplet instabilities". First we will

consider the triplet instability problem in Hartree Fock (HF) theory since it is well known and documented,[113–116] then the discussion will be widened to TD-DFT.

Figure 1.27 shows the potential energy curve for H_2, calculated by Tozer and coworkers.[117] Unrestricted Hartree-Fock (UHF) theory uses different orbitals for the α and β electrons while restricted Hartree-Fock (RHF) uses a single molecular orbital twice, multiplied once by α and once by β. We would expect the energies of the two spin states (singlet and triplet) to converge as the two hydrogen atoms dissociate; this is exactly what was shown by the group for the two UHF calculations. In contrast, they showed that the $^1\Sigma_g^+$ RHF energy became too high as the molecule dissociated due to ionic components in the wave function (an unphysical result of the calculation). For UHF the $^3\Sigma_u^+$ and $^1\Sigma_g^+$ states became degenerate at high values of R, but for RHF the $^3\Sigma_u^+$ state was much lower than $^1\Sigma_g^+$, showing that the RHF calculations for H_2 are unstable with respect to the breaking of spin-symmetry.

Exact orbital exchange in DFT

Exact orbital exchange in DFT is the HF exchange energy expression, evaluated using Kohn-Sham orbitals. Many groups use hybrid functionals[118–127] with a fixed amount of exact orbital exchange, α, (e.g. as B3LYP, 20%[128–130] and PBE0, 25%[131;132]) for DFT calculations, in place of generalised gradient approximations (GGAs) such as PBE.[132;133] This is because GGAs generally underestimate excitation energies; introduction of exact exchange increases these energies, particularly in singlet excitations, although in some cases the energies become significantly lower for triplets. More recently, Coulomb-attenuated or range-separated functionals have also been used since they have been shown to improve calculation of long-range, charge-transfer type excitation energies but maintain a good approximation of localised excitations.[134–138] These functionals vary the amount of exact orbital exchange as a function of the inter-electron distance, r_{12}; for example, CAM-B3LYP[134] has an initial α of 19%, increasing to 65% at high r_{12}. It is perhaps unsurprising therefore that DFT functionals incorporating some degree of exact orbital exchange will

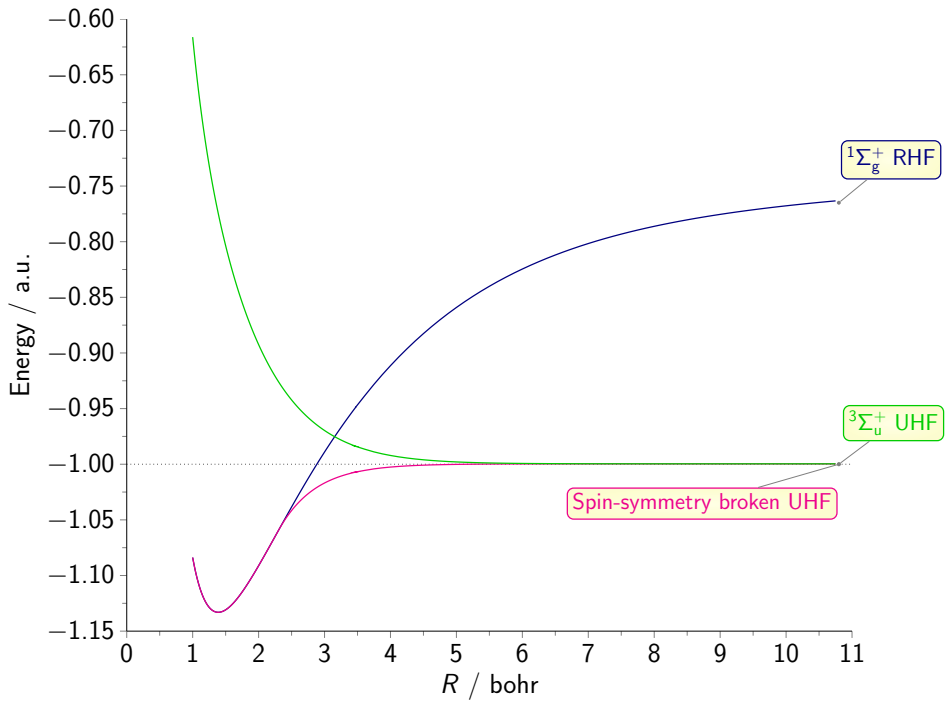

Figure 1.27: HF electronic energy of H_2 calculated as a function of bond length.[117]

suffer from the same triplet stability difficulties as HF.

Measuring stability

Tozer and coworkers showed that the "stability measures" of a given geometry could be quantified by consideration of the eigenvalue in the electronic Hessian, which becomes negative with low stability.[117;139] This indicates that specific orbital rotations of an identified space-spin symmetry (similar to the rotations involved when describing excited states) can result in lower total energies (see Appendix, Figure 9.1 for examples calculated for H_2).

The similarity in the equations used to calculate excited state energies and stabilities[140;141] means that geometries with a low stability are more likely to be associated with an inaccurate total energy. The group showed that this was indeed the case by calculating excitation energies of H_2 as a function of bond length. Contrary to the exact excitation energy which tends to zero with

dissociation of the H−H bond, the difference in energy between the curves in Figure 1.27 (ΔSCF excitation energy) becomes negative (see Appendix, Figure 9.1) as a consequence of the ground state energy being significantly too high. The group showed that when the HF stability was high (>2 eV) excitation energies did not seem to suffer, but lower stabilities than this gave low excitation energies, the extreme example being negative stabilities precipitating imaginary excitation energies. The same analysis with TD-DFT showed a similar correlation though the threshold at which stabilites became too low was less well defined for Coulomb-attenuated functionals since the amount of exchange will vary between compounds.

The Tamm-Dancoff approximation

Tozer and coworkers recommended the use of the Tamm-Dancoff (TDA) approximation for calculating excitation energies with low triplet stabilities.[117;139] This allows excitations between occupied and virtual orbital pairs while precluding de-excitations. The group calculated singlet and triplet excitation energies of four small molecule compounds (ethene, butadiene, benzoquinone, naphthalene) as a function of α with both TD-DFT and TDA.[117] The results for butadiene are shown in Figure 1.28. They showed that for the singlets, GGAs ($\alpha = 0$) underestimated the energies, which then increased with increasing α. For the triplet excitation, energies decreased with increasing exchange, dramatically dropping below 0 for 1^3B_u. TDA increased the excitation energies in each case, even for the very low or negative excitation energies. They showed for all the molecules that TDA generally improves the excitation energies compared to the reference values. Peach and Tozer later showed the use of TDA with CAM-B3LYP for reliable calculation of low-overlap, low stability excitation energies.[142]

1.7 Franck-Condon principle

During an electronic transition, the Franck-Condon (FC) principle states that the probability for the transition is greater when the two vibrational wave functions have high overlap.[144–146] This is because the nuclei are much heavier than the electrons, so the electronic transitions proceed much faster than the

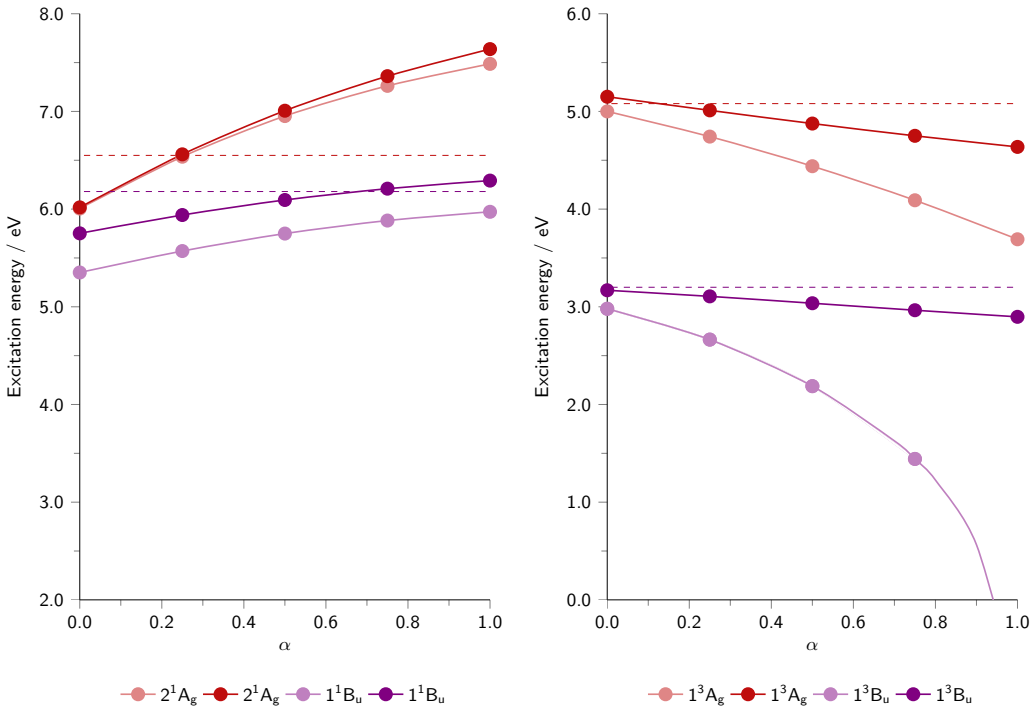

Figure 1.28: Singlet (left) and triplet (right) excitation energies of butadiene as a function of exact exchange (α). Dashed lines show reference values.[143] Lighter colours show TD-DFT excitations and darker colours those computed by TDA.[117]

nuclei can respond. Excitations then proceed without a change in geometry so the highest intensity band is the one where the nuclei have the highest probability of being at the same initial geometry. Franck-Condon states are therefore normally electronically and vibrationally excited. A quantum mechanical description of the theory states that the intensity of each vibronic transition will be proportional to the square of the overlap integral of the two vibrational wave functions in the transition. An illustration of this is shown in Figure 1.29, which shows that as distortion increases the 0−0 band decreases in intensity relative to the other bands.

1.7.1 Calculating electronic excitation properties with vibrational structure

Excitation energies calculated by those methods described in Section 1.6 are often used to predict the absorption spectra of complexes.[107;148;149] For $S_0 \rightarrow$

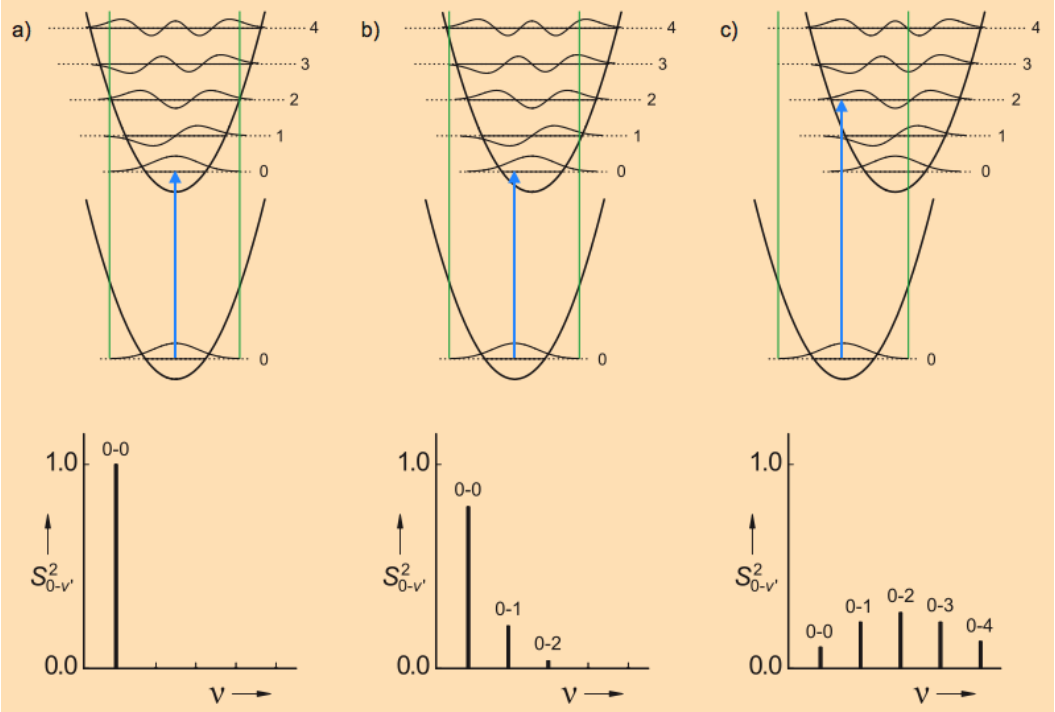

Figure 1.29: Illustration of the quantum mechanical model for Franck-Condon overlap with increasing distortion from a-c.[147]

S_n excitations the output from the calculation is usually an excitation energy and an oscillator strength (f), showing the probability of the excitation. Measured at room temperature, absorption spectra are a mixture of many different excitations, both electronic and vibrational so that broad bands, often incorporating more than one excitation, are obtained. It is often therefore desirable to "convolute" these computationally obtained energies for comparison to experimental results. The most common way to achieve this is to place a Lorentzian or Gaussian curve over each excitation with a fixed energy of broadening (e.g. 0.1 eV) at half the oscillator strength maximum. Various researchers achieve this either manually[150] or using a program such as GaussSum,[104;151–154] or SWizard.[110]

One example of manual convolution of absorption excitations was recently given by Li *et al.*[150] The group optimised the ground state geometry of each of the six N^N^C-coordinated complexes shown in Figure 1.30 then calcu-

lated the 40 lowest singlet excitations at that geometry using TD-DFT. Each individual excitation (shown by the vertical lines in Figure 1.30) was then broadened by a Gaussian function with a line width of 0.1 eV to give the spectra shown. The calculations were performed using the conductor polarized continuum model (CPCM)[155] for DCM and the experimentally obtained spectra shown were obtained from solutions of DCM at room temperature. This gave reasonable reproduction of the trend in absorption energies between the complexes, though the energies of the calculated bands are blue-shifted from the experimental values. Consideration of the oscillator strength of each excitation allows more informed consideration of which orbitals are affecting that region of the spectrum so that those with insignificant probabilities will not dominate and can be ignored. For example, the group showed that where R = NO_2, excitations to S_3, S_4 and S_6 dominated the spectra so only these orbitals were considered (Figure 1.31).

Though there have been some studies on the calculation of FC integrals,[156–158] they are computationally demanding for large molecular systems and are usually reserved for small molecule study.[159–164] For example, Ziegler and coworkers used TD-DFT to predict and study the absorption spectra of MnO_4^-, TcO_4^-, RuO_4^- and OsO_4^-.[165] They optimised the singlet excited states using TD-DFT and the ground state by direct minimisation of the SCF energy. Franck-Condon factors were calculated from two vibrational mode calculations at the two different electronic states of the molecule. The energies and intensities obtained from this calculation were then broadened using Lorentzian functions with a half-width of 60 cm^{-1}. This approach (as illustrated by MnO_4^-, Figure 1.32) shows a good reproduction of the absorption spectrum structure though the energies were lower in the calculated spectra.

1.8 Modelling solvent

Unless otherwise specified, DFT calculations are performed in the gas phase in vacuum. Since these conditions are difficult to reproduce experimentally and different solvents can have a profound effect on the emission properties observed, it is often desirable to specify solvent in the calculations. The two

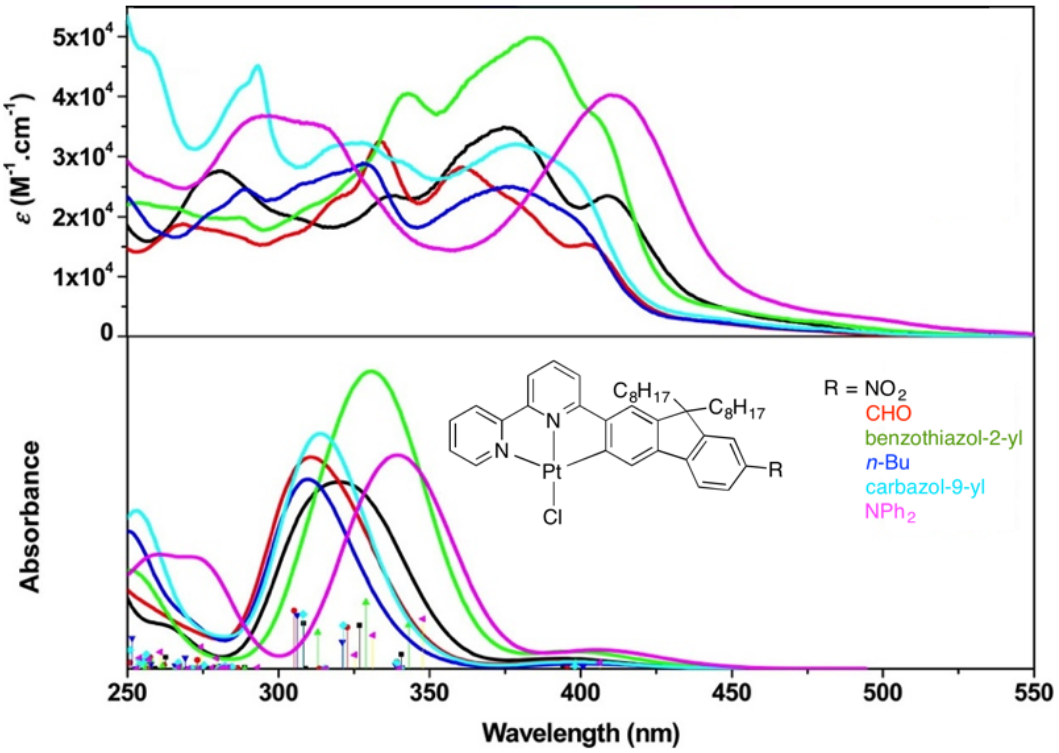

Figure 1.30: Top: experimental UV-vis absorption spectra at 298 K in DCM. Bottom: calculated absorption spectra; vertical lines show individual excitations and their oscillator strengths. Calculations performed with CAM-B3LYP with the LANL08 basis set for Pt and 6-31G for all other atoms.*[150]

Excited state and properties	Hole	Electron
S_3 $f_{osc} = 0.2279$ 340 nm	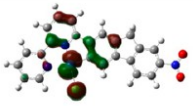	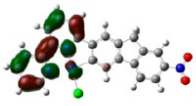
S_4 $f_{osc} = 0.6786$ 327 nm	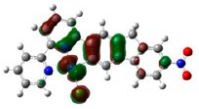	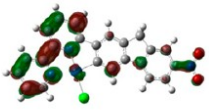
S_6 $f_{osc} = 0.7102$ 308 nm	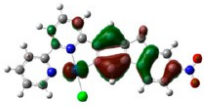	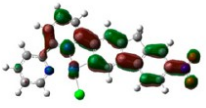

Figure 1.31: Natural transition orbitals for the transitions corresponding to the main absorption bands for the complex shown in Figure 1.30 where R = NO_2.[150]

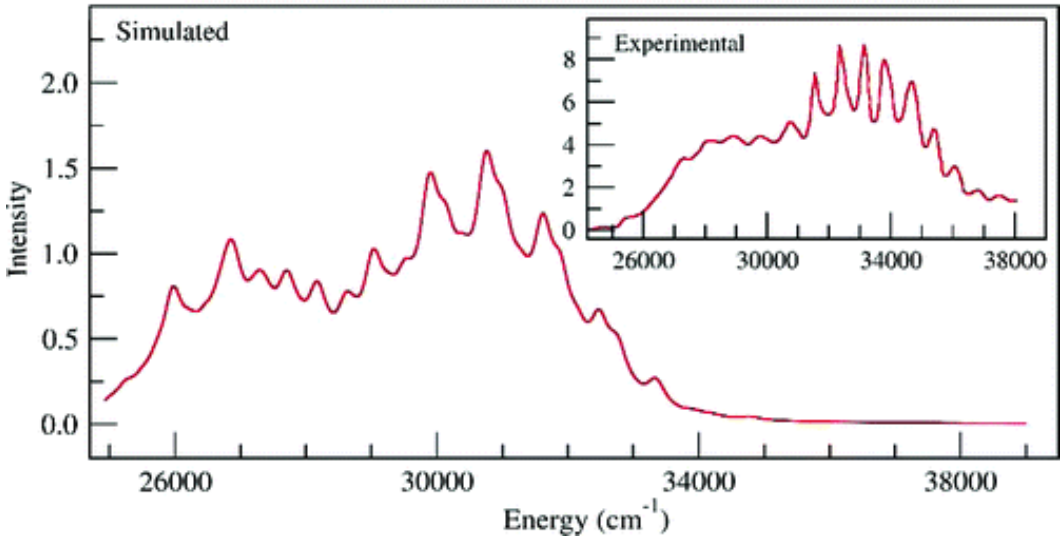

Figure 1.32: Experimental and simulated second and third bands of MnO_4^-.[165]

main approaches for estimation of solvent effects are explicit and implicit models. Explicit models treat every solvent molecule individually, calculating their interaction with one another and the compound of interest. Though this has been attempted for some small molecule systems, it is computationally demanding so is not used routinely in larger systems.[166]

Implicit solvent models describe the area around the compound of interest as a structureless continuum. For example, the Polarisable Continuum Model (PCM)[167] is often used in calculations of large molecules (such as platinum complexes) by many groups.[108;110;150] This approach omits specific solvent interactions but describes the polarity of the environment.

Inclusion of solvent in a calculation can have a significant effect on the excitation energies calculated. Che and Tong calculated the phosphorescent emission energies of five Pt(II) complexes (structures shown in Figure 1.33, these compounds will be discussed in more detail in Section 1.9.1) by optimising both the T_1 and S_0 geometries and calculating E^{0-0}.[154] They performed these calculations both in solvent and in vacuum for all five complexes, the energies for which are shown in Figure 1.33. Not only are the energies themselves

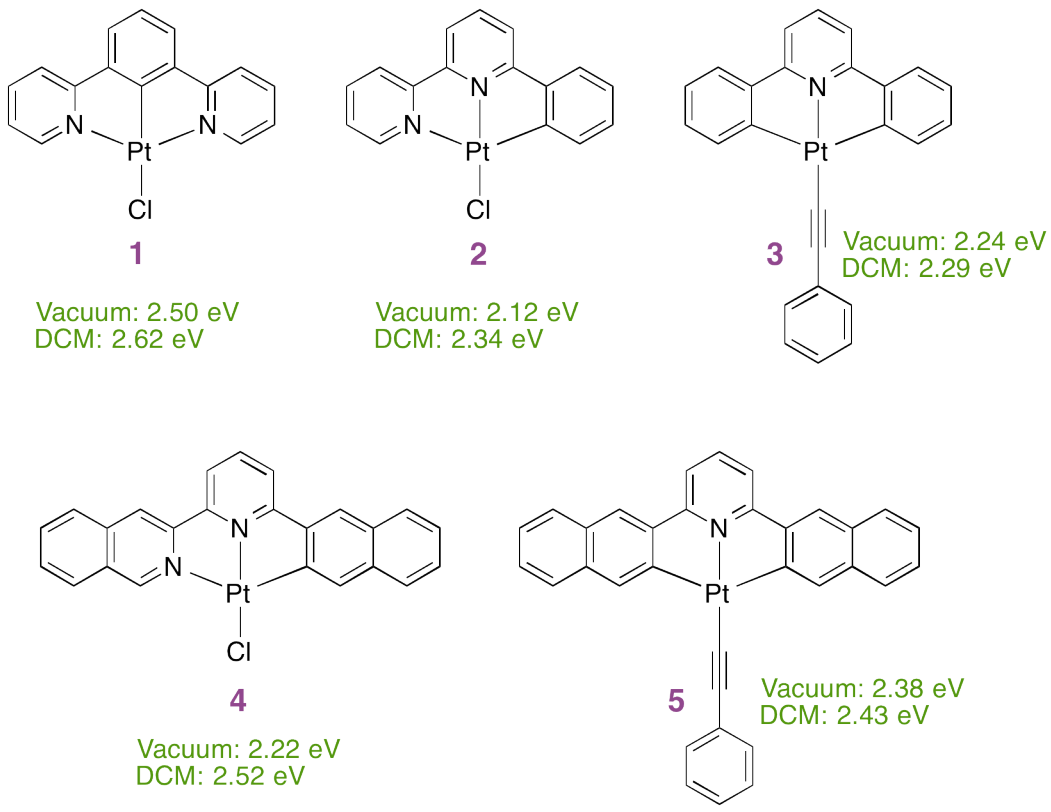

Figure 1.33: Structures and calculated phosphorescence emission energies of the complexes studied by Tong and Che (energies shown for both DCM and vacuum).[154] *The $T_1 \rightarrow S_0$ energies were calculated by the energy difference between the T_1 and S_0 optimised geometries.*

different but also the trend between them. In vacuum, energies of emission increase:

$$\mathbf{2} < \mathbf{4} < \mathbf{3} < \mathbf{5} < \mathbf{1}$$

In DCM emission energies increase:

$$\mathbf{3} < \mathbf{2} < \mathbf{5} < \mathbf{4} < \mathbf{1}$$

This highlights the importance of solvent inclusion in some calculations since they can have a large effect on the energies calculated.

1.9 DFT calculations for intensity

Estimations of phosphorescence efficiencies in the literature are rare compared to discussion of orbitals and excitation energies. The inclusion of SOC in cal-

culations, to enable the estimation of k_r, is far from routine. There are however some examples from groups who have attempted to rationalise the emission efficiencies of Pt(II) complexes using DFT. Some examples are outlined below.

1.9.1 DFT calculations on N^N^C, C^N^C and N^C^N complexes

DFT and TD-DFT methods have been employed by Tong and Che to try to explain why terdentate C^N^C-coordinated Pt(II) complexes showed weak luminescence at room temperature, N^N^C were weakly emissive and N^C^N were highly intense emitters.[154]

TD-DFT calculations were performed on the five complexes shown in Figure 1.33 to attempt to understand the different emission properties observed in a study highlighting the complexity of rationalising Φ_{lum}. The group calculated the radiative rate constant for each complex then considered its possible non-radiative decay pathways with the intention of understanding three main observations:

1. **1** has a high emission efficiency but **2** is only weakly emissive in solution at 298 K
2. **3** is non-emissive at 298 K, despite the increased strength in ligand field from **1** and **2**
3. the effect of π conjugation in **4** and **5** on emission efficiency

Rates of radiative decay were calculated by looking at a combination of three factors. First, SOC matrix elements between the emissive triplet and singlet excited states; second, the energy ratio between those two states and finally, the oscillator strength of the $S_n \rightarrow S_0$ transition with which the emissive triplet state undergoes SOC. k_r calculated for each complex is shown in Table 1.1. They reasoned that emission in **1** was in fact coming from the T_2 state since the radiative rate constant was much higher for that transition (109×10^4 s^{-1}) and Stokes shift for the $S_0 \rightarrow T_2$ excitation at the T_1 optimised geometry (3500 cm^{-1}) was more like the value obtained experimentally (4600 cm^{-1})[17;52] than the Stokes shift of the $S_0 \rightarrow T_1$ excitation (8100 cm^{-1}).

Complex[a]	Φ_{lum}	$T_1 \rightarrow S_0$ / eV	k_r 10^4 / s^{-1}
1	0.60[17;52]	2.62	1.04
2	0.20[168]	2.34	1.70
3	0.025[168]	2.29	0.785
4	–[42]	2.52	5.23
5	0.002[154]	2.43	0.0153

Table 1.1: Experimental quantum yields, phosphorescent energies (calculated in DCM) and calculated rates of radiative decay ($T_1 \rightarrow S_0$) for the five complexes studied by Tong and Che.[154] [a]Complex labels refer to those shown in Figure 1.33

Rates of non-radiative decay were considered more qualitatively through distortion between the excited triplet and ground states and the energy difference between those two states (since a smaller gap will lead to faster non-radiative decay).

The group showed that (unlike the other three complexes) compounds **2** and **3** underwent significant distortion away from planarity at the T_1 excited state (Figure 1.34) suggesting a possible route for non-radiative decay. They also showed that the calculated energies of emission (E^{0-0} between optimised T_1 and S_0 geometries in DCM) (shown in Figure 1.33) decreased in the order:

$$\mathbf{1} > \mathbf{4} > \mathbf{5} > \mathbf{2} > \mathbf{3}$$

This suggests, for example, that **3** will have a higher rate of non-radiative decay than **1**. The complexity of considering d-orbital splitting was also underlined since a compromise must be made between the large splitting between occupied and unoccupied d orbitals needed to make them thermally inaccessible for quenching[87] and the necessity for them to be close in energy for efficient SOC between excited singlet and triplet states. For example, they calculated **2** and **3** to have the smallest d-orbital splittings between the two highest lying occupied d orbitals, (Δdd_{occ}, at the S_0 geometry), giving the largest SOC and the highest k_r. Clearly this is not the case since **2** is weakly emissive[169] and **3**

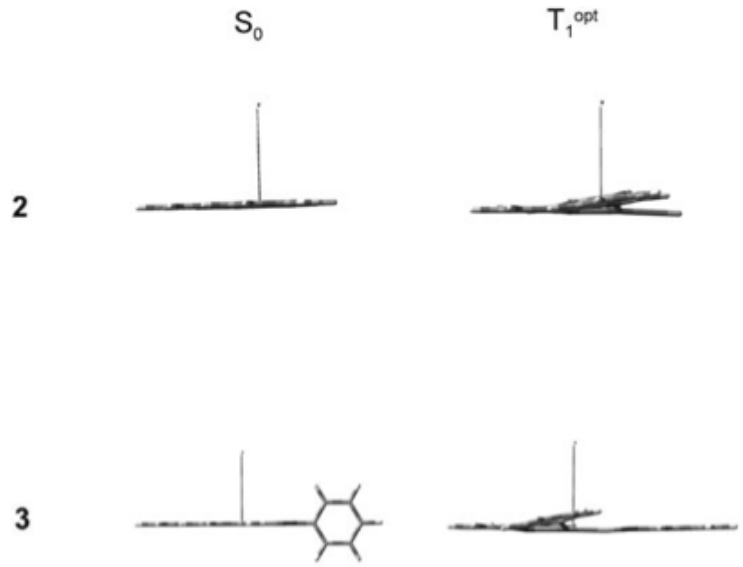

Figure 1.34: Optimised S_0 (left) and T_1 (right) geometries of compounds 2 (top) and 3 (bottom). Complexes are viewed from the side to show distortion away from planarity.[154]

is non-emissive[42] in DCM at 298 K. Conversely, **3** and **5** had high dd* splitting which should reduce their k_{nr} but these compounds also had poor emission efficiencies.[42;154]

These calculations illustrate then that predicting efficiency of emission is a complex process where many different factors must be considered. Calculation of radiative rate constants alone is not sufficient since non-radiative processes must also be considered which are much more difficult to quantify. Emission from the T_2 excited state (as assigned for **1**) is rare (Kasha's rule states that phosphorescent emission will occur from the lowest triplet excited state) and should be assigned with caution since unexpectedly low excitation energies could be due to triplet instabilities.

1.9.2 Increase in luminescence efficiency in dimeric complexes

Kataoka *et al.* have recently reported the theoretical study of the two Pt(II) complexes shown in Figure 1.35.[108] The 2-phenyl-6-(1*H*-pyrazol-3-yl)-pyridine ligand shown coordinated to platinum in Figure 1.35 has received interest from

several synthetic groups.[170–172] Interestingly, the neutral dimer complex exhibits a significantly higher quantum yield of phosphorescence (0.59 in DMF at 300 K) than the chloro-substituted complex ($\Phi_{lum} = 0.14$ in DMF at 300 K). A similar phenomenon has been reported for various other complexes: the dimer exhibits greater emission efficiency than the mono-nuclear platinum(II) complex.[37;38] The group analysed the complexes using DFT and TD-DFT to investigate their ground and excited state geometries, their absorption and emission processes and to investigate the difference in quantum yields of luminescence observed.

The optimised ground state (S_0) structures of the two complexes were compared with crystal structure geometries. It was found that the geometries were generally in good agreement with one another. There are one or two exceptions to this, for example the Pt−Cl bond length was longer in the optimised geometry (compared to the crystal structure) due to intermolecular forces in the crystal. It should be noted that each geometry optimisation was started at the crystal structure geometry. TD-DFT calculations were performed at the optimised S_0 geometry; the calculated excitation energies and oscillator strengths showed good agreement with the general shape of the experimental spectra though the energies themselves were slightly low. It is possible that this is a result of geometry optimisation from the crystal structure geometry: if a local minimum has been found due to symmetry constraints then the ground state will be too high in energy, resulting in lower excitation energies.

The group also optimised the S_1 and T_1 excited state geometries from the crystal structure, by TD-DFT, showing that excitation energies for $T_1 \rightarrow S_0$ emission gave red-shifted values from experimental results for both the monomer (553 nm calculated, 501 nm experimental) and the dimer (560 nm calculated, 503 nm experimental). For both complexes the excitations were $^3\pi - \pi^*/^3$MLCT in character (Figure 1.35, bottom), with the second ligand playing almost no role in the excitation for the dimer. They concluded that the second ligand played a role only in rigidifying the complex to prevent distortion leading to non-radiative decay.

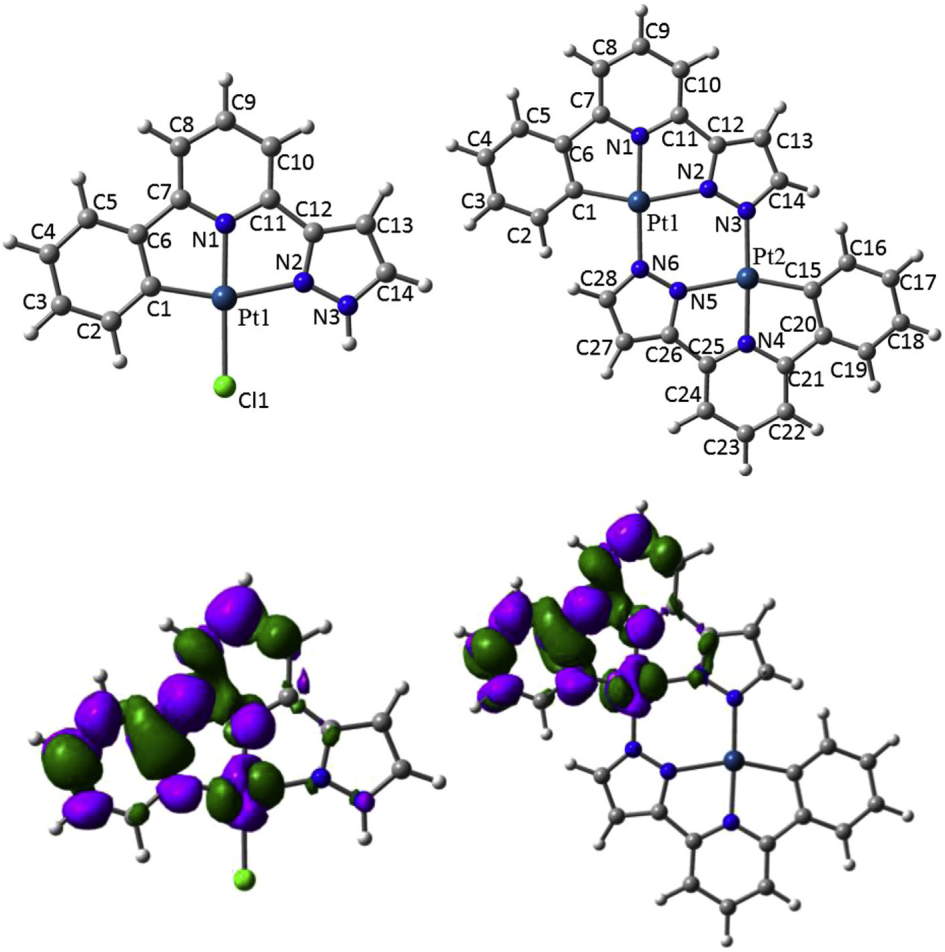

Figure 1.35: Top: ground state optimised geometries of the complexes studied by Kataoka et al.[108] *Bottom: density difference plots for the $S_0 \rightarrow T_1$ excitation at the T_1 geometry. Purple and green zones show increase and decrease of electron density respectively.*[108]

1.9.3 Estimating distortion

Monkman and coworkers made and studied a series of Pt(II) complexes with one bidentate, N^C-coordinated ligand and the other two coordination sites filled either by an acetylacetonate ligand or one chloride and one sulfoxide group.[173] Two examples are shown in Figure 1.36, both of which showed almost negligible emission in solution at room temperature, and the group employed DFT and TD-DFT techniques in an attempt to understand why.

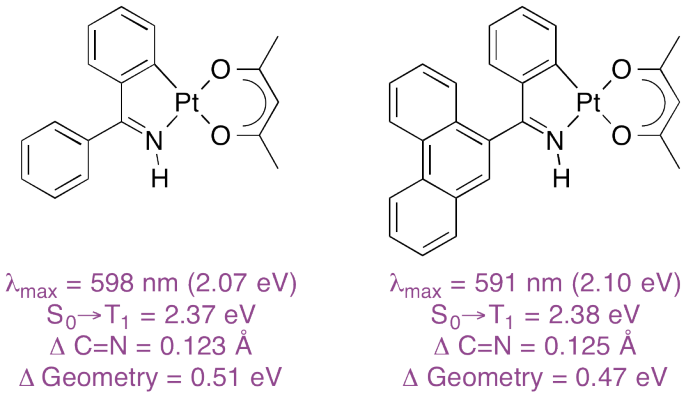

Figure 1.36: Structures and properties of the complexes studied by Monkman and coworkers. λ_{max} represents the experimentally measured emission in DCM at 298 K, $S_0 \rightarrow T_1$ the calculated excitation at the ground state geometry, Δ C=N the change in C=N bond length between the S_0 and T_1 geometries and Δ Geometry the difference between the energy of the ground state geometry (S_0) and the single point singlet calculation at the triplet geometry (T_1).[173]

For both compounds shown in Figure 1.36 they observed that the $S_0 \rightarrow T_1$ excitation calculated at the S_0 and T_1 geometries gave very different excitation energies from those observed experimentally, suggesting that the T_1 excited state geometries were very different from the ground state geometries for these compounds. Optimisation of the T_1 excited state geometry revealed that elongation of the C=N bond occurs in the excited state compared to the ground state geometry. They also observed that single point singlet calculations at the T_1 geometry gave reasonably different SCF energies from the ground state geometries, illustrating the difference between the two geometries and concluded that the combination of all these results show significant excited state distortion leading to non-radiative decay.

Though a helpful analysis, widespread application of this technique should be approached with caution since it relies heavily on small differences in computed energies. We have already seen that these can suffer in the triplet state from instabilities. Inherent errors in DFT and TD-DFT also mean that an error of at least 0.3 eV[115;116;139;141;174–179] is present in most calculations so that over-interpretation of calculated values is not advised.

1.10 Objectives

This brief review has highlighted the wide variety of luminescent platinum complexes present in the literature and various techniques for enhancing certain photophysical properties. By careful ligand design, compounds can be tailored to absorb and emit over a wide range of wavelengths. Different efficiencies of emission can also be achieved, from complexes which do not emit at room temperature to those with extremely high quantum yields. While much of this ligand design is systematic, for example increased rigidity leads to slower rates of non-radiative decay, often the results can be unexpected.

DFT and TD-DFT have been shown to be useful tools in both predicting and rationalising certain photophysical properties of these types of complexes. The theory is utilised by many groups but often using different techniques. Detailed calculations analysing the theory itself are often performed on small molecule systems so that it is difficult then to get an idea of the accuracy of different methods.

This project presents a combined theoretical and experimental approach to a better understanding of the accuracy and application of DFT in predicting and rationalising the excited state behaviour of platinum complexes, particularly luminescent efficiencies. Conversely, it is also concerned with further investigating the experimental properties of platinum derivatives and the effect of ligand manipulation on their excited state properties.

2

Pt(II) and Pt(IV) complexes of ligands based on 1,3-dipyridylbenzene

2.1 Chapter outline

In this chapter, the photophysical properties of a series of N^C^N-coordinated Pt(II) complexes will be discussed. Williams and coworkers reported the synthesis and photophysical properties of terdentate Pt(II) complexes, cyclometallated at the C-2 position of the benzene ring, of the form shown in Figure 2.1. These complexes exhibited unusually high quantum yields of luminescence, the parent complex (R and R′ = H) with a quantum yield of 0.60 in degassed dichloromethane.[52] The group also showed how alteration of substituents at R and R′ could be used to tune the wavelength of emission, reporting a series of cyclometallated complexes of this form with a wide-ranging wavelength of emission.[17]

The complexes (shown in Figure 2.2) were originally prepared and their photophysical properties studied by a previous member of the group, Lisa Murphy.[180] Some examples and other new derivatives discussed in later chapters were prepared during this work, the synthesis of which is closely related so will be discussed together here. PtL$^{1-4}$Cl and PtLF$^{1-4}$Cl, made by Lisa Murphy

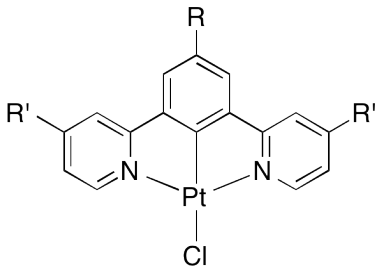

Figure 2.1: General structure of the N^C^N-coordinated Pt(II) complexes.

(Figure 2.2) provide two series of closely related compounds where absorption and emission differ subtly as the position of a methyl group is shifted round the pyridine rings. They will be used to consider the accuracy of the standard procedures which are generally employed for the prediction of these properties for phosphorescent compounds.

The experimentally obtained photophysical results will first be outlined, before consideration of the ability of TD-DFT to replicate the trends observed. This chapter is predominantly concerned with the calculation of absorption energies. They will be discussed in detail, considering methods of convolution, and various mathematical parameters such as basis set, choice of functional and modelling of solvent. The ability of TD-DFT to replicate the phosphorescent emission energies of the compounds will then briefly be discussed along with an excursus on the relative difficulties and accuracies of such calculations.

Alongside discussion of the synthesis of the Pt(II) complexes we will also describe the synthesis of some closely related Pt(IV) compounds. The properties of the Pt(IV) analogues will be returned to towards the end of the chapter when their stability (with regard to decomposition) under various conditions will be investigated. The experimentally obtained photophysical properties of the Pt(IV) compounds will then be discussed and, finally, using the same techniques as developed for the Pt(II) compounds, the ability of DFT to model their absorption properties, relative both to one another, and to their reduced platinum(II) analogues, will be considered.

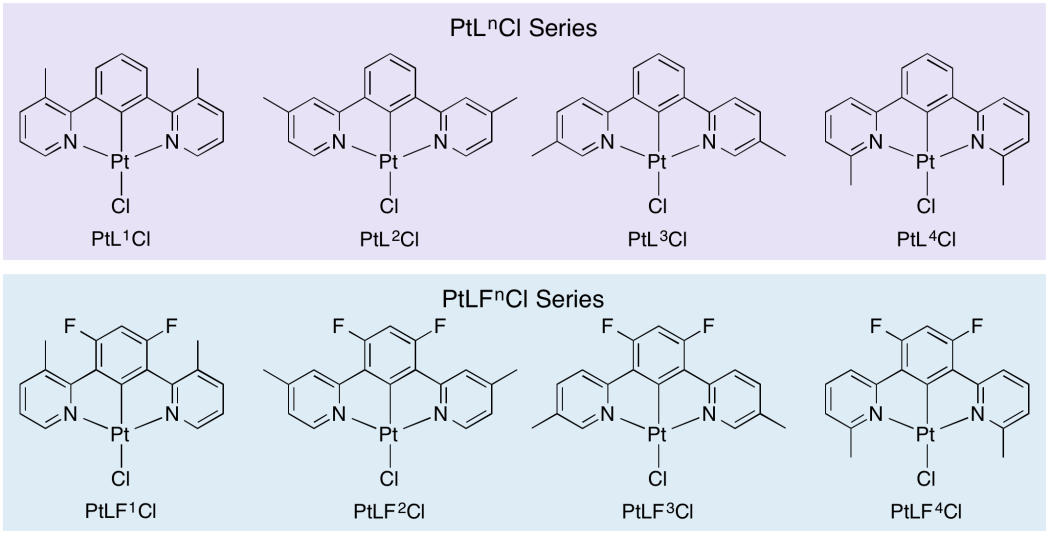

Figure 2.2: The chemical structures of the two series of complexes studied.

2.2 Synthesis

The eight previously made platinum(II) complexes, for which we will consider the modelling of absorption spectra in this chapter, are shown in Figure 2.2. The compounds can be divided into two sets of four: those with a fluorine atom at the 3 and 5 positions on the benzene ring, PtLF^{n}Cl, and those without, PtL^{n}Cl. This conveniently provides two sets of very closely related complexes for analysis by TD-DFT.

2.2.1 Ligand synthesis

Stille cross-coupling

Ligands HL^1 and HLF$^{1-4}$ (Figure 2.3) were synthesised via the Stille cross-coupling reaction.[180] First, pyridyl stannane precursors were made via a two-step process (as shown in Scheme 2.1) by lithiation at the 2-pyridyl position, followed by nucleophilic substitution with Bu_3SnCl. With one exception (*vide infra*), 2-bromo substituted pyridines were directly lithiated by mixing with *n*-BuLi, at 0 °C, to give exchange of the bromine for lithium.[181] In the case of HLF^2 however, the lithiated pyridine was formed directly from

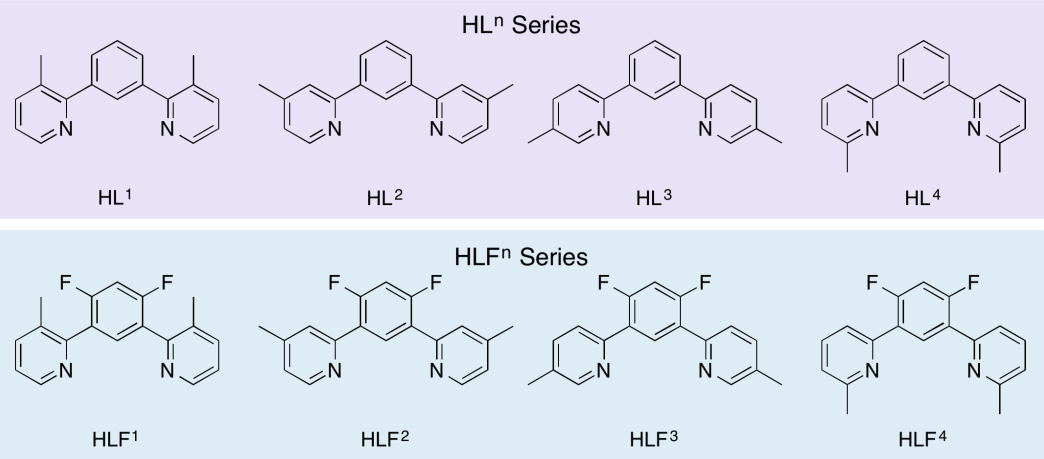

Figure 2.3: The chemical structures of the two series of ligands studied.

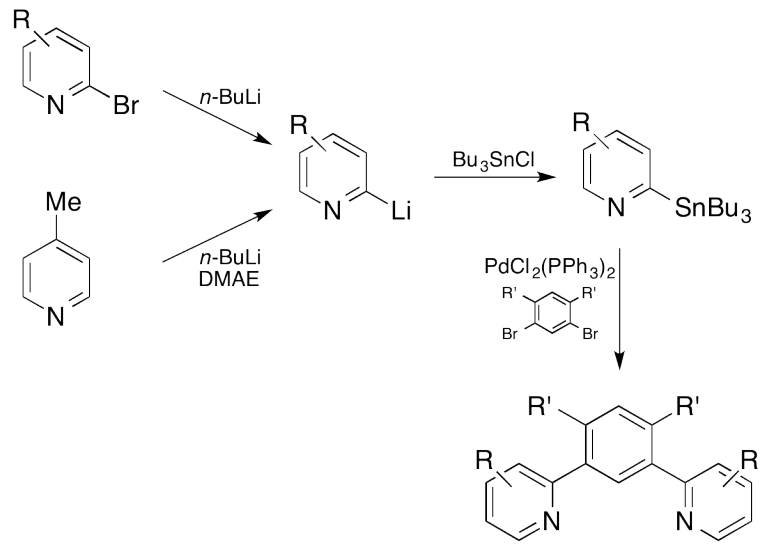

Scheme 2.1: Schematic representation of the ligand formation using Stille cross-coupling. R represents a methyl group at each of the positions 3-6 around the pyridine ring and R′ represents either a fluorine or hydrogen atom. DMAE = dimethylaminoethanol.

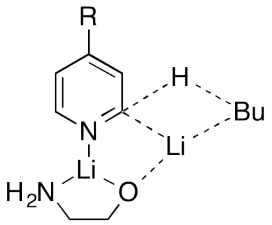

Figure 2.4: Mixed lithium aggregate intermediate

4-methylpyridine, instead of the 2-bromo analogue, according to a route developed by Kaminski *et al.*,[182] where *n*-BuLi was first mixed with dimethylaminoethanol (DMAE), in dry hexane, before addition of the 4-functionalised pyridine molecule. Upon addition, a mixed lithium aggregate intermediate is formed (Figure 2.4). The increased acidity of the proton at the position *ortho* to the nitrogen, combined with proximity within the aggregate, leads to selective *ortho* lithiation. It should be noted, however, that this method is only reliably selective for 4-substituted pyridines since its use where there is substitution at other positions in the ring would lead to a mixture of isomers.

Once the lithiated product was obtained, it was converted to the stannane analogue by mixture with tributyltin chloride. Since the stannanes were found to partly decompose during column chromatography, they were used without purification, and an estimate of conversion of the reactants to products was taken from the ^{1}H NMR spectrum (by comparing integrals of the aromatic region of the spectrum with the integrals of the aliphatic region).

The crude stannane was next coupled to 1,3-dibromobenzene, using the bis-(triphenylphosphine)palladium(II) chloride catalyst under inert conditions which gave, after purification by column chromatography, the pure ligand.

Suzuki-Miyaura cross-coupling

Ligands HL^3 and HL^4 (Figure 2.3) were synthesised in the same project via the Suzuki-Miyaura cross-coupling reaction (Scheme 2.2), using Na_2CO_3 as a base and a dimethoxyethane/water (1:1) solvent system, in the presence of a

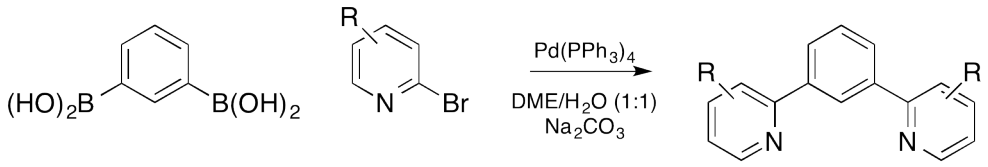

Scheme 2.2: Schematic representation of the ligand formation using Suzuki-Miyaura cross-coupling. R represents a methyl group at positions 5 or 6 of the pyridine ring.

$Pd(PPh_3)_4$ catalyst. The solvent, base and ligand precursors were degassed using the freeze-pump-thaw methodology and placed under an atmosphere of nitrogen, before addition of the catalyst. The mixture was then heated under nitrogen, at 85 °C, for two days before purification by column chromatography. Ligands HL^6 and HL^7 were also made using the Suzuki-Miyaura cross-coupling reaction, according to literature procedures.

During the present work, the unsubstituted ligand HL^5 was synthesised by two different methods: conventionally for this ligand, by a Stille cross-coupling reaction (discussed in Section 2.2.1) and also using a Suzuki-Miyaura cross-coupling reaction. The use of 1,3-benzene-diboronic acid to prepare HL^1 by a Suzuki-Miyaura reaction has not previously been reported, despite the potential benefits such a method would offer over the Stille cross-coupling (e.g. innocuous side-products and a one-step reaction). We found that the compound could indeed be prepared by such a method, in the one-step process outlined in Scheme 2.2 (more details are given in Chapter 8). The identity of the ligand, formed by both techniques, was confirmed by ^{1}H NMR spectroscopy, which was in good agreement with literature values for this well reported compound. Indeed, aside from the obvious benefits afforded by the use of a one-step reaction (compared to the three steps required by Stille), the avoidance of toxic heterocyclic stannane reagents, and undesirable reactants such as butyl lithium, we found that the yield obtained in the case of the Suzuki-Miyaura method (70%) was significantly higher than that obtained by the Stille (55%).

2.2.2 Cyclometallation of ligands to give Pt(II) complexes

Two methods were used for cyclometallation of the ligands to give platinum(II) complexes (Scheme 2.3). The first involved reaction of the ligand with K_2PtCl_4, in either acetic acid or a mixture of MeCN and H_2O (3:1) at reflux under nitrogen. Purification was then achieved by isolating the precipitated solid, using centrifugation, and washing it with various solvents, before extraction into DCM.

Microwave cyclometallation was achieved in a reaction analogous to the one described by Wang *et al.*,[183] using a mixture of acetic acid and water (9:1) as the solvent, at a much higher concentration, for just thirty minutes. The use of the microwave allowed higher temperatures of reaction than the boiling point of the solvent (in this case 160 °C) which, combined with the increased concentration of the reactants in solution, is thought to be the reason for the elevated rate of reaction. We found an even higher yield than Wang *et al.* (91% compared to 80%), perhaps due to the degassing of the reaction mixture, in our case, leading to less decomposition. This technique was also used for the first time to generate PtL^5Br by reaction of the ligand with K_2PtBr_4. This method led to improved yields at the same time as decreasing reaction times. It was also used for complexes PtL^6Cl and PtL^7Cl, with similar results.

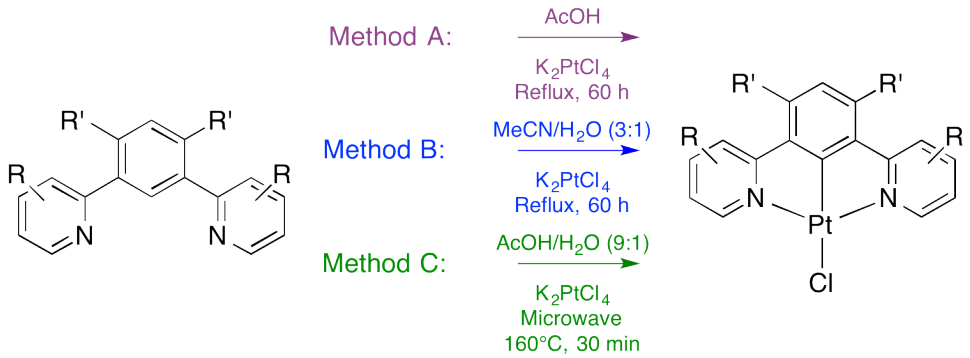

Scheme 2.3: Schematic representation of the three methods used for cyclometallation of the ligand. R represents a methyl group at each of the positions 3-6 of the pyridine ring and R′ represents either a fluorine or hydrogen atom.

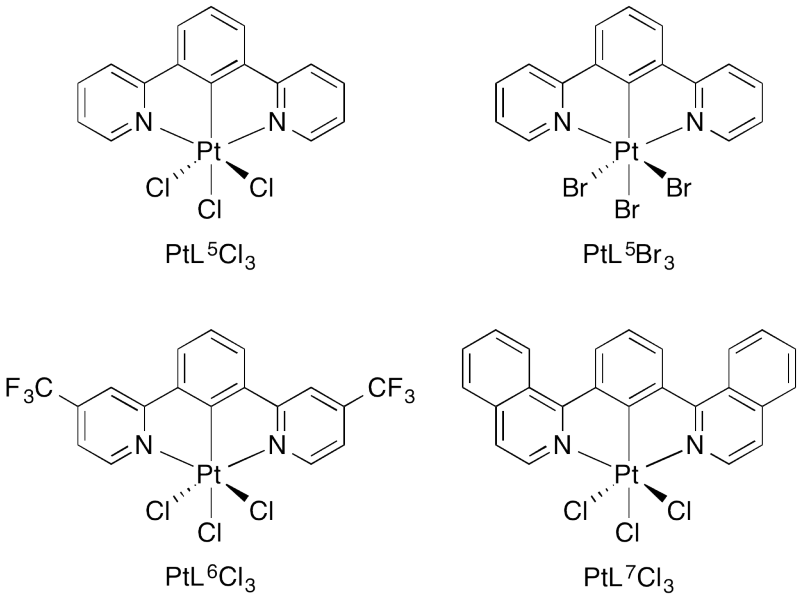

Figure 2.5: Molecular structures of the four tri-halogenated Pt(IV) complexes synthesised.

2.2.3 Oxidation of Pt(II) to Pt(IV)

While this study is primarily concerned with the synthesis and study of Pt(II) complexes, it was decided to investigate their oxidised derivatives too: N^C^N-coordinated Pt(IV) complexes. Since these compounds are isoelectronic with their Ir(III) analogues, which have been shown to be highly emissive, it is interesting to see what the phosphorescent properties of these previously investigated Pt(IV) complexes are. A brief excursus will follow on the synthesis and characterisation of the compounds made of this type.

Synthesis of tri-halogenated platinum(IV) complexes

Initially, oxidation of the Pt(II) species was attempted by reaction with copper(II) chloride.[184] $CuCl_2$ and the Pt(II) complex were added to a mixture of methanol and DCM (1:1), and stirred at room temperature for 24 h. CuCl was then removed by filtration and the product purified from the solvent mixture. Although this procedure was successful, there was not a complete conversion of reactants to products so it was decided to use a procedure that had been previously developed in the group.

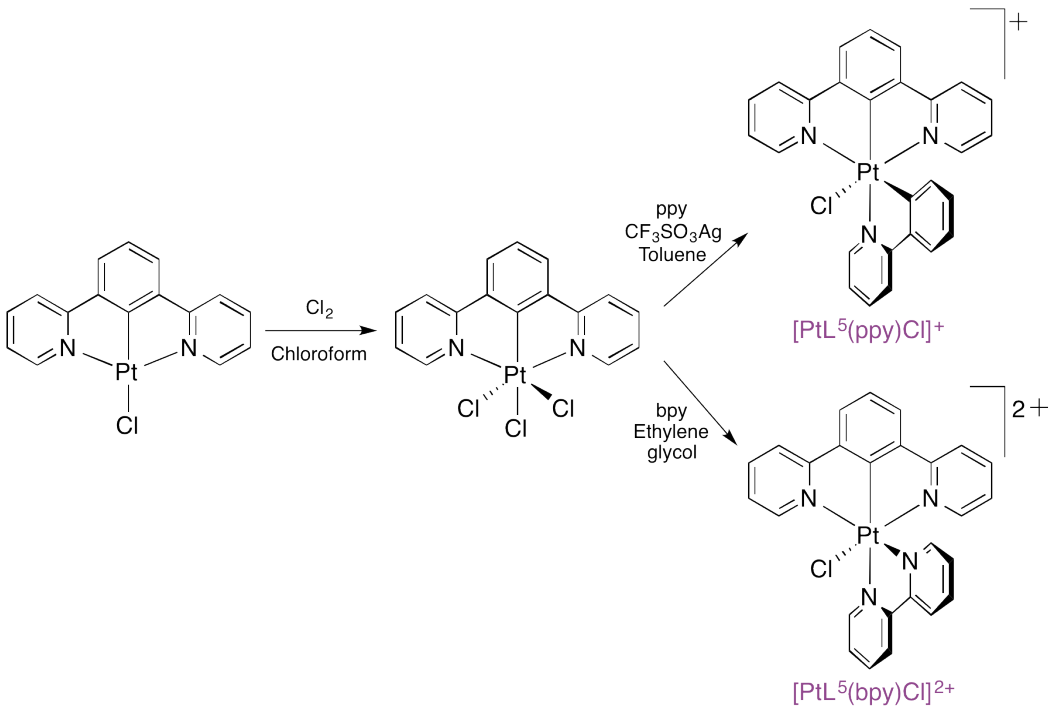

Scheme 2.4: Synthetic pathway to Pt(IV) complexes.

According to a procedure developed by Lisa Murphy [180] for five related N^C^N-coordinated Pt(II) complexes, three new tri-chloro Pt(IV) complexes were synthesised. The oxidation was achieved by taking up the Pt(II) complex in a small volume of chloroform and bubbling chlorine gas through the solution for 30 minutes, with the exclusion of light. The solution became paler in colour after just a couple of minutes, indicating that oxidation had taken place, though chlorine was added for some time afterwards to try to ensure complete conversion. The solvent was removed quickly under reduced pressure since decomposition of the product was observed in solution in the presence of light (see Section 2.5.2). In each case the Pt(IV) complex was obtained as a powder, paler in colour than its Pt(II) analogue.

In an attempt to find less harsh (and experimentally demanding) methods for oxidation of Pt(II), bromine and iodine were investigated as potential oxidising agents. A similar technique as for Cl_2 was used for the oxidation,

using PtL^5X as the test species. In each case the halogen, X_2, was added in large excess to the respective halide-substituted PtL^5X complex, in a solution of chloroform. The mixture was then stirred with the exclusion of light for various amounts of time (in the case of Br_2 it was found that the reaction had proceeded after 24 h). The product precipitated from solution and could therefore be easily obtained by centrifugation and subsequent washings. As expected, oxidation by bromine was slower and there were traces of PtL^5Br in the product (either due to decomposition or incomplete conversion) whilst there was little evidence of a reaction occurring with I_2 (even after 72 h).

The PtL^nCl_3 products appeared pure by ^{1}H NMR and mass spectrometry but upon photophysical analysis, traces of the Pt(II) complex were seen in the emission spectrum. Since these compounds are so emissive compared to their Pt(IV) analogues, only a tiny amount of the starting material would need to be present to dominate the entire emission spectrum. It is thought that the compounds readily decompose, probably to something similar to the Pt(II) starting material, upon irradiation with light. This will be further discussed in Section 2.5.2.

Synthesis of other platinum(IV) complexes

Von Zelewsky et al. showed that reaction of some Pt(II) complexes with an alkyl halide (as both reactant and solvent) oxidised the Pt(II) compound to give the Pt(IV) product (with the halide and alkyl group as the two new ligands).[185] Unfortunately, attempts at synthesis of Pt(IV) complexes containing a tridentate ligand and one monodentate ligand according to this method, shown in Scheme 2.5, gave only a mixture of starting materials and decomposition products (after 2 h heating at 60 °C).

Newman *et al.* showed that a similar reaction proceeded by first oxidation and then cyclometallation[186] (Scheme 2.6) so the compound will be first oxidised (since we know that this can be done cleanly and to completion); and then the bidentate ligand coordinated, rather than the one-step oxidation and coordination employed by Jenkins and Bernhard (Scheme 2.6).[187] We synthe-

sised two N^C^N-coordinated Pt(IV) complexes from PtL^5Cl_3: one with a cyclometallated bidentate ligand, $[PtL^5(ppy)Cl]^+$ formed upon reaction with ppyH, and one with two coordinating pyridine rings, $[PtL^5(bpy)Cl]^{2+}$ from reaction with bpy (Scheme 2.4). Both reactions were conducted with the exclusion of light to prevent decomposition (see Section 2.5.2).

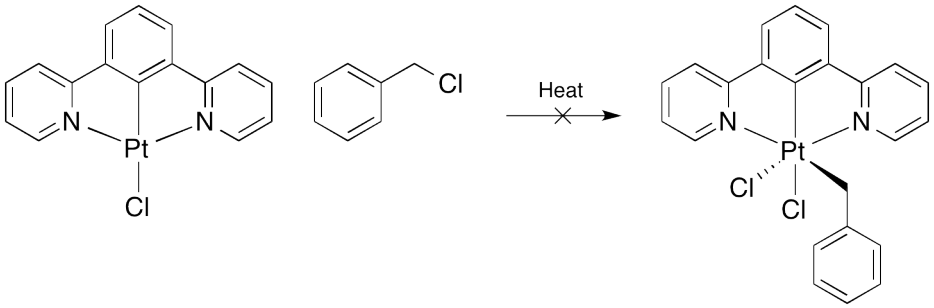

Scheme 2.5: Attempted preparation of a Pt(IV) complex using benzyl chloride.

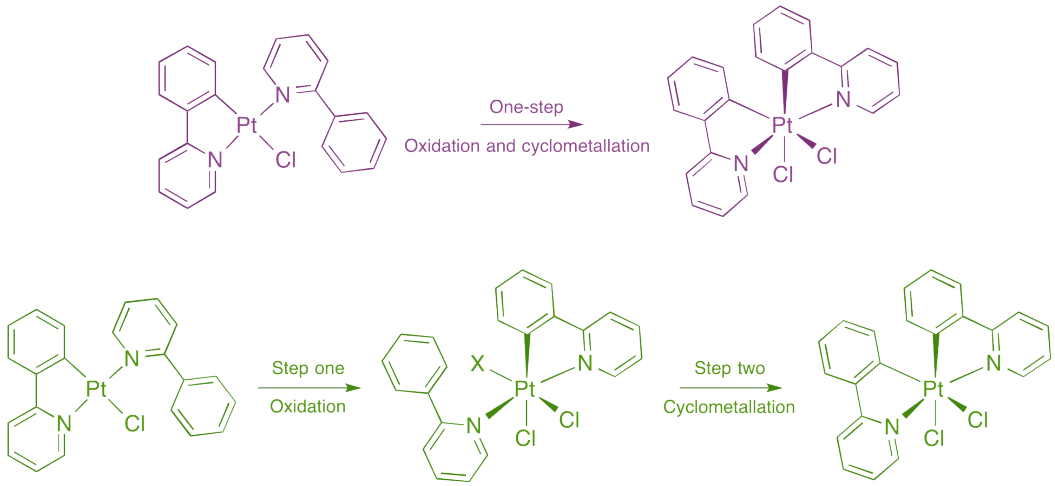

Scheme 2.6: The two routes used for synthesis of Pt(IV) complexes. The one-step reaction used by Jenkins and Bernhard (top) is shown in purple and the two-step oxidation and cyclometallation employed by Newman et al. (bottom) in green.

For the ppy complex, $[PtL^5(ppy)Cl]^+$, silver trifluoromethanesulfonate was added as a chloride scavenger to help drive the reaction. The pure product was obtained by changing the counter ion from triflate to Cl^- to improve

the solubility of the complex in water, allowing impurities to be removed by washing the solution with DCM. Changing the counter ion back to PF_6^- then allowed washing with water. Use of acetonitrile during the preparation and manipulation of this compound was necessarily avoided since it is a potentially coordinating solvent. Unlike its precursor, once formed, this complex appeared to be stable with respect to light and showed no traces of the Pt(II) compound by NMR, mass spectrometry and even emission spectroscopy.

The bpy-substituted complex proved to be more complicated to synthesise than its cyclometallated analogue. While it was found that the use of the chloride scavenger was unnecessary for formation of the product, initial attempts at synthesis in a mixture of polar, protic solvents (MeCN:H_2O 3:1), with an excess of bpy, heated at reflux for 48 h, showed no appreciable formation of product, merely a red solid containing the bipyridine. We were concerned about the ability of the acetonitrile molecule to bind to the platinum so the solvent was changed to ethylene glycol (which also enabled higher reaction temperatures). When heated at reflux for 12 h, a dark red solution was obtained which, once purified by conversion to the PF_6^- salt, yielded a red product which included a mixture of bipyridine, Pt(II) starting material and the desired Pt(IV) product. Finally it was found that gradual heating (as described in Chapter 8) discouraged the entropically favoured production of Pt(II) starting material. Purification was achieved by taking the reaction mixture and purifying immediately using HPLC. This gave a white powder whose NMR spectrum was consistent with the desired Pt(IV) product − we are unsure as to the origin of the deep red impurity. All of these reactions were performed under nitrogen with the exclusion of light wherever possible.

In a proof-of-principle reaction, it was shown possible to alter the ancillary Cl^- ligand on $[PtL^5(ppy)Cl]^+$ for 1-ethynyl-3,5-bis(trifluoromethyl)benzene. Initially, a mixture of methanol and acetone, 7:1, was used, the acetone to improve the solubility of the complex. The complex was taken up in the solvent with sodium hydroxide and the acetylide and stirred for 19 h. Under these conditions no reaction occurred. Upon addition of a catalytic amount of copper iodide, however, with a further 2 h stirring at room temperature, some

formation of product was shown to occur by mass spectrometry. We therefore postulate that with longer reaction times and possibly a higher temperature of reaction, a greater yield could be obtained.

Characterisation of platinum(IV) complexes

Oxidation of PtL^5Cl to PtL^5Cl_3 resulted in deshielding and a consequent downfield shift of signals in the proton NMR spectrum (Figures 2.6 and 2.7). The heteronuclear coupling constand between ^{195}Pt and H^6 in the ligand was also reduced. This proton is shifted further downfield on moving from PtL^5Cl_3 to PtL^5Cl_3 (9.54 and 9.72 ppm respectively, Figure 2.8). This mirrors the behaviour of their Pt(II) analogues, PtL^5Cl and PtL^5Br, which have shifts of 9.34 and 9.56 ppm respectively. Both Pt(IV) compounds are deshielded relative to their Pt(II) counterparts. A HRMS spectrum was obtained of PtL^5Cl_3, with a peak corresponding to the mono-cation (after removal of one Cl^- ion), confirming the identity of this compound and in keeping with previously reported data.[180]

Substitution of two chloride ions by either bpy or ppy results in an upfield shift of the proton at the 6-position of the pyridine ring (on the tridentate ligand), the effect of which is greater in the cyclometallated bidentate ligand (7.95 ppm) than for bpy (8.36 ppm). There is also a change in shift of the cyclometallated carbon atom of the N^C^N ligand upfield from the Pt(II) compound (160.7 ppm for $[PtL^5(ppy)Cl]^+$, 154.0 ppm for $[PtL^5(bpy)Cl]^{2+}$, compared to 161.8 ppm for PtL^5Cl). Both these compounds display the expected added protons from the bidentate ligand, upfield of the N^C^N protons. Only one isomer of $[PtL^5(ppy)Cl]^+$ was observed: that with the nitrogen atom of the bidentate ligand *trans* to the carbon atom of the tridentate ligand. Assignment of this isomer was achieved by comparison of the NMR spectrum with that of an iridium analogue where a NOSEY spectrum had been obtained[188] and also by consideration of the crystal structure (*vide infra*). Formation of this isomer uniquely is presumably due to the unfavourable *trans* disposition of the two cyclometallated carbon atoms in the other isomer. Analysis by mass spectrometry of $[PtL^5(bpy)Cl]^{2+}$ showed peaks for both the +1 and +2 fragments

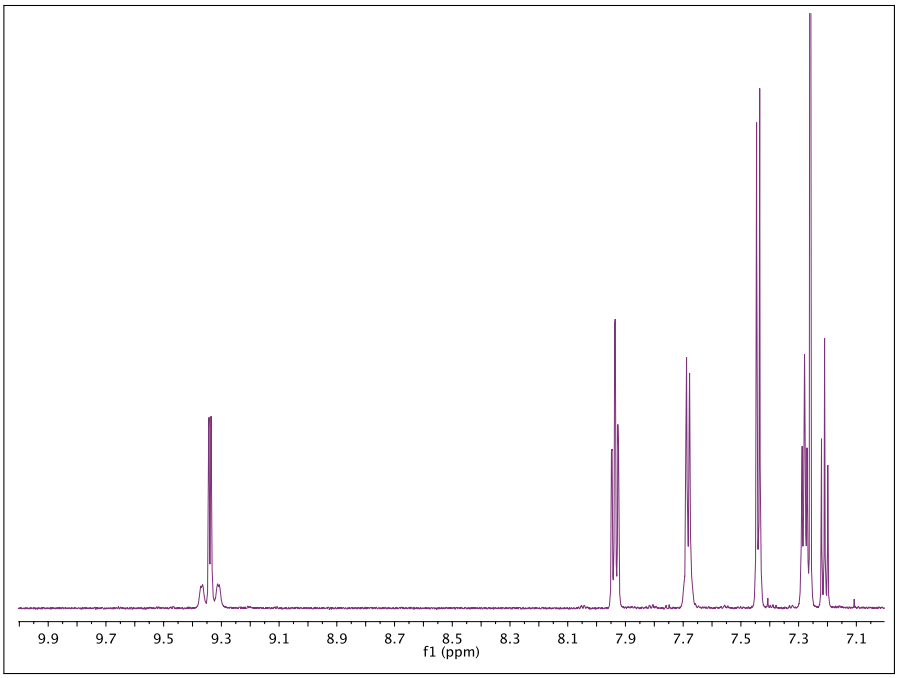

Figure 2.6: ^{1}H NMR spectrum of the aromatic region of $PtL^{5}Cl$ in $CDCl_3$, at 700 MHz NMR.

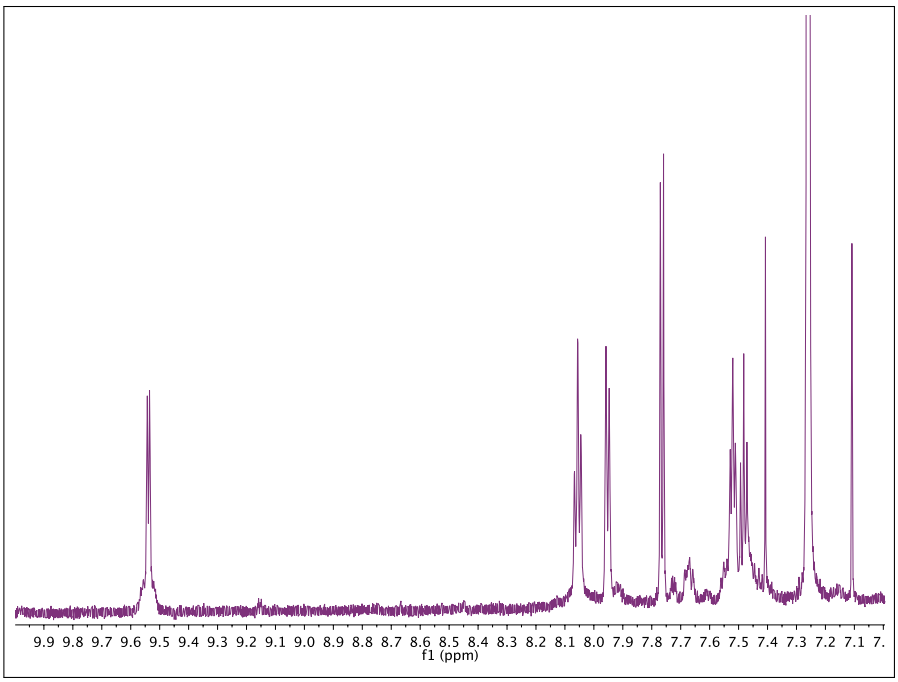

Figure 2.7: ^{1}H NMR spectrum of the aromatic region of $PtL^{5}Cl_3$ in $CDCl_3$, at 700 MHz.

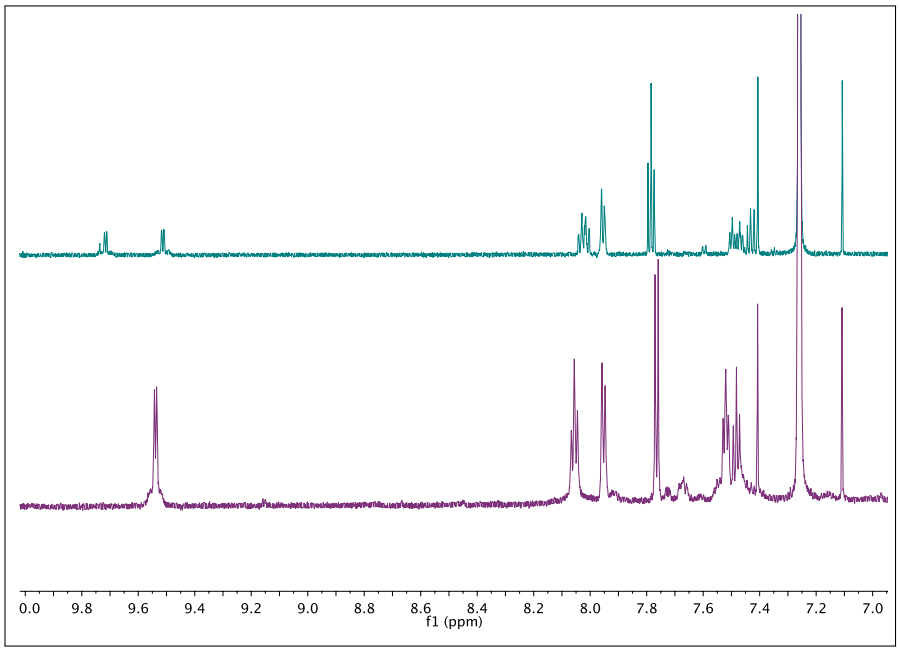

Figure 2.8: ^1H NMR spectrum of the aromatic region of PtL^5Br_3 (top) and PtL^5Cl_3 (bottom), both in $CDCl_3$ and run with a 700 MHz NMR spectrometer. PtL^5Br_3 could not be formed without a large amount of the starting material, PtL^5Br remaining which is also present in the spectrum.

according to whether the compound had either one or no counter ions present.

Small crystals of $[PtL^5(ppy)Cl]^+$ and $[PtL^5(bpy)Cl]^{2+}$ were obtained by slow evaporation from acetone and their molecular structure determined by X-ray diffraction, the structures of which are shown in Figures 2.9 and 2.10 respectively. The geometries are distorted octahedral and a summary of the important bond lengths and angles about platinum can be seen in Table 2.1. Each carbon atom is *trans* to a nitrogen rather than to another carbon in $[PtL^5(ppy)Cl]^+$ to reduce the unfavourable trans interaction of the two carbon atoms. The Pt−Cl bond is longer for the ppy-substituted complex than for bpy, and much more like that of the Pt(II) complex, PtL^5Cl which has a Pt−Cl bond length of 2.417(2) Å and a Cl also *trans* to a carbon atom.[51] Both complexes display a Pt−Cl bond which is shorter and more like Pt(II) than two related (though substituted) N^C^N and N^C-coordinated Ir(III) complexes (which have bonds of 2.462(2) and 2.469(1) Å in length).[189] The Pt-C

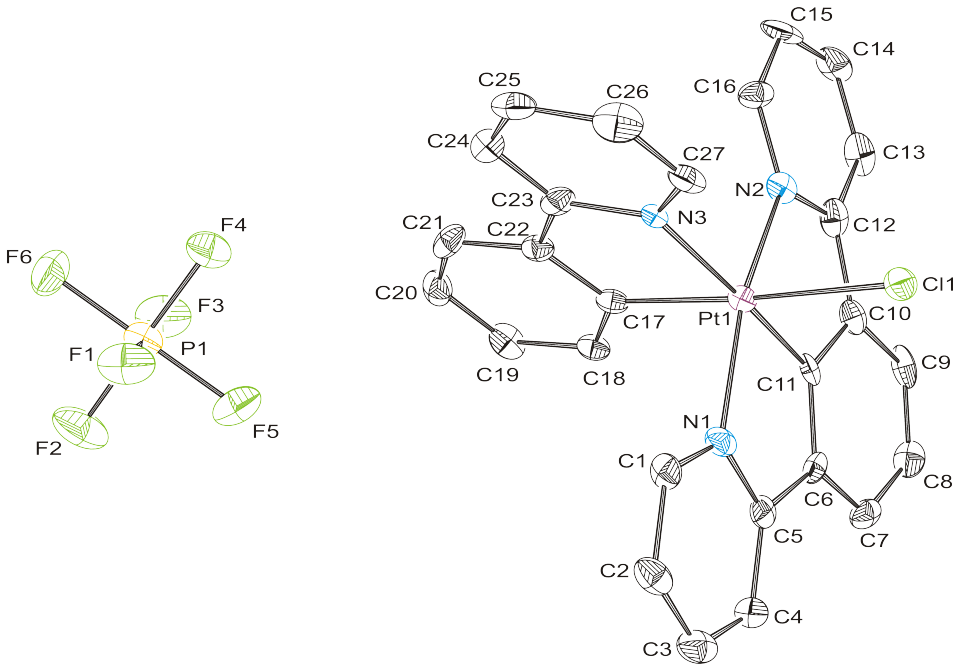

Figure 2.9: Crystal structure of $[PtL^5(ppy)Cl][PF_6]$ *from acetone*

bond of the N^C^N ligand is elongated in both these structures compared to the Pt(II) complex which is 1.907(8) Å, and is slightly longer in the bpy analogue compared to the ppy. The elongation of this bond is presumably to reduce steric interactions, which are introduced upon oxidation of Pt(II), since there are more groups attached to the platinum centre. The N−Pt−N angle is roughly the same between all three complexes (PtL^5Cl angle 161.1(2)°). To our knowledge there is no Ir(III) complex in the literature for comparison with the bpy Pt(IV) compound.

Comparison of these new Pt(IV) structures with those of PtL^5Cl_3 (which has Pt−C and Pt−Cl bond lengths of 1.945(4) and 2.3189(10), 2.3195(10) and 2.4457(11) Å respectively)[180] shows little change of the Pt−C bond length for $[PtL^5(ppy)Cl]^+$ and a slight elongation in $[PtL^5(bpy)Cl]^{2+}$. The Pt−Cl bond is slightly longer in $[PtL^5(ppy)Cl]^+$ than $[PtL^5(bpy)Cl]^{2+}$ since it is *trans* to the Pt−C bond in the former. The Pt−Cl bond lenth increases in the order:

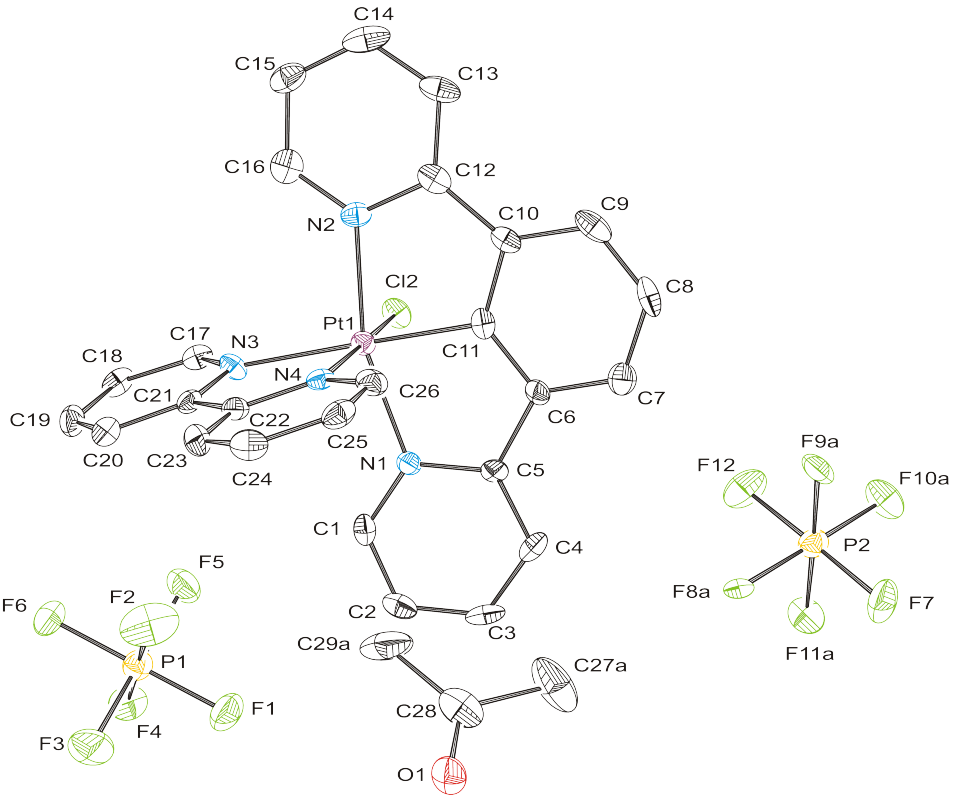

Figure 2.10: Crystal structure of $[PtL^5(bpy)Cl][PF_6]_2$ *from acetone*

$$[\mathbf{PtL^5(bpy)Cl}]^{2+} < \underset{\textbf{(Cl } \textit{trans} \textbf{ to Pt}-\textbf{N)}}{\mathbf{PtL^5Cl_3}} < [\mathbf{PtL^5(ppy)Cl}]^{+} < \underset{\textbf{(Cl } \textit{trans} \textbf{ to Pt}-\textbf{C)}}{\mathbf{PtL^5Cl_3}}$$

It can be seen from Table 2.1 that the Pt−C and Pt−N bonds are longer on the ppy ligand than the N^C^N ligand. This is probably due to proximity of the tridentate ligand to the Pt atom, allowing close bonding of three atoms, while if the ppy is close this is only advantageous to two bonding atoms. Steric interactions prevent both ligands from being close in space to the Pt at once.

	$[PtL^5(ppy)Cl]^+$	$[PtL^5(bpy)Cl]^{2+}$
Bond lengths:		
Pt–N	2.0450, 2.0533	2.0558(1), 2.0585(1)
Pt–C	1.9410	1.9668(1)
Pt–N	2.1335	2.0361(1), 2.1476(1)
Pt–C	2.0218(1)	–
Pt–Cl	2.4186(1)	2.3038(1)
Bond angles:		
N–Pt–N	161.05	161.76
N–Pt–C	80.69 80.47	80.61 81.16
N–Pt–Cl	90.75 91.14	90.26 90.10
N–Pt–N	99.20 99.49	99.02, 88.16, 99.11, 93.22
N–Pt–C	90.82 89.27	–
C–Pt–N	176.80	175.96 96.61
C–Pt–C	96.45	–
C–Pt–Cl	89.59	88.87
N–Pt–N	–	79.36
N–Pt–C	80.36	–
N–Pt–Cl	93.61	95.16 173.98
C–Pt–Cl	173.94	–

Table 2.1: Selected bond lengths (Å) and bond angles (°) found for the Pt(IV) crystal structures. Purple text indicates atoms bound from the N^C^N ligand while green text shows atoms from the bpy or ppy ligand.

2.3 Photophysical properties of Pt(II) complexes

2.3.1 Absorption properties of PtL^nCl and $PtLF^nCl$

The experimental UV-vis absorption spectra of $PtL^{1-4}Cl$ and $PtLF^{1-4}Cl$ in DCM are shown in Figure 2.11. It can be seen that the non-fluorinated complexes absorb at a lower energy than their fluorinated counterparts and that there is a well-defined band at about 340 nm in the former group with no obvious corresponding band in the latter. It was also reported that the $PtL^{1-4}Cl$ series display a formally forbidden S→T transition although these bands were shown to be very weak due to their formally forbidden nature (Table 2.2).

Figure 2.12 shows the UV-vis absorption spectra of PtL^3Cl and $PtLF^3Cl$ in various different solvents. It can be seen that both display negative solvatochromism in the lowest energy $S_0 \rightarrow S_n$ absorption band.

2.3.2 Emission properties of PtL^nCl and $PtLF^nCl$

The wavelengths of emission of the $PtL^{1-4}Cl$ and $PtLF^{1-4}Cl$ complexes are shown in Table 2.3. The $PtLF^{1-4}Cl$ series all emit at a higher energy than their non-fluorinated counterparts.

2.4 TD-DFT studies of Pt(II) complexes

2.4.1 Simulated absorption spectra of Pt(II) complexes

In this section we will discuss, in some depth, the ability of DFT to predict the absorptive properties of the two series of complexes: $PtL^{1-4}Cl$ and $PtLF^{1-4}Cl$. Simulation of these properties has been investigated for similar compounds by other groups.[190;191] In many ways, the prediction of the absorption of light by a compound is much more straightforward than calculation of the emissive properties, some of the complexities of which will be discussed in later chapters. One of the complications attributable to absorption, but not emission, however, is that for excitation of the ground state molecule to a singlet excited state, any one of a large number of singlet excited states can

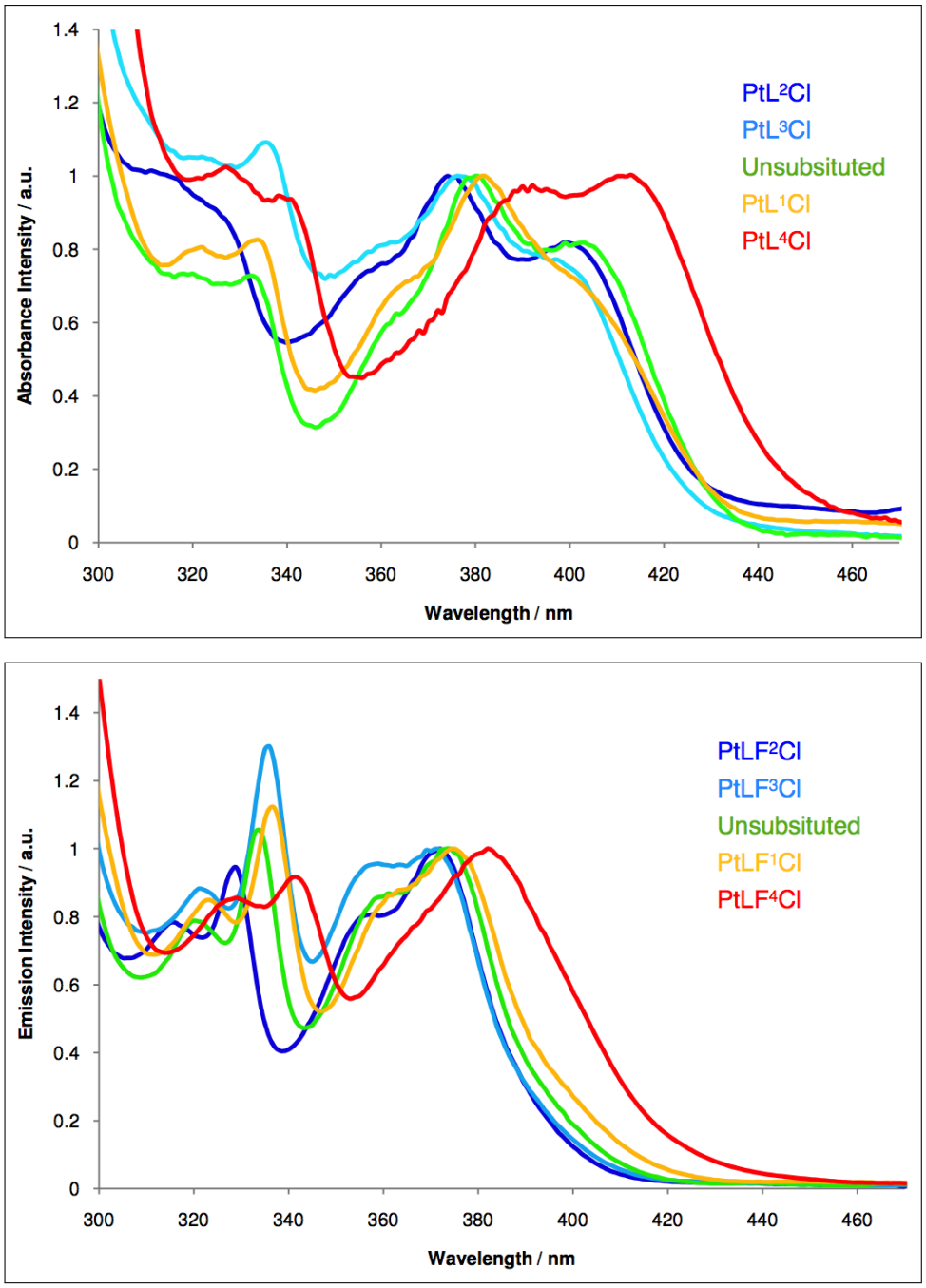

Figure 2.11: Normalised UV-vis absorption spectra of PtL^{n}Cl (top) and PtLF^{n}Cl (bottom) series in DCM at 298 K. The intensity of the absorption band at ~380 nm is normalised for ease of comparison. The unsubstituted complex (shown in green) represents the Pt(II) complex in each case with no methyl groups. Figures taken from Lisa Murphy's thesis.[180]

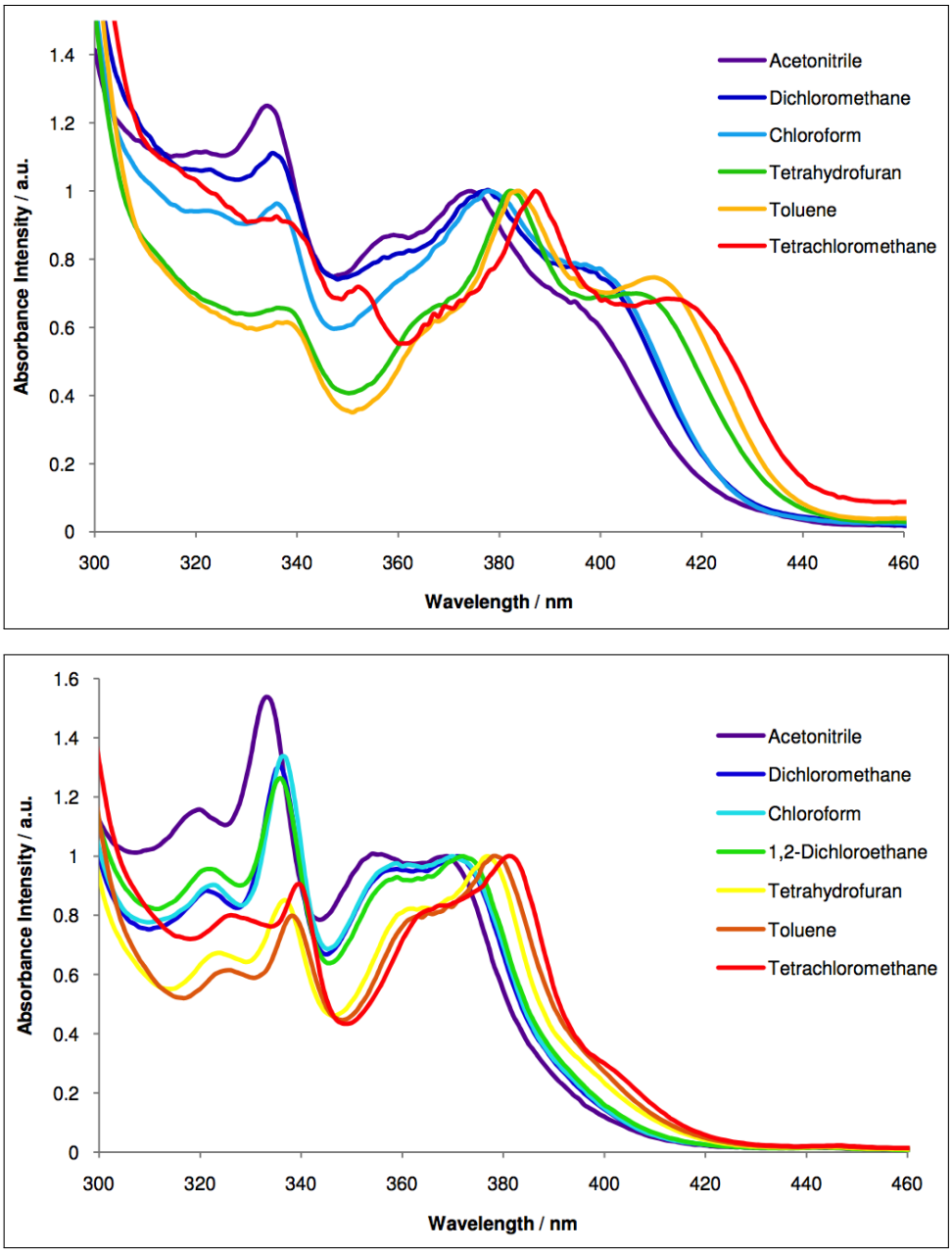

Figure 2.12: Normalised UV-vis absorption spectra of PtL^3Cl (top) and $PtLF^3Cl$ (bottom) in different solvents at 298 K. The intensity of the absorption band at ∼380 nm is normalised for ease of comparison. Figures taken from Lisa Murphy's thesis.[180]

	Absorbance λ_{max}/ nm (ε / L mol^{-1}cm^{-1})
PtL^{1}Cl	322 (5180), 334 (5289), 363 *sh* (4383), 382 (6333), 405 *sh* (4299), 459* *sh*, 489*
PtL^{2}Cl	326 (7820), 356 (6420), 374 (8930), 400 (7040), 479* (260)
PtL^{3}Cl	335 (12350), 360 (9150), 370 (11210), 399 (8464), 455* *sh* (280), 490* (130)
PtL^{4}Cl	327 (6500), 339 *sh* (6030), 390 *sh* (6440), 413 (6730), 492* (310)
PtLF^{1}Cl	323 (6030), 336 (8010), 361 (6030), 375 (7110), 444*(110),474* (90)
PtLF^{2}Cl	316 (8910), 329 *sh* (10790), 358 (9000), 372 (11320), 433* (180), 462* (150)
PtLF^{3}Cl	322 (5820), 336 (8620), 358 (6330), 372 (6730), 442* (110), 473* (80)
PtLF^{4}Cl	292 (13890), 329 (5550), 341 (5980), 382 (6480), 475* (120)

*Table 2.2: Wavelengths of absorption of PtL^{n}Cl and PtLF^{n}Cl series at 298 K in DCM. *Forbidden $S_0 \rightarrow T_1$ absorption bands.*

be accessed. Indeed it has even been shown that some compounds can absorb to a triplet excited state. Some of these transitions are more favourable than others. For example, the excitation from $S_0 \rightarrow S_1$ may be so unfavourable that it is not seen at all, other excitations may be weak, and excitation from S_0 to S_5 (for example) may dominate the low energy region of the absorption spectrum. For this reason, when considering the TD-DFT calculation of the absorption spectrum, it is easiest to compare the experimental spectrum with a convoluted spectrum rather than individual excitations.

For each given excitation TD-DFT will calculate a single point energy along with an indication of the probability of that excitation, the oscillator strength

	Emission λ_{max} / nm	Energy of triplet state / eV[a]
PtL^{1}Cl	497, 529, 565 *sh*	2.49
PtL^{2}Cl	487, 521, 560	2.55
PtL^{3}Cl	494, 528, 565 *sh*	2.51
PtL^{4}Cl	506, 529 569 *sh*	2.45
PtLF^{1}Cl	487, 513, 555 *sh*	2.55
PtLF^{2}Cl	467, 498, 529	2.65
PtLF^{3}Cl	478, 510, 543 *sh*	2.59
PtLF^{4}Cl	494, 530, 565 *sh*	2.51

Table 2.3: Wavelenth of phosphorescent emission and energy of the T_1 triplet state of PtL^{n}Cl and PtLF^{n}Cl series at 298 K in DCM. [a] Estimated from wavelength of 0−0 band.

(f). Experimentally we measure extinction coefficients which show how strongly the sample absorbs light at a given wavelength. The calculated oscillator strength gives an indication of the probability of a transition between energy levels occurring. Since TD-DFT calculations are generally run at 0 K, this does not take into account broadening by vibration which can be added in later, generally by convolution of the excitations and oscillator strengths found. Usually this is achieved by putting a set width (often 0.6 eV) at half the line maximum and drawing a Gaussian shaped curve over the top.[192] All the Gaussian curves are then added together to give the predicted spectrum. There are other ways of creating such a spectrum (one of which will be discussed later in this section) but these are usually too computationally demanding for general use. In this section we will discuss the ability of DFT to reproduce experimental trends in the absorption spectra of the mentioned compounds with consideration of how the inclusion of various computational parameters affects the trends observed. The TD-DFT results obtained will be presented as convoluted absorption spectra.

Unless otherwise stated, DFT and TD-DFT calculations presented in this chapter were performed using PBE0, in vacuum with the LANL2DZ basis set

for platinum and cc-pVDZ for all other atoms. Where indicated a PCM for solvent was applied. Ground state and triplet excited state geometries were optimised by direct minimisation of the SCF energy and checked to be a true minimum by frequency calculations at the same level of theory. Convolution of excitation energies for absorption spectra was achieved using a 0.6 eV full width at half maximum Gaussian. Various combinations altering the functional, point of inclusion of solvent model and different basis sets were used as indicated throughout to investigate the importance and significance of each on the results obtained.

Calculations in vacuum

Initial attempts to reproduce the trends in absorption spectra of $PtL^{1-4}Cl$ and $PtLF^{1-4}Cl$ were conducted in vacuum, using PBE0, with basis sets LANL2DZ for platinum and cc-pVDZ for all other atoms. The S_0 ground state geometry was first optimised, then the first ten singlet excitations at this geometry computed. The convoluted spectra produced are shown in Figure 2.13. In general this method produced reasonable results. The trend between the two series of complexes, PtL^nCl and $PtLF^nCl$ was correct, with a blue shift seen for the fluorinated compounds, as seen in the experimental spectra. The difference in calculated wavelength of absorption between the two series was also good, for example, the λ_{max} of PtL^3Cl and $PtLF^3Cl$ were 399 and 372 nm experimentally and 404 and 371 computationally (Table 2.4).

Within each series (with the exception of $PtLF^2Cl$) the general trends were well reproduced despite the very small difference in energy between them. The difference between λ_{max} of the absorption bands was less well reproduced: comparison of Figure 2.11 with 2.13 shows that the relatively large gap between PtL^1Cl and PtL^4Cl observed experimentally is not reproduced by these calculations.

Calculations with a PCM for solvent

Since photophysical measurements are usually conducted in a solvent at high dilution (to reduce the probability of aggregate or excimer formation) and

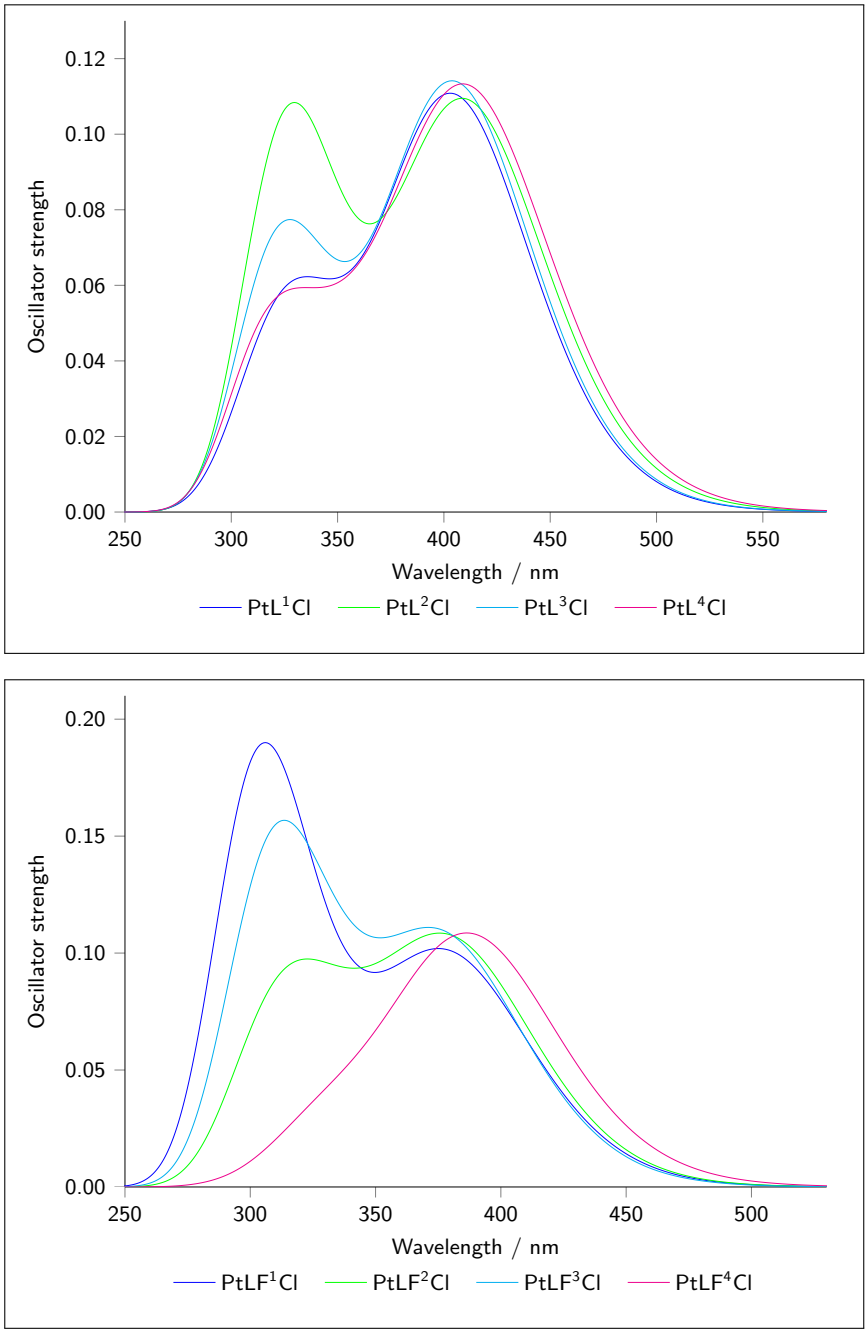

Figure 2.13: Convoluted absorption spectra of PtL^nCl (top) and $PtLF^nCl$ (bottom) series, calculated by TD-DFT. Excitation energies calculated are shown in the Appendix, Tables 9.1 and 9.2.

	Calculated λ_{max} / nm	Experimental λ_{max} / nm
PtL^{1}Cl	403	405 *sh*
PtL^{2}Cl	408	400
PtL^{3}Cl	404	399
PtL^{4}Cl	409	413
PtLF^{1}Cl	375	375
PtLF^{2}Cl	376	372
PtLF^{3}Cl	371	372
PtLF^{4}Cl	386	382

Table 2.4: Wavelenth of the lowest energy $S_0 \rightarrow S_n$ absorption band from Figure 2.13. Equivalent experimental values are shown for comparison.

these solvents can affect the energies of absorption and emission obtained, it is desirable to include such solvents in the calculation. Inclusion of solvent increases computational time so it is often omitted entirely or included only in the TD-DFT calculation. Inclusion of large numbers of individual solvent molecules around the compound of interest to calculate their interaction with it would make the time-cost of calculations prohibitively high. Instead of this, many groups use a polarisable continuum model (PCM) for solvent where spheres are drawn around each atom of the molecule and a dielectric constant applied to the space outside the spheres. The drawback of such a technique is that intermolecular interactions (such as π-stacking) are not taken into account. We will now assess the effect of a PCM for solvent and the effect of its inclusion on both geometry optimisation and TD-DFT calculations for the absorption spectra of PtL^{3}Cl and PtLF^{3}Cl.

Figure 2.14 shows the calculated absorption spectra of PtL$^{1-4}$Cl and PtLF$^{1-4}$Cl where both the geometry optimisation and TD-DFT calculations included a PCM for DCM (the solvent used experimentally). The excitation energies obtained are higher in energy than those computed in vacuum. Inclusion of solvent in this way correctly increases the wavelength of the lowest energy

band of PtL^4Cl, so that the gap between this band and the same band in PtL^2Cl is 14 nm (c.f. 13 nm experimentally). The other three complexes all have their lowest energy band at essentially the same position, only varying between the three by 2 nm. The same is true of the $PtLF^nCl$ series.

Further investigations were pursued considering only PtL^3Cl and $PtLF^3Cl$. Figure 2.15 shows the convoluted absorption spectra of these two complexes in six solvents of varying polarity. The geometry was first optimised in vacuum, then the solvent model applied for the TD-DFT calculations. The spectra show that for the lowest energy band the negative solvatochromism displayed experimentally is correctly predicted in both cases.

Figure 2.16 compares absorption spectra generated where the solvent model is included at different points in the calculations. Method A takes the ground state geometry computed in vacuum and applies a solvent for the TD-DFT calculations while Method B includes solvent for both geometry and TD-DFT. In general, the point of inclusion makes little difference, though in acetonitrile, a highly polar solvent (dielectric constant = 37.5), the band at ∼300 nm decreases by 0.11 eV with Method B. Excitations calculated in vacuum at the crystal structure geometry are also shown. This geometry is often used for such calculations since it is a known, experimental geometry and also saves on computational time. Since we have seen, though, that the excitation energies calculated are dependent on the geometry used, the results could be skewed by use of a geometry which has been obtained due to the intermolecular interactions present in the formation of the crystal structure.

Calculations with different basis sets and functionals

Calculations where larger basis sets are used are generally considered to be more accurate though they take longer to compute; computational accuracy does not necessarily give results closer in energy to those obtained experimentally since, for example, calculations simulate in the gas phase at 0 K. They can also encounter more difficulty in converging. Choice of basis set is, as with all factors, a compromise between using one small enough to obtain results

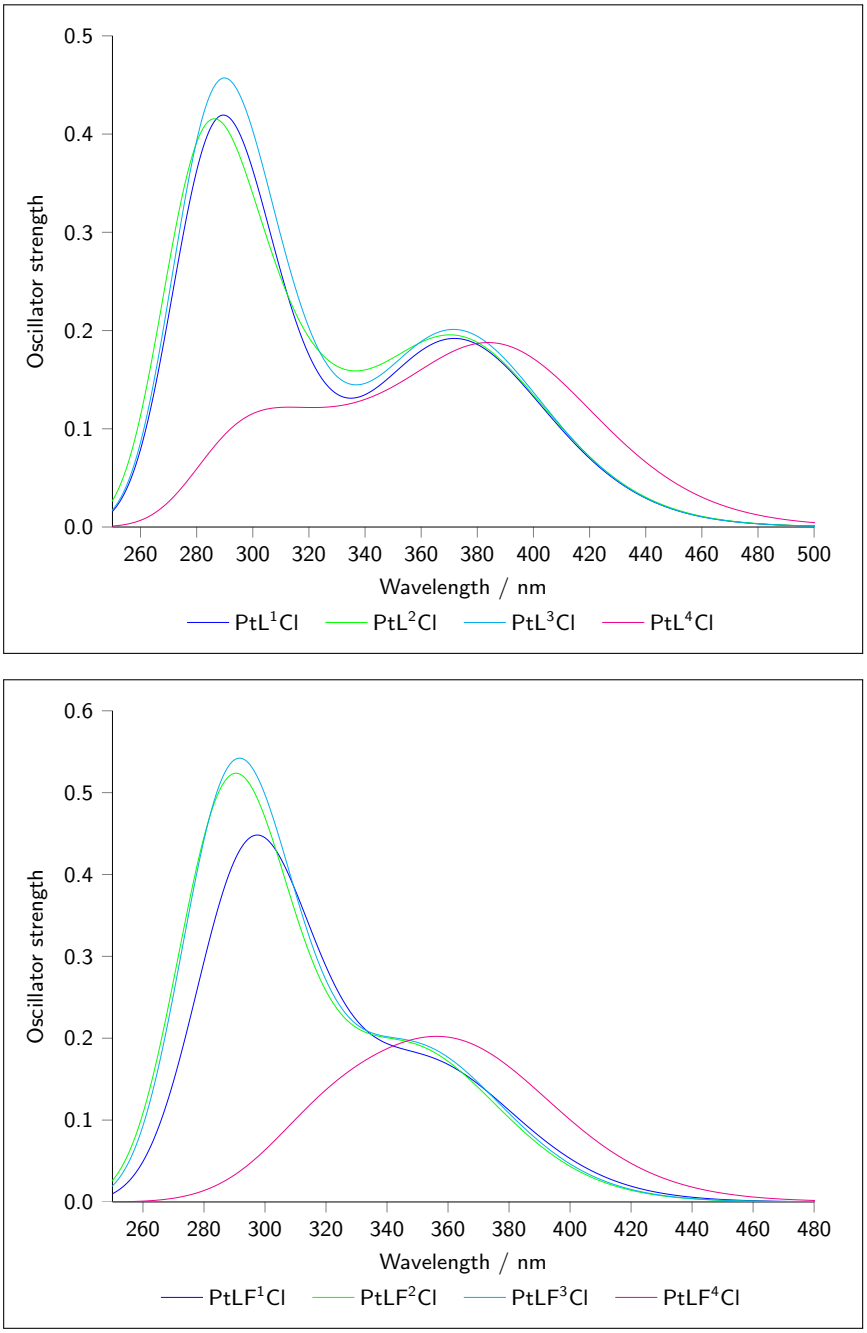

Figure 2.14: Convoluted absorption spectra of PtL^nCl (top) and $PtLF^nCl$ (bottom) series calculated with a PCM solvent model for DCM (for all calculations). Excitation energies calculated are shown in the Appendix, Tables 9.3 and 9.4.

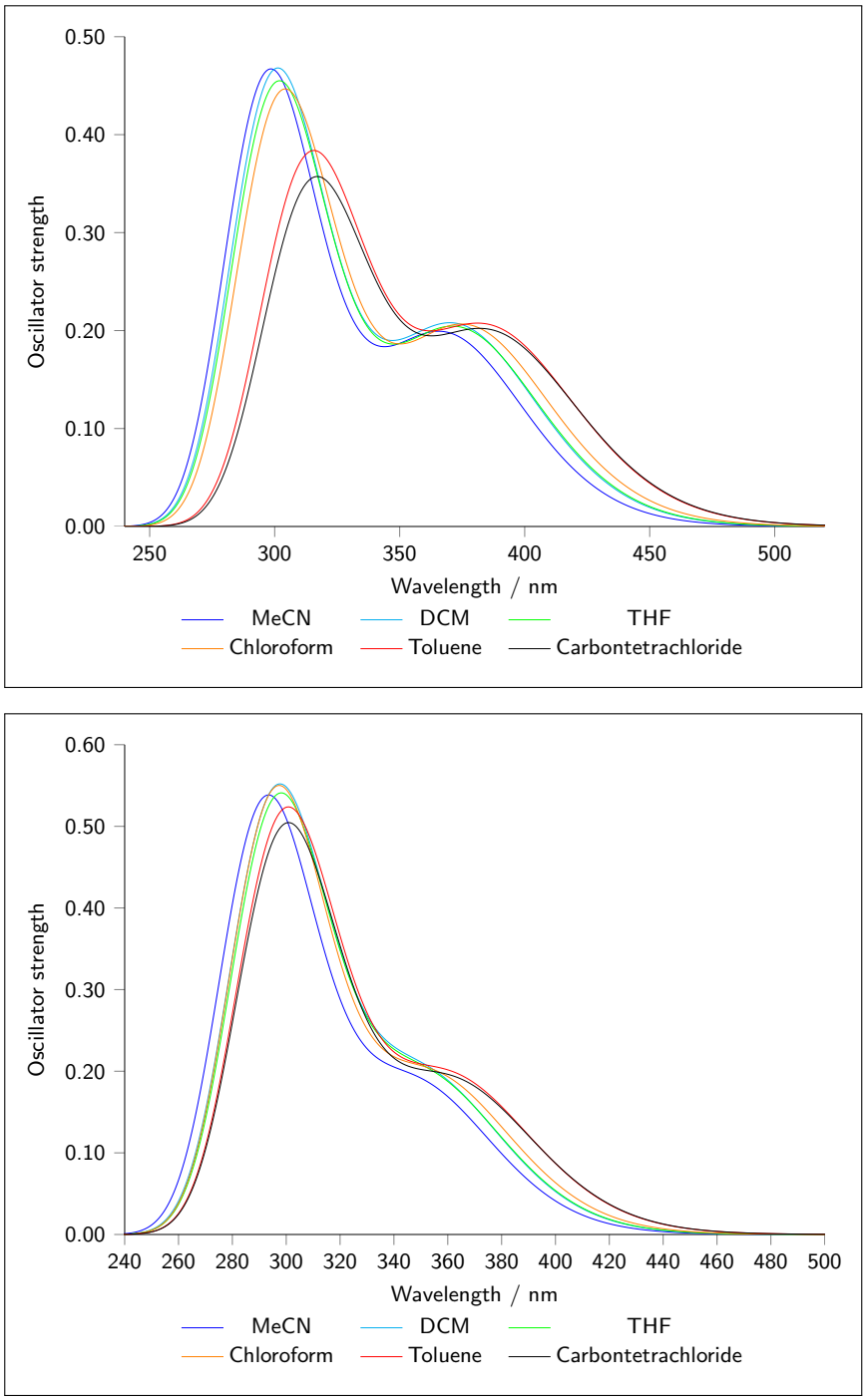

Figure 2.15: Convoluted absorption spectra of PtL^3Cl (top) and $PtLF^3Cl$ (bottom) calculated by TD-DFT in various solvents. The ground state geometry was first optimised in vacuum, then the excitation energies obtained using TD-DFT, with a PCM of the indicated solvent applied. Excitation energies calculated are shown in the Appendix, Tables 9.5 and 9.6.

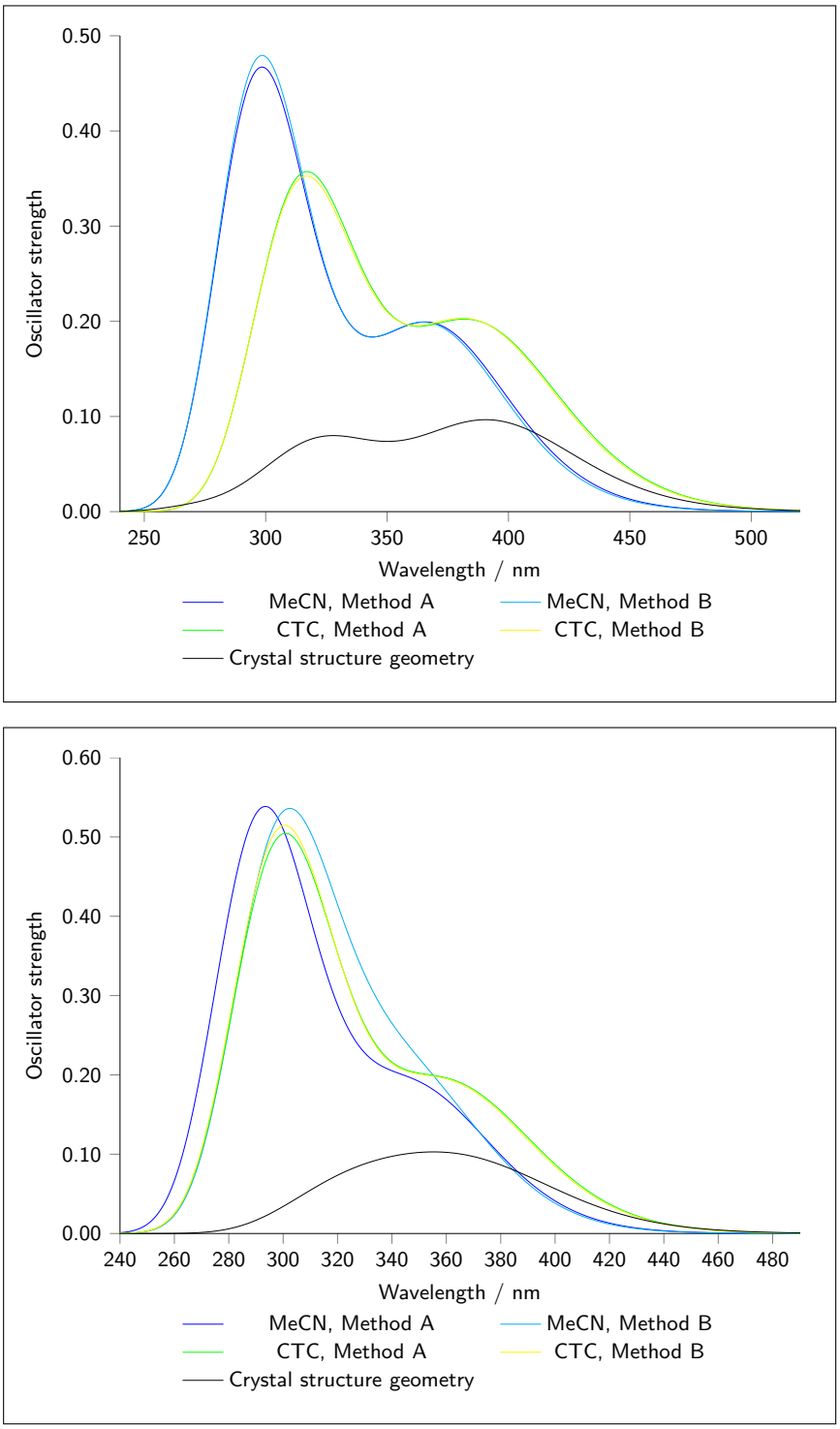

Figure 2.16: Convoluted absorption spectra of PtL^3Cl (top) and $PtLF^3Cl$ (bottom) calculated by TD-DFT. Method A: the ground state geometry was first optimised in vacuum then the excitation energies obtained using TD-DFT with a PCM of the indicated solvent applied. Method B: both the ground state geometry optimisation and the TD-DFT were calculated with a PCM applied. The black line indicates TD-DFT calculations in vacuum at the crystal structure geometry. Excitation energies calculated are shown in the Appendix, Table 9.7.

in a reasonable time-span and one large enough to give reasonably reliable results. The spectra from TD-DFT excitations using four different basis sets (at the cc-pVDZ geometry) for PtL^3Cl and $PtLF^3Cl$ are shown in Figure 2.17. They show the λ_{max} varying significantly depending on the basis set used in each case.

Figure 2.18 shows the convoluted absorption spectra for the same two compounds where the geometry was also computed using the indicated basis set. In this second example of varying basis sets, aug-cc-pVDZ is not shown since, despite several attempts, a geometry optimisation using this basis set could not be made to converge. For the rest of the discussion cc-pVDZ will be used for all atoms except platinum since this appeared to give reasonable results, similar to that of cc-pVTZ but in a more achievable time span.

Finally, convoluted absorption spectra were calculated with various basis sets and the functional altered to CAM-B3LYP to see if longer-range interactions had any effect on excitation energies calculated. Again, cc-pVDZ and cc-pVTZ gave very similar results but calculations with cc-pVDZ were much quicker. CAM-B3LYP will be used in later chapters where there are compounds with low orbital-overlap excitations so that a long-range corrected functional is necessary to accuarately describe the processes taking place.

Simulated absorption spectra of Pt(II) complexes without convolution

As previously alluded to, it is possible to calculate the absorption spectra of compounds using TD-DFT but without merely placing a Gaussian curve over the excitation: instead the calculation takes into account the vibrations of the ground and excited states of the molecule during calculation of the excitation intensities. To evaluate the vibrations, the structure of each individual excited state must be computed, followed by a frequency calculation at that structure. In two proof-of-principle calculations this was attempted for PtL^3Cl and $PtLF^3Cl$, in vacuum, using PBE0 (the same parameters as used for Figure 2.13). Due to the computationally demanding nature of these calculations, only the first five singlet excitations were computed for each. Whilst a

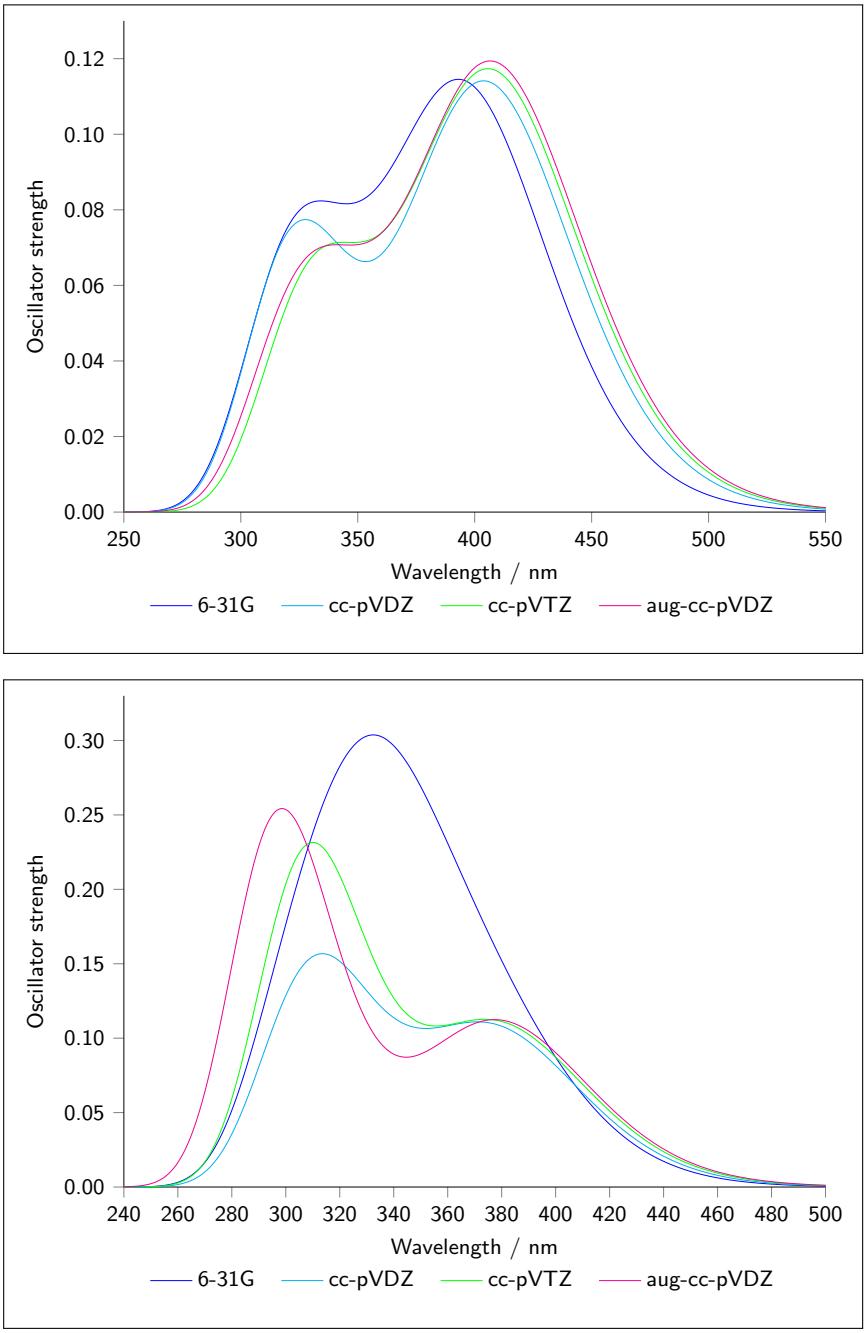

Figure 2.17: Convoluted absorption spectra of PtL^{3}Cl (top) andPtLF^{3}Cl (bottom) calculated by TD-DFT. Geometries were calculated with cc-pVDZ and LANL2DZ, then TD-DFT excitations calculated with LANL2DZ for Pt and the indicated basis set for the other atoms. Excitation energies calculated are shown in the Appendix, Tables 9.8 and 9.9.

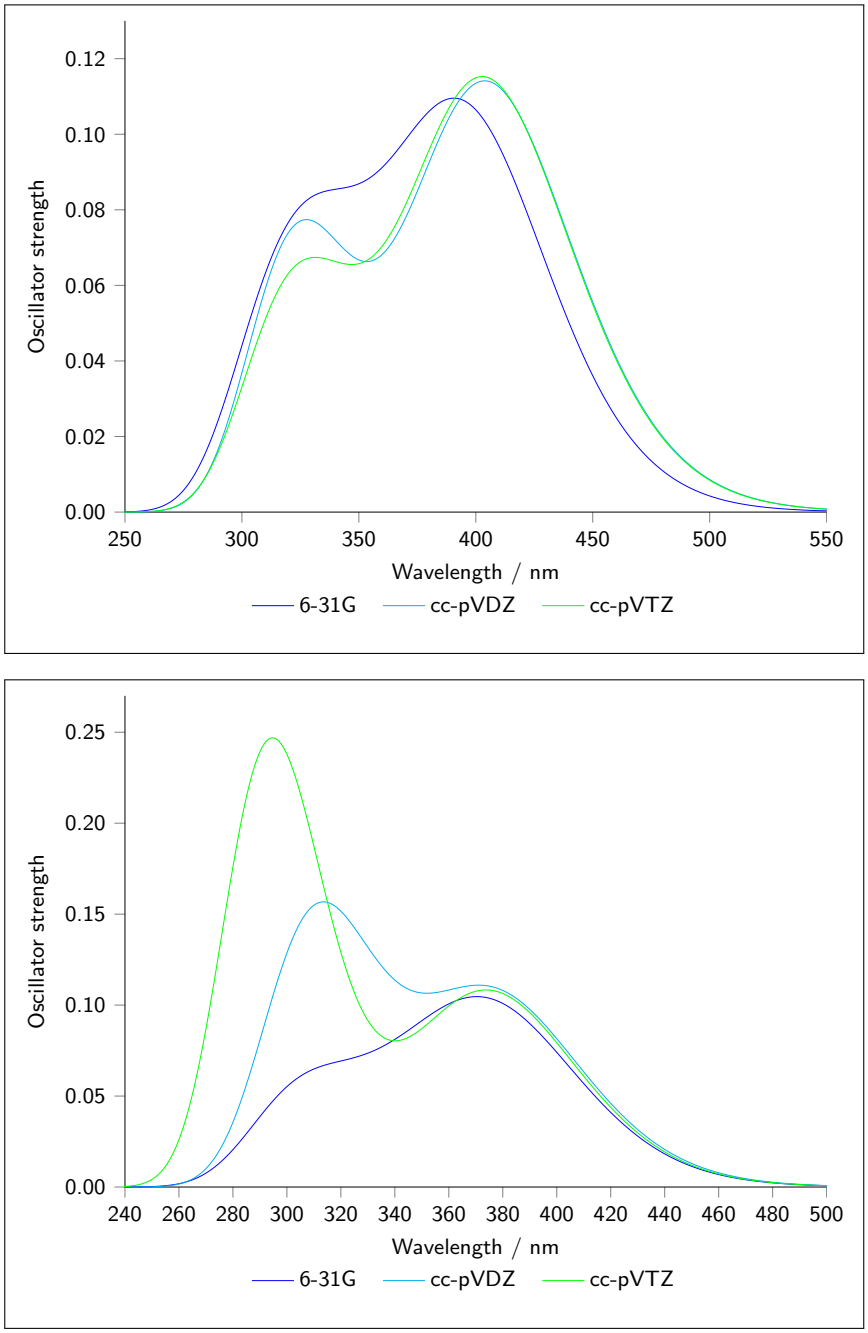

Figure 2.18: Convoluted absorption spectra of PtL^{3}Cl (top) and PtLF^{3}Cl (bottom). Calculations were run with LANL2DZ for Pt and the indicated basis set for the other atoms for both the geometry optimisation and TD-DFT. Excitation energies calculated are shown in the Appendix, Tables 9.8 and 9.9.

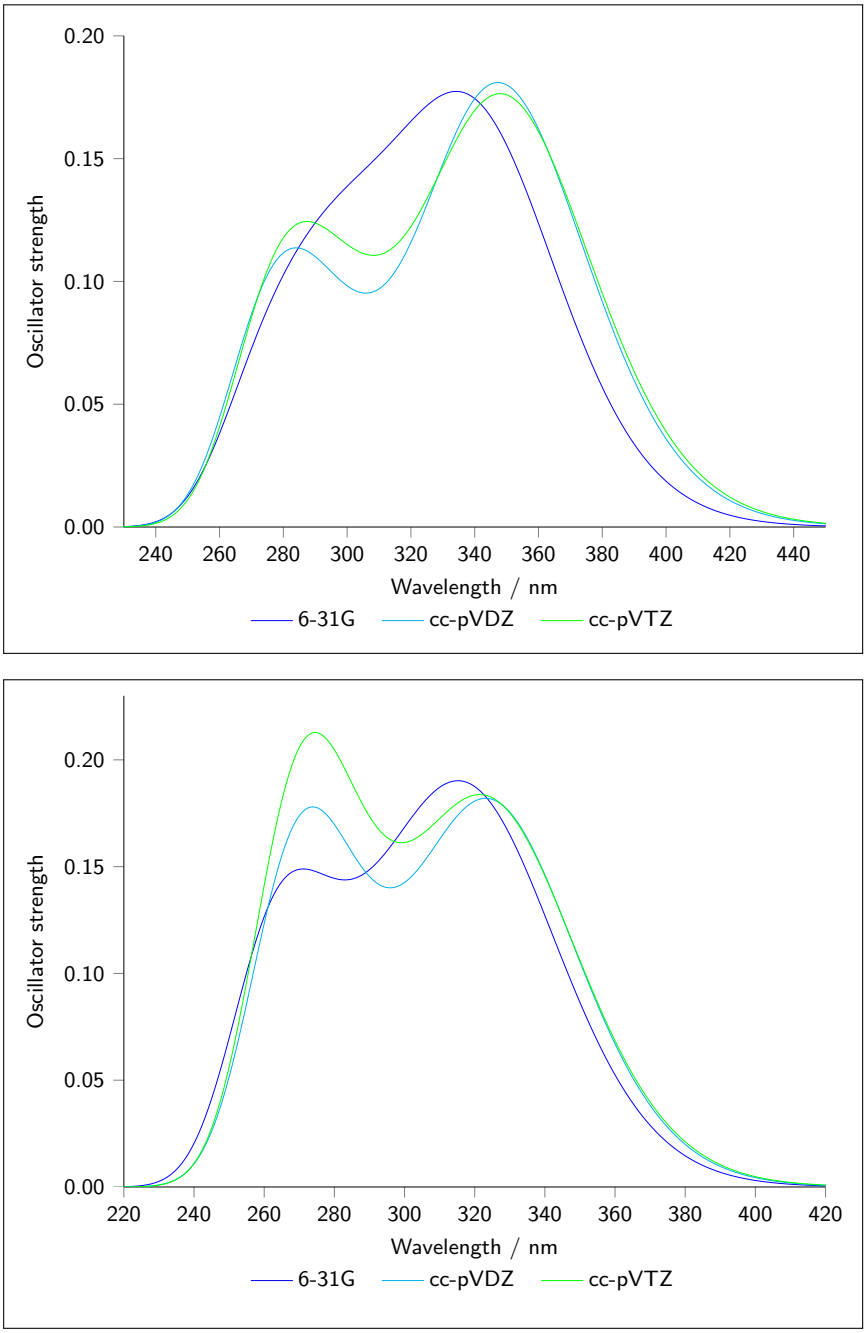

Figure 2.19: Convoluted absorption spectra of PtL^3Cl (top) and $PtLF^3Cl$ (bottom) calculated by TD-DFT using CAM-B3LYP. Excitation energies calculated are shown in the Appendix, Table 9.10.

result more similar to room temperature experimental spectra is obtained by calculations such as these, the calculation time required is vastly increased. For example, in the case of $PtLF^3Cl$, calculating the absorptive properties for 20 excited states using conventional methods (optimisation of the ground state geometry followed by TD-DFT calculations to find the energy of the excitations) took just over 23 h cpu time. Meanwhile, the same calculation using this method took nearly 5.4 years cpu time. For this reason, while it was possible to re-run calculations shown to have imaginary frequencies when using the first method, it is not practical to keep repeating calculations using the second method, and consequently some of the results have imaginary frequencies, showing that they are not at a true minimum.[a] Singlet excited state geometries calculated for PtL^3Cl were also shown to have imaginary frequencies.[b] Although geometry optimisations and frequency calculations were successfully performed, Franck-Condon excitation energies could not be computed due to a problem with the Gaussian program (possibly from calculations requiring consideration of so many different vibrational modes.)

The same calculations were therefore performed for benzene for the S_0 and S_1 geometries to give an idea of the quality of spectrum that might be obtained. Both the experimental absorption spectrum (in DCM at 298 K) and the calculated spectrum are shown in Figure 2.20. The calculated spectrum (although shifted to a higher energy) shows good reproduction of the spectrum structure, especially when taking into account that DFT simulates at 0 K and experimental results were obtained at 298 K. Calculations were performed with PBE0, using cc-pVDZ, in vacuum.

2.4.2 Calculated emission energies of PtL^nCl and $PtLF^nCl$

Comparison of Tables 2.3 and 2.5 show that the excitation energies calculated for triplet emission by TD-DFT do not give a very good reproduction of the

[a] For $PtLF^3Cl$: S1 geometry, 2 imaginary frequencies, 817.82 i cm^{-1} and 104.09 i cm^{-1}; S2 geometry, 1 imaginary frequency, 7.80 i cm^{-1}; S4 geometry, 1 imaginary frequency, 174.70 i cm^{-1}.

[b] For PtL^3: S2 geometry, 1 imaginary frequency, 46 i cm^{-1}.16; S5, 1 imaginary frequency, 41.44 i cm^{-1}.

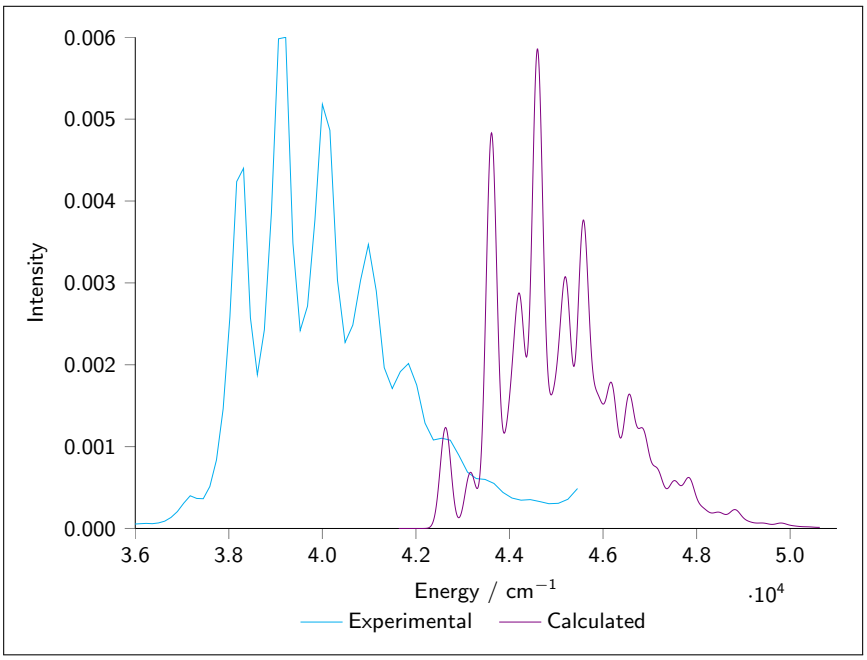

Figure 2.20: Experimental (298 K, in DCM solution) and theoretical (taking into account Franck-Condon factors) absorption spectra of benzene.

	Energy / eV	Wavelength / nm	Experimental wavelength / nm
PtL^{1}Cl	2.07	600	497
PtL^{2}Cl	1.00	1236	487
PtL^{3}Cl	0.87	1429	494
PtL^{4}Cl	0.68	1817	506
PtLF^{1}Cl	0.85	1465	487
PtLF^{2}Cl	2.19	565	467
PtLF^{3}Cl	1.02	1217	478
PtLF^{4}Cl	1.03	1199	494

Table 2.5: Calculated excitation energies for phosphorescent excitation from S_0 to T_1 at the T_1 excited state geometry for the PtL^{n}Cl and PtLF^{n}Cl series of compounds. Experimental wavelengths correspond to the 0,0 band at 298 K in DCM.

experimental trends observed. Unlike the values calculated for absorption, not only are the trends incorrect, but the magnitude varies dramatically. The calculation of triplet excitations can be fraught with difficulty for various reasons (such as triplet instabilities in high overlap compounds like these, see Chapter 1, Section 1.6.1) and there are a number of ways to calculate them both by direct optimisation of the triplet geometry and by TD-DFT. This will be the subject of some of the following chapters.

2.5 Pt(IV) complexes

2.5.1 Photophysical properties of Platinum(IV) complexes

The synthesis and photochemistry of terdentate Pt(II) complexes has been extensively studied in recent years and many brightly emissive examples discovered. In contrast, little is known of the photophysical properties of cyclometallated Pt(IV) complexes which are isoelectronic with their Ir(III) analogues. The first cyclometallated Pt(IV) complexes made were non-emissive at room temperature.[193] However, some, incorporating multiple ring systems with two cyclometallating ligands, showed room temperature emission[194] since the ligand field is sufficiently strong to displace the d-d* states to a high enough energy that they no longer provide a deactivation pathway at room temperature. Another example of this is given by Kunkely and Vogler in their discussion of methyl Pt(IV) complexes.[195] They show that $[Pt(bpy)(CH_3)_3I]$ displays room temperature emission while $[Pt(bpy)_2Cl_2]^{2+}$ does not. The anionic ligands raise the metal d orbital, thus promoting MLCT and increasing k_r.

The UV-vis absorption spectrum for PtL^5Cl_3 is shown in Figure 2.22 alongside that of its parent compound, PtL^5Cl for comparison. It can be seen that upon oxidation to the Pt(IV) species the lowest energy absorption bands are displaced to higher energy than the Pt(II) species. At room temperature, no emission could be detected from PtL^5Cl_3. Although this compound is clearly a weak emitter, the high quantum yield of emission from its decomposition product (PtL^5Cl) swamps the spectrum so that even if some is present it is too weak to be seen by comparison.

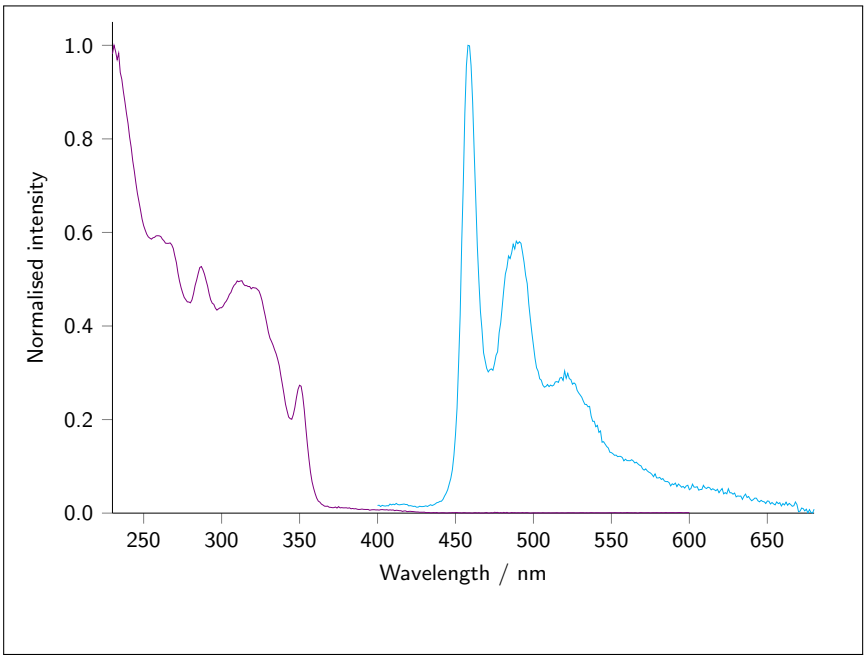

Figure 2.21: Normalised UV-vis absorption spectrum (purple) and emission spectrum (blue) of $[PtL^5(ppy)Cl]^+$ *in DCM solution at 298 K.*

Coordination of a second, bidentate ligand was achieved, giving $[PtL^5(ppy)Cl]^+$ and $[PtL^5(bpy)Cl]^{2+}$. Despite the increase in ligand field strength and ligand rigidity of these compounds compared to PtL^5Cl_3, no room temperature emission was observed for $[PtL^5(bpy)Cl]^{2+}$ and only weak, blue, structured emission for $[PtL^5(ppy)Cl]^+$ (Figure 2.21). Synthesis of $[PtL^7(ppy)Cl]^+$ is desirable since the phosphorescent efficiency of both $[PtL^5(ppy)Cl]^+$ and $[PtL^5(bpy)Cl]^{2+}$ are poor. It is hoped that the lower energy provided by delocalisation of electrons over this ligand could match the lower energy of the platinum in this higher oxidation state, thus optimising the emissive properties of the compound. The same is true of the CF_3 substituted complex, $[PtL^6(ppy)Cl]^+$, however in this case the lower energy would be achieved by the electron withdrawing character of the CF_3 groups.

2.5.2 Stability of Platinum(IV) complexes

As previously mentioned, although ^{1}H NMR analysis of PtL^5Cl_3 showed no detectable traces of impurities, once the photophysical properties of the compound were studied the emission spectrum was dominated by the Pt(II) compound, PtL^5Cl. The Pt(II) compound is vastly more emissive than the Pt(IV) analogue so any traces remaining will dominate the emission spectrum. Despite extensive attempts at synthesis of a pure sample, the emission spectrum continued to be dominated by PtL^5Cl. For this reason, a series of studies were undertaken to investigate if decomposition from Pt(IV) to Pt(II) could be occurring during irradiation of the sample with light whilst taking the measurements. Figure 2.22 shows the normalised absorption spectra of PtL^5Cl and of PtL^5Cl_3 before and after 5 h irradiation of light with a UV lamp (at a peak wavelength of 254 nm). It shows that irradiation of the sample introduces a new band to the spectrum at ∼365 nm which is lower energy than that of the Pt(IV) compound, but not as low as Pt(II).

Time dependent studies of the decomposition of Pt(IV) complexes PtL^5Cl_3 and PtL^5Br_3 were undertaken under various conditions. The absorption spectrum was measured every 30 minutes during exposure of the sample to UV light. Figure 2.23 follows the decomposition of PtL^5Cl_3 and PtL^5Br_3 in DCM. The rate constant for decomposition of PtL^5Cl_3 in DCM was calculated as 2×10^4 s^{-1} (assuming 5 hours to be time = ∞). Analysis of the compound by mass spectrometry, after 6 days in a solution of acetonitrile, with intermittent UV irradiation showed decomposition to the Pt(II) complex and coordination of acetonitrile in the place of chloride. Decomposition of the bromo analogue is more rapid than that of the chloro.

Figure 2.24 compares the decomposition of PtL^5Cl_3 in different solvents: chloroform and acetonitrile (DCM is shown in Figure 2.23). The effect of ambient light on the sample is shown in the Appendix, Figure 9.3 − it shows that there is no measurable decomposition of the sample under these conditions. Also shown in this figure is the spectrum of a sample kept in solution in the dark for 45 h as a control for these experiments. This sample also shows no

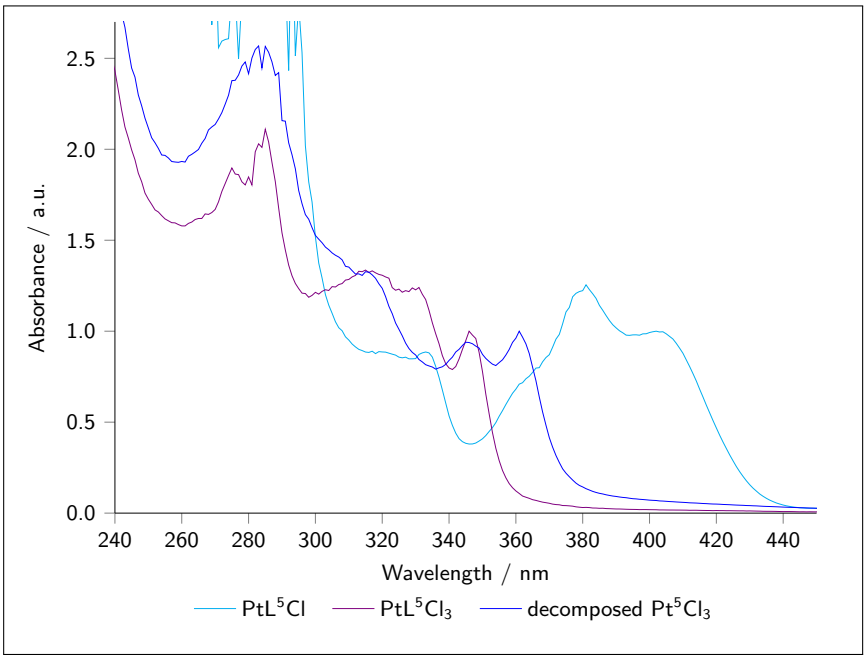

Figure 2.22: Normalised UV-vis absorption spectra of PtL^5Cl, PtL^5Cl_3 and PtL^5Cl_3 after 5 h UV irradiation, all compounds in DCM. The intensity of the lowest energy absorption band is normalised for ease of comparison.

measurable decomposition.

The effect of heat on decomposition of PtL^5Cl_3 was also investigated (Figure 9.3). The sample was heated at reflux, in chloroform, with the exclusion of light for 20 h but showed no signs of decomposition. The same is true of a sample stored in the solid state in ambient light for three months.

2.5.3 DFT of platinum(IV) complexes

As illustrated by Figure 2.22, oxidation of PtL^5Cl to PtL^5Cl_3 results in a shift of the lowest energy absorption band to a higher energy. Calculation and convolution of the first ten singlet excitations at the ground state geometry for PtL^5Cl and PtL^5Cl_3 in DCM (Figure 2.25), shows the same pattern. In PtL^3Cl, the $S_0 \rightarrow S_1$ transition dominates the low energy region of the spectrum (Figure 2.26) while for PtL^5Cl_3, it is the $S_0 \rightarrow S_8$ transition that domintates (Figure 2.27). In this transition, the density difference plots show

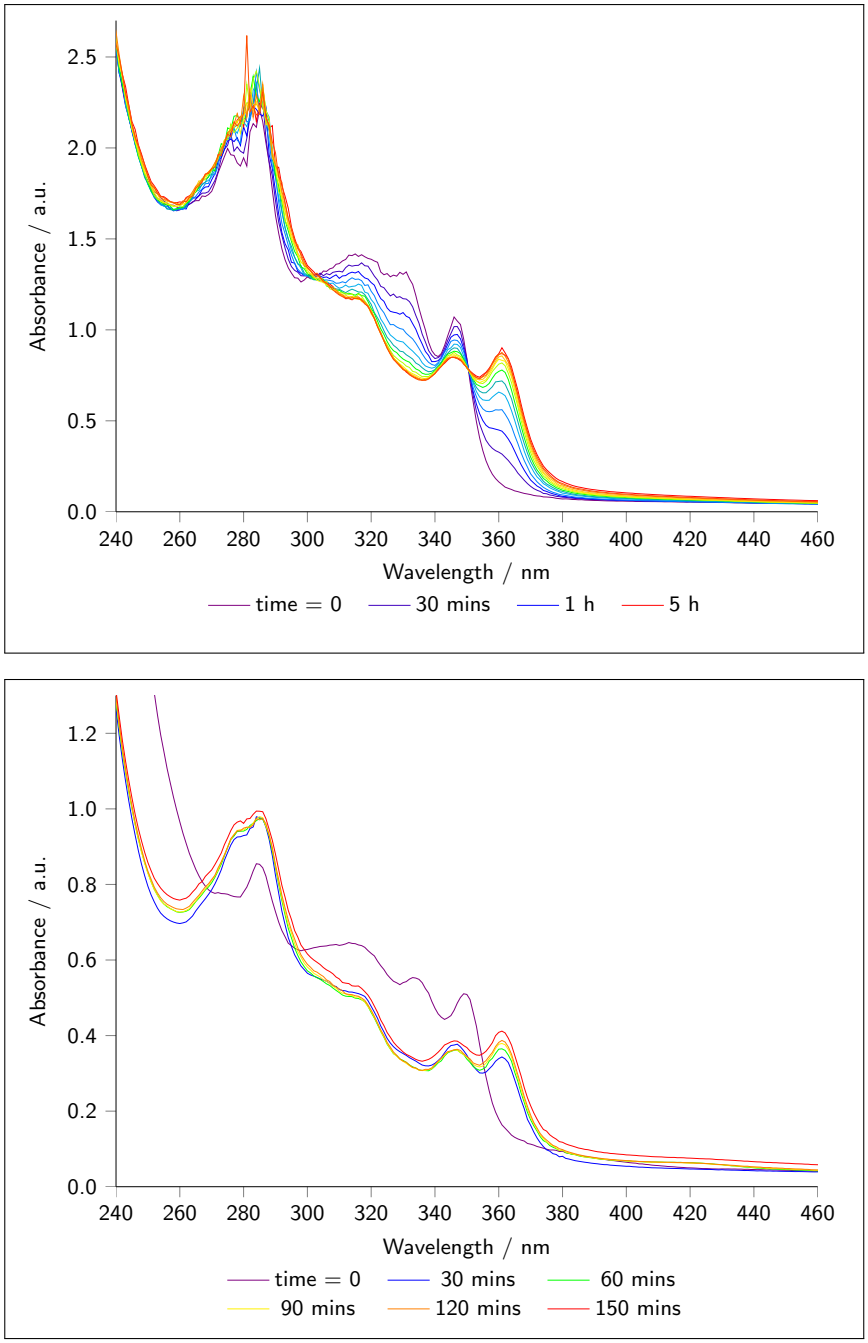

Figure 2.23: UV-vis absorption spectra of PtL^5Cl_3 in DCM (top) and PtL^5Br_3 in DCM (bottom). Measurements were taken every 30 minutes and the progress of the decomposition can be seen as you move from purple plots to red.

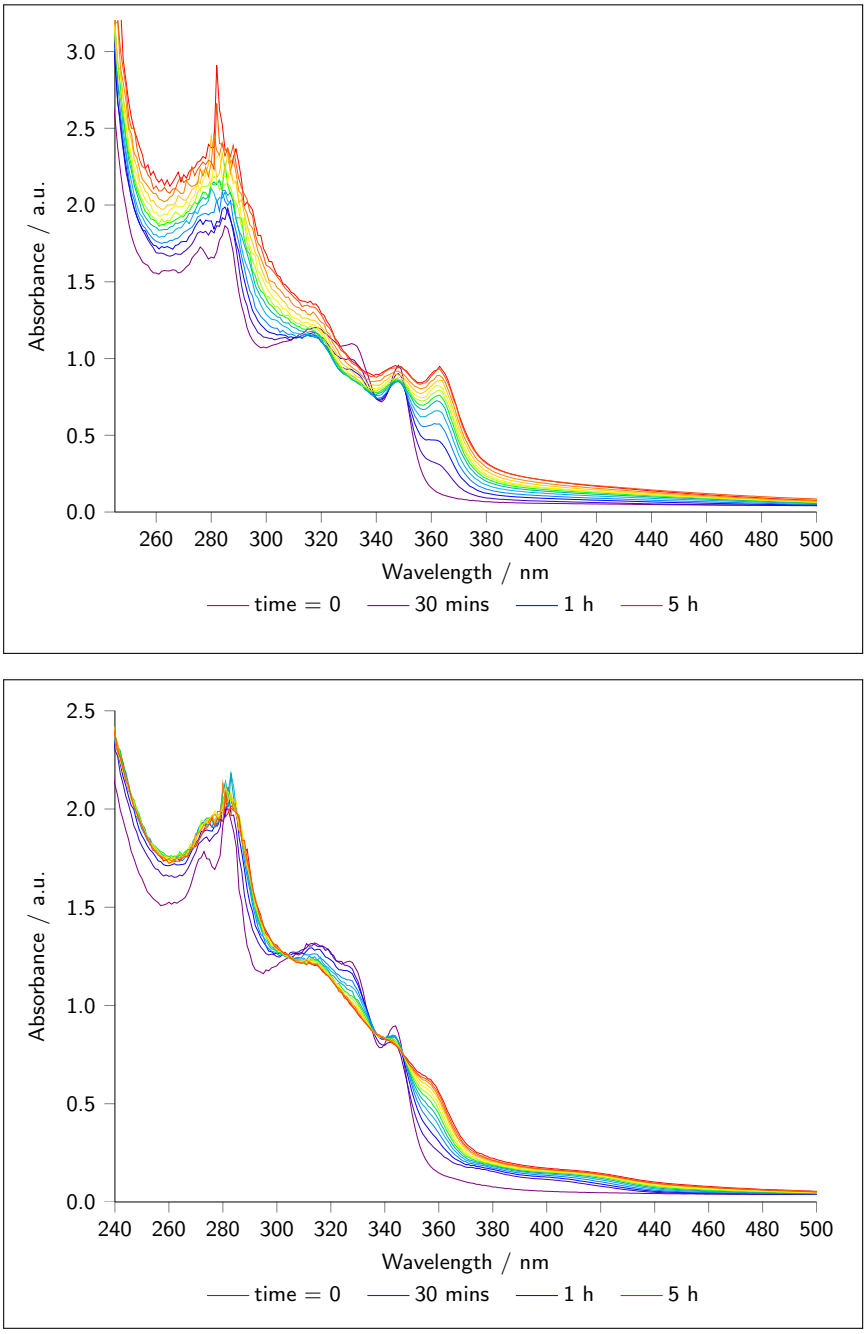

Figure 2.24: UV-vis absorption spectra of PtL^5Cl_3 in chloroform (top) and MeCN (bottom). Measurements were taken every 30 minutes and the progress of the decomposition can be seen as you move from purple plots to red.

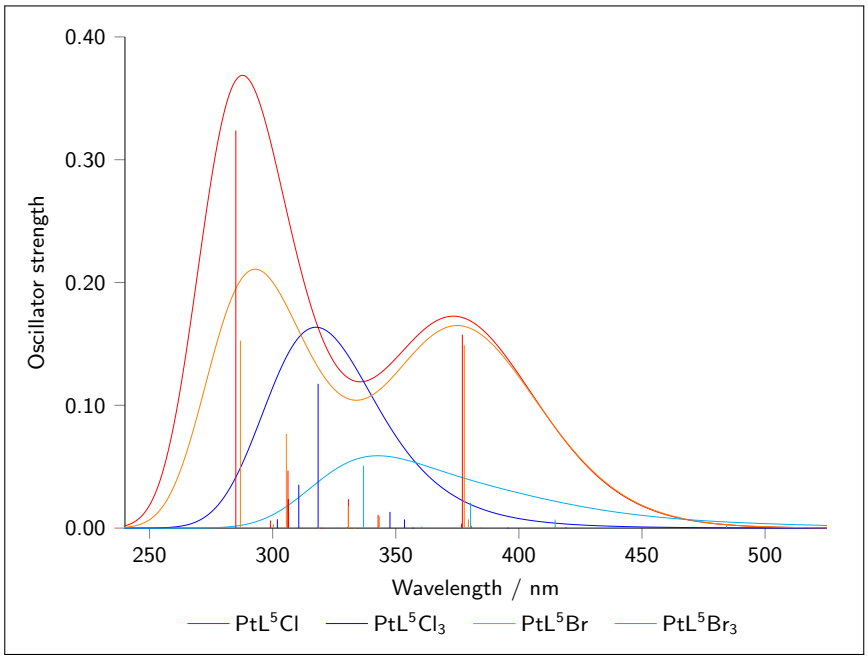

Figure 2.25: Convoluted absorption spectra of PtL^5Cl, PtL^5Cl_3, PtL^5Br and PtL^5Br_3 calculated by TD-DFT in DCM. Individual excitations are shown by the vertical lines.

that the HOMO will be partially on the electron withdrawing chlorine atoms which stabilise the HOMO, increasing the energy of the absorption band. Consideration of the $S_0 \rightarrow S_1$ plots alone (excitation wavelength = 419 nm) would suggest the reverse but the oscillator strength is so low in this case (f = 0.0006) that this transition is probably too weak to be observed. The same pattern is seen for the bromo analogues.

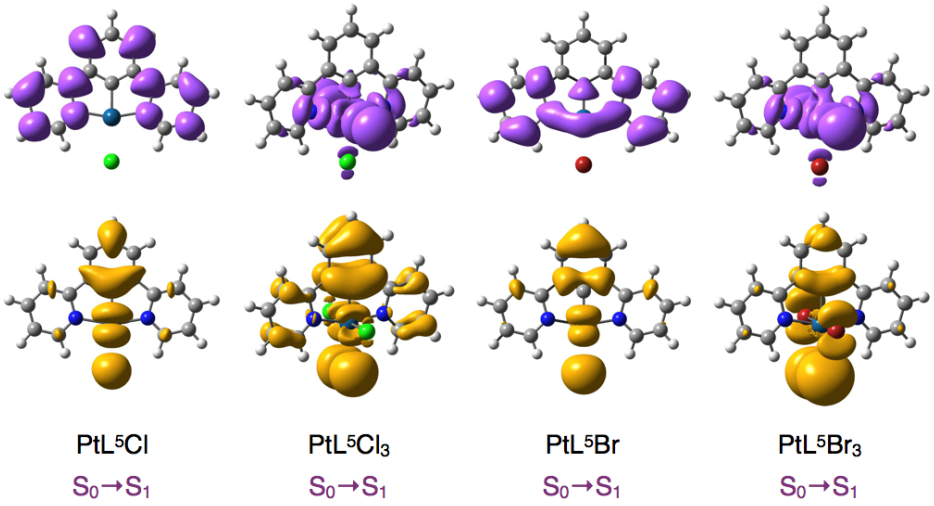

Figure 2.26: Density difference plots for excitation from the ground state to S_1 for PtL^{5}Cl, PtL^{5}Cl$_3$, PtL^{5}Br and PtL^{5}Br$_3$ calculated by TD-DFT in DCM.

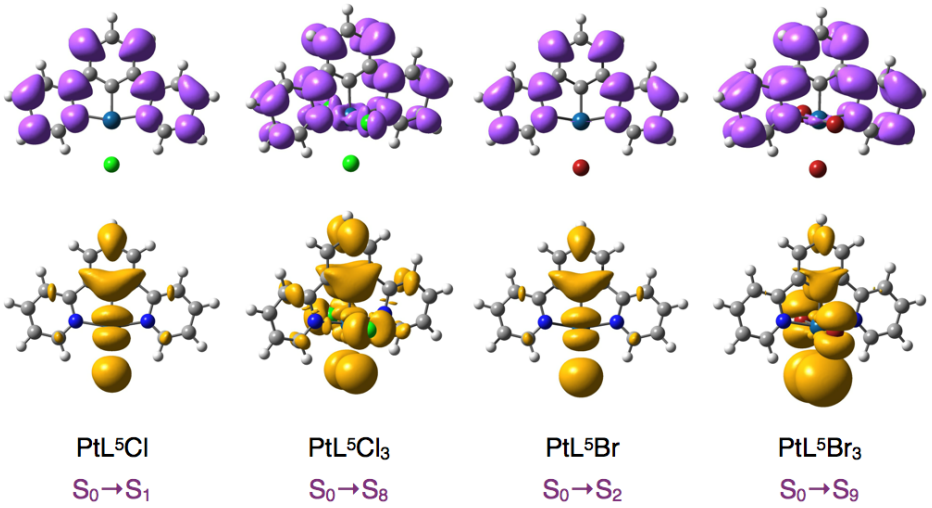

Figure 2.27: Density difference plots for excitation from the ground state to the the excited state shown for PtL^{5}Cl, PtL^{5}Cl$_3$, PtL^{5}Br and PtL^{5}Br$_3$ calculated by TD-DFT in DCM. In each case the excitation shown is the one found to dominate the low end of the spectrum in Figure 2.25. Excitation energies calculated are shown in the Appendix, Table 9.11

2.6 Concluding remarks

The synthesis and photophysical properties of some Pt(II) and Pt(IV) derivatives of PtL^5Cl have been discussed along with a computational study of their behaviour. Though the tri-halogenated Pt(IV) complexes were unstable in solution and under UV irradiation, those with a second, bidentate ligand ($[PtL^5(ppy)Cl]^+$ and $[PtL^5(bpy)Cl]^{2+}$) were shown to be stable. The low-energy region of the absorption spectra could be reproduced with a reasonable degree of accuracy by TD-DFT, reproducing both the general trend between compounds in solution and the solvatochromic response exhibited by two example complexes. The differing energies of absorption between the Pt(II) and Pt(IV) complexes in light of such calculations was understood with the aid of density difference plots, once the transition dominating the low energy region of the spectrum had been identified. Analysis of different basis sets, points of inclusion for a solvent model and functionals informed further the behaviour of each of these mathematical parameters for DFT and TD-DFT calculations in later chapters.

3

Synthesis and photophysical properties of N^C^N-coordinated Pt(II) complexes incorporating thiolate coligands

3.1 Chapter outline

In this chapter we will discuss two sets of compounds: the first, PtL^5SR and PtL^8SR (shown in Figure 3.1), was synthesised by a previous member of the group.[a] Then, in the course of this project, electrochemical and solvatochromic properties of those compounds were investigated, alongside TD-DFT studies, in an attempt to better understand the photophysical processes taking place. The second set of compounds (shown in Figure 3.2) was later synthesised and studied in the same manner, to see if the trends observed in the first set were carried through to the second, and what effect substituents on the N^C^N ligand had on the properties observed.

This chapter will concentrate on experiment, considering the synthesis of this class of compound and describing photophysical properties in comparison with

[a]Synthesis and preliminary photophysical study of PtL^5SR and PtL^8SR at both 298 K (in DCM) and 77 K (in EPA glass) were performed by William Tarran.[196]

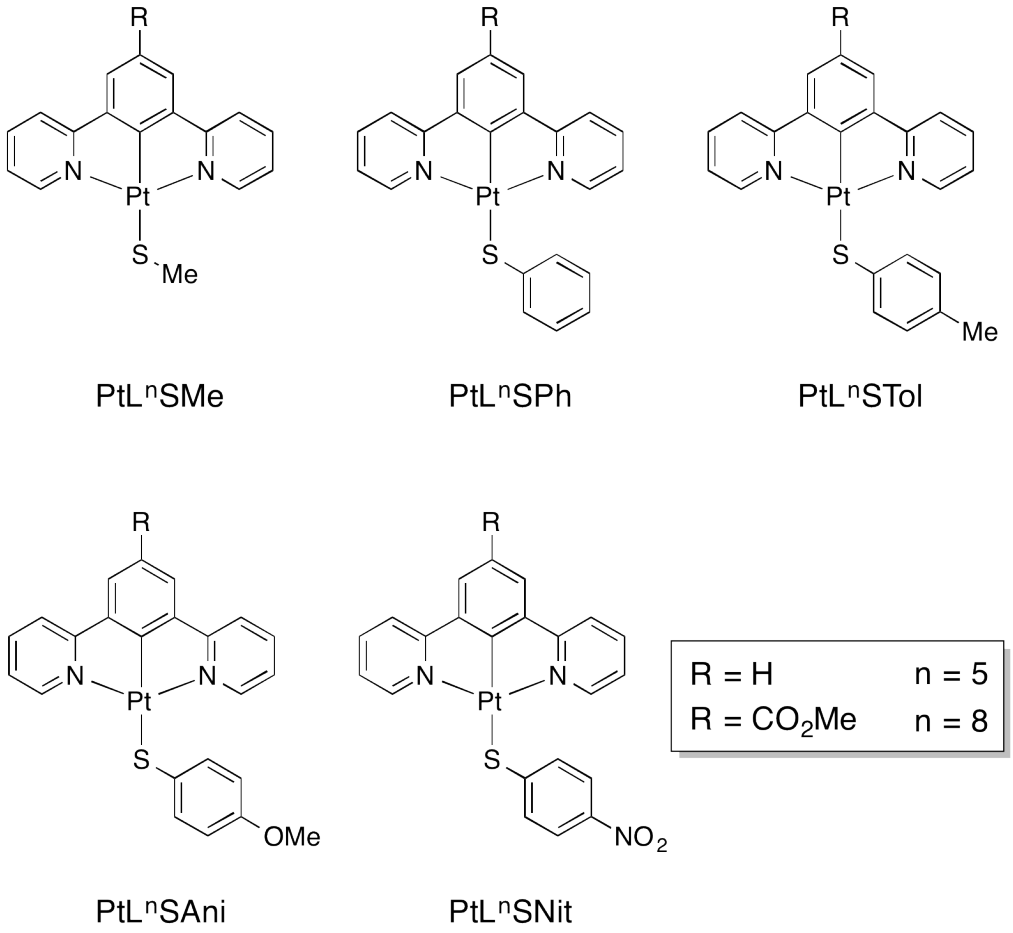

Figure 3.1: Structural formulae of the ten thiolate complexes prepared by William Tarran.

those of PtL^{5}Cl. This will highlight the dramatic change brought about by substitution of a chloride ancillary ligand by a thiolate. The following chapter describes the in-depth theoretical study of the complexes, considering the importance of both solvent and functional when attempting to predict the type of transition occurring in absorption or emission, the orbitals involved and the energy associated with it.

3.2 Synthesis of complexes

The six new complexes, PtL$^{6-9}$STol and PtL$^{6-9}$SNit, were synthesised in the same way as the previously reported PtL$^{5/8}$SR complexes. Each was prepared

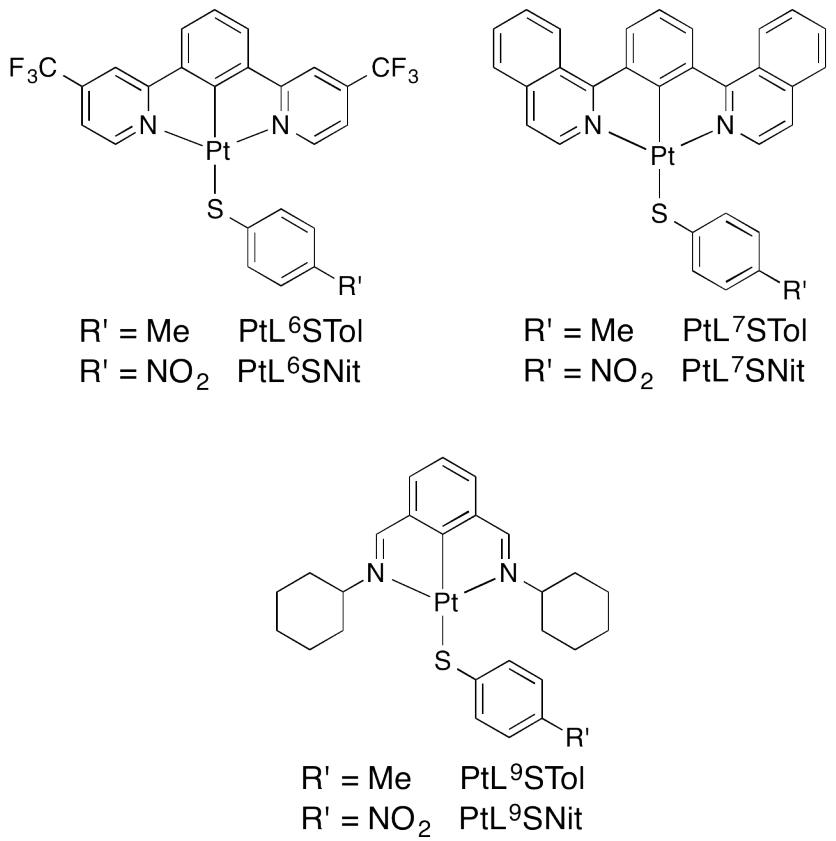

Figure 3.2: Structural formulae of the six new thiolate complexes prepared in this work.

from the parent chloro compound (PtL^6Cl, PtL^7Cl and PtL^9Cl) by addition of the complex to a degassed solution of the potassium salt of the desired thiolate (ArS^-K^+) in methanol, as illustrated in Scheme 3.1. The potassium thiolate was prepared immediately before use and the reaction proceeded at room temperature, precipitating the products as intensely red, orange or yellow solids. The compounds were then washed successively with water, methanol and diethyl ether to give the analytically pure product.

Although synthesis of PtL^7SNit was attempted, it was not possible to obtain a pure sample. There was some evidence of product formation by mass spectrometry but NMR spectroscopy showed there to be a mixture of products in every case:

$$\mathbf{(ASAP^+)}\ \boldsymbol{m/z} = \mathbf{681.1}\ [\mathbf{M} + \mathbf{H}]^+;$$

HRMS (AP$^+$) m/z = 679.0836 calculated for $[C_{30}H_{19}N_3O_2S^{194}Pt]^+$ 679.0825

Some attempts were made at purification by extensive washings but to no avail. Due to the instability of the complexes in solution, other attempts towards purification were abandoned.

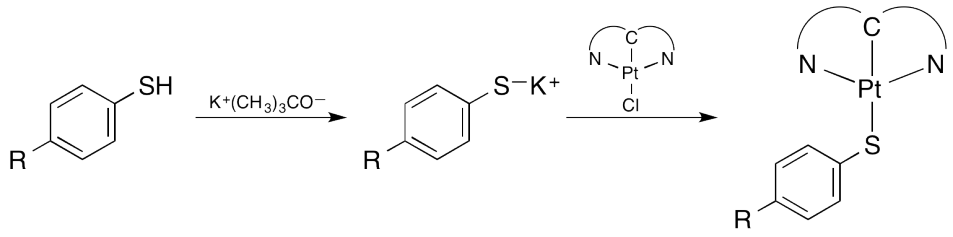

Scheme 3.1: General scheme for the synthesis of complexes with a thiolate ancillary ligand.

Characterisation of new thiolate complexes

Evidence for the successful synthesis of these complexes was compiled predominantly through ^{1}H and ^{13}C NMR spectroscopy. Though very stable in the solid state, the complexes were found to decompose relatively quickly in solution. It was found that decomposition proceeded much more rapidly in $CDCl_3$ than in DMSO-d_6. While it was not possible to obtain a proton spectrum in $CDCl_3$ before significant decomposition had occurred, analysis in DMSO-d_6 even allowed for the time consuming ^{13}C spectrum to be obtained. This is illustrated in Figures 3.3 to 3.5. The ^{1}H spectrum in DMSO-d_6 (Figure 3.3) shows the expected set of signals with no evidence of any impurities. Figure 3.4 shows that in $CDCl_3$, after 20 minutes there is a mixture of products and a consequently very complicated NMR spectrum. After 72 hours however, the spectrum looks quite similar to that of the chloro-substituted product, PtL^{9}Cl (shown in Figure 3.6 for reference), suggesting that the thiolate ligand has dissociated. The NMR spectra showed similar resonance peaks in each case to the parent chloro complex with the addition of the expected peaks from the thiolate ligand.

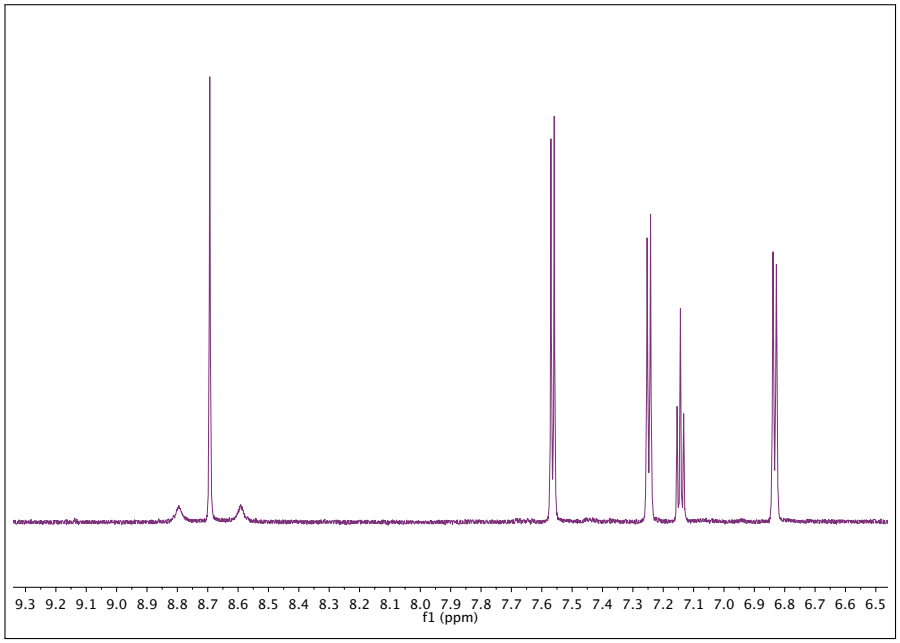

Figure 3.3: ^1H NMR spectrum of the aromatic region of PtL^{9}STol in DMSO-d_6, run at 700 MHz.

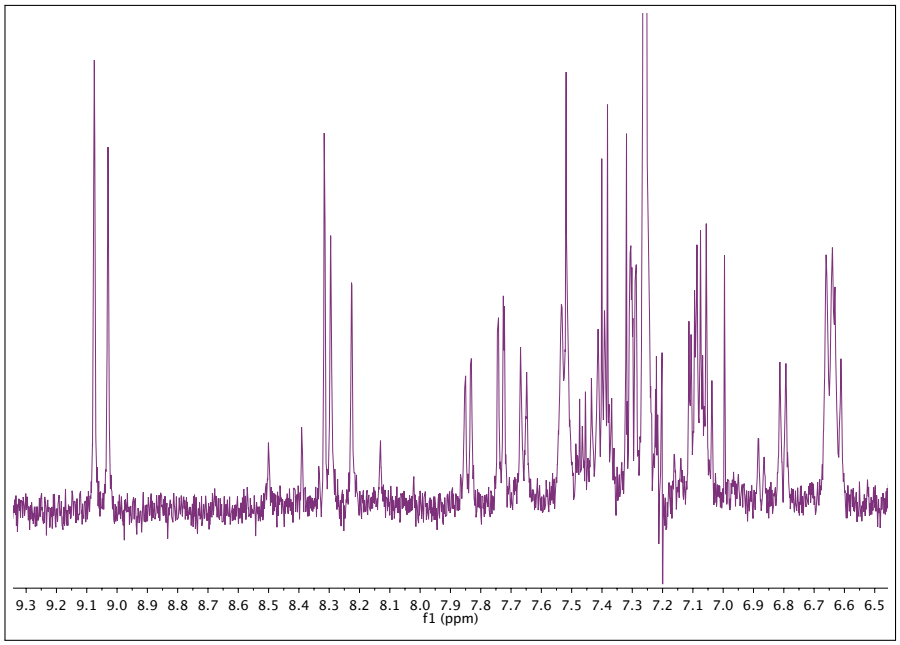

Figure 3.4: ^1H NMR spectrum of the aromatic region of PtL^{9}STol in $CDCl_3$, run at 400 MHz, within 20 minutes of the sample being prepared.

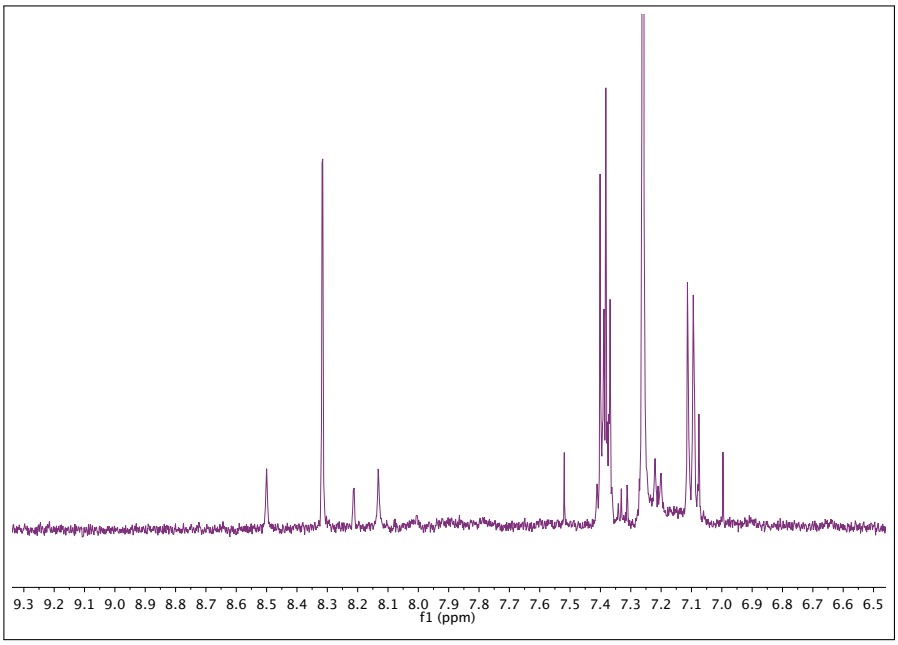

Figure 3.5: ^{1}H NMR spectrum of the aromatic region of PtL^{9}STol in $CDCl_3$, run at 400 MHz, after 72 hours (from the same sample as for Figure 3.4).

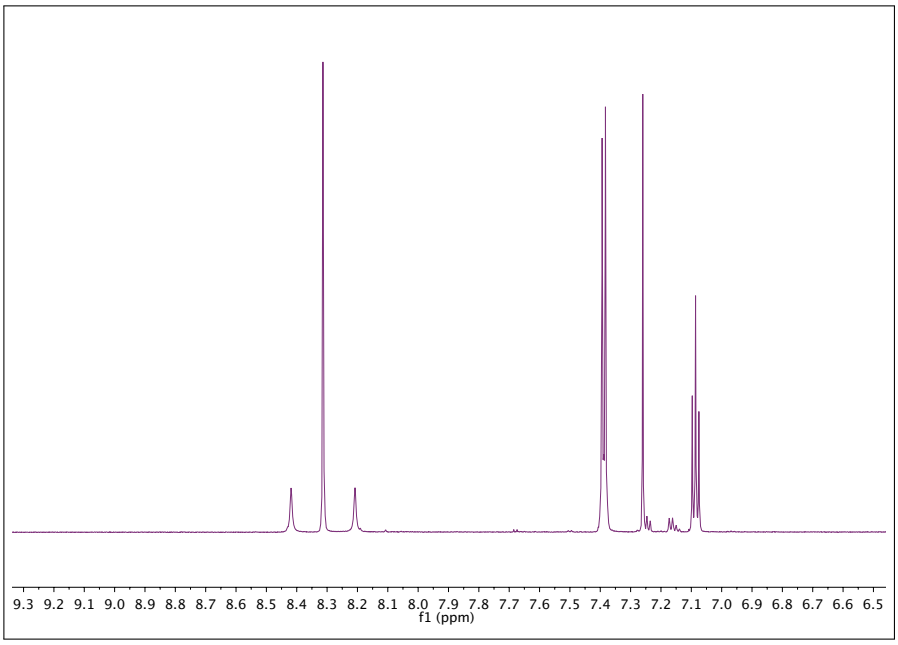

Figure 3.6: ^{1}H NMR spectrum of the aromatic region of PtL^{9}Cl in $CDCl_3$ run at 700 MHz.

Solid state ASAP allowed for analysis of the compounds by mass spectrometry without decomposition complications that had previously been observed using electrospray ionisation. It also had the added advantage of a lower susceptibility to fragmentation, enabling observation of molecular ion peaks with the thiolate ancillary ligand still bound.

3.3 Electrochemistry of PtL$^{5/8}$SR

The PtL^{5}SR and PtL^{8}SR series of compounds were studied electrochemically to investigate their ground-state redox potentials by cyclic voltammetry. Measurements were taken of each compound in a solution of DCM, in the presence of Bu_4NPF_6 (0.1 M) as the supporting electrolyte. The values obtained can be seen in Table 3.1, relative to the ferrocene | ferrocenium couple (Fc | Fc^+) under the same conditions.

In the region -0.4 to $+0.3$ V all of the complexes exhibit a well-defined, irreversible oxidation wave. In each case, this oxidation wave is cathodically shifted from the parent, chloro-substituted complex (values for which are also shown in Table 3.1). The trend in oxidation potentials of the four aryl thiolate complexes (R = OMe < Me < H < NO_2) qualitatively reflects the electron-donating character of the thiolate substituent (R = OMe > Me > H > NO_2). Of the thiolate series, the two methanethiolate complexes are the most readily oxidised ($E_p{}^{ox}$ ∼0.35 V). The PtL^{8}SR series exhibits a small cathodic shift from the PtL^{5}SR series.

A reduction wave is also displayed by all of the aryl thiolate complexes at ~ -1.45 V. At high scan rates the wave is partially reversible, with peak-to-peak separation of 200 − 300 mV. At lower scan rates, < 100 mV s^{-1}, the return wave becomes poorly defined.

A number of studies, particularly by Eisenberg *et al.*[197 198 199 200] and by Weinstein *et al.*,[201 202 203 204] have investigated related complexes of the form Pt(N^N)(S^S), (where N^N represents a diimine ligand such as bipyridine and S^S a chelating dithiolate or two mono-dentate thiolate ligands). It is interesting to compare

	$E_p{}^{ox}-E_{1/2}{}^{red}$	$E_p{}^{ox}$ /V$^{(b)}$	$E_{1/2}{}^{red}$ / V$^{(b)}$ (/ mV)
PtL^{5}SMe	1.72	−0.36	−1.36
PtL^{5}SPh	1.36	−0.03	−1.39 (240)
PtL^{5}STol	1.26	−0.10	−1.36 (220)
PtL^{5}SAni	1.35	−0.12	*(c)*
PtL^{5}SNit	1.62	+0.26	−1.36
			−1.73 (160)
PtL^{8}SMe	-	−0.35	*(c)*
PtL^{8}SPh	1.37	−0.07	−1.44 (290)
PtL^{8}STol	1.27	−0.11	−1.38 (280)
PtL^{8}SAni	1.21	−0.22	−1.43 (250)
PtL^{8}SNit	1.58	+0.13	−1.45 (200)
			−1.87 (90)

Table 3.1: (b) Using Bu_4NPF_6 (0.1 M) as the supporting electrolyte. Peak potentials are given for the oxidations, all of which were irreversible, and for those reductions where the return wave was poorly defined. For reductions showing return waves, the quoted values refer to $E_{1/2}$ and the peak-to-peak separation is given in parenthesis. Values refer to a scan rate of 100 mV s^{-1}, and are quoted relative to Fc^+ | Fc. (c) The reduction wave was poorly defined for this complex.

these studies with the thiolate systems described above. They also show an irreversible oxidation process and one or two reversible (or partially reversible) reduction processes. Similar results have been reported for terpyridyl analogues of the form Pt[(N^N^N)SR]$^+$.[205] In-depth studies using EPR, resonance Raman spectroscopy and TD-DFT calculations indicate that the reduction is based predominantly on the diimine ligand. The oxidation meanwhile involves the metal and thiolate ligands instead.[206]

3.4 Photophysical properties of the complexes

3.4.1 Absorption

Within a few minutes of addition of the chloro-complex to potassium thiolate solution, a dramatic deepening in colour was observed from the pale, yellow, chloro-complex to an intensely red, orange or yellow thiolate complex, indicating a significant change in the absorptive properties of the compound. The spectral origins of this can be observed by comparison of the energy of UV-vis absorption bands of $PtL^{5/8}SR$ and of $PtL^{5/8}Cl$ (Figure 3.7 and Table 3.2): the thiolate complexes absorb much further into the red region of the spectrum than the chloro-complexes. Comparison of PtL^8SPh to PtL^8Cl shows that while both display common intense bands in the far UV (λ_{max} = 380 nm for PtL^8Cl and 373 nm for PtL^8SPh), the longest wavelength spin-allowed band in PtL^8Cl is a shoulder (397 nm) while the thiolate, PtL^8SPh, has a well defined, intense, broad band centred at 465 nm, with no equivalent transition in the PtL^8Cl spectrum.

PtL^5SR and PtL^8SR

Comparison of the absorption spectra within the PtL^5SR series reveals a marked difference between the nitro substituted compound, PtL^5SNit, and the other four which are all very similar to one another (Figure 3.8). In the case of the nitro complex, the low energy region of the spectrum shows a very intense band at 415 nm (ε = 17100 M^{-1} cm^{-1}) which probably incorporates the bands of the type displayed in this region by the other four complexes, suggesting that there must be one extra, very intense transition in PtL^5SNit. Other complexes incorporating 4-nitrophenylthiolate with other metal ions have exhibited similarly intense bands in the same region of the absorption spectrum.[207] The same pattern is seen for the PtL^8SR series, the spectra of which are better defined in the low-energy region and slightly red-shifted compared to their PtL^5SR analogues. The aryl-substituted thiolates, excluding the nitro, increase in λ_{max} in the order:

phenyl < tolyl < anisyl

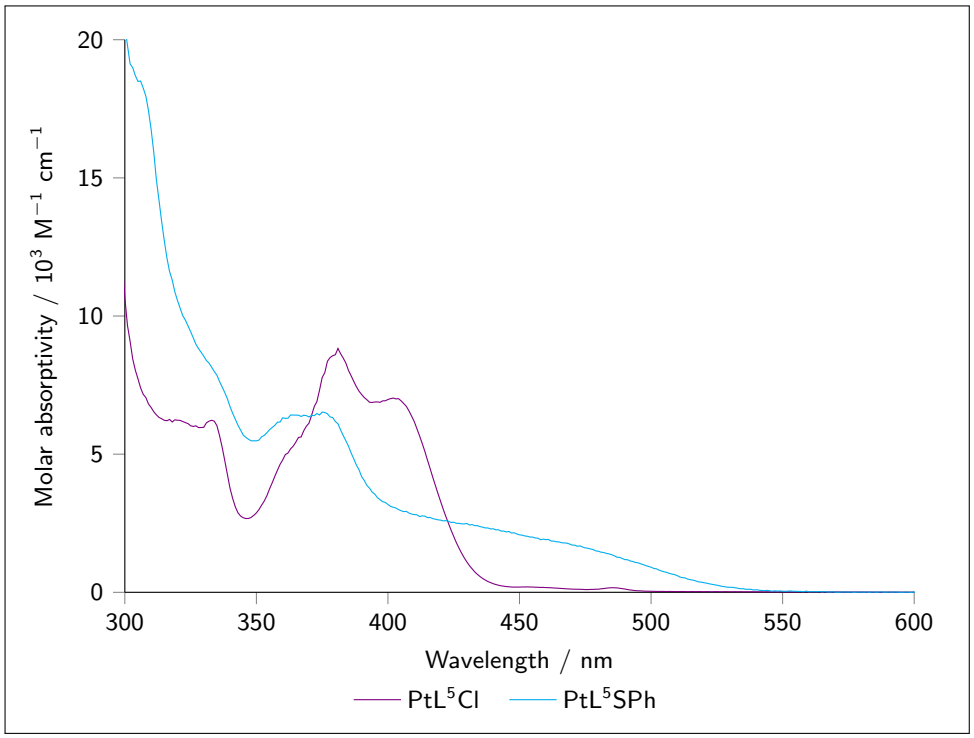

Figure 3.7: Absorption spectra of PtL^{5}Cl and PtL^{5}SPh in DCM at 298 K.

PtL^{6}SR and PtL^{7}STol

Figure 3.9 shows the absorption spectra of PtL^{6}STol and PtL^{6}Cl with maxima and extinction coefficients shown in Table 3.3. PtL^{6}STol absorbs further into the red region of the spectrum than PtL^{5}SR or PtL^{8}SR, tailing off at around 600 nm. The same is true of PtL^{7}STol which shows a very similar, though slightly more structured, absorption spectrum (Figure 3.10).

Figure 3.9 shows that while the absorption spectrum of PtL^{6}SNit is red-shifted from PtL^{6}Cl, its absorption does not extend nearly so far into the red region of the spectrum as PtL^{6}STol. The strongly absorbing band at 414 nm is essentially the same position as that of PtL^{5}SNit at 415 nm although without the shoulder displayed by the latter.

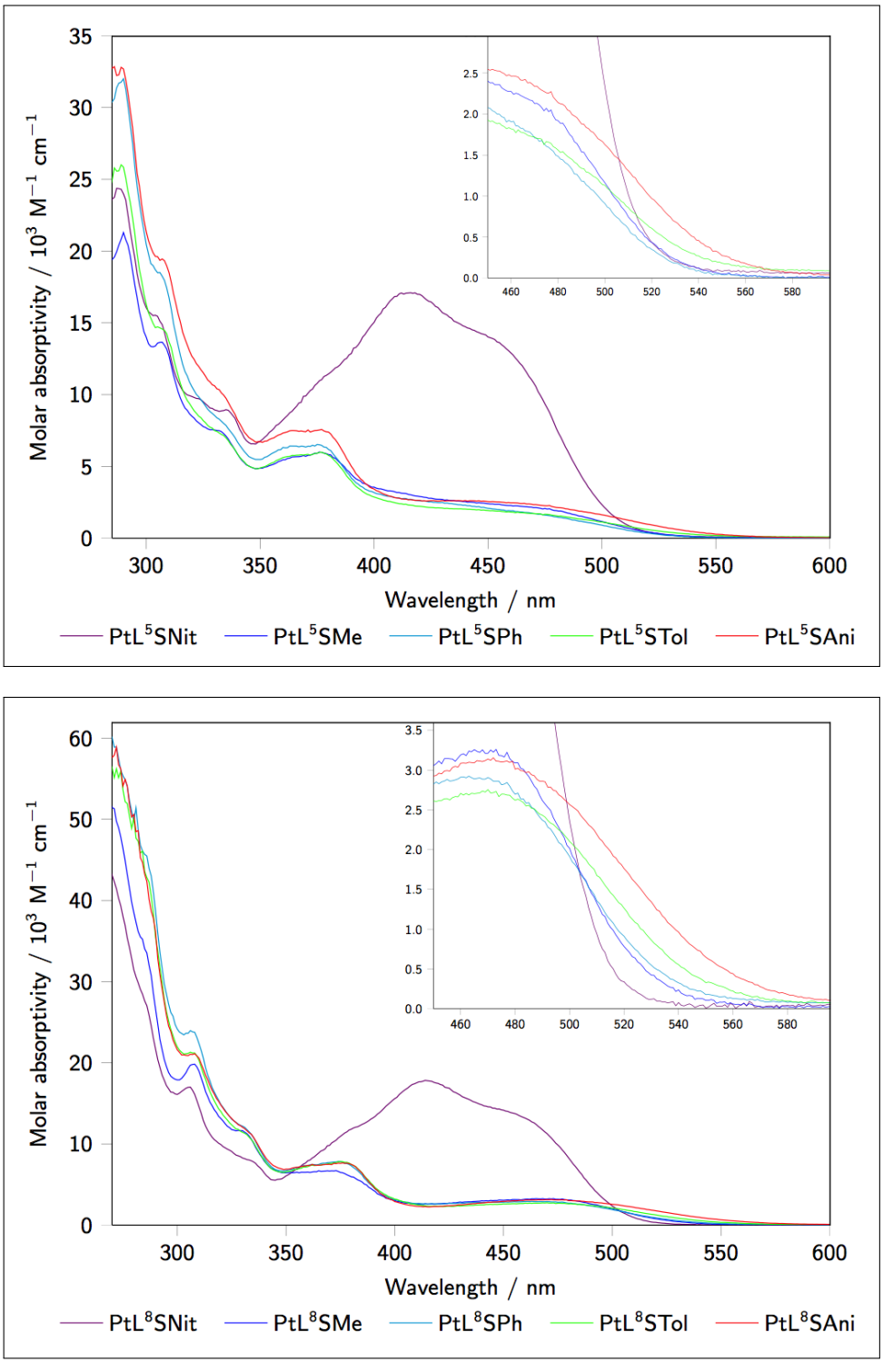

Figure 3.8: Absorption spectra of PtL^{5}SR (top) and PtL^{8}SR (bottom) in DCM at 298 K.

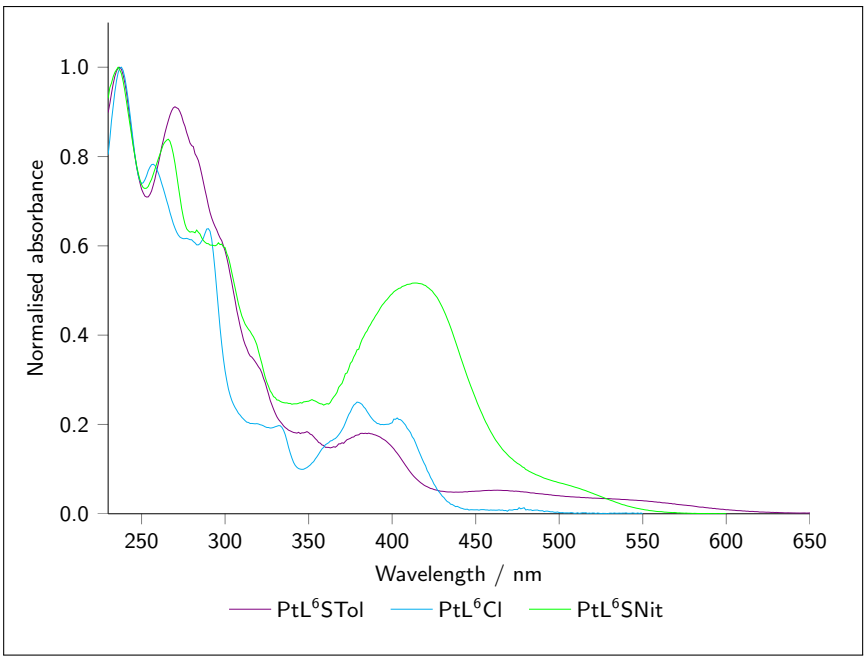

Figure 3.9: Absorption spectra of PtL^{6}Cl, PtL^{6}STol and PtL^{6}SNit in DCM at 298 K. The spectra have been normalised to the same absorbance at the high energy band ∼240 nm for ease of comparison.

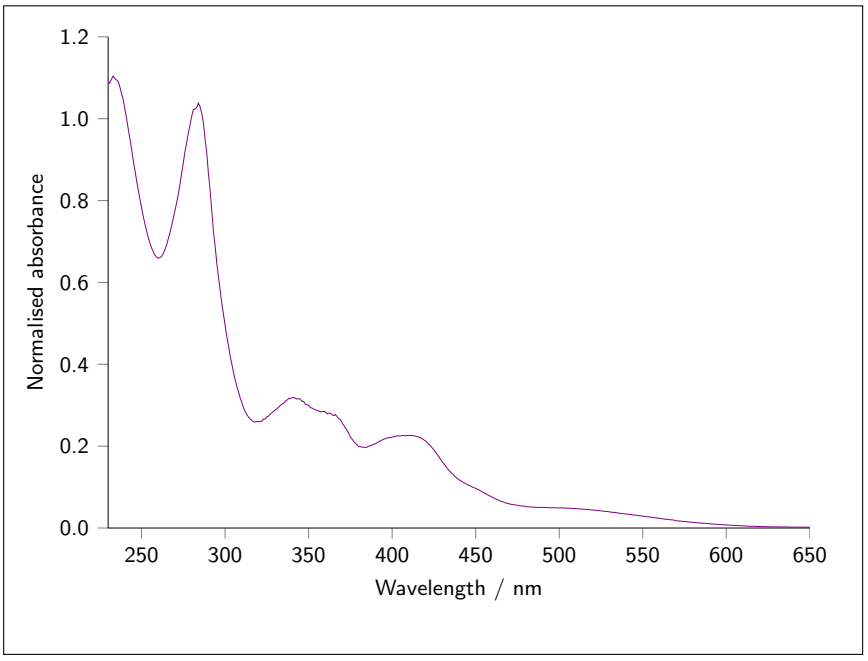

Figure 3.10: Absorption spectrum of PtL^{7}STol in DCM at 298 K.

	Absorption λ_{max} /nm [(a)] (ε /M^{-1} cm^{-1})
PtL^{5}Cl	332 (6510), 380 (8690), 401 (7010), 454 (270), 485 (240)
PtL^{5}SMe	332 (7490), 365 (5660), 377 (5980), 465*sh* (2210)
PtL^{5}SPh	363 (6420), 376 (6510), 452 *sh* (2040)
PtL^{5}STol	363 (5700), 377 (5990), 460 *sh* (1820)
PtL^{5}SAni	365 (7490), 377 (7580), 463 *sh* (2450)
PtL^{5}SNit	305 (15500), 335 (8950), 376 *sh* (11000), 415 (17100), 455 *sh* (13600)
PtL^{8}Cl	329 (7560), 380 (9990), 397 (7880), 446 (180), 478 (200)
PtL^{8}SMe	307 (19800), 330 *sh* (11600), 369 (6690), 468 (3250)
PtL^{8}SPh	330 *sh* (12200), 360 (7350), 373 (7780), 465 (2890)
PtL^{8}STol	332 *sh* (11100), 362 (7380), 375 (7820), 469 (2720)
PtL^{8}SAni	332 *sh* (11600), 362 (7490), 376 (7660), 472 (3150)
PtL^{8}SNit	305 (17000), 333 *sh* (8030), 378 (11500), 415 (17800), 455 *sh* (13800)

Table 3.2: UV-vis absorption data for the PtL^{5}SR and PtL^{8}SR series of compounds and their chloro-analogues (for reference) at 298 K in DCM. (a) Absorption maxima > 300 nm.

PtL^{9}SR

The absorption spectra of PtL^{9}Cl and its thiolate derivatives PtL^{9}STol and PtL^{9}SNit are shown in Figure 3.11. The lowest energy absorption band of PtL^{9}SNit is strongly absorbing with a λ_{max} of 423 nm and a shoulder at 470 nm - in essence it is very similar to the absorption spectra of the other related nitro compounds. The absorption spectrum of the tolyl-substituted analogue is much more blue-shifted than PtL$^{5/8}$STol; it shows similar wavelengths of absorption as PtL^{9}Cl, though the spectrum is much less structured. Complexes of L^9 show the largest difference between λ_{max} of the lowest energy band for their nitro and tolyl thiolate complexes of any of the complexes discussed.

	Absorption λ_{max} /nm [(a)] (ε /M^{-1} cm^{-1})
PtL^{6}STol	237 (71200), 270 (65900), 295 *sh* (45800), 319 *sh* (23400), 349 (11600), 386 (11700), 461 (3660), 530 *sh* (2380)
PtL^{6}SNit	236 (41800), 266 (35700), 283 (26500), 296 (25500), 316 *sh* (17100), 352 (10900), 414 (22600), 497 *sh* (3180)
PtL^{7}STol	234 (110000), 284 (105000), 341 (30400), 362 *sh* (25600), 410 (20400), 450 *sh* (6230), 502 *sh* (6390)
PtL^{9}STol	259 *sh* (37300), 270 *sh* (32900), 372 *sh* (4670)
PtL^{9}SNit	252 (20900), 290 *sh* (7590), 339 (6750), 425 (13800), 466 *sh* 11600

Table 3.3: UV-vis absorption data for PtL^{6}SR, PtL^{7}STol and PtL^{9}SR at 298 K in DCM. (a) Absorption maxima > 230 nm.

3.4.2 Luminescence

Emission of PtL^{5}SR and PtL^{8}SR

The emission properties of the PtL^{5}SR and PtL^{8}SR series, measured by William Tarran,[196] are summarised in Table 3.4 and the luminescence spectra at 298 K in DCM are shown in Figure 3.12. All 12 compounds are luminescent in solution, at room temperature, upon excitation with high energy light. Exchange of the chloride ancillary for a thiolate (PtL$^{5/8}$Cl to PtL$^{5/8}$SR) alters the nature of the emission spectrum from highly structured in the green region of the spectrum to broad and red-shifted to the deep red part of the spectrum. The λ_{max} of emission decreases between the complexes in the order:

PtL^{5}Cl > PtL^{5}SPh > PtL^{5}SMe > PtL^{5}STol > PtL^{5}SAni > PtL^{5}SNit

The same pattern is shown for the PtL^{8}R series with one exception: PtL^{8}SMe (λ_{max} = 642 nm) and PtL^{8}SPh (λ_{max} = 643 nm) swap order, but the differ-

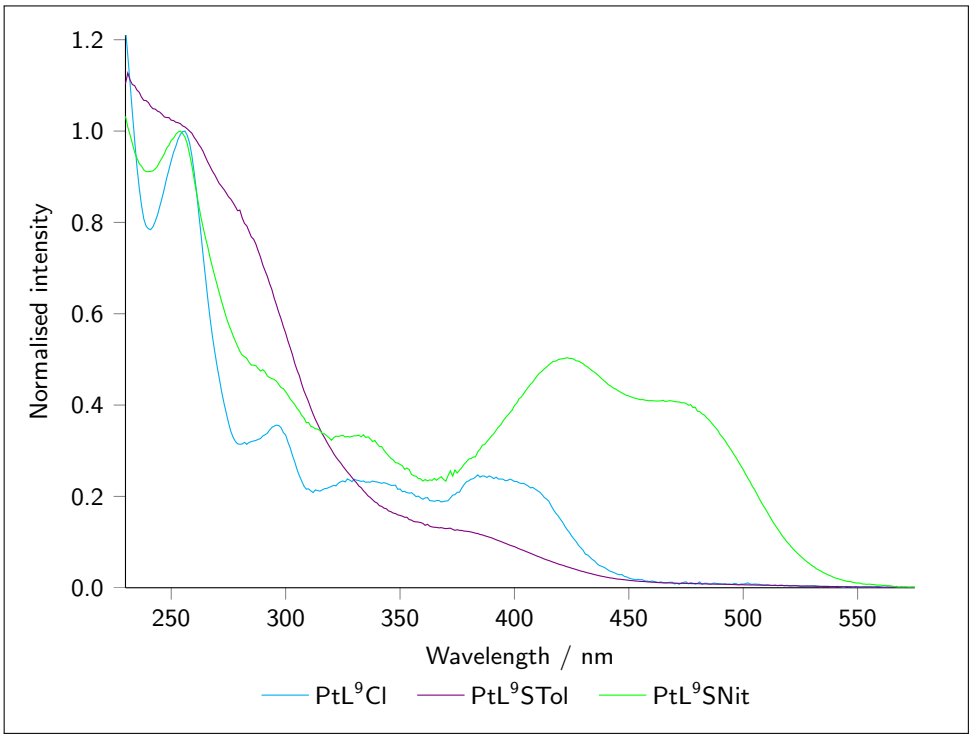

Figure 3.11: Absorption spectra of PtL^{9}Cl, PtL^{9}STol and PtL^{9}SNit in DCM at 298 K. The spectra have been normalised to the same absorbance at the high energy band ~255 nm for ease of comparison.

ence in magnitude between the two is negligible. Comparison of PtL^{5}Cl with PtL^{5}SPh shows that, as well as the loss of vibrational structure and red shift in the emission spectrum of the thiolate complex, the quantum yield is significantly reduced (from 0.60 to 0.17) and the lifetime decreased by an order of magnitude (7.2 μs to 0.77 μs). Though the thiolate quantum yield is significantly reduced from PtL^{8}Cl, 0.17 is still exceptionally high for a compound emitting in such a deeply red region of the spectrum (634 nm). The energy gap law states that as the excited state energy decreases (or wavelength of emission increases), the rate of non-radiative decay of a complex will increase exponentially. The same pattern is shown for the PtL^{8}SR series. With the exception of the two nitro-substituted compounds, the thiolate complexes of L^8 are red-shifted compared to the corresponding L^5 analogues. The nitro-substituted complexes, PtL^{5}SNit and PtL^{8}SNit, have much longer lifetimes than the other aryl thiolates:

$$\mathbf{PtL^{5/8}SNit \gg PtL^{5/8}SPh > PtL^{5/8}STol > PtL^{5/8}SAni}$$

The luminescence quantum yields follow the same order as the lifetimes, with the exception of the nitro-compounds, which have small quantum yields despite their long lifetimes. The radiative rate constants of the nitro complexes are two or three orders of magnitude smaller than the other thiolate complexes. Table 3.4 also shows that the emission of all ten thiolate complexes is blue shifted at 77 K compared to room temperature measurements, and that the largest shift is displayed for the $PtL^{5/8}SNit$ complexes. Finally, it can be seen that the emission spectrum of PtL^5SMe is essentially the same as that of PtL^5SPh (the same is true of the PtL^8SR series) but that the methyl substituted compound exhibits much weaker emission, with a lower quantum yield, and a shorter lifetime.

Emission of PtL^6SR, PtL^7STol and PtL^9SR

All five of the new complexes were luminescent at 77 K in EPA glass and all except PtL^6STol emitted in solution at 298 K (Table 3.5). Selected excitation spectra are shown in the Appendix (Figure 9.4). As with the PtL^5SR and PtL^8SR compounds, low temperature emission was blue-shifted from that at room temperature. PtL^9STol appeared to decompose particularly quickly in solution so it was not possible to obtain a complete set of measurements for this compound and the quantum yield shown was measured in aerated solution to prevent decomposition during degassing.

Figure 3.13 shows that upon substitution of the chloride ligand by STol, the emission changed from highly structured to broad and red-shifted, as for PtL^5SR and PtL^8SR. The quantum yields were also reduced by more than an order of magnitude, so much so in the case of PtL^6STol that no room temperature emission was observed. The emission wavelength of these three compounds increases in the order:

$$\mathbf{PtL^9STol < PtL^7STol < PtL^6STol}$$

Both PtL^6SNit and PtL^9SNit are red-shifted from their chloro-analogues, but while PtL^9SNit is red-shifted from PtL^9STol, PtL^6SNit is blue-shifted from

	Emission λ_{max} / nm	Φ_{lum} $\times 10^2$	τ / ns degassed	$k^Q{}_{O_2}$ / 10^8 $M^{-1}s^{-1}$ (b)	k_r / 10^3 s^{-1} (c)	Σk_{nr} / 10^4 s^{-1} (c)	Emission 77 K λ_{max} / nm	τ / μs
PtL^{5}Cl	491, 524, 562	60	7200	9.1	83	5.5	486, 516, 548	6.4
PtL^{5}SMe	636	2.6	430	54	60	230	538	6.6
PtL^{5}SPh	634	17	770	65	220	110	539	6.8
PtL^{5}STol	661	6.9	510	53	140	180	548	7.4
PtL^{5}SAni	691	1.4	48	110	290	2100	570	8.2
PtL^{5}SNit	714	0.21	7400	2.6	0.28	13	574, 610	760
PtL^{8}Cl	481, 513, 550	58	8000	4.4	72	5.3	478, 510, 547	7.0
PtL^{8}SMe	642	3.8	510	90	75	190	558	6.6
PtL^{8}SPh	643	16	880		180	95	550	7.8
PtL^{8}STol	668	6.0	370		160	250	581	8.9
PtL^{8}SAni	701	0.35	29		120	3400	597	9.5
PtL^{8}SNit	703	0.64	11300	8.0	0.57	8.8	567, 603	470

Table 3.4: Luminescence data for the PtL^{5}R and PtL^{8}R complexes in DCM solution at 298 K and in EPA$^{(a)}$ at 77 K.

(a) EPA = diethyl ether / isopentane / ethanol, 2:2:1 v/v. (b) $k^Q{}_{O_2}$ is the bimolecular rate constant for quenching by molecular oxygen at 298 K, estimated from the relative emission intensities in degassed and aerated solutions, assuming [O_2] at 1 atm pressure of air = 2.2 mmol dm^{-3}. (c) k_r and Σk_{nr} are the radiative and non-radiative rate constants estimated from the quantum yield and lifetime at 298 K.

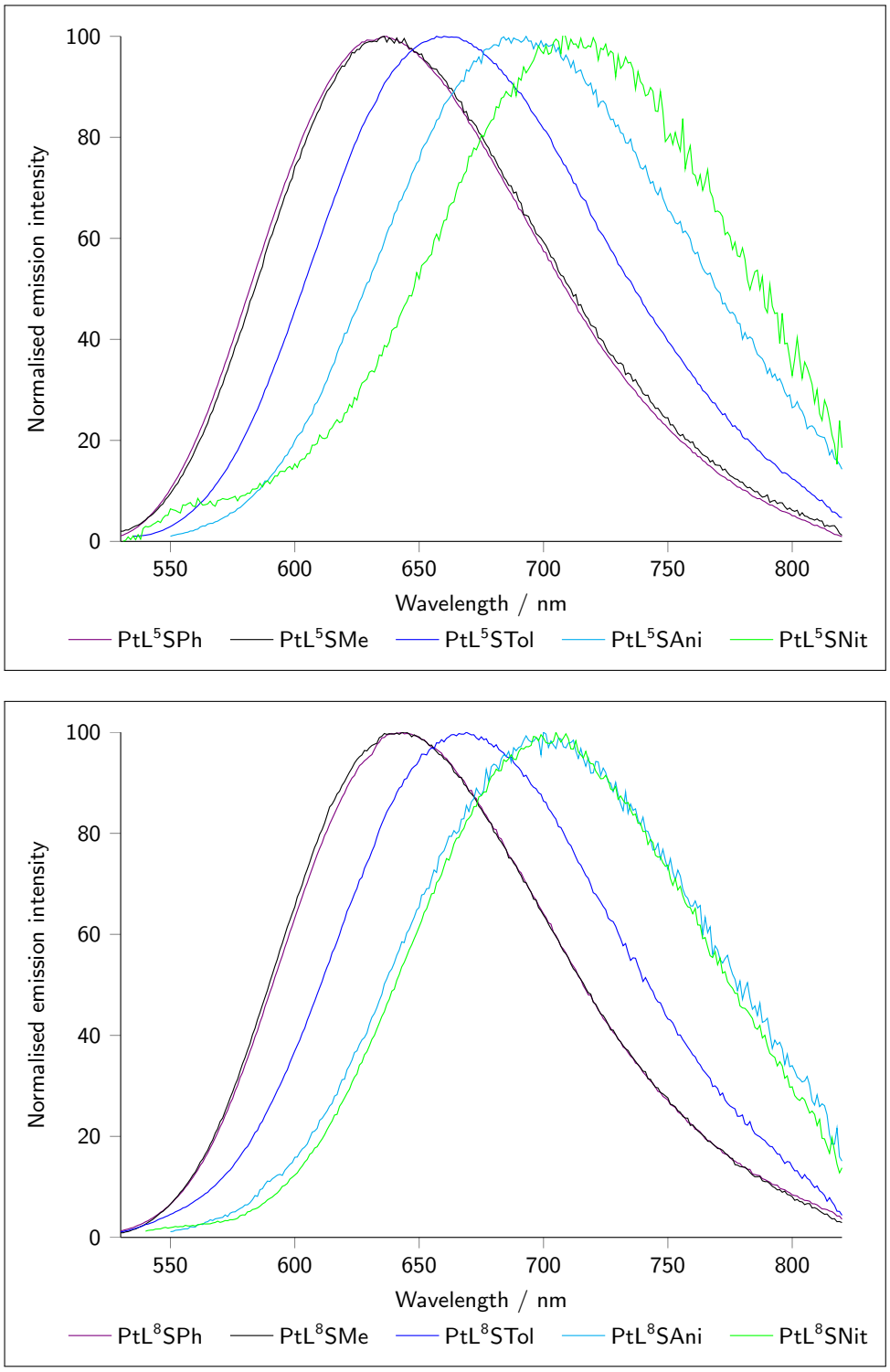

Figure 3.12: Normalised emission spectra of PtL^{5}SR (top), and PtL^{8}SR (bottom) in DCM at 298 K.

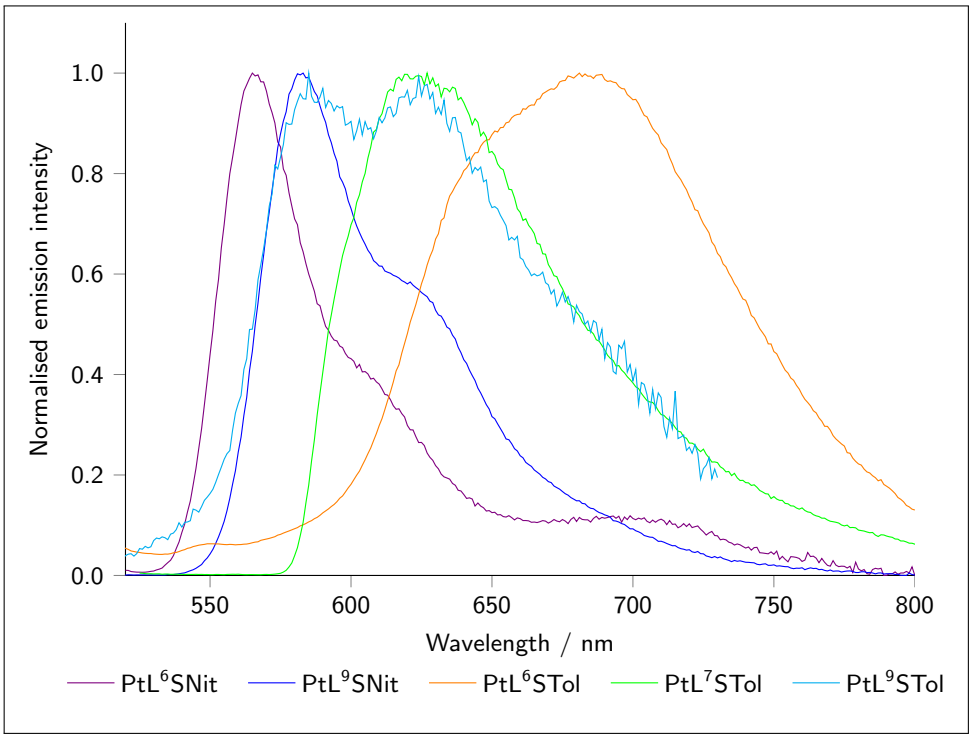

Figure 3.13: Normalised emission spectra of PtL^{6}SR, PtL^{7}STol and PtL^{9}SNit in EPA glass at 77 K. PtL^{9}STol is in aerated DCM at 298 K.

PtL^{6}STol. PtL^{6}SNit is the only complex in either series whose low temperature lifetime (850 ns in EPA glass) is shorter than at 298 K (9700 ns in a degassed solution of DCM).

3.4.3 Solvatochromism of PtL$^{5/8}$SPh and PtL$^{5/8}$SNit

The effect of solvent on the absorption and emission properties of PtL^{8}SPh (Figures 3.14 and 3.15) and PtL^{8}SNit (Figures 3.16 and 3.17) was investigated in the course of this project (Table 3.6). PtL^{8}SPh displays negative solvatochromism in the low energy absorption band (Figure 3.14): the λ_{max} shifts from 494 nm in toluene, to 453 nm in acetonitrile. In contrast, the intensely absorbing, low energy band at ~415 nm of PtL^{8}SNit, shows little evidence of solvatochromism (Figure 3.16).

	Emission λ_{max} / nm	Φ_{lum} $\times 10^2$	τ / ns degassed [aerated]	$k^Q{}_{O_2}$ / 10^8 $M^{-1}s^{-1}$ (b)	k_r / 10^3 s^{-1} (c)	Σk_{nr} / 10^4 s^{-1} (c)	Emission 77 K λ_{max} / nm	τ / μs
PtL^{6}Cl	518, 548	37	5000 [1000]	3.6	74	13	511, 549, 591	6.0
PtL^{6}STol							681	1.4
PtL^{6}SNit	627	25	9700 [760]	5.5	26	7.7	565, 604 *sh*	0.85
PtL^{7}Cl	592	7.2	3500		21	27	586	5.9
PtL^{7}STol	601, 646, 701	0.24	2400 [520]	6.8	0.97	41	627	0.75
PtL^{9}Cl	556, 599, 647, 719, 804	1.8	700 [310]	8.2	25	140	532, 578, 632, 692, 772	2.1
PtL^{9}STol	573, 637	0.10$^{(d)}$						
PtL^{9}SNit	725	0.45	690		6.6	150	583, 617 *sh*	290

Table 3.5: Luminescence data for PtL^{6}R, PtL^{7}R and PtL^{9}R in DCM solution at 298 K and in EPA$^{(a)}$ at 77 K. Values for PtL^{6}Cl[208] and PtL^{7}Cl[183] were taken from the literature and are shown for comparison.

(a) EPA = diethyl ether / isopentane / ethanol, 2:2:1 v/v. (b) $k^Q{}_{O_2}$ is the bimolecular rate constant for quenching by molecular oxygen at 298 K, estimated from the relative emission intensities in degassed and aerated solutions, assuming [O_2] at 1 atm pressure of air = 2.2 mmol dm^{-3}. (c) k_r and Σk_{nr} are the radiative and non-radiative rate constants estimated from the quantum yield and lifetime at 298 K. (d) In aerated solution since decomposition occurred too quickly in this case to give time for degassing.

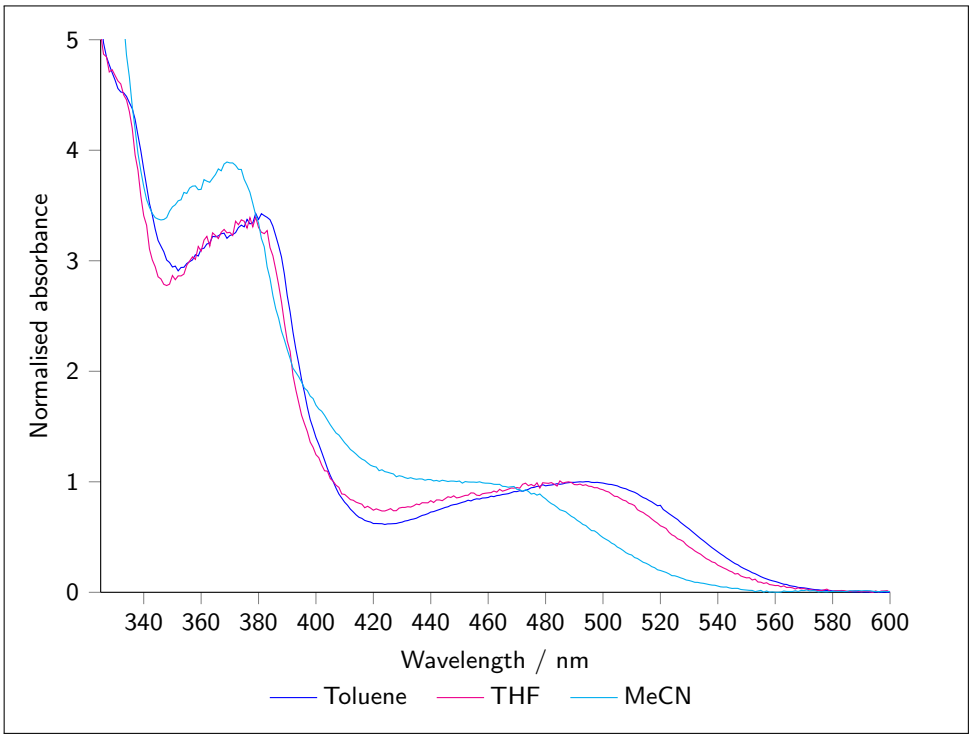

Figure 3.14: Absorption spectra PtL^{8}SPh in four solvents of varying polarity at 298 K. The spectra have been normalised to the same absorbance at longest-wavelength maximum to aid comparison.

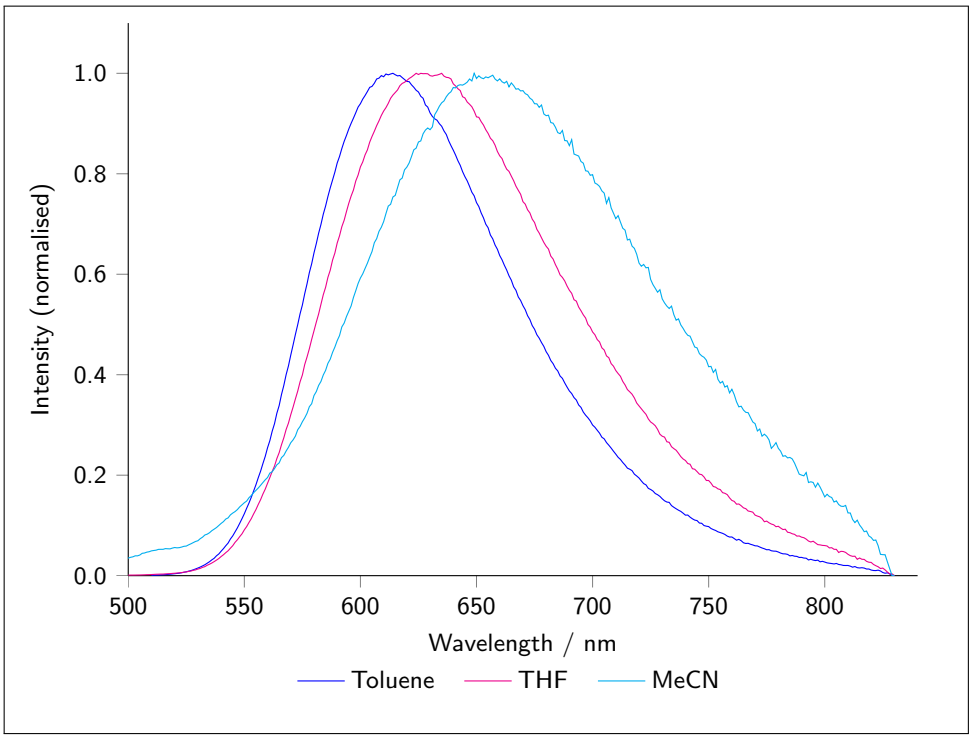

Figure 3.15: Normalised emission spectra of PtL^{8}SPh in various solvents at 298 K.

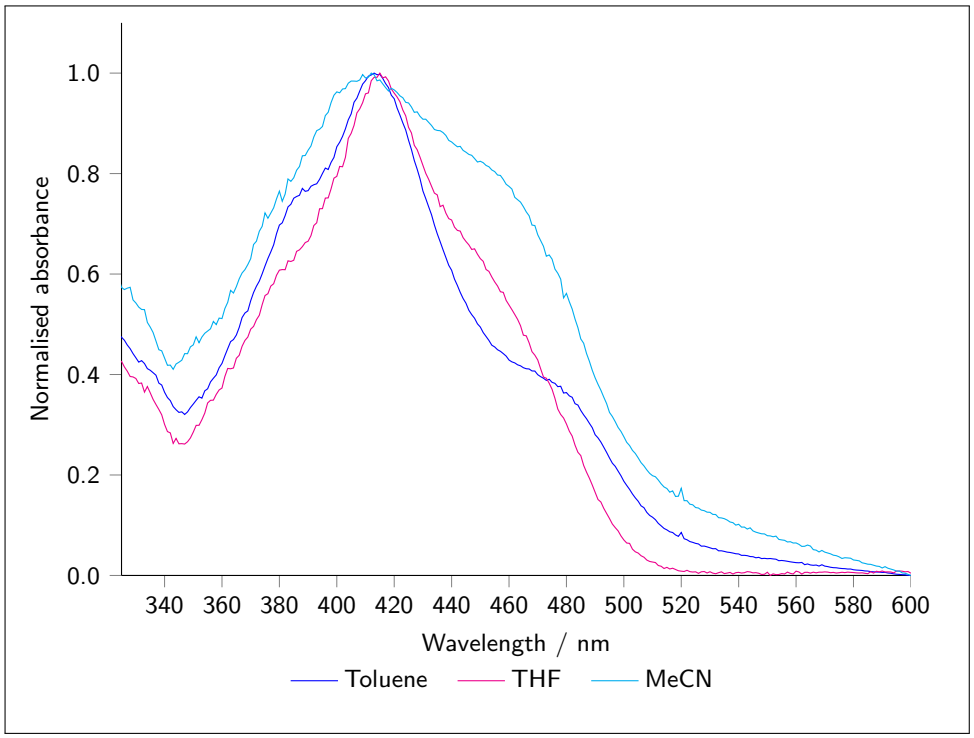

Figure 3.16: Absorption spectra PtL^{8}SNit in four solvents of varying polarity at 298 K. The spectra have been normalised to the same absorbance at longest-wavelength maximum to aid comparison.

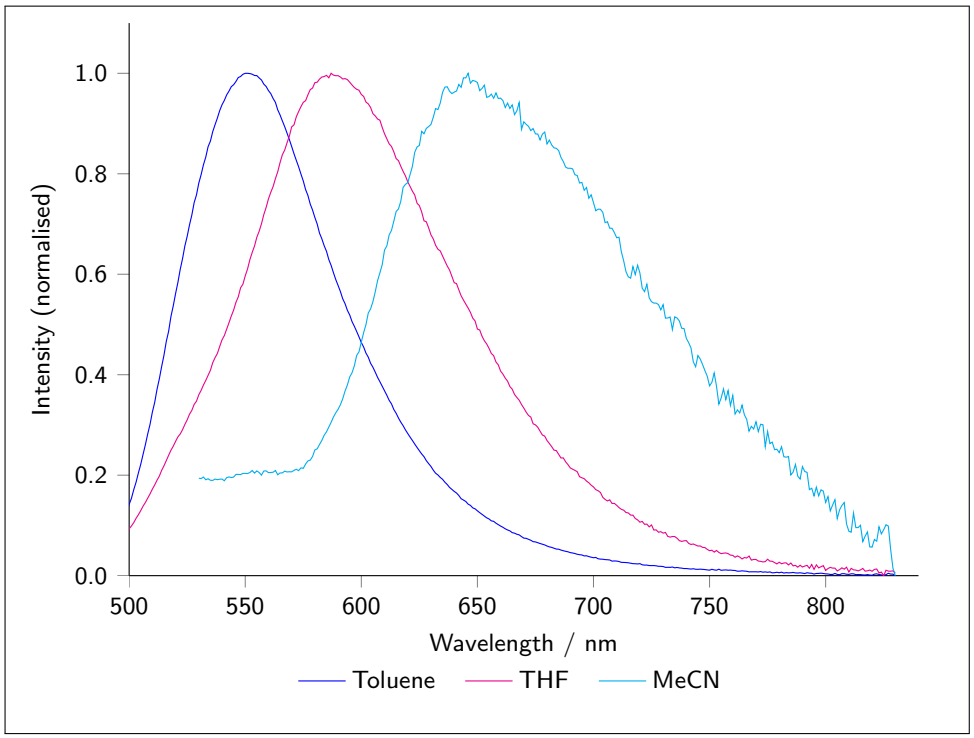

Figure 3.17: Normalised emission spectra of PtL^{8}SNit in various solvents at 298 K.

	Solvent	Emission λ_{max} / nm	Φ_{lum} $\times 10^2$	τ / ns degassed	k_r / 10^3 s^{-1} (a)	Σk_{nr} / 10^4 s^{-1} (a)
PtL^{8}SPh	Toluene	614	25	1232	21	61
	THF	624	1.6	927	170	91
	Acetonitrile	649	7.2	250	290	370
PtL^{8}SNit	Toluene	550	29	6285	46	11
	THF	587	2.7	7090	3.8	14
	Acetonitrile	646	0.36	3080	1.2	32

Table 3.6: Luminescence data for PtL^{8}SPh and PtL^{8}SNit in various solvents at 298 K (solvents shown in order of increasing polarity).

(a) k_r and Σk_{nr} are the radiative and non-radiative rate constants estimated from the quantum yield and lifetime.

3.5 TD-DFT studies and discussion of electronic properties of the complexes

In this section a summary of the final results from Chapter 4 will be given to enable discussion of the experimental results alongside analysis by TD-DFT. A more detailed discussion of the pros and cons of various methods and modelling of different parameters will then be given in the following chapter.

3.5.1 Emission

PtL^{5}SR and PtL^{8}SR

The density difference plots for the $S_0 \rightarrow T_1$ excitation at the T_1 geometry of PtL^{5}SR and PtL^{8}SR (calculated in DCM with PBE0) are shown in Figure 3.18. In general they show that there is very little difference between the plots for PtL^{5}SR and PtL^{8}SR: the ester group of PtL^{8}SR has almost no role in the excitation at all. PtL$^{5/8}$SPh, PtL$^{5/8}$STol, PtL$^{5/8}$SAni and to a lesser extent PtL$^{5/8}$SMe all show the same type of excitation: charge transfer from

the thiolate ligand to the platinum and N^C^N ligand. In contrast, the density difference plots of PtL$^{5/8}$SNit show a high overlap excitation with both electron depletion and accretion plots centred on the thiolate ligand.

A combined study of the electrochemical and photophysical properties of these complexes alongside TD-DFT studies yields insight into the nature of the excitations taking place. The density difference plots of PtL$^{5/8}$SPh, PtL$^{5/8}$STol, PtL$^{5/8}$SAni and PtL$^{5/8}$SMe show that the excited state of these complexes is $d_{Pt}/\pi_{RS} \rightarrow \pi^*_{NCN}$ in nature. This charge-transfer excited state explains many of the photophysical properties of these compounds. First, the red-shift in λ_{max} of emission for PtL^{8}SR compared to PtL^{5}SR is due to the electron-withdrawing ester group in the former, stabilising the LUMO (which is located on the N^C^N ligand and Pt metal) and reducing the energy of emission. The stabilising effect of this group is small since it is located on the central phenyl ring of the N^C^N ligand which, as shown in the density difference plots, has a low contribution to the LUMO. The increase in energy of emission upon cooling of these complexes to 77 K is consistent with a low overlap, charge-transfer excitation since reorganisation of the solvent to stabilise the excited state is not possible in frozen glass, unlike room temperature measurements. As previously mentioned, with increasing electron-donating ability of the thiolate ligand, there is a decrease in the energy of emission; the more electron-donating substituents favouring a charge transfer excitation. Consideration of the electrochemical measurements alongside the photophysical ones shows a linear correlation of the first three aryl thiolates (SPh, STol and SAni) between their emission energies and $[E^{ox}-E^{red}]$. Interestingly the nitro-substituted complex does not follow this trend (Figure 3.19). A line of best fit through these first three compounds gives a gradient of 7800 cm^{-1} /V.

Analysis of the density difference plots for PtL$^{5/8}$SNit shows a very different excitation character: the excited state is localised on the thiolate ligand with almost no involvement of the metal or N^C^N ligand. The long lifetimes and low rates of radiative decay of these complexes, despite high orbital overlap, seem therefore to be due to a low contribution of the metal in the excited state of the ILCT. This difference in character explains the discrepancies between

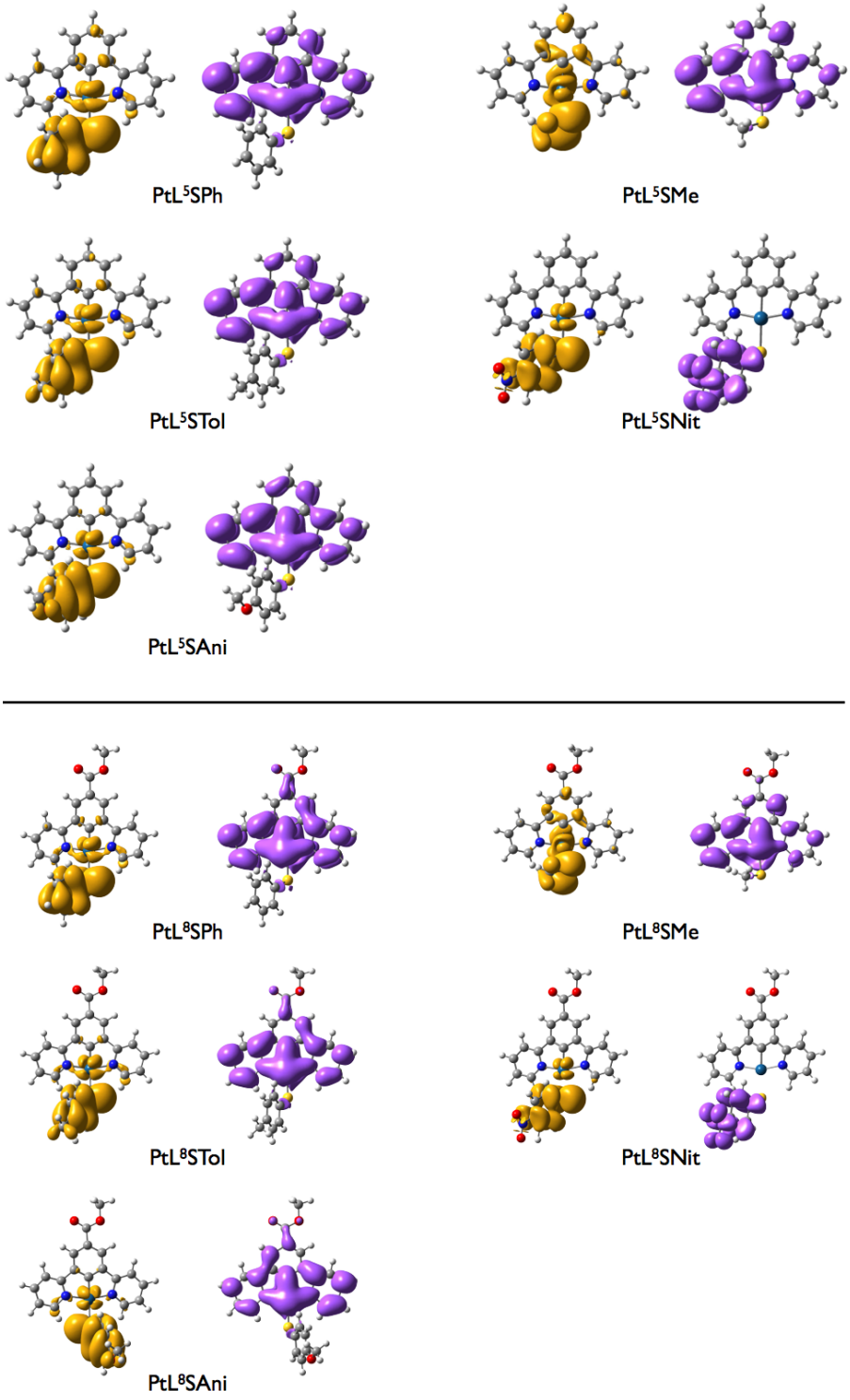

Figure 3.18: Density difference plots of the $S_0 \rightarrow T_1$ excitation at the T_1 geometry for PtL^{5}SR (top) and PtL^{8}SR (bottom), calculated with PBE0, with a PCM for DCM, basis sets: LANL2DZ for platinum and cc-pVDZ for all other atoms.

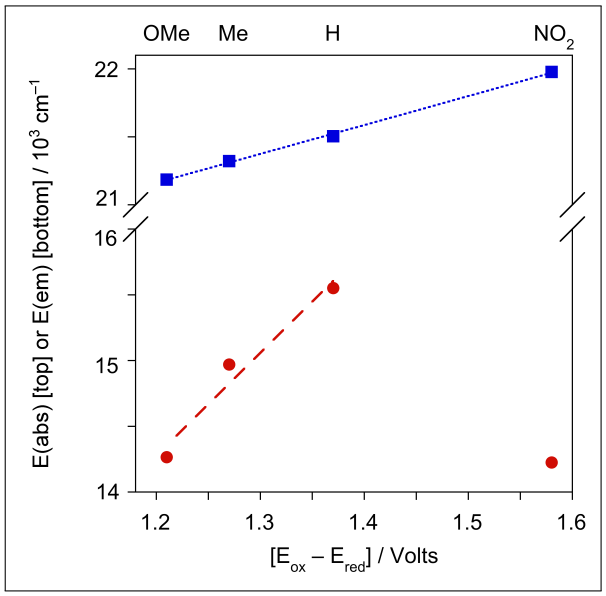

Figure 3.19: Energy of absorption(top) and emission(bottom) versus the difference between the oxidation and reduction potentials of PtL^{8}SR. The blue dotted line through the absorption data points represents the linear best fit for all four complexes, gradient = 2100 cm^{-1}/V. The red dashed line for the emission data represents the best fit for the phenyl, tolyl and anisyl complexes, but excluding the nitro analogue; gradient = 7800 cm^{-1}/V.

this compound and the others in the series in Figure 3.19. A plot of {ln k_{nr}} against the emission energy of the thiolate complexes (estimated from their emission maxima) is shown in Figure 3.20 for PtL$^{5/8}$SR. Omission of the two nitro-substituted complexes from the line of best fit shows a convincing linear relationship between the other eight complexes. PtL^{5}SNit and PtL^{8}SNit have lower k_{nr} than expected for their emission energies were a charge-transfer excited state to be adopted, providing further evidence for a difference in nature of the excitation for these two compared to the other compounds in the series.

PtL^{6}SR, PtL^{7}STol and PtL^{9}SR

The equivalent density difference plots for PtL$^{6/9}$STol and PtL$^{6/9}$SNit are shown in Figure 3.21. For the nitro-substituted complexes they show the same transition as PtL$^{5/8}$SNit: a high overlap excitation based on the thiolate ligand. The tolyl analogues show a charge-transfer excitation from the thiolate

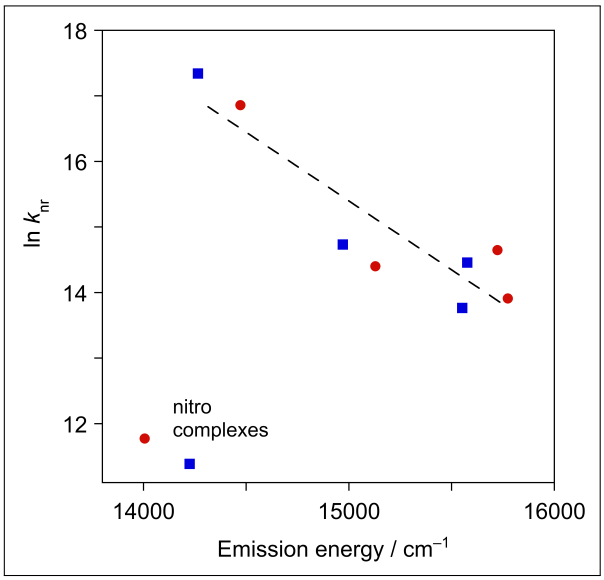

Figure 3.20: A plot to show $\{ln\ k_{nr}\}$ versus the emission energy of the PtL$^{5/8}$SR complexes. PtL^{5}SR are shown by the red circles and PtL^{8}SR by the blue squares. The line shown is the least-squares linear fit through all data points except for PtL$^{5/8}$SNit (which are shown in the bottom left corner of the graph).

ligand to the platinum and N^C^N ligand. PtL^{9}STol displays less delocalisation in the electron accretion plot than the other compounds since it has no aromatic rings, while PtL^{7}STol shows extended electron delocalisation, incorporating the quinoline groups. The electron augmentation plot of PtL^{6}STol incorporates the CF_3 groups, the electron-withdrawing nature of which should therefore affect the energy of the "LUMO".

Since the LUMO for the low-overlap, tolyl-substituted compounds is centred on the N^C^N ligand and Pt, the different ligands about platinum have a significant effect on the emission observed. The CF_3 group and delocalised electrons of the quinoline ligand (PtL^{6}STol and PtL^{7}STol respectively) stabilise the LUMO, giving a red shift in emission. In contrast, the limited delocalisation over the imine ligand, combined with the electron-donating cyclohexyl groups of PtL^{9}STol, destabilises the LUMO giving a blue shift (Figure 3.13). The predicted red-shift in PtL^{6}STol to such a low energy is one possible explanation for lack of room temperature emission: the higher rate

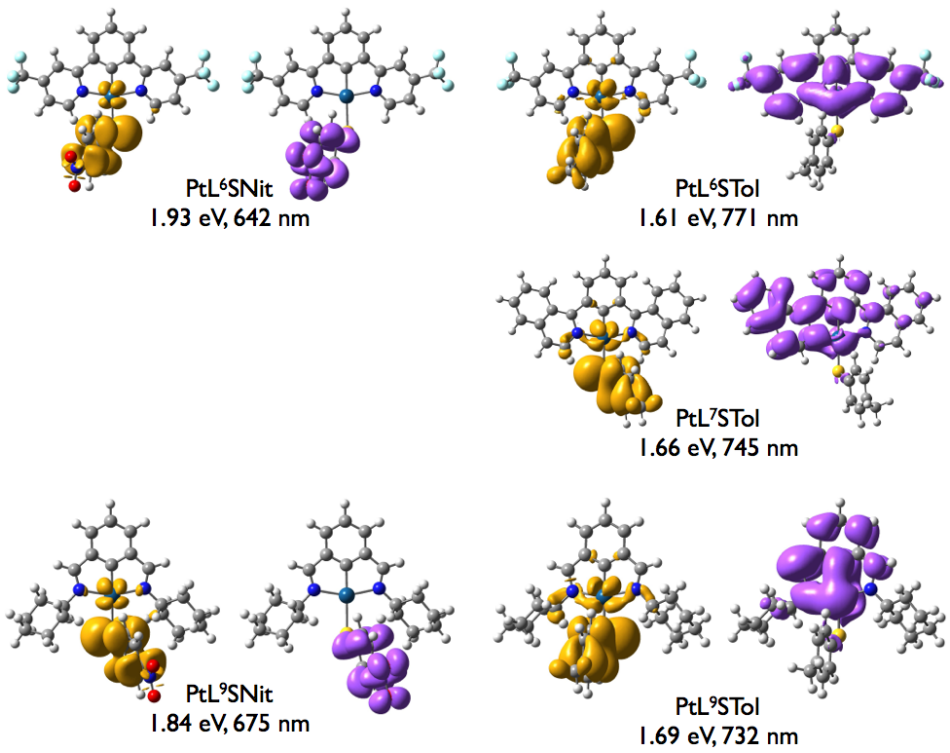

Figure 3.21: Density difference plots of the $S_0 \rightarrow T_1$ excitation at the T_1 geometry for PtL$^{6/9}$SNit, PtL$^{6/9}$STol and PtL^{7}STol in DCM.

of non-radiative decay (predicted by the energy gap law) could be inhibiting emission. Orbitals involved in emission of the two nitro-substituted complexes, PtL^{6}SNit and PtL^{9}SNit, are centred on the thiolate ligand so are less affected by the N^C^N ligand and its substituents. Like PtL$^{5/8}$SNit, PtL^{6}SNit and PtL^{9}SNit have a reduced rate of radiative decay compared to their parent chloro-compounds since there is less metal character, making the transition less allowed. The shorter lifetime of PtL^{6}SNit at low temperature, compared to room temperature, could be due to a change in the emissive state. The electron withdrawing CF_3 groups reduce the energy of the N^C^N ligand, making it closer to that of the nitro-thiolate ligand. Emission from PtL^{6}SNit at 77 K could therefore be more like the low-overlap excitation seen for PtL^{6}SNit.

3.5.2 Absorption

The new band introduced in the low energy region of the thiolate-complex absorption spectrum can be rationalised as a new low-energy charge-transfer state, also reported in related diimine complexes.[206] The electron rich sulfur is expected to give a HOMO localised over the thiolate and the metal atom. This is in contrast to the chloro ancillary complex where the most electron rich component is the metal atom and the cyclometallated carbon of the ligand. In both cases the LUMO should remain largely on the pyridyl rings of the N^C^N ligand. TD-DFT calculations on PtL^{8}SPh showed this to be the case; $S_0 \rightarrow S_1$ and $S_0 \rightarrow S_2$ excitations dominate the low energy region of the simulated absorption spectrum, their density difference plots are shown in Figure 3.22. The low energy region of the charge-transfer complex absorption spectra is dominated by this $d_{Pt}/\pi_{RS} \rightarrow \pi^*_{NCN}$, non-centrosymmetric movement of electron density, giving rise to the solvatochromic response observed.

The strongly absorbing bands present in the nitro-substituted complexes appear to be due to the addition of an ILCT excitation (Figure 3.22), explaining why no solvatotchromic response was seen for the band at 415 nm for PtL^{8}SNit. The nitro-substituted complexes also showed weaker excitations for the charge transfer-type excitation, $d_{Pt}/\pi_{RS} \rightarrow \pi^*_{NCN}$ which is the origin of the lower energy bands which did show some change in energy with polarity of solvent. The effect was not so great as for PtL^{8}SPh however since there was some ILCT character involved in the excitation.

PtL^{6}SR and PtL^{7}STol

Addition of an electron-withdrawing CF_3 group to the 4-position of each pyridine ring of PtL^{5}Cl gives PtL^{6}Cl and a red shift in the absorption spectrum.[208] This is due to the electron withdrawing nature of the CF_3 groups which stabilise the pyridyl ring-based LUMO as discussed in Chapter 4. Substitution of the Cl^- for a thiolate group, producing a complex where excitations are charge transfer in nature should then decrease the energy of the LUMO further, without affecting the position of the HOMO, shifting the ab-

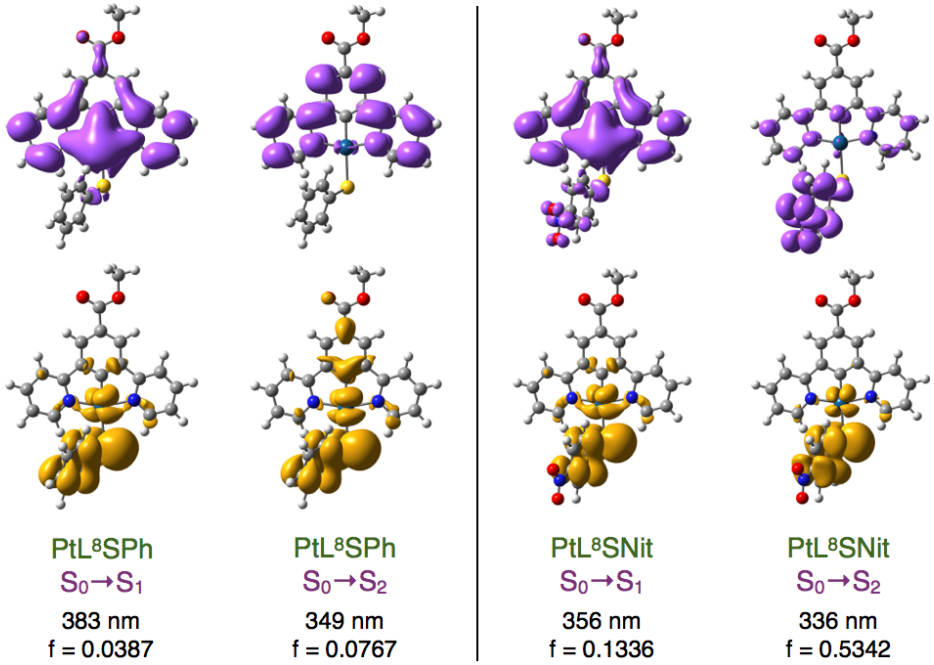

Figure 3.22: Density difference plots of the $S_0 \rightarrow S_n$ excitations at the S_0 geometry for PtL^{8}STol and PtL^{8}SNit in DCM, calculated with CAM-B3LYP, in DCM, with cc-pVDZ and LANL2DZ for Pt.

sorption even further to the red. This is indeed the case for PtL^{6}STol, the excitations are similar in nature to those of PtL^{8}STol (density difference plots for PtL^{6}STol are shown in Chapter 4). The absorption spectrum of PtL^{7}STol is similar to that of PtL^{6}STol. In this case, the LUMO is stabilised by delocalisation of electrons over extended π-conjugation. In contrast, for PtL^{6}SNit, the electron density remains on the nitro ligand upon excitation, therefore the absorption spectrum is similar to that of PtL^{5}SNit and PtL^{8}SNit, without the increase in red shift shown for PtL^{6}STol, since the CF_3 groups are uninvolved in the excitation. Density difference plots of $S_0 \rightarrow S_n$ excitations for these complexes are shown in Chapter 4.

The energies of the absorption bands of PtL^{9}STol are perhaps counterintuitive since, though a change is shown in the absorption spectrum upon

replacement of the chloride by the STol group, the absorption spectrum is blue-shifted rather than red. For the chloro complex, PtL^{9}Cl, the N^C^N ligand is involved in both the HOMO and LUMO while for PtL^{9}STol it only contributes to the LUMO. As for the emission, the electron-donating cyclohexyl groups, combined with the reduced electron-delocalisation over the imine ligand, destabilise the LUMO, compared to the other thiolate complexes, increasing the energy gap and giving the observed blue shift. Comparison of all five STol-substituted complexes shows an increase in wavelength of the lowest-energy absorption band with increasing electron-withdrawing nature of the substituent group:

$$\mathbf{PtL^9STol} < \mathbf{PtL^5STol} < \mathbf{PtL^8STol} < \mathbf{PtL^{6/7}STol}$$

3.6 Concluding remarks

We have seen that substitution of the chloro ligand of the well-known Pt(dpyb)Cl-type complexes has a profound effect on the electronic properties of the molecule. With the exception of PtL^{9}R, a red-shift in both the absorption and emission spectra is observed upon coordination of a mono-dentate thiolate ligand. The luminescence quantum yields were reduced by such a substitution but were still high for platinum(II) complexes emitting in this region of the spectrum.

In general two types of excited states were observed and assigned based on their properties and accompanying TD-DFT studies: ILCT when an electron-withdrawing, nitro-substituted thiolate ligand was coordinated and $d_{Pt}/\pi_{RS} \rightarrow \pi^*_{NCN}$ for phenyl, tolyl, anisol and methyl-substituted thiolates.

Comparison of PtL^{5}SR, PtL^{6}SR, PtL^{7}STol, PtL^{8}SR and PtL^{9}SR series allowed study of the role of the N^C^N ligand in the charge-transfer type excitations. Substitution of functional groups on the pyridine rings of this ligand allowed control over the energy of the LUMO while having little effect on the HOMO.

4

A computational study of N^C^N-coordinated Pt(II) complexes incorporating thiolate coligands

4.1 Chapter outline

Chapter 3 described the synthesis and photophysical properties of various N^C^N-coordinated platinum(II) complexes incorporating a monodentate thiolate ligand. A short summary of TD-DFT calculations performed on these molecules was presented in order to understand the excitations taking place. This chapter will now expound upon those results, showing different methods for the calculations presented and analysing their success at predicting the observed characteristics.

Given what we have seen experimentally about the photophysical behaviour of these compounds, there are three main trends we would hope to be reproducible using DFT: the difference in the type of transition of the nitro-substituted complexes, the trend in energy of emission between the compounds and finally their emission energies in different solvents. Each of these will be discussed in turn. The ten compounds of the general formulae PtL^5SR and

PtL^8SR will be discussed first and in detail, with complexes PtL^6SR and PtL^9SR considered at the end of the chapter, as test cases, to see if the principles determined hold true for a differing set of compounds.

Unless otherwise stated, DFT and TD-DFT calculations presented in this chapter were performed in vacuum, using PBE0. Where solvent is indicated, a PCM for the specified solvent was applied. The LANL2DZ basis set was used for platinum and cc-pVDZ for all other atoms. Ground state and triplet excited state geometries were optimised by direct minimisation of the SCF energy and checked to be a true minimum by frequency calculations at the same level of theory as the geometry optimisation. Convolution of absorption spectra was achieved using a 0.6 eV full-width-at-half-maximum Gaussian.

4.2 Predicting the correct transition

Chapter 3 discussed how the nitro-substituted complexes (PtL^5SNit and PtL^8SNit) showed phosphorescent emission of different character from the other compounds in the series: $PtL^{5/8}SNit$ excitations were centred on the thiolate ligand, rather than the charge transfer transitions seen for the other complexes. Naturally it is expected that this would be reflected in the orbital plots generated from DFT for the transition from the T_1 excited state to the S_0 ground state. We would expect to see from these density difference plots an excitation similar to the schematic example of high overlap shown in Figure 4.1 for $PtL^{5/8}SNit$ and the low overlap, charge transfer excitation for the other $PtL^{5/8}SR$ complexes. We will now consider the aptitude of different theoretical models for predicting the nature of these transitions.

4.2.1 Presentation of orbital plots

It is well known that, contrary to the rather simplistic explanation often used to teach the concept of emission, emission of light from T_1 to S_0 does not always involve purely the HOMO and LUMO orbitals. Instead, any given transition is usually made up of many small contributions from various other orbitals. In order for simplified visualisation of the processes occurring, the orbitals with the highest contribution to the relevant transition are usually

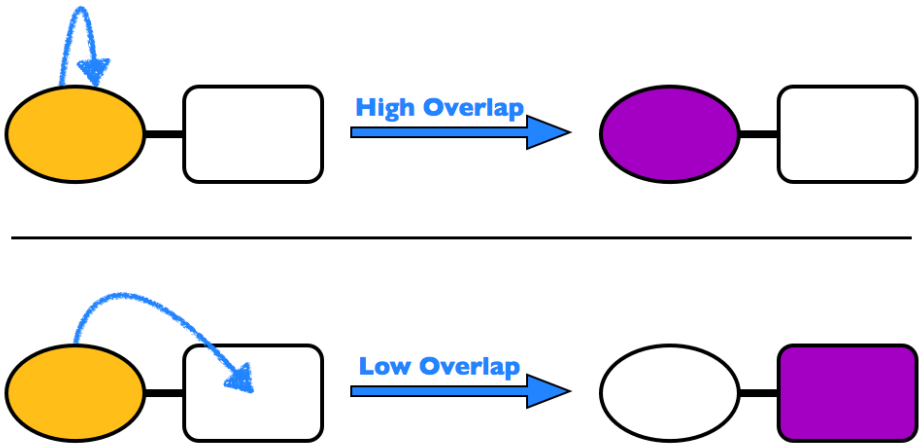

Figure 4.1: A cartoon schematic to show the types of excitations expected for the different thiolate complexes. The oval represents the thiolate ligand and the rectangle the platinum atom and N^C^N ligand. Orange and purple represent zones of electron depletion and augmentation respectively upon excitation of the molecule.

shown along with their respective contributions. The user must then attempt to manually overlay each of these in their head to understand the transition that is taking place. Figure 4.2 and Table 4.1 show the orbital plots and their relative contributions for T_1 to S_0 emission for PtL^5SPh. This can be compared to the density difference plot for the same calculation, also shown in Figure 4.2 (in the box). It can be seen that in this example case, consideration of the orbital plots alone could lead to the incorrect transition being assigned; in contrast the density difference plot clearly shows electron density rearranging, but remaining upon the thiolate ligand unambiguously. For this reason we will henceforth use density difference plots of the lowest energy triplet transition for the remainder of this discussion.

4.2.2 Predicting the correct orbital plots for the nitro compound

Initial, simplistic calculations on the PtL^5R and PtL^8R series of compounds (PBE0, cc-pVDZ and LANL2DZ) do not show the pattern in transitions that we would expect from the experimentally obtained data. While the four charge transfer-type compounds do indeed show movement of the electron from the thiolate ligand to the platinum and N^C^N ligand, this type of transition is

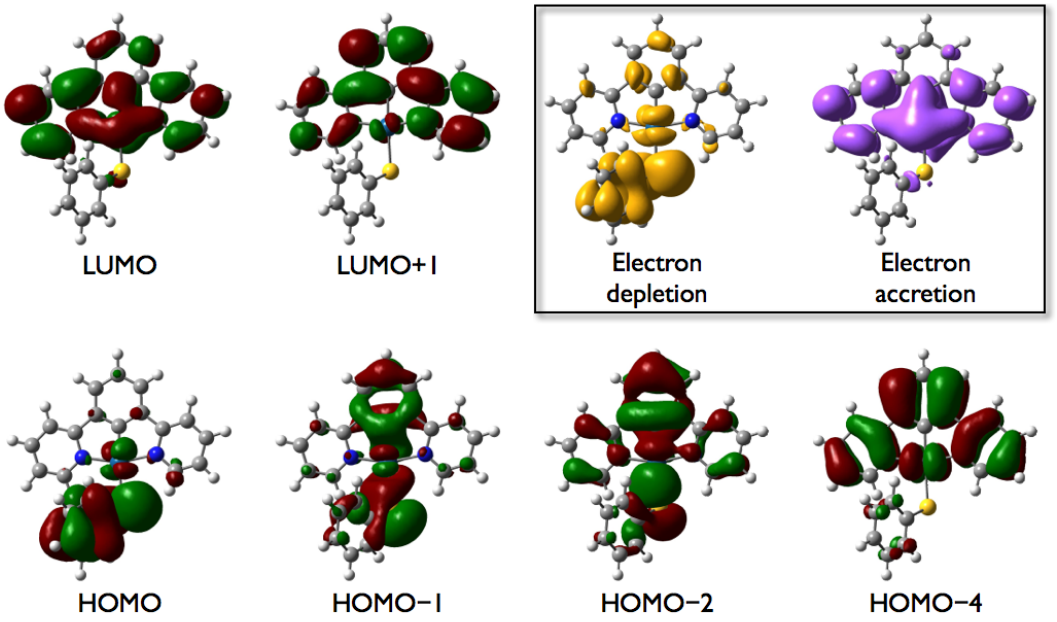

Figure 4.2: Orbital plots at the T_1 geometry for PtL^{5}SPh; PBE0 geometry, CAM-B3LYP TD-DFT.

Transition			Contribution
HOMO−4	→	LUMO+1	0.140
HOMO−2	→	LUMO	−0.159
HOMO−1	→	LUMO	−0.137
HOMO	→	LUMO	0.602
HOMO	→	LUMO+1	−0.177

Table 4.1: Orbital contributions for emission from T_1 to S_0 for PtL^{5}SPh; PBE0 geometry, CAM-B3LYP TD-DFT.

also predicted for the nitro-substituted complex. For PtL^5SNit and PtL^8SNit we would expect to see the electron density remaining on the thiolate ligand in the excited state - this ligand-centred transition would explain the lower energy of emission, the longer life times and the trends in solvatochromism. This pattern is shown in Figure 4.3 for both series, PtL^5SR and PtL^5SR.

A series of calculations were next carried out to investigate the effect of a PCM solvent model on the density difference plots observed. The results of this are shown in Figures 4.4 and 4.5 which show that such an inclusion dramatically affects the type of transition observed, as does the point at which it is included in the calculation. For the "correct" density difference plots to be observed, it is essential that the solvent of choice is included for both the geometry optimisation and the time-dependent studies. Surprisingly this is true for both the polar solvent, DCM and the non-polar hexane. It is therefore not merely the case that one state is stabilised by the presence of a particular solvent, rather that the inclusion of any solvent at all affects the results observed. We can see this effect demonstrated in a more quantitative manner by looking at the energies of the lowest triplet excitation in each case. For both solvents, performing the geometry optimisation in the solvent with the subsequent TD-DFT calculation in vacuum achieves a value much closer to the value where both calculations are in solvent than when optimisation is in vacuum and TD-DFT in solvent. In other words, looking at DCM in Figure 4.4, result (d) is more similar to (e) than to (c). Perhaps this is unsurprising since experimentally the polarity of the solvent can cause a different excited state geometry to be stabilised, giving a solvatochromic response. We would therefore expect the presence of solvent to have a greater effect on the geometry and thus the emission observed than if applied at a fixed geometry. Unsurprisingly, the polar solvent, DCM, has a much greater effect on the excitation energies calculated than the non-polar solvent hexane.

For obvious reasons it is important to see that, with the same solvent treatment, the other complexes retain their predicted charge transfer character. This is indeed the case, as illustrated with the examples of PtL^8SPh and PtL^5SPh, shown in Figures 4.6 and 4.7 respectively.

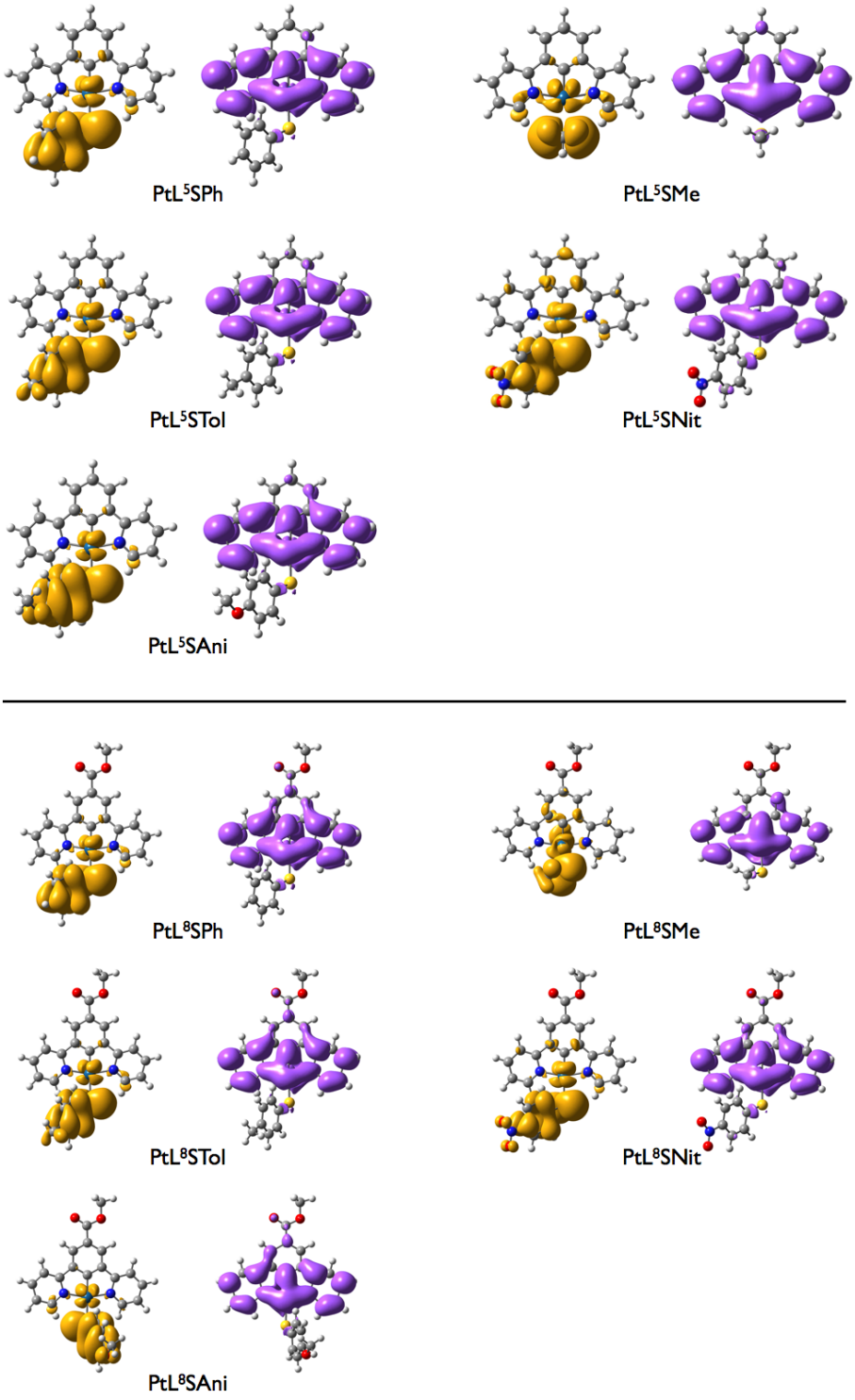

Figure 4.3: Density difference plots of the $S_0 \rightarrow T_1$ excitation at the T_1 geometry for PtL^{5}SR (top) and PtL^{8}SR (bottom) in vacuum.

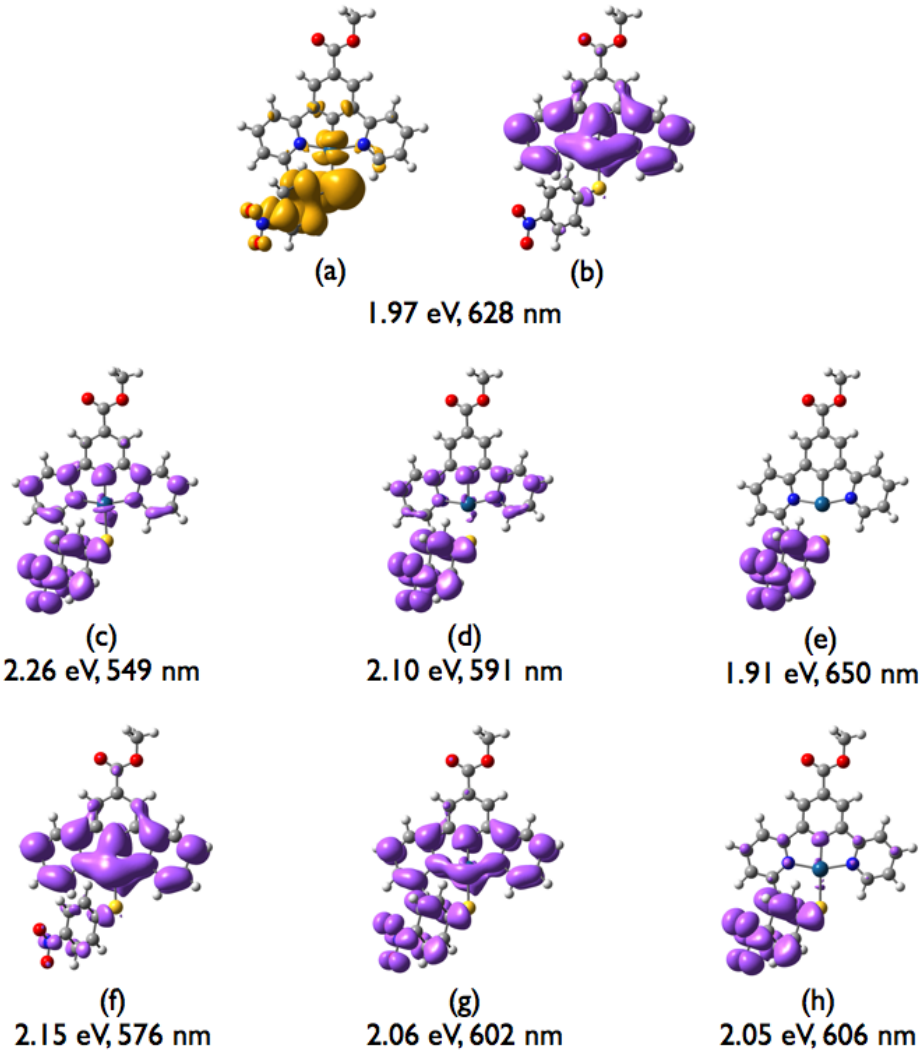

Figure 4.4: Density difference plots for PtL^{8}SNit. Energies shown correspond to the $S_0 \rightarrow T_1$ excitation. Plots showing where the electron density is moving from are only shown for one example since they are all essentially the same (they can be seen in the Appendix, Figure 9.5). (a) and (b) show "HOMO" and "LUMO" equivalents respectively, for both geometry and TD-DFT in vacuum, (c) geometry calculated in vacuum, TD-DFT in DCM, (d) geometry in DCM, TD-DFT in vacuum, (e) geometry and TD-DFT both in DCM, (f) geometry calculated in vacuum, TD-DFT in hexane, (g) geometry in hexane, TD-DFT in vacuum, (h) geometry and TD-DFT both in hexane.

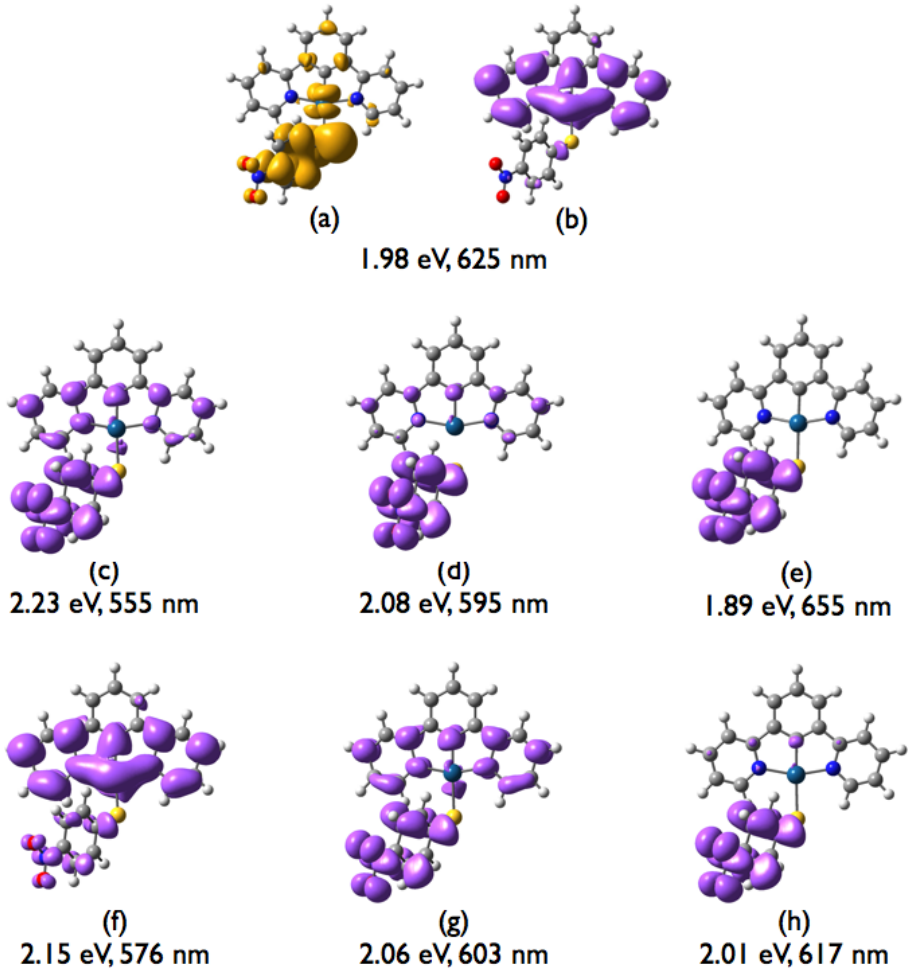

Figure 4.5: Density difference plots for PtL^{5}SNit. Electron depletion plots in the Appendix, Figure 9.6. See Figure 4.4 for details.

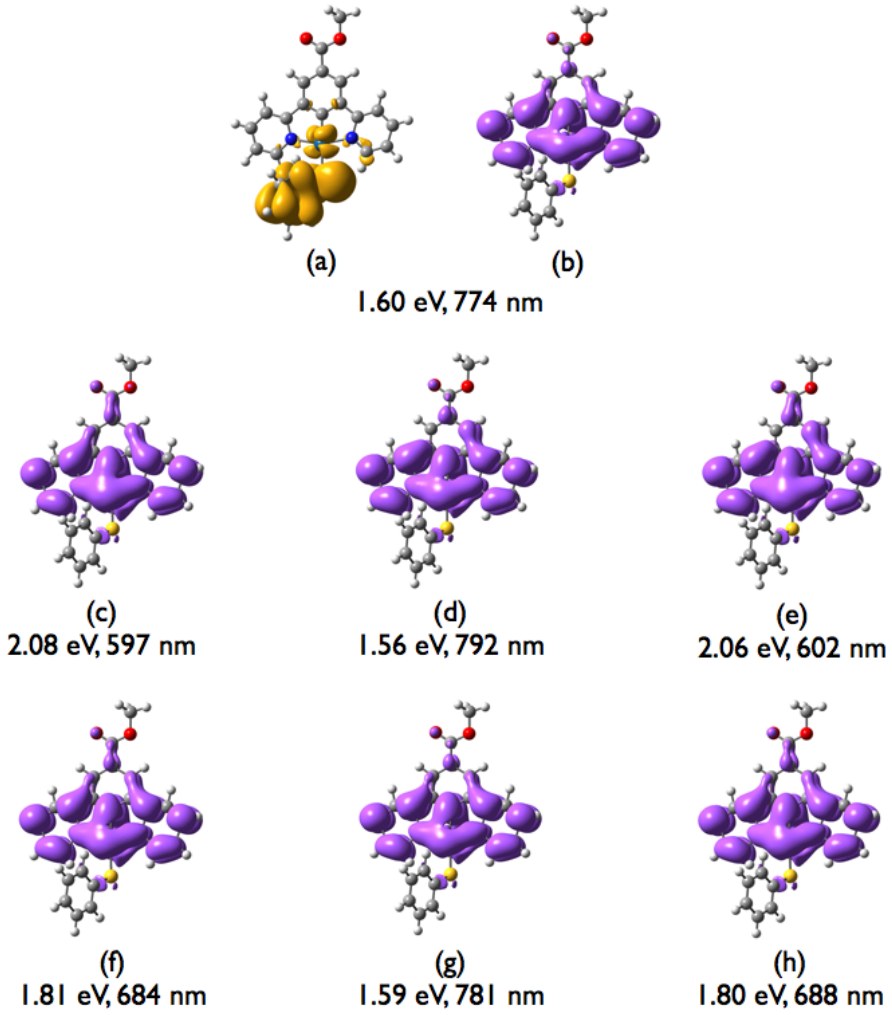

Figure 4.6: Density difference plots for PtL^{8}SPh. Electron depletion plots in the Appendix, Figure 9.7. See Figure 4.4 for details.

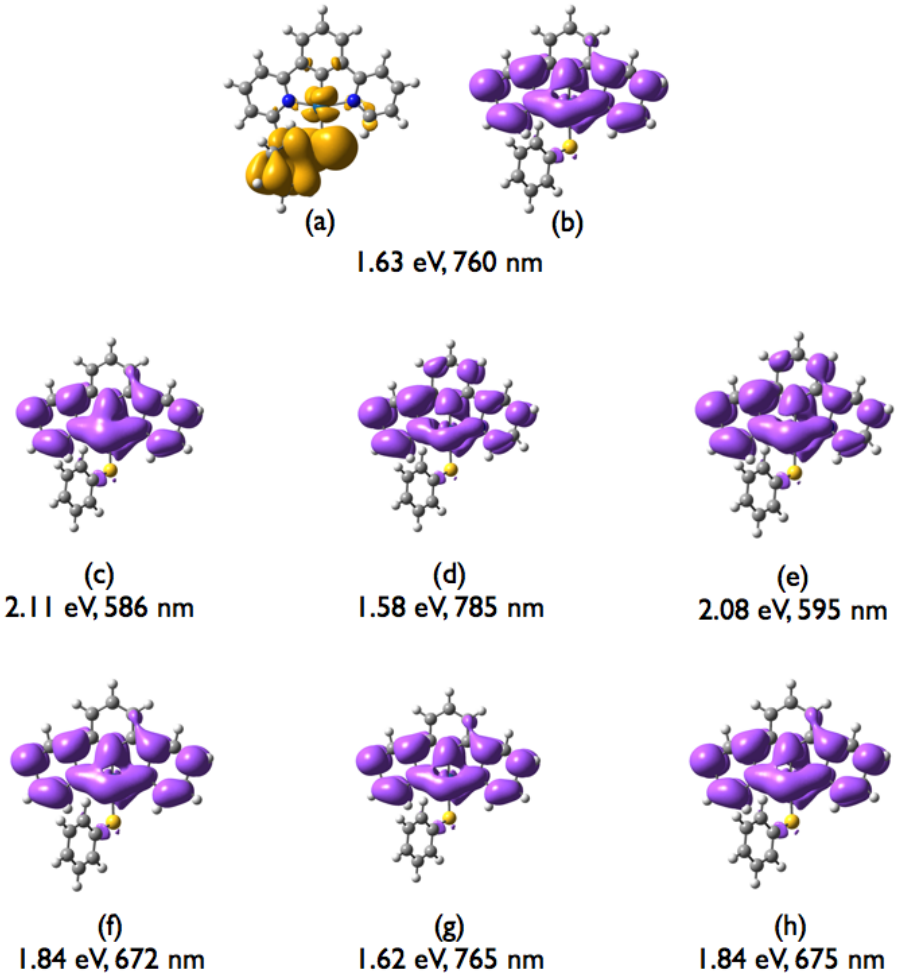

Figure 4.7: Density difference plots for PtL^{5}SPh. Electron depletion plots in the Appendix, Figure 9.8). See Figure 4.4 for details.

4.3 Predicting trends between complexes in absorption

In an attempt to reproduce the trends in absorption energy observed experimentally between PtL^5SR and PtL^8SR, the first ten singlet excitations at the ground state geometry (in DCM using the PCM) were computed using both PBE0 and CAM-B3LYP. The latter was used since it has been shown that charge-transfer transitions with low orbital overlap, which can be quantified by Λ,[174] are not usually well described by hybrid functionals such as PBE0, but are better represented by the use of long range corrected functionals such as CAM-B3LYP.[209;210]

Figures 4.8 to 4.11 show that in each case the strongly absorbing band seen in each nitro complex (PtL^5SNit and PtL^8SNit) is clearly displayed. In keeping with experimentally obtained data, λ_{max} for this band is higher in energy than the lowest energy band of each of the charge-transfer type compounds. For both PBE0 and CAM-B3LYP the trend in wavelength of the lowest energy absorption band is the same as observed experimentally (Chapter 3, Table 3.2). While PBE0 predicts excitation energies which are too low in energy in comparison to experimental data, CAM-B3LYP predicts energies which are too high for the four charge-transfer type compounds. However, the difference in energy between the excitations is marginally better for CAM-B3LYP than PBE0.

4.4 Predicting trends between complexes in emission

We will now consider the energy of phosphorescent emission of these complexes to see if DFT can be used to predict the trends exhibited. It is worth noting that direct comparison of experimental data with theory is not possible. Calculations such as these are undertaken with many assumptions: the calculations simulate at 0 K, in the gas phase and often in a vacuum (or a PCM solvent model, considering only general polarity and constrictive nature in space of addition of solvent, not interactions between the compound of interest and individual solvent molecules). The theory also assumes that there is no interaction of the compound with other species (either of the same kind,

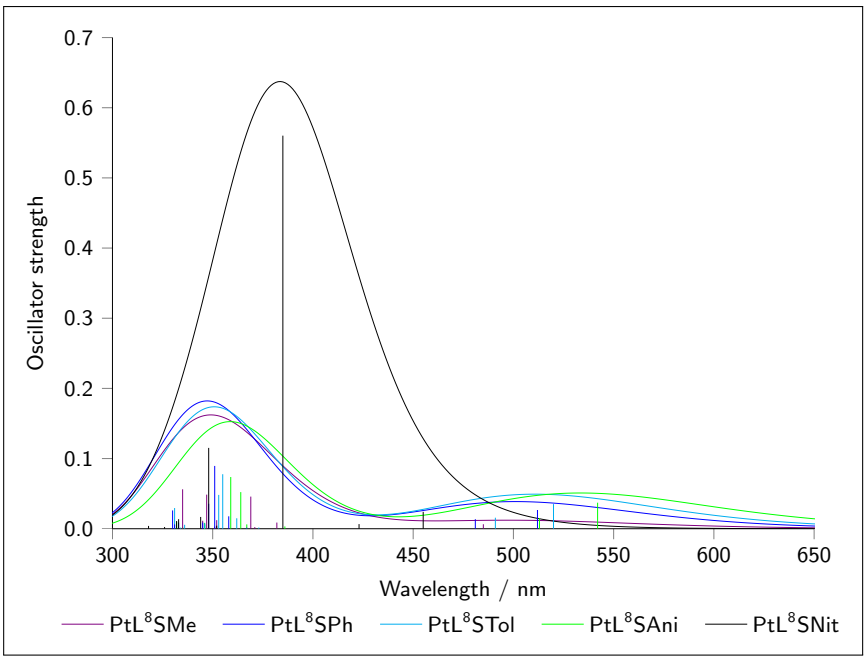

Figure 4.8: Convoluted absorption spectra of PtL^{8}SR in DCM, calculated by TD-DFT. Excitations calculated are shown in the Appendix in Table 9.12.

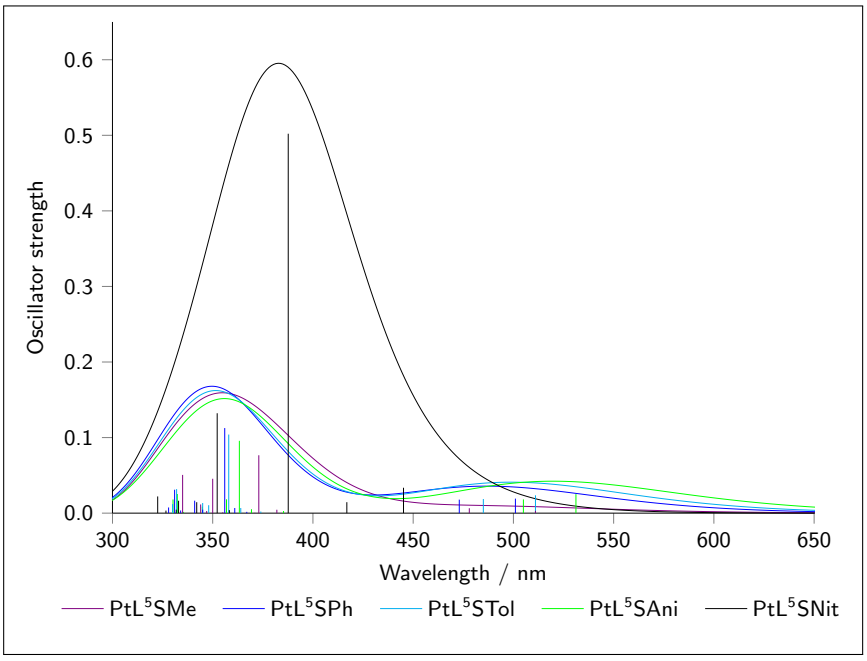

Figure 4.9: Convoluted absorption spectra of PtL^{5}SR in DCM, calculated by TD-DFT. Excitations calculated are shown in the Appendix in Table 9.13.

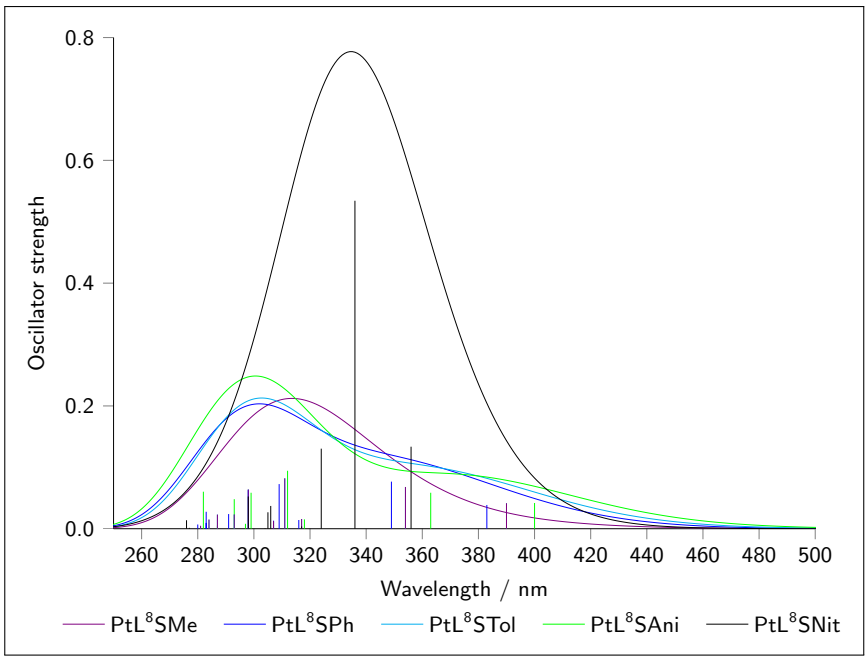

Figure 4.10: Convoluted absorption spectra of PtL^{8}SR in DCM, calculated by TD-DFT with CAM-B3LYP. Excitations calculated are shown in the Appendix in Table 9.14.

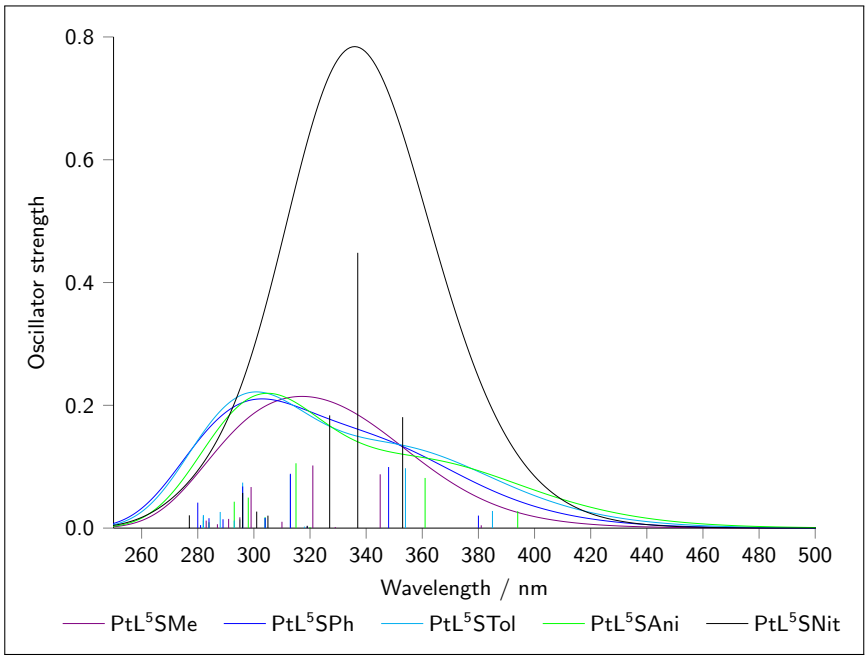

Figure 4.11: Convoluted absorption spectra of PtL^{5}SR in DCM, calculated by TD-DFT with CAM-B3LYP. Excitations calculated are shown in the Appendix in Table 9.15.

or, for example, with oxygen) which has been shown to have a profound effect on the emissive properties observed.[19;211] Experimentally, the probability of interactions with other compounds present can be significantly reduced by using high dilution (separating individual molecules of the studied compound). For these reasons we will consider only the trends observed within the series, rather than trying to compare individual calculated energies with their experimental counterparts.

Table 3.4 (Chapter 3) illustrates well the difficulty of predicting trends in emission energy. It can be seen that three pairs of complexes (PtL^5SAni and PtL^8STol, PtL^5STol and PtL^8SMe, and PtL^5SMe and PtL^5SPh) swap order in their emission energy between 298 K (in DCM) and 77 K (EPA glass). All values also increase to a higher energy upon cooling; the difference is between 0.3 and 0.4 eV. We know that both solvent (see Section 4.5) and temperature can have a large effect on the energy of emission that is observed. It is therefore difficult to know which results to compare with (since calculations are simulated at 0 K), or what to attempt to account for in the calculation in terms of solvent, since the lowest temperature measurements are necessarily done in EPA glass which cannot be easily modelled in calculations. The difference in the trends between these two sets of data are shown with the violet and black lines in Figure 4.12 for 0 K and 298 K respectively. At 0 K, the excitations should be essentially free of solvent effects since the low temperature prevents reorganisation of solvent molecules which are therefore unable to stabilise the excited state.

For these reasons, only general trends between the energies of emission of the thiolate compounds will be discussed. Tables 4.2 and 4.3 show that the prediction of even these trends is fraught with difficulty, certain compounds when calculated never fit the trend in energy shown experimentally. Since the character of the excitation is different for $PtL^{5/8}SNit$ and $PtL^{5/8}SMe$ do not contain an aromatic ring, it is more difficult to compare calculations of these four with the charge-transfer, aromatic thiolate complexes. These compounds will therefore only be considered in their pairs and not with the rest of the set.

	Experimental		Method A		Method B		Method C		Method C2		Method D	
	/ nm	/ eV	/ nm	/ eV	/ nm	/ eV	/ nm	/ eV	/ nm	/ eV	/ nm	/ eV
PtL^{5}SNit	714	1.74	625	1.98	555	2.23	655	1.89	543	2.28	621	2.00
PtL^{8}SAni	701	1.77	966	1.28	691	1.80	706	1.76	569	2.18	710	1.75
PtL^{8}SNit	703	1.77	628	1.97	549	2.26	650	1.91	538	2.31	615	2.02
PtL^{5}SAni	691	1.80	924	1.34	666	1.86	688	1.80	556	2.23	691	1.80
PtL^{8}STol	668	1.86	821	1.51	624	1.99	631	1.96	546	2.27	634	1.96
PtL^{5}STol	661	1.88	802	1.55	610	2.03	621	2.00	535	2.32	623	1.99
PtL^{8}SMe	642	1.93	847	1.46	671	1.85	688	1.80	535	2.32	681	1.82
PtL^{8}SPh	643	1.93	774	1.60	597	2.08	602	2.06	534	2.32	603	2.06
PtL^{5}SMe	636	1.95	653	1.90	519	2.39	678	1.83	523	2.37	670	1.85
PtL^{5}SPh	634	1.96	760	1.63	586	2.11	595	2.08	523	2.37	597	2.08

Table 4.2: Excitation energies calculated for the thiolate series of complexes with experimental results for reference. Excitation energies are listed from highest experimental value to lowest for easy comparison of trends. Experimental results at 298 K in DCM.

	Experimental		Method C		Method C2		Method E		Method F	
	/ nm	/ eV	/ nm	/ eV	/ nm	/ eV	/ nm	/ eV	/ nm	/ eV
PtL^{5}SNit	714	1.74	0.30	4167	482	2.57	559	2.22	614	2.02
PtL^{8}SAni	701	1.77	2.39	518	469	2.65	501	2.47	501	2.47
PtL^{8}SNit	703	1.77	2.00	621	479	2.59	611	2.03	611	2.03
PtL^{5}SAni	691	1.80	−0.33	−3730	470	2.64	513	2.42	513	2.42
PtL^{8}STol	668	1.86	0.34	3655	468	2.65	496	2.50	496	2.50
PtL^{5}STol	661	1.88	0.40	3077	470	2.64	464	2.67	512	2.42
PtL^{8}SMe	642	1.93	0.92	1343	466	2.66	548	2.26	548	2.26
PtL^{8}SPh	643	1.93	0.13	9570	467	2.65	496	2.50	496	2.50
PtL^{5}SMe	636	1.95	0.27	4549	468	2.65	545	2.27	545	2.27
PtL^{5}SPh	634	1.96	0.44	2819	469	2.64	512	2.42	512	2.42

Table 4.3: Excitation energies calculated with CAM-B3LYP for the thiolate series of complexes with experimental results for reference. Excitation energies are listed from highest experimental value to lowest for easy comparison of trends. Experimental results at 298 K in DCM.

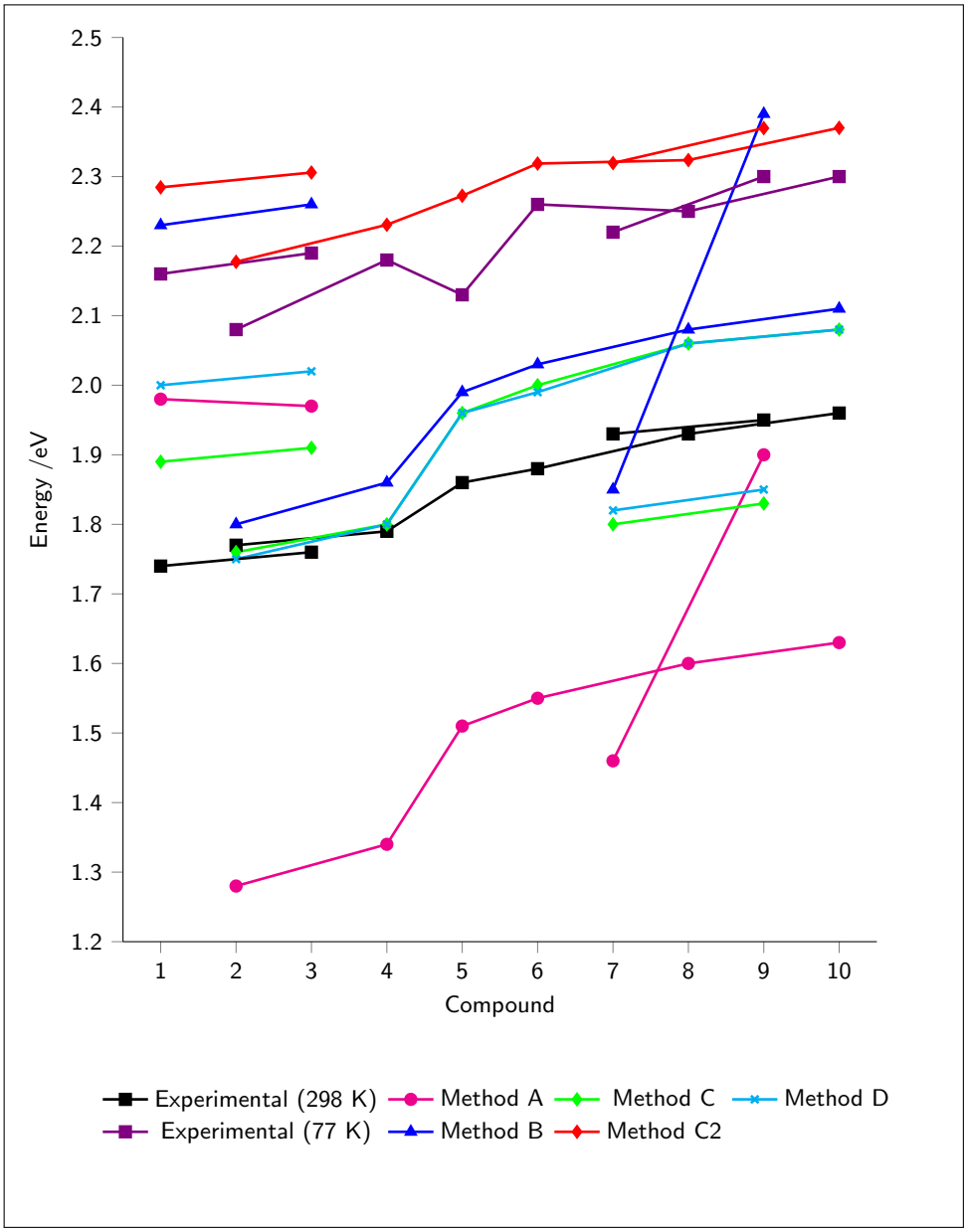

Figure 4.12: A graph to show the trend in excitation energies calculated for the thiolate series of complexes with experimental results (at 298 K in DCM and at 77 K in EPA) for reference. Compound 1: PtL^{5}SNit, 2: PtL^{8}SAni, 3: PtL^{8}SNit, 4: PtL^{5}SAni, 5: PtL^{8}STol, 6: PtL^{5}STol, 7: PtL^{8}SMe, 8: PtL^{8}SPh, 9: PtL^{5}SMe, 10: PtL^{5}SPh.

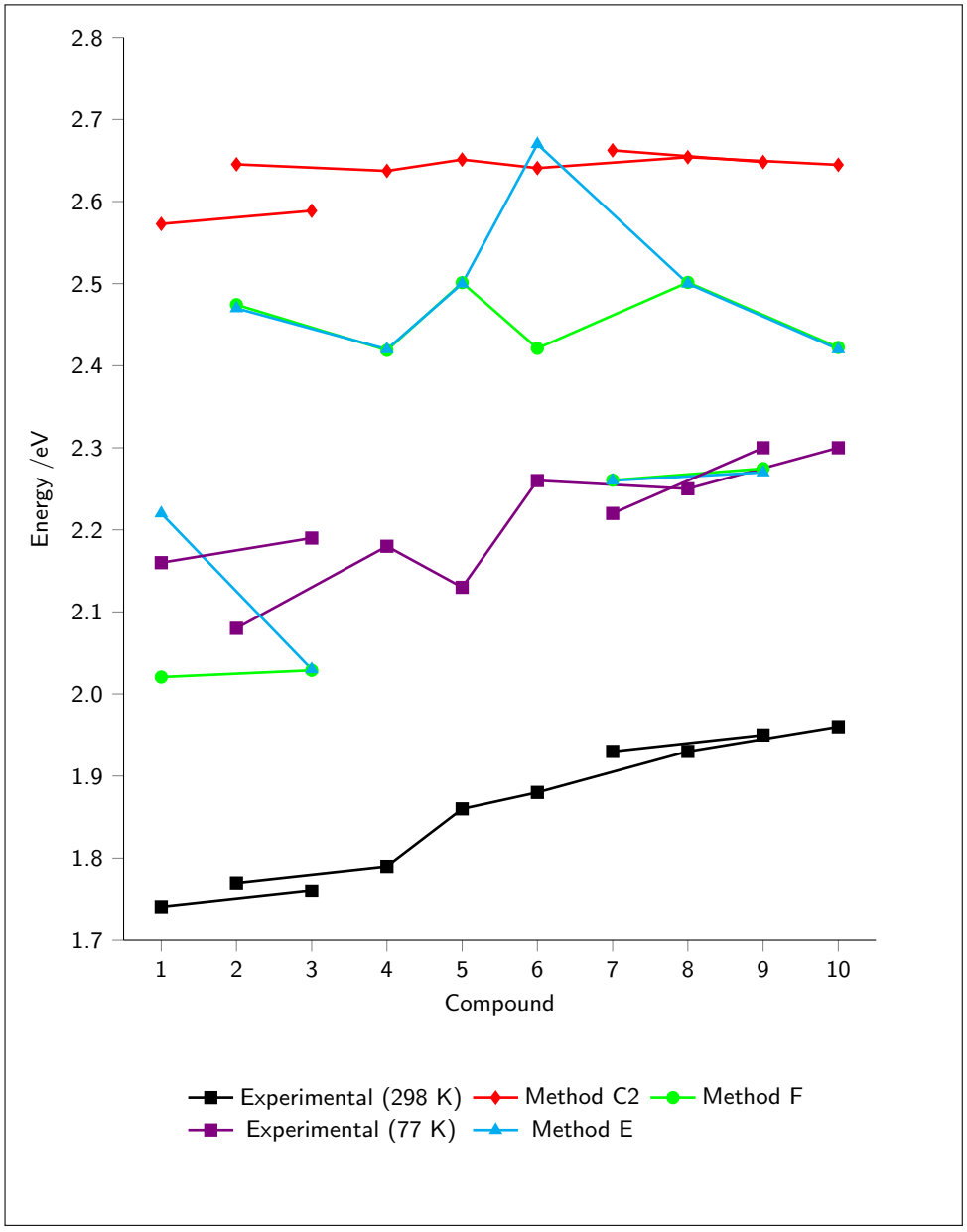

Figure 4.13: A graph to show the trend in excitation energies calculated for the thiolate series of complexes with experimental results (at 298 K in DCM and at 77 K in EPA) for reference. Compound 1: PtL^{5}SNit, 2: PtL^{8}SAni, 3: PtL^{8}SNit, 4: PtL^{5}SAni, 5: PtL^{8}STol, 6: PtL^{5}STol, 7: PtL^{8}SMe, 8: PtL^{8}SPh, 9: PtL^{5}SMe, 10: PtL^{5}SPh.

	PBE0: Method A		PBE0: Method C	CAM-B3LYP: Method C
	Stability	Λ	Stability	Stability
PtL^{5}SMe	1.69	0.18	1.59	0.30
PtL^{5}SPh	1.56	0.29	1.59	0.23
PtL^{5}STol	1.48	0.28	1.59	0.20
PtL^{5}SAni	1.30	0.25	1.59	−0.19
PtL^{5}SNit	1.64	0.35	1.43	0.03
PtL^{8}SMe	1.26	0.42	1.60	0.68
PtL^{8}SPh	1.54	0.29	1.64	0.02
PtL^{8}STol	1.46	0.27	1.64	0.12
PtL^{8}SAni	1.25	0.22	1.63	1.41
PtL^{8}SNit	1.66	0.34	1.44	1.27

Table 4.4: Stabilities and Λ values calculated for the thiolate series of complexes.

Method A: geometry and TD-DFT calculations both run in vacuum. Method C: geometry and TD-DFT calculations both run in DCM.

4.4.1 PBE0 calculations

Various different methods were used in an attempt to reproduce the trends in energy seen between the complexes experimentally. The different methods (*vide infra*) varied in their point of inclusion of solvent as well as the model used to predict the energy of $T_1 \rightarrow S_0$ emission; the results outlined in Figure 4.12 all used PBE0 as the functional. The $S_0 \rightarrow T_1$ excitation was calculated in each case at the geometry optimised as indicated.

Method A: *Geometry* − T_1 geometry calculated, optimised in vacuum
TD-DFT − calculated in vacuum

Method B: *Geometry* − T_1 geometry calculated, optimised in vacuum
TD-DFT − calculated with a PCM for DCM

Method C: *Geometry* − T_1 geometry calculated, optimised with a PCM for DCM
TD-DFT − calculated with a PCM for DCM

Method C2: *Geometry* − S_0 geometry calculated, optimised with a PCM for DCM
TD-DFT − calculated with a PCM for DCM (since this is at the S_0 geometry, this is really the formally forbidden $S_0 \rightarrow T_1$ absorption rather than emission)

Method D: *Geometry* − T_1 geometry optimised with a PCM for DCM
Excitations − calculated using TDA with a PCM for DCM

Table 4.2 and Figure 4.12 show that most techniques using PBE0 as a functional give reasonably good results at predicting the trend in emission between all ten complexes. Indeed, all methods A-D give the same general trend for the aromatic charge transfer compounds as for the experimental results at 298 K in DCM. The lowest energy excitations are calculated entirely in vacuum (Method A) with the excitation energies increasing upon inclusion of solvent (DCM). Calculations in vacuum for both geometry and TD-DFT show an exaggerated trend between the complexes: the gaps in energy between each are generally much bigger than observed experimentally, especially in the case of the two PtL^nSMe complexes. The incorrect relationship between the energies of PtL^5SNit and PtL^8SNit should be ignored since, as previously discussed, the incorrect excitation is being described (Section 4.2.2). Method B (geometry optimisation in vacuum, TD-DFT in DCM) is also inaccurate since the density difference plots showed some charge transfer character for $PtL^{5/8}SNit$. The effect was not so pronounced though which is reflected in the

excitation energies calculated. Inclusion of a PCM solvent for DCM for both calculations (geometry and TD-DFT), Method C, shows probably the closest reproduction of the experimental results in DCM with values calculated for the two OMe-substituted thiolates exceptionally close. Method C2 shows the trend predicted when the first triplet excitation is calculated at the singlet geometry (geometry and TD-DFT in DCM). This is a commonplace technique in the literature which circumvents difficulties encountered with triplet instabilities (discussed in Chapter 1, Section 1.6.1) in the geometry optimisation (although these are still present when calculating the excitations themselves) and optimising to a state which is not the true triplet minimum. In this case the general trend is similar to that observed experimentally although, as expected, the energy of the excitation in each case is increased. Calculation using this method relies upon the geometry of the triplet excited state being very close to that of the ground state.

Compounds which exhibit a high level of overlap between excited and ground state orbitals have recently been shown to be highly susceptible to triplet instabilities. This can lead to unexpectedly low calculated energies of emission from T_1 for these compounds. Stability calculations on PtL^5SNit and PtL^8SNit show that calculations on both of these compounds experience such difficulties (Table 4.4), explaining the low energies of emission calculated. Tozer and co-workers showed that this can be overcome in small molecules with the use of the Tamm-Dancoff approximation (TDA).[117] Method D therefore applies the TDA to the geometries which were previously calculated in DCM with PBE0. It is interesting to see that while there is very little difference in the excitation energy calculated for the charge transfer-type compounds, there is a significant increase in the excitation energy calculated for both of the nitro compounds ($\sim$0.2 eV) presumably since these two compounds were adversely affected by a low triplet stability. Unfortunately in this case however, the use of TDA does not improve upon the trends calculated with conventional DFT for the aryl-substituted, charge-transfer type complexes. This is perhaps unsurprising since the low overlap and moderately acceptable stability at the calculated triplet geometries is not too much of a problem in this case.

4.4.2 CAM-B3LYP calculations

We will now briefly consider the use of CAM-B3LYP with these charge transfer complexes to see what effect a long range corrected functional has on the energies calculated and trends observed. Once again, different methods were used to see how well each reproduced the experimental trends in energy. In this case, most calculations were performed with CAM-B3LYP though, where indicated, some geometries were optimised using PBE0. Methods C and C2 are those outlined in Section 4.4.1, using CAM-B3LYP in place of PBE0 as the functional.

Method E: *Geometry* – T_1 geometry optimised with PBE0 and a PCM for DCM
Excitations – calculated using TDA with CAM-B3LYP

Method F: *Geometry* – T_1 geometry optimised with PBE0 and a PCM for DCM
Excitations – calculated using TD-DFT with CAM-B3LYP and a PCM for DCM

It is clear from a first glance at Figure 4.13 (Table 4.3) that calculations using the CAM-B3LYP functional give very different results from those using PBE0. The most noticeable change is the significantly higher excitation energies which are greater in most cases than even the low temperature experimental results. It seems that, in general, the trends are also less well described. Excitations calculated using Method C (geometry and TD-DFT with CAM-B3LYP at the T_1 geometry in DCM) are not included in Figure 4.13 since the energies are extremely low.

Calculations where the geometry optimisation and TD-DFT were both performed using CAM-B3LYP (both in vacuum and in DCM) are not shown in Figure 4.13 since the excitation energies calculated were exceptionally low (Table 4.3). Many different minima were found (each with no imaginary frequencies) when the geometry was calculated using this functional. It is thought that the stabilities were so low that the T_1 geometry itself was ad-

versely affected, giving a false minimum. Despite this, study of the density difference plots showed that the correct type of transition in each case was still predicted. This phenomenon is further discussed in Chapter 6. Since it was suspected that triplet instabilities had compromised the CAM-B3LYP geometries, CAM-B3LYP excitations at a PBE0 geometry were computed to see what effect this had on the trends observed. This was done using both TD-DFT and the Tamm-Dancoff approximation (TDA). Excitation energies calculated with TDA are not susceptible to triplet instabilities (see Chapter 1, Section 1.6.1). Figure 4.13 shows that for most of the compounds (excepting PtL^5SNit and PtL^5STol) there was very little difference between energies calculated with TDA and TD-DFT. Both of these techniques gave a poor representation of the experimental trends though perhaps this is unsurprising since we have seen that the combination of both geometry and TD-DFT have a significant impact on the excitation energies, so that if each is calculated using a different functional, inconsistent results will be obtained.

The importance of the geometry optimisation is underlined by the trend produced by calculation of the $S_0 \rightarrow T_1$ excitation at the ground state geometry with CAM-B3LYP in DCM. While the relationship between PtL^5SNit and PtL^8SNit is correctly reproduced (albeit at a much higher energy, as we would expect when calculating this value as an absorptive process, rather than emissive), the other eight complexes show roughly the same energy for the $S_0 \rightarrow T_1$ excitation. This can be explained upon consideration of the density difference plots for this transition, Figures 4.14 and 4.15: entirely the wrong transition is being described. The thiolate ligand has virtually no effect on the excitation energies calculated because it is not involved in the predicted transition. For these compounds then, despite their charge transfer nature, it seems that PBE0 is a better choice of functional for description of phosphorescent emission since it is not so susceptible to the triplet instability problem when calculating the T_1 excited state geometry (CAM-B3LYP has a higher α at high r_{12} than PBE0, see Chapter 1). Tozer and co-workers have shown that use of TDA with CAM-B3LYP excitations can help eliminate complications with triplet instabilities when calculating the excitations themselves.[142] Since CAM-B3LYP predicts the trend better than PBE0 for absorption in these

compounds and stability with CAM-B3LYP is low, ideally, a CAM-B3LYP TDA geometry would be calculated for each of these compounds. Subtle differences in the geometry of the complexes could make the small alterations necessary for correct reproduction of the trends. If a geometry can be found with circumvention of the triplet instability problem, then TDA excitation energies calculated at this geometry may reproduce the experimental trend better. Unfortunately these calculations were outside the scope of this project since calculations were performed with QChem which was unable to perform TDA geometry optimisations with a PCM solvent model, using CAM-B3LYP or PBE0 as the functional. Finally, it should be noted that inherent errors in DFT and TD-DFT calculations mean that an error of at least 0.3 eV is present in most calculations (as outlined in Chapter 1). This error covers the whole span of experimental emission energies (both at 298 and 77 K). It could therefore be considered that trends calculated by TD-DFT are in fact quite good.

4.5 Predicting trends in solvatochromism

Chapter 3, Section 3.4.3 outlined the experimental dependence of the thiolate complexes on solvent for wavelengths of absorption and emission. Since we have seen the importance of the inclusion of solvent in TD-DFT calculations for the generation of reliable results, it is important to investigate whether this method can predict solvatochromic shifts in energy using the PCM solvent model. In order to investigate the reliability of these solvent calculations, the absorption and emission properties of two of the complexes, in various solvents, were measured experimentally, and the corresponding TD-DFT calculations performed for comparison. One charge transfer complex, PtL^8SPh, and one ILCT, PtL^8SNit, were investigated and the results summarised in Chapter 3, Table 3.6.

4.5.1 Solvatochromism in absorption

It is difficult to know which transitions are responsible for a change in energy of absorption since, unlike emission, many transitions are possible from the singlet ground state to any number of singlet (or even in some cases the

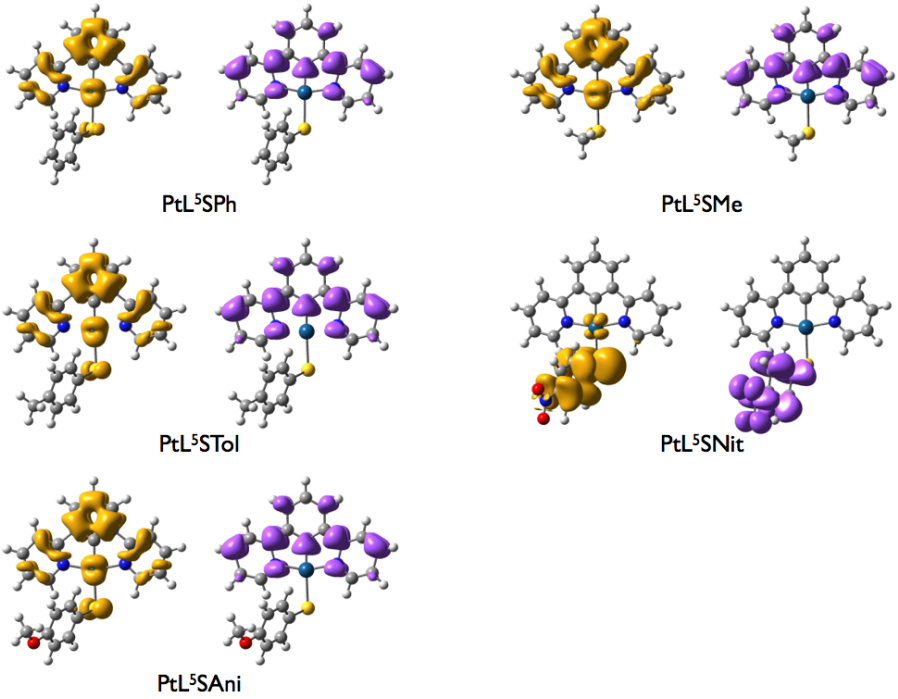

Figure 4.14: Density difference plots of absorption from S_0 to T_1 for PtL^{5}R series of complexes in DCM, calculated with CAM-B3LYP.

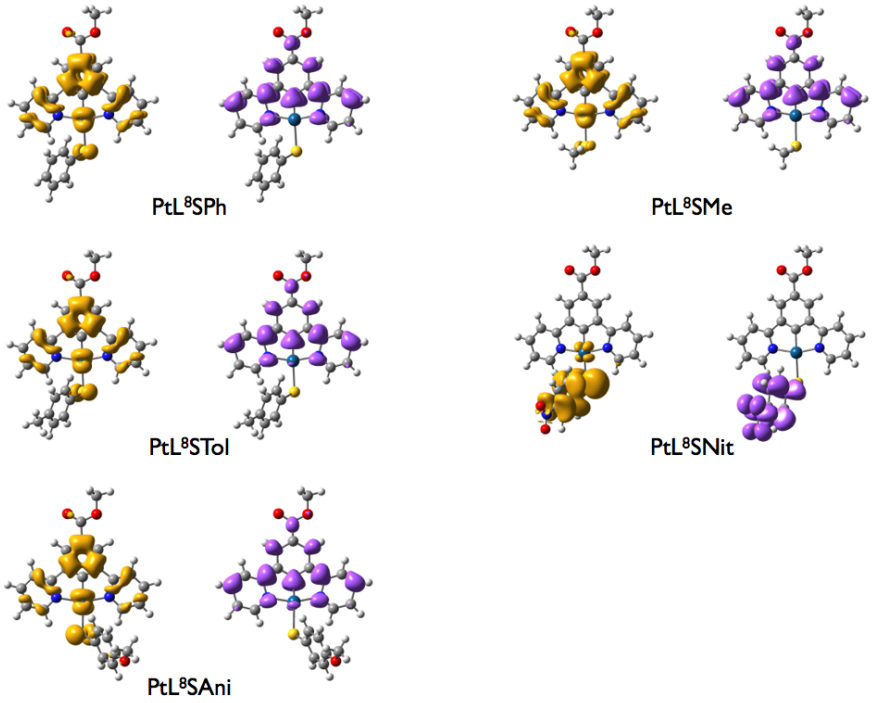

Figure 4.15: Density difference plots of absorption from S_0 to T_1 for PtL^{8}R series of complexes in DCM, calculated with CAM-B3LYP.

triplet) excited states. It is unsurprising therefore that when trying to simulate the trend exhibited by the lowest energy band in the absorption spectrum by looking at the lowest energy singlet absorption at the ground state geometry, we find negative solvatochromism predicted for both PtL^8SPh and PtL^8SNit (Appendix, Table 9.16). Indeed the density difference plots for $S_0 \rightarrow S_1$ show transitions that are charge transfer from the thiolate ligand to the N^C^N ligand/platinum in character, even for PtL^8SNit.

Figures 4.16 and 4.17 show density difference plots for the first two and three singlet excitations for PtL^8SPh and PtL^8SNit respectively, at the ground state geometry, in THF. Reference to the simulated absorption spectrum (Figure 4.18) and the excitations calculated to generate it (Appendix, Table 9.16) show that for PtL^8SPh, the low energy region of the absorption spectrum is dominated by the lowest energy $S_0 \rightarrow S_1$ transition, with moderate influence from $S_0 \rightarrow S_2$. Figure 4.16 shows that both of these excitations are charge-transfer in nature and therefore their energy will be highly influenced by polarity of solvent. The TD-DFT in this case correctly predicts negative solvatochromism in the lowest energy band of the absorption spectrum both by looking at the lowest energy singlet excitation ($S_0 \rightarrow S_1$) and by production of a convoluted absorption spectrum. Equivalent plots of the two complexes in MeCN and DCM are shown in the Appendix, Figures 9.10 and 9.12 respectively.

PtL^8SNit also shows the two lowest energy excitations ($S_0 \rightarrow S_1$ and $S_0 \rightarrow S_2$) as charge transfer in character, displaying wavelengths dependent on solvent polarity (Figure 4.17) but, as illustrated in Figure 4.19, these transitions are so weak they have very little influence on the overall spectrum. Instead, the whole of this region of the spectrum is dominated by the $S_0 \rightarrow S_3$ excitation at ∼385 nm. Figure 4.17 shows that this excitation is centred on the thiolate ligand and therefore is not influenced to such a degree by choice of solvent. It does however show very slight positive solvatochromism, in keeping with the experimentally obtained spectra (Chapter 3, Figure 3.16).

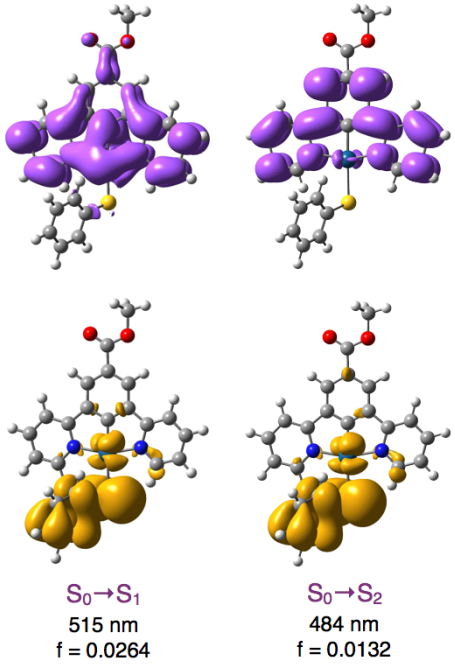

Figure 4.16: Density difference plots for the first two excitations of PtL^{8}SPh in THF at the ground state geometry with oscillator strength for each transition (f).

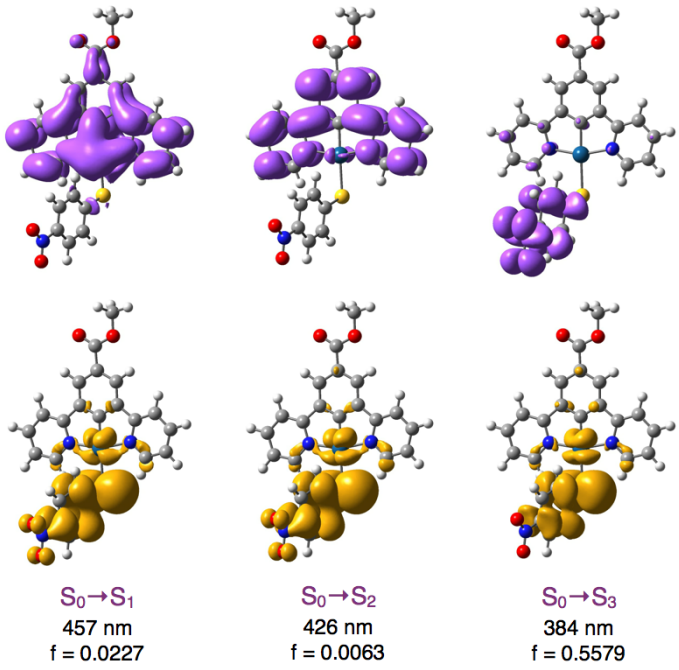

Figure 4.17: Density difference plots for the first three excitations of PtL^{8}SNit in THF at the ground state geometry with oscillator strength for each transition (f).

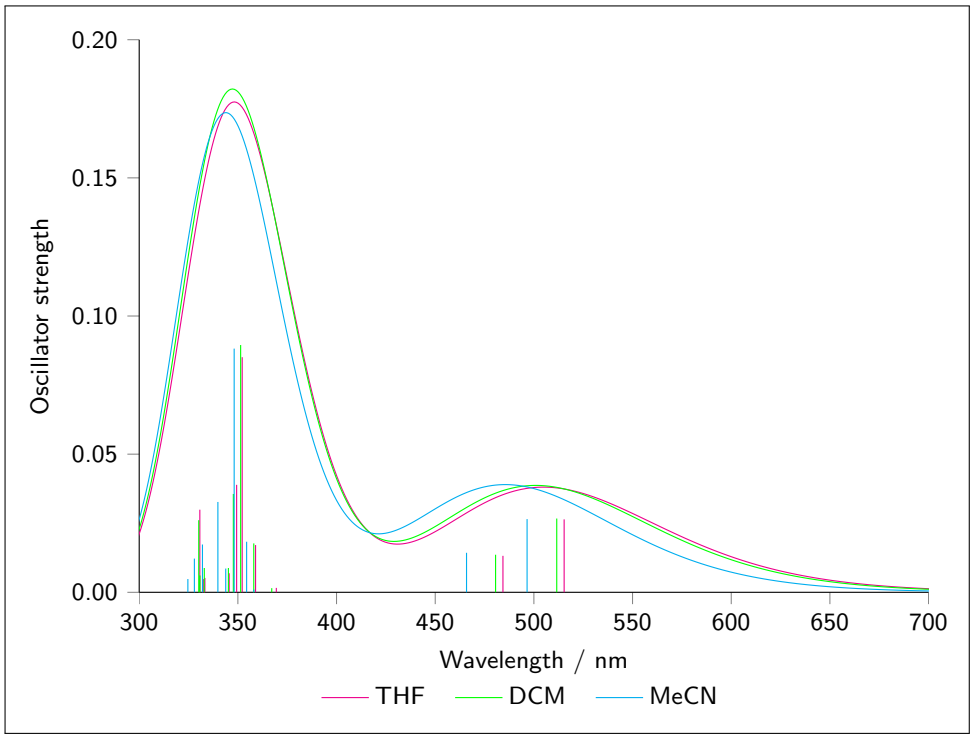

Figure 4.18: Convoluted absorption spectra PtL^{8}SPh in three solvents of varying polarity, calculated by TD-DFT. Vertical lines show excitation energies and oscillator strengths (values shown in Appendix, Table 9.16); the curve shows the convoluted spectrum.

4.5.2 Solvatochromism in emission

Figure 3.15 (in Chapter 3) shows that PtL^{8}SPh gives a red shift in emission with increasing polarity of solvent. Perhaps unexpectedly, Figure 3.17 (Chapter 3) shows that PtL^{8}SNit also gives a red shift in emission with increasing polarity in contrast to behaviour exhibited in absorption. In fact, the shift in wavelength is greater in PtL^{8}SNit than PtL^{8}SPh. Examination of density difference plots for the $S_0 \rightarrow T_1$ excitation at the triplet excited state geometry in various solvents (Figures 4.20 (MeCN), 4.21 (DCM), 4.22 (THF) and 4.23 (toluene)) shows the thiolate-centred excitation which is influenced by change in solvent. Scrutiny of the orbital plots in these figures alongside their relative contributions to the excitation (Table 4.5) suggests a possible origin for this solvatochromic response: with decreasing polarity, a small degree of charge transfer character enters the excitation. We know from PtL^{8}SPh that

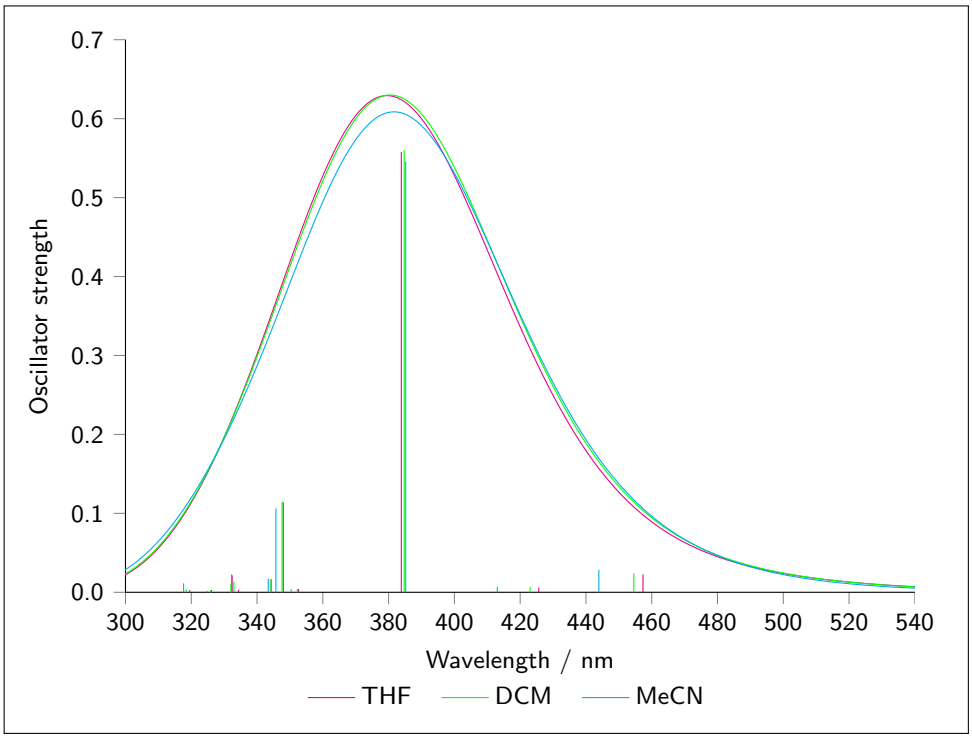

Figure 4.19: Convoluted absorption spectra PtL^{8}SNit in three solvents of varying polarity, calculated by TD-DFT. Vertical lines show excitation energies and oscillator strengths (values shown in Appendix, Table 9.16); the curve shows the convoluted spectrum.

the more polar solvents induced a red shift in emission which partly explains the effect seen here. This is compounded in this case by the change in excitation type as illustrated in Figure 4.24. The charge-transfer excitations were higher in energy than those centred exclusively on the thiolate ligand. Therefore inclusion of some charge transfer character in the excitation (as in the case of THF and toluene) will induce a blue shift in the emission energy. The exaggerated shift in energy with change in solvent is then a combination of the red shift induced by the non-polar solvent, combined with the red shift precipitated by change in character of emission towards charge-transfer in the non-polar solvents. This is reflected in the predicted energies of emission in each of these solvents, shown in Table 4.5.

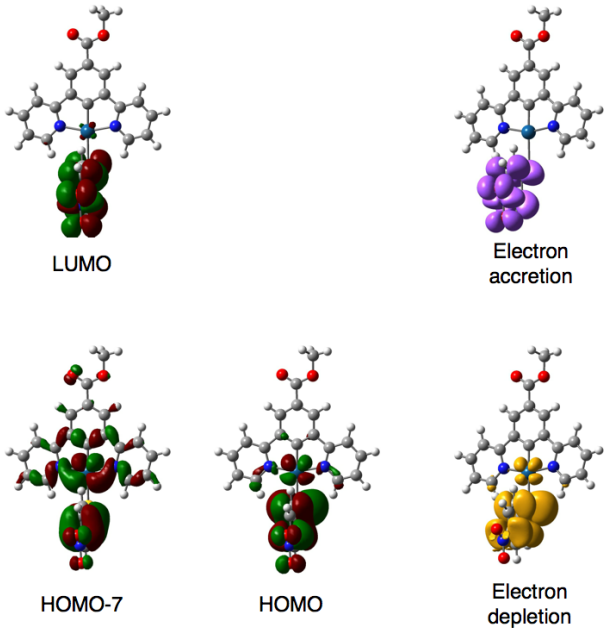

Figure 4.20: Orbital and density difference plots of the $S_0 \rightarrow T_1$ excitation of PtL^{8}SNit at the T_1 geometry in MeCN.

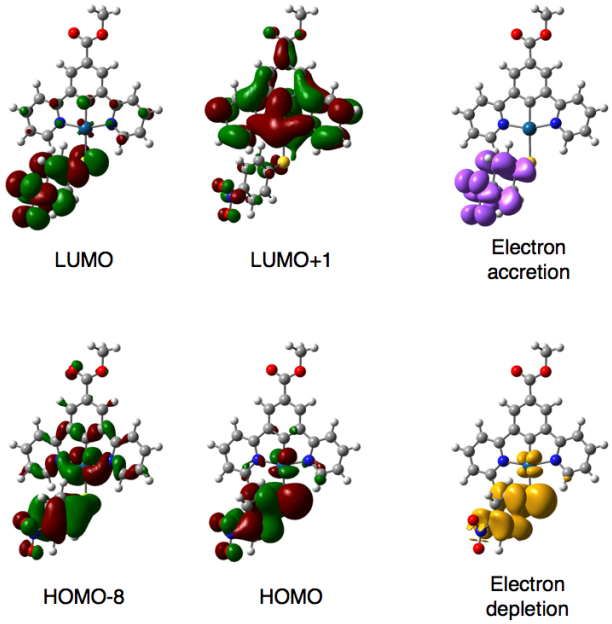

Figure 4.21: Orbital and density difference plots of the $S_0 \rightarrow T_1$ excitation of PtL^{8}SNit at the T_1 geometry in DCM.

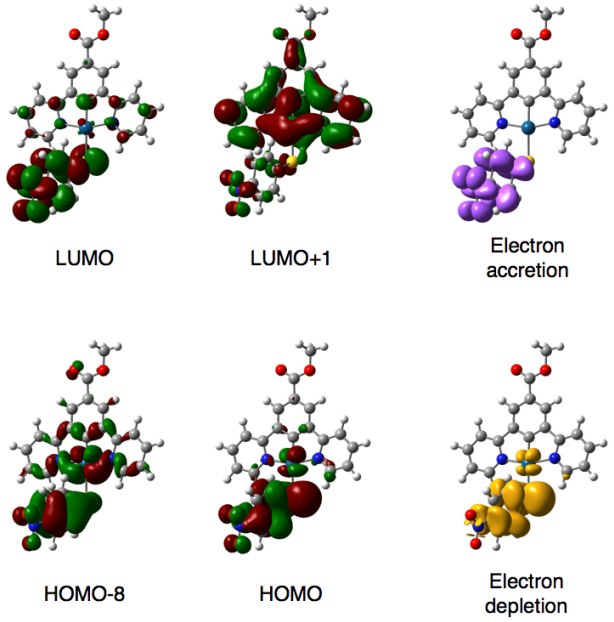

Figure 4.22: Orbital and density difference plots of the $S_0 \rightarrow T_1$ excitation of PtL^{8}SNit at the T_1 geometry in THF.

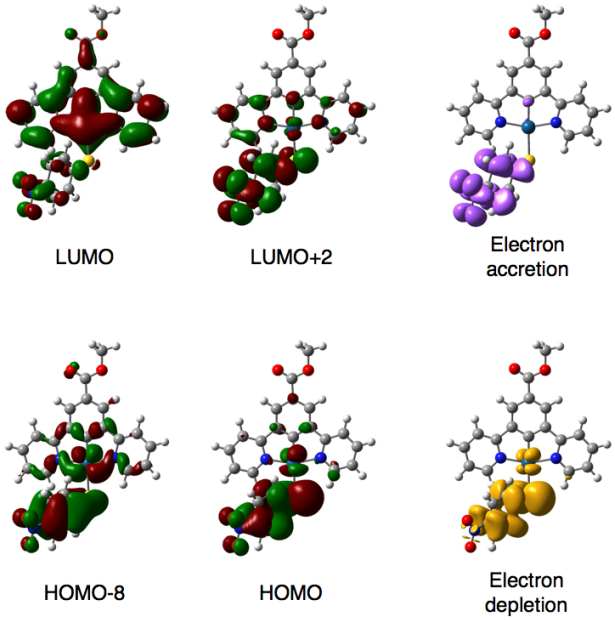

Figure 4.23: Orbital and density difference plots of the $S_0 \rightarrow T_1$ excitation of PtL^{8}SNit at the T_1 geometry in toluene.

Transition	Contribution
MeCN$^{(a)}$ *(37.5)*$^{(b)}$ *661 nm*$^{(c)}$	
HOMO−7 → LUMO	−0.112
HOMO → LUMO	0.692
DCM *(8.9) 650 nm*	
HOMO−8 → LUMO	0.110
HOMO → LUMO	0.675
HOMO → LUMO+1	0.155
THF *(7.6) 647 nm*	
HOMO−8 → LUMO	0.107
HOMO → LUMO	0.663
HOMO → LUMO+1	0.198
Toluene *(2.4) 620 nm*	
HOMO−8 → LUMO+2	0.104
HOMO → LUMO	−0.362
HOMO → LUMO+2	0.579

Table 4.5: Orbital contributions for the $S_0 \rightarrow T_1$ excitation at the T_1 geometry for PtL^{8}SNit in the indicated solvent. $^{(a)}$ **solvent modelled**, $^{(b)}$*(dielectric constant of solvent),* $^{(c)}$ λ_{max} *predicted.*

4.6 DFT of PtL^{6}SR and PtL^{9}SR

4.6.1 Absorption

Convoluted absorption spectra of PtL^{6}STol, PtL^{6}SNit, PtL^{9}STol and PtL^{9}SNit are shown in Figures 4.25 (PBE0) and 4.26 (CAM-B3LYP). As for PtL$^{5/8}$SR, and as outlined in the experimental data, the nitro-substituted compound in both cases shows one very intensely absorbing band (at ∼340 nm with CAM-B3LYP) which is due to the thiolate-centred ILCT (Figures 4.29 and 4.31 for PtL^{6}SNit and PtL^{9}SNit respectively, equivalent density difference plots for PBE0 are shown in the Appendix). The weaker absorbing band tailing into

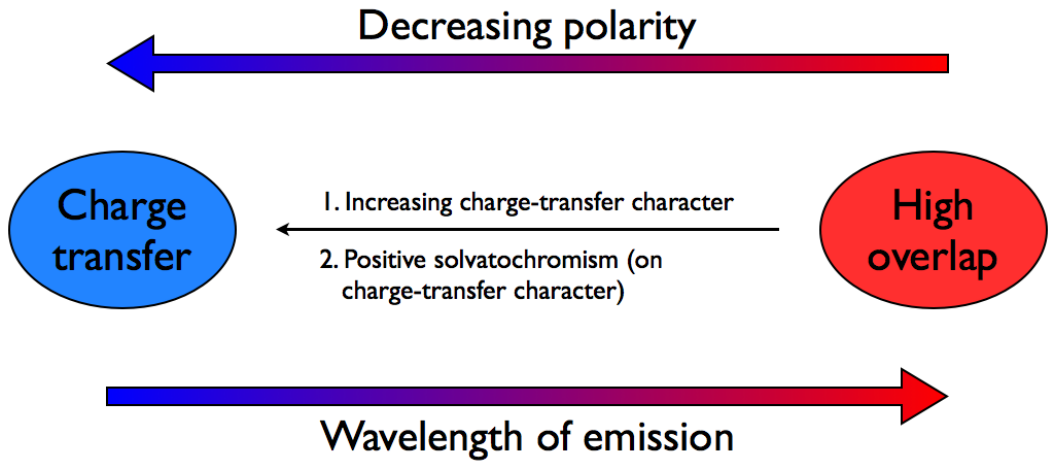

Figure 4.24: Illustration of the proposed reasons for the solvatochromic response shown by PtL^{8}SNit.

the red region of the spectrum of PtL^{6}STol and PtL^{9}STol can be attributed to the $S_0 \rightarrow S_1$ and $S_0 \rightarrow S_2$ charge transfer excitations which have lower oscillator strengths as shown in Figures 4.28 and 4.30.

Figure 4.25 shows that the trend in energy of the lowest energy absorption band between the three PtL^{9}R complexes when calculated with PBE0 is incorrect: in PtL^{9}STol this band extends far into the red region of the spectrum. When the calculation is repeated using the CAM-B3LYP functional (Figure 4.26), a much lower wavelength is predicted for this band, in keeping with the experimental spectrum. This is presumably due to the LUMO-destabilising nature of the cyclohexyl groups being taken into account with the long range corrected functional. PtL^{6}R shows the same pattern though less dramatically; though the trend is correct with PBE0 (Figure 4.25), the difference in energy of the absorption bands of the different complexes is exaggerated while it is correctly muted by CAM-B3LYP (Figure 4.26).

4.6.2 Emission

Density difference plots for the $S_0 \rightarrow T_1$ excitation at the triplet excited state geometry for PtL$^{6/9}$STol and PtL$^{6/9}$SNit are shown in Chapter 3, Figure 3.21.

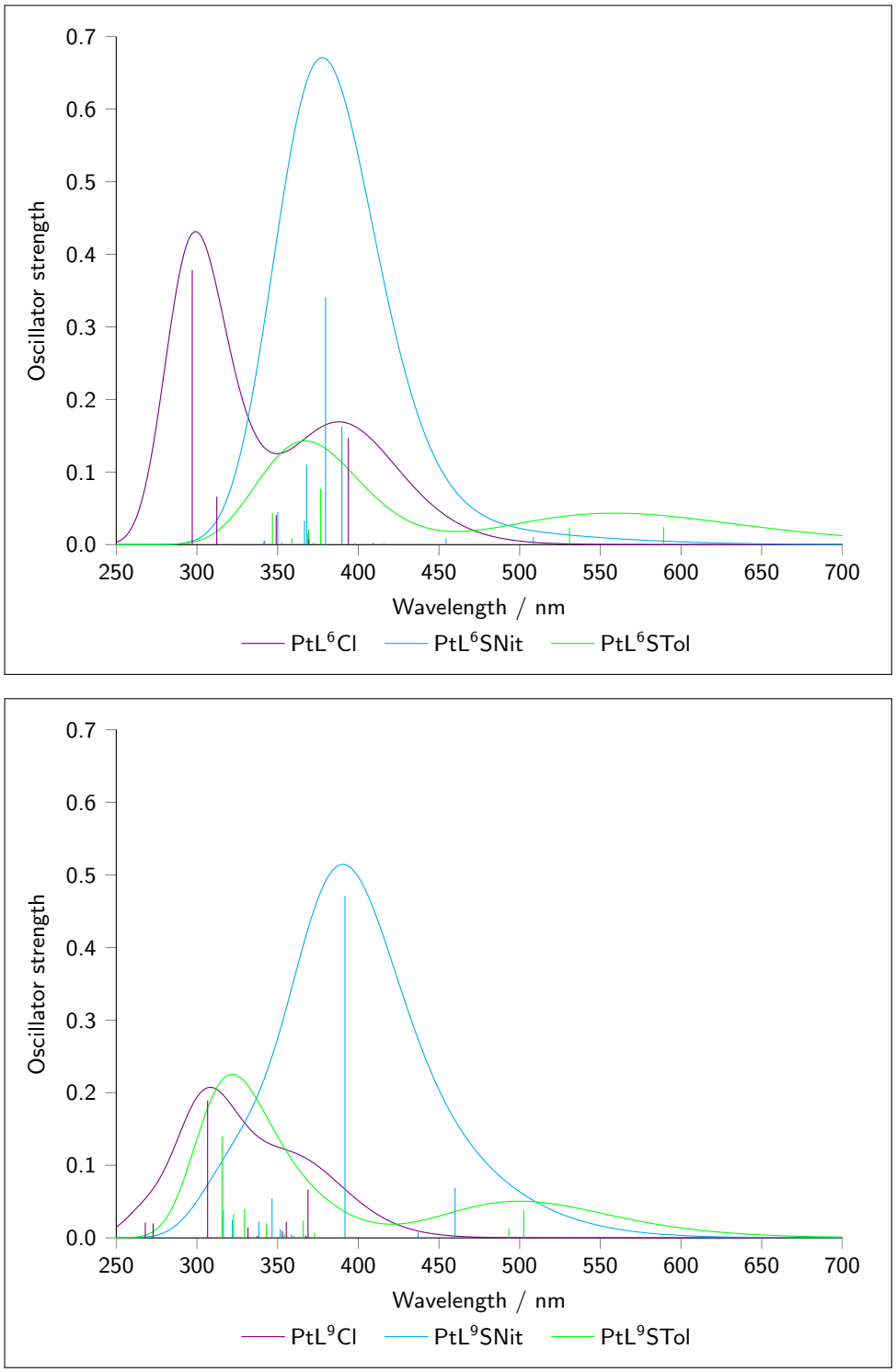

Figure 4.25: Convoluted absorption spectra of PtL^6SNit and PtL^6STol (top) and PtL^9SNit and PtL^9STol (bottom) in DCM, calculated by TD-DFT. Excitations calculated are shown in the Appendix, Table 9.17, density difference plots in Figures 9.13, 9.15 and 9.17.

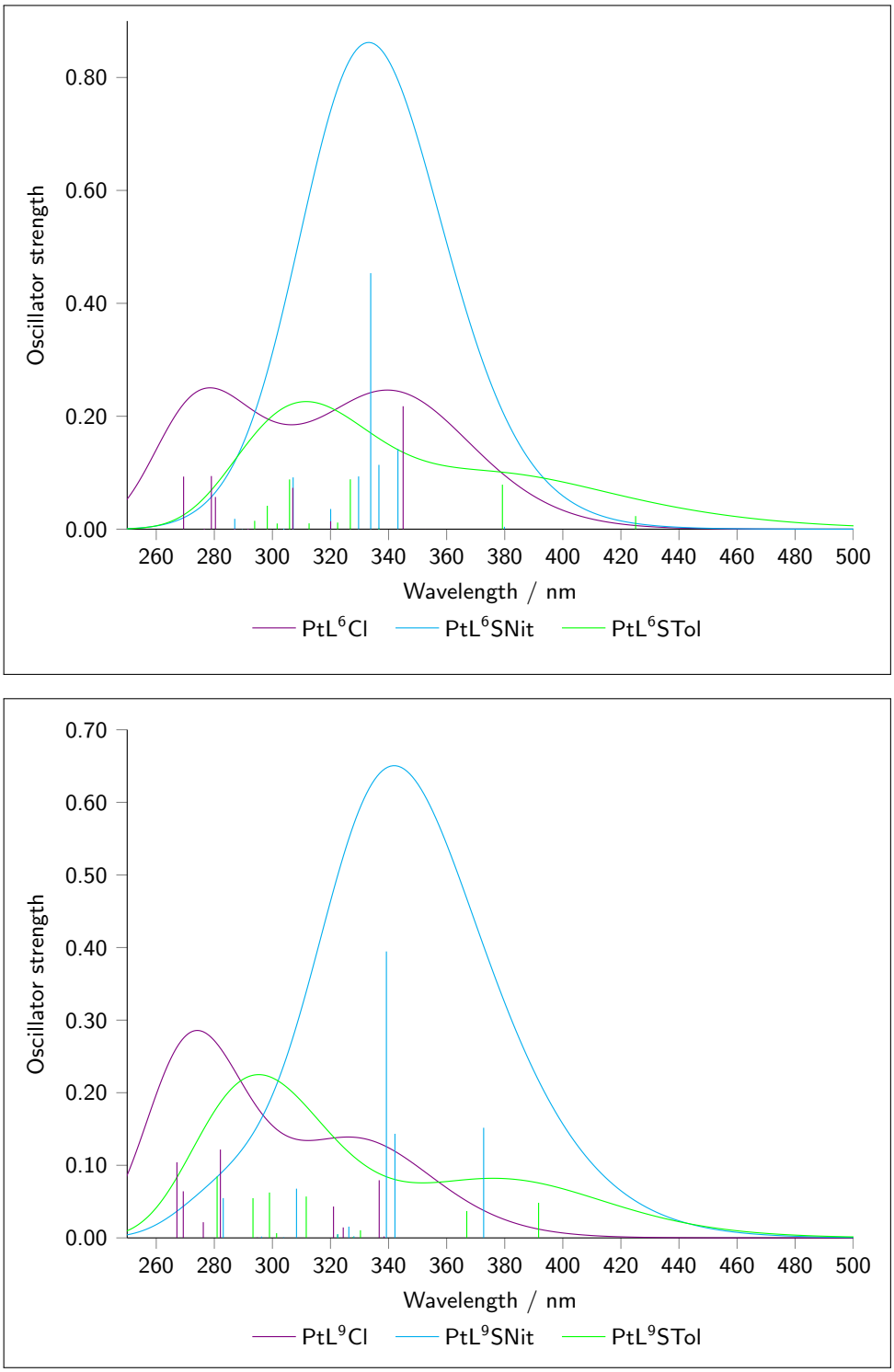

Figure 4.26: Convoluted absorption spectra of PtL^{6}SNit and PtL^{6}STol (top) and PtL^{9}SNit and PtL^{9}STol (bottom) in DCM, calculated by TD-DFT with CAM-B3LYP. Excitations calculated are shown in the Appendix, Table 9.18.

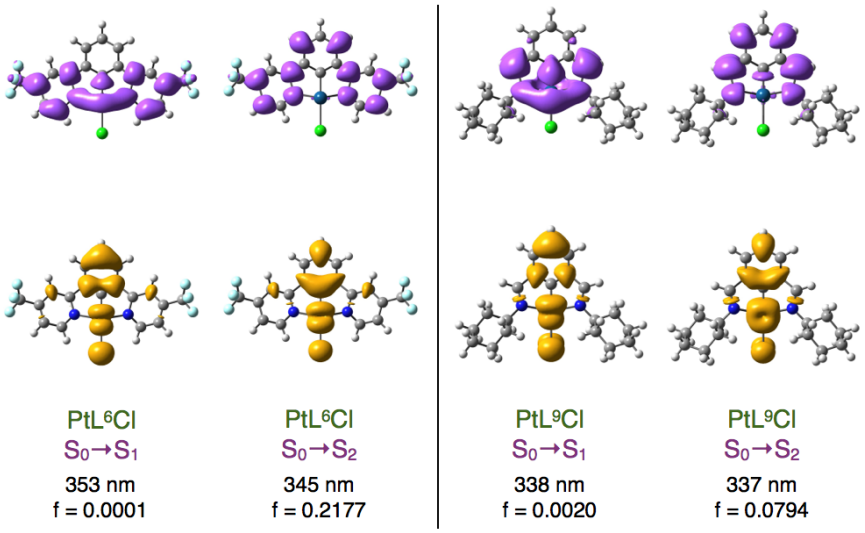

Figure 4.27: Density difference plots for the first two excitations of PtL^{9}Cl and PtL^{6}SCl in DCM at the ground state geometry with oscillator strength for each transition (f). Calculations were run with CAM-B3LYP.

They show that for both PtL^{6}SR and PtL^{9}SR DFT predicts a charge-transfer transition for the two STol-substituted compounds and a thiolate-based transition in the case of the nitro compound, in line with the experimentally obtained results. The excitation energies also shown in Chapter 3, Figure 3.21 show that the red-shift of PtL^{6}STol relative to PtL^{9}STol is correctly predicted, as is the red-shift of the PtL^{6}STol relative to its SNit counterpart. Despite the correct transition being assigned, PtL^{9}STol is predicted to be lower in energy of emission than PtL^{9}SNit, though this is perhaps unsurprising since we have seen that different types of transitions cannot always be predicted accurately within a trend, especially when one is low in orbital overlap (PtL^{9}STol) and the other is high (PtL^{9}SNit).

4.7 Concluding remarks

This chapter has discussed the merits and shortcomings of DFT calculations on two groups of complexes. The first, made up of two series of closely related compounds (PtL^{5}SR and PtL^{8}SR), were used as a test set to investigate the ability of TD-DFT to reproduce trends in absorption and emission energies,

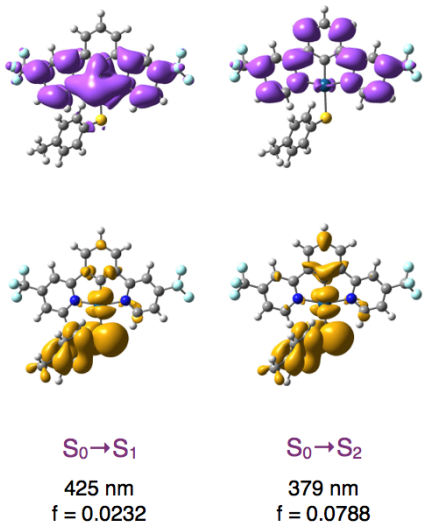

Figure 4.28: Density difference plots for the first two excitations of PtL^{6}STol in DCM at the ground state geometry with oscillator strength for each transition (f). Calculations were run with CAM-B3LYP.

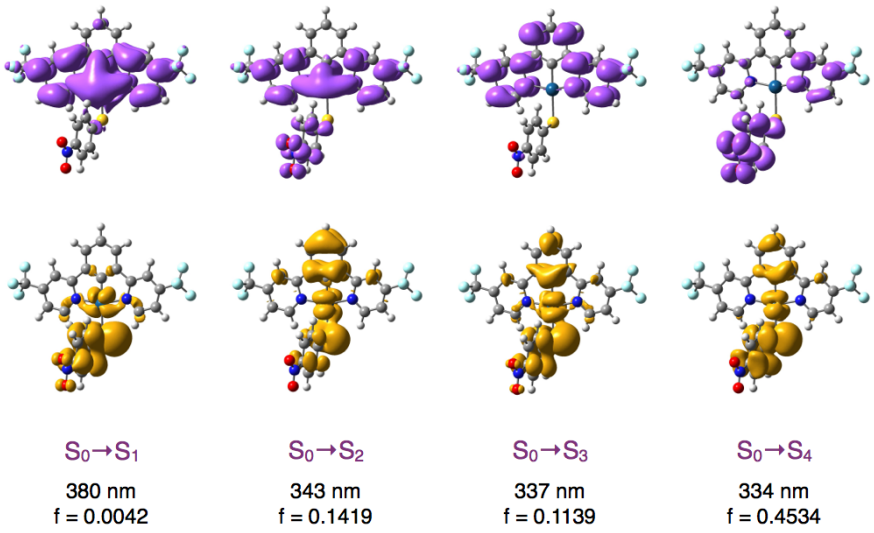

Figure 4.29: Density difference plots for the first four excitations of PtL^{6}SNit in DCM at the ground state geometry with oscillator strength for each transition (f). Calculations were run with CAM-B3LYP.

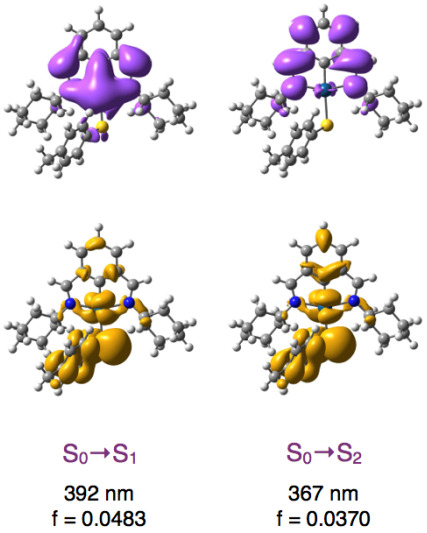

Figure 4.30: Density difference plots for the first two excitations of PtL^{9}STol in DCM at the ground state geometry with oscillator strength (f). Calculations were run with CAM-B3LYP.

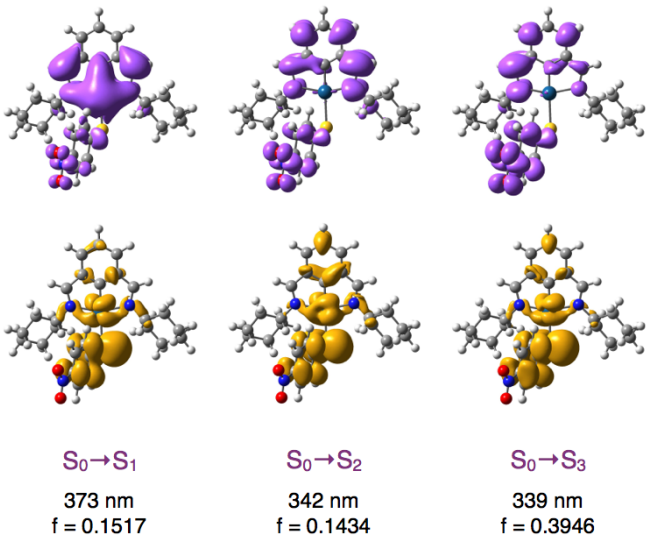

Figure 4.31: Density difference plots for the first three excitations of PtL^{9}SNit in DCM at the ground state geometry with oscillator strength for each transition (f). Calculations were run with CAM-B3LYP.

along with their correct density difference plots. Studies on these complexes showed the importance of solvent inclusion at all stages of the calculation (both geometry optimisation and TD-DFT) for prediction of the correct orbital plots and assignment of excitation character.

For all the series of complexes studied (PtL^5SR, PtL^6SR, PtL^8SR and PtL^9SR), trends predicted in absorption energies were closer to experimentally obtained results when using a long range corrected functional, CAM-B3LYP, than with PBE0. For emission the reverse was true due to lower triplet stabilities when using CAM-B3LYP than PBE0. TDA excitations were calculated at the DFT-optimised T_1 geometry, though it is suggested that the geometries themselves had been adversely affected by the low stabilities. For these reasons, TDA excitations at a TDA geometry, using CAM-B3LYP, are suggested as a possible route to the best reproduction of experimental trends. In general, singlet absorption is much more straightforward to predict than phosphorescent emission since there is less difficulty in ensuring you have the true ground state minimum (instead of a localised triplet minimum) and triplet instabilities do not need to be taken into account.

Trends in solvatochromism of the complexes were also reproduced and accounted for by analysis of the orbital plots for the relevant complexes.

5

Pt(II) complexes of ligands based on 1,3-diiminobenzene

5.1 Introduction

In this chapter we will consider a series of tridentate imine-based ligands for use in Pt(II) complexes. Previous work on some of these complexes investigated their use as catalysts,[212] while we intended to study their emission properties. Such ligands might be used to synthesise relatively cheap, easy-to-make Pt(II) complexes in which a simple imine C=N unit replaces the pyridyl rings of the complexes of Chapters 2-4. The ligands can be formed by a simple condensation reaction between an aldehyde and an amine without recourse to the Pd catalysts required for the dipyridylbenzene ligands. This method allows a great number of ligands to be synthesised relatively easily since the reaction can take as little as thirty minutes to reach equilibrium. A large variety of R and R′ substituents are possible, allowing for diversity of products (Figure 5.1).

Synthesis of these imine (R′ = H, R = C_nH_m) ligands will first be discussed in this chapter, then their ketimine (R′ = Me) and oxime (R = OC_nH_n) analogues. We will then consider the synthesis of the complexes along with ancillary ligand metathesis. The photophysical properties of the complexes will be discussed in Section 5.3 and interpreted using DFT calculations in

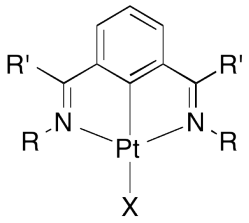

Figure 5.1: General structure of complexes with 1,3-diiminobenzene ligands.

Section 5.4. DFT calculations have been successfully used to rationalise the drastically differing quantum yields of emission measured among the series of complexes.

5.2 Synthesis

5.2.1 Synthesis of ligands

In this investigation, three series of ligands were synthesised: imines, ketimines and bis-oximes. The ligands made are shown in Figure 5.2.

Imine formation - introduction

The condensation of a carbonyl group with an amine to give an imine (Scheme 5.1) is a reversible reaction. Since the discovery of Schiff bases in 1864,[213] they have been widely used in chemical reactions and thoroughly researched.[214] Imine formation is normally carried out in anhydrous organic solvents, which pushes the equilibrium position towards the condensation product through loss of water.[215]

It is well known that the rate-determining step of decomposition (shown in Scheme 5.2) is imine hydrolysis (step 1) when at neutral or alkaline pH.[216] In addition, it has been demonstrated that the rate of hydrolysis of retinylidenemethylamine (a Schiff base) is significantly slower in acidic conditions than in neutral. This is attributed to a change in the rate determining step from step 1 of the reaction to step 2 when at a low pH. While formation of the imine group is affected by general acid catalysis, the presence of a strong acid in

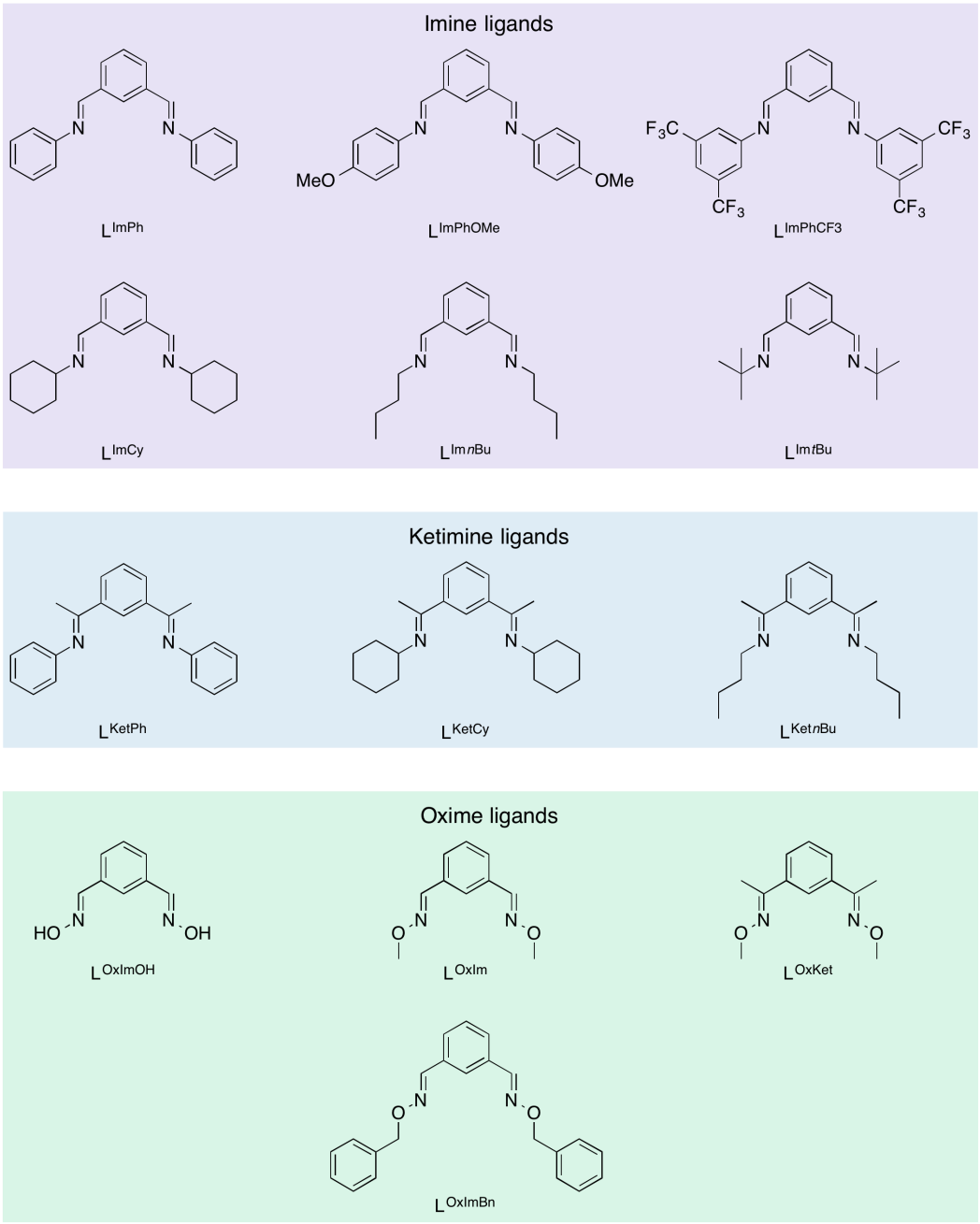

Figure 5.2: The chemical structures of the three sets of ligands synthesised.

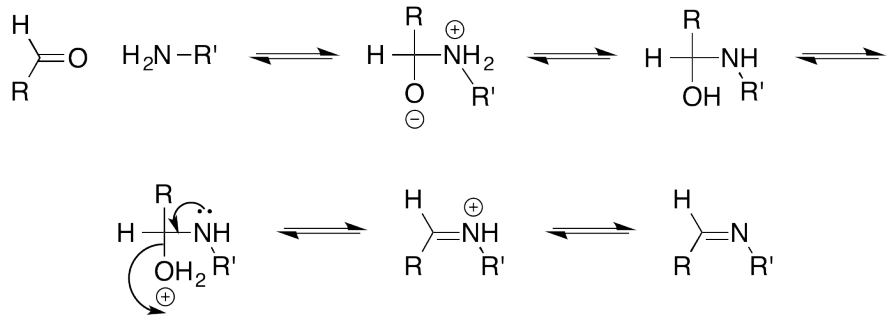

Scheme 5.1: Mechanism for the reaction of carbonyls with amines to give imines.

the reaction mixture will protonate the amine, removing it from the reaction mixture and shifting the position of the equilibrium towards its formation.[216] It is clear, therefore, that the pH of imine chemistry is an important factor in determining the speed and position of equilibrium that is obtained, the importance of which was seen upon attempts to cyclometallate these ligands (Section 5.2.2).

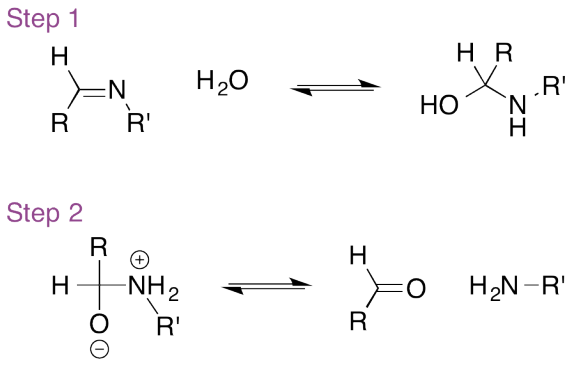

Scheme 5.2: Hydrolysis of imines to give carbonyl and amine species.

Imine ligand formation

Ligand synthesis followed that described by Fossey and Richards[212] (Scheme 5.3), though some difficulty was met in reproduction of reported results. Fossey *et al.* drove formation of imine to completion by reflux of a small excess of amine with the aldehyde, in ethanol, for thirty minutes. The solvent was then removed, the product taken up in ethyl acetate and rapidly filtered through

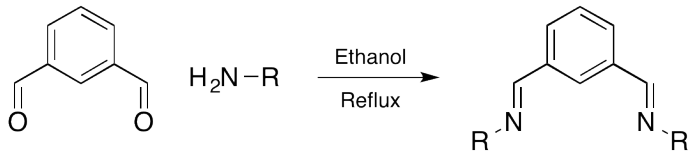

Scheme 5.3: Formation of N^C^N imine ligands.

a small plug of silica to remove the amine. This gave a product containing a small amount of aldehyde (for example 6% in the case of L^{ImPh}) which they removed by recrystallisation from ethyl acetate/petroleum ether. Though this procedure was repeated with success for the phenyl substituted imine, on repetition for the cyclohexyl substituted analogue we found that extensive hydrolysis of the imine occurred upon filtration through silica. This is presumably due to the presence of water in the silica and to its slightly acidic nature. The apparent higher stability of the phenyl substituted imine could be due to an extended system of delocalised electrons encompassing both the phenyl group and the imine bond. An adapted method was therefore necessary for the synthesis of the cyclohexyl compound and other aliphatic substituted imines.

We will first consider synthesis of the cyclohexyl-substituted ligand, L^{ImCy}, since this informed the method used for synthesis of the other ligands. Since excess amine was used to drive the reaction to completion, this was the impurity which had to be removed upon completion of the reaction. Various different purification techniques were employed to attempt its removal without causing hydrolysis of the product, including extremely fast filtering through a silica plug (which caused hydrolysis), selective precipitation (taking up the mixture in ethyl acetate followed by addition of hexane), and removal of the amine by heating the product on the high vacuum line (since the boiling point of the amine is 134.5°C[217]). All of these were to no avail.

Since all attempts at removing the amine were unsuccessful, synthesis was attempted using an excess of aldehyde to drive the reaction. The same difficulty was encountered since the aldehyde has similar solubility properties to the imine product; purification by recrystallisation was unsuccessful. Finally,

synthesis was attempted with the aldehyde and amine groups in equimolar quantities. All glassware and equipment was extensively dried prior to use to exclude water, so that equilibrium would not be shifted (according to Le Chatelier's principle) towards reactants. The reaction showed very good conversion and, after washing with cold hexane (0°C), the pure product was obtained in good yield. Synthesis of $L^{ImPhOMe}$ and L^{ImPhCF_3} was also achieved by use of equimolar quantities of reactants to avoid the need for purification, once again delivering the pure product in high yield.

Synthesis of butyl-substituted imines was more straightforward than their phenyl and cyclohexyl analogues since both *n*-butylamine and *t*-butylamine have low boiling points (77 and 44 - 46°C respectively).[217] This meant that the amine could be used in a large excess, driving the position of the equilibrium towards the products. The amine was then easily removed under reduced pressure upon completion. In order to reach a boiling point high enough for reaction of the two molecules, the reaction mixture was heated under nitrogen (to exclude atmospheric water) in a sealed flask rather than using a condenser. This meant that the low boiling point amines were not lost through evaporation, keeping them in solution to react with the aldehyde groups. This gave complete conversion to L^{Im^nBu} and L^{Im^tBu} with no need for further purification.

Characterisation of imine ligands

Condensation of an amine and isophthalaldehyde to give the imine ligand species resulted in a significant upfield shift of the N=C−H proton in the ^{1}H NMR spectrum. For example, the O=C−H proton of isophthalaldehyde has a chemical shift of 10.13 ppm (in $CDCl_3$), while the equivalent proton in L^{ImCy} has a shift of 8.34 ppm. The other three aromatic protons were also shifted upfield though the magnitude was not so large.

Crystals of $L^{ImPhOMe}$ suitable for analysis by X-ray diffraction were obtained by slow evaporation from a mixture of methanol and DCM. The structure obtained and packing adopted by this molecule are shown in Figure 5.3. The structure confirmed the identity of the compound. It is interesting to note

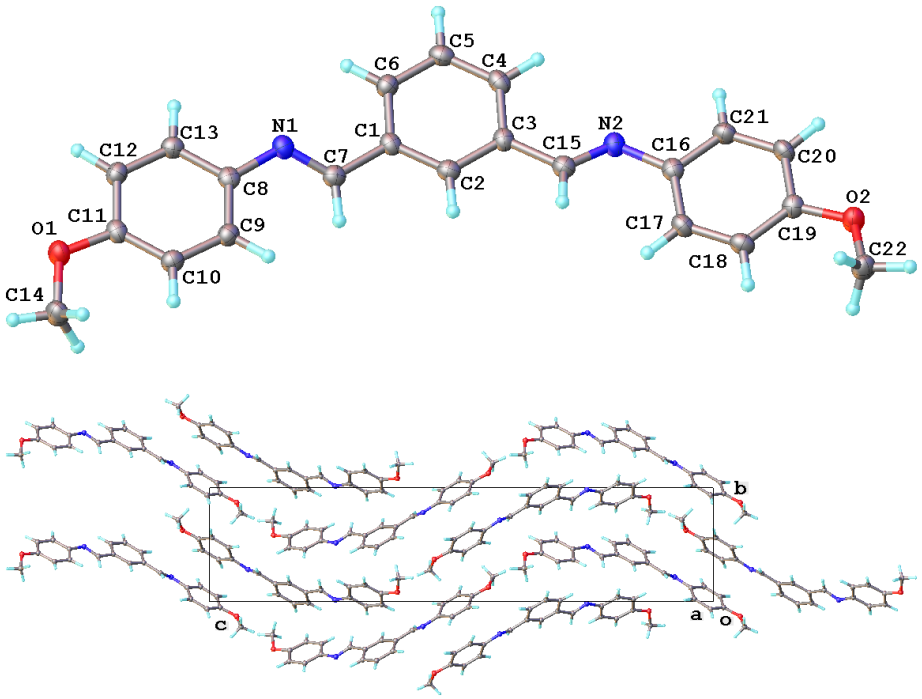

Figure 5.3: Crystal structure (top) and illustration of the packing (bottom) adopted by $L^{ImPhOMe}$.

that despite the number of aromatic rings included in this molecule there are no $\pi - \pi$ interactions.

Ketimine ligand formation

Due to the ease with which the imines were hydrolysed and the difficulty which was then encountered upon attempts to cyclometallate them (*vide infra*), it was decided to synthesise a series of ketimine ligands. These would be more sterically hindered, preventing the approach of water molecules to the sp^2 carbon centre and therefore making them more stable towards hydrolysis. The ketimines were synthesised according to the method shown in Scheme 5.4. Unsurprisingly, the synthesis of ketimines required harsher conditions than those used for their imine analogues, since the carbonyl carbon is more sterically hindered and less electrophilic. Synthesis of these novel molecules was based on a route for ketimine formation described by Malkov *et al.*[218] where the reactants were heated in dry toluene, under nitrogen and

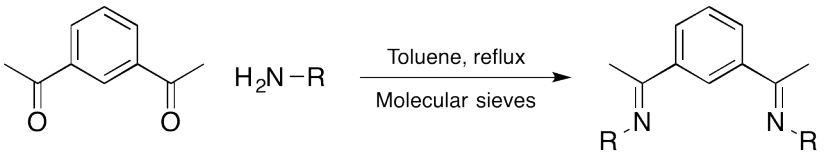

Scheme 5.4: Formation of N^C^N ketimine ligands.

in the presence of molecular sieves. Synthesis of the cyclohexyl substituted compound was initially attempted to refine the synthetic process since some difficulty was encountered in getting complete conversion to the bis-ketimine. Once this was achieved, phenyl and butyl substituted compounds were synthesised using the same method with relative ease.

Several different methods were attempted for the synthesis of the cyclohexyl-substituted ketimine ligand, L^{KetCy} since it was found that, as for the imine analogues, hydrolysis often occurred during purification of the product. Although in this case there was some success with purification by recrystallisation from hexane, there was significant product loss and the compound obtained still retained a small amount of impurity.

Initially, cyclohexylamine was reacted in a slight excess with 1,3-diacetylbenzene in dry toluene (using oven dried glassware), in the presence of activated molecular sieves and with a calcium chloride drying tube. The reaction mixture was heated at reflux overnight with the aim to remove water molecules produced using the molecular sieves, shifting the equilibrium in favour of the products. While some conversion of reactants to products was observed, complete conversion did not occur and as mentioned above, purification by filtration of a DCM solution through silica to remove the amine led to the hydrolysis product. Repetition of this reaction with the ketone and amine functional groups in a 1:1 molar ratio did not give complete conversion to products.

Synthesis of the ketimine ligand was attempted in ethanol since polar solvents are good at stablising localised charges formed in transition states; ethanol was used as the solvent for synthesis of the imine ligands with great success.

Unfortunately, reflux of the ketone with cyclohexylamine for 5 hours in ethanol (in the presence of activated molecular sieves) showed almost no conversion of reactants to products at all. This is probably due in part to the significantly reduced temperature of reaction in ethanol (b.p. of 79°C) compared to toluene (110°). Alcohol solvents also tend to contain a small amount of water which, if not all removed by the molecular sieves, would shift the position of equilibrium away from the product. For this reason the toluene solvent system was returned to.

During the overnight reflux of the reaction mixture, the molecular sieves became broken up into fine particles and the efficiency of their removal of water was questioned. We therefore attempted the reaction with activated molecular sieves placed in a soxhlet condenser to see if this allowed a more efficient removal of water. Three times the volume of toluene was required for use of the soxhlet condenser resulting in the increased reaction time of 36 hours. Very little condensation product was observed at all under these conditions. This is probably due to two contributing factors: first, the increased volume of solvent and second, the absence of the molecular sieves from the reaction mixture. Though the volume of solvent was increased by a factor of three, the length of time was also increased. It should also be considered that the soxhlet condenser works in cycles, filling up and emptying, therefore the volume of solvent in the reaction mixture is always varying and rarely the full amount. The decrease in conversion of reactants to products cannot entirely be explained by the decrease in concentration. It is likely that the molecular sieves played a catalytic role in the reaction when used in the reaction flask itself. The addition of a reaction surface is known to increase rates of such reactions, even though the precise details of how it does so remain unclear, and it can reasonably be suggested that this is the case here.

Finally, the reaction was carried out in the presence of molecular sieves but with a second quantity of sieves added half way through the reaction time. The additional sieves would make up for any inefficiencies from the first batch breaking up. The reaction time was extended to 48 hours and the ketone and amine functional groups combined in a 1:1 ratio. This resulted in near

complete conversion of reactants to products and the small amount of starting material was removed by washing of the product with cold hexane (0°C).

The corresponding ketimine ligand of aniline was then prepared simply using the same procedure and the product obtained in a high yield (87%). The synthesis of the *n*-butyl analogue was carried out with a large excess of amine, in dry toluene and in the presence of molecular sieves. The purification was simple since the excess amine (combined with removal of water) drove the reaction to completion. The amine could then be easily removed under reduced pressure, after the removal of the molecular sieves, by filtration.

Synthesis of the *t*-butyl substituted compound was also attempted (Scheme 5.5). The synthetic method used for the other three compounds was unsuccessful in this case, presumably due to the boiling point of *t*-butylamine (44-46°C) which is much lower than that of toluene and the reaction temperature previously used. Since the boiling point was so low, the amine was added in large excess (5:1 molar ratio) and the reaction carried out at 110°C in toluene in a sealed flask, under nitrogen. Almost no conversion of reactants was observed though a small amount of the monomeric species was seen by ^{1}H NMR spectroscopy. To ensure that the lack of reaction was not due to loss of the amine, the reaction was repeated with extra *t*-butylamine added half way through the reaction time (along with the molecular sieves) but after 48 hours at reflux temperature still only a small amount of the monomeric product was detected and it was concluded that the product formation was likely to be hindered due to the steric constraints of *t*-butylamine. While it is possible that given a long period of time the product may have formed, it was decided that the length of time of reaction required and volume of amine needed (to replace any lost during the reaction) were too great to pursue synthesis of this product.

Characterisation of ketimine ligands

The ketimine ligands were characterised by ^{1}H and ^{13}C NMR spectroscopy and high resolution mass spectrometry. The two solid ketimine ligands (cyclo-

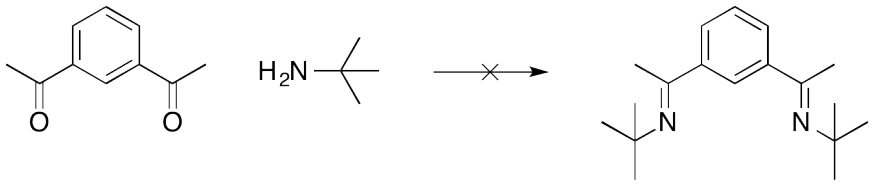

Scheme 5.5: Unsuccessful method attempted for synthesis of ^{t}butyl-substituted ketimine ligand.

hexyl and phenyl substituted) were also characterised by elemental analysis. Crystals of these two compounds suitable for X-ray diffraction analysis were obtained by slow evaporation from DCM, and the resulting structures are shown in Figures 5.4 and 5.5. The structures confirmed the identity of the compounds. Interestingly, the conformations adopted by these two molecules around the bonds labelled C7-C9 are different. For the phenyl-substituted compound the phenyl groups on the nitrogen atoms are in a different plane to the rest of the molecule despite the fact that this must prevent the possibility of extended conjugation across the whole molecule. This is due to steric constraints between this group and the methyl substituent on the imine group. The difference in geometry between the two compounds could be due to the difference in size between the two substituent groups or perhaps just to different packing effects.

Bis-oxime ligand formation

A great deal of difficulty was encountered upon attempting to cyclometallate the imine and ketimine ligands to platinum due to competitive hydrolysis of the ligand (see Section 5.2.2). For this reason, oximes were considered in place of the imine/ketimine groups, since oximes are more stable to hydrolysis. The electronegative oxygen can take part in delocalisation of the double bond, reducing the $\delta+$ on the carbon atom and making the group less susceptible to nucleophilic attack. The oxime functional group is synthesised by condensation of a ketone or aldehyde group with hydroxylamine[219] (Scheme 5.6).

At a neutral pH the attack of the nitrogen atom on the carbonyl compound is fast. The overall rate of the reaction therefore depends on the equilibrium

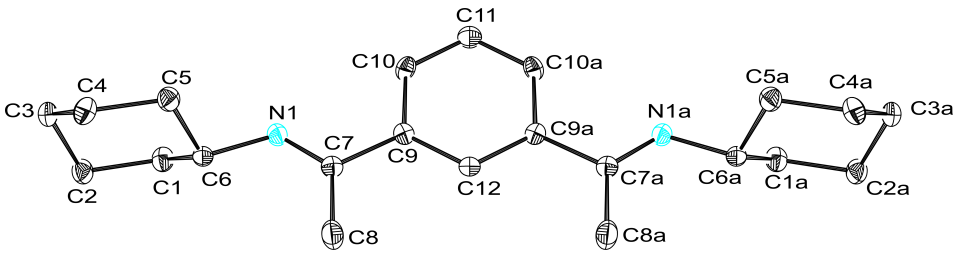

Figure 5.4: Crystal structure of L^{KetCy}

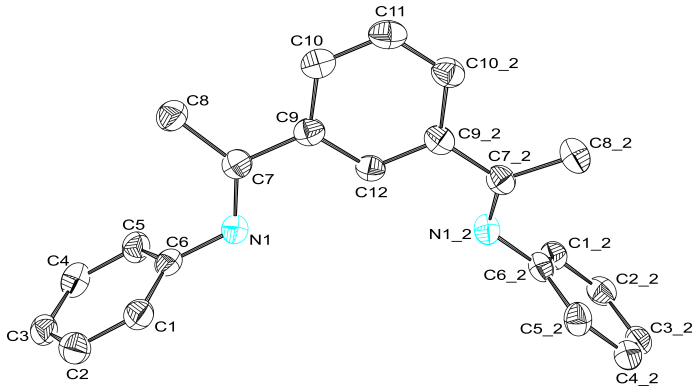

Figure 5.5: Crystal structure of L^{KetPh}

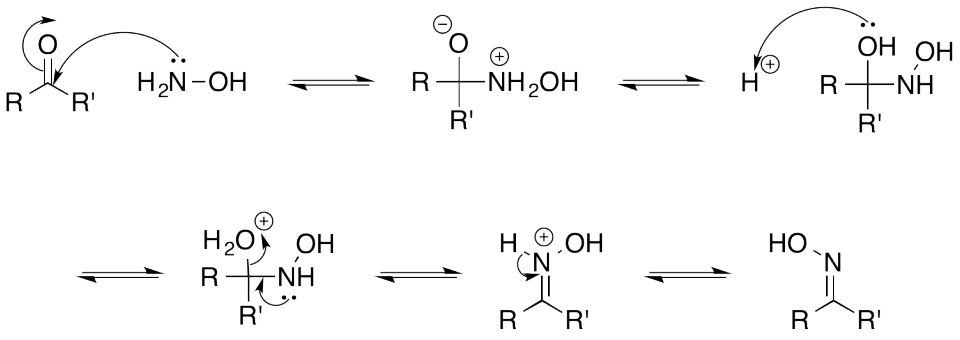

Scheme 5.6: Mechanism for the formation of an oxime.

concentration of the addition compound and on the rate of its acid-catalysed dehydration. Under acidic conditions the rate limiting step is the attack of the free nitrogen base on the carbonyl compound and is not dependent on general acid catalysis.[220]

Synthesis of L^{OxImBn} (Figure 5.2) was attempted according to a method similar to one described by Godineau *et al.*[221] The reaction was carried out in a solution of sodium acetate (which acts as a buffer), in DCM, at room temperature. A mixture of isomers was obtained according to the conformation around the C=N double bonds. This problem was not encountered for imine and ketimine ligand synthesis since the reaction was performed at high temperature, giving the thermodynamic product and $Z \rightarrow E$ isomerisation in imines probably has a lower energy barrier. The isomers and any remaining starting material were separated from each other with ease by column chromatography and the desired *EE* isomer was isolated for characterisation. The fractions containing the other isomers (*EZ* and *ZZ*) were combined and the solvent removed. This mixture of isomers was then put under an atmosphere of nitrogen and heated strongly for two lots of 2.5 minutes, giving $\sim 60\%$ conversion to the *EE* isomer, the thermodynamic product. For this reason, if the reaction were to be repeated, heating upon completion of the reaction and before purification should give a greater yield. Alternatively, carrying out the reaction with heating in a different polar, aprotic solvent with a higher boiling point (such as DMF or acetonitrile), should give a higher yield of the desired product. It is testament to the stabilising presence of the oxygen atom in the molecule that the compound resisted hydrolysis both in the presence of water and during purification by column chromatography. As discussed later (Section 5.2.2), the product showed little hydrolysis even when heated under reflux in acetic acid while similar imine and ketimine molecules showed extensive degradation. Ligands L^{OxImOH}, L^{OxIm} and L^{OxKet} were also synthesised using this method.

5.2.2 Synthesis of complexes

Significant difficulty was encountered in the cyclometallation of the imine and ketimine ligands to platinum since both series of ligands were found to be very

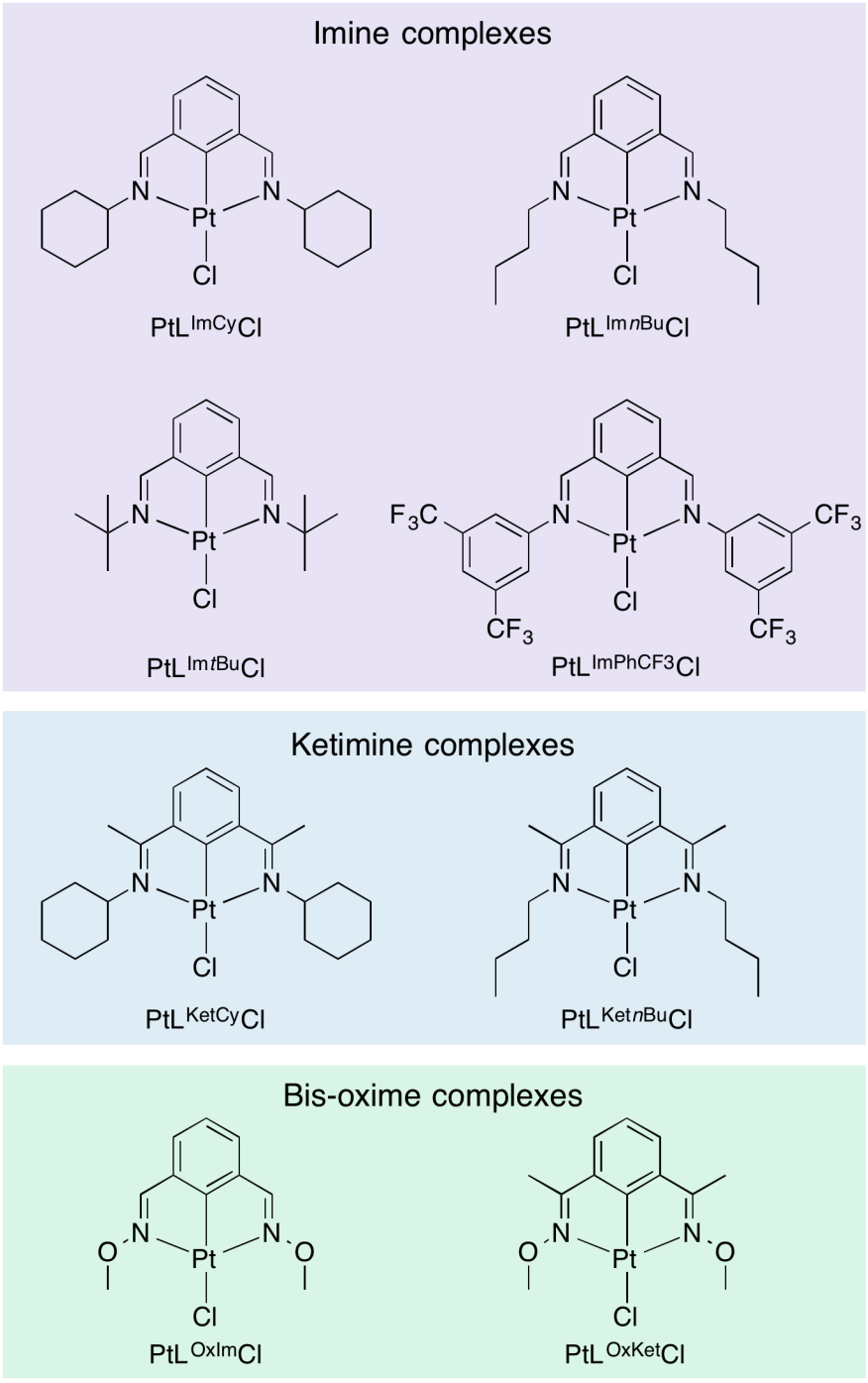

Figure 5.6: The chemical structures of the three sets of complexes synthesised.

water-sensitive. Decomposition of the imine series was characterised by the disappearance of the imine proton in the ^{1}H NMR spectrum, and appearance of the aldehyde proton. Despite the increased steric protection afforded to the ketimine ligands there seemed to be no difference between the two series of ligands in their propensity to hydrolysis. This difficulty of competitive hydrolysis was not encountered with the oxime series due to the stabilising effect of the oxygen atoms.

Synthesis of the complexes was initially attempted according to the procedure described by Fossey and Richards[212] for both the cyclohexyl and phenyl substituted imines and for the cyclohexyl substituted ketimine, but all to no avail. Analysis of the reaction products by ^{1}H NMR spectroscopy showed complete hydrolysis of ligands to their starting materials with no formation of the platinum complex. Though this method has previously been used with success, hydrolysis of the compounds is unsurprising since (as previously discussed) the decomposition of the imine bond is acid catalysed. Furthermore, acidification of the amine decomposition product removes this molecule from the equilibrium, driving the position of the equilibrium towards hydrolysis. Nevertheless, water must be present for this decomposition to occur. For this reason, extensive care was taken in drying both the glassware, the solvent and the hygroscopic potassium tetrachloroplatinate in an attempt to prevent the breakdown of the compounds.

Synthesis of the metallated products was successfully achieved by use of trimethylphosphate which has been used in other cyclometallation reactions.[222] Difficulty was encountered, however, in complete removal of such a high boiling point solvent (197°C) from the product. Despite extensive attempts at extraction, chromatography, recrystallisation, vaccum distillation and washings, the solvent present could only be reduced, never removed entirely. The cyclometallated product seemed to show some solvatochromic response (by eye) and it is suspected that the compound forms an adduct or clathrate with the trimethyl phosphate, explaining why it is so difficult to separate.

Since hydrolysis of the ligands was the main barrier to successful cyclometalla-

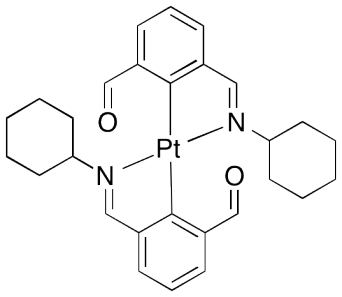

Figure 5.7: Proposed structure of by-product formed upon attempts to cyclometallate L^{ImCy}.

tion, it was postulated that reaction of the ligands with potassium tetrachloroplatinate in an alcohol would allow the ligands to re-form once hydrolysed. Binding of the ligands to the platinum would then remove them from the equilibrium mixture, driving the reaction towards the formation of products. Though formation of the Pt(II) complex was not observed after reaction in propanol (probably due to the reduced reaction temperature), some formation of complex was observed in butan-1-ol. Attempted cyclometallation in butan-1-ol seemed to favour formation of a second product. Analysis of the mixture by mass spectrometry showed a combination of products and a peak with a platinum isotope pattern corresponding to the compound shown in Figure 5.7.

Finally, cyclometallation was achieved in acetic acid with drying of both solvent and metal salt prior to synthesis by reflux of both in the presence of acetic anhydride, reaction of which with any water present in the potassium tetrachloroplatinate crystals would result in the production of acetic acid. This was followed by addition of a large excess of ligand, allowing for some sacrificial degradation. This method was successful and purification was achieved either by passing the product through a small plug of silica or, for some complexes, by HPLC. Hydrolysis of the excess ligand for the aromatic amine ligands resulted in reaction between the amine and acetic acid molecules to give the corresponding acetamide, small crystals of which were obtained and analysed by X-ray diffraction (Figure 5.8).

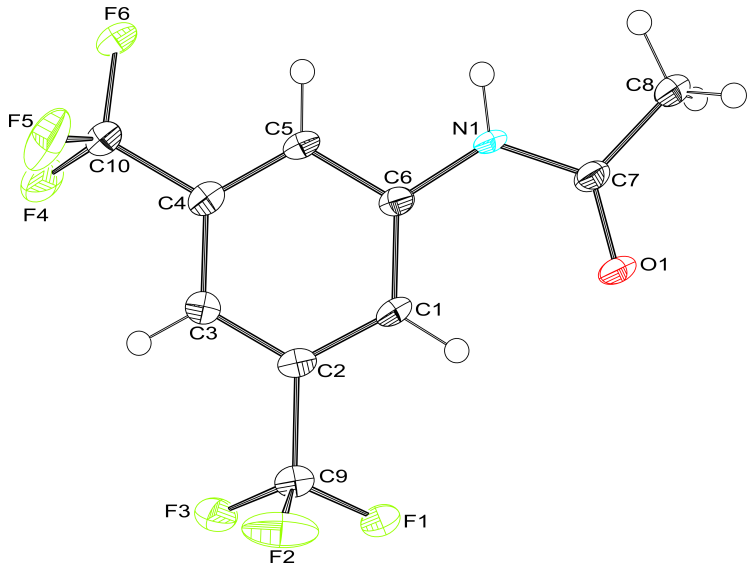

Figure 5.8: Crystal structure of acetamide produced upon attempts to cyclometallate PtL^{ImCF_3}Cl.

Characterisation of complexes

The identity of each of the complexes was confirmed by ^{1}H and ^{13}C NMR spectroscopy. Successful cyclometallation of the ligand showed the introduction of platinum satellites in the ^{1}H spectrum for the protons at positions 3 and 5 of the benzene ring and, for the imine complexes, the N=C−H proton. High resolution mass spectrometry also confirmed the identity of the species; all of the data for compounds previously reported was in good agreement with the literature values.

Small crystals, suitable for X-ray diffraction, were obtained of PtL$^{\mathrm{ImPhCF_3}}$Cl ($CDCl_3$), PtL$^{\mathrm{Ket^nBu}}$Cl (methanol/water), PtL$^{\mathrm{OxIm}}$Cl (DCM) and PtL$^{\mathrm{OxKet}}$Cl ($CDCl_3$) by slow evaporation from the indicated solvents (Figures 5.9 - 5.12). The crystal structures of PtL$^{\mathrm{Im^tBu}}$Cl and PtL$^{\mathrm{ImPh}}$Cl have previously been determined by Fossey and Richards.[212] A summary of some of the important bond lengths and angles of PtL$^{\mathrm{ImPhCF_3}}$Cl, PtL$^{\mathrm{Ket^nBu}}$Cl, PtL$^{\mathrm{OxIm}}$Cl and PtL$^{\mathrm{OxKet}}$Cl is shown in Table 5.1.

$PtL^{ImPhCF_3}Cl$ shows a nearly planar environment around the Pt atom with only very slight twisting out of the plane (presumably to minimise steric interactions). The two pendant phenyl groups are twisted relative to the rest of the molecule, preventing delocalisation of electrons over the whole molecule. This is also true of $PtL^{ImPh}Cl$[212] and in fact the L^{KetPh} ligand (see Section 5.2.1, Figure 5.5). $PtL^{Ket^nBu}Cl$ shows a very small distortion away from planarity about one of the nitrogen atoms; again it is assumed that this is to minimise steric interactions due to the increased interactions introduced by the combination of methyl groups alongside *n*-butyl pendants. $PtL^{OxIm}Cl$ shows some bowing around the C−Pt−Cl but has the two less bulky OMe groups pointing in the same direction. The same is true of $PtL^{OxKet}Cl$.

In all these cases the N−Pt−N angle is more strained than for the platinum(II) complex of 1,3-di(2-pyridyl)benzene, PtL^5Cl (161.1(2)°), this is particularly pronounced in the two oxime complexes, $PtL^{OxIm}Cl$ and $PtL^{OxKet}Cl$ which have values of around 157° for this angle. The C−Pt−Cl bond is also distorted in these new complexes, again particularly in the oximes which are contorted away from the linear 180° which we would expect (PtL^5Cl is 179.0(3)°). The Pt−C bond lengths are longer for the oxime complexes than for the imine and ketimine compounds but are all on average around the same length as PtL^5Cl (1.907(8) Å). This is also true of the Pt−Cl bond (2.417(2) Å for PtL^5Cl). In contrast all of the C=N bonds are much shorter for these new compounds compared to PtL^5Cl which has lengths of 1.365(9) and 1.374(9) Å, which is not a true C=N bond since the bond order is ~ 1.5 instead of 2.

The packing of $PtL^{ImPhCF_3}Cl$ is made up of sheets of the planar section of the molecules with the pendant groups in between. Each molecule is rotated 90° to the ones above and below it, maximising $\pi-\pi$ stacking while minimising unfavourable steric interactions (see Figure 5.9). The crystal of $PtL^{OxKet}Cl$ was shown to contain two non-equivalent geometries of the complex as shown in Figure 5.12. There seem to be no other electronic interactions in the packing of the other complexes (extended packing shown in Appendix).

	PtL^5Cl	$PtL^{ImPhCF_3}Cl$	$PtL^{Ket^nBu}Cl$	$PtL^{OxIm}Cl$	$PtL^{OxKet}Cl$
Bond Lengths / Å					
Pt−N	2.042(6) 2.033(6)	2.051(3) 2.069(3)	2.0430 2.0437	2.035 2.0334	2.0090, 2.0246 2.0130, 2.0218
Pt−C	1.907(8)	1.893(4)	1.8994	1.9282	1.9143 1.9143
Pt−Cl	2.417(2)	2.3764(9)	2.3864	2.4031	2.4257 2.4378
N=C	1.365(9) 1.374(9)	1.315(5) 1.320(5)	1.3027 1.3164	1.2867 1.2997	1.3172, 1.3061 1.2998, 1.3106
Bond Angles / °					
N−Pt−N	161.1(2)	158.7(1)	159.47	156.57	156.98 156.60
C−Pt−Cl	179.0(3)	177.8(1)	178.03	173.95	173.24 178.51
N−Pt−C	80.9(3) 80.2(3)	79.3(1) 79.4(1)	79.71 79.77	78.58 78.00	78.50, 78.53 78.33, 78.34
N−Pt−Cl	99.8(2) 99.1(2)	99.46(9) 101.79(8)	99.15 101.37	101.28 101.95	99.37, 103.62 100.23, 103.11

Table 5.1: Selected bond lengths (Å) and bond angles (°) found for the complexes shown. Purple text indicates the second molecule in the unit cell - in this case the crystals grew based around a two molecule system. Values for PtL^5Cl reported by Cárdenas et al.[51]

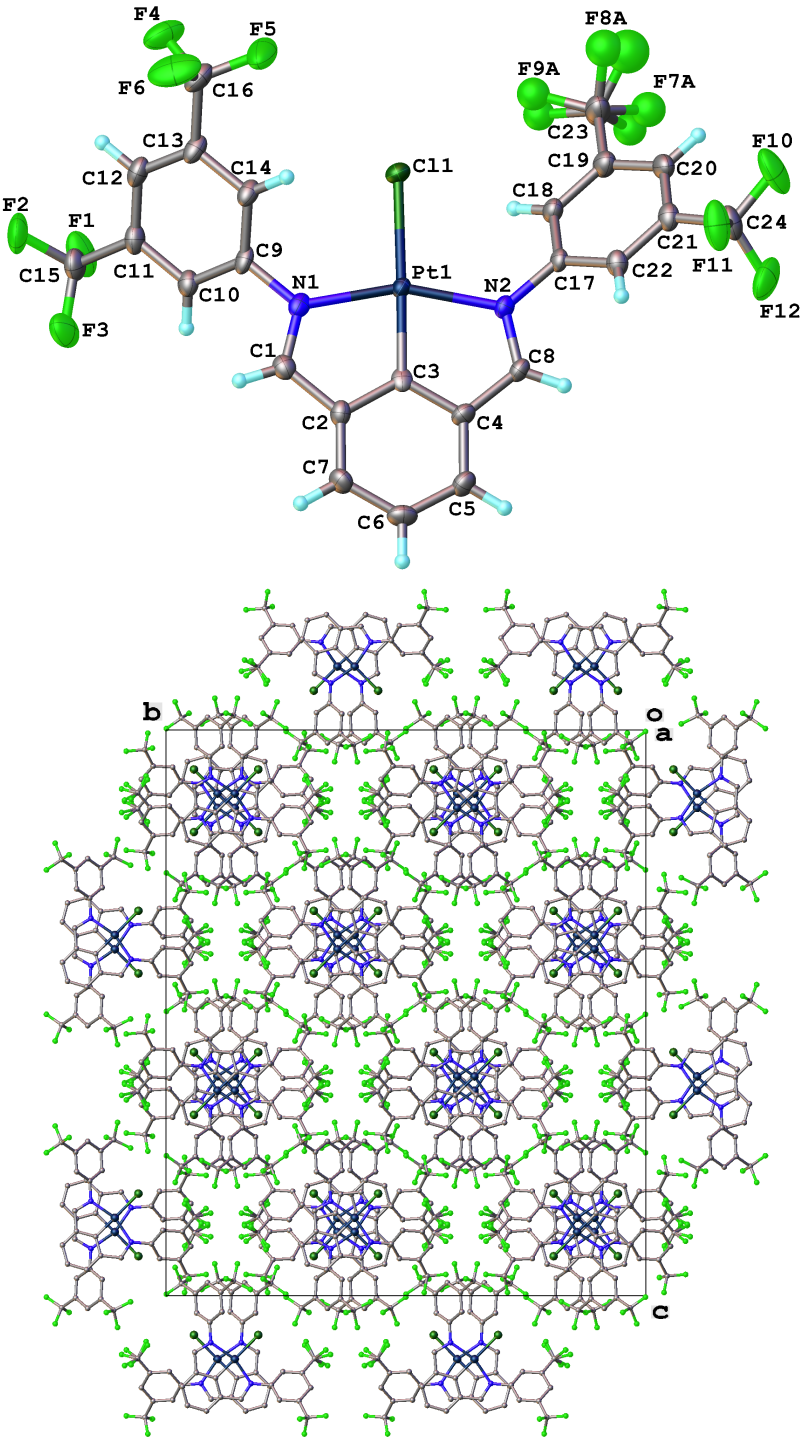

Figure 5.9: Crystal structure of PtL^{ImPhCF_3}Cl.

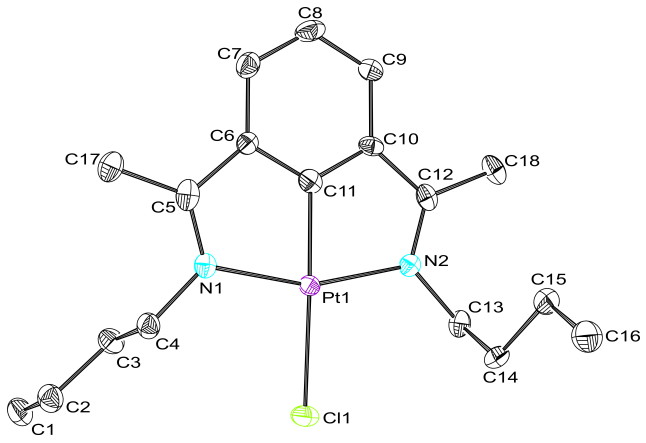

Figure 5.10: Crystal structure of PtL$^{Ket^{n}Bu}$Cl. Packing shown in Appendix, Figure 9.18.

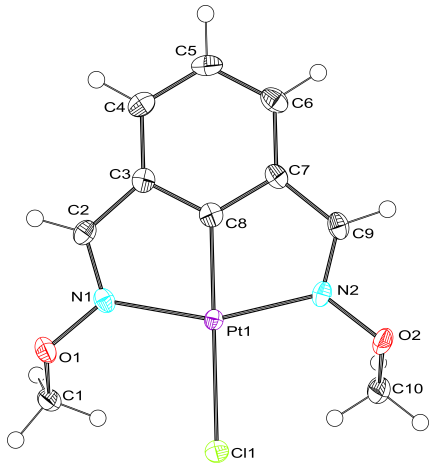

Figure 5.11: Crystal structure of PtL^{OxIm}Cl. Packing shown in Appendix, Figure 9.19.

5.2.3 Metathesis of the ancillary ligand

Substitution of the chloride ancillary ligand for a stronger field ligand should increase ligand field splitting, increasing the energy of the d-d state, reducing likelihood of its population and therefore reducing non-radiative decay. Substitution of this ligand has been attempted with success by several groups in related complexes such as Pt(N^N^C)Cl, who have converted the chloride to ligands such as cyanides or acetylides.[29–32]

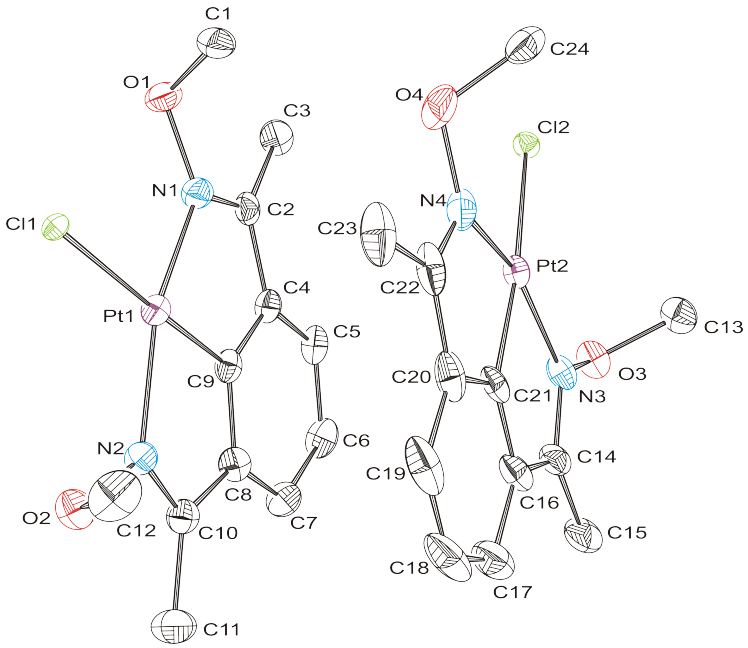

Figure 5.12: Crystal structure of PtL^{OxKet}Cl. Packing shown in Appendix, Figure 9.20.

The chloride ligand of an example imine complex, PtL^{ImCy}Cl was substituted by various other ancillary ligands to see what effect this had on the photophysical properties of the molecule. The chemical structures of the four complexes made are shown in Figure 5.13. Synthesis and photophysical characterisation of PtL^{ImCy}STol and PtL^{ImCy}SNit have been discussed more fully in Chapter 3 (Sections 3.2 and 3.4 respectively).

Synthesis of PtL^{ImCy}C$_2$Ar

The chloride ancillary ligand of PtL^{ImCy}Cl was substituted for an acetylide using a technique similar to that of Baik *et al.* for other N^C^N-coordinated Pt(II) complexes but without the use of a chloride scavenger.[60] The reaction proceeded under mild conditions at room temperature, the acetylide deprotonated by sodium hydroxide, then once reacted with the platinum complex, the product retrieved from solution as a light yellow precipitate (Scheme 5.7). Purification was achieved by washing with methanol. Although stable enough to acquire a crystal structure, PtL^{ImCy}C$_2$Ar did show some decomposition in

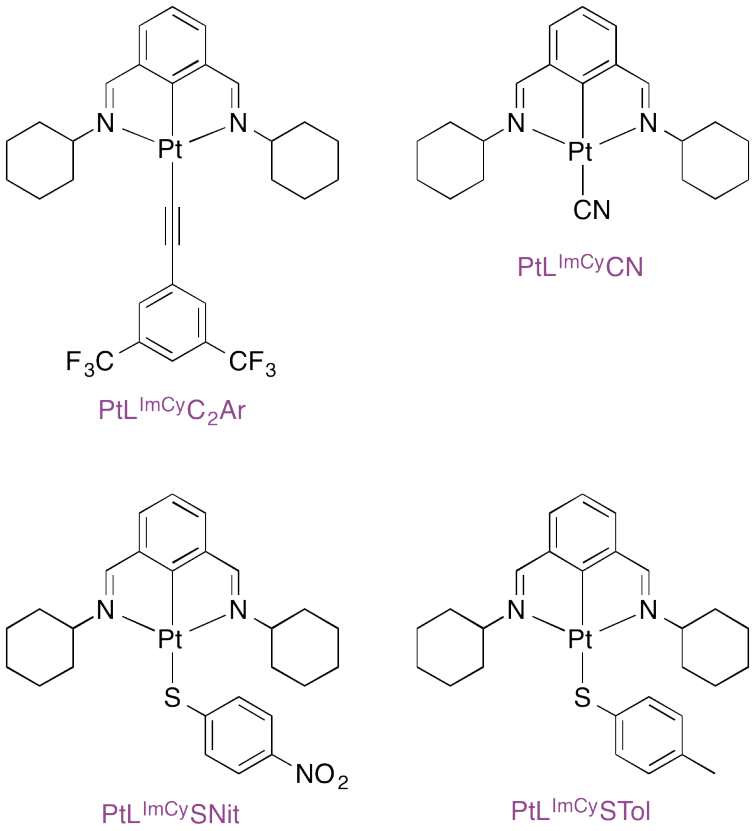

Figure 5.13: The chemical structures of the complexes synthesised incorporating a monodentate ligand other than chloride.

DCM. The electron-withdrawing CF_3 groups of the acetylide ligand help to stabilise the Pt−C bond in its unfavourable position: *trans* to another cyclometallated bond.

Synthesis of $PtL^{ImCy}CN$

Substitution of the chloride ligand by CN was also attempted though with limited success (Scheme 5.8). A solution of KCN and $PtL^{ImCy}Cl$ in methanol were stirred for ∼12 h at room temperature to give a pale, yellow solid. Analysis of this product in the solid state by ASAP mass spectrometry (at both high and low resolution) showed data in line with formation of the correct product:

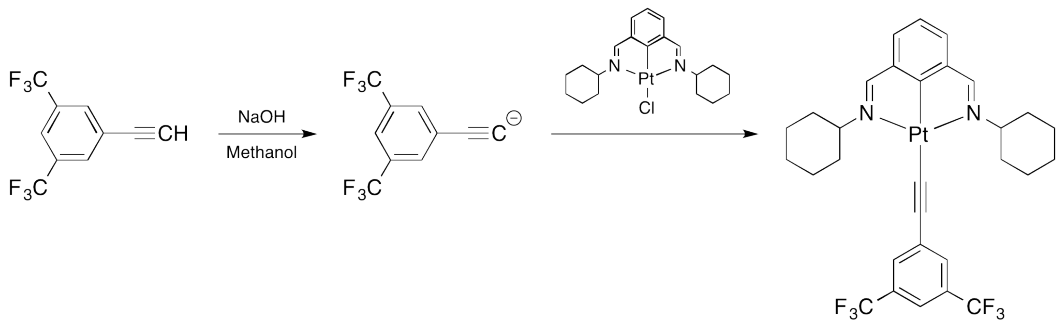

Scheme 5.7: Formation of $PtL^{ImCy}C_2Ar$.

(ASAP$^+$) m/z = 517.2 [M + H]$^+$; HRMS (AP$^+$) m/z = 515.1829 [M]$^+$; calculated for [$C_{21}H_{27}N_3{}^{194}Pt$]$^+$ 515.1832.

Solvation of the compound for analysis by NMR (or photochemical analysis) induced rapid decomposition.

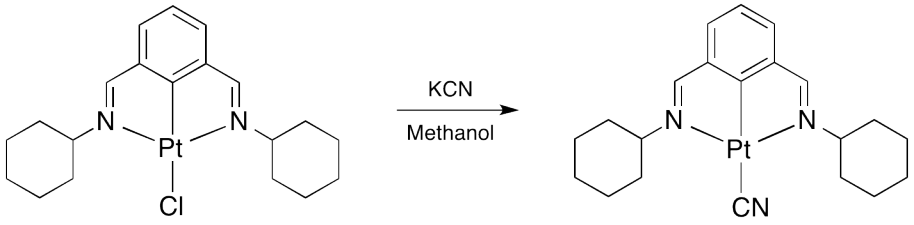

Scheme 5.8: Formation of $PtL^{ImCy}CN$.

Characterisation of $PtL^{ImCy}C_2Ar$

A small crystal of $PtL^{ImCy}C_2Ar$ was obtained by slow evaporation from deuterated chloroform. Its structure is shown in Figure 5.14 with some selected bond lengths and angles in Table 5.2. It is interesting to note that the acetylide group is contorted out of the plane of the molecule, with the C≡C−C bond at 170.55° rather than the linear 180°. Both CF_3 groups and one of the cyclohexyl rings are disordered. The C−Pt bond of the ancillary ligand is quite long for a cyclometallated bond (2.0499 Å) due to the unfavourable *trans* effect of two such carbon atoms. The C−Pt bond of the N^C^N is slightly longer than the equivalent bond in the other chloride-substituted complexes

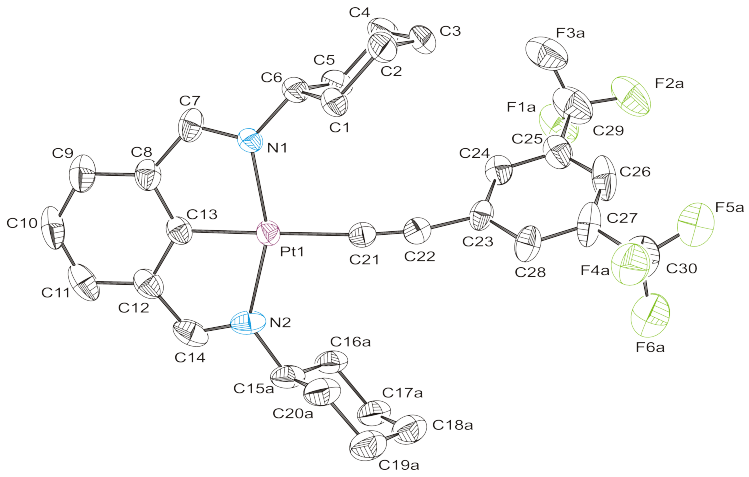

Figure 5.14: Crystal structure of PtL^{ImCy}C$_2$Ar. Packing shown in Appendix, Figure 9.21.

Bond lengths / Å		*Bond angles / °*	
N–Pt	2.0734, 2.0684	**N–Pt–N**	156.75
C–Pt	1.9430	**N–Pt–C**	78.42, 78.33
C–Pt	2.0499	**N–Pt–C**	101.11, 102.14
C≡C	1.2012	**C–Pt–C**	179.05
		Pt–C≡C	174.42
		C≡C–C	170.55

Table 5.2: Selected bond lengths (Å) and angles (°) found for the crystal structure of PtL^{ImCy}C$_2$Ar. Purple text indicates atoms bound from the N^C^N ligand while green text shows atoms from the acetylide ancillary ligand.

(see Table 5.1) due to the same effect.

Analysis by ^{1}H and ^{19}F NMR showed the expected extra peaks but analysis by ^{13}C NMR was not possible due to decomposition of the complex in solution over longer periods of time. ASAP mass spectrometry showed the expected molecular ion peak.

5.3 Photophysical properties of the complexes

5.3.1 Absorption

The absorption spectra of the new complexes were recorded in DCM at room temperature. They show bands with high extinction coefficients in the far UV and moderately intense bands at longer wavelengths, around 450-420 nm.

As illustrated by Figure 5.15, the absorption wavelengths of $PtL^{ImCy}Cl$ and $PtL^{KetCy}Cl$ are very similar to that of PtL^5Cl, with the band at ∼400 nm overlapping for all three complexes. The low energy absorption bands were slightly more intense in PtL^5Cl (Table 5.3). The new complexes show slightly less structured spectra than PtL^5Cl and lack the additional band displayed at 380 nm. $PtL^{ImCy}Cl$ and $PtL^{KetCy}Cl$ absorb more strongly between 340 and 360 nm than PtL^5Cl. They showed no evidence of the weak, spin-forbidden $S_0 \rightarrow T_n$ excitations shown by PtL^5Cl at longer wavelengths.[52]

The five alkyl-substituted imine and ketimine complexes ($PtL^{ImCy}Cl$, $PtL^{KetCy}Cl$, $PtL^{Im^nBu}Cl$, $PtL^{Im^tBu}Cl$ and $PtL^{Ket^nBu}Cl$) all show very similar absorption spectra (Figures 5.15 and 5.16); their lowest energy absorption band (∼390 nm) increases in wavelength in the order:

$$\mathbf{PtL^{Im^tBu}Cl} < \mathbf{PtL^{ImCy}Cl} < \mathbf{PtL^{Im^nBu}Cl} < \mathbf{PtL^{KetCy}Cl} < \mathbf{PtL^{Ket^nBu}Cl}$$

with a difference of only 1250 cm^{-1} between the λ_{max} of $PtL^{Im^tBu}Cl$ and $PtL^{Ket^nBu}Cl$. The absorption spectra of the imine complexes is more structured than that of the ketimines.

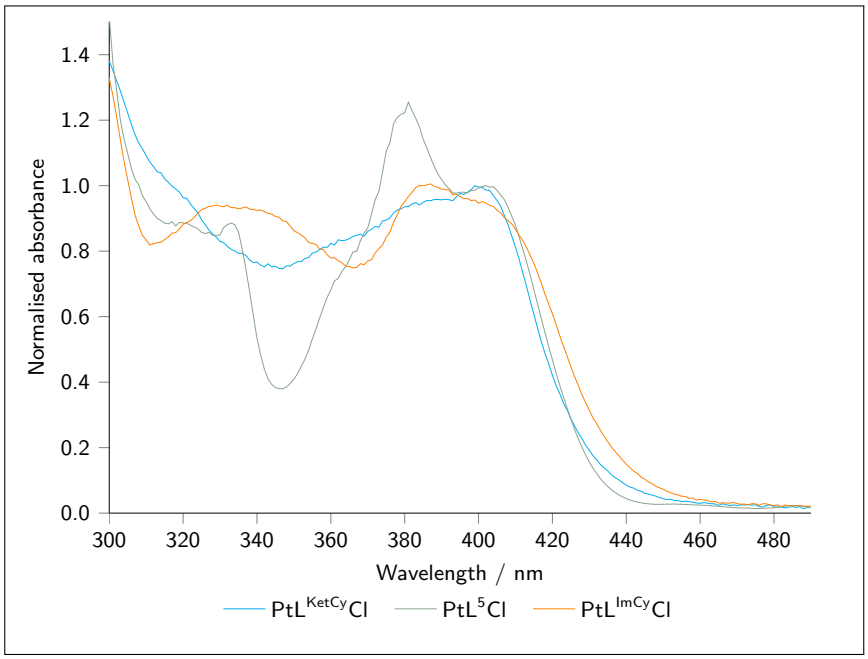

Figure 5.15: Normalised absorption spectra of PtL^{ImCy}Cl, PtL^{KetCy}Cl and PtL^{5}Cl in DCM.

The absorption spectrum of PtL^{ImCF_3}Cl is red-shifted from all of the other compounds, the lowest energy absorption band has a λ_{max} of 426 nm, compared to 385 nm for PtL^{ImCy}Cl (Figure 5.17). In contrast, PtL^{OxKet}Cl is blue-shifted from all the other compounds (λ_{max} = 379 nm).

5.3.2 Emission

The emission spectra of the new complexes were recorded both in degassed DCM at room temperature (Figures 5.18, 5.19 and 5.20) and in EPA glass at 77 K. With the exception of PtL^{OxKet}Cl, the platinum(II) complexes shown in Figure 5.6 were all luminescent in solution at room temperature. They showed low energy, red emission at 298 K ($\lambda_{max} \sim 600$ nm) with the 0−1 band highest in relative intensity. Emission spectra of the new complexes were obtained at different concentrations. This had no effect on the structure of the spectra obtained, indicating that there was no emission from excimer formation. There was a slight blue shift in emission energy upon cooling to 77 K. Quantum yields of luminescence were relatively low, ranging from ∼2% for some of the

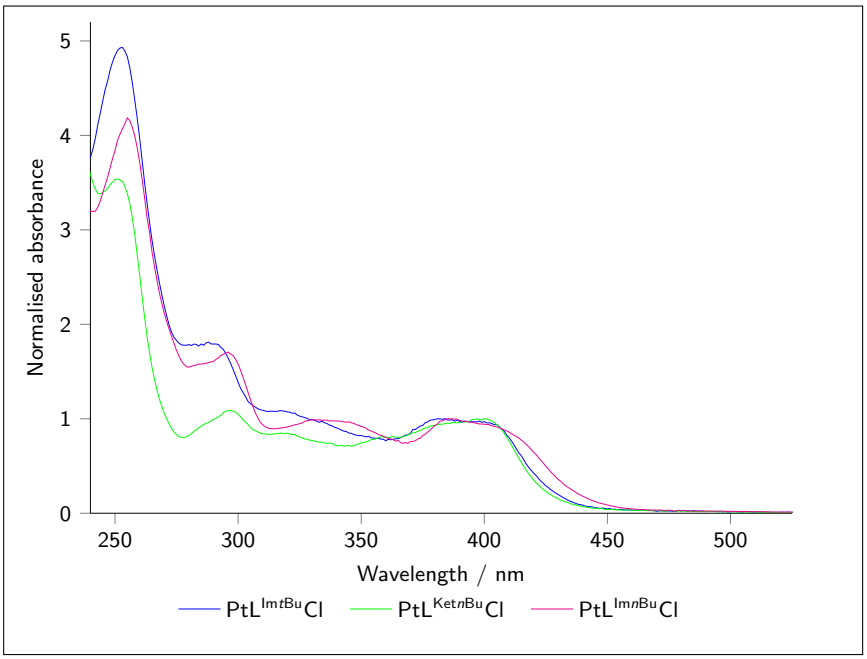

Figure 5.16: Normalised absorption spectra of the three butyl-substituted derivatives in DCM.

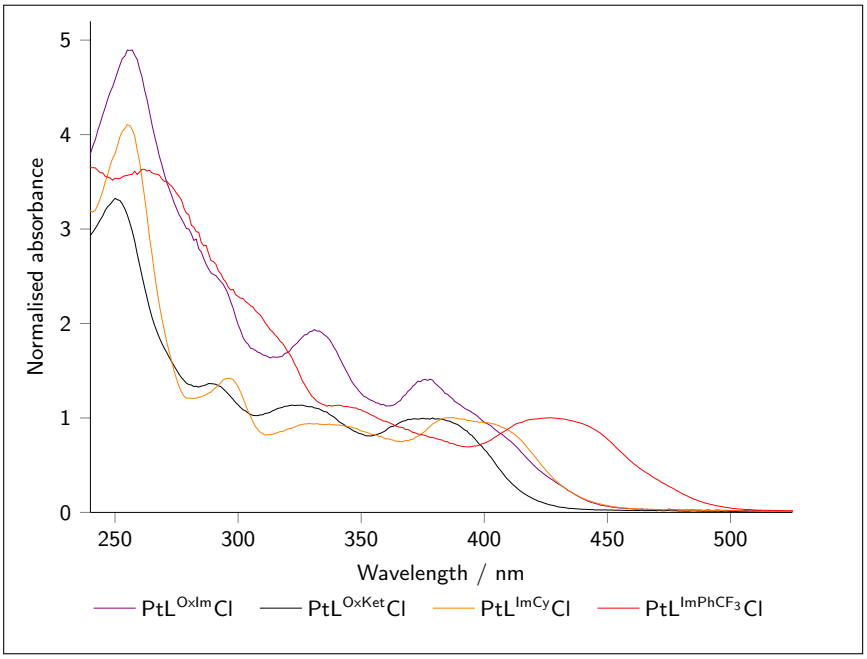

Figure 5.17: Normalised absorption spectra of $PtL^{OxIm}Cl$, $PtL^{OxKet}Cl$, $PtL^{ImCy}Cl$ and $PtL^{ImCF_3}Cl$ in DCM.

	Absorption λ_{max} / nm [(a)] (ε / M^{-1} cm^{-1})
$PtL^{5}Cl$	332 (6510), 380 (8690), 401 (7010), 454 (270), 485 (240)
$PtL^{ImCy}Cl$	255 (34100), 295 (8590), 329 (6530), 385 (6060)
$PtL^{Im^{n}Bu}Cl$	254 (26000), 296 (10800), 330 (6130), 387 (6230)
$PtL^{Im^{t}Bu}Cl$	253 (20700), 288 (7010), 317 (4220), 381 (3860)
$PtL^{ImPhCF_3}Cl$	262 (29100), 312 *sh* (15200), 339 (8720), 426 (7780)
$PtL^{KetCy}Cl$	253 (15600), 296 (5950), 399 (4070)
$PtL^{Ket^{n}Bu}Cl$	251 (21400), 297 (6530), 400 (6120)
$PtL^{OxIm}Cl$	257 (16200), 331 (6030), 378 (4390), 398 *sh* (3150)
$PtL^{OxKet}Cl$	250 (16500), 288 (6480), 326 (5430), 379 (4720)
$PtL^{ImCy}C_2Ar$	286 (15400), 352 *sh* (6530), 387 (5370), 415 *sh* (4870)

Table 5.3: UV-vis absorption data for the imine, ketimine and oxime complexes in DCM solution at 298 K. [(a)] Absorption maxima > 250 nm.

imine complexes to $PtL^{OxKet}Cl$ which showed no room temperature emission. Lifetimes of emission in degassed DCM varied between 13 ns ($PtL^{OxIm}Cl$) and 740 ns ($PtL^{Im^nBu}Cl$). A summary of the emission properties for the complexes studied is shown in Table 5.4.

Comparison of $PtL^{ImCy}Cl$ and PtL^5Cl shows that the emission properties of these two N^C^N-coordinated Pt(II) complexes are very different from one another. Emission from $PtL^{ImCy}Cl$ is much lower in energy than PtL^5Cl and shows a red shift of 2380 cm^{-1} between the two 0−0 bands (at room temperature, in DCM). The quantum yield is also significantly reduced from 60% (PtL^5Cl) to just 1.8%. While both compounds display highly structured emission spectra, the ratio of the band intensity changes. The 0−0 band is most intense for PtL^5Cl while the 0−1 band is for $PtL^{ImCy}Cl$ at both room temperature (DCM) and 77 K (EPA glass). The degassed lifetime (τ_{deg}) is an order of magnitude shorter for $PtL^{ImCy}Cl$ (700 ns) than for PtL^5Cl (7200 ns). In stark contrast to PtL^5Cl, $PtL^{ImCy}Cl$ shows no evidence of excimer formation.

The reduced emission quantum yield of in $PtL^{ImCy}Cl$ compared to PtL^5Cl is due to a combination of a slightly reduced k_r in the new compound and a significantly increased k_{nr} (by two orders of magnitude), as illustrated in Figure 5.21. The excited state energy of $PtL^{ImCy}Cl$ is significantly lower than PtL^5Cl, which increases the rate of non-radiative decay. Intuitively it is presumed that the dramatic increase in the rate of non-radiative decay is also due to intramolecular energy transfer to the C=N bonds of $PtL^{ImCy}Cl$, combined with increased flexibility within the ligand allowing for non-radiative decay through molecular motion.

The reduction in intermolecular interactions and lack of excimer formation in $PtL^{ImCy}Cl$ compared to PtL^5Cl is presumably due to the steric protection afforded by the bulky substituent groups in the former, preventing the close approach of molecules that is required for the necessary orbital overlap (or possibly due to lack of complementarity in electron density distribution at the ground and excited states). Shortened excited state lifetimes will also disfavour excimer formation.

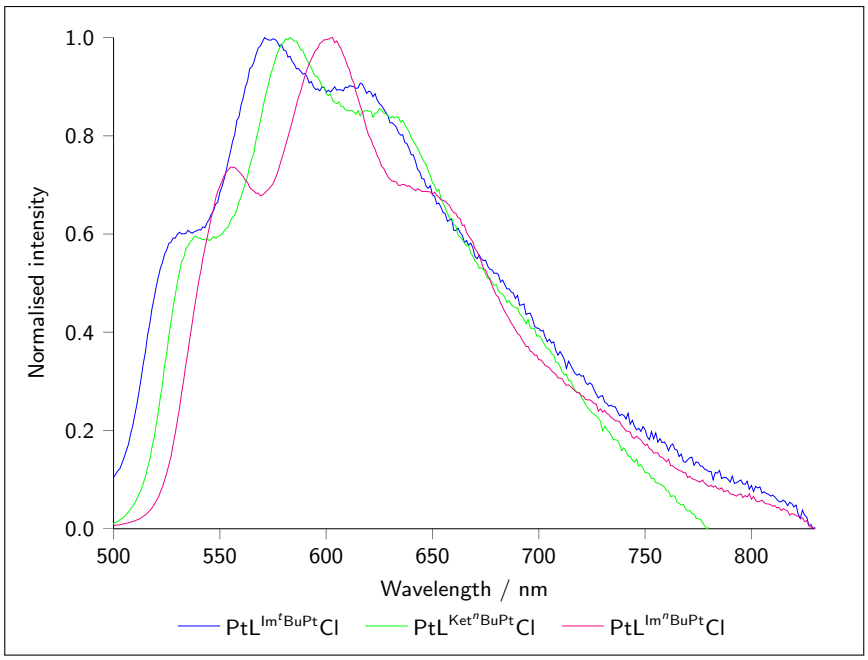

Figure 5.18: Normalised emission spectra of the three butyl-substituted derivatives in degassed DCM at 298 K.

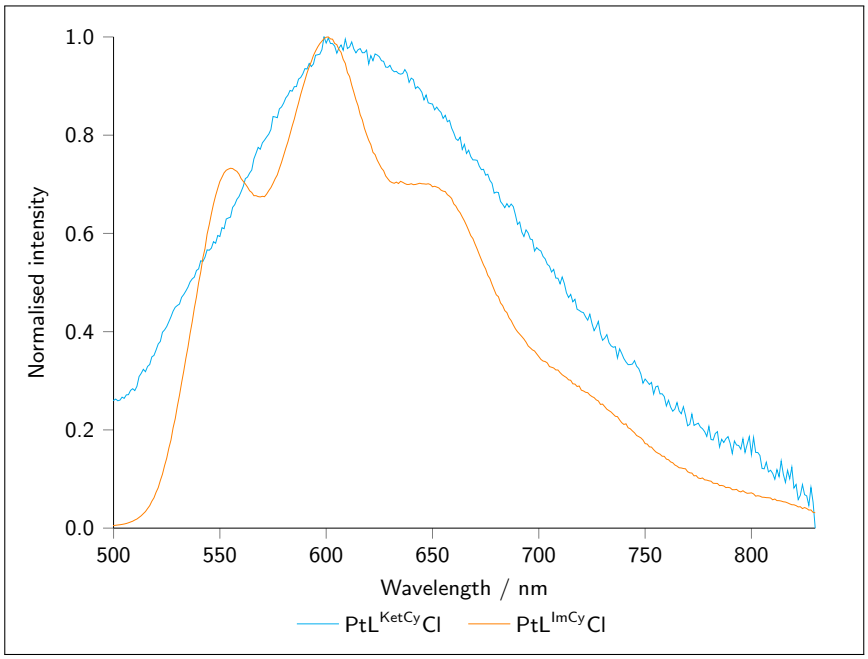

Figure 5.19: Normalised emission spectra of the two cyclohexyl-substituted derivatives in degassed DCM at 298 K.

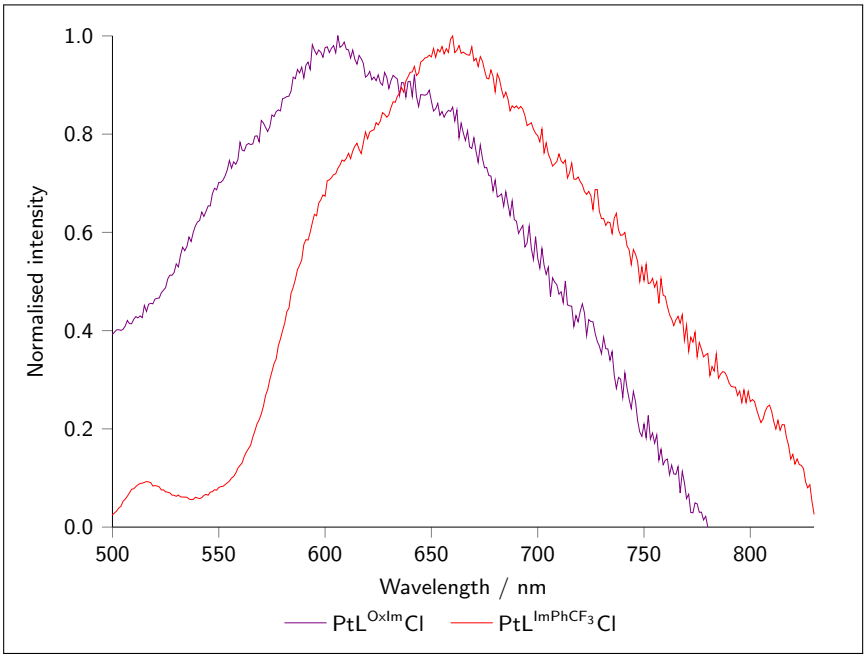

Figure 5.20: Normalised emission spectra of $PtL^{OxIm}Cl$ and $PtL^{ImPhCF_3}Cl$ in degassed DCM at 298 K.

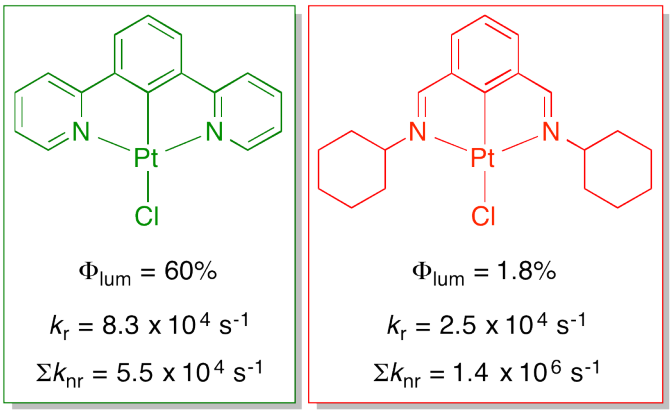

Figure 5.21: A diagram to summarise some of the emission properties of PtL^5Cl (left) and $PtL^{ImCy}Cl$ (right).

	Emission λ_{max} / nm (298 K)	Φ_{lum} $\times 10^2$	τ / ns degassed [aerated]	$k^Q{}_{O_2}$ / 10^8 $M^{-1}s^{-1}$ (b)	k_r / 10^4 s^{-1} (c)	Σk_{nr} / 10^6 s^{-1} (c)	Emission 77 K λ_{max}(**0−0**) / nm	τ / μs
$\mathbf{PtL^{ImCy}Cl}$	556, 599, 647, 719, 804	1.8	700 [310]	8.2	2.5	1.4	**532**, 578, 632, 692, 772	2100
$\mathbf{PtL^{Im^nBu}Cl}$	556, 600, 650	1.7	740 [330]	7.6	2.3	1.3	**532**, 580, 636, 694	630
$\mathbf{PtL^{Im^tBu}Cl}$	536, 575, 615	0.096	38 [37]	3.2	2.5	26	**514**, 558, 610, 668, 738	570
$\mathbf{PtL^{ImPhCF_3}Cl}$	660	0.22	-	-	-	-	**577**, 627, 687	-
$\mathbf{PtL^{KetCy}Cl}$	585	0.12	41 [36]	15	2.9	24	**536**, 572, 621, 685	720
$\mathbf{PtL^{Ket^nBu}Cl}$	537, 579, 635	0.88	370 [210]	9.3	2.4	2.7	**530**, 576, 628, 696 *sh*	720
$\mathbf{PtL^{OxIm}Cl}$	597	0.022	13 [12]	29	1.7	77	**508**, 543, 586, 642, 704	580
$\mathbf{PtL^{OxKet}Cl}$	-	-	-	-	-	-	-	-
$\mathbf{PtL^{ImCy}C_2Ar}$	559, 601, 650 *sh*	2.8	650 [250]	11	4.3	1.5	**531**, 577, 634, 694	790

Table 5.4: Luminescence data for the imine, ketimine and oxime complexes in DCM solution at 298 K and in EPA[(a)] at 77 K. Quantum yields are measured relative to [Ru(bpy)$_3$]Cl$_2$ in H_2O.

(a) EPA = diethyl ether / isopentane / ethanol, 2:2:1 v/v. (b) $k^Q{}_{O_2}$ is the bimolecular rate constant for quenching by molecular oxygen at 298 K, estimated from the relative lifetimes in degassed and aerated solutions, assuming [O_2] at 1 atm pressure of air = 2.2 mmol dm^{-3}. (c) k_r and Σk_{nr} are the radiative and non-radiative rate constants estimated from the quantum yield and lifetime at 298 K.

Comparison of diimine complexes with one another

During the course of this work, similar imine complexes were made and their photophysical properties studied by Raftery and co-workers.[223] They altered the 4-position of the benzene ring to various delocalised electron systems, finding through TD-DFT studies that this pendant arm was significantly involved in the excitations taking place. The phosphorescent emission of our complexes gave structured emission in the red region of the spectrum with λ_{max} ∼600 nm, similar to that of those other imine compounds previously reported.[223] Unlike the other imine compounds reported, the most intense band for all of the imine and ketimine complexes was the 0−1, suggesting a significant degree of distortion between the ground and excited states. There was a slight blue-shift in the emission maxima at low temperature, an effect which was slightly augmented in the imines compared to the ketimines.

The λ_{max} of emission was remarkably similar for $PtL^{ImCy}Cl$, $PtL^{KetCy}Cl$, $PtL^{Im^nBu}Cl$ and $PtL^{Ket^nBu}Cl$ (Figures 5.23 and 5.22), while $PtL^{Im^tBu}Cl$ shows a slight blue shift. In contrast, $PtL^{OxIm}Cl$ shows a significant blue-shift in emission energy of 2380 cm^{-1} from $PtL^{ImCy}Cl$ (for λ_{max} at 77 K) and $PtL^{ImPhCF_3}Cl$ is red-shifted from all the other compounds (for λ_{max} a shift of 1350 cm^{-1} compared to $PtL^{ImCy}Cl$ at 77 K).

Despite the very similar energies of emission of most of the complexes, Table 5.4 shows that both the quantum yields and lifetimes vary significantly. $PtL^{ImCy}Cl$ and $PtL^{Im^nBu}Cl$ had quantum yields an order of magnitude higher than those imine complexes previously reported.[223] Comparison of $PtL^{ImCy}Cl$ and $PtL^{KetCy}Cl$ shows that upon addition of the methyl groups to give the ketimine derivative, the quantum yield is reduced by an order of magnitude, as is k_{nr}, while k_r remains roughly the same, as illustrated in Figure 5.25 (each of the lifetimes is also reduced by an order of magnitude). The same is true of the three butyl-substituted complexes, the quantum yields of which decrease (k_{nr} increases) in the order:

$$\mathbf{PtL^{Im^nBu}Cl > PtL^{Ket^nBu}Cl > PtL^{Im^tBu}Cl}$$

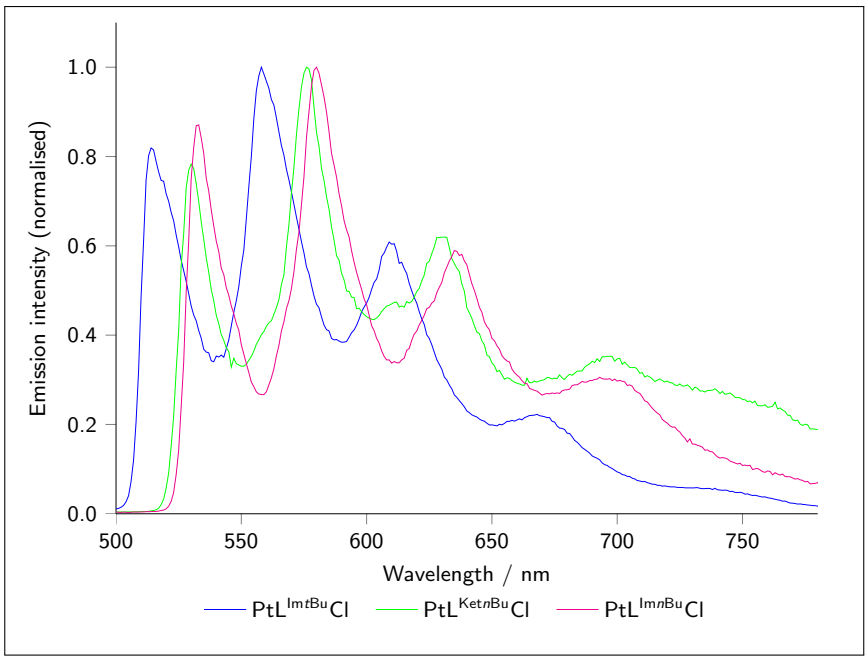

Figure 5.22: Normalised emission spectra of the three butyl-substituted derivatives in EPA glass at 77 K.

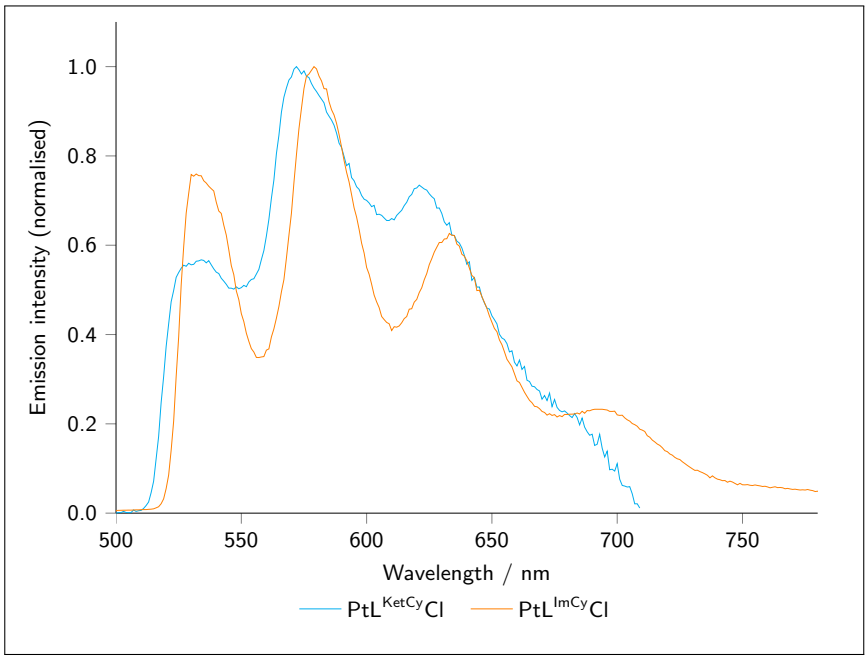

Figure 5.23: Normalised emission spectra of the two cyclohexyl-substituted derivatives in EPA glass at 77 K.

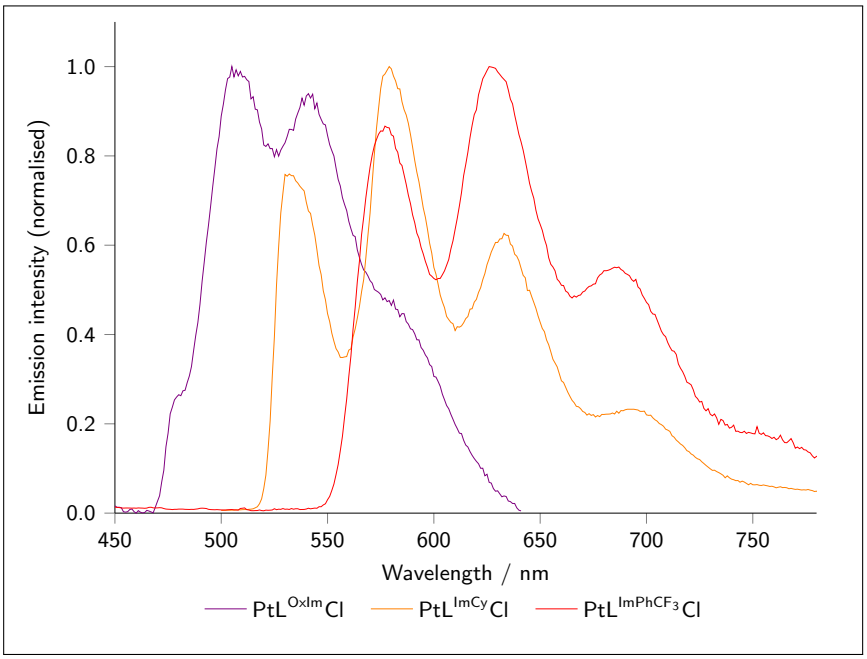

Figure 5.24: Normalised emission spectra of $PtL^{OxIm}Cl$, $PtL^{ImCy}Cl$ and $PtL^{ImPhCF_3}Cl$ in EPA glass at 77 K.

	Intensity of 0−0	Intensity of 0−1	Intensity of 0−2
$\mathbf{PtL^{ImCy}Cl}$	0.76	1	0.61
$\mathbf{PtL^{KetCy}Cl}$	0.56	1	0.73
$\mathbf{PtL^{Im^nBu}Cl}$	0.87	1	0.59
$\mathbf{PtL^{Ket^nBu}Cl}$	0.78	1	0.62
$\mathbf{PtL^{Im^tBu}Cl}$	0.82	1	0.60

Table 5.5: Experimental values for the intensity of the 0−n vibronic bands relative to the intensity of the 0−1 vibronic band for the imine and ketimine complexes at 77 K in EPA glass.

Table 5.5 shows the intensities of the 0−0 and 0−2 vibronic bands relative to the intensity of the 0−1 vibronic band for the various imine and ketimine complexes. The 0−0 band is highest in relative intensity for those compounds with higher quantum yields, suggesting that the higher rates of non-radiative decay are due to increased distortion in the excited state.

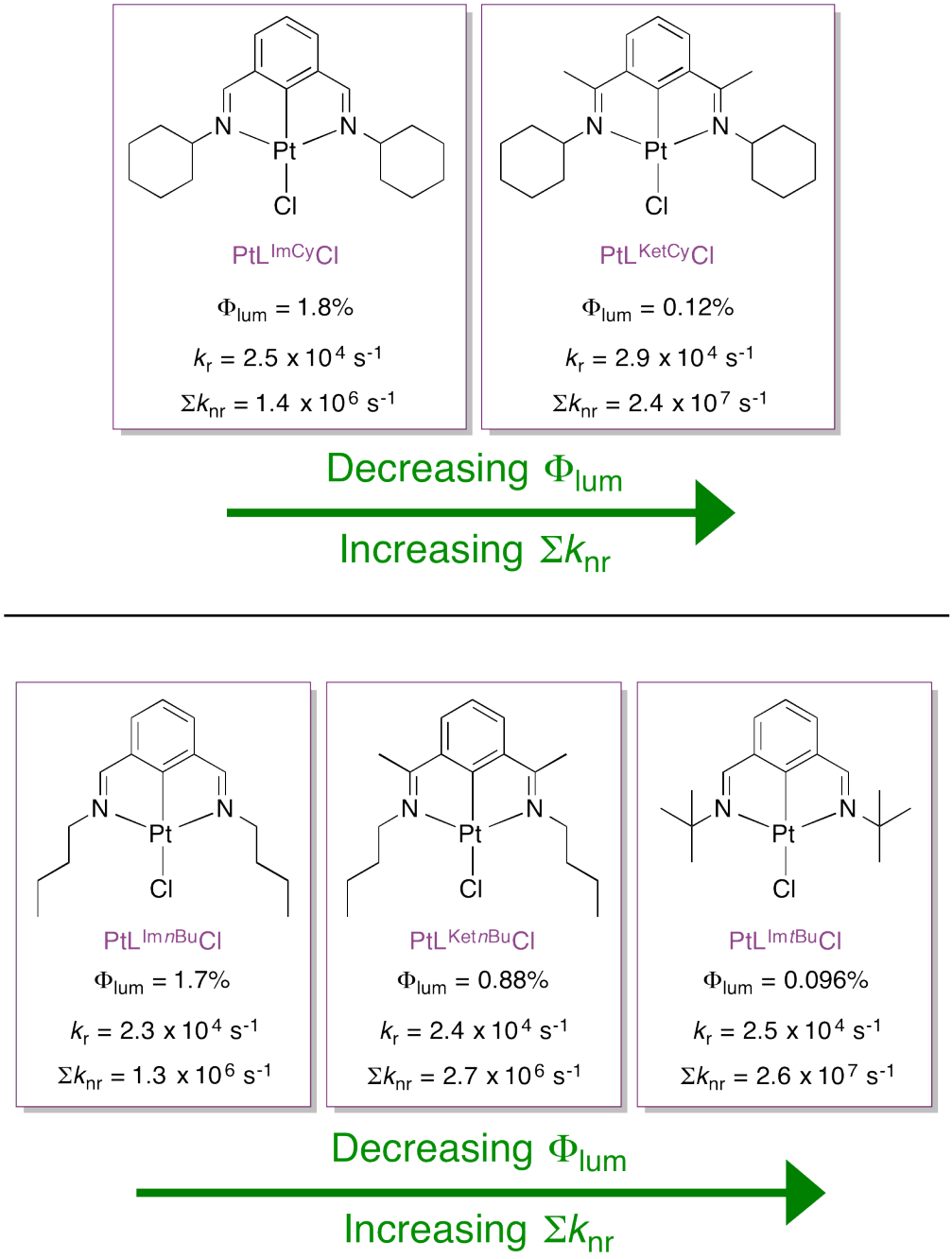

Figure 5.25: A diagram to summarise the trends in quantum yields and rates of radiative and non-radiative decay for the cyclohexyl (top) and butyl (bottom) substituted complexes.

5.3.3 Photophysical properties of the $PtL^{ImCy}X$ complexes (X ≠ Cl)

As discussed in Chapter 3, substitution of the chloride ancillary ligand of $PtL^{ImCy}Cl$ by a thiolate has a profound effect on the absorption and emission properties of the complex: the absorption spectra change dramatically in structure for both $PtL^{ImCy}STol$ and $PtL^{ImCy}SNit$: there is a loss of structure for $PtL^{ImCy}STol$ and the nitro complex absorbs much further into the red region of the spectrum. The structure of the emission spectra is also altered, with the 0−0 band becoming highest in relative intensity for the thiolate complexes, which was accompanied by a smaller shift in the λ_{max} and a reduction in the quantum yield of luminescence.

The absorption and emission spectra of $PtL^{ImCy}C_2Ar$ are shown in Figures 5.26 and 5.27 respectively, alongside those of $PtL^{ImCy}Cl$ for comparison. Figure 5.26 shows that the acetylide ligand introduces a new low energy band into the absorption spectrum, with a shoulder at 415 nm. (c.f. 385 nm for $PtL^{ImCy}Cl$). The acetylide ligand also introduces a strongly absorbing band at 286 nm, with an extinction coefficient of 15400 M^{-1} cm^{-1}. The emission spectrum of $PtL^{ImCy}C_2Ar$ shows almost no distinction from that of $PtL^{ImCy}Cl$ (Figure 5.27), although the quantum yield increased from 0.018 to 0.028, alongside a slight increase in the rate of radiative decay, k_r (Table 5.4).

5.3.4 OLED generation

Introduction to OLEDs

Part of the impetus towards the synthesis of these complexes was their potential for use in OLEDs. Some PtL^8Cl-type complexes have previously been incorporated into OLEDs, with substitution of the ester group for groups with varying electron-donating and withdrawing properties allowing for tuning of emission colour.[224] When incorporated into OLEDs, these compounds displayed high external quantum efficiencies (4-16% ph e^{-1}).

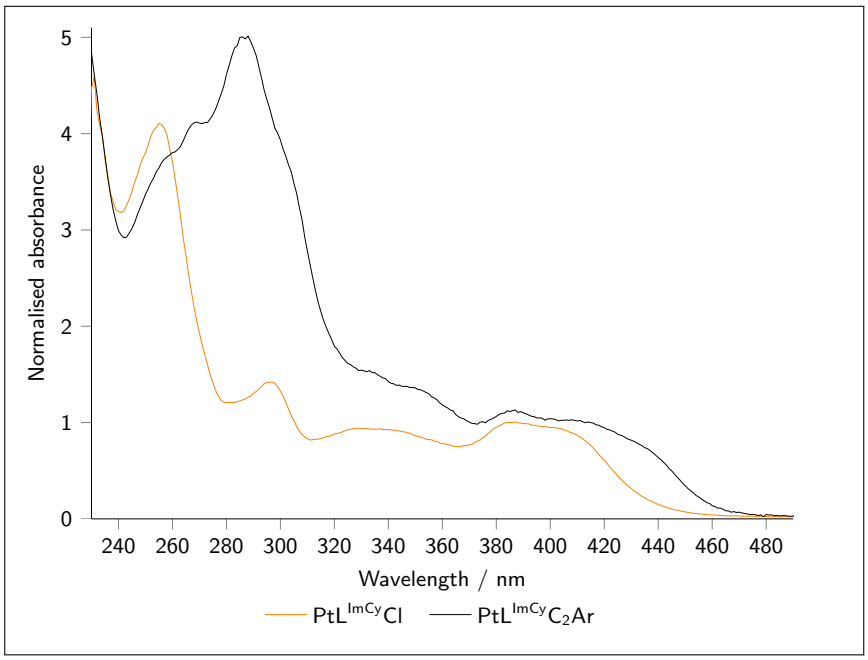

Figure 5.26: Absorption spectra of $PtL^{ImCy}Cl$ and $PtL^{ImCy}C_2Ar$ in DCM at 298 K, normalised at the longest wavelength absorption band.

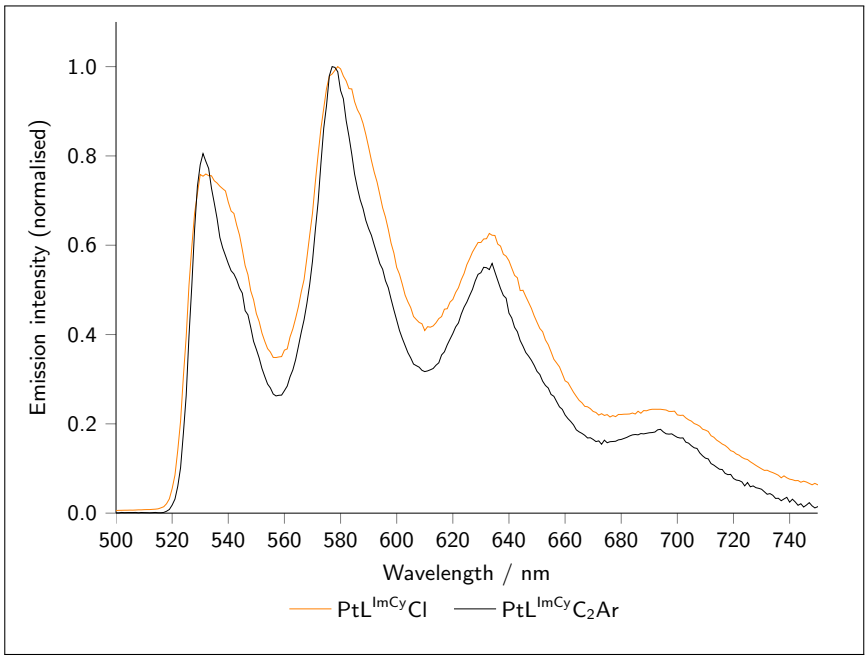

Figure 5.27: Normalised emission spectra of $PtL^{ImCy}Cl$ and $PtL^{ImCy}C_2Ar$ at 77 K in EPA glass. Spectra in degassed DCM at 298 K are shown in the Appendix, Figure 9.22.

Complexes incorporating a substituted dipyridylbenzene (dpyb) ligand require cross-couping reactions and the use of palladium catalysts in their synthesis (see Chapter 8 for details) which are often considered undesirable for use in OLEDs since small Pd impurities can lead to defects in the devices.[225] These imine ligands, synthesised by a simple condensation reaction and without the use of such catalysts, are potentially interesting for OLED applications. The imine-type complexes also showed no sign of excimer formation. Excimers have been used for WOLED production,[226] but are not desirable in every device since their formation changes the wavelength of emission and can reduce efficiency.

$PtL^{ImCy}Cl$ in an OLED

$PtL^{ImCy}Cl$ was investigated for use in OLEDs since it showed one of the highest quantum yields of luminescence and its synthesis did not require the use of HPLC, enabling it to be made in relatively large quantities with ease. Two OLEDs were made by our collaborator in Bologna, Dr Cocchi, one with the emissive layer (EML) made of 5% $PtL^{ImCy}Cl$ in TCTA and the other with a neat film of the complex. Both devices had the configuration:

ITO / TPD:PC [75%:25%] (60 nm) **/ TCTA** (10 nm) **/ EML** (30 nm) **/ TAZ** (30 nm) **/ LiF** (0.5 nm) **/ Al** (100 nm)

Figure 5.28 shows the electroluminescence spectra of the two devices, showing that the electroluminescent emission is coming from the active layer itself, with a slightly higher intensity for the device where the EML is made from 5% $PtL^{ImCy}Cl$. The turn-on voltage is lower in the blend device, which can also achieve a higher brightness at the same voltage compared to the neat film device (Figure 5.29). Although the blend device has a lower efficiency compared to the neat film, its efficiency is more stable at higher currents compared to the latter (Figure 5.30). The efficiency for both devices is poor (1%), perhaps unsurprisingly given the solution state quantum yield for this complex (1.8%). No "excimer-like" emission was seen in the neat film device in contrast to PtL^5Cl devices.

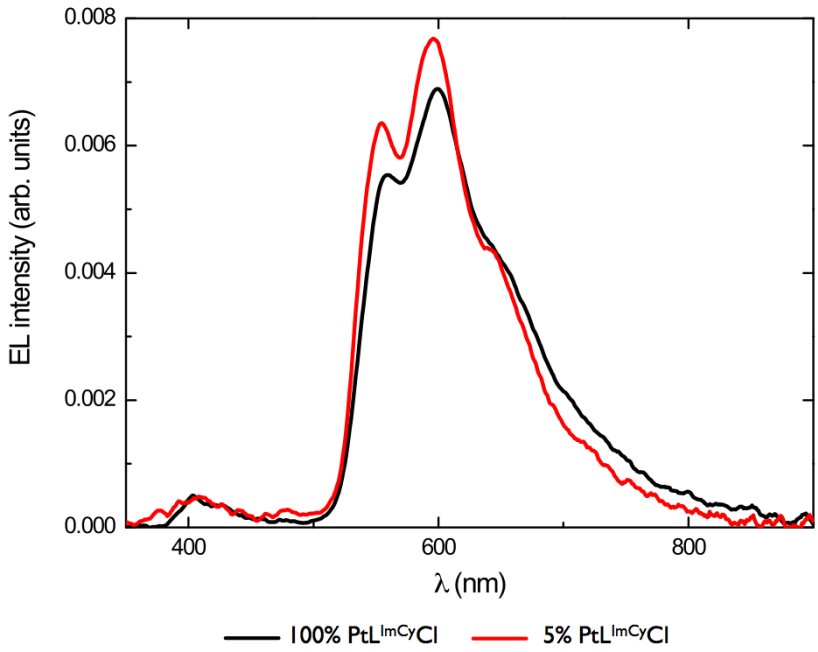

Figure 5.28: Electroluminescence spectra of the two OLEDs incorporating $PtL^{ImCy}Cl$ as a neat film or doped at 5% by mass in TCTA.

5.4 Density functional theory calculations

Unless otherwise stated, DFT and TD-DFT calculations described in this chapter were performed using PBE0 in DCM using a PCM for solvent. The LANL2DZ basis set was used for platinum and cc-pVDZ for all other atoms. Ground state and triplet excited state geometries were optimised by direct minimisation of the SCF energy and checked to be a true minimum by frequency calculations at the same level of theory.

5.4.1 Absorption of $PtL^{Im/Ket/Ox}Cl$

The ground state geometries of each of the eight complexes were optimised by direct minimisation of the SCF energy; those compounds where crystal structures were obtained showed a good correlation between the theoretical and experimental structures with the exception of the nitrogen substituents, which is unsurprising due to their high degree of flexibility (see Appendix,

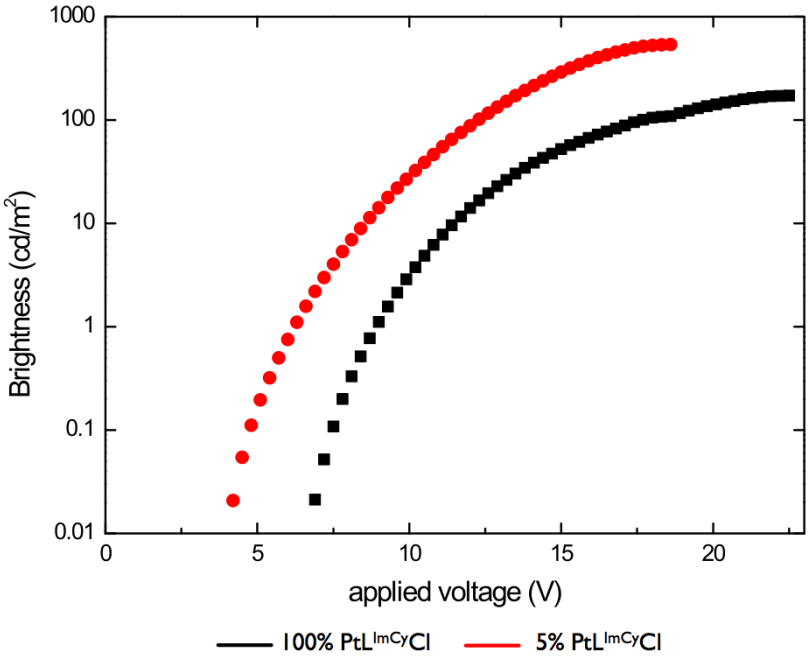

Figure 5.29: Brightness-voltage plots of the two OLEDs incorporating $PtL^{ImCy}Cl$.

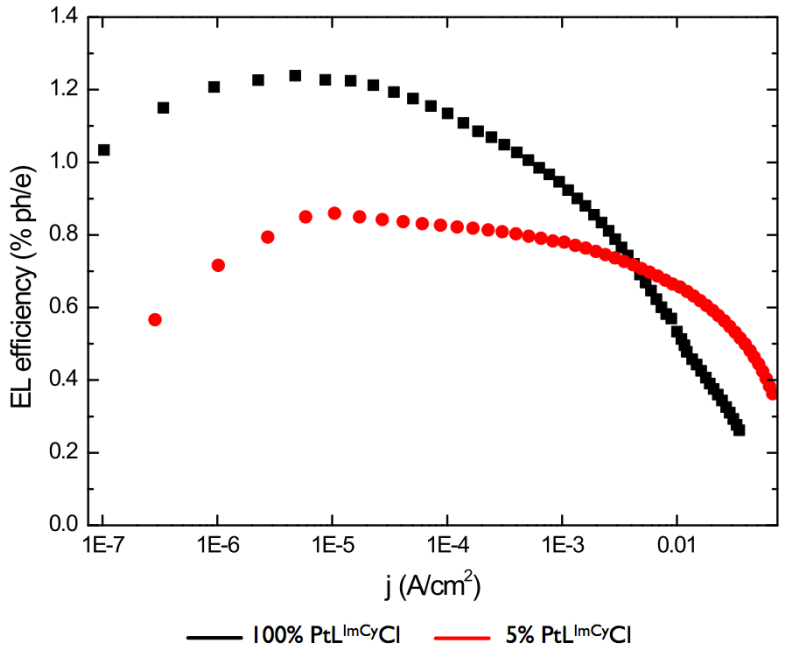

Figure 5.30: Electroluminescence quantum efficiency-electric current density plots of the two OLEDs incorporating $PtL^{ImCy}Cl$.

Figure 9.23). The convoluted absorption spectra of $PtL^{ImCy}Cl$, $PtL^{KetCy}Cl$, $PtL^{OxKet}Cl$ and $PtL^{ImPhCF_3}Cl$ are shown in Figure 5.31. The vertical lines represent the individual excitations calculated by TD-DFT, which are also shown in Table 9.19. Both these show that the low energy region of the spectrum is dominated in each case by the $S_0 \rightarrow S_1$ excitation, the density difference plots for which are shown in Figure 5.32. Figure 5.31 shows that, like the experimentally obtained spectra, the wavelength of the low-energy absorption band is remarkably similar for $PtL^{ImCy}Cl$ and $PtL^{KetCy}Cl$; $PtL^{OxKet}Cl$ is blue-shifted from these two and $Pt^{ImPhCF_3}Cl$ is significantly red-shifted from all the other compounds. Consideration of the density difference plots for each of these gives insight into the electronic origin of these observations: $PtL^{ImCy}Cl$ and $PtL^{KetCy}Cl$ both have very similar excitations while $PtL^{OxKet}Cl$ incorporates the electron-donating OMe group and $PtL^{ImPhCF_3}Cl$ shows delocalisation over the CF_3-substituted phenyl rings at the S_1 excited state.

Figures 5.33 and 5.34 show the equivalent spectra and density difference plots for the butyl-substituted compounds and $PtL^{OxIm}Cl$. $PtL^{Im^tBu}Cl$, $PtL^{Im^nBu}Cl$ and $PtL^{Ket^nBu}Cl$ show the same transition as $PtL^{ImCy}Cl$ and $PtL^{KetCy}Cl$ for $S_0 \rightarrow S_1$, and this transition once again dominates the low energy region of the spectrum. Neither the alkyl-pendant groups, nor the methyl groups of the ketimine complexes play a significant role in the excitation, showing why substitution of one for another has little effect on the absorption spectrum obtained. The electron-donating OMe groups of $PtL^{OxIm}Cl$ are not significantly involved in the $S_0 \rightarrow S_1$ excitation so there is less of a blue-shift for this complex than for $PtL^{OxKet}Cl$, but the spectrum is slightly blue-shifted from the other complexes since the presence of the OMe groups will still necessarily affect the nature of the complex.

The loss of structure in the absorption spectra of the ketimines compared to the imines observed experimentally is also shown in the convoluted absorption spectra. According to the TD-DFT calculations, this loss of structure appears to be due to both the increased proximity of the $S_0 \rightarrow S_1$ and $S_0 \rightarrow S_8$ excitations, and also the increased intensity of the $S_0 \rightarrow S_4$ excitation in $PtL^{KetCy}Cl$ and the $S_0 \rightarrow S_3$ excitation in $PtL^{Ket^nBu}Cl$.

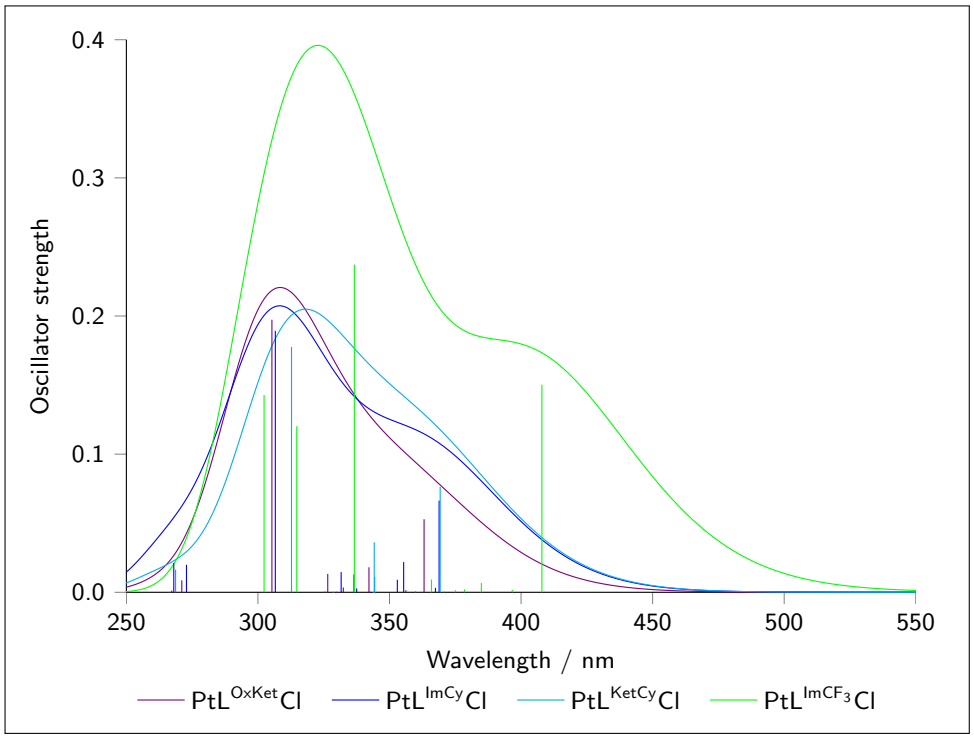

Figure 5.31: Convoluted absorption spectra of $PtL^{ImCy}Cl$, $Pt^{KetCy}Cl$, $PtL^{OxKet}Cl$ and $PtL^{ImPhCF_3}Cl$, calculated by TD-DFT. Excitations shown in the Appendix, Table 9.19.

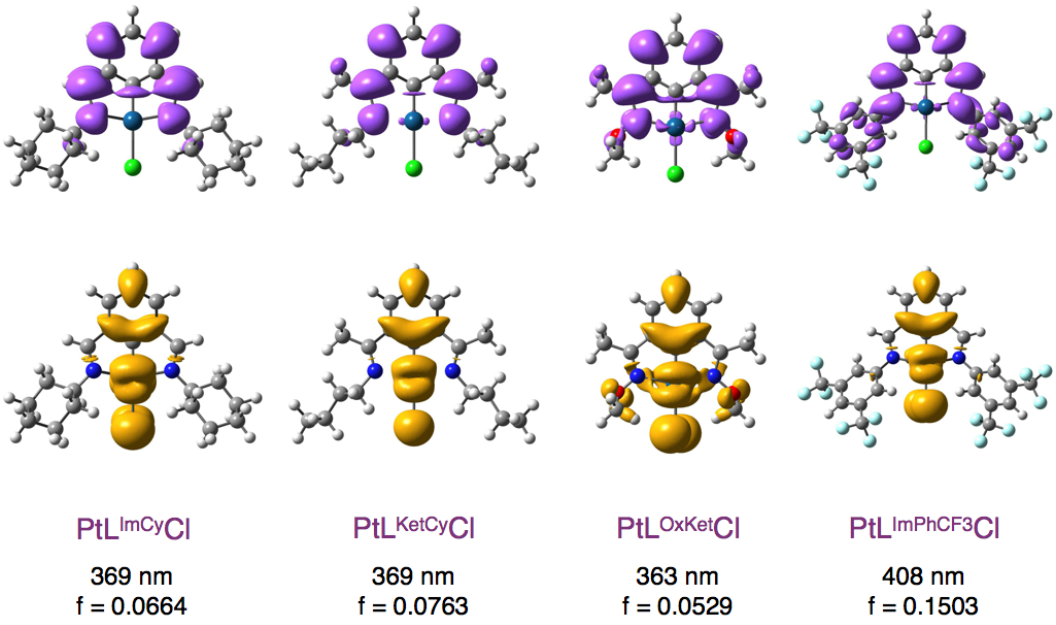

Figure 5.32: Density difference plots for the $S_0 \rightarrow S_1$ excitation at the ground state geometry for $PtL^{ImCy}Cl$, $Pt^{KetCy}Cl$, $PtL^{OxKet}Cl$ and $PtL^{ImPhCF_3}Cl$, calculated by TD-DFT.

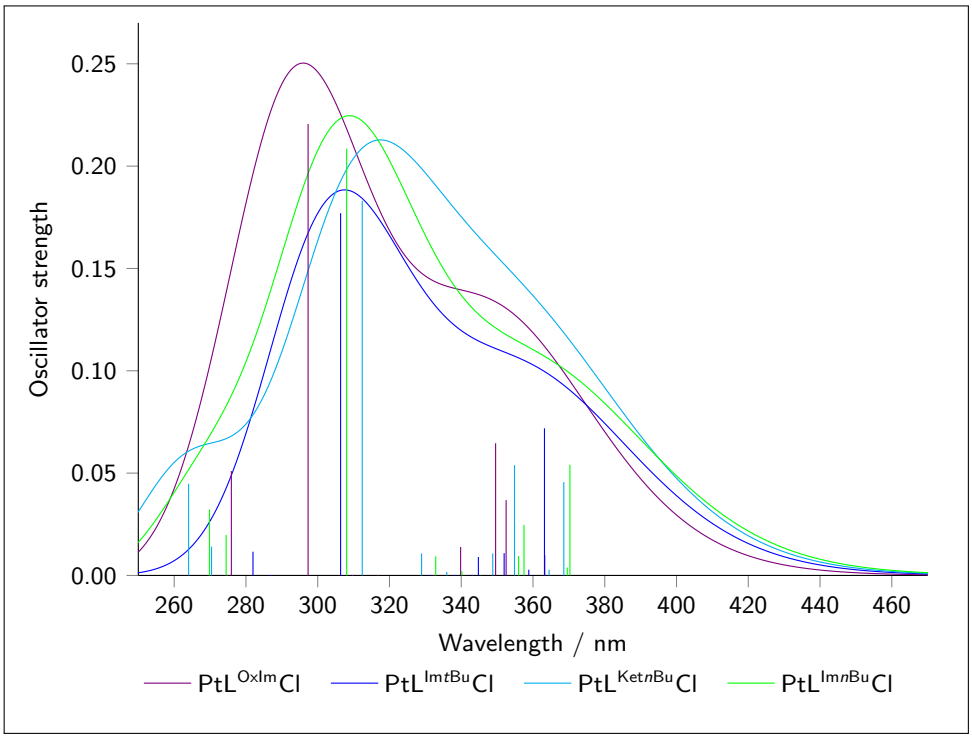

Figure 5.33: Convoluted absorption spectra of $PtL^{Im^tBu}Cl$, $PtL^{Im^nBu}Cl$, $PtL^{Ket^nBu}Cl$ and $PtL^{OxIm}Cl$, calculated by TD-DFT. Excitations shown in the Appendix, Table 9.20.

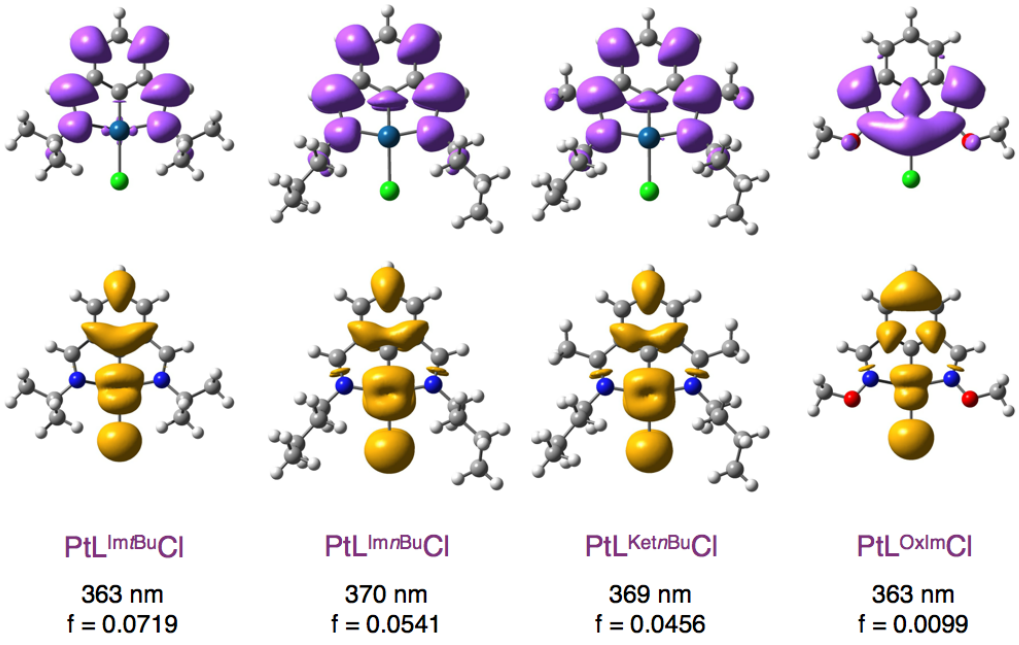

Figure 5.34: Density difference plots for the $S_0 \rightarrow S_1$ excitation at the ground state geometry for $PtL^{Im^tBu}Cl$, $PtL^{Im^nBu}Cl$, $PtL^{Ket^nBu}Cl$ and $PtL^{OxIm}Cl$, calculated by TD-DFT.

	S_0 geometry		T_1 geometry	
	S_0	S_1	S_0	T_1
$\mathbf{PtL^{ImCy}Cl}$	−0.488	−0.386	−0.482	−0.489
$\mathbf{PtL^{ImCy}C_2Ar}$	−0.821	−0.502	−0.827	−0.831

Table 5.6: Mulliken charges on the ancillary ligand of the two $PtL^{ImCy}R$ complexes at the ground and excited states. Those calculated at the S_0 geometry, representing absorption, are shown on the left and at the T_1 geometry (emission) on the right.

5.4.2 Absorption and emission of $PtL^{ImCy}C_2Ar$

Figures 5.35 and 5.36 show that while the acetylide ligand is involved in the absorption excitation in the low energy end of the spectrum (the $S_0 \rightarrow S_1$ transition is almost charge transfer in nature), it plays almost no part in emission. The Mulliken charges on the ancillary ligand of $PtL^{ImCy}Cl$ and $PtL^{ImCy}C_2Ar$ of the excitations for absorption and emission are shown in Table 5.6. The difference between the Mulliken charge on the ancillary ligand for $S_0 \rightarrow S_1$ (at the ground state geometry - absorption) is −0.319 (−0.103 for the Cl of $PtL^{ImCy}Cl$) while for $S_0 \rightarrow T_1$ (at the T_1 geometry-emission), it is just 0.004 (0.007 for $PtL^{ImCy}Cl$). This explains why the absorption spectra of $PtL^{ImCy}Cl$ and $PtL^{ImCy}C_2Ar$ are so different from one another while their emission properties are essentially the same: the ancillary ligand plays a large role in absorption (in the low energy region of the spectrum) but almost none in emission. Equivalent density difference plots for $PtL^{ImCy}Cl$ are shown in Figures 5.32 and 5.37.

5.4.3 Emission of $PtL^{Im/Ket/Ox}Cl$

Density difference plots of the excitation

Density difference plots for the $S_0 \rightarrow T_1$ excitation at the T_1 geometry for each of the eight chloro-substituted complexes are shown in Figure 5.37. The plots show a transition with a high degree of orbital overlap including a moderate involvement of the nitrogen-pendant groups in the excitation. The involvement of the pendant groups in $PtL^{ImPhCF_3}Cl$, $PtL^{OxIm}Cl$

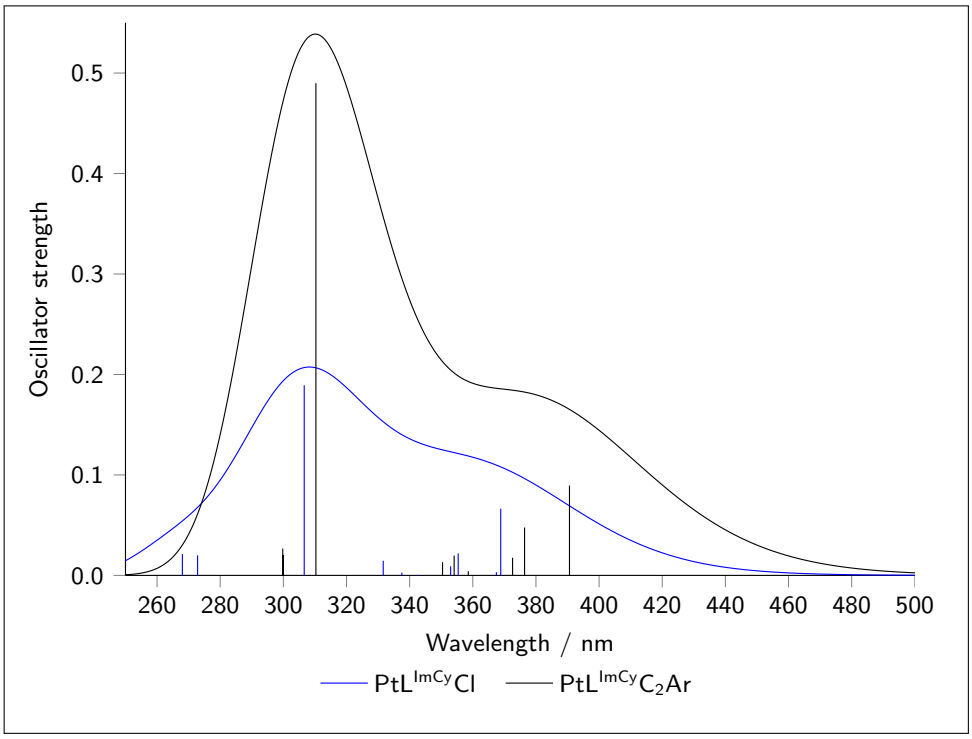

Figure 5.35: Convoluted absorption spectra of $PtL^{ImCy}Cl$ and $PtL^{ImCy}C_2Ar$, calculated by TD-DFT. Excitations shown in the Appendix, Tables 9.21 and 9.19.

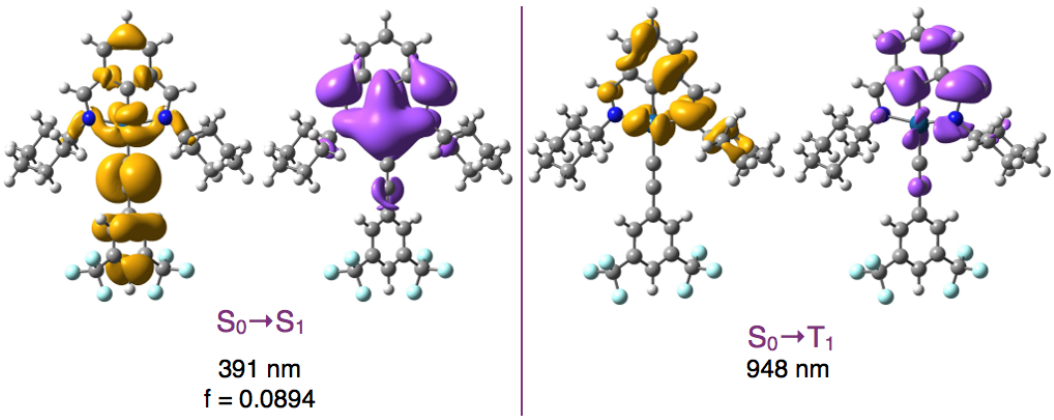

Figure 5.36: Density difference plots for the $S_0 \rightarrow S_1$ excitation at the ground state geometry (left) and $S_0 \rightarrow T_1$ excitation at the T_1 excited state geometry (right) for $PtL^{ImCy}C_2Ar$, calculated by TD-DFT.

and $PtL^{OxKet}Cl$ complexes explains why these groups alter the emission energy of these three complexes: delocalisation of electrons over the aromatic pendant rings in $PtL^{ImPhCF_3}Cl$ and electron-donating OMe groups of the two oxime complexes. The blue-shift observed experimentally for the two oxime complexes is due to destabilisation of the LUMO by the electron-donating −OMe group, increasing the energy of emission. The red-shift in the experimental emission spectrum of $PtL^{ImPhCF_3}Cl$ can be attributed to delocalisation of electrons over the pendant phenyl groups (according to the density difference plots), which was not possible with the other, alkyl derivatives.

While the alkyl substituents of the other five complexes are involved in the excitation, as are the methyl groups of the ketimines, these groups have very little effect on the energy of emission since the difference between the groups is minimal and their contribution to the overall excitation is small. The low variation in experimental energy of emission also suggests that neither the methyl groups of the ketimines, nor the alkyl pendants have very much influence on the excited state energy of the complexes. The ability of TD-DFT to calculate the excitation energies themselves was poor (*vide infra*), though the density difference plots are qualitatively informative, showing that each of the alkyl-substituted complexes are essentially showing the same type of emission.

Non-radiative decay due to distortion

As discussed in Section 5.3.2, the emission efficiency of the eight complexes considered in this chapter varies dramatically, despite similar energies and characteristics of emission. Estimation of the rates of radiative and non-radiative decay for each of these complexes from their lifetimes of emission shows that while the rate of radiative decay, k_r, remains approximately constant, the rate of non-radiative decay, Σk_{nr} varies by nearly two orders of magnitude. There are many and varied routes of non-radiative decay for an excited state complex (such as solvent interaction, aggregate formation and deactivating d-d states) but this discussion will focus on distortion.

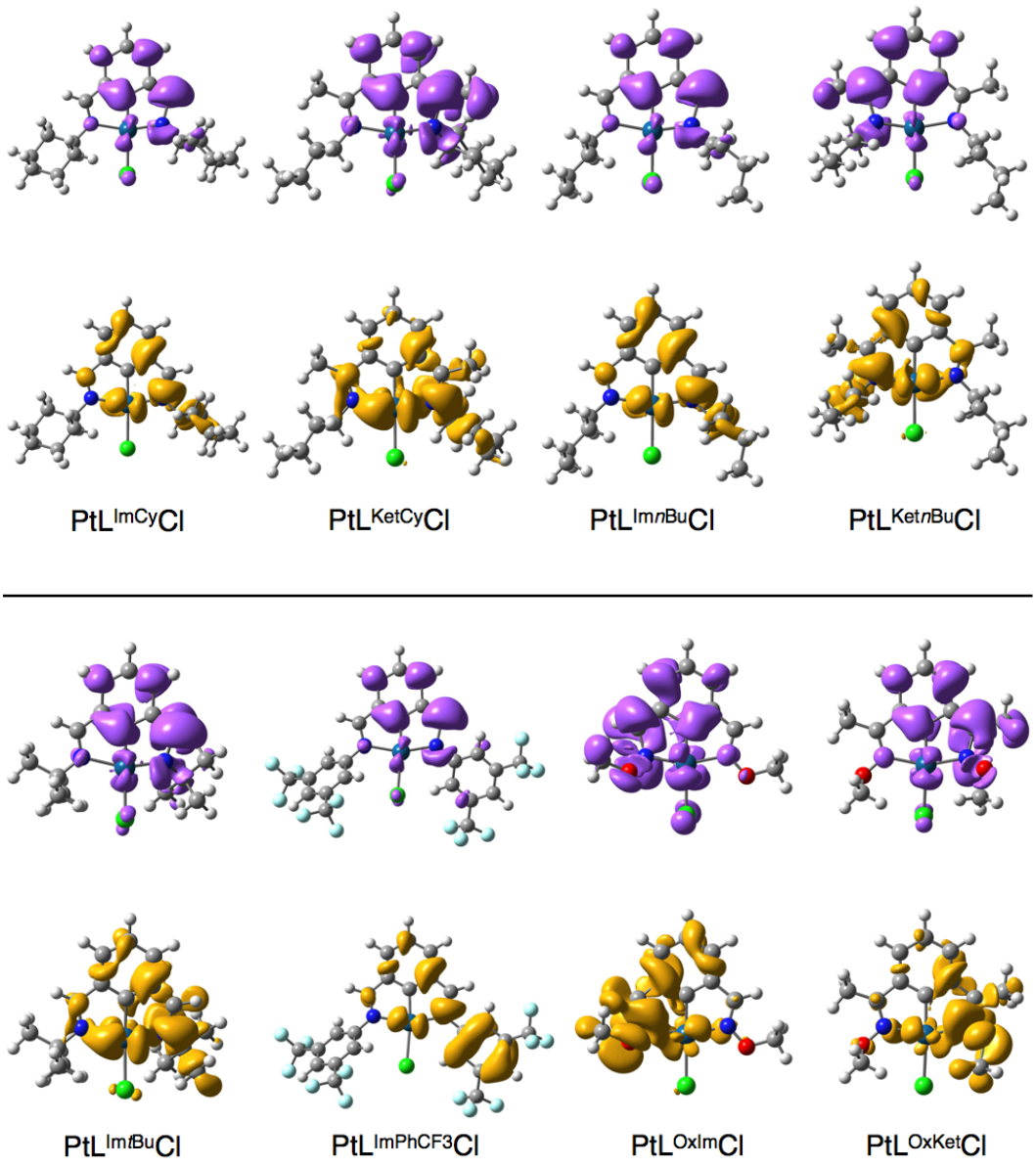

Figure 5.37: Density difference plots for the $S_0 \rightarrow T_1$ excitation at the T_1 excited state geometry for the imine, ketimine and oxime complexes, calculated by TD-DFT.

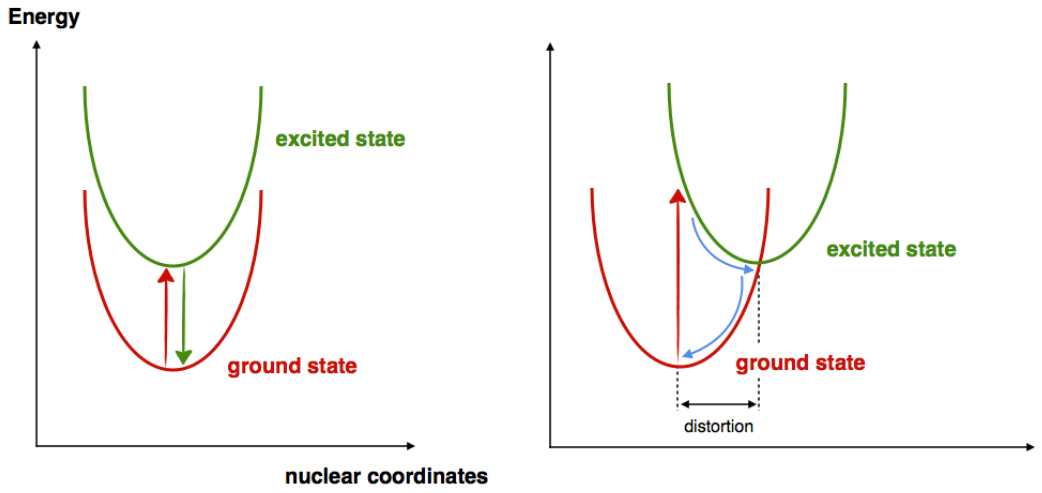

Figure 5.38: A schematic diagram to show routes of non-radiative decay enabled by distortion.

Figure 5.38 shows a schematic diagram of two possible excitations: the left where there is no distortion between the S_0 ground state and the T_1 excited state, and the right where there is significant distortion between the two states. Where there is no distortion, relaxation of the excited state to the ground state gives emission of light (unless there is some other deactivating process). In the second example, the excited state energy curve is shifted with respect to that of the ground state, giving a crossing point between the two curves and allowing non-radiative decay to occur (blue arrows on the right hand side diagram).

When undertaking calculations of this kind it is common to assume that the ground state and triplet excited states of metal complexes will be the same; triplet excitations can often be performed at either the ground state geometry or at the crystal structure geometry. Both of these techniques present problems, the first is the equivalent to $S_0 \rightarrow T_1$ absorption and will therefore predict an emission energy that is too high, while the second takes a solid-state geometry which has been formed through a combination of packing and solvent interactions, at the ground state geometry. Since the excitation energies are heavily dependent on geometry, it is important to calculate the correct geometry to ensure that the right excitation process is being described by the calculation. When calculating the triplet excited state geometry it is

also common to optimise from the ground state geometry in order to reduce the necessary calculation time. This technique is also not optimal since, as we will see in this section, triplet excited state geometries are not necessarily symmetrical and due to the nature of the calculation itself, once a symmetric geometry has been obtained, other non-symmetrical geometries cannot be found resulting in a false minimum.

Figures 5.39 and 5.40 show the superimposed S_0 and T_1 geometries of each of the complexes, both optimised by direct minimisation of the SCF ground and triplet states. Table 5.7 gives a quantitative indication of the distortion of the T_1 excited state versus the S_0 ground state alongside the rates of non-radiative decay for reference. The large increase in Σk_{nr} (of an order of magnitude) from $PtL^{ImCy}Cl$ to $PtL^{KetCy}Cl$ is accompanied by an increase in the RMSD of 0.2 Å. The three butyl-substituted complexes increase in distortion in the order:

$$\mathbf{PtL^{Im^{\mathit{n}}Bu}Cl} < \mathbf{PtL^{Ket^{\mathit{n}}Bu}Cl} < \mathbf{PtL^{Im^{\mathit{t}}Bu}Cl}$$

This correlates with their increase in rate of non-radiative decay and consequently the decrease in their quantum yields.

Unsurprisingly, the two oxime complexes and $PtL^{ImPhCF_3}Cl$ do not fit in with the trend of the other five aliphatic complexes since the functional groups present (and the aromatic rings in $PtL^{ImPhCF_3}Cl$) change the nature and energy of the excitation taking place. Table 5.7 does show, though, that $PtL^{OxKet}Cl$ distorts more in the triplet state than $PtL^{OxIm}Cl$, which suggests a possible origin for the lack of emission of $PtL^{OxKet}Cl$ at room temperature. $PtL^{OxIm}Cl$ showed a substantial degree of distortion and a high rate of non-radiative decay (7.7×10^7 s^{-1}), resulting in a very low quantum yield of 0.022%. A further increase in the rate of non-radiative decay through distortion would then presumably result in a lack of room temperature emission.

Rate of radiative decay

Table 5.8 shows that while the rate of radiative decay remains approximately constant for the related alkyl-substituted complexes, it is reduced to

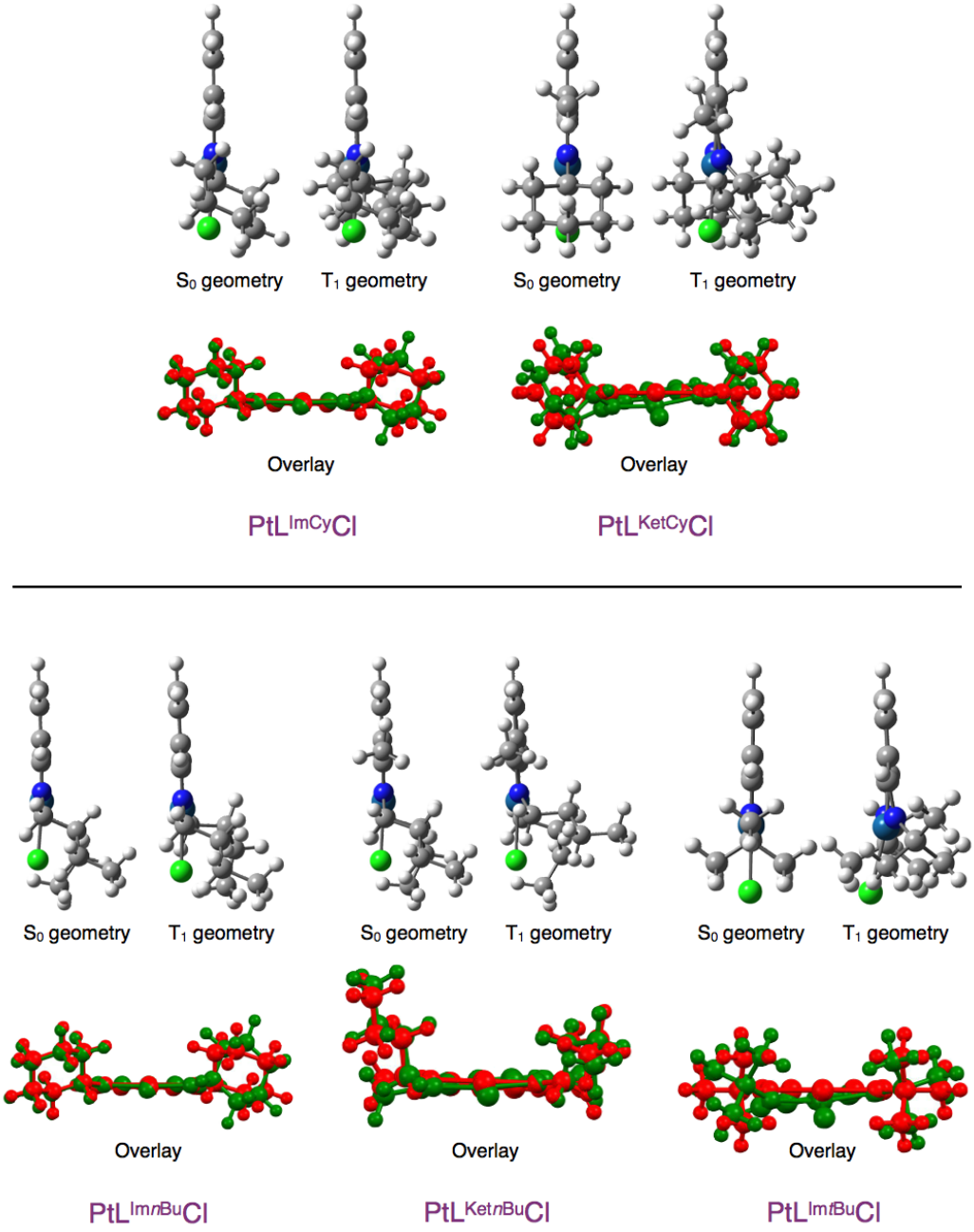

Figure 5.39: Geometries (side-view) and superimposed structures (viewed along the Cl−Pt bond) of the S_0 ground state (red) and T_1 excited state (green) for the five aliphatic complexes, calculated by DFT.

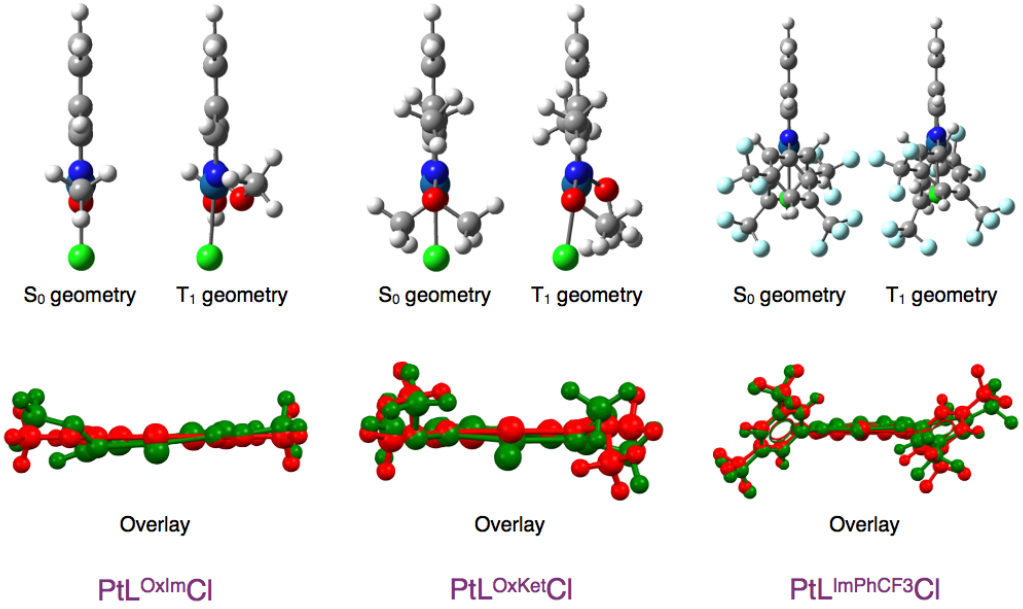

Figure 5.40: Geometries (side-view) and superimposed structures (viewed along the Cl−Pt bond) of the S_0 ground state (red) and T_1 excited state (green) for the PtL^{OxIm}Cl, PtL^{OxKet}Cl and PtL^{ImPhCF_3}Cl, calculated by DFT.

	RMSD / Å	Σk_{nr} / 10^6 s^{-1}
$\mathbf{PtL^{ImCy}Cl}$	0.34	1.4
$\mathbf{PtL^{Im^nBu}Cl}$	0.20	1.3
$\mathbf{PtL^{Im^tBu}Cl}$	0.47	26
$\mathbf{PtL^{ImPhCF_3}Cl}$	0.49	-
$\mathbf{PtL^{KetCy}Cl}$	0.54	24
$\mathbf{PtL^{Ket^nBu}Cl}$	0.36	2.7
$\mathbf{PtL^{OxIm}Cl}$	0.31	77
$\mathbf{PtL^{OxKet}Cl}$	0.54	-

Table 5.7: Root-mean-square displacement and rate of non-radiative decay of the S_0 ground state and T_1 excited state geometries of each of the eight complexes, calculated by DFT.

	$\Lambda^{[a]}$	k_r / 10^4 s^{-1}
$PtL^{ImCy}Cl$	0.58	2.5
$PtL^{Im^nBu}Cl$	0.59	2.3
$PtL^{Im^tBu}Cl$	0.62	2.5
$PtL^{ImPhCF_3}Cl$	0.65	-
$PtL^{KetCy}Cl$	0.66	2.9
$PtL^{Ket^nBu}Cl$	0.62	2.4
$PtL^{OxIm}Cl$	0.45	1.7
$PtL^{OxKet}Cl$	0.47	-

Table 5.8: TD-DFT values for lambda and metal character, and experimental k_r of each of the eight complexes. Λ was calculated in vacuum at the DCM geometry.

1.7×10^4 s^{-1} for $PtL^{OxIm}Cl$. The reduction in the radiative rate constant correlates with a decrease in the orbital overlap of the transition, quantified by lambda (Λ). It is interesting to note the slight increase in the rate of radiative decay for each of the distorting complexes, despite the decrease in quantum yield (which has been attributed to non-radiative decay through excited state distortion). For example, $PtL^{ImCy}Cl$ has a lower rate of radiative decay than $PtL^{KetCy}Cl$ (2.5×10^4 and 2.9×10^4 s^{-1} respectively), which again, correlates with an increase in Λ.

TD-DFT calculation of emission energies

The energies for the $S_0 \rightarrow T_1$ excitation at the T_1 geometry for each of the eight complexes, corresponding to the density difference plots shown in Figure 5.37, are shown in Table 5.9; neither the magnitude of the energies, nor the general trends between the complexes are correct. In Chapter 3 we showed that, due to the low overlap involved in the excitation, a long range corrected functional (CAM-B3LYP) was needed to correctly predict the trends in excitation energies and the increased propensity of the CAM-B3LYP functional towards triplet instabilities in the calculations was also discussed. While triplet instabilities are less often encountered with PBE0, higher orbital

	Energy / eV	Energy / nm
$\mathbf{PtL^{ImCy}Cl}$	1.29	962
$\mathbf{PtL^{Im^nBu}Cl}$	1.32	941
$\mathbf{PtL^{Im^tBu}Cl}$	0.97	1280
$\mathbf{PtL^{ImPhCF_3}Cl}$	1.29	965
$\mathbf{PtL^{KetCy}Cl}$	0.73	1690
$\mathbf{PtL^{Ket^nBu}Cl}$	1.17	1060
$\mathbf{PtL^{OxIm}Cl}$	0.37 i	3400 i
$\mathbf{PtL^{OxKet}Cl}$	0.64 i	1940 i

Table 5.9: Energies for the $S_0 \rightarrow T_1$ excitation at the T_1 geometry for each of the eight complexes. i = imaginary value.

overlap in the excitation increases their likelihood. These imine, ketimine and oxime complexes show a large degree of orbital overlap in their $S_0 \rightarrow T_1$ excitation so that even when using the PBE0 functional difficulties are encountered, giving the low excitation energies shown in Table 5.9. For the oximes, they become so low that a negative value is obtained.

As previously discussed, there are many and various ways to calculate the phosphorescence emission energy. The results of some of these for the three butyl-substituted complexes, as a test set, are shown in Table 5.10 along with the experimental values for comparison. With the exception of $S_0 \rightarrow T_1$ absorption, none of the values shown give an accurate representation of the trends observed experimentally.

Excitation energies calculated at the SCF geometry are much lower than those obtained experimentally but are greatly improved by the use of TDA. While the TD-DFT excitation energies for all the triplet geometry calculations are much too low, the values calculated at the TD-DFT geometry are particularly poor and show imaginary excitations for all three complexes. In each of these calculations the triplet instability is so high that, as for the thiolate complexes,

	$PtL^{Im^nBu}Cl$		$PtL^{Im^tBu}Cl$		$PtL^{Ket^nBu}Cl$	
	eV	nm	eV	nm	eV	nm
Experimental (298 K)[a]	2.23	556	2.31	536	2.31	537
Experimental (77 K)[b]	2.33	532	2.41	514	2.34	530
$S_0 \rightarrow T_1$ absorption[c]	2.38	520	2.45	506	2.45	505
SCF, T_1 geometry	1.32	941	0.97	1280	1.17	1060
SCF/TDA[d]	2.43	510	1.52	813	1.53	808
TD-DFT, T_1 geometry[e]	−0.92	−1350	−0.96	−1290	−0.91	−1370
TD-DFT/TDA[f]	0.70	1780	0.61	2040	0.63	1970
RI-CC2[g]	1.79	1050	0.81	1530	0.56	2210
RI-CC2[h]	1.27	973	1.06	1170	0.79	1570

Table 5.10: Energies calculated for the $S_0 \rightarrow T_1$ excitation of the three butyl-substituted complexes.

[a] Measurements taken in DCM solution. [b] Measurements taken in EPA glass. [c] Excitation at the S_0 optimised geometry, calculations performed in vacuum. [d] Excitation calculated by TDA at the T_1 SCF geometry. [e] Excitation at the T_1 geometry, optimised by TD-DFT, calculations performed in vacuum and due to the computationally demanding nature of the calculation, frequency calculations were not performed to ensure a minimum had been found. [f] Excitation calculated by TDA at the T_1 TD-DFT geometry. [g] RI-CC2 for both geometry optimisation and excitations, performed by our collaborator, Andreas Köhn [h] TD-DFT excitations, calculated with PBE0 in vacuum, at the geometry from (g).

the geometries themselves have been compromised. The effect is magnified in calculation of the TD-DFT geometry since the triplet excitation is involved in the optimisation of the geometry. TDA excitation energies at this geometry improve on the values obtained so that they are all positive but they are still far too low in energy compared to the experimental values. Even excitation energies calculated by RI-CC2 are significantly lower in energy than observed experimentally.

It is possible that the geometries themselves have been adversely affected by low triplet stability, this is certainly the case for those optimised by TD-

DFT. The trends in energy might therefore be improved by optimisation with TDA, as for the thiolate complexes discussed in Chapter 4. It is unsurprising, though, that where there is a large degree of distortion between the excited state and ground state, prediction of excitation energies is poor. In the complex where there is little distortion ($PtL^{Im^nBu}Cl$), the energy for the $S_0 \rightarrow T_1$ excitation, computed at the SCF geometry, using TDA to avoid triplet instability (2.43 eV, 510 nm) is remarkably similar to experimental values (2.33 eV, 532 nm at 77 K). The excitation energies for $PtL^{Im^tBu}Cl$ and $PtL^{Ket^nBu}Cl$ decrease with increasing distortion, the opposite to the experimental trend. Excitation energies calculated where there is no distortion, at the singlet ground state, reproduce the trend well. The prediction of low excitation energies where there is significant distortion at the excited state geometry will be further discussed in Chapter 6.

5.5 Concluding remarks

The photophysical properties of eight Pt(II), chloro-substituted, imine complexes have been studied; they show phosphorescent emission in the red region of the spectrum. The five alkyl-substituted complexes show remarkably similar emission spectra to one another but quantum yields that vary by over two orders of magnitude (from 1.8 to 0.022%). The difference in quantum yield can be attributed, by the use of DFT, to non-radiative decay pathways through distortion between the ground state and excited state geometries, which is more prevalent in some compounds than others. Substitution of the chloride for another ancillary ligand (such as acetylide) dramatically affects the absorptive properties of the compound, but not the emission. TD-DFT showed that this ancillary ligand was only involved in the absorption excitations, not the emission. Due to the high level of excited state distortion, excitation energies could not be reproduced by TD-DFT calculations; $S_0 \rightarrow T_1$ excitations at the ground state geometry did show good reproduction of the trends observed.

6

The triplet excited states of methyl-substituted benzenes

6.1 Introduction

Triplet instabilities showed a significant, detrimental effect on the reliable prediction of the excitation energies of many of the compounds studied in previous chapters; in some cases the predicted energies were even negative. In some examples, TDA calculations at the DFT geometry still showed implausibly low excitation energies, suggesting that the T_1 geometry itself was adversely affected. In large complexes, where little is already known about the nature of the excited state adopted, it is difficult to fully comprehend whether such problems are due to the computational methods employed, or to the physical nature of the compounds themselves. Furthermore, such large compounds require very time consuming calculations so that more computationally expensive investigations (such as coupled cluster or TDA geometries) are not routinely feasible.

Theoretical studies of pairs of compounds such as $PtL^{5/8}SPh$ and $PtL^{5/8}STol$ (Chapter 3) or $PtL^{ImCy}Cl$ and $PtL^{KetCy}Cl$ (Chapter 5) seemed to show that compounds where extra methyl groups were included suffered more from the triplet instability problem. It was decided to conduct a combined experimental and theoretical study on a series of model organic compounds to see if such

effects could be reproduced, enabling detailed study and a better understanding of the processes taking place.

In this chapter the photophysical properties of a series of benzene-based compounds with increasing numbers of methyl substituents will be discussed. The compounds (shown in Figure 6.1) were purchased, purified and their photophysical properties studied as a simplified example of some of the compounds that we have discussed in other chapters for the purpose of probing the influence of proximal methyl groups. Since these compounds are small and well characterised they provide a set that can be investigated in detail by theoretical calculations alongside their experimental photophysical properties. They also displayed excitations high in orbital overlap (with correspondingly high Λ values) making them particularly susceptible to triplet instabilities.

6.2 Computational details

Unless otherwise stated, DFT calculations described in this chapter were performed using PBE0 with cc-pVDZ. All calculations were performed in vacuum. T_1 and S_0 geometries were optimised by direct minimisation of the SCF energy and checked to be a true minimum by frequency calculations at the same level of theory. TDA geometry optimisations and excitations were performed with B3LYP and cc-pVDZ, in vacuum, by Michael Peach.

6.3 The compounds

The thirteen compounds we will consider in this chapter are shown in Figure 6.1. They can be broadly divided into groups according to how many methyl groups they possess. For example, ArMe2, ArMe2a and ArMe2b form a group of isomers that all contain two methyl substituents, but differ in their relative disposition. The photophysical properties of many of these compounds have been previously discussed in various papers,[227–229] though, to our knowledge, this is the only study of the complete set displaying the phosphorescence of all thirteen of them.

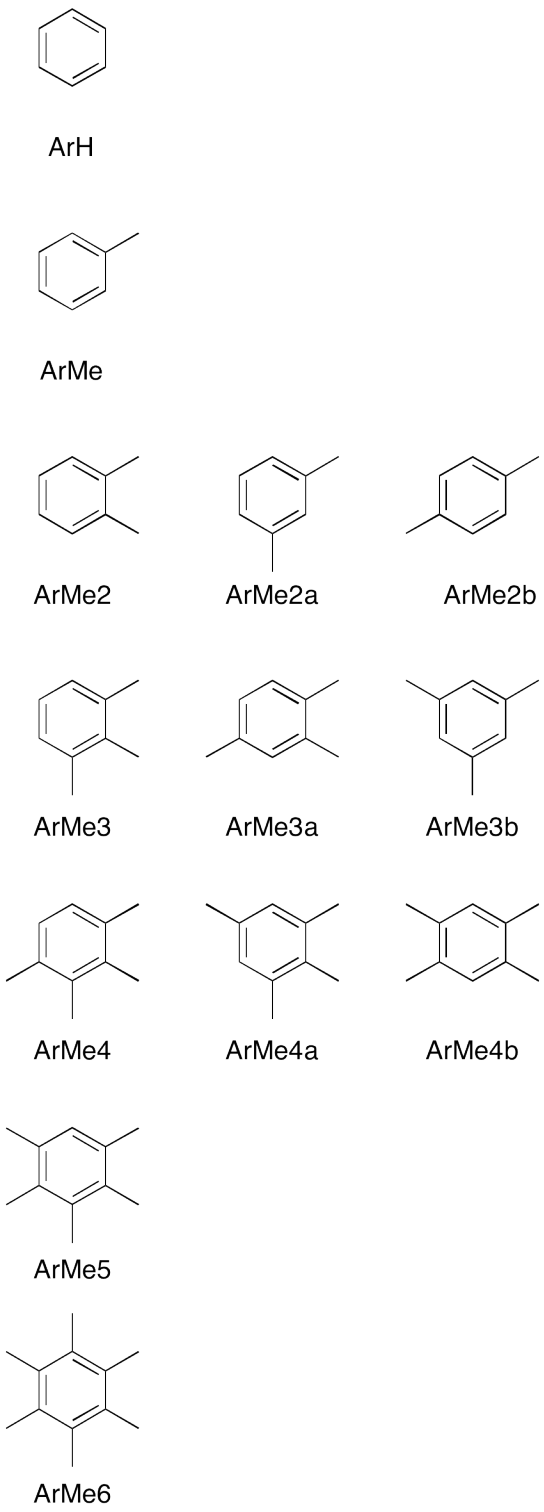

Figure 6.1: The chemical structures of the aromatic compounds studied.

6.4 Experimental photophysical data

The thirteen substituted-benzene compounds showed fluorescence bands between ∼260 and 330 nm and phosphorescence between ∼350 and 480 nm in MP (methylcyclohexane and isopentane in a 3:1 v/v ratio) glass at 77 K. A summary of their phosphorescent emission energies and quantum yields is shown in Table 6.1. Increasing numbers of methyl substituents resulted in a red shift in phosphorescent emission and a partial loss of vibrational structure. The full spectra (including the fluorescence of each compound) are shown in the Appendix, Figures 9.24 to 9.36.

Quantum yields of phosphorescence were measured in MP glass, relative to toluene ($\Phi_{phos} = 0.26$).[227] The determination of quantum yields is, unfortunately, susceptible to considerable uncertainty and variation from one measurement to the next, particularly for measurements at low temperature involving short λ excitation. For this reason, an average was taken of three readings. The values obtained should still only be used as a general guide for comparison within each series rather than considered as an absolute value.

Within the xylene series (ArMe2) it can be seen that the quantum yields increase as the methyl groups move further away from one another around the ring:

$$\textit{ortho} < \textit{meta} < \textit{para}$$

This correlates with an increase in the intensity of the 0−0 band relative to that of λ_{max} (Figure 6.2). The same pattern can be seen with benzene compared to toluene: the ratio of the intensity of the 0−0 band to the intensity at λ_{max} is higher for toluene than benzene (Figure 6.3) and the quantum yield of phosphorescence is also higher. The pattern is less clear in the tri and tetra-substituted series (Figures 6.4 and 6.5 respectively). For the former, the quantum yield increases as the methyl groups are spaced further apart:

$$\textbf{ArMe3} < \textbf{ArMe3a} < \textbf{ArMe3b}$$

In the tetramethyl-substituted complexes ArMe4a is more emissive than the other three:

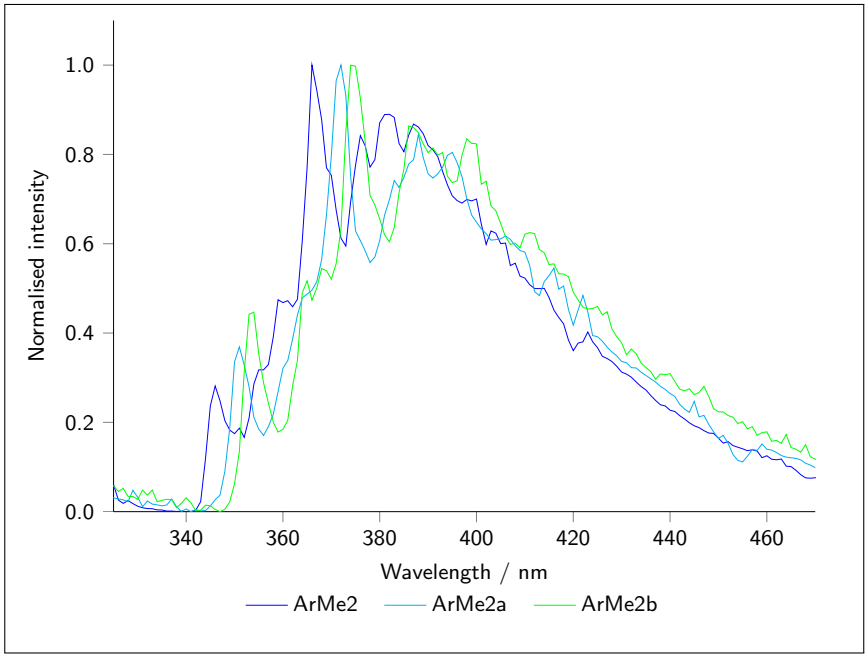

Figure 6.2: Phosphorescent emission spectra of ArMe2, ArMe2a and ArMe2b at 77 K in MP.

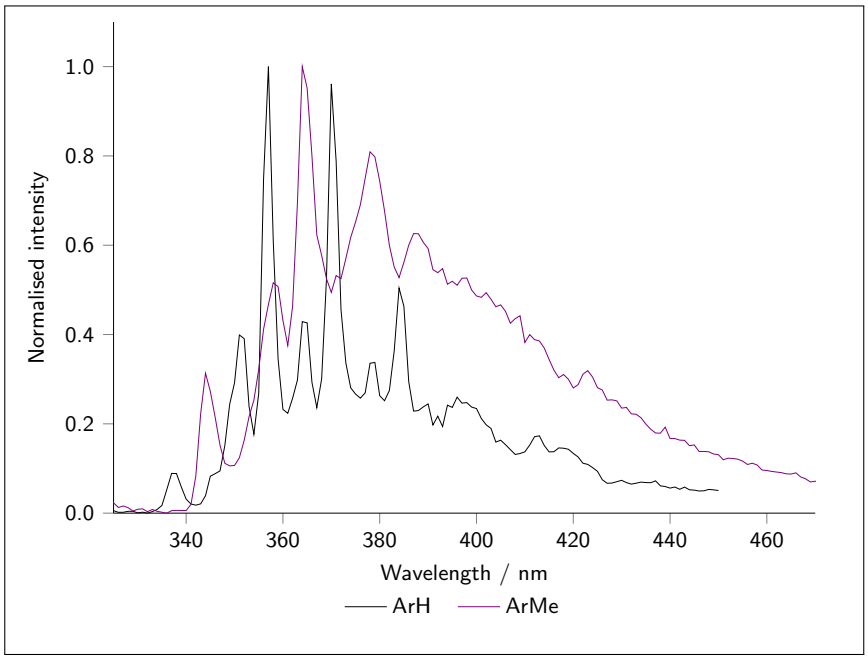

Figure 6.3: Phosphorescent emission spectra of ArH and ArMe at 77 K in MP.

	Experimental		Φ_{phos}
	/ nm	/ eV	
ArH	337	3.68	0.11
ArMe	344	3.60	0.26
ArMe2	346	3.58	0.34
ArMe2a	351	3.53	0.46
ArMe2b	354	3.50	0.51
ArMe3	350	3.54	0.33
ArMe3a	355	3.49	0.37
ArMe3b	355	3.49	0.45
ArMe4	360 *sh*	3.44	0.34
ArMe4a	355	3.49	0.54
ArMe4b	357	3.47	0.45
ArMe5	398[a]	3.12	0.34
ArMe6	442[a]	2.81	0.23

Table 6.1: Emission wavelengths of the 0−0 band for each of the substituted-benzene compounds at 77 K, in MP glass. [a]λ_{max}*, 0−0 band indistinguishable. Quantum yields were calculated relative to toluene.*[227]

ArMe4a < **ArMe4b** < **ArMe4**

ArMe5 and ArMe6 show decreased Φ_{phos} from the tetramethyl-substituted compounds. They both show poorly structured emission (Figure 6.6) and weak phosphorescence compared to the fluorescence spectrum (Appendix, Figures 9.35 and 9.36).

6.4.1 Experimental photophysical conclusions

Taking ArMe2, ArMe2a and ArMe2b as an example series, the increase in quantum yield through the series might be due (at least in part) to a decrease in distortion of the T_1 excited state relative to the S_0 ground state, given that

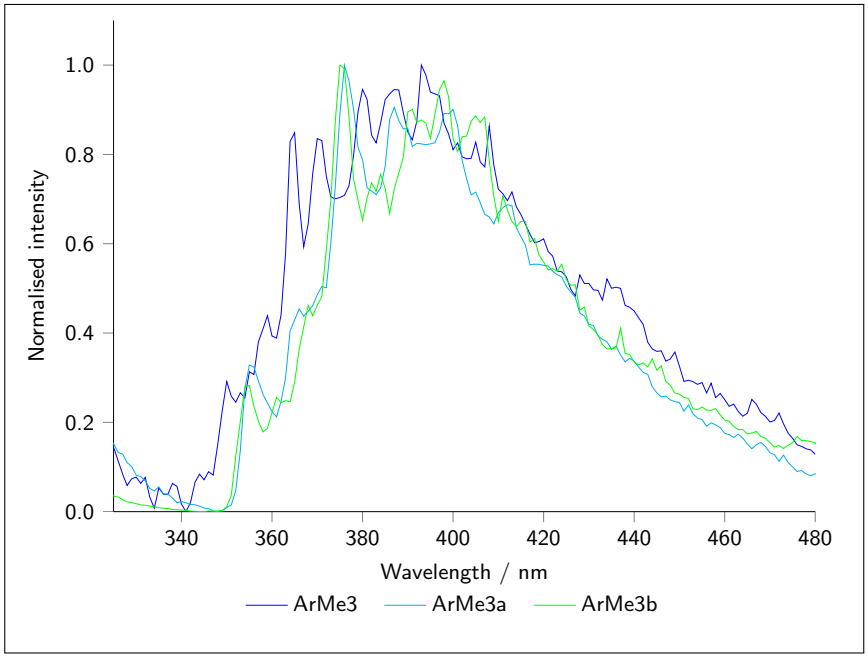

Figure 6.4: Phosphorescent emission spectra of ArMe3, ArMe3a and ArMe3b at 77 K in MP.

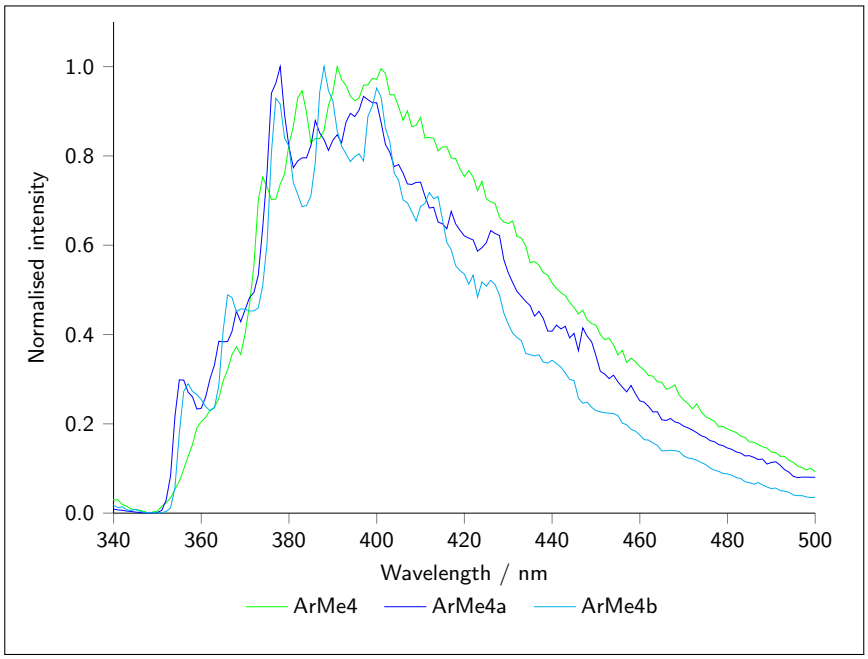

Figure 6.5: Phosphorescent emission spectra of ArMe4, ArMe4a and ArMe4b at 77 K in MP.

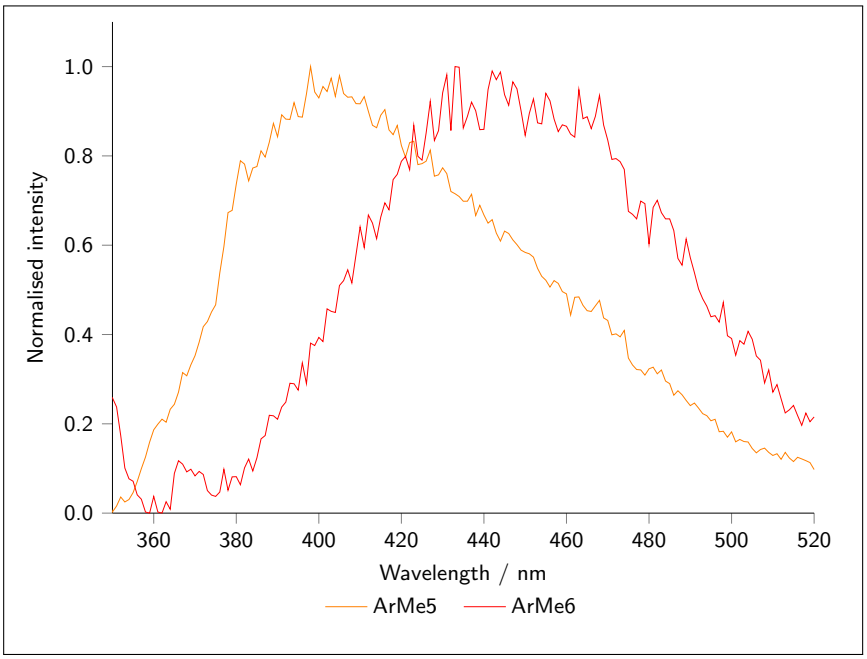

Figure 6.6: Phosphorescent emission spectra of ArMe5 and ArMe6 at 77 K in MP.

the relative intensity of the 0−0 band increases in this order (see Chapter 1, Section 1.7). Since the three compounds are isomeric, there is unlikely to be a significant difference in the excitation taking place and all three have similar energies of emission. The same pattern is seen in the ArMe3 series although the trend in the 0−0 band is not so clear.

Distortion may also explain the difference in emission intensities of the other compounds: the reduced quantum yields in ArMe5 and ArMe6, despite the increased number of methyl groups, is presumably due to distortion from steric crowding of the groups at the excited state.

6.5 Computational studies on benzene triplet state

The small size of benzene lends itself well to computational study since high level calculations can be performed on a reasonable time scale. Indeed coupled cluster calculations have recently been reported for all twelve fluorine-substituted benzene compounds.[230] It has also been shown that at a pla-

nar symmetrical geometry their excitation energies can be reproduced with good accuracy.[231] For these reasons there are many studies of benzene and its derivatives in the literature at different levels of theory. Various experimental spectroscopic and semi-empirical theoretical studies have suggested that the triplet excited state geometry of benzene is D_{2h} in symmetry.[232–240]

6.5.1 DFT calculations

Optimisation of the T_1 excited state geometry of benzene from various different non-symmetrical starting geometries gave a structure with D_{2h} symmetry, shown on the left of Figure 6.7, geometry A. This geometry has two elongated C−C bonds (1.52 Å compared to 1.39 Å) opposite to one another, in keeping with structures previously discussed in the literature.[232–240] In an attempt to see if another, lower energy geometry could be found by starting from a distorted structure, the optimised T_1 geometry of 1,2,3-trimethylbenzene (ArMe3) was used as a starting geometry for optimisation of benzene with the three methyl groups replaced by hydrogen atoms. The resulting geometry of this calculation is also shown in Figure 6.7, on the right hand side, geometry B. It can be seen that the ring is twisted away from planarity and the bond lengths altered. Neither of the two geometries showed any imaginary frequencies. Interestingly, this new, lower symmetry geometry is lower in energy than the first.

TD-DFT calculation of the $S_0 \rightarrow T_1$ excitation at each geometry showed an emission energy of 2.84 eV (437 nm) for geometry A and just 0.59 eV (2110 nm) for geometry B. While the excitation energy calculated at geometry A is quite low in energy compared to the experimental spectrum (Figure 6.3), the energy calculated at geometry B is extremely low, reminiscent of some of the excitation energies calculated at distorted structures in previous chapters. It is also interesting to note that stability calculations at each geometry show a much lower stability for geometry B (0.12) than geometry A (1.64). Excitation energies, stabilities and Λ for the two geometries are shown in Table 6.2. The lowest energy, distorted structure will be referred to for the remainder of this discussion.

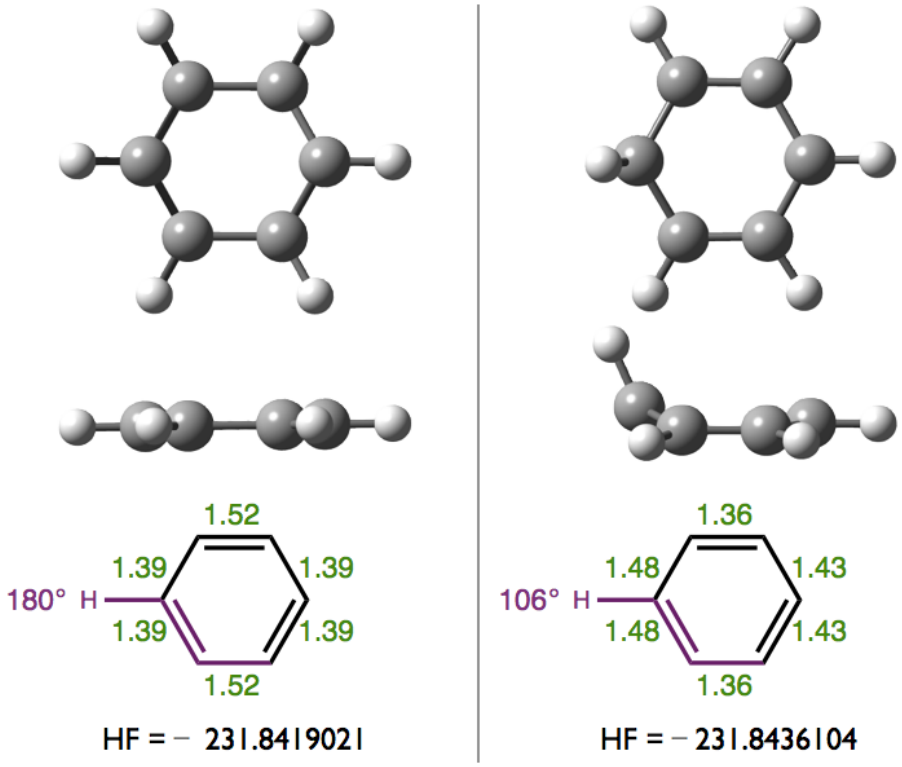

Figure 6.7: T_1 excited state geometry A (left) and geometry B (right), optimised for benzene by DFT. Geometry energies are given in hartrees. The C−C bond lengths (Å) are shown in green and the dihedral angle in purple.

6.5.2 CCSD calculations

CCSD calculations at the two geometries shown in Figure 6.7 showed that, contrary to the DFT results, the D_{2h} geometry is in fact the lowest energy configuration of benzene at the T_1 excited state. This suggests that optimisation of the T_1 geometry can in some cases lead to a lowest energy geometry being obtained which is not in fact the true minimum, despite the lowest energy geometry normally being considered to be the true one.

	Geometry A	Geometry B
Energy / eV	2.84	0.59
Wavelength / nm	437	2110
Stability	1.64	0.12
Λ	0.92	0.86
TDA energy / eV	3.32	1.55
TDA wavelength / nm	373	802

Table 6.2: Excitation energies, stabilities and Λ for the $S_0 \rightarrow T_1$ excitation of benzene at the two different T_1 geometries. TDA excitation energies are calculated at the two DFT geometries with PBE0.

6.5.3 TDA and TD-DFT geometry optimisation

Section 6.5.1 showed that for both geometries A and B of benzene, the stability for the excitation was low, resulting in low excitation energies from TD-DFT. Excitation energies calculated with TDA circumvented this problem, giving higher energy excitations in each case. Although use of TDA for calculation of the excitation energies improved the values obtained, the energies were still low, especially for the lowest energy geometry, B. We suspected that the low stability was adversely affecting the geometries themselves, leading to the low excitation energies and ultimately to the incorrect geometry being predicted as the lowest energy conformation. Geometry optimisation using TDA was therefore attempted.

The T_1 geometry optimised by TDA is shown in Figure 6.8; it is D_{2h} in symmetry and the lowest energy geometry found, even when starting from the geometry of ArMe3 - there was no distorted geometry as for DFT. The $S_0 \rightarrow T_1$ excitation energy was 3.37 eV, similar to that of geometry A, when the excitation energy was calculated by Tamm-Dancoff. This suggests that while DFT can in some cases predict an incorrect geometry as the lowest T_1 state, TDA correctly predicted the geometry for benzene.

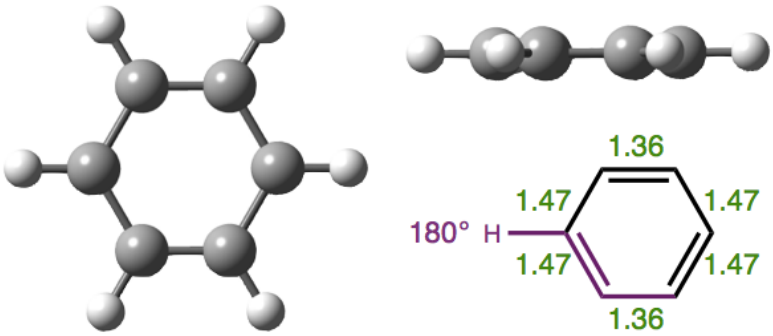

Figure 6.8: T_1 excited state geometry optimised for benzene by TDA. The C−C bond lengths (Å) are shown in green and the dihedral angle in purple

6.6 Calculations on substituted benzene compounds

Section 6.5 showed that DFT incorrectly predicted the lowest energy triplet geometry of benzene if starting from a distorted structure but that TDA predicted the correct one. We will now widen the discussion to the other substituted-benzene compounds to see if this occurrence can be more widely observed, or if it is an isolated case. Chapter 5 showed that optimisation of the T_1 geometry and comparison of it to the S_0 geometry could be used to predict increased rates of non-radiative decay and subsequent lowering of quantum yields. Although rates of radiative and non-radiative decay could not be measured experimentally for these benzene analogues, it is interesting to see if distortion in the excited state relative to the ground state correlates with decreased efficiency of emission. Those compounds where the 0−0 band in the emission spectrum is lower compared to λ_{max} should also be those which display a large degree of distortion. Geometries calculated using DFT will first be discussed, then those computed with TDA.

6.6.1 DFT geometries

The T_1 excited state geometries of the thirteen benzene-derivative compounds calculated by DFT are shown in Figures 6.9, 6.10 and 6.11. RMSD values between the ground state and T_1 excited state geometries are shown in Table 6.3 alongside their experimental quantum yields. There appears to be a weak

	DFT RMSD / Å	TDA RMSD / Å	Φ_{phos}
ArH	0.1274	0.0521	0.11
ArMe	0.0632	0.0498	0.26
ArMe2	0.0557	0.3492	0.34
ArMe2a	0.0504	0.1298	0.46
ArMe2b	0.0492	0.0478	0.51
ArMe3	0.5644	0.4965	0.33
ArMe3a	0.0524	0.0891	0.37
ArMe3b	0.0487	0.0457	0.45
ArMe4	0.0452	0.4700	0.34
ArMe4a	0.5624	0.4703	0.54
ArMe4b	0.2309	0.2068	0.45
ArMe5	0.2927	0.4740	0.34
ArMe6	0.5437	0.4649	0.23

Table 6.3: RMSD between the S_0 and T_1 geometries of the benzene derivatives calculated by DFT and TDA. TDA calculations were performed with B3LYP, as were their corresponding ground state geometries. Quantum yields of phosphorescence are shown for comparison.

correlation between those compounds which indicated distortion experimentally and those predicted to do so theoretically. The exception to this is the ArMe4 series which shows the inverse of the expected relationship.

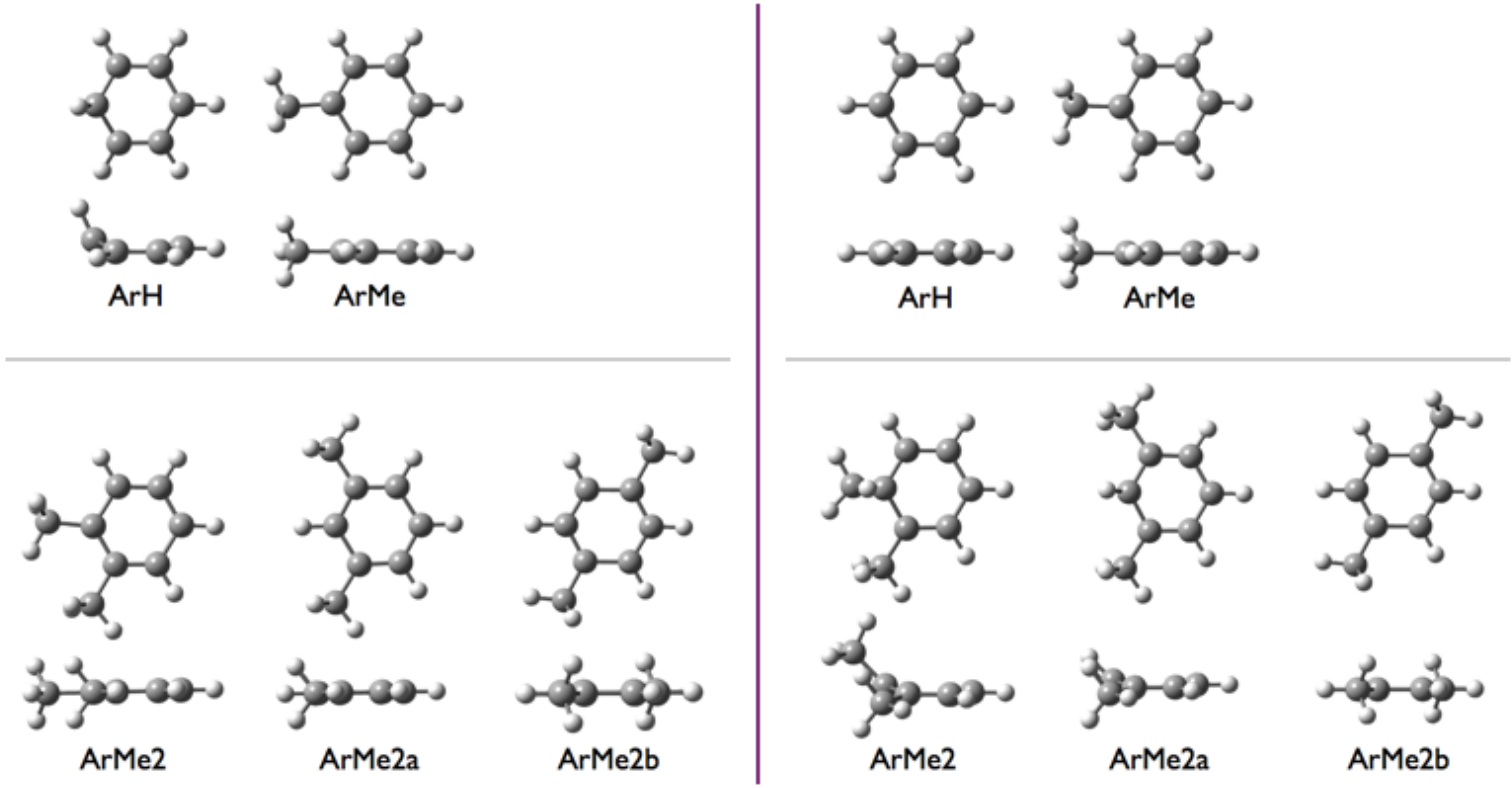

Figure 6.9: Lowest energy T_1 excited state geometries of benzene derivatives, calculated by DFT (left) and TDA (right). ArH optimised from distorted geometry.

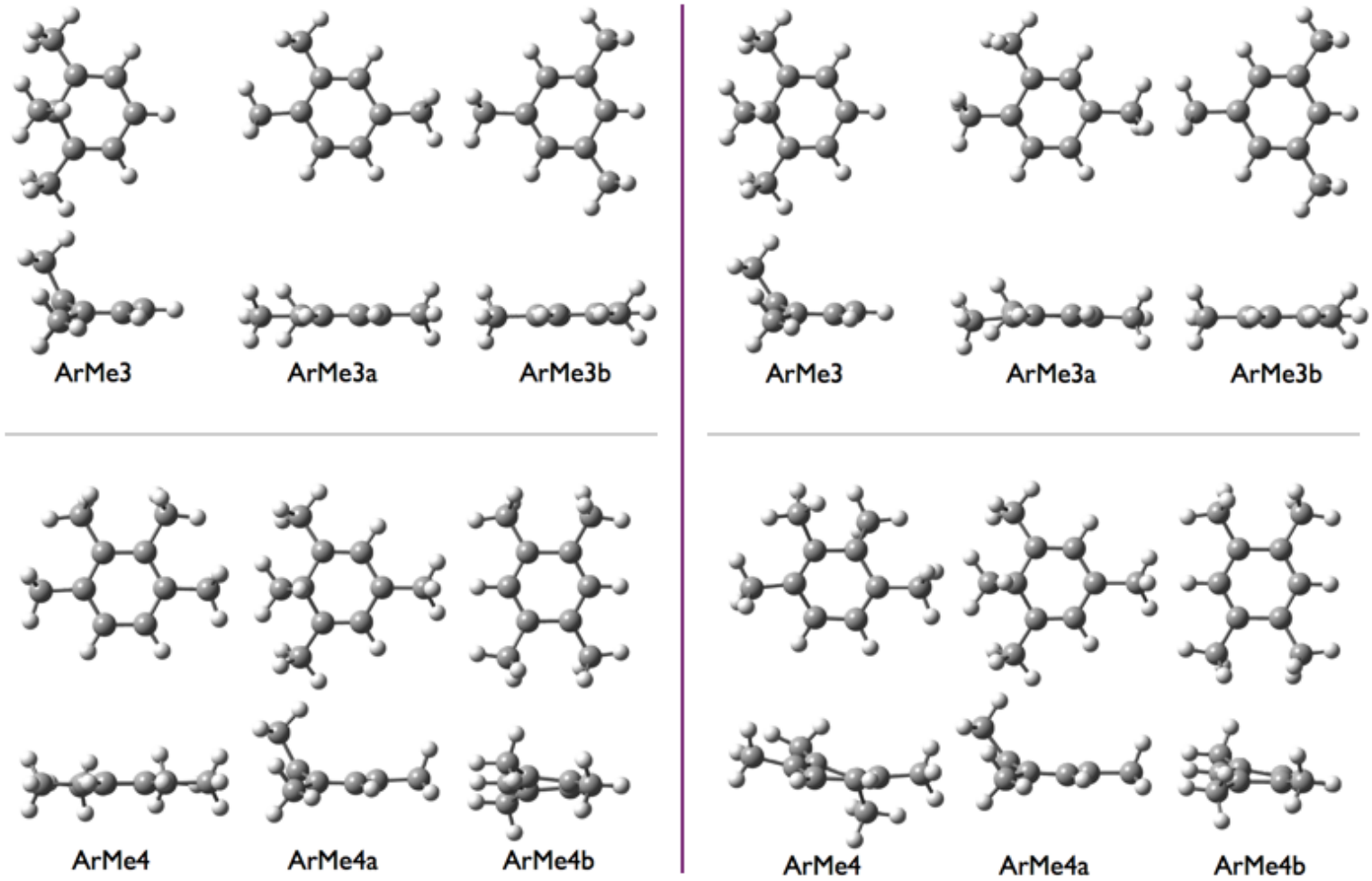

Figure 6.10: Lowest energy T_1 excited state geometries of benzene derivatives, calculated by DFT (left) and TDA (right).

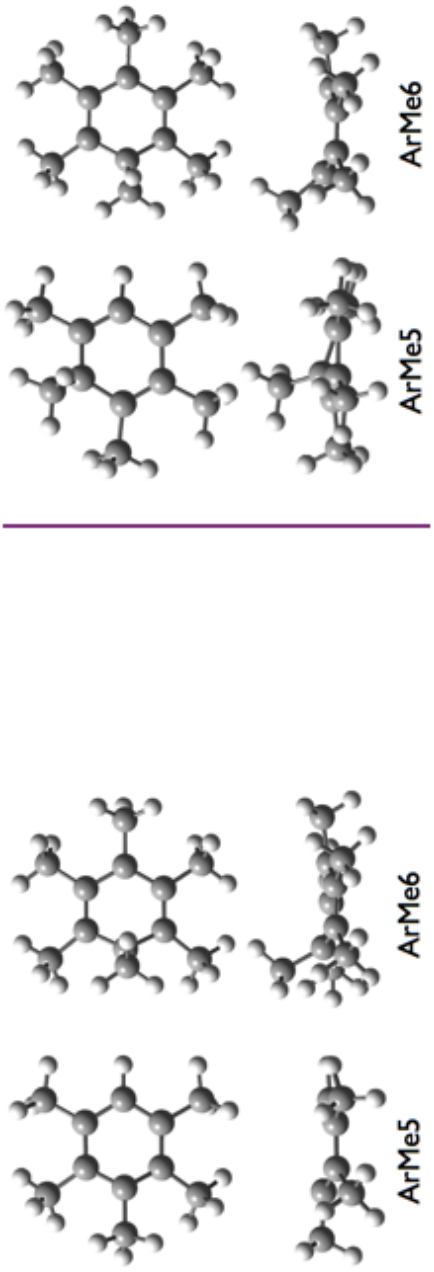

Figure 6.11: Lowest energy T_1 excited state geometries of benzene derivatives, calculated by DFT (left) and TDA (right).

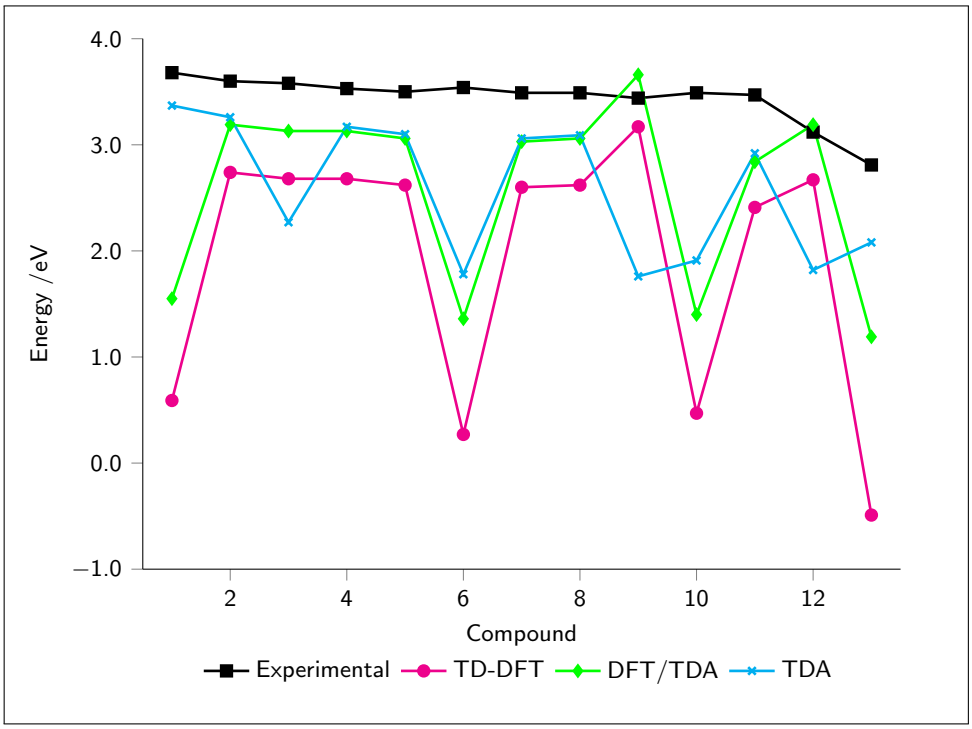

Figure 6.12: A graph to show the trend in excitation energies calculated for the compounds with experimental results (at 77 K in MP) for reference. Compound numbers refer to those in Table 6.4.

The excitation energies calculated by TD-DFT are shown in Table 6.4 alongside experimental values for the 0−0 band for comparison. The energies predicted by TD-DFT at the DFT-optimised T_1 geometry are shown in Table 6.4 and plotted with the experimental values in Figure 6.12. As we saw for benzene, some of the compounds with very distorted geometries showed excitation energies that were very low; ArMe6 was the extreme case with an imaginary excitation energy of −0.49 eV. Excitations calculated using TDA at the DFT geometry did show an increase in energy and all excitations calculated were positive but they were still much too low and did not fit the experimental trend observed.

		Experimental		TD-DFT	DFT/TDA	TDA
		/ nm	/ eV	/ eV	/ eV	/ eV
1	**ArH**	337	3.68	0.59	1.55	3.37
2	**ArMe**	344	3.60	2.74	3.19	3.26
3	**ArMe2**	346	3.58	2.68	3.13	2.27
4	**ArMe2a**	351	3.53	2.68	3.13	3.17
5	**ArMe2b**	354	3.50	2.62	3.06	3.10
6	**ArMe3**	350	3.54	0.27	1.36	1.78
7	**ArMe3a**	355	3.49	2.60	3.03	3.06
8	**ArMe3b**	355	3.49	2.62	3.06	3.09
9	**ArMe4**	360 *sh*	3.44	3.17	3.66	1.76
10	**ArMe4a**	355	3.49	0.47	1.40	1.91
11	**ArMe4b**	357	3.47	2.41	2.84	2.92
12	**ArMe5**	398[a]	3.12	2.67	3.19	1.82
13	**ArMe6**	442[a]	2.81	-0.49	1.19	2.08

Table 6.4: Excitation energies of the benzene derivatives calculated by TD-DFT, TDA at the DFT geometry and TDA at the TDA geometry. Experimental spectra were obtained at 77 K, in MP glass and refer to the 0–0 band. [a]λ_{max} *since the 0–0 band is indistinguishable.*

6.6.2 TDA geometries

The geometries for the thirteen compounds optimised using TDA are shown in Figures 6.9, 6.10 and 6.11. These geometries are very different from those optimised by DFT, a fact which is highlighted by the differences shown in the RMSDs between the two methods (Table 6.3). For example, the RMSD of ArMe2 according to DFT is just 0.0557 Å, but 0.3492 Å at the TDA geometry. Conversely, the RMSD of ArH decreases from 0.1274 Å to just 0.0521 Å with TDA. The trends in RMSD correlate much better with those in quantum yields of phosphorescence for the TDA geometries than they did for those calculated with DFT. There is a more convincing decrease in the RMSD from ArMe2

through to ArMe2b, correlating with the increase in quantum yield which is visually represented in the relative heights of the bands in the emission spectra (Figure 6.2):

	ArMe2	<	**ArMe2a**	<	**ArMe2b**
Φ_{phos}	0.34		0.46		0.51
RMSD	0.35		0.13		0.05

The only exception to this correlation is ArMe4a. This compound has the highest quantum yield in the ArMe4X series, but also the highest RMSD. While the RMSD is high for the geometry optimised by both DFT and TDA, it is lower for TDA (0.4703 Å , compared to 0.5624 Å with DFT) and essentially the same degree of distortion as ArMe4 (RMSD = 0.4700 Å). It could be that inclusion of a solvent model in the TDA geometry optimisation (which is not at present possible with QChem) could alter the geometry found.

While there is a visible improvement in the trend in predicted excitation energies calculated by TDA from those computed by TD-DFT (Figure 6.12), the trend is still dissimilar to the experimental one. Noticeably, the compounds with the low excitation energies are those predicted to show significant distortion both experimentally and according to TDA. For example, ArMe2 shows 2.27 eV for $S_0 \rightarrow T_1$ compared to 3.17 and 3.10 eV for ArMe2a and ArMe2b respectively.

6.7 Concluding remarks

The emission spectra of benzene and its twelve methyl-substituted derivatives have been measured and trends in their quantum yields of phosphorescence established. The quantum yields alongside relative intensities of bands in the emission spectra were used to indicate distortion in the excited state of the compounds relative to the ground state. The relative distortions were compared and contrasted with RMSD between the T_1 and S_0 geometries for the thirteen compounds calculated by both DFT and TDA.

Analysis of the results (along with coupled cluster calculations) showed that DFT can, in some cases, predict the incorrect lowest energy T_1 geometry. This was illustrated by calculations on benzene and widened to the larger set of compounds; the TDA and DFT geometries were dissimilar and the TDA geometries showed a better correlation with the experimental results obtained. Compounds showing a large degree of distortion between the ground and excited states consistently showed poor correlation between predicted and experimental energies of emission. Care should therefore be taken when using optimised triplet DFT geometries in case the incorrect geometry is assigned: the lowest energy geometry is not necessarily the correct one. It should be noted however that these compounds were the extreme example with exceptionally high orbital overlap (leading to low stability) and were designed specifically to test this theory.

7

Application of TD-DFT to other contemporary Pt(II) complexes

7.1 Introduction

The computational studies in Chapters 2 and 3 focused predominantly on the use of TD-DFT to predict absorption and emission energies respectively. Chapter 6 discussed the use of distortion at the triplet state geometry to predict relative rates of non-radiative decay in small, organic, molecules while Chapter 5 augmented this discussion to a series of larger, phosphorescent, Pt(II) complexes. Equation 7.1 shows that the quantum yield of luminescence is dependent on both the rate of radiative and non-radiative decay, such that a sufficiently low value of the former, or a high of the latter, can result in a lack of detectable room temperature emission from any given compound.

$$\Phi_{lum} = \frac{k_r}{k_r + \Sigma k_{nr}} \tag{7.1}$$

It is well known that both the degree of orbital overlap and the magnitude of metal character in a given transition have significant influence on the rate of radiative decay, k_r, for phosphorescent emission. The Franck-Condon principle states that transitions with a high degree of orbital overlap will be more favourable than those with a low degree of overlap, and will therefore proceed at a faster rate (see Chapter 1, Section 1.7). Orbital overlap can be quantified

computationally using TD-DFT, calculating Λ as discussed in Chapter 3. The heavy metal atom in a complex, such as platinum or ruthenium, introduces spin-orbit coupling, making formally forbidden intersystem crossing (ISC) and phosphorescent emission more allowed. For this reason, compounds with a high degree of metal character in the phosphorescent transition are likely to have a high k_r, since the transition should be more allowed, while the inverse is true of those with a low degree of metal character.

There are many factors affecting the rate of non-radiative decay, not all of which can be easily quantified (such as quenching by interaction with other molecules e.g. solvent interactions, aggregate formation, O_2 quenching). One of the significant contributors to Σk_{nr} which can be quantified is geometric distortion between the excited state and ground state, the increasing degree of which facilitates non-radiative decay in line with the energy gap law.

In previous chapters we have seen various examples of compounds synthesised with their photophysical properties rationalised, explained or predicted with the use of DFT. While it is important to study some such sets in detail in order to fully understand the effect of various parameters on the values and properties predicted, it is also important to apply these techniques to a wider variety of complexes, to see if the same theories hold true, precipitating reliable results. In this chapter, various different compounds (made by other groups or people) will be considered to see if the DFT can reliably account for their photophysical properties, using the techniques outlined in the previous chapters, with a particular focus on quantum yield of emission. At the end of this chapter values for Mulliken charges on the Pt atom, Λ (for orbital overlap) and RMSD (for distortion) for all complexes discussed are summarised in one large table together (Table 7.6) for comparison of different complexes with one another.

7.1.1 DFT calculations

Apart from the exceptions outlined in the text, DFT and TD-DFT calculation described in this chapter were performed using PBE0, in DCM, using a PCM

for solvent. The LANL2DZ basis set was used for platinum and cc-pVDZ for all other atoms. Ground state and triplet excited state geometries were optimised by direct minimisation of the SCF energy and checked to be a true minimum by frequency calculations at the same level of theory. Convolution of absorption spectra was achieved using a 0.6 eV full width at half maximum Gaussian.

Chapter 3 showed the importance of the inclusion of solvent in some calculations for prediction of the correct transition. The exceptions in the text are those where published results were reported in vacuum; solvent calculations were also performed to ensure the correct transition was predicted. PBE0 was chosen as a functional due to the increased triplet instabilities experienced by CAM-B3LYP. In such calculations, geometry optimisation by direct minimisation of the SCF energy using PBE0 can be used initially to assess the type of transition taking place, then the functional and method altered if necessary (e.g. CAM-B3LYP with TDA).

7.2 $PtL^{1-4}Cl$ and $PtLF^{1-4}Cl$ compounds revisited

Table 7.1 shows that the efficiency of emission of the $PtL^{1-4}Cl$ and $PtLF^{1-4}Cl$ compounds (discussed in Chapter 2) varies dramatically: $PtLF^{2}Cl$ has a very high quantum yield of 0.87 while $PtLF^{4}Cl$ has a low quantum yield of just 0.02. The only difference between these two compounds (which have fairly similar energies of emission, 467 and 494 nm respectively) is the position of the methyl groups on the pyridine ring.

The quantum yields of the $PtL^{n}Cl$ series increase in the order:

$$\mathbf{PtL^{4}Cl} < \mathbf{PtL^{3}Cl} < \mathbf{PtL^{1}Cl} < \mathbf{PtL^{2}Cl}$$

The same pattern is shown for the $PtLF^{n}Cl$ series, with the exception of $PtLF^{1}Cl$, which has a low quantum yield. While there is some variation of both energy of emission and orbital overlap (Λ) with position of the methyl group, neither are of significant magnitude to explain the vastly different efficiencies of emission observed. Inspection of the geometries and density difference plots of these eight complexes shows that, unlike the other compounds,

	Emission λ_{max} / nm	Φ_{lum}	k_r / 10^4 s^{-1}	Σk_{nr} / 10^4 s^{-1}
PtL^{1}Cl	497, 529, 565 *sh*	0.51	6.6	6.3
PtL^{2}Cl	487, 521, 560	0.73	7.3	2.7
PtL^{3}Cl	494, 528, 565 *sh*	0.13	1.2	7.8
PtL^{4}Cl	506, 529, 569 *sh*	0.03	–	–
PtLF^{1}Cl	487, 513, 555 *sh*	0.39	5.3	8.4
PtLF^{2}Cl	467, 498, 529 *sh*	0.87	11	1.6
PtLF^{3}Cl	478, 510, 543 *sh*	0.67	6.4	3.1
PtLF^{4}Cl	494, 530, 565 *sh*	0.02	–	–

Table 7.1: Luminescence data for PtL$^{1-4}$Cl and PtLF$^{1-4}$Cl in degassed DCM solution at 298 K. k_r and Σk_{nr} are the radiative and non-radiative rate constants estimated from the quantum yield and lifetime at 298 K.

PtL^{4}Cl, PtLF^{1}Cl and PtLF^{4}Cl show significant distortion away from planarity at both the S_0 and T_1 geometries, due to steric interactions between the methyl groups and either the chlorine or fluorine atoms (Figure 7.1). This distortion occurs to such an extent that the density difference plots of the $S_0 \rightarrow T_1$ excitation at the T_1 geometry are altered (Figure 7.2). Furthermore, these three complexes show distortion between the S_0 and T_1 geometries, leading to non-radiative decay (Figure 7.3). Consideration of the relative intensities of the vibronic bands in the emission spectra of these complexes (Table 7.2) confirms experimentally that there is distortion between the two states since the intensity of the 0−1 vibronic band relative to the 0−0 band is increased in PtL^{4}Cl, PtLF^{1}Cl and PtLF^{4}Cl compared to the other five compounds.

Table 7.1 shows that the increased efficiency of emission of PtL^{2}Cl compared to PtL^{1}Cl, and PtL^{1}Cl over PtL^{3}Cl, is due to both an increase in the rate of radiative decay, k_r, and a decrease in the rate of non-radiative decay, k_{nr}. Distortion is lowest for PtL^{2}Cl (decreasing k_{nr}) and highest for PtL^{1}Cl, while Λ is highest for PtL^{3}Cl (increasing k_r) and lowest for PtL^{2}Cl. The overall efficiency of emission of these is then due to subtle differences in a variety of

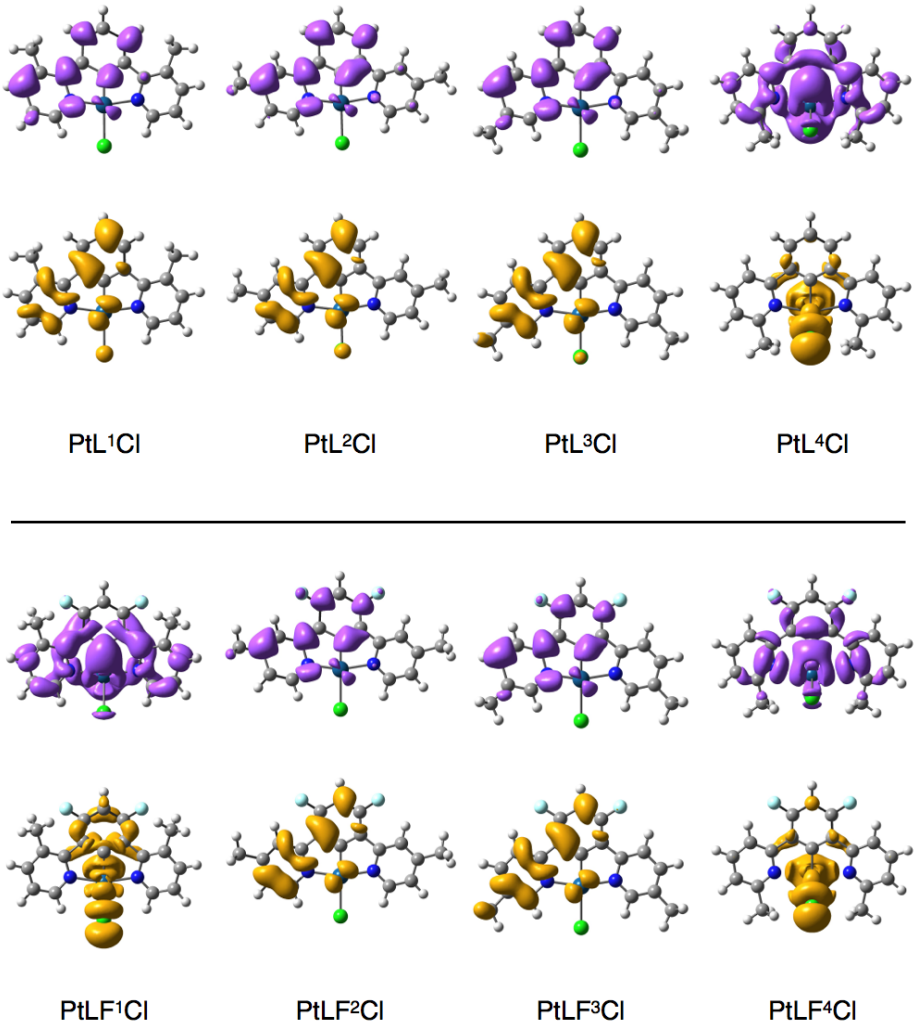

Figure 7.1: Density difference plots for the $S_0 \rightarrow T_1$ excitation of PtL$^{1-4}$Cl (top) and PtLF$^{1-4}$Cl at the triplet excited state geometry, T_1.

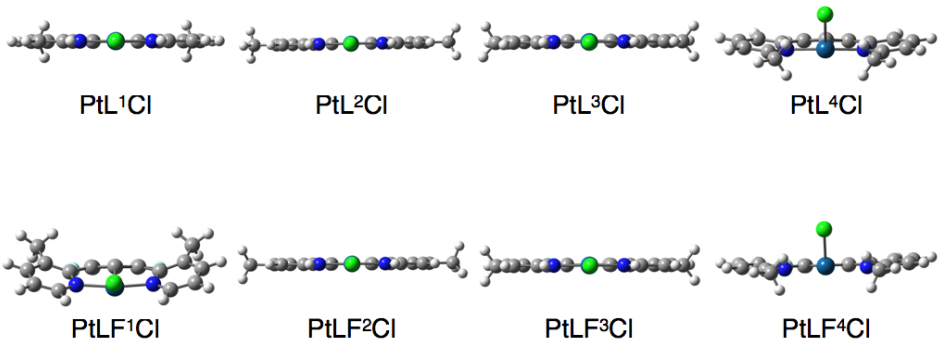

Figure 7.2: PtL$^{1-4}$Cl (top) and PtLF$^{1-4}$Cl at the triplet excited state geometry, T_1, viewed along the Cl−Pt−C bond.

	Intensity of 0−0	Intensity of 0−1	Intensity of 0−2
PtL^{1}Cl	1	0.66	0.27
PtL^{2}Cl	1	0.60	0.28
PtL^{3}Cl	1	0.58	0.24
PtL^{4}Cl	1	0.70	0.30
PtLF^{1}Cl	1	0.86	0.43
PtLF^{2}Cl	1	0.55	0.23
PtLF^{3}Cl	1	0.56	0.23
PtLF^{4}Cl	1	0.70	0.36

Table 7.2: Experimental values for the intensity of the 0−n vibronic bands relative to the intensity of the 0−0 vibronic band for the PtL^{n}Cl and PtLF^{n}Cl series of complexes.

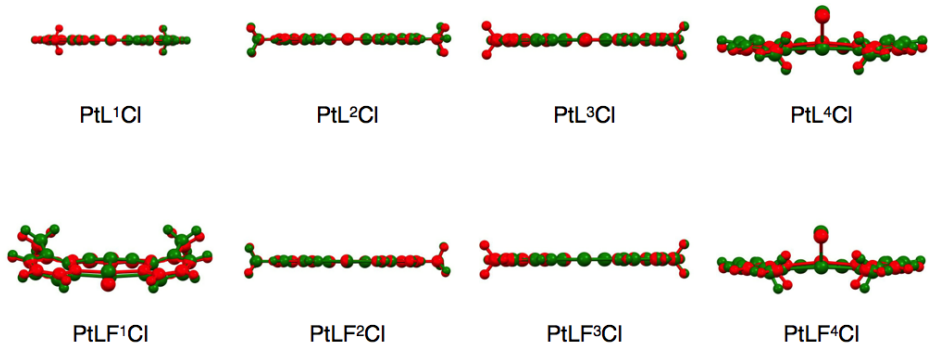

Figure 7.3: Superimposed structures of the S_0 ground state (red) and T_1 excited state (green) for the eight $PtL^{1-4}Cl$ (top) and $PtLF^{1-4}Cl$ complexes, viewed along the Cl−Pt−C bond.

factors.

7.3 Acetylacetonate compounds

7.3.1 Introduction and experimental considerations

A series of *ortho*-platinated complexes bound to various β-diketonate ligands of the form [Pt(N^C)(O^O)] were synthesised by Spencer *et al.* to study their liquid crystal and luminescent properties.[241] Complexes of this type usually have an excited state located on the metal and cyclometallated ligand, with the second (in this case β-diketonate) an innocent auxiliary ligand, having little effect on the emission properties observed. The compounds investigated were those shown in Figure 7.4, with long alkoxy chains R and R′ on either end of the ppy ligand. The tfac complex showed formation of two different isomers, designated *cis* and *trans* according to the relative positions of the CF_3 group and the pyridyl ring about platinum. While one could be favoured in synthesis, it could not be achieved specifically, and a single isomer could not be obtained for photophysical study. Despite this, by recrystallisation, a 36:1 ratio could be purified and study of this alongside a sample of a 1:1 mixture of the isomers allowed some understanding of the electronic properties of the individual isomers. It was concluded that the *trans* isomer emitted at a higher energy than the *cis*, but with a significantly lower quantum yield since, when in a 1:1 ratio, emission from the *cis* dominated the spectrum (Figure

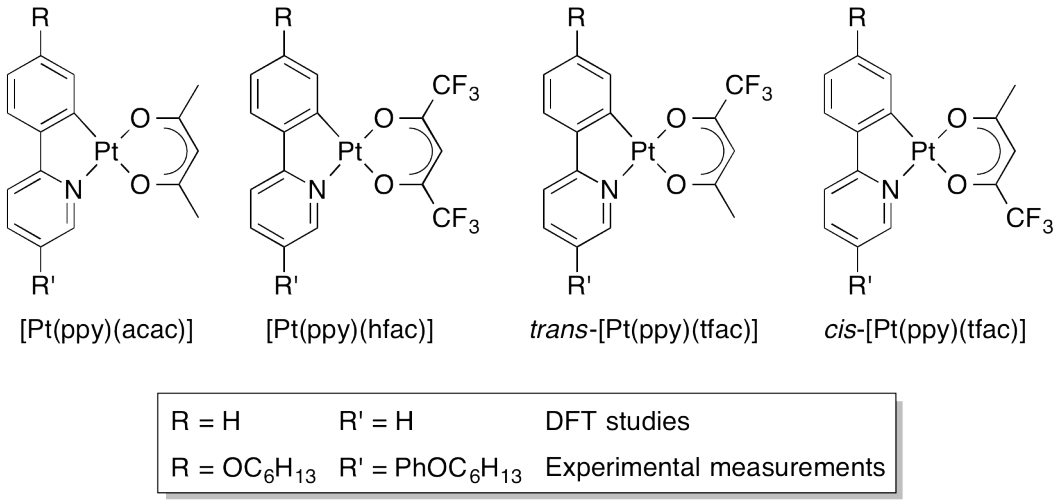

Figure 7.4: The chemical structures of the four acac complexes studied.

7.5). Unexpectedly, the hfac complex was not emissive at room temperature. Given that the O^O ligand was not initially expected to be involved in the excited state, the drastic drop in emission efficiency upon alteration of this ligand from acac or tfac to hfac was surprising.

In an attempt to understand the range of emission efficiencies observed, DFT calculations were performed on the four analogous complexes shown in Figure 7.4 where R = R′ = H. The alkoxy chains were removed from those studied experimentally, since the effect had been shown to be the same over a range of substituents, and because the extra computational time associated with such long chains was prohibitive.

7.3.2 Ground state studies

The ground state geometries of the four compounds shown in Figure 7.4 were optimised by DFT with both PBE0 and CAM-B3LYP, in vacuum and with a PCM for DCM. All four methods gave essentially the same results, those shown are for PBE0 with DCM. Some of the key bond lengths and angles calculated for *cis*-[Pt(ppy)(tfac)] and *trans*-[Pt(ppy)(tfac)] at the S_0 geometry are shown in Figure 7.6. They show good agreement with those found for a

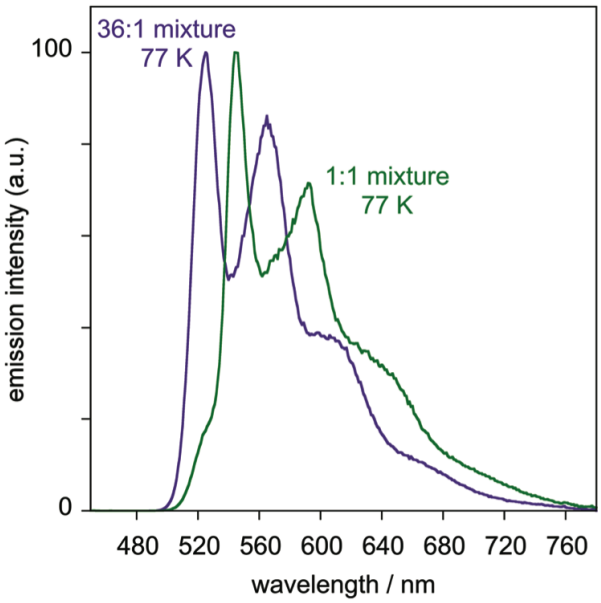

Figure 7.5: The emission spectra of [Pt(ppy)(tfac)] in EPA glass at 77 K. Green line: the spectrum of the 1:1 mixture of isomers. Purple line: corresponding spectrum of the sample in which one isomer has been concentrated to 36:1 by fractional recrystallisation.

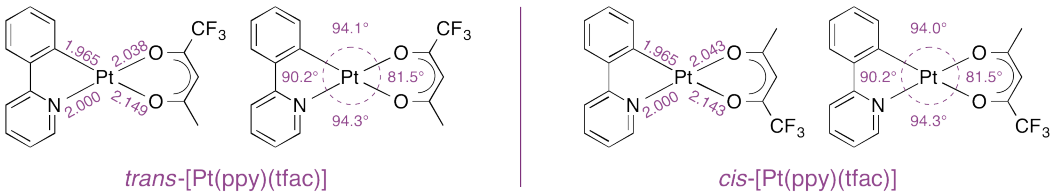

Figure 7.6: Bond lengths (Å) and angles (°) calculated by DFT for trans-[Pt(ppy)(tfac)] and cis-[Pt(ppy)(tfac)] at the ground state geometry.

closely related compound in the crystal structure of the *trans* isomer with a methyl group on the phenyl ring. Figure 7.6 shows that, despite the difference in quantum yield observed experimentally, there is little difference in bond lengths and angles between the two isomers at the ground state geometry.

Density difference plots for the $S_0 \rightarrow T_1$ excitation at the ground state geometry are shown in Figure 7.7; they show a marked difference between [Pt(ppy)(hfac)] and the other three compounds. While [Pt(ppy)(hfac)] shows electron depletion from the aryl ring of the ppy ligand and augmentation on

the hfac ligand, the other three complexes display rearrangement of electron density on the ppy ligand upon excitation, consistent with normal excited states in these complexes: $d_{Pt}/\pi_{N\wedge C} \rightarrow \pi^*_{N\wedge C}$ (mixed MLCT/LLCT). The change in excitation shown for [Pt(ppy)(hfac)] can presumably be attributed to the stabilisation of the π^* orbitals by the electron-withdrawing groups to such an extent that the LUMO is positioned there instead. Interestingly, the LUMO of [Pt(ppy)(hfac)] is very similar to the LUMO+2 of [Pt(ppy)(acac)] (Figures 9.38 and 9.37), in keeping with the findings of Ghedini *et al.* who showed that for some related cyclometallated Pt(II) and Pd(II) complexes the LUMO and LUMO+1 swapped between the acac and hfac complexes.[242] The excitation associated with [Pt(ppy)(hfac)] has a lower orbital overlap (Λ = 0.42), perhaps explaining in part the lower quantum yield observed due to the lower rate of radiative decay.

7.3.3 Triplet excited state studies

Optimisation of the first triplet excited state geometry, T_1, for each of the four complexes shows another probable origin for the variation of emission efficiency between the four complexes. Figure 7.8 shows the T_1 geometry of each complex superimposed upon its respective ground state geometry, S_0. It clearly shows that [Pt(ppy)(acac)] undergoes virtually no geometrical distortion upon excitation while, to varying degrees, all of the other three do, the largest change in geometry being shown by [Pt(ppy)(hfac)]. The significant distortion in [Pt(ppy)(hfac)] resulting in an increase in non-radiative decay, combined with decrease in radiative decay already discussed, suggests an origin for the lack of emission displayed by the hfac complexes in general.

The distortion of *cis*-[Pt(ppy)(tfac)] and *trans*-[Pt(ppy)(tfac)] again provide a possible explanation for the difference in emission efficiencies displayed by these two isomers. Quantification of the extent of distortion by calculation of the root-mean-square displacement of the atoms between the two states (S_0 and T_1) shows that the extent of distortion increases in the order:

[Pt(ppy)(acac)] < ***cis*-[Pt(ppy)(tfac)]** < ***trans*-[Pt(ppy)(tfac)]** < **[Pt(ppy)(hfac)]**

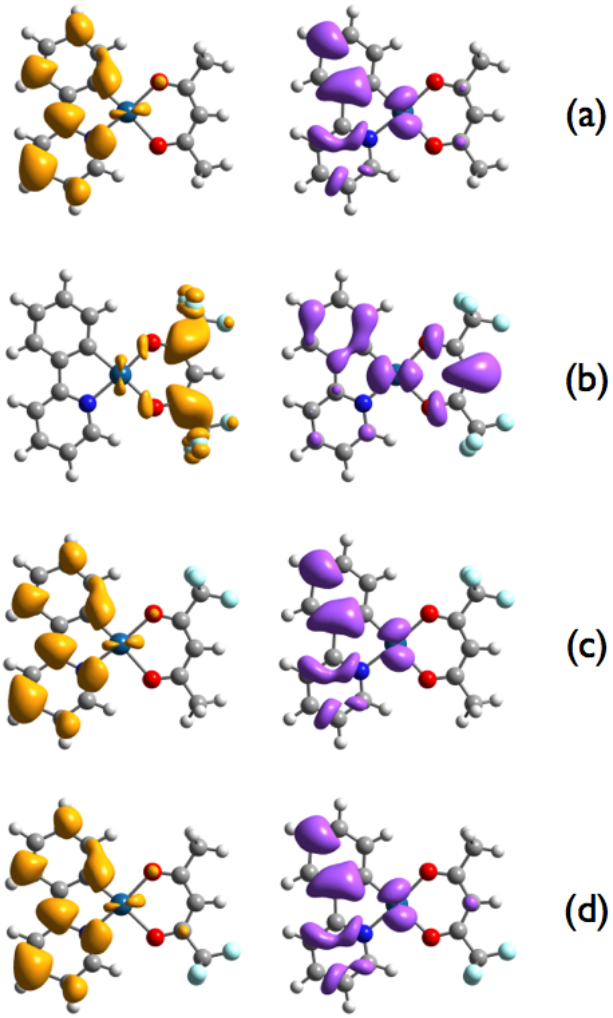

Figure 7.7: Density difference plots for the $S_0 \rightarrow T_1$ excitation of the four complexes at the ground state geometry: (a) [Pt(ppy)(acac)]; (b) [Pt(ppy)(hfac)]; (c) trans-[Pt(ppy)(tfac)]; (d) cis-[Pt(ppy)(tfac)].

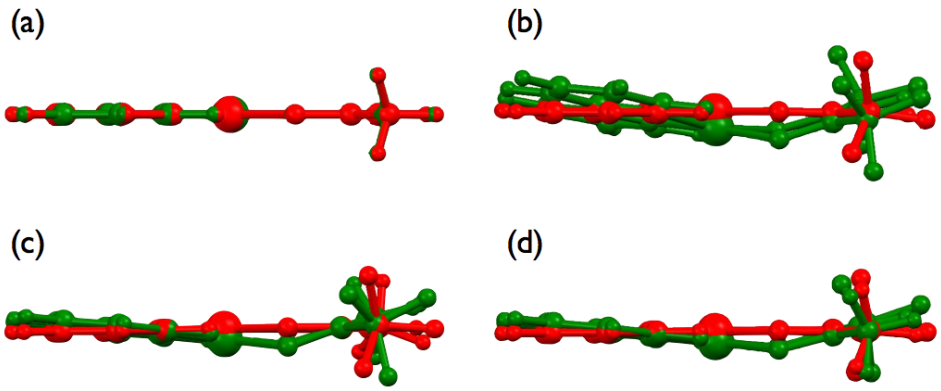

Figure 7.8: Superimposed structures of the S_0 ground state (red) and T_1 excited state (green) for the four complexes of Figure 7.4. (a) [Pt(ppy)(acac)]; (b) [Pt(ppy)(hfac)]; (c) trans-[Pt(ppy)(tfac)]; (d) cis-[Pt(ppy)(tfac)].

This suggests that the *trans* isomer distorts more in the triplet state than the *cis*, leading to a greater rate of non-radiative decay and therefore less efficient emission.

7.4 Effects of cis/trans isomerisation on emission in styryl-appended platinum complexes

7.4.1 Experimental studies

The compound shown in Figure 7.9 was synthesised by Nisic *et al.* for studies into its potential for use in OLEDs.[4] The absorption and emission properties of the complex were found to change upon irradiation with light as, upon irradiation, the *trans* isomer isomerised to the *cis* (Figure 7.10). Prior to irradiation, weak green phosphorescence was observed at room temperature in the form of a highly structured emission spectrum with the 0−0 band highest in intensity, the spectrum being very similar in nature to that of PtL^5Cl. At 77 K, in EPA glass, a vibrational structured emission was observed in the red region of the spectrum (λ = 600-800 nm). After irradiation, there was a substantial increase in the intensity of emission which remained green and structured with the 0−0 band highest in intensity. The low temperature emission spectrum showed a new set of bands between 480 and 600 nm (typical

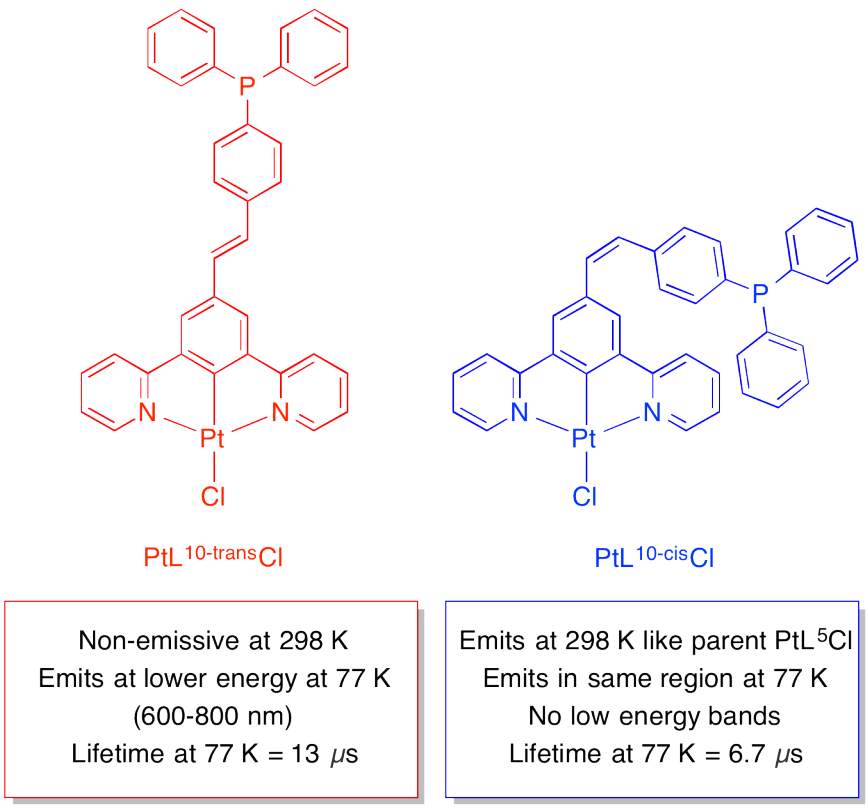

Figure 7.9: The chemical structures of the two isomers studied.

for PtL^5Cl-type emission) together with (though much more intense than) the lower energy bands observed prior to irradiation. A change was also observed in the absorption spectrum following irradiation, the complex absorbed more weakly for $\lambda > 310$ nm and at a higher energy lacked the lower energy shoulder centred around 425 nm..

It was concluded that the higher energy emission was attributable to the *cis* isomer whose emission was of the same character as PtL^5Cl both at room temperature and 77 K. The lower energy bands observed at 600-800 nm were only seen at 77 K and emanated from the *trans* isomer which did not emit at room temperature. The *cis* isomer absorbed more weakly and to a higher energy than the *trans*. In an attempt to reproduce the experimentally obtained trends to confirm the behaviour of each isomer and to better understand the

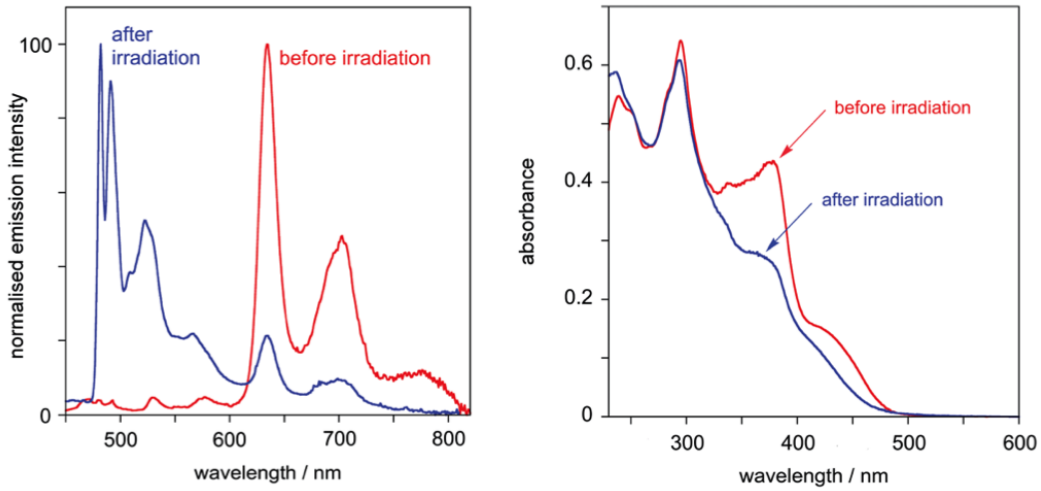

Figure 7.10: Left: emission spectra of PtL^{10}Cl at 77 K in EPA glass before and after UV irradiation. Right: absorption spectra of PtL^{10}Cl in DCM at 298 K before and after irradiation with a UV lamp for 7 minutes.

origin of their difference in photophysical properties, both were studied by TD-DFT at the ground state and the triplet excited state geometry, T_1.

7.4.2 Ground state DFT studies

As found experimentally, the convoluted absorption spectrum shows that the *cis* isomer of PtL^{10}Cl absorbs less intensely, and at a higher energy than the *trans* (Figure 7.11). Analysis of the density difference plots for the first three $S_0 \rightarrow S_n$ excitations (Figure 7.13) shows that each of the three transitions is essentially the same in nature for both isomers, but higher in energy and with a lower oscillator strength for *cis*. The spectrum in both cases is dominated by the $S_0 \rightarrow S_3$ transition in which the pendant participates in both the electron accretion and depletion plots.

7.4.3 Excited state DFT studies

Figure 7.14 shows the density difference plots for the $S_0 \rightarrow T_1$ excitation at the T_1 excited state geometry for both isomers of PtL^{10}Cl. These show that for emission, the transition is very different for the two isomers. PtL^{10-cis}Cl shows

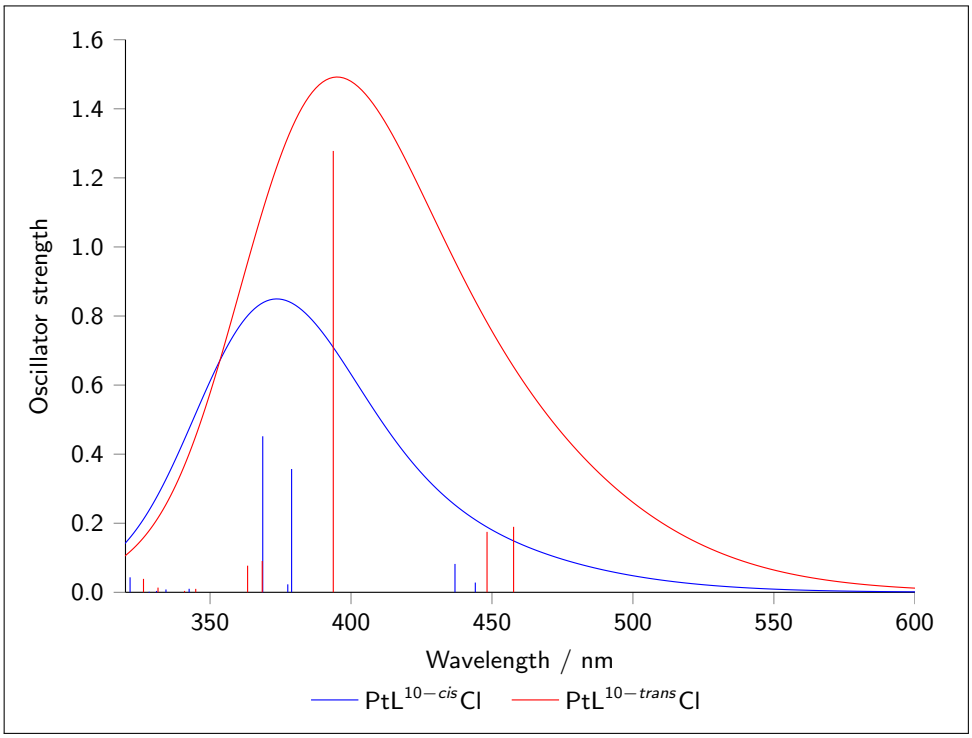

Figure 7.11: Convoluted absorption spectra of PtL^{10-cis}Cl and PtL$^{10-trans}$Cl calculated by TD-DFT at the ground state optimised geometry. Individual excitations are shown by the vertical lines (also shown in Appendix, Table 9.23).

almost no pendant involvement in the excitation, which looks very like that of the compound without the pendant, PtL^{5}Cl in character.[53] In contrast, the density difference plots for PtL$^{10-trans}$Cl show movement of the electron density almost entirely on the pendant itself. The low metal character involved in emission for this complex means that despite the high orbital overlap (Λ = 0.64 for *trans*, 0.39 for *cis*), emission from the triplet state is weak with a rate of radiative decay too low to be observed at room temperature and resulting in a lifetime at 77 K which is longer for *trans* than for *cis* (13 and 6.7 μs respectively). The extended conjugation for PtL$^{10-trans}$Cl results in the lower emission energy which is similar to that of *E*-stilbene phosphorescence (λ_{max} = 580).[243]

Despite the high degree of distortion shown for the *cis* isomer, it is thought that distortion of the triplet excited state relative to the singlet ground state,

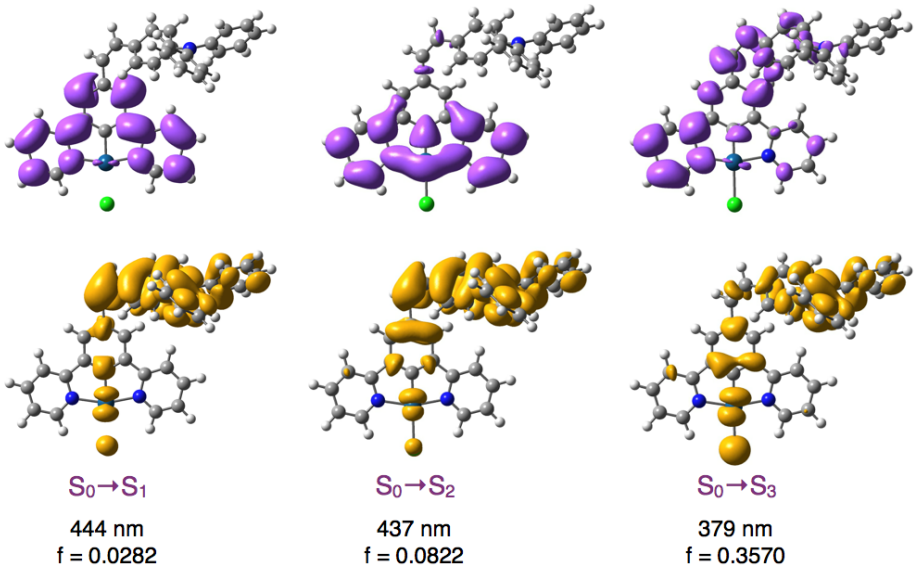

Figure 7.12: Density difference plots for excitation of $PtL^{10-cis}Cl$ *at the optimised ground state geometry,* S_0.

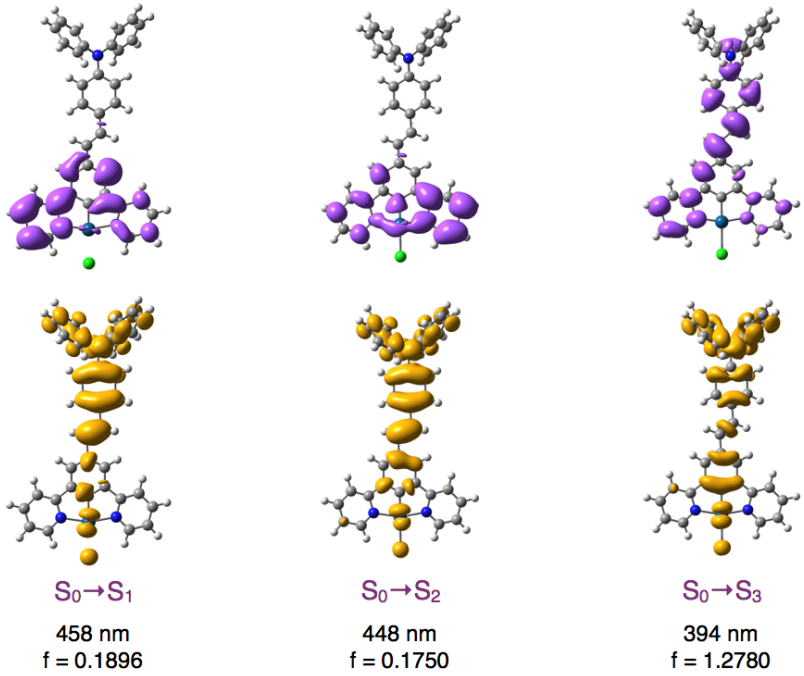

Figure 7.13: Density difference plots for excitation of $PtL^{10-trans}Cl$ *at the optimised ground state geometry,* S_0.

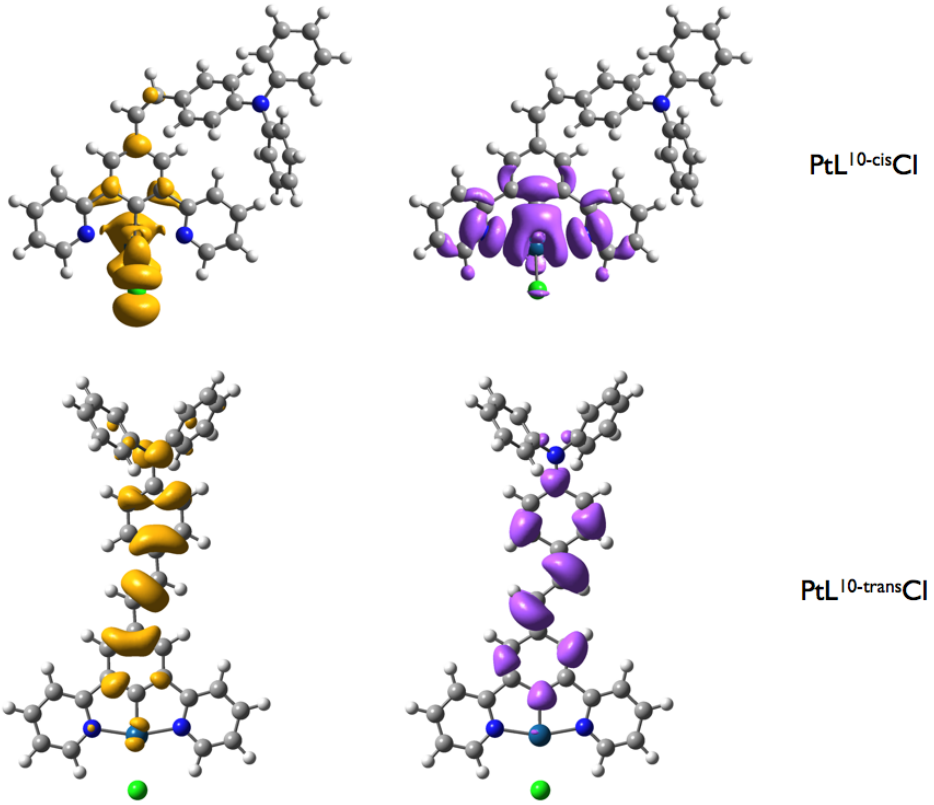

Figure 7.14: Density difference plots for the $S_0 \rightarrow T_1$ excitation of $PtL^{10-cis}Cl$ (top) and $PtL^{10-trans}Cl$ (bottom) at the triplet excited state geometry, T_1.

leading to non-radiative decay, is not in this case a significant factor. In fact while the RMSD is 1.7906 Å (compared to 0.0563 Å for the *trans* isomer), upon comparison of the structure of the two states after removal of the pendant moiety, the RMSD is reduced to 0.0147 Å (0.0126 Å for *trans*), showing that the displacement was just due to a slight movement in the whole pendant, resulting in a extremely high value for the complex as a whole (Figure 7.15). Since the pendant arm is not involved in the transition in the case of the *cis* isomer, and due to the nature of its origin, this is thought to be unimportant.

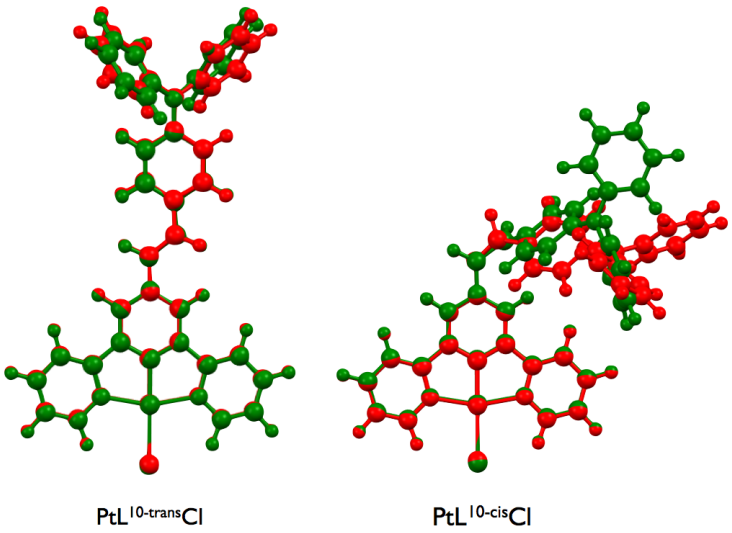

Figure 7.15: Superimposed structures of the S_0 ground state (red) and T_1 excited state (green) for the two isomers of PtL^{10}Cl.

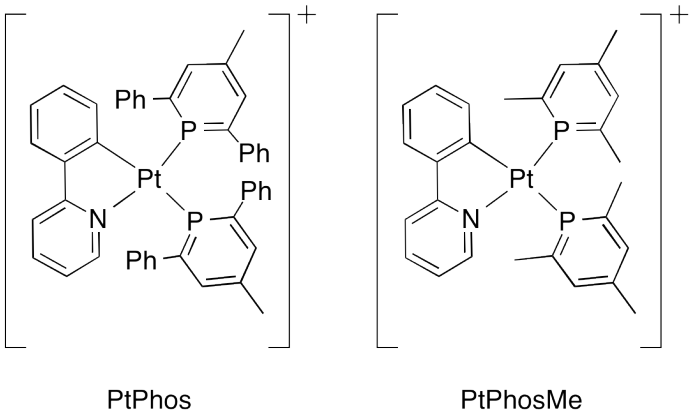

Figure 7.16: The chemical structures of the two phosphinine complexes studied.

7.5 Platinum complexes with a phosphinine ligand

7.5.1 Introduction and experimental considerations

Moussa *et al.* synthesised the first example of a luminescent, cyclometallated, Pt(II) complex with a phosphinine co-ligand, PtPhos, shown in Figure 7.16.[244] Although there are a few reports on the coordination chemistry of

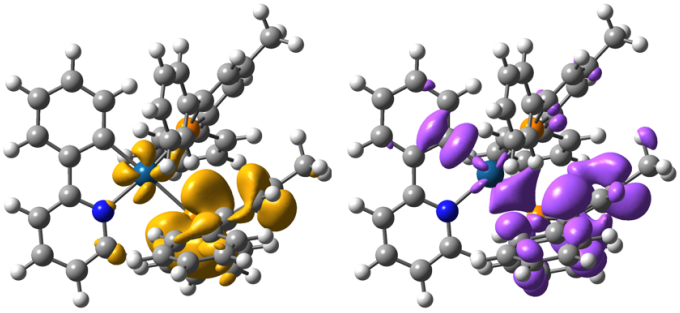

Figure 7.17: Density difference plots for excitation of PtPhos at the triplet excited state geometry, T_1.

phosphinines with Pt(II),[245;246] there are no studies into the electronic excited states of such compounds. A cyclometallated, *tris*-P^C coordinated Ir(II) complex was recently shown to be non-emissive even at low temperature due to non-radiative decay.[247] PtPhos displayed phosphorescent emission at 77 K in EPA glass ($\lambda_{max} = 586$ nm) with a long lifetime of 230 μs. The low temperature emission spectrum was very similar to that of the phosphorescence band displayed by the phosphinine proligand, only without an accompanying fluorescence band, and the phosphorescence lifetime was two orders of magnitude shorter for the complex. This suggested that the T_1 excited state was similar in character to that of the proligand, incorporating enough metal character to promote intersystem crossing and emission from $T_1 \rightarrow S_0$, thus increasing the radiative rate constant and shortening the lifetime.

7.5.2 DFT calculations

PtPhos

Density difference and orbital plots for the $S_0 \rightarrow T_1$ excitation at the triplet geometry (calculated with PBE0 in DCM) are shown in Figures 7.17 and 7.18 respectively, with orbital contributions shown in Table 7.3. The excitation is shown to be predominantly HOMO $\rightarrow$ LUMO in character, with both sets of orbitals centred on the phosphinine ligand *trans* to the cyclometallated carbon. Although there is precedent for this type of transition,[84;85] it is unusual since, as highlighted in Section 7.3, in Pt(N^C)-type complexes the excitation is

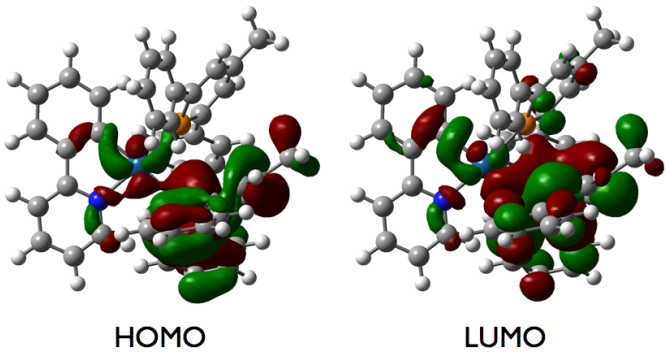

Figure 7.18: HOMO and LUMO orbital plots for excitation of PtPhos at the triplet excited state geometry, T_1.

Transition	Contribution
PtPhos	
HOMO → LUMO	0.739
HOMO ← LUMO	0.280
PtPhosMe	
HOMO → LUMO	0.659
HOMO → LUMO+2	−0.126
HOMO ← LUMO	0.101

Table 7.3: Dominant orbital contributions for excitation from S_0 to T_1 at the triplet excited state geometry of PtPhos and PtPhosMe.

more normally centred on the cyclometallated ligand. The excitation has a high degree of orbital overlap ($\Lambda = 0.76$) but despite this the rate of radiative decay is low which is probably due to the low metal character associated with the transition, resulting in the long lifetime.

PtPhosMe

DFT calculations were also performed on PtPhosMe (Figure 7.16), initially in an attempt to reduce calculation time involved in investigating PtPhos. Figures 7.19 and 7.20 show though that the excitation $S_0 \rightarrow T_1$ excitation (at

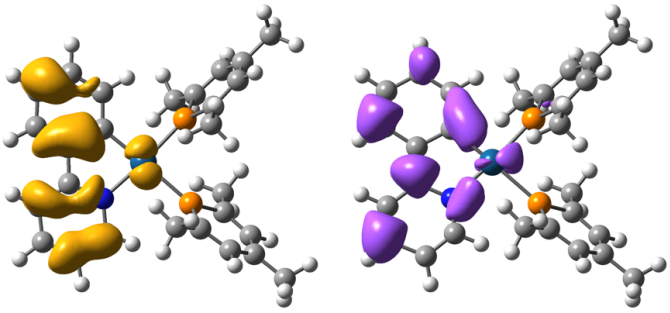

Figure 7.19: Density difference plots for excitation of PtPhosMe at the triplet excited state geometry, T_1.

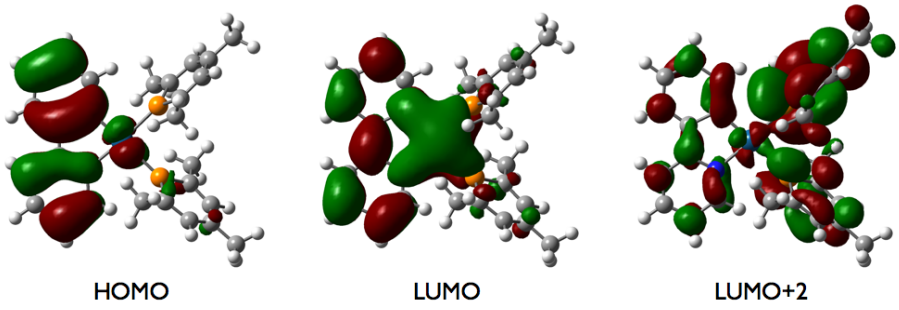

Figure 7.20: HOMO and LUMO orbital plots for excitation of PtPhosMe at the triplet excited state geometry, T_1.

the triplet geometry) is very different for this compound from that observed for PtPhos, serving as a reminder that it is not always possible to replace bulky, computationally expensive groups with smaller ones as models as is commonplace in the literature. The excitation is based instead on the ppy ligand and involves a greater degree of metal character suggesting a much higher rate of radiative decay would exist for this compound, increasing the efficiency of emission.

7.6 Pt(II) compounds of ligands featuring 6-membered chelate rings

7.6.1 Introduction

As previously discussed, the N^N^N-coordinated $[Pt(tpy)Cl]^+$ is non-emissive in solution at room temperature despite its rigid terdentate ligand.[248] This

is thought to be because of a rather weak ligand field as a result of the poor N−Pt−N angle. Maximum orbital overlap would be achieved by a ligand with a bite angle of 180° while tpy only achieves an angle of 163.5(7)° in [Pt(tpy)Cl]ClO_4.[249] This reduction in efficiency of emission is again illustrated by two ruthenium complexes, $[Ru(tpy)_2]^{2+}$ and $[Ru(bpy)_3]^{2+}$. The former, with N−Ru−N angles of 158.3(3) - 159.1(2)° and a subsequently weaker ligand field is essentially non-emissive at room temperature,[250–253] while $[Ru(bpy)_3]^{2+}$ has a quantum yield of 0.028 even in aerated aqueous solution at room temperature.[254]

Larger bite angles afforded by 6-membered chelation have proved a possible route to more efficient emission. Use of 2-(8-quinolyl)-1,10-phenanthroline as a ligand gives an N^N^N-coordinated Pt(II) complex with one 5-membered and one 6-membered chelate ring, with a quantum yield of 0.002 in DCM at room temperature, due to the relieved ring strain.[255] Two complexes, each incorporating two 6-membered chelates around Pt(II) with N^C^N coordination, were therefore synthesised by previous members of the group to investigate whether the emissive properties of the complexes could be made more efficient in this way (Figure 7.22).

Perhaps surprisingly, neither complex showed improved efficiency of emission compared to the 5-membered chelate ring, N^C^N-coordinated complex, PtL^5Cl. $PtL^{11}Cl$ had a quantum yield of luminescence (in degassed DCM solution at room temperature) of just 1.6%[28] (compared to 60% for PtL^5Cl) while $PtL^{12}Cl$ showed no room temperature emission at all (Figure 7.22).[256] Although the energy of emission of $PtL^{11}Cl$ at 298 K (in DCM) was very low (λ_{max} = 645 nm), the rate of non-radiative decay was extremely low (7×10^4 s^{-1} compared to 5.5×10^4 s^{-1} for PtL^5Cl - λ_{max} = 491 nm). The reduced efficiency of emission was therefore due to a low rate of radiative decay (10^3 s^{-1}).

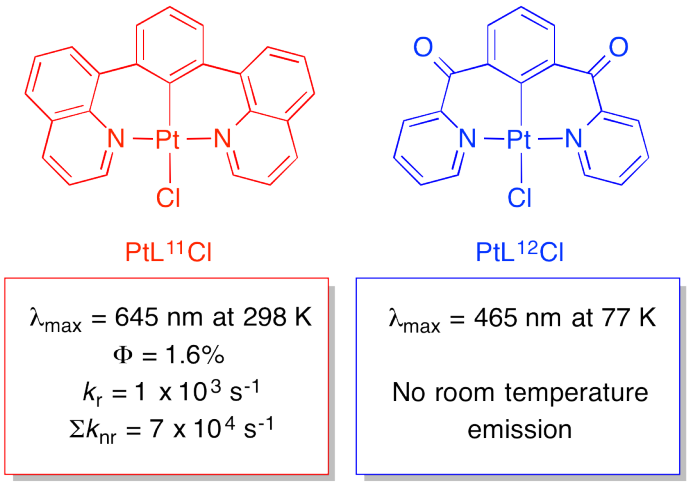

Figure 7.21: The chemical structures and emission properties of the Pt(II) complexes with two 6-membered chelate rings.

7.6.2 Calculations

TD-DFT was employed to help understand the reduced efficiencies of these complexes compared to similar complexes with 5-membered chelate rings. Optimised ground state geometries of the two complexes are shown in Figure 7.22. They show that the 6-membered chelate rings about platinum did indeed relieve ring strain, giving N^C^N angles of 179.2° and 179.6° for $PtL^{11}Cl$ and $PtL^{12}Cl$ respectively (compared to 161.2° for $PtL^{5}Cl$). Both geometries show twisting of the ligand to achieve this angle (Figure 7.22). The ground state and triplet state geometries of both complexes were very similar, with RMSDs of just 0.1416 ($PtL^{11}Cl$) and 0.1528 ($PtL^{12}Cl$), in keeping with the low rate of non-radiative decay observed experimentally for $PtL^{11}Cl$.

Orbital and density difference plots for the $S_0 \rightarrow T_1$ excitation of $PtL^{11}Cl$ and $PtL^{12}Cl$ at the T_1 geometry are shown in Figures 7.23 and 7.24 respectively. $PtL^{11}Cl$ shows moderate orbital overlap for the excitation ($\Lambda = 0.60$) but low metal character. The combination of the two of these results in the low rate of radiative decay observed experimentally. $PtL^{12}Cl$ shows lower orbital overlap ($\Lambda = 0.40$) than $PtL^{11}Cl$ and a higher Mulliken charge on the platinum atom at both S_0 and T_1 states of the T_1 geometry (Table 7.6), indicating a lower

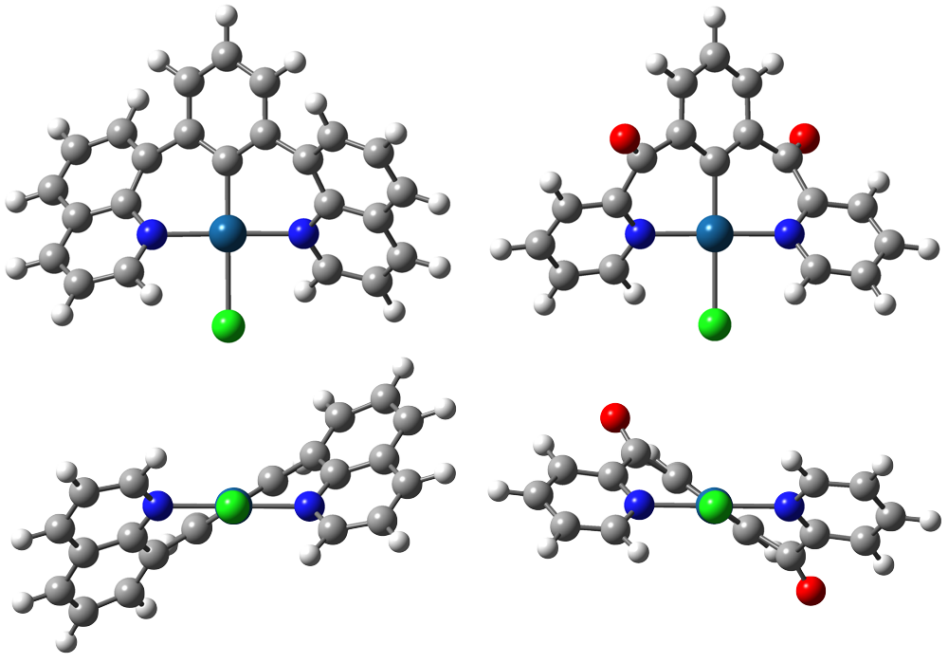

Figure 7.22: S_0 optimised geometries of PtL^{11}Cl (left) and PtL^{12}Cl (right), viewed from the front (top) and along the Cl−Pt−C bond (bottom).

involvement of the platinum in the excitation. This combination of factors could therefore be reducing the rate of radiative decay to such a degree that no room temperature emission is observed.

7.7 Compounds with a tetradentate ligand

7.7.1 Introduction

As discussed in Chapter 1, rigidity within the ligand can help to prevent distortion, reducing the propensity to non-radiative decay by this route. In sharp contrast to the high quantum yield of PtL^{5}Cl, *cis*-[Pt(ppy)$_2$] (with two bidentate ligands) exhibits little emission at room temperature. This is due to D_{2d} distortion in the excited state.[93] A tetradentate ligand, made up of two ppy groups, bound by an −NPh linker, and bound with C^N^N^C-coordination to Pt(II), was synthesised by Vezzu *et al.*[94] The increased rigidity afforded by the tetradentate ligand prevents D_{2d} distortion, and the positioning of the carbon atoms *cis* to one another prevents unfavourable *trans* interactions.

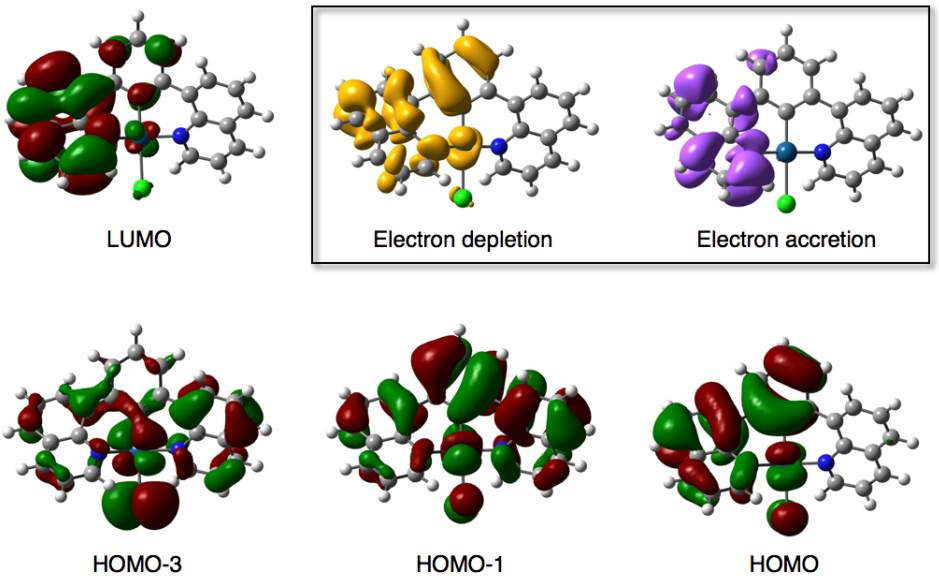

Figure 7.23: Orbital and density difference plots for the $S_0 \rightarrow T_1$ excitation of $PtL^{11}Cl$ at the T_1 geometry.

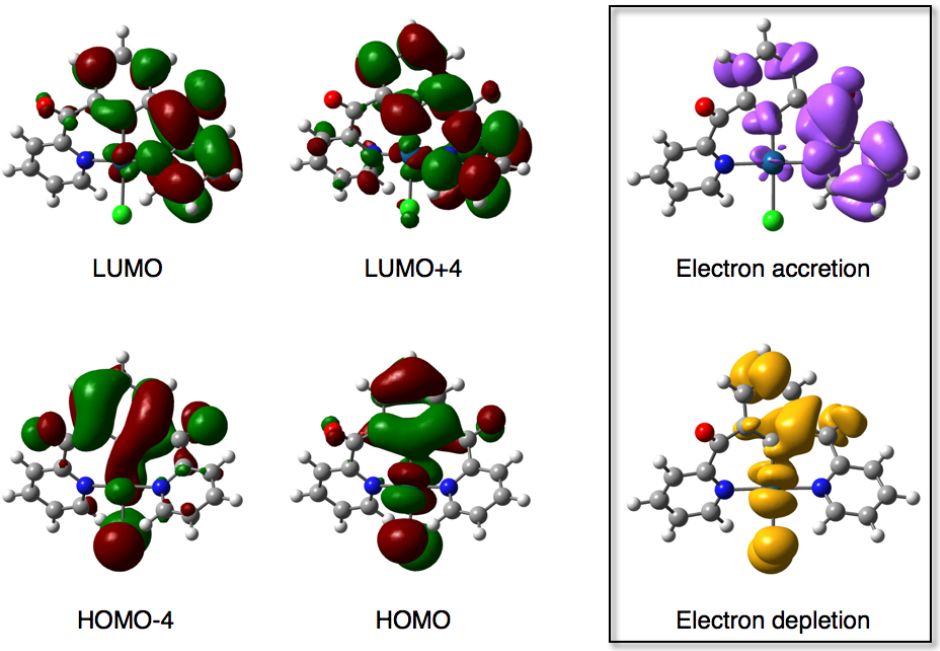

Figure 7.24: Orbital and density difference plots for the $S_0 \rightarrow T_1$ excitation of $PtL^{12}Cl$ at the T_1 geometry.

Transition			Contribution
$PtL^{11}Cl$			
HOMO−3	→	LUMO	−0.117
HOMO−1	→	LUMO	−0.253
HOMO	→	LUMO	0.624
HOMO	←	LUMO	0.133
$PtL^{12}Cl$			
HOMO−4	→	LUMO	−0.235
HOMO	→	LUMO	0.610
HOMO	→	LUMO+4	−0.106

Table 7.4: Dominant orbital contributions for excitation of PtL^{11} and PtL^{12} from S_0 to T_1 at the triplet excited state geometry.

The compound most like *cis*-[Pt(ppy)$_2$] showed highly efficient emission with a quantum yield of 0.74 (in degassed 2-methyltetrahydrofuran at 298 K). The only difference between this complex and *cis*-[Pt(ppy)$_2$] was the linker between the two N^C ligands; the two complexes showed similar excited states in TD-DFT studies. The significant increase in emission can then be attributed to the increased rigidity.

In view of the possible advantages in emission offered by increased rigidity, two tetradentate Pt(II) complexes were made by previous members of the group to investigate their luminescent properties. Both are shown in Figure 7.25; PtL^{13} was found to be highly emissive with a quantum yield of 0.74 in solution at room temperature[257] while PtL^{14} was only emissive at 77 K.[258]

7.7.2 Calculations

Comparison of the ground state and T_1 excited state geometries of the two tetradentate platinum(II) complexes showed that both had very little distortion between the two geometries. The RMSD of PtL^{13} was 0.0211 Å and PtL^{14} was 0.0283 Å, indicating that the increased rigidity of the tetradentate ligand

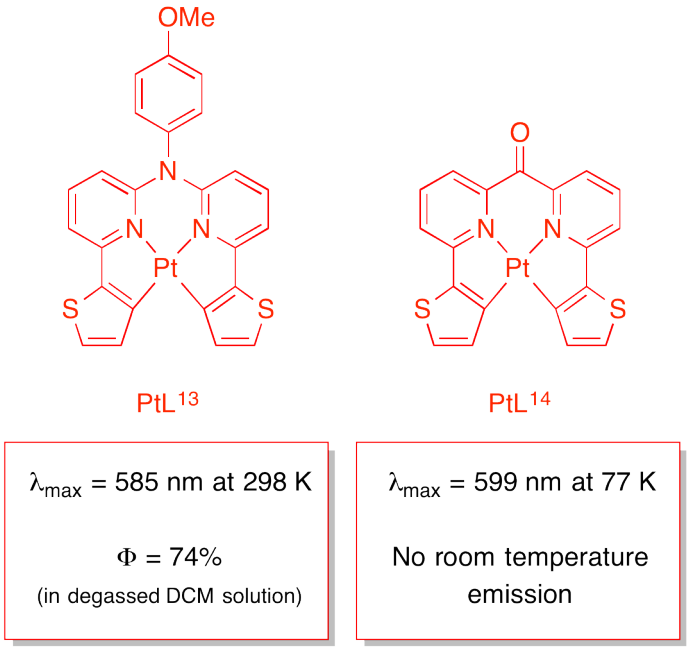

Figure 7.25: The chemical structures of the two complexes with a tetradentate ligand.

did prevent distortion between the ground state and excited state geometries for these two complexes.

For PtL^{13}, the low rate of non-radiative decay, combined with high orbital overlap ($\Lambda = 0.68$) and moderate contribution of the metal to the excited state (Figure 7.26) resulted in a high quantum yield of luminescence (0.74 in degassed DCM solution). This was despite a relatively low energy of emission ($\lambda_{max} = 585$ nm in DCM at 298 K).

In spite of the similarity of the ground state and excited state geometries of PtL^{14} and its structural similarity to PtL^{13}, no room temperature emission was observed. Low temperature emission (at 77 K in EPA glass) from PtL^{14} showed λ_{max} of 599 nm indicating that it emits in the same region of the spectrum as PtL^{13}. This suggests that the effect is not a result of non-radiative decay due to lower energy emission. Comparison of Figures 7.26 and 7.27 alongside the Mulliken charges on platinum for both complexes (Table 7.6) shows that the metal character of the excitation in PtL^{14} is reduced from that

Transition			Contribution
PtL^{13}			
HOMO−1	→	LUMO	−0.142
HOMO	→	LUMO	0.630
HOMO	→	LUMO+1	0.217
HOMO	←	LUMO	0.110
PtL^{14}			
HOMO	→	LUMO	0.693

Table 7.5: Dominant orbital contributions for excitation of PtL^{13} and PtL^{14} from S_0 to T_1 at the triplet excited state geometry.

in PtL^{13}. The Mulliken charges of PtL^{14} are much higher at both the ground and excited states than on PtL^{13}. The orbital overlap is also reduced (Λ = 0.46 for PtL^{14} compared to 0.68 for PtL^{13}). The combination of reduced metal character and lower orbital overlap then points to a reduced rate of radiative decay in PtL^{13} compared to PtL^{14}; this leads to a reduced quantum yield of luminescence.

7.8 Concluding remarks

In this chapter we have seen the importance of both minimising the rate of non-radiative decay and maximising the rate of radiative decay for efficiency of emission and high quantum yields of luminescence. Methods discussed in previous chapters for predicting non-radiative decay through distortion have been applied successfully to a wider variety of platinum(II) complexes. Discussion of orbital overlap (quantified by Λ) and metal character of excitations have provided a route to better predict rates of radiative decay using DFT. While obtaining numerical values which depict geometrical distortion and orbital overlap is relatively straightforward, considering the contribution of the metal atom to the excitation is much more qualitative and a combination of orbital plots and Mulliken charge analysis had to be used. Ideally, future work in this area could focus on deriving a means to obtain a more quantita-

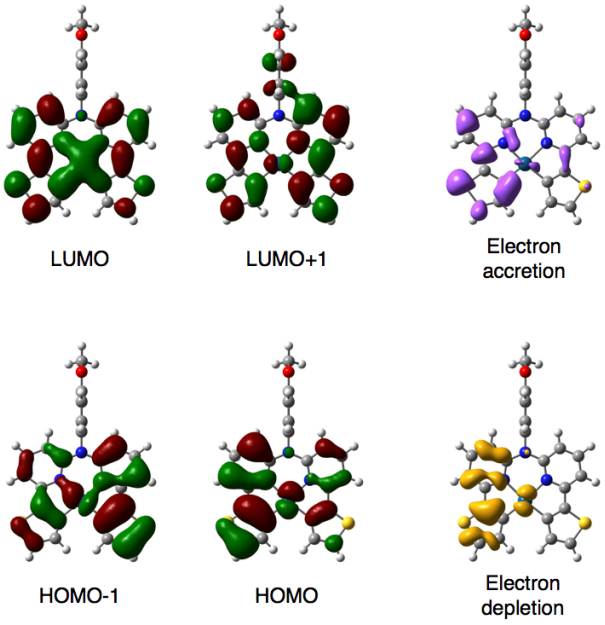

Figure 7.26: Orbital and density difference plots for excitation of PtL[13] from S_0 to T_1 at the triplet geometry.

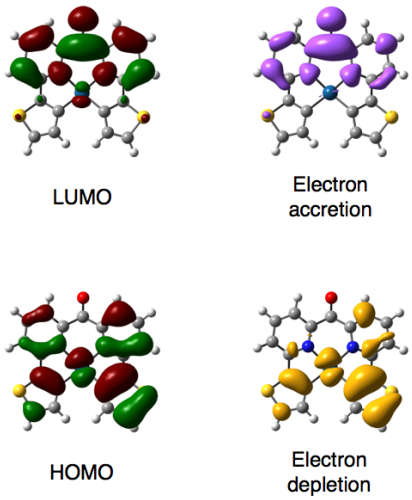

Figure 7.27: Orbital and density difference plots for excitation of PtL[14] from S_0 to T_1 at the triplet geometry.

	S_0 Mulliken charge	T_1 Mulliken charge	Λ	RMSD / Å
PtL^{1}Cl	0.720	0.678	0.63	0.0253
PtL^{2}Cl	0.722	0.674	0.62	0.0236
PtL^{3}Cl	0.708	0.668	0.65	0.0246
PtL^{4}Cl	0.571	0.573	0.58	0.2204
PtLF^{1}Cl	0.657	0.634	0.55	0.2389
PtLF^{2}Cl	0.724	0.696	0.64	0.0232
PtLF^{3}Cl	0.712	0.692	0.65	0.0247
PtLF^{4}Cl	0.571	0.611	0.61	0.2648
[Pt(ppy)(acac)]	0.769	0.736	0.64	0.0261
[Pt(ppy)(hfac)]	0.922	0.898	0.42	0.4185
***trans*-[Pt(ppy)(tfac)]**	0.796	0.779	0.49	0.3101
***cis*-[Pt(ppy)(tfac)]**	0.807	0.790	0.46	0.2496
PtL^{10-cis}Cl	0.631	0.633	0.39	1.5608
PtL$^{10-trans}$Cl	0.628	0.628	0.64	0.2605
PtPhos	0.431	0.456	0.76	2.0603
PtPhosMe	0.392	0.390	0.68	0.0969
PtL^{11}Cl	0.601	0.596	0.60	0.1416
PtL^{12}Cl	0.769	0.721	0.40	0.1528
PtL^{13}Cl	0.943	0.927	0.68	0.0211
PtL^{14}Cl	1.134	1.119	0.46	0.0283

Table 7.6: Values for Mulliken charges on Pt, Λ (to quantify orbital overlap) and distortion (RMSD) for the twenty complexes studied in this chapter. S_0 and T_1 excited state Mulliken charges are for platinum at the T_1 geometry. Λ was calculated using PBE0 in vacuum and, just for PtPhos, 6-31G as a basis set on all atoms except Pt. Root-mean-square displacement between the ground state and T_1 excited state geometries of each of the complexes, calculated by DFT.

tive measure of this value where only the electron concerned in the excitation is considered instead of the overall charge on the metal atom.

8

Experimental

8.1 Materials and equipment

8.1.1 General experimental

All solvents used were Analar quality (with the exception of acetonitrile which was HPLC grade) and were used without further purification. Dry, air-free solvents were obtained by passing through a Pure Solv 400 solvent purification system. Water was purified using the $\text{Purite}_{\text{STILL}}$ Plus^{TM} system and had a conductivity of 0.04 μS cm^{-1}. Unless stated otherwise all reagents were used as supplied from commercial sources. Reactions requiring an inert atmosphere were carried out using Schlenk line techniques under an atmosphere of dry nitrogen.

Thin layer chromatography (TLC) was carried out on silica plates (Merck Art 5554) which were fluorescent upon irradiation at 254 nm. Column chromatography was carried out using silica (Merck Silica Gel 60, 230-400 mesh). HPLC was achieved using an analytical Varian LC-diode array detector, then a semi-prep Varian LC- UV-vis detector. A gradient solvent system of acetonitrile/water was used.

8.1.2 Characterisation techniques

^{1}H NMR spectra were recorded in the indicated solvents on Mercury-400, Varian-200, Varian-500, Varian VNMRS-600 or Huple-VNMRS-700 MHz instruments. ^{13}C spectra were recorded at 126 MHz on the Varian Inova-500 or at 176 MHz on the Huple-VNMRS-700 MHz. Chemical shifts are quoted relative to the appropriate protio-solvent resonances, and all J values are given in Hz. Owing to chemical shift anisotropy, ^{195}Pt$-^{1}$H couplings become poorly resolved at high fields (e.g. 700 MHz) and so in some cases it is not possible to record the corresponding J value.

Low-resolution electrospray mass spectra (ES) were recorded using a Thermo Finnigan LTQ FT mass spectrometer, with methanol or acetonitrile as the carrier solvent. Accurate ES mass spectra were obtained using either a LCT Premier XE mass spectrometer (Waters Ltd, UK) or a LTQ FT mass spectrometer (Thermo-Finnigan Corporation).

C, H and N analysis was achieved using an Exeter Analytical E-440 elemental analyser.

8.1.3 Photophysical characterisation

UV/Vis absorption spectra were measured using a Biotek Instruments UVIKON XS spectrometer operating with LabPower software. The sample was held in a quartz cuvette of 1 cm path length, and spectra were recorded against a reference of pure solvent held in a matched cuvette. Extinction coefficients were determined using a dilution method, and graphical application of the Beer-Lambert law:

$$\mathrm{A} = \varepsilon \, \mathrm{l} \, \mathrm{c} \tag{8.1}$$

A represents absorbance, ε molar absorptivity, l the path length and c the concentration of the sample.

Solution-based emission and excitation spectra were acquired on a Jobin Yvon-

Spex Fluoromax-2 spectrometer. All samples were contained within quartz cuvettes of 1 cm path length. Samples that were to be measured in the absence of air were placed in quartz cuvettes that were modified with appropriate glassware to allow connection to a high vacuum line. To remove air prior to the measurement, the sample was degassed within the cuvette by three freeze-pump-thaw cycles. Emission was recorded at 90° to the excitation source, and appropriate filters were used when required to remove second-order peaks. All emission spectra were corrected after acquisition for dark count and for the spectral response of the detector. Excitation spectra were automatically corrected upon measurement for lamp output, through use of a beam splitter which directs 8% of the excitation light to a reference photodiode.

The quantum yields were determined relative to a reference solution containing $[Ru(bpy)_3]Cl_2$. The quantum yield of this complex is well established in air-equilibrated H_2O to be 0.028.[254] To measure the quantum yield, a sample of complex in DCM was prepared so that the absorbance at the chosen excitation wavelength was below 0.1, to minimise inner-filter effects. A solution containing $[Ru(bpy)_3]Cl_2$ with similar optical density was prepared, and the emission spectra of the complex and reference were measured under identical conditions (i.e. same excitation wavelength, same slit size). The quantum yield was determined from the absorbance and emission data by use of Equation 8.2 (applicable only for solutions of low optical density):

$$\Phi = \Phi_{st} \left[\frac{I}{I_{st}}\right] \left[\frac{OD_{st}}{OD}\right] \left[\frac{n^2}{n_{st}^2}\right] \tag{8.2}$$

Φ represents the quantum yield, I the overall integrated intensity, OD the optical density at the chosen wavelength and n^2 the refractive index of the solvent; the subscript *st* denotes the standard and all other values the sample.

Lifetimes were determined using an Edinburgh Instruments OB 920 fluorimeter. Luminescence lifetimes of the complexes up to approximately 10 μs were measured by time-correlated single-photon counting method, using an EPL-375 pulsed-diode laser as excitation source (374 nm excitation, pulse length of 60 ps). The laser repetition rate was selected so that the pulse period was at least 5-10 times longer than the complex lifetime. The emission was detected

at 90° to the excitation source, after passage through a monochromator, using a Peltier-cooled R928. Lifetimes in excess of 10 μs were measured by multichannel scaling, and a xenon flash lamp was used as the excitation source (excitation wavelength matched to a suitable absorption band of the complex, pulse length of 2 μs).

The lifetimes were obtained by least-squares fitting to a mono-exponential decay and goodness-of-fit was assessed from the residuals. Low temperature (77 K) experiments were performed using a glass vacuum cold finger apparatus built in house. A small amount of sample was dissolved in a 2:2:1 solvent mix of ether/isopentane/ethanol (EPA), and placed into a glass tube. The cold finger was filled with liquid nitrogen and the tube containing the sample was inserted. EPA forms an amorphous glass upon freezing, which has a very low propensity for cracking.

8.1.4 Electrochemistry

Cyclic voltammetry of the complexes was performed with a μAutolab Type III potentiostat using GPES Manager software. Three electrodes were inserted into the sample: a glassy-carbon working electrode, and platinum wire reference and working electrodes. Sample concentrations of ∼1 mM in DCM were used with 0.1 M $[Bu_4N][PF_6]$ as the electrolyte, which was recrystallised and rigorously dried before use. These solutions were purged with nitrogen gas for ten minutes with stirring, then the measurements recorded without stirring. Voltammograms obtained were referenced to the ferrocene-ferrocenium couple ($E_{1/2}$ = 0.42 V vs. SCE).

8.1.5 DFT and TD-DFT calculations

DFT geometry optimisations, frequency, stability and TD-DFT excitation calculations were performed using Gaussian 09.[259] For platinum, the Los-Alamos LANL2DZ effective core potentials (ECPs) were used to treat the core electrons, in combination with the LANL2DZ basis set for the valence electrons.

Basis sets used for other atoms along with choice in functional are indicated in the main body of the text. Frequency calculations were performed at each geometry at the same level of theory as the optimisation to ensure that the geometries do indeed correspond to minima on the potential energy surface. Geometries and orbitals were visualised using Gaussview 5.0; the default contour value of 0.02 au was used for each of them. Densities were also plotted using Gaussview 5.0, where the default contour value of 0.0004 au^2 was used.

Values for Λ and TDA excitation energies were calculated using Dalton 2011 [260] with the indicated basis sets and functionals. TDA geometries were optimised and their frequency calculations performed in Q-Chem 4.0. [261] Coupled cluster calculations were performed by our collaborators using Turbomole v6.5.

8.2 Synthesis of ligands and ligand precursors

Preparation of 2-(tributylstannyl)pyridine

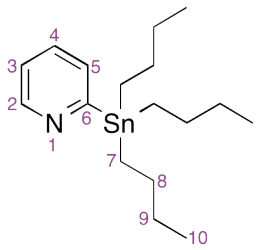

2-Bromopyridine (5.0 g, 31.6 mmol) was placed in a two-necked round bottom flask fitted with a condenser and suba seal. Dry THF (25 mL) was added to the flask under nitrogen and the reaction mixture cooled to −78°C in dry ice. *n*-Butyl lithium (34.8 mmol, 2.5 M in hexane) was added over a period of 20 minutes then the reaction mixture was stirred for a further 90 minutes. Bu_3SnCl (10.29 g, 31.6 mmol) in dry THF (6 mL) was then added under nitrogen over a period of 20 minutes before stirring for a further 90 minutes. The reaction mixture was then allowed to warm to room temperature. Water (30 mL) was added to the mixture and stirred for 10 minutes. The product was

extracted into diethyl ether (5 × 50 mL), dried over Na_2SO_4, filtered and the solvent removed under reduced pressure to give 2-(tributylstannyl)pyridine as a brown oil, 70% pure based on ^{1}H NMR integrals; (ES$^+$) m/z = 366.1 [M + H]$^+$; HRMS (ES$^+$) m/z = 366.1550 [M + H]$^+$; calculated for $[C_{17}H_{32}N^{116}Sn]^+$ 366.1552. Experimental data obtained was in good agreement with the literature.[262]

Preparation of L^5 - Stille method

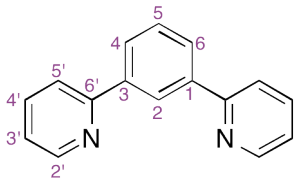

70% pure 2-(tributylstannyl)pyridine (671 mg, 1.27 mmol of compound), 1,3-dibromobenzene (150 mg, 0.64 mmol), bis-(triphenylphosphine)palladium(II) chloride (16.5 mg, 0.014 mmol), lithium chloride (197 mg, 4.65 mmol) and toluene (5 mL) were added to a dry Schlenk tube and degassed using the freeze, pump, thaw method. The mixture was then heated under nitrogen at 150°C for three days. After cooling to room temperature, saturated potassium fluoride solution (1.3 mL) was added and the solution was stirred for 30 minutes. The precipitated solid was removed by filtration and washed with toluene (4 mL). Sodium hydrogen carbonate solution (10%, 7 mL) was added to the combined filtrates, the product extracted into dichloromethane (3 × 15 mL) and dried over magnesium sulfate. The product was filtered, the solvent removed under reduced pressure and the product purified by column chromatography (hexane / diethyl ether gradient, 100 / 0 to 10 / 90 on silica) to give the product as a brown, oily solid (114 mg, 55%); δ H (700 MHz; $CDCl_3$) 8.72 (2 H, ddd, J 1.0, J 1.9 and J 4.8, H$^{2'}$), 8.63 (1 H, td, J 0.6 and J 1.8, H^2), 8.06 (2 H, dd, J 1.8 and J 7.7, H^4 and H^6), 7.85 (2 H, dt, J 1.0 and J 7.9, H$^{5'}$), 7.77 (2 H, td, J 1.8 and J 7.7, H$^{4'}$), 7.59 (1 H, td, J 0.6 and J 7.7, H^5), 7.25 (2 H, m, H$^{3'}$); δ C (700 MHz; $CDCl_3$) 157.2 (C^3), 149.6 (C$^{2'}$), 139.8 (C^3

and C^1), 136.8 ($C^{4'}$), 129.2 (C^5), 127.5 (C^4 and C^6), 125.5 (C^2), 122.2 ($C^{3'}$), 120.7 ($C^{5'}$); (ES^+) m/z = 233.2 $[M + H]^+$; HRMS (ES^+) m/z = 233.1074 $[M + H]^+$; calculated for $[C_{16}H_{13}N_2]^+$ 233.1079. Experimental data obtained was in good agreement with the literature.[262]

Preparation of L^5 - Suzuki-Miyaura method

Benzene-1,3-diboronic acid (150 mg, 0.91 mmol), bromopyridine (286 mg, 1.81 mmol) and sodium carbonate (7.5 mL, 1 M) were added with DME (7.5 mL) to a Schlenk tube and degassed using the freeze, pump, thaw method. The tetrakis(triphenylphosphine) palladium(0) catalyst (52 mg, 0.044 mmol) was then added under a flow of nitrogen and the mixture heated at reflux overnight. Water (5 mL) was then added and the product was extracted into DCM (3×30 mL) before drying over potassium carbonate. The solution was filtered and the solvent removed under reduced pressure before drying on the high vacuum line giving a yellow oil. The product was purified by column chromatography on silica (hexane / ethylacetate gradient, 100 / 0 to 70 / 30) to give the product as a brown oily solid (147 mg, 70%). Experimental data obtained was in good agreement with the literature.[262]

Preparation of L^6

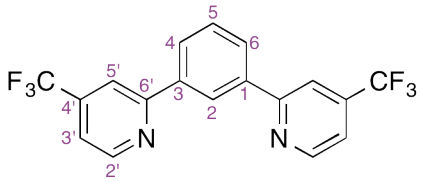

Benzene-1,3-diboronic acid (200 mg, 1.21 mmol), 2-bromo-4-(trifluoromethyl) pyridine (0.39 mL, 3.15 mmol), sodium carbonate (845 mg, 7.97 mmol), methanol (7 mL) and toluene (7 mL) were placed in a Schlenk tube fitted with a magnetic stirrer bar and condenser. The mixture was degassed using

the freeze, pump, thaw method and placed under an atmosphere of nitrogen. The tetrakis(triphenylphosphine) palladium(0) catalyst (92 mg, 0.08 mmol) was then added under a stream of nitrogen and the mixture heated at reflux for 48 hours before cooling to room temperature. The solvent was then removed under reduced pressure and the residue taken up in DCM (30 mL) and water (20 mL) before extraction of the product into DCM (3 × 20 mL). The mixture was dried over magnesium sulfate and filtered. Al_2O_3 (0.9 chromatographic grade) was added, the suspension shaken several times and the alumina removed by filtration to give the crude product. The ligand was then taken up in DCM and flushed through a plug of silica, the solvent removed under reduced pressure and the residue dried on the high vacuum line to give the analytically pure product (106 mg, 24%): δ H (400 MHz; $CDCl_3$) 8.92 (2 H, d, *J* 4.8, $H^{2'}$), 8.73 (1 H, t, *J* 1.6, H^2), 8.14 (2 H, dd, *J* 1.6 and *J* 7.6, H^3 and H^4), 8.04 (2 H, t, *J* 0.8, $H^{5'}$), 7.66 (1 H, t, *J* 8, H^5), 7.50 (2 H, dd, *J* 0.8 and *J* 4.8, $H^{3'}$; (ES^+) *m/z* = 369.0 $[M + H]^+$; HRMS (ES^+) *m/z* = 369.0835 $[M + H]^+$; calculated for $[C_{18}H_{11}N_2F_6]^+$ 369.0826. The experimental data obtained was in good agreement with the literature.[208]

Preparation of L^7

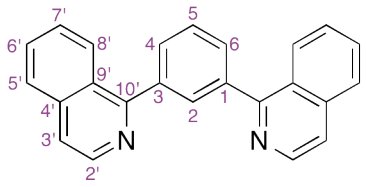

Benzene-1,3-diboronic acid (228 mg, 1.38 mmol) and 1-chloroisoquinoline (445 mg, 2.72 mmol) were placed in a Schlenk tube fitted with a condenser and stirrer bar together with toluene (10 mL), ethanol (10 mL), water (5 mL) and sodium carbonate (806 mg, 7.60 mmol). The mixture was degassed using the freeze, pump, thaw method and placed under an atmosphere of nitrogen. The tetrakis(triphenylphosphine) palladium(0) catalyst (45 mg, 0.04 mmol) was added under a stream of nitrogen and the mixture heated at reflux for

36 hours. After cooling to room temperature, water (9 mL) was added and the product extracted into DCM (3 × 50 mL). The extracts were dried over anhydrous potassium carbonate, filtered and the solvent removed under reduced pressure. The brown solid was recrystallised from acetonitrile to give the analytically pure product as an off-white solid (314 mg, 69%); δ H (400 MHz; $CDCl_3$) 8.62 (2 H, d, J 5.8, $H^{2'}$), 8.19 (2 H, d, J 8.4, $H^{5'}$ or $H^{8'}$), 8.05 (1 H, t, J 1.8, H^{2}), 7.85 (4 H, m, $H^{5'}$ or $H^{8'}$), 7.72 (1 H, t, J 5.0, H^{5}), 7.64 (4 H, m, $H^{6'/7'}$), 7.51 (2 H, m, $H^{4/6}$); (ES^+) m/z = 333.1 $[M + H]^+$; HRMS (ES^+) m/z = 333.1374 $[M + H]^+$; calculated for $[C_{24}H_{17}N_2]$ 333.1392. Analytical data obtained was in good agreement with the literature.[28]

8.2.1 Synthesis of imine ligands

Isophthalaldehyde, the amine and ethanol were added to an oven-dried flask fitted with a magnetic stirrer bar and a reflux condenser. The reactants were heated at reflux under nitrogen for three hours then the solvent was removed under reduced pressure.

Preparation of L^{ImPh}

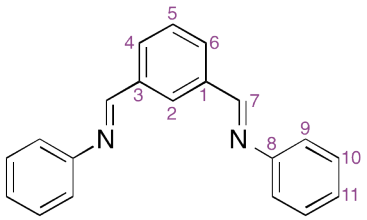

Isophthalaldehyde (500 mg, 3.72 mmol), aniline (800 mg, 8.56 mmol) and ethanol (40 mL) were added to an oven dried flask fitted with a magnetic stirrer bar, a reflux condenser and a calcium chloride drying tube. The reactants were heated at reflux for 45 minutes then the ethanol was removed under reduced pressure. The resulting oil was adsorbed onto silica and passed quickly through a small plug of silica (in 50 mL portions of 25% ethyl acetate

in hexane). After analysis by TLC, fractions containing the desired product were combined and the solvent removed under reduced pressure to give a pale yellow solid. This was recrystallised from ethyl acetate/petroleum ether to give L^{ImPh} as a pale, yellow powder (650 mg, 61%); Found: C, 84.48; H, 5.69; N, 9.96%. $C_{20}H_{16}N_2$ requires C, 84.48; H, 5.67; N, 9.85%; δ H (700 MHz; $CDCl_3$) 8.54 (2 H, s, H^7), 8.41 (1 H, s, H^2), 8.05 (2 H, dd, J 2.0 and J 8.0, H^4 and H^6), 7.59 (1 H, t, J 8.0, H^5), 7.41 (4 H, m, H^9), 7.25 (6 H, m, H^{10} and H^{11}); δ C (700 MHz; $CDCl_3$) 159.5 (C^7), 151.7 (C^8), 136.7 (C^1 and C^3), 131.2 (C^4 and C^6), 129.3 (C^2), 129.2 (C^5), 129.2 (C^9), 126.2 (C^{11}), 120.9 (C^{10}); (ES^+) m/z = 285.4 $[M + H]^+$; HRMS (ES^+) m/z = 285.1398 $[M + H]^+$; calculated for $[C_{20}H_{17}N_2]^+$ 285.1392. Analytical data obtained was in good agreement with the literature.[212]

Preparation of $L^{ImPhOMe}$

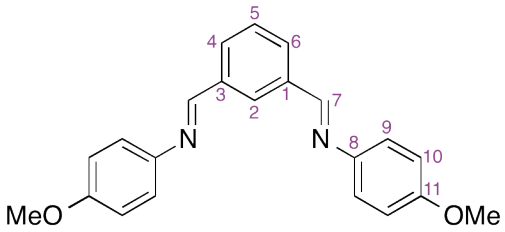

Isophthalaldehyde (500 mg, 3.73 mmol), *p*-anisidine (919 mg, 7.46 mmol) and ethanol (25 mL). Recrystallisation from ethanol gave the product as a pale yellow solid (580 mg, 45%); Found: C, 76.71; H, 5.79; N, 8.01. $C_{22}H_{20}N_2O_2$ requires C, 76.72, H, 5.85, N, 8.13%; δ H (600 MHz; $CDCl_3$) 8.56 (2H, s, H^7), 8.37 (1H, s, H^2), 8.00 (2H, dd, J 1.8 and J 7.8, H^4 and H^6), 7.56 (1H, t, J 7.8, H^5), 7.27 (4H, m, H^{10}), 6.95 (4H, m, H^6), 3.84 (6H, s, CH_3); δ C (500 MHz; $CDCl_3$) 158.71 (C^{11}), 157.74 (C^7), 144.82 (C^8), 137.27 (C^1 and C^3), 130.90 (C^4 and ^{6}), 129.39 (C^5), 129.16 (C^2), 122.49 (C^{10}), 114.66 (C^9), 55.72 (CH_3); (ES^+) m/z = 345.3 $[M + H]^+$; HRMS (ES^+) m/z = 345.1614 calculated for $[C_{22}H_{21}N_2O_2]^+$ 345.1603.

Preparation of L^{ImCF_3}

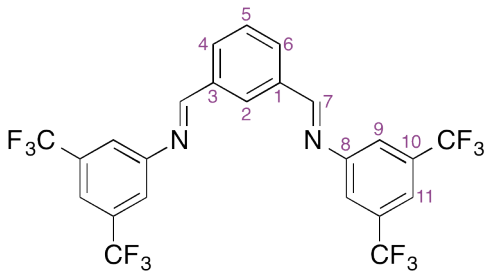

Isophthalaldehyde (200 mg, 1.49 mmol), 3,5-bis(trifluoromethyl) aniline (0.6 mL, 3.84 mmol) and ethanol (5 mL). The product was a white powder (0.80 g, 97%); Found: C, 51.73; H, 2.15; N 4.96. $C_{23}H_{12}F_{12}N_2$ requires C, 51.81; H, 2.17; N, 5.04%; ν_{max}/ cm^{-1} 1640 (N=C); δ H (500 MHz; $CDCl_3$) 8.58 (2H, s, H^7), 8.51 (1H, t, *J* 1.7, H^2), 8.12 (2H, dd, *J* 1.7 and *J* 7.7, H^4 and H^6), 7.77 (2H, s, H^{11}), 7.68 (1H, t, *J* 7.7, H^5), 7.65 (4H, s, H^9); δ C (500 MHz; $CDCl_3$) 161.8 (C^7), 152.8 (C^8), 136.0 (C^1 and C^3), 132.6 (q, *J* 133.1, CF_3), 132.5 (C^4 and C^6), 129.7 (C^2), 129.6 (C^5), 123.1 (d, *J* 272.9, C^{10}), 121.0 (m, C^9), 119.5 (m, C^{11}); δ F (400 MHz; $CDCl_3$) −63.31; (ES$^+$) *m/z* = 557.2 [M + H]$^+$; HRMS (ES$^+$) *m/z* = 557.0845 [M + H]$^+$; calculated for $[C_{24}H_{13}N_2F_{12}]^+$ 557.0887.

Preparation of L^{ImCy}

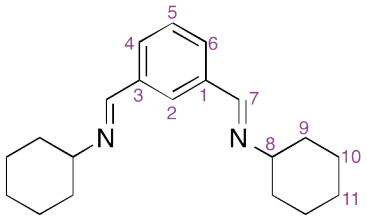

Isophthalaldehyde (500 mg, 3.73 mmol), cyclohexylamine (721 mg, 7.27 mmol) and ethanol (26 mL). The crude solid was washed twice with hexane

to give L^{ImCy} as a white, oily solid (1.02 g, 92%); ν_{max}/ cm^{-1} 1644 (N=C); δ H (700 MHz; $CDCl_3$) 8.34 (2 H, s, H^7), 8.03 (1 H, s, H^2), 7.77 (2 H, dd, J 1.5 and J 8.0, H^4 and H^6), 7.42 (1 H, t, J 8.0, H^5), 3.20 (1 H, m, H^8), 1.83 and 1.36 (8 H, m, H^{10}), 1.73 and 1.58 (8 H, m, H^9), 1.68 and 1.26 (4 H, m, H^{11}); δ C (700 MHz; $CDCl_3$) 158.2 (C^7), 137.0 (C^1 and C^3), 129.7 (C^4 and C^6), 128.7 (C^5), 127.57 (C^2), 65.9 (C^8), 34.3 (C^9), 25.6 (C^{11}), 24.8 (C^{10}); (ES^+) m/z = 297.0 $[M + H]^+$; HRMS (ES^+) m/z = 297.2345 $[M + H]^+$; calculated for $[C_{20}H_{29}N_2]^+$ 297.2331.

Preparation of L^{Im^nBu}

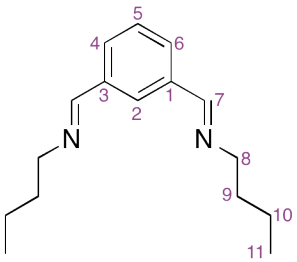

Isophthalaldehyde (200 mg, 1.49 mmol), n-butylamine (1 mL, 10 mmol) and ethanol (5 mL) were added to a 50 mL, oven dried flask fitted with a magnetic stirrer bar. In this instance, the flask was flushed with nitrogen, sealed and heated at reflux for three hours. The solvent and excess amine were removed under reduced pressure to give L^{Im^nBu} as a colourless oil (370 mg, 100%); ν_{max}/ cm^{-1} 1645 (N=C); δ H (500 MHz; $CDCl_3$) 8.30 (2 H, s , H^7), 8.03 (1 H, s , H^2), 7.79 (2 H, dd, J 1.5 and J 7.5, H^4 and H^6), 7.44 (1 H, t, J 7.5, H^5), 3.62 (4 H, td, J 1.5 and J 2.0, H^8), 1.69 (4 H, m, H^9), 1.40 (4 H, m, H^{10}), 0.96 (6 H, t, J 7.5, H^{11}); δ C (500 MHz; $CDCl_3$) 160.5 (C^7), 137.0 (C^1 and C^3), 129.9 (C^4 and C^6), 129.1 (C^5), 128.2 (C^2), 61.7 (C^8), 33.2 (C^9), 20.7 (C^{10}), 14.1 (C^{11}); (ES^+) m/z = 245.4 $[M + H]^+$; HRMS (ES^+) m/z = 245.2012 $[M + H]^+$; calculated for $[C_{16}H_{25}N_2]^+$ 245.2012.

Preparation of L^{Im^tBu}

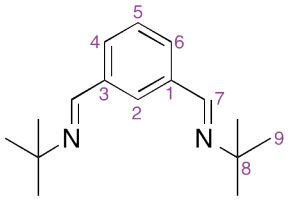

Isophthalaldehyde (200 mg, 1.49 mmol), *tert*-butylamine (0.5 mL, 5 mmol) and ethanol (5 mL) were added to a 50 mL oven dried flask fitted with a magnetic stirrer bar. The flask was flushed with nitrogen, sealed and heated at reflux for three hours. The solvent and excess amine were removed under reduced pressure to give L^{Im^tBu} as a white powder (366 mg, 100%); Found C, 77.95, H, 9.77, N, 11.30. $C_{16}H_{24}N_2$ requires C, 78.14, H, 9.90; N, 11.46%; ν_{max}/ cm^{-1} 1682 (N=C); δ H (500 MHz; $CDCl_3$) 8.33 (2 H, s, H^7), 8.07 (1 H, t, *J* 1.5, H^2), 7.80 (2 H, dd, *J* 1.5 and *J* 7.5, H^4 and H^6), 7.44 (1 H, t, *J* 7.5, H^5), 1.30 (18 H, s, H^9); δ C (500 MHz; $CDCl_3$) 155.3 (C^7), 137.7 (C^1 and C^3), 129.6 (C^4 and C^6), 129.0 (C^2), 128.0 (C^5), 57.6 (C^8), 30.0 (C^9); (ES^+) *m/z* = 245.3 $[M + H]^+$; HRMS (ES^+) *m/z* = 245.2018 $[M + H]^+$; calculated for $[C_{16}H_{25}N_2]^+$ 245.2018. Analytical data obtained was in good agreement with the literature.[212]

8.2.2 Synthesis of ketimine ligands

1,3-Diacetylbenzene, the amine and toluene were placed in an oven dried, round bottomed flask fitted with a magnetic stirrer bar and reflux condenser. Activated 4 Å molecular sieves were added to the flask (1.25 g) and the reactants were heated at reflux, under nitrogen for 48 hours. Half way through this time period a further 1.25 g of molecular sieves were added. The molecular sieves were then removed from the reaction mixture by filtration and were washed with toluene (2 × 2 mL). The washings were combined with the filtrate and the solvent (along with any excess amine) removed under reduced

pressure.

Preparation of L^{KetPh}

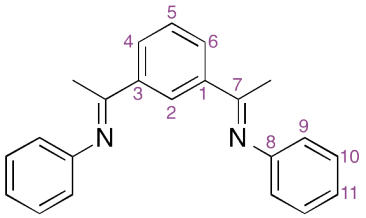

1,3-Diacetylbenzene (100 mg, 0.62 mmol), aniline (287 mg, 3.08 mmol) and toluene (5 mL) to give a yellow solid. The crude product was washed with cold hexane (2×1 mL) to give L^{KetPh} as a pale, yellow powder (169 mg, 87%); Found C, 83.23; H, 6.43; N, 8.57. $C_{22}H_{20}N_2$ requires C, 84.58; H, 6.45; N, 8.97%; ν_{max}/ cm^{-1} 1685 (N=C); δ H (500 MHz; $CDCl_3$) 8.57 (1 H, dt, J 1.5 and J 15, H^5), 8.07 (2 H, m, H^4 and H^6), 7.55 (1 H, m, H^2), 7.37 (4 H, m, H^9), 7.13 (6 H, m, H^{10} and H^{11}), 2.68 (6 H, s, CH_3); δ C (500 MHz; $CDCl_3$) 129.6, 129.3, 129.0, 123.7, 119.7, 115.5, 81.8, 27.1, 17.9; (ES^+) m/z = 313.2 $[M + H]^+$; HRMS (ES^+) m/z = 313.1706 $[M + H]^+$; calculated for $[C_{22}H_{21}N_2]^+$ 313.1705.

Preparation of L^{KetCy}

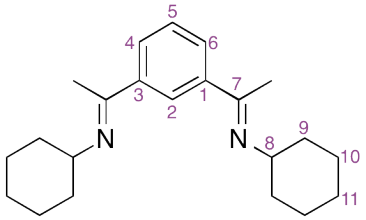

1,3-Diacetylbenzene (500 mg, 3.08 mmol), cyclohexylamine (611 g, 6.16 mmol) and toluene (15 mL). The crude product was washed with cold hexane

(6 × 1 mL) to give L^{KetCy} as a colourless, crystalline solid (480 mg, 48%); Found: C, 80.22; H, 9.66; N, 8.05. $C_{22}H_{32}N_2$ requires C, 81.43; H, 9.94; N, 8.63%; ν_{max}/ cm^{-1} 1682 (N=C); δ H (700 MHz; $CDCl_3$) 8.04 (1 H, t, *J* 2.0, H^2), 7.72 (2 H, dd, *J* 1.5 and *J* 7.5, H^4 and H^6), 7.34 (1 H, t, *J* 7.5, H^5), 3.47 (2 H, m, H^8), 2.26 (6 H, t, *J* 7.0, CH_3), 1.83 and 1.38 (8 H, m, H^{10}), 1.68 and 1.55 (8 H, m, H^9), 1.28 (4 H, m, H^{11}); δ C (700 MHz; $CDCl_3$) 162.9 (C^7), 142.3 (C^1 and C^3), 128.2 (C^2), 127.7 (C^4 and C^6), 125.3 (C^5), 60.3 (C^8), 33.8 (C^9), 26.0 (C^{11}), 25.2 (C^{10}), 15.7 (CH_3); (ES^+) *m/z* = 325.4 $[M + H]^+$; HRMS (ES^+) *m/z* = 325.2641 $[M + H]^+$; calculated for $[C_{22}H_{33}N_2]^+$ 325.2644.

Preparation of L^{Ket^nBu}

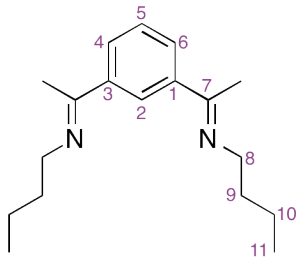

1,3-Diacetylbenzene (200 mg, 1.23 mmol), *n*-butylamine (0.5 mL, 5 mmol) and toluene (5 mL) the flask was sealed, flushed with nitrogen and no reflux condenser used in this instance to give L^{Ket^nBu} as a light brown oil (252 mg, 75%); ν_{max}/ cm^{-1} 1684 (N=C); δ H (500 MHz; $CDCl_3$) 8.10 (1 H, t, *J* 1.5, H^2), 7.76 (2 H, dd, *J* 2.0 and *J* 8.0, H^4 and H^6), 7.36 (1 H, t, *J* 7.5, H^5), 3.48 (4 H, t, *J* 7.5, H^8), 2.25 (6 H, s, CH_3), 1.73 (4 H, m, *J* 7.5, H^9), 1.46 (4 H, m, *J* 7.5, H^{10}), 0.97 (6 H, t, *J* 7.0, H^{11}); δ C (500 MHz; $CDCl_3$) 165.1 (C^7), 141.8 (C^1 and C^3), 128.3 (C^2), 127.7 (C^4 and C^6), 125.1 (C^5), 52.3 (C^8), 33.3 (C^9), 21.1 (C^{10}), 15.9 (CH_3), 14.3 (C^{11}); (ES^+) *m/z* = 273.3 $[M + H]^+$; HRMS (ES^+) *m/z* = 273.2331 $[M + H]^+$; calculated for $[C_{18}H_{29}N_2]^+$ 273.2331.

8.2.3 Synthesis of oxime ligands

Isophthalaldehyde, the amine hydrochloride salt, sodium acetate and dichloromethane were added to a flask fitted with a magnetic stirrer bar and stirred at room temperature for 20 hours. The reaction mixture was then quenched with water (10 mL) and stirred for a further hour. The crude product was extracted into dichloromethane (3 × 10 mL), dried over magnesium sulfate, filtered and the solvent removed under reduced pressure. The product was purified by column chromatography on silica with dichloromethane.

Preparation of L^{OxImOH}

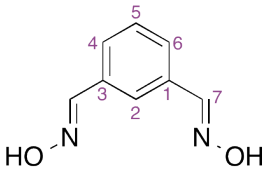

Isophthalaldehyde (300 mg, 2.24 mmol), hydroxylamine hydrochloride (228 mg, 3.28 mmol), sodium acetate (606 mg, 7.39 mmol) and DCM (15 mL) were placed in a clean, dry Schlenk tube which was flushed with nitrogen then stoppered and stirred at room temperature for 24 h. Water (30 mL) was then added and the suspension stirred for a further 90 min. The DCM was then removed under reduced pressure and the product extracted into ethylacetate (5 × 40 mL). The solvent was then removed under reduced pressure and the product dried on the high vacuum line to give the product as a white powder (148 mg, 55%); $\nu_{\max}$/ cm^{-1} 1694 (N=C); δ H (400 MHz; $CO(CD_3)_2$) 8.04 (2 H, s, H^7), 7.75 (1 H, t, J 1.5, H^2), 7.50 (2 H, dd, J 1.5 and J 7.5, H^4 and H^6), 7.29 (1 H, t, J 7.5, H^5), 2.79 (2 H, s, OH); (ES $^-$) m/z = 163.2 $[M\text{-}H]^-$; HRMS (ES$^-$) m/z = 163.0513 $[M - H]^-$; calculated for $[C_8H_7N_2O_2]^-$ 163.058.

Preparation of L^{OxIm}

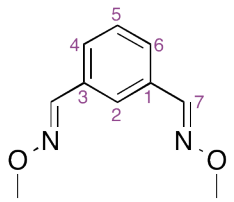

Isophthalaldehyde (100 mg, 0.75 mmol), methoxyamine hydrochloride (108 mg, 1.6 mmol), sodium acetate (202 mg, 2.5 mmol) and DCM (6 mL) to give the product as a clear oil (12 mg, 22%); δ H (700 MHz; $CDCl_3$) 8.06 (2 H, s, H^7), 7.77 (1H, t, *J* 1.7, H^2), 7.59 (2 H, dd, *J* 1.7 and *J* 7.8, H^4 and H^6), 7.38 (1 H, t, *J* 7.7, H^5), 3.99 (6 H, s, CH_3); δ C (700 MHz; $CDCl_3$) 147.9 (C^7), 132.7 (C^3 and C^1), 129.0 (C^5), 128.1 (C^4 and C^6), 125.5 (C^2), 62.1 (CH_3); (ES^+) *m/z* = 193.2 $[M + H]^+$; HRMS (ES^+) *m/z* = 193.0987 $[M + H]^+$; calculated for $[C_{10}H_{13}N_2O_2]^+$ 193.0977.

Preparation of L^{OxKet}

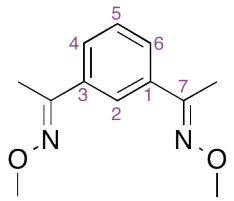

1,3-Diacetylbenzene (100 mg, 0.62 mmol), methoxyamine hydrochloride (103 mg, 1.2 mmol), sodium acetate (202 mg, 2.5 mmol) and acetonitrile (5 mL) were added to a clean, dry Schlenk tube and heated at reflux for 2 h. The solvent was then removed under reduced pressure and the product taken up in water (10 mL) and DCM (25 mL). The product was extracted into DCM (3 × 25 mL), dried over magnesium sulfate, filtered and the solvent removed under reduced pressure to give the product in a mixture of three isomers as

a cloudy white oil (121 mg, 89%); δ H (700 MHz; $CDCl_3$) 7.89 (1H, t, J 1.9, H^2), 7.64 (2H, dd, J 1.8 and J 7.8, H^4 and H^6), 7.36 (1H, t, J 7.8, H^5), 4.01 (6H, s, OCH_3), 2.24 (6H, s, CH_3); δ C (700 MHz; $CDCl_3$) 154.7 (C^3 and C^1), 137.2 (C^7), 128.8 (C^5), 127.0 (C^4 and C^6), 124.1 (C^2), 62.3 (OCH_3), 13.1 (CH_3); (ES^+) m/z = 221.2 $[M + H]^+$; HRMS (ES^+) m/z = 221.1298 $[M + H]^+$; calculated for $[C_{12}H_{17}N_2O_2]^+$ 221.1290.

Preparation of L^{OxImBn}

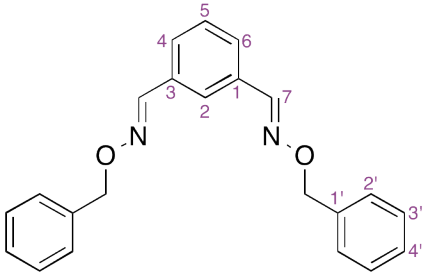

Isophthalaldehyde (100 mg, 0.74 mmol), *O*-benzylhydroxylamine hydrochloride (207 mg, 1.68 mmol), sodium acetate (202 mg, 2.46 mmol) and dichloro methane (6 mL). The product was purified by column chromatography on silica with dichloromethane. The desired isomer (*EE*) was retrieved from the column first (then the others later). Removal of solvent under reduced pressure gave a white oil (71 mg, 28%); δ H (700 MHz; $CDCl_3$) 8.14 (1 H, s, H^7), 7.76 (1 H, s, H^2), 7.59 (2 H, dd, J 1.5 and J 7.5, H^4 and H^6), 7.42 (4 H, d, J 7.5, $H^{2'}$), 7.37 (4 H, t, J 7.5, $H^{3'}$), 7.32 (2 H, t, J 7.0, $H^{4'}$), 5.23 (4 H, s, CH_2); δ C (500 MHz; $CDCl_3$) 148.4 (C^7), 137.4 ($C^{1'}$), 132.8 (C^1 and C^3), 129.0 (C^5), 128.5 ($C^{3'}$), 128.4 ($C^{2'}$), 128.2 (C^4 and C^6), 128.0 ($C^{4'}$), 125.7 (C^2), 76.5 (CH_2); (ES^+) m/z = 345.3 $[M + H]^+$, m/z = 367.3 $[M + Na]^+$; HRMS (ES^+) m/z = 345.1614 $[M + H]^+$; calculated for $[C_{22}H_{21}N_2O_2]^+$ 345.1603.

8.3 Synthesis of Pt(II) complexes

8.3.1 Synthesis of Pt(II) complexes of heterocyclic ligands

Potassium tetrachloroplatinate, acetic acid and the chosen ligand were placed in a Schlenk tube fitted with a magnetic stirrer bar and condenser. The suspension was degassed using the freeze, pump, thaw method and heated at reflux, under an atmosphere of nitrogen for 60 hours. The mixture was then cooled to room temperature and the acetic acid removed by centrifugation to give the crude product.

Preparation of PtL^5Cl

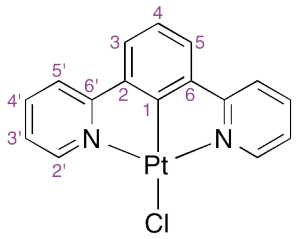

1,3-Dipyridylbenzene (70 mg, 0.30 mmol), potassium tetrachloroplatinate (147 mg, 0.35 mmol) and acetic acid (9 mL) were placed in a clean, dry Schlenk tube fitted with a condenser and magnetic stirrer bar and degassed using the freeze, pump, thaw method. The mixture was then heated at reflux for 60 hours under nitrogen before cooling to room temperature. The crude, solid product was removed from the solvent by separation on the centrifuge then washed first with water (4 mL), then methanol (4 mL) and finally diethyl ether (4 mL). The product was then extracted into DCM and the solvent removed under reduced pressure to give PtL^5Cl as a yellow solid (70 mg, 51%); δ H (700 MHz; $CDCl_3$) 9.34 (2 H, m with coupling to ^{195}Pt, $H^{2'}$), 7.94 (2 H, td, J 1.6 and J 7.6, $H^{4'}$), 7.68 (2 H, m, $H^{5'}$), 7.44 (2 H, d, J 7.7, H^3 and H^5), 7.28 (2 H, ddd, J 1.4, J 5.6 and J 7.3, $H^{3'}$), 7.21 (1 H, t, J 7.6, H^4); δ C (700 MHz; $CDCl_3$) 167.3 ($C^{2'}$), 161.8 (C^1), 152.2 ($C^{4'}$), 140.9 (C^2 and C^6), 139.1

($C^{6'}$), 124.1 (C^3 and C^5), 123.1 ($C^{3'}$), 122.9 (C^4), 119.2 ($C^{5'}$); (ES^+) m/z = 426.0 $[M - Cl]^+$; HRMS (AP^+) m/z = 425.0547 $[M - Cl]^+$; calculated for $[C_{16}H_{11}N_2{}^{194}Pt]^+$ 425.0549. Experimental data obtained was in good agreement with the literature.[262]

8.3.2 Synthesis of Pt(II) complexes of heterocyclic ligands by microwave irradiation

The platinum salt, ligand, acetic acid and water were placed in a microwave vial fitted with a magnetic stirrer bar and the vial sealed. The vessel was degassed through a syringe needle, using the freeze, pump, thaw method and placed under an atmosphere of nitrogen. The suspension was heated at 160°C for 30 minutes fixed hold time before cooling to room temperature. The solvent was removed by centrifugation to give the crude product.

Preparation of PtL^5Cl

1,3-Dipyridylbenzene (109 mg, 0.47 mmol), potassium tetrachloroplatinate (200 mg, 0.48 mmol), acetic acid (1.2 mL) and water (0.3 mL). The crude product was washed with water (5 mL), then methanol (5 mL), then diethyl ether (5 mL) before extraction into DCM. The solvent was removed under reduced pressure and the complex dried on the high vacuum line to give the analytically pure product (197 mg, 91%). Experimental data obtained was in good agreement with the literature.[262]

Preparation of PtL^5Br

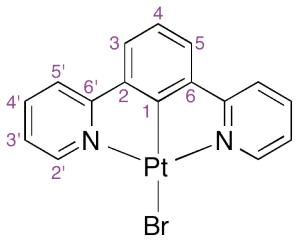

1,3-Dipyridylbenzene (29 mg, 0.12 mmol), potassium tetrabromoplatinate (75 mg, 0.13 mmol), acetic acid (0.9 mL) and water (0.1 mL). The crude product was washed with water (3 mL), then methanol (3 mL) and finally ether (3 mL). The complex was extracted into DCM and the solvent removed under reduced pressure to give the analytically pure product (35 mg, 58%); δ H (400 MHz; $CDCl_3$) 9.56 (2H, ddd with coupling to ^{195}Pt, J 0.8, J 1.6 and J 5.7, $H^{2'}$), 7.93 (2H, ddd, J 1.6, J 7.6 and J 8.1, $H^{4'}$), 7.69 (2H, ddd with coupling to ^{195}Pt, J 0.8, J 1.5 and J 8.0, $H^{5'}$), 7.45 (2H, d with coupling to ^{195}Pt, J 7.6, H^3 and H^5), 7.27 (3H, m, H^4 and $H^{3'}$); (ASAP$^+$) m/z = 506.0 $[M]^+$.

Preparation of PtL^6Cl

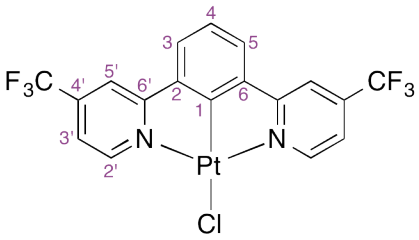

L^6 (86 mg, 0.23 mmol), potassium tetrachloroplatinate (100 mg, 0.24 mmol), acetic acid (2.7 mL) and water (0.3 mL). The crude product was washed with methanol (3×5 mL), water (3×5 mL), ethanol (3×5 mL) then ether (3×5 mL) before drying on the high vacuum line to give the analytically pure product as an orange solid (125 mg, 91%); δ H (700 MHz; $CDCl_3$) 9.53

(2H, d with coupling to Pt, $H^{2'}$), 7.87 (2H, s, $H^{5'}$), 7.59 (2H, d, J 7.7, H^3 and H^5), 7.51 (2H, dd, J 1.8 and J 5.9, $H^{3'}$), 7.33 (1H, t, J 7.7, H^4); δ C (700 MHz; $CDCl_3$) 168.6 ($C^{6'}$), 163.5 (C^1), 153.3 ($C^{2'}$), 141.1 (d, J 34.9, $C^{4'}$), 139.9 (C^2 and C^6), 125.5 (C^3 and C^5), 123.5 (C^4), 122.2 (d, J 273.9, CF_3), 119.3 ($C^{3'}$), 115.4 ($C^{5'}$); δ F (600 MHz; $CDCl_3$) −65.1 (CF_3); (ASAP$^+$) $m/z = 562.0$ $[M - Cl]^+$; HRMS (AP$^+$) $m/z = 602.0533$ calculated for $[C_{20}H_{12}N_3F_6{}^{194}Pt]^+$ 602.0562

Preparation of PtL^7Cl

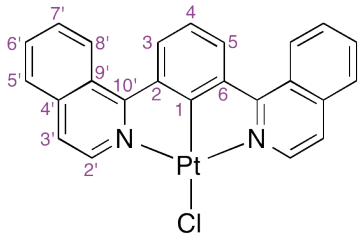

General procedure E was followed: 1-[3-(isoquinolin-1-yl)phenyl]isoquinoline (97 mg, 0.29 mmol), potassium tetrachloroplatinate (134 mg, 0.32 mmol), acetic acid (1.35 mL) and water (0.15 mL). The crude product was washed with methanol (3 × 3 mL), water (3 × 3 mL), ethanol (3 × 3 mL) and ether (3 × 3 mL), then extracted into DCM. The solvent was removed under reduced pressure and the compound dried on the high vacuum line to give the analytically pure product (73 mg, 45 %); δ H (400 MHz; $CDCl_3$) 9.51 (2H, d, J 6.4, $H^{2'}$), 8.97 (2 H, d, J 8.8, $H^{5'}$ or $H^{8'}$), 8.28 (2H, d, J 8, $H^{3/5}$), 7.94 (2 H, d, J 8, $H^{5'}$ or $H^{8'}$), 7.84 (2 H, m, $H^{6'}$ or $H^{7'}$), 7.76 (2 H, m, $H^{6'}$ or $H^{7'}$), 7.67 (2 H, d, J 6.3, H^3), 7.43 (1 H, t, J 7.8, H^4); (ASAP$^+$) $m/z = 560.1$ $[M]^+$; HRMS (AP$^+$) $m/z = 560.0544$ $[M]^+$; calculated for $[C_{24}H_{15}N_2Cl^{194}Pt]^+$ 560.0551.

8.3.3 Synthesis of Pt(II) complexes of imine ligands

Potassium tetrachloroplatinate, acetic acid and acetic anhydride were placed in a dry Schlenk fitted with a magnetic stirrer bar and condenser. The suspen-

sion was degassed using the freeze, pump, thaw method and heated at 80°C for 40 minutes under nitrogen. The mixture was then allowed to cool to room temperature and the ligand added before being degassed again. The suspension was heated at reflux for 60 hours under nitrogen before being allowed to cool to room temperature. The solvent was removed under reduced pressure, the resulting solid taken up in DCM and flushed through a small plug of silica.

Preparation of $PtL^{ImCy}Cl$

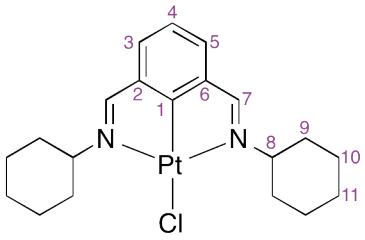

Potassium tetrachloroplatinate (50 mg, 0.12 mmol), acetic acid (3 mL), acetic anhydride (0.1 mL), L^{ImCy} (180 mg, 0.61 mmol). The isolated orange solid was washed with hexane (9 × 2.5 mL) to give the product as an orange solid (37.8 mg, 60%); δ H (700 MHz; $CDCl_3$) 8.31 (2 H, s with coupling to ^{195}Pt, J 74, H^7), 7.39 (2 H, d, J 7.6, H^3 and H^5), 7.09 (1 H, t, J 7.6, H^4), 4.15 (2 H, tdd, J 2.0, J 5.5 and J 11.8, H^8), 2.18 (4 H, d, J 11.7, $H^9{}_{eq}$), 1.86 (4 H, m, $H^{10}{}_{eq}$), 1.70 (6 H, m, $H^9{}_{ax}$ and $H^{11}{}_{eq}$), 1.46 (4 H, qt, J 3.6 and J 13.3, $H^{10}{}_{ax}$), 1.24 (2 H, qt, J 3.8 and J 13.2, $H^{11}{}_{ax}$); δ C (700 MHz; $CDCl_3$) 173.3 (C^1), 172.3 (C^7), 141.9 (C^2 and C^6), 126.2 (C^3 and C^5), 122.3 (C^4), 67.8 (C^8), 33.2 (C^9), 25.4 (C^{11}), 25.3 (C^{10}); (ES$^+$) m/z = 490.1 $[M - Cl]^+$; HRMS (ES$^+$) m/z = 489.1812 $[M - Cl]^+$; calculated for $[C_{20}H_{27}N_2{}^{194}Pt]^+$ 489.1801. Analytical data obtained was in good agreement with the literature.[212]

Preparation of $PtL^{Im^nBu}Cl$

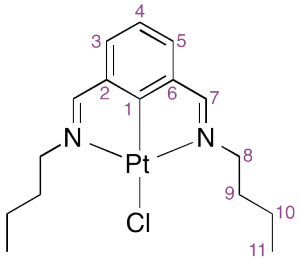

Potassium tetrachloroplatinate (50 mg, 0.12 mmol), acetic acid (3 mL), acetic anhydride (0.1 mL), L^{Im^nBu} (117 mg, 0.48 mmol). The isolated orange solid was purified by HPLC to give the product as an orange solid (16 mg, 28%); δ H (700 MHz; $CDCl_3$) 8.26 (2 H, s with coupling to Pt J 77, H^7), 7.41 (2 H d with coupling to Pt J 7 and J 7, H^3 and H^5), 7.10 (1 H, t, J 7.6, H^4), 4.01 (4 H, m, J 7, H^8), 1.93 (4 H, p, J 7, H^9), 1.38 (4 H, m, J 4, H^{10}), 0.95 (6 H, t, J 7.4, H^{11}); δ C (700 MHz; $CDCl_3$) 175.3 (C^7), 141.4 (C^6 and C^2), 126.1 (C^3 and C^5), 122.3 (C^4), 61.1 (C^8), 32.5 (C^9), 19.7 (C^{10}), 13.7 (C^{11}); (ES^+) m/z = 466.37 $[M - Cl]^+$; HRMS (AP^+) m/z = 437.1483 $[M - Cl]^+$; calculated for $[C_{16}H_{23}N_2{}^{194}Pt]^+$ 437.1488. Analytical data obtained was in good agreement with the literature.[212]

Preparation of $PtL^{Im^tBu}Cl$

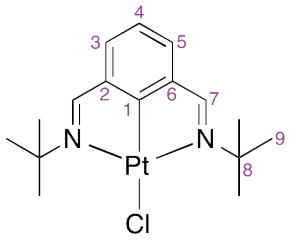

Potassium tetrachloroplatinate (50 mg, 0.12 mmol), acetic acid (3 mL), acetic anhydride (0.1 mL), L^{Im^tBu} (117 mg, 0.48 mmol). The isolated orange

solid was recrystallised from DCM/diethyl ether to give the product as an orange solid (18 mg, 32%); δ H (700 MHz; $CDCl_3$) 8.26 (2 H, s with coupling to Pt, J 76, H^7), 7.38 (2 H, d, J 7.6, H^3 and H^5), 7.13 (1 H, t, J 7.6, H^4), 1.71 (18 H, s, H^9); δ C (700 MHz; $CDCl_3$) 171.9 (C^7), 170.8 (C^8), 142.7 (C^2 and C^6), 127.4 (C^3 and C^5), 122.8 (C^4), 65.9 (C^1), 30.1 (C^9); (ES^+) m/z = 466.34 $[M - Cl]^+$; HRMS (AP^+) m/z = 437.1488 $[M - Cl]^+$; calculated for $[C_{16}H_{23}N_2{}^{194}Pt]^+$ 437.1488. Analytical data obtained was in good agreement with the literature.[212]

Preparation of $PtL^{ImPhCF_3}Cl$

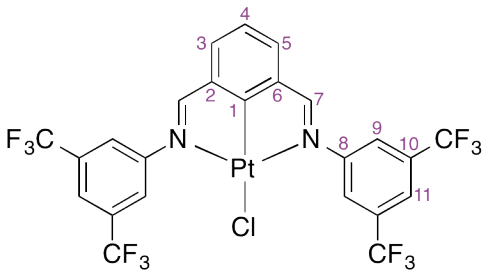

Potassium tetrachloroplatinate (50 mg, 0.12 mmol), L^{ImPhCF_3} (268 mg, 0.48) and acetic acid (3 mL). After cooling to room temperature the product remained in solution so the solvent was removed under reduced pressure and the crude product purified by column chromatography (on silica, eluting with toluene) to give the analytically pure product as a red solid (21 mg, 22%); Found: C, 36.75; H, 1.37; N, 3.48. $C_{24}H_{11}ClF_{12}N_2Pt$ requires C, 36.68; H, 1.37; N, 3.48%; δ H (700 MHz; $CDCl_3$) 8.71 (2H, s with coupling to Pt, J 154, H^7), 8.00 (4H, s, H^9), 7.87 (2H, s, H^{11}), 7.82 (2H, s, H^{11}), 7.82 (2H, d, J 7.7, H^3 and H^5), 7.36 (1H, J 7.7, H^4); δ C (700 MHz; $CDCl_3$) 179.5 (C^1), 179.4 (C^7), 148.8 (C^8), 141.5 (C^2 and C^6), 132.2 (q, J 34.1, CF_3), 130.2 (C^3 and C^5), 124.9 (q, J 4, C^9), 123.7 (C^4), 122.3 (p, J 3.8, C^{11}), 120.4 (C^{10}); δ F (600 MHz; $CDCl_3$) −62.9 (CF_3); (AP^+) m/z = 790.0 $[M - Cl + MeCN]^+$; HRMS (AP^+) m/z = 790.0629 calculated for $[C_{26}H_{14}N_3F_{12}{}^{194}Pt]^+$ 790.0623.

Preparation of $PtL^{KetCy}Cl$

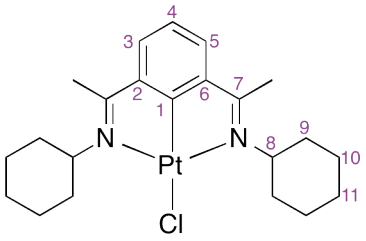

Potassium tetrachloroplatinate (50 mg, 0.12 mmol), acetic acid (2.5 mL), acetic anhydride (0.1 mL), L^{KetCy} (132 mg, 0.41 mmol). The isolated solid was purified by HPLC to give the product as an orange solid (19 mg, 28%); δ H (500 MHz; $CDCl_3$) 7.24 (2H, d, J 7.8, H^3 and H^5), 7.13 (1H, t, J 7.3, H^4), 4.19 (2H, s, H^8), 2.99 (4H, s, $H^9{}_{eq}$), 2.45 (6H, s, CH_3), 1.89 (4H, d, J 13.3, $H^{10}{}_{eq}$), 1.58 (8H, m, $H^9{}_{ax}$ and H^{11}), 1.30 (4H, m, $H^{10}{}_{ax}$); δ C (500 MHz; $CDCl_3$) 181.4 (C^1), 167.9 (C^7), 144.1 (C^2 and C^6), 127.1 (C^3 and C^5), 121.3 (C^4), 64.9 (C^8), 30.0 (C^9), 25.4 (C^{10}), 24.3 (C^{11}), 15.8 (CH_3); (ES^+) m/z = 517.3 $[M - Cl]^+$; HRMS ($ASAP^+$) m/z = 517.2115 $[M - Cl]^+$; calculated for $[C_{22}H_{31}N_2{}^{194}Pt]^+$ 517.2114.

Preparation of $PtL^{Ket^nBu}Cl$

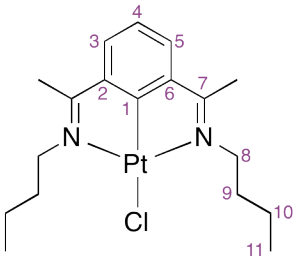

Potassium tetrachloroplatinate (100 mg, 0.24 mmol), acetic acid (4 mL), acetic anhydride (0.1 mL), L^{Ket^nBu} (262 mg, 0.96 mmol). The isolated solid was purified by HPLC to give the product as an orange solid (24 mg, 20%); δ

H (500 MHz; $CDCl_3$) 7.26 (2 H, d, H^3 and H^5), 7.13 (1H, t, J 5, H^4), 4.14 (4 H, m, J 8.0, H^8), 2.39 (6H, t, J 4.5, CH_3), 1.82 (4H, m, J 7.5, H^9), 1.47 (4 H, m, J 7.5, H^{10}), 0.981 (6 H, t, J 7.5, H^{11}); δ C (500 MHz; $CDCl_3$); 182.9 (C^7), 170.7 (C^1), 144.0 (C^2 and C^6), 126.7 (C^3 and C^5), 121.3 (C^4), 54.7 (C^8), 32.2 (C^9), 20.5 (C^{10}), 14.9 (CH_3), 14.2 (C^{11}); (ASAP$^+$) m/z = 466.2 [M − Cl]$^+$; HRMS (ASAP$^+$) m/z = 466.18211 [M − Cl]$^+$; calculated for $[C_{18}H_{27}N_2{}^{194}Pt]^+$ 465.17954.

Preparation of $PtL^{OxIm}Cl$

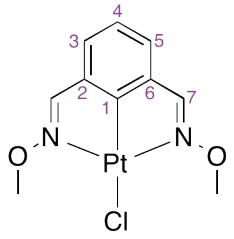

Potassium tetrachloroplatinate (50 mg, 0.12 mmol), acetic acid (2 mL), acetic anhydride (0.1 mL), L^{OxIm} (51 mg, 0.27 mmol). The isolated solid was recrystallised from DCM to give the product as an orange solid (9 mg, 18%); ν_{max}/ cm^{-1} 1686 (N=C); δ H (500 MHz; $CDCl_3$) 8.60 (2H, s with coupling to Pt J 76, H^7), 7.44 (2H, d with coupling to Pt J 4.0 and J 7.5, H^3 and H^5), 7.22 (1H, t, J 8, H^4), 4.24 (6H, s, CH_3); δ C (500 MHz; $CDCl_3$) 170.77 (C^7), 168.79 (C^4), 135.94 (C^2 and C^6), 126.37 (C^3 and C^5), 124.34 (C^1), 65.14 (CH_3); (ES$^+$) m/z = 385.1 [M − Cl]$^+$; HRMS (AP$^+$) m/z = 385.0460 [M − Cl]$^+$; calculated for $[C_{10}H_{11}N_2O_2{}^{194}Pt]^+$ 385.0447.

Preparation of $PtL^{OxKet}Cl$

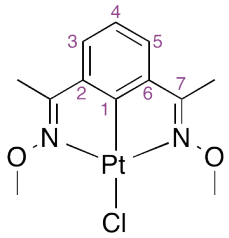

Potassium tetrachloroplatinate (75 mg, 0.18 mmol), acetic acid (2 mL), acetic anhydride (0.1 mL), L^{OxKet} (122 mg, 0.55 mmol). The isolated solid was recrystallised from DCM to give the product as an orange solid (18 mg, 22%); δ H (500 MHz; $CDCl_3$) 7.33 (2H, d, H^3 and H^5), 7.25 (1H, t, J 7, H^4), 4.17 (6H, s, OCH_3), 2.47 (6H, t, J 4.5, CH_3); δ C (500 MHz; $CDCl_3$) 179.8 (C^2 and C^6), 167.0 (C^7), 138.4 (C^4), 126.6 (C^3 and C^5), 123.5 (C^1), 64.0 (OCH_3), 13.7 (CH_3); (ES^+) m/z = 415.2 $[M - Cl]^+$; HRMS (AP^+) m/z = 413.0768 $[M - Cl]^+$; calculated for $[C_{12}H_{15}N_2O_2{}^{194}Pt]^+$ 413.0760.

8.4 Synthesis of Pt(IV) complexes

8.4.1 Synthesis of trichloro-Pt(IV) complexes

The platinum(II) complex was taken up in chloroform and chlorine gas (generated in a separate flask by addition of concentrated hydrochloric acid to potassium permanganate) bubbled through the solution, with stirring, for 30 minutes. The solvent was removed under reduced pressure and the compound taken up again in chloroform (25 mL). The solvent was removed once again under reduced pressure (this enabled complete removal of any residual chlorine) and the products dried on the high vacuum line.

Preparation of PtL^5Cl_3

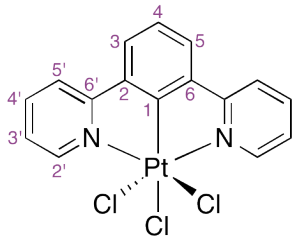

PtL^5Cl (20 mg, 0.04 mmol) and chloroform (20 mL). The product was obtained as a pale yellow powder (21 mg, 99%); δ H (700 MHz; $CDCl_3$) 9.54 (2H, d with coupling to ^{195}Pt, J 5.4, $H^{2'}$), 8.05 (2H, t, J 7.7, $H^{4'}$), 7.95 (2H, d, J 8.2, $H^{5'}$), 7.76 (2H, d, J 7.7, H^3 and H^5), 7.52 (2H, t, J 6.7, $H^{3'}$), 7.48 (1H, t, J 7.8, H^4); (AP^+) m/z = 497.0 $[M - Cl]^+$; HRMS (AP^+) m/z = 494.9922 $[M - Cl]^+$; calculated for $[C_{16}H_{11}N_2Cl_2{}^{194}Pt]^+$ 494.9926.

Preparation of PtL^7Cl_3

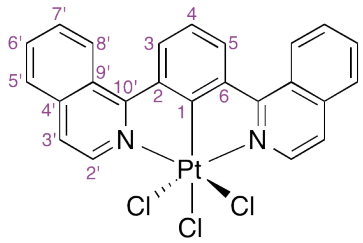

PtL^7Cl (20 mg, 0.04 mmol) and chloroform (25 mL) to give the product (24 mg, 96%); δ H (700 MHz; $CDCl_3$) 9.70 (2 H, d, J 7.5, $H^{2'}$), 9.04 (2 H, d, J 8.4, $H^{5'}$ or $H^{8'}$), 8.55 (2 H, d, J 8.0, H^3 and H^5), 8.11 (2 H, d, J 8.0, $H^{5'}$ $H^{8'}$), 7.93 (3 H, m, H^4 and $H^{6'}$ or $H^{7'}$), 7.71 (2 H, m, $H^{6'}$ or $H^{7'}$), 7.53 (2 H, m, $H^{3'}$); ($ASAP^+$) m/z = 596.0 $[M - Cl]^+$.

Preparation of PtL^5Br_3

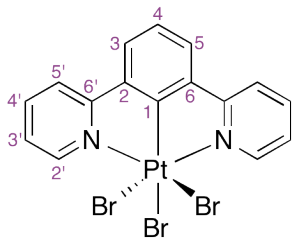

PtL^5Br (34 mg, 0.07 mmol) was taken up in chloroform (25 mL) in a round bottomed flask. Bromine (0.05 mL, 0.97 mmol) was added, the flask stoppered and the solution stirred for 24 hours. The yellow precipitate was isolated by centrifugation, washed with chloroform (3×4 mL) and dried on the high vacuum line to give the product (14 mg, 30%); δ H (700 MHz; $CDCl_3$) 9.72 (2H, m, $H^{2'}$), 8.02 (2H, m, $H^{4'}$), 7.95 (2H, d, J 7.9, $H^{5'}$), 7.78 (2H, t, J 7.6, H^3 and H^5), 7.48 (2H, m, $H^{2'}$), 7.43 (1H, t, J 7.6, $H^{2'}$). Some of the platinum(II) starting material was found in analysis of the product since the Pt(IV) complex is unstable.

Preparation of $[PtL^5(ppy)Cl]^+$

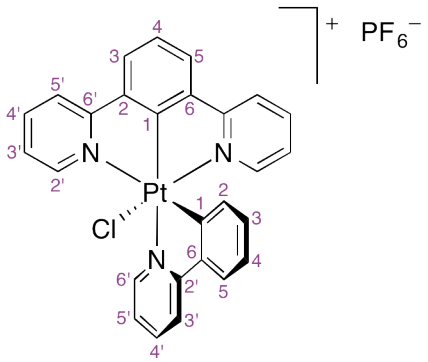

PtL^5Cl (50 mg, 0.11 mmol) was oxidised to PtL^5Cl_3 (*vide supra*). The resultant complex was taken up in toluene (6 mL) with silver trifluoromethanesulfonate (65 mg, 0.25 mmol) and 2-phenylpyridine (25 mg, 0.16 mmol). The

mixture was heated at reflux, under nitrogen, with the exclusion of light for 24 hours. After cooling to room temperature, the precipitated solid was isolated on the centrifuge and washed with toluene (2 × 3 mL). The crude product was extracted into acetone (3 × 5 mL) and the solvent removed under reduced pressure. The product was then dissolved in the minimum volume of acetone and a saturated solution of KCl in acetone added drop wise to precipitate the chloride salt of the complex. This was isolated on the centrifuge, taken up in water and washed with DCM (5 × 20 mL). The water was removed under reduced pressure. The PF_6^- salt was obtained by taking the complex up in the minimum volume of water and pouring it into excess solution of saturated KPF_6 in water to precipitate the product. The solid was isolated by centrifugation and then washed with water (5 × 3 mL) before drying on the high vacuum line to give the analytically pure product (14 mg, 17%); δ H (700 MHz; $(CD_3)_2CO$) 9.91 (1H, ddd, *J* 0.8, *J* 1.6 and *J* 5.5, ppy-$H^{6'}$), 8.68 (1H, d, *J* 8.3, ppy-$H^{3'}$), 8.57 (1H, td, *J* 1.7 and *J* 5.8, ppy-$H^{4'}$), 8.49 (2H, dd, *J* 1.4 and *J* 8.0, $H^{5'}$), 8.28 (2H, d, *J* 7.8, H^3 and H^5), 8.27 (2H, td, *J* 1.5 and *J* 8.2, $H^{4'}$), 8.09 (2H, m, ppy-H^5 and ppy-$H^{5'}$), 7.95 (2H, dd with coupling to Pt, $H^{2'}$), 7.82 (1H, t, *J* 7.8, H^4), 7.45 (2H, ddd, *J* 1.5, *J* 5.9 and *J* 7.5, $H^{3'}$), 7.19 (1H, ddd, *J* 1, *J* 7.2 and *J* 7.8, ppy-H^4), 6.95 (1H, m, ppy-H^3), 6.18 (1H, dd with coupling to Pt, ppy-H^2); δ C (700 MHz; $(CD_3)_2CO$) 166.1 ($C^{6'}$), 162.1 (ppy-C^6), 160.7 (C^1), 150.8 ($C^{2'}$), 149.1 (ppy-$C^{6'}$), 143.4 ($C^{4'}$), 143.2 (ppy-$C^{4'}$), 141.9 (ppy-$C^{2'}$), 138.9 (C^2), 136.0 (ppy-C^5), 132.9 (ppy-C^3), 130.7 (ppy-C^2), 128.7 (C^3 and C^5), 128.4 (ppy-C^4), 128.3 (C^4), 127.6 (ppy-$C^{5'}$), 127.0 ($C^{3'}$), 126.9 (ppy-C^1), 124.0 ($C^{5'}$), 123.0 (ppy-$C^{3'}$); (ES^+) m/z = 616.2 $[M + H]^+$; HRMS (ES^+) m/z = 614.0901 calculated for $[C_{27}H_{19}N_3Cl^{194}Pt]^+$ 614.0894.

Preparation of $[PtL^5(bpy)Cl]^{2+}$

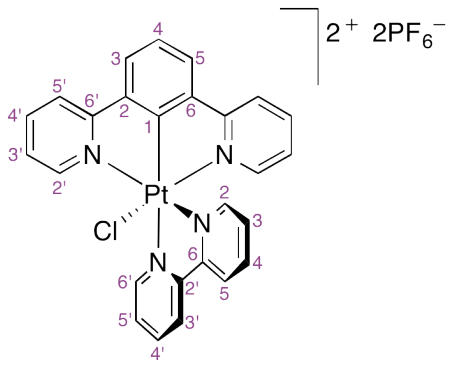

PtL^5Cl (20 mg, 0.04 mmol) was oxidised to PtL^5Cl_3 (*vide supra*). The resultant complex was then taken up in ethylene glycol (2 mL) with 2,2-bipyridine (41 mg, 0.26 mmol) and stirred at room temperature, under nitrogen with the exclusion of light for 30 minutes. The mixture was then gradually heated: 1.5 hours at 40°C, 30 minutes at 75°C, 30 minutes at 80°C and 16 hours at 100°C. After cooling to room temperature the dark red solution was purified by HPLC. After removal of solvent under reduced pressure, the PF_6^- salt was obtained by taking the complex up in the minimum volume of water and pouring it into excess solution of saturated KPF_6 in water to precipitate the product. The solid was obtained by centrifugation and then washed with water (5×3 mL) before drying on the high vacuum line to give the analytically pure product (9 mg, 25%); δ H (700 MHz; D_2O) 9.77 (1 H, d, J 5.3, bpy-$H^{6'}$), 8.95 (1 H, d, J 8.2, bpy-$H^{3'}$), 8.82 (1 H, t, J 8.1, bpy-$H^{4'}$), 8.73 (1 H, d, J 8.1, bpy-H^2), 8.43 (1 H, dd, J 5.3 and J 8.0, bpy-$H^{5'}$), 8.36 (2 H, d J 8.0, $H^{2'}$), 8.32 (1 H, t, J 7.9, bpy-H^3), 8.24 (2 H, d, J 7.8, $H^{3'}$), 8.22 (2 H, d, J 8.1, H^3 and H^5), 7.92 (1 H, t, J 7.9, H^4), 7.81 (1 H, d, J 6.1, bpy-H^5), 7.76 (2 H, d, J 6.0, $H^{5'}$), 7.52 (1 H, t J 6.9, bpy-H^4), 7.42 (2 H, t, J 6.8, $H^{4'}$); δ C (700 MHz; D_2O) 164.0 (C^2 and C^6), 155.0 (bpy-C^6), 154.0 (C^1), 153.4 (bpy-$C^{2'}$), 149.9 ($C^{5'}$), 148.8 (bpy-C^5), 148.4 (bpy-$C^{6'}$), 144.4 (bpy-C^3), 144.2 (bpy-$C^{4'}$), 144.1 ($C^{3'}$), 137.6 ($C^{6'}$), 130.7 (bpy-$C^{5'}$), 130.0 (C^4), 130.0 (bpy-C^4), 129.3 (C^3 and C^5), 127.1 (bpy-C^2), 127.0 ($C^{4'}$), 126.6 (bpy-$C^{3'}$), 124.4 ($C^{2'}$); (ES^+) m/z = 308.5 $[M]^{2+}$, m/z = 763.6 $[M + PF_6]^+$; HRMS (ES^+) m/z = 759.0519 [M +

$PF_6]^+$; calculated for $[C_{26}H_{19}N_4F_6PCl^{192}Pt]^+$ 582.8916.

8.5 Metathesis of the ancillary ligand

Preparation of PtL^5I

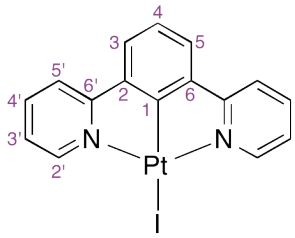

PtL^5Cl (40 mg, 0.09 mmol) was suspended in acetone (8 mL) and silver trifluoromethanesulfonate (28 mg, 0.11 mmol) added. The mixture was stirred for 1.5 hours at room temperature. The precipitated silver chloride was removed by centrifugation and potassium iodide (28 mg, 0.17 mmol) added to the acetone solution which was subsequently stirred for a further 2 hours. The complex was precipitated from the reaction mixture, isolated by centrifugation and washed with ethanol (2 mL), then water (2 mL), then ether (2 mL) before drying on the high vacuum line to give the analytically pure product (31 mg, 65%); δ H (400 MHz; $CDCl_3$) 9.90 (2H, m with coupling to ^{195}Pt J 45, $H^{2'}$), 7.91 (2 H, td, J 1.6 and 7.8, $H^{4'}$), 7.68 (2 H, m, $H^{5'}$), 7.45 (2 H, d, J 7.7, H^3 and H^5), 7.25 (3 H, m, H^4 and $H^{3'}$; (ASAP$^+$) m/z = 553.0 $[M]^+$; HRMS (AP$^+$) m/z = 551.9598 calculated for $[C_{16}H_{11}N_2I^{194}Pt]^+$ 551.9594.

Preparation of $PtL^{ImCy}Acet$

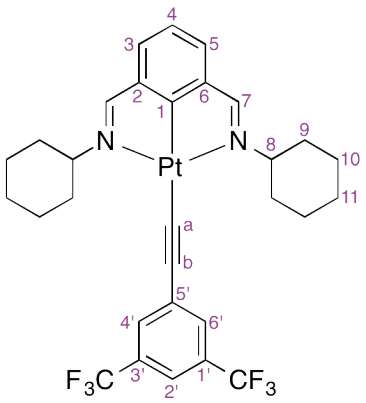

1-Ethynyl-3,5-bis(trifluoromethyl)benzene (7 mg, 0.03 mmol) and sodium hydroxide (1 mg, 0.03 mmol) were taken up in methanol (5 mL) and stirred at room temperature for 30 minutes. $PtL^{ImCy}Cl$ (15 mg, 0.03 mmol) was then added and the mixture stirred for 12 hours at room temperature. The product was precipitated, isolated on the centrifuge, washed with methanol (1 mL) and dried on the high vacuum line to give the analytically pure product (10 mg, 46%); δ H (700 MHz; $CDCl_3$) 8.47 (2H, s with coupling to Pt J 66, H^7), 7.79 (2H, s, $H^{4'}$ and $H^{6'}$), 7.59 (1H, s, $H^{2'}$), 7.45 (2H, d, J 7.7, H^3 and H^5), 7.09 (1H, t, J 7, H^4), 3.90 (2H, t, J 10.5, H^8), 2.10 (4H, d, overlapping signals, $H^{9}{}_{eq}$), 2.06 (4H, q, J 11.9, $H^{9}{}_{ax}$), 1.91 (4H, d, J 14, $H^{10}{}_{eq}$), 1.70 (2H, d, J 12.6, $H^{11}{}_{eq}$), 1.41 (4H, q, J 12.6, $H^{10}{}_{ax}$), 1.24 (2H, q, J 12.6, $H^{11}{}_{ax}$); δ F (700 MHz; $CDCl_3$) −63.205 (CF_3); (ASAP$^+$) m/z = 727.2 $[M + H]^+$; HRMS (AP$^+$) m/z = 726.1961 $[M]^+$; calculated for $[C_{30}H_{30}N_2F_6{}^{194}Pt]^+$ 726.1940.

Preparation of $PtL^{ImCy}CN$

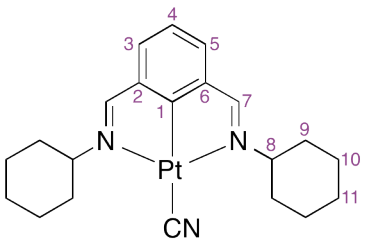

$PtL^{ImCy}Cl$ (30 mg, 0.02 mmol) and potassium cyanide (8 mg, 0.12 mmol) were placed in a clean, dry Schlenk, in methanol (5 mL) and stirred at room temperature for 16 hours. The methanol was then removed under reduced pressure and the products taken up in DCM, washed with water (10 mL), dried over $MgSO_4$, filtered and the solvent removed under reduced pressure. The product was dried on the high vacuum line (4 mg, 34%). ($ASAP^+$) m/z = 517.2 $[M + H]^+$; HRMS (AP^+) m/z = 515.1829 $[M]^+$; calculated for $[C_{21}H_{27}N_3{}^{194}Pt]^+$ 515.1832.

8.5.1 Substitution of chloride ancillary for a thiolate ligand

The chosen thiolate ligand and methanol were placed in a Schlenk tube and degassed using the freeze, pump, thaw method before being placed under an atmosphere of nitrogen. Potassium *tert*-butoxide was then added under a stream of nitrogen and the resultant solution stirred for 5 minutes. The platinum(II) complex was then added, as a solid, under a stream of nitrogen and the mixture stirred for 16 hours. The crude product was obtained as a precipitate which was isolated on the centrifuge.

Preparation of PtL^{6}STol

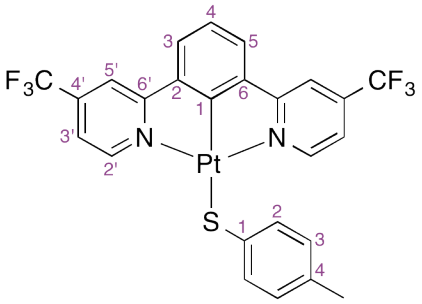

p-Thiocresol (22 mg, 0.18 mmol), methanol (3 mL), potassium *tert*-butoxide (19 mg, 0.17 mmol) and PtL^{6}Cl (40 mg, 0.07 mmol). The crude product was washed with methanol (5 × 4 mL) and dried on the high vacuum line to give the analytically pure product (34 mg, 71%): δ H (600 MHz; $(CD_3)_2SO$) 9.39 (2H, d with coupling to ^{195}Pt, J 8.1, H$^{2'}$), 8.50 (2H, s, H$^{5'}$), 8.06 (2H, d, J 7.7, H^3 and H^5), 7.81 (2H, m, H$^{3'}$), 7.34 (3H, m, H^4 and SAr-H^2), 6.78 (2H, d, J 8.1, SAr-H^3), 2.12 (3H, s, CH_3); δ C (600 MHz; $(CD_3)_2SO$) 170.7 (C^1), 169.5 (C$^{6'}$), 154.1 (C$^{2'}$), 144.0 (SAr-C^1), 140.3 (C^2 and C^6), 139.4 (C$^{4'}$), 132.1 (SAr-C^2), 130.1 (SAr-C^4),128.5 (SAr-C^3), 126.8 (C^3 and C^5), 124.0 (C^4), 122.6 (CF_3), 120.3 (C$^{3'}$), 116.9 (C$^{5'}$), 20.4 (CH_3); δ F (400 MHz; $(CD_3)_2SO$) −63.55 (CF_3); (ASAP$^+$) m/z = 686.1 [M + H]$^+$; HRMS (AP$^+$) m/z = 683.0605 [M + H]$^+$; calculated for $[C_{25}H_{17}N_2F_6S^{192}Pt]^+$ 683.0627.

Preparation of PtL^{6}SNit

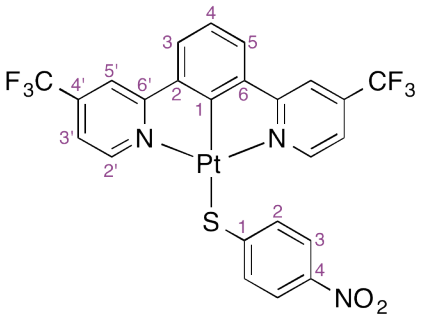

4-Nitro-thiophenol (27 mg, 0.17 mmol), methanol (2 mL), potassium *tert*-butoxide (19 mg, 0.17 mmol) and PtL^6Cl (40 mg, 0.07 mmol). The crude product was washed first with methanol (5 × 4 mL), then with ether (5 × 3 mL). The deep red solid was dried on the high vacuum line to give the analytically pure product (33 mg, 66%): δ H (400 MHz; $(CD_3)_2SO$) 9.20 (2 H, d, *J* 6.0, $H^{2'}$), 8.50 (2 H, s, $H^{5'}$), 8.02 (2 H, d, *J* 7.6, H^3 and H^5), 7.79 (4 H, m, H^{Nit-2} and H^{Nit-3}), 7.61 (2 H, d, *J* 8.8, $H^{3'}$), 7.32 (1 H, t, *J* 7.2, H^4); (ASAP$^+$) *m/z* = 717.0 $[M + H]^+$; HRMS (AP$^+$) *m/z* = 714.0322 $[M + H]^+$; calculated for $[C_{24}H_{14}N_3O_2F_6S^{192}Pt]^+$ 714.0321.

Preparation of PtL^7STol

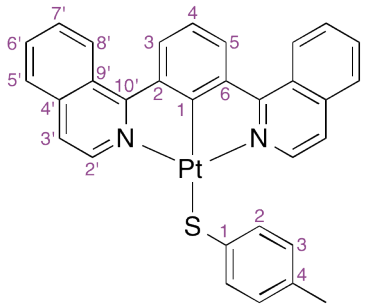

p-Thiocresol (5 mg, 0.04 mmol), methanol (3 mL), potassium *tert*-butoxide (7 mg, 0.06 mmol) and PtL^7Cl (20 mg, 0.04 mmol). The crude product was washed first with methanol (3 × 2 mL), then ether (3 × 2 mL). The pale yellow solid was dried on the high vacuum line to give the analytically pure product (21 mg, 74%): δ H (400 MHz; $(CD_3)_2SO$) 9.41 (2 H, d, *J* 8, $H^{2'}$), 9.13 (2 H, d, *J* 8, $H^{5'}$ or $H^{8'}$), 8.55 (2 H, d, *J* 8, $H^{3/5}$), 8.12 (2 H, d, *J* 8, $H^{5'}$ or $H^{8'}$), 8.00 (2 H, t, *J* 8, $H^{6'}$ or $H^{7'}$), 7.90 (4 H, m, $H^{Tol-2/3}$), 7.54 (1 H, t, *J* 8, H^4), 7.41 (2 H, d, *J* 8, $H^{6'}$ or $H^{7'}$), 6.77 (2 H, d, *J* 8, H^3); (ASAP$^+$) *m/z* = 648.1 $[M]^+$; HRMS (AP$^+$) *m/z* = 648.1132 calculated for $[C_{31}H_{22}N_2S^{194}Pt]^+$ 648.1132.

Preparation of $PtL^{ImCy}STol$

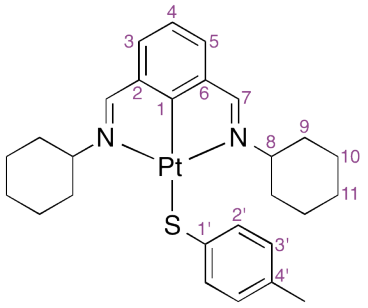

p-Thiocresol (6 mg, 0.05 mmol), methanol (3 mL), potassium *tert*-butoxide (8 mg, 0.07 mmol) and $PtL^{ImCy}Cl$ (25 mg, 0.05 mmol). The crude product was washed first with methanol (3 × 2 mL), then ether (3 × 2 mL). The pale yellow solid was dried on the high vacuum line to give the analytically pure product (18 mg, 59%): δ H (700 MHz; $(CD_3)_2SO$) 8.69 (2H, s with coupling to Pt J 70, H^7), 8.5645 (2H, d, J 7.7, H^3 and H^5), 7.25 (2H, d, J 7.7, SAr-$H^{2'}$), 7.14 (1H, t, J 7.7, H^4), 6.83 (2H, d, J 8.4, SAr-$H^{3'}$), 3.77 (2H, tt, J 2.8 and J 11.2, H^8), 2.18 (3H, s, CH_3), 1.91 (4H, d, J 11.2, $H^9{}_{eq}$), 1.67 (4H, d, J 12.6, $H^{10}{}_{eq}$), 1.53 (2H, d, J 12.6, $H^{11}{}_{eq}$), 1.44 (4H, q, J 12.6, $H^9{}_{ax}$), 1.07 (2H, q, J 12.6, $H^{11}{}_{ax}$), 0.99 (4H, q, J 12.6, $H^{10}{}_{ax}$); δ C (700 MHz; $(CD_3)_2SO$) 176.45 (C^7), 145.31 (SAr-$C^{4'}$), 142.74 (C^2), 133.52 (SAr-$C^{2'}$), 131.23 (SAr-$C^{1'}$), 128.67 (SAr-$C^{3'}$), 127.43 (C^3), 122.88 (C^4), 66.43 (C^8), 40.46 (C^1), 33.88 (C^9), 25.78 (C^{10}), 25.65 (C^{11}), 21.09 (CH_3); (ASAP$^+$) m/z = 614.2 $[M + H]^+$, m/z = 654.2 $[M + MeCN]^+$; HRMS (AP$^+$) m/z = 612.2068 $[M]^+$; calculated for $[C_{27}H_{34}N_2S^{194}Pt]^+$ 612.2070.

Preparation of $PtL^{ImCy}SNit$

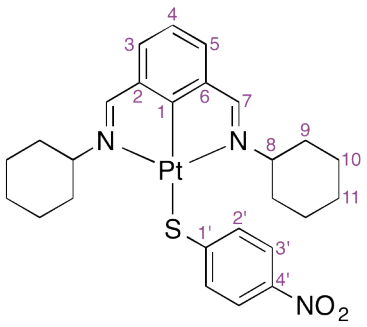

4-Nitro-thiophenol (8 mg, 0.05 mmol), methanol (3 mL), potassium *tert*-butoxide (8 mg, 0.07 mmol) and $PtL^{ImCy}Cl$ (25 mg, 0.05 mmol). The crude product was washed first with methanol (5 × 4 mL), then with ether (5 × 3 mL) before drying on the high vacuum line to give the analytically pure product (21 mg, 65%): δ H (400 MHz; $(CD_3)_2SO$) 8.70 (2 H, s with coupling to Pt, J 144, H^7), 8.86 (2 H, d, J 9.3, H^3 and H^5), 7.57 (4 H, m, $H^{2'}$ and $H^{3'}$), 7.19 (1 H, t, J 7.6, H^4); 3.78 (2 H, t, J 12.2, H^8), 1.92 (4 H, d, J 11.8, H^9_{eq}), 1.69 (4 H, d, J 12.6, H^{10}_{eq}), 1.52 (6 H, m, H^9_{ax} and H^{11}_{eq}), 1.02 (6 H, m, H^{10}_{ax} and H^{11}_{ax}); (ASAP$^+$) m/z = 644.2 $[M + H]^+$; HRMS (AP$^+$) m/z = 644.1829 calculated for $[C_{26}H_{32}N_3O_2S^{194}Pt]^+$ 644.1842.

9

Appendix

9.1 Publications arising from work discussed in this thesis

'Phosphorescent, liquid-crystalline complexes of platinum(II): influence of the beta-diketonate co-ligand on mesomorphism and emission properties'
Matthew Spencer, Amedeo Santoro, Gemma R. Freeman, Álvaro Díez, Paul R. Murray, Javier Torroba, Adrian C. Whitwood, Lesley J. Yellowlees, J. A. Gareth Williams and Duncan W. Bruce
Dalton Trans., 2012, **41**, 14244-14256.
This article features on the front cover of the issue.

Book chapter: 'Metal complexes of pincer ligands: excited states, photochemistry and luminescence' in 'Organometallic Pincer Chemistry'
Gemma R. Freeman and J. A. Gareth Williams
Top. Organomet. Chem., 2013, **40**, 89-130.

'Platinum(II) complexes with cyclometallated 5-π-delocalized-donor-1,3-di(2-pyridyl)benzene ligands as efficient phosphors for NIR-OLEDs'
Filippo Nisic, Alessia Colombo, Claudia Dragonetti, Dominique Roberto, Adriana Valore, Joanna M. Malicka, Massimo Cocchi, Gemma R Freeman and J. A. Gareth Williams
J. Mater. Chem. C, 2014, **2**, 1791-1800.

'An unprecedented cyclometallated platinum(II) complex incorporating a phosphinine co-ligand: synthesis and photoluminescence behaviour'
Jamal Moussa, Thomas Cheminel, Gemma R. Freeman, Lise-Marie Chamoreau, J. A. Gareth Williams and Hani Amouri
Dalton Trans., 2014, **43**, 8162-8165.

'Platinum(II) complexes of N^C^N-coordinating 1,3-di(2-pyridyl)benzene ligands: thiolate co-ligands lead to strong red luminescence from charge-transfer states'
William A. Tarran, Gemma R. Freeman, Lisa Murphy, Adam M. Benham, Ritu Kataky and J. A. Gareth Williams
Inorg. Chem., 2014, **53**, 5738-5749.

9.2 Conferences attended

Young and early careers researchers' meeting: Photochemistry group, Durham; 13^{th} January 2010.

Controlling photophysical properties of metal complexes: Toward molecular photonics (COST meeting), Prague; 17^{th} - 19^{th} May 2010.
Poster presentation: "*An easy route to terdentate Pt(II) complexes*"

Universities of Scotland inorganic chemistry conference, Durham; 8^{th} - 9^{th} July 2010.
Poster presentation: "*New terdentate ligands for light-emitting Pt(II) complexes*"

RSC Photochemistry group and Dublin chemistry: Photochemistry and photochemical techniques, Dublin; 16^{th} - 18^{th} May 2011.
Oral presentation: "*New terdentate ligands for light-emitting complexes*"

19^{th} International symposium on the photochemistry and photophysics of coordination compounds, Strasbourg; 3^{rd} - 7^{th} July 2011.
Oral presentation: "*New terdentate ligands for light-emitting metal complexes*"

LEA Rennes-Durham meeting, Durham; 3^{rd} - 4^{th} April 2012.

Photoactivatable metal complexes: from theory to therapy, London; 18^{th} - 19^{th} June 2012.
Flash poster presentation: "*Time-resolved emission imaging microscopy (TREM) with highly luminescent metal complexes*"

9.3 Work outside the department

26^{th} - 30^{th} March 2012, laser microscopy laboratory, Rutherford-Appleton Laboratories, Oxfordshire. Two-photon excitation imaging studies of a series of Pt(II) complexes within cells.

9.4 Crystal structure data

Crystal data and structure refinement for $L^{ImPhOMe}$:

Identification code	13srv241	
Empirical formula	$C_{22}H_{20}N_2O_2$	
Formula weight	344.40	
Temperature	120 K	
Wavelength	0.71073 Å	
Crystal system	Orthorhombic	
Space group	$P2_12_12_1$	
Unit cell dimensions	a = 5.7513(4) Å	$\alpha = 90°$.
	b = 8.2979(5) Å	$\beta = 90°$.
	c = 36.710(2) Å	$\gamma = 90°$.
Volume	1751.9(2) $Å^3$	
Z	4	
Density (calculated)	1.306 Mg/m^3	
Absorption coefficient	0.084 mm^{-1}	
F(000)	728.0	
Crystal size	$0.44 \times 0.42 \times 0.12$ mm^3	
Theta range for data collection	2.22 to 57°.	
Index ranges	$-7 \leq h \leq 7, -11 \leq k \leq 11, -49 \leq l \leq 49$	
Reflections collected	16394	
Independent reflections	4447 [R(int) = 0.0619]	
Data / restraints / parameters	4447 / 0 / 315	
Goodness-of-fit on F^2	1.001	
Final R indices [I>2sigma(I)]	R1 = 0.0440, wR2 = 0.1000	
R indices (all data)	R1 = 0.0603, wR2 = 0.0.1064	
Largest diff. peak and hole	0.26 and -0.19 e.$Å^{-3}$	

Crystal data and structure refinement for L^{KetCy}:

Identification code	10srv055	
Empirical formula	$C_{22}H_{32}N_2$	
Formula weight	324.50	
Temperature	120(2) K	
Wavelength	0.71073 Å	
Crystal system	Orthorhombic	
Space group	Pnma	
Unit cell dimensions	a = 10.1990(3) Å	$\alpha = 90°$.
	b = 36.0846(10) Å	$\beta = 90°$.
	c = 5.1886(2) Å	$\gamma = 90°$.
Volume	1909.54(11) $Å^3$	
Z	4	
Density (calculated)	1.129 Mg/m^3	
Absorption coefficient	0.065 mm^{-1}	
F(000)	712	
Crystal size	$0.26 \times 0.25 \times 0.20$ mm^3	
Theta range for data collection	3.39 to 25.03°.	
Index ranges	$-11 \leq h \leq 12, -42 \leq k \leq 42, -6 \leq l \leq 6$	
Reflections collected	12671	
Independent reflections	1709 [R(int) = 0.0403]	
Completeness to theta = 25.00°	99.8 %	
Absorption correction	Semi-empirical from equivalents	
Max. and min. transmission	1.000 and 0.807	
Refinement method	Full-matrix least-squares on F^2	
Data / restraints / parameters	1709 / 0 / 113	
Goodness-of-fit on F^2	1.241	
Final R indices [I>2sigma(I)]	R1 = 0.0664, wR2 = 0.1338	
R indices (all data)	R1 = 0.0741, wR2 = 0.1369	
Largest diff. peak and hole	0.190 and -0.225 e.$Å^{-3}$	

Crystal data and structure refinement for L^{KetPh}:

Identification code	10srv099	
Empirical formula	$C_{22}H_{20}N_2$	
Formula weight	312.40	
Temperature	120(2) K	
Wavelength	0.71073 Å	
Crystal system	Monoclinic	
Space group	C 2/c	
Unit cell dimensions	a = 19.4573(13) Å	$\alpha = 90°$.
	b = 7.1105(4) Å	$\beta = 109.304(2)°$.
	c = 12.7922(8) Å	$\gamma = 90°$.
Volume	1670.31(18) $Å^3$	
Z	4	
Density (calculated)	1.242 Mg/m^3	
Absorption coefficient	0.073 mm^{-1}	
F(000)	664	
Crystal size	$0.22 \times 0.20 \times 0.10$ mm^3	
Theta range for data collection	2.22 to 25.03°.	
Index ranges	$-23 \leq h \leq 23, -6 \leq k \leq 8, -15 \leq l \leq 15$	
Reflections collected	4736	
Independent reflections	1481 [R(int) = 0.0482]	
Completeness to theta = 25.00°	100.0 %	
Absorption correction	Semi-empirical from equivalents	
Max. and min. transmission	1.000 and 0.769	
Refinement method	Full-matrix least-squares on F^2	
Data / restraints / parameters	1481 / 0 / 111	
Goodness-of-fit on F^2	1.030	
Final R indices [I>2sigma(I)]	R1 = 0.0634, wR2 = 0.1642	
R indices (all data)	R1 = 0.0921, wR2 = 0.1957	
Largest diff. peak and hole	0.434 and -0.239 e.$Å^{-3}$	

Crystal data and structure refinement for $PtL^{Ket^nBu}Cl$:

Identification code	10srv176	
Empirical formula	$C_{18}H_{27}ClN_2Pt$	
Formula weight	501.96	
Temperature	120(2) K	
Wavelength	0.71073 Å	
Crystal system	Orthorhombic	
Space group	P 21 21 21	
Unit cell dimensions	a = 5.07110(10) Å	$\alpha = 90°$.
	b = 14.0644(3) Å	$\beta = 90°$.
	c = 25.1994(5) Å	$\gamma = 90°$.
Volume	1797.27(6) $Å^3$	
Z	4	
Density (calculated)	1.855 Mg/m^3	
Absorption coefficient	7.955 mm^{-1}	
F(000)	976	
Crystal size	$0.40 \times 0.12 \times 0.10$ mm^3	
Theta range for data collection	2.17 to 25.02°.	
Index ranges	$-6 \leq h \leq 5, -16 \leq k \leq 16, -29 \leq l \leq 29$	
Reflections collected	10806	
Independent reflections	3153 [R(int) = 0.0304]	
Completeness to theta = 25.00°	99.9 %	
Absorption correction	Semi-empirical from equivalents	
Max. and min. transmission	1.000 and 0.436	
Refinement method	Full-matrix least-squares on F^2	
Data / restraints / parameters	3153 / 0 / 204	
Goodness-of-fit on F^2	1.035	
Final R indices [I>2sigma(I)]	R1 = 0.0174, wR2 = 0.0382	
R indices (all data)	R1 = 0.0194, wR2 = 0.0389	
Absolute structure parameter	0.358(8)	
Largest diff. peak and hole	1.231 and -0.534 e.$Å^{-3}$	

Crystal data and structure refinement for $PtL^{OxIm}Cl$:

Identification code	10srv190	
Empirical formula	$C_{10}H_{11}ClN_2O_2Pt$	
Formula weight	421.75	
Temperature	120(2) K	
Wavelength	0.71073 Å	
Crystal system	Orthorhombic	
Space group	Pbca	
Unit cell dimensions	a = 11.2334(2) Å	$\alpha = 90°$.
	b = 12.0769(2) Å	$\beta = 90°$.
	c = 16.7780(4) Å	$\gamma = 90°$.
Volume	2276.18(8) $Å^3$	
Z	8	
Density (calculated)	2.461 Mg/m^3	
Absorption coefficient	12.549 mm^{-1}	
F(000)	1568	
Crystal size	$0.40 \times 0.12 \times 0.12$ mm^3	
Theta range for data collection	2.43 to 26.37°.	
Index ranges	$-11 \leq h \leq 14, -15 \leq k \leq 15, -16 \leq l \leq 20$	
Reflections collected	11241	
Independent reflections	2329 [R(int) = 0.0297]	
Completeness to theta = 25.00°	100.0 %	
Absorption correction	Semi-empirical from equivalents	
Max. and min. transmission	1.000 and 0.369	
Refinement method	Full-matrix least-squares on F^2	
Data / restraints / parameters	2329 / 0 / 147	
Goodness-of-fit on F^2	1.087	
Final R indices [I>2sigma(I)]	R1 = 0.0187, wR2 = 0.0417	
R indices (all data)	R1 = 0.0236, wR2 = 0.0435	
Largest diff. peak and hole	1.438 and -0.940 e.$Å^{-3}$	

Crystal data and structure refinement for $PtL^{ImPhCF_3}Cl$:

Identification code	13srv181	
Empirical formula	$C_{24}H_{11}ClF_{12}N_2Pt$	
Formula weight	785.89	
Temperature	120 K	
Crystal system	Orthorhombic	
Space group	Fddd	
Unit cell dimensions	a = 14.8776(2) Å	$\alpha = 90°$.
	b = 33.7860(6) Å	$\beta = 90°$.
	c = 39.8394(7) Å	$\gamma = 90°$.
Volume	20025.5(6) $Å^3$	
Z	32	
Density (calculated)	2.085 Mg/m^3	
Absorption coefficient	5.819 mm^{-1}	
F(000)	11904.0	
Crystal size	$0.4927 \times 0.1243 \times 0.0591$ mm^3	
Theta range for data collection	5.48 to 64.08°.	
Index ranges	$-21 \leq h \leq 21, -49 \leq k \leq 49, -59 \leq l \leq 57$	
Reflections collected	95510	
Independent reflections	6657 [R(int) = 0.0674]	
Completeness to theta = 25.00°	100.0 %	
Absorption correction	Semi-empirical from equivalents	
Max. and min. transmission	1.000 and 0.369	
Refinement method	Full-matrix least-squares on F^2	
Data / restraints / parameters	6657 / 15 / 358	
Goodness-of-fit on F^2	1.056	
Final R indices [I>2sigma(I)]	R1 = 0.0284, wR2 = 0.0664	
R indices (all data)	R1 = 0.0409, wR2 = 0.0701	
Largest diff. peak and hole	1.56 and -1.11 e.$Å^{-3}$	

Crystal data and structure refinement for $PtL^{ImCy}C_2Ar$:

Identification code	12srv038	
Empirical formula	$C_{30}H_{30}F_6N_2O_{0.72}Pt$	
Formula weight	739.17	
Temperature	120(2) K	
Wavelength	0.71073 Å	
Crystal system	Trigonal	
Space group	P−3	
Unit cell dimensions	a = 18.2589(3) Å	$\alpha = 90°$.
	b = 18.2589(3) Å	$\beta = 90°$.
	c = 14.7397(3) Å	$\gamma = 120°$.
Volume	4255.67(13) $Å^3$	
Z	6	
Density (calculated)	1.731 Mg/m^3	
Absorption coefficient	4.998 mm^{-1}	
F(000)	2171	
Crystal size	$0.29 \times 0.21 \times 0.14$ mm^3	
Theta range for data collection	2.58 to 29.25°.	
Index ranges	$-19 \leq h \leq 24, -24 \leq k \leq 23, -18 \leq l \leq 20$	
Reflections collected	38686	
Independent reflections	7068 [R(int) = 0.0503]	
Completeness to theta = 27.00°	99.9 %	
Absorption correction	Analytical	
Max. and min. transmission	0.519 and 0.364	
Refinement method	Full-matrix least-squares on F^2	
Data / restraints / parameters	7068 / 620 / 524	
Goodness-of-fit on F^2	1.040	
Final R indices [I>2sigma(I)]	R1 = 0.0408, wR2 = 0.0853	
R indices (all data)	R1 = 0.0589, wR2 = 0.0947	
Largest diff. peak and hole	2.094 and −1.619 e.$Å^{-3}$	

Crystal data and structure refinement for $PtL^{OxKet}Cl$:

Identification code	12srv035	
Empirical formula	$C_{12}H_{15}ClN_2O_2Pt$	
Formula weight	449.80	
Temperature	120(2) K	
Wavelength	0.71073 Å	
Crystal system	Monoclinic	
Space group	P 21/c	
Unit cell dimensions	a = 7.3897(2) Å	$\alpha = 90°$.
	b = 17.5102(4) Å	$\beta = 91.383(2)°$.
	c = 20.6523(4) Å	$\gamma = 90°$.
Volume	2671.53(11) $Å^3$	
Z	8	
Density (calculated)	2.237 Mg/m^3	
Absorption coefficient	10.699 mm^{-1}	
F(000)	1696	
Crystal size	$0.3874 \times 0.2038 \times 0.1145$ mm^3	
Theta range for data collection	2.76 to 29.25°.	
Index ranges	$-10 \leq h \leq 10, -23 \leq k \leq 21, -28 \leq l \leq 27$	
Reflections collected	24679	
Independent reflections	6379 [R(int) = 0.0319]	
Completeness to theta = 27.00°	99.2 %	
Absorption correction	Analytical	
Max. and min. transmission	0.363 and 0.123	
Refinement method	Full-matrix least-squares on F^2	
Data / restraints / parameters	6379 / 0 / 333	
Goodness-of-fit on F^2	1.083	
Final R indices [I>2sigma(I)]	R1 = 0.0287, wR2 = 0.0689	
R indices (all data)	R1 = 0.0335, wR2 = 0.0712	
Largest diff. peak and hole	2.310 and -0.930 e.$Å^{-3}$	

Crystal data and structure refinement for $[PtL^5(ppy)Cl]^+$:

Identification code	12srv082	
Empirical formula	$C_{27}H_{19}ClF_6N_3PPt$	
Formula weight	760.96	
Temperature	120(2) K	
Wavelength	0.71073 Å	
Crystal system	Monoclinic	
Space group	P 21/n	
Unit cell dimensions	a = 11.3178(3) Å	$\alpha = 90°$.
	b = 13.8020(4) Å	$\beta = 95.380(3)°$.
	c = 16.1527(5) Å	$\gamma = 90°$.
Volume	2512.07(13) $Å^3$	
Z	4	
Density (calculated)	2.012 Mg/m^3	
Absorption coefficient	5.797 mm^{-1}	
F(000)	1464	
Crystal size	$0.11 \times 0.08 \times 0.05$ mm^3	
Theta range for data collection	3.57 to 26.37°.	
Index ranges	$-14 \leq h \leq 14, -17 \leq k \leq 17, -11 \leq l \leq 20$	
Reflections collected	11451	
Independent reflections	5121 [R(int) = 0.0580]	
Completeness to theta = 26.00°	99.8 %	
Absorption correction	Analytical	
Max. and min. transmission	0.773 and 0.568	
Refinement method	Full-matrix least-squares on F^2	
Data / restraints / parameters	5121 / 12 / 352	
Goodness-of-fit on F^2	0.994	
Final R indices [I>2sigma(I)]	R1 = 0.0440, wR2 = 0.0599	
R indices (all data)	R1 = 0.0673, wR2 = 0.0694	
Largest diff. peak and hole	1.216 and -1.274 e.$Å^{-3}$	

Crystal data and structure refinement for $[\mathbf{PtL^5(bpy)Cl}]^{2+}$:

Identification code	12srv145	
Empirical formula	$C_{29}H_{25}ClF_{12}N_4OP_2Pt$	
Formula weight	966.01	
Temperature	120(2) K	
Wavelength	0.71073 Å	
Crystal system	Triclinic	
Space group	P−1	
Unit cell dimensions	a = 9.4819(3) Å	$\alpha = 75.837(3)°$.
	b = 12.0126(4) Å	$\beta = 79.211(3)°$.
	c = 15.1624(5) Å	$\gamma = 74.144(3)°$.
Volume	1597.36(9) $Å^3$	
Z	2	
Density (calculated)	2.008 Mg/m^3	
Absorption coefficient	4.665 mm^{-1}	
F(000)	936	
Crystal size	$0.17 \times 0.11 \times 0.09$ mm^3	
Theta range for data collection	2.49 to 26.37°.	
Index ranges	$-11 \leq h \leq 11, -15 \leq k \leq 12, -16 \leq l \leq 18$	
Reflections collected	12869	
Independent reflections	6518 [R(int) = 0.0557]	
Completeness to theta = 26.00°	99.9 %	
Absorption correction	Analytical	
Max. and min. transmission	0.710 and 0.549	
Refinement method	Full-matrix least-squares on F^2	
Data / restraints / parameters	6518 / 180 / 545	
Goodness-of-fit on F^2	1.005	
Final R indices [I>2sigma(I)]	R1 = 0.0454, wR2 = 0.0600	
R indices (all data)	R1 = 0.0627, wR2 = 0.0646	
Largest diff. peak and hole	1.445 and −1.075 e.$Å^{-3}$	

9.5 Chapter 1

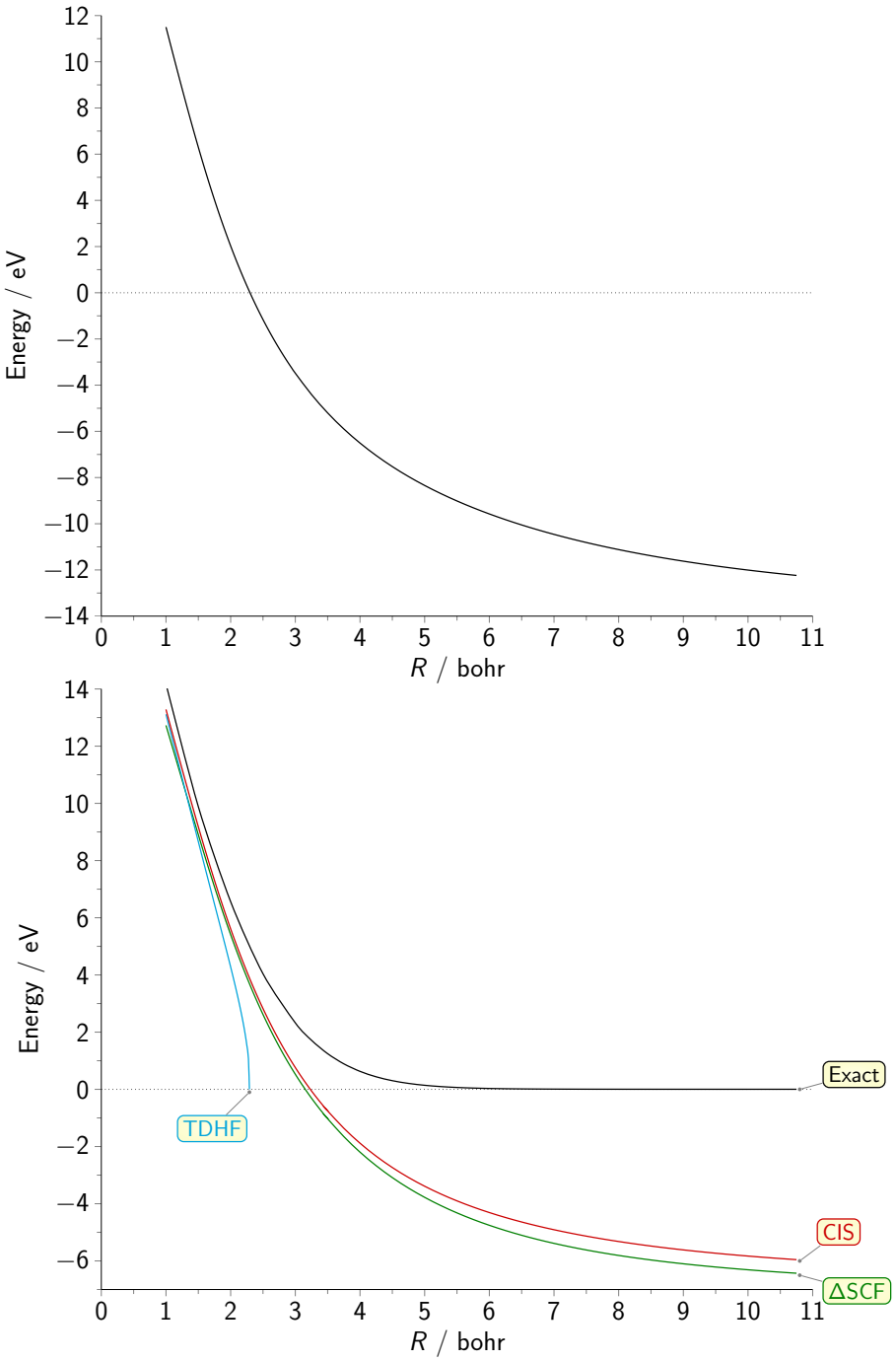

Figure 9.1: Top: ${}^3\Sigma_u^+$ stability measure of H_2. HF Bottom: ${}^1\Sigma_g^+ \rightarrow {}^3\Sigma_u^+$ excitation energies for H_2 as a function of bond length.

9.6 Chapter 2

Excited state	PtL^1Cl		PtL^2Cl		PtL^3Cl		PtL^4Cl	
	λ /nm	f	λ /nm	f	λ /nm	f	λ /nm	f
1	405	0.1025	411	0.1013	406	0.0025	416	0.0886
2	403	0.0055	398	0.0064	406	0.1091	413	0.0062
3	361	0.0000	362	0.0000	365	0.0000	392	0.0166
4	352	0.0055	357	0.0001	352	0.0050	376	0.0006
5	347	0.0001	348	0.0056	349	0.0005	359	0.0048
6	341	0.0000	347	0.0000	341	0.0000	352	0.0252
7	335	0.0278	334	0.0422	337	0.0183	339	0.0000
8	332	0.0136	329	0.0307	331	0.0007	326	0.0001
9	315	0.0020	320	0.0001	323	0.0410	319	0.0007
10	313	0.0176	319	0.0339	316	0.0168	318	0.0440

Table 9.1: First ten singlet excitations of $PtL^{1-4}Cl$, calculated by TD-DFT.

Excited state	**PtLF^{1}Cl**		**PtLF^{2}Cl**		**PtLF^{3}Cl**		**PtLF^{4}Cl**	
	λ /nm	f	λ /nm	f	λ /nm	f	λ /nm	f
1	394	0.0057	385	0.0077	392	0.0031	404	0.0074
2	381	0.0863	382	0.0902	379	0.0972	393	0.0205
3	355	0.0030	357	0.0000	359	0.0000	388	0.0758
4	348	0.0056	342	0.0060	345	0.0059	359	0.0004
5	338	0.0091	337	0.0189	342	0.0037	353	0.0038
6	327	0.0002	337	0.0001	331	0.0000	334	0.0281
7	325	0.0000	325	0.0000	325	0.0000	333	0.0008
8	323	0.0158	321	0.0382	322	0.0001	330	0.0011
9	305	0.0051	311	0.0027	320	0.0568	318	0.0000
10	304	0.1697	308	0.0415	307	0.1006	306	0.0033

Table 9.2: First ten singlet excitations of PtLF$^{1-4}$Cl, calculated by TD-DFT.

Excited state	$\mathbf{PtL^1Cl}$		$\mathbf{PtL^2Cl}$		$\mathbf{PtL^3Cl}$		$\mathbf{PtL^4Cl}$	
	λ /nm	f	λ /nm	f	λ /nm	f	λ /nm	f
1	378	0.0034	376	0.1750	378	0.0009	393	0.0065
2	375	0.1755	369	0.0039	375	0.1885	392	0.1567
3	343	0.0107	337	0.0112	341	0.0107	358	0.0073
4	332	0.0275	329	0.0000	334	0.0149	348	0.0251
5	326	0.0000	329	0.0490	326	0.0000	345	0.0355
6	317	0.0000	314	0.0000	318	0.0000	332	0.0042
7	304	0.0451	310	0.0653	306	0.1017	317	0.0423
8	301	0.0000	306	0.0000	303	0.0000	314	0.0058
9	294	0.1025	293	0.0604	299	0.0096	301	0.0036
10	286	0.2896	283	0.3336	287	0.3855	295	0.0739

Table 9.3: First ten singlet excitations of $PtL^{1-4}Cl$, calculated by TD-DFT in DCM.

Excited state	**PtLF^{1}Cl**		**PtLF^{2}Cl**		**PtLF^{3}Cl**		**PtLF^{4}Cl**	
	λ /nm	f	λ /nm	f	λ /nm	f	λ /nm	f
1	372	0.0034	358	0.0045	366	0.0007	386	0.0080
2	357	0.1432	353	0.1459	353	0.1599	370	0.1349
3	342	0.0098	336	0.0113	341	0.0109	355	0.0053
4	338	0.0084	335	0.0252	339	0.0109	350	0.0307
5	315	0.0003	315	0.0000	316	0.0000	328	0.0327
6	311	0.0042	312	0.0000	312	0.0000	324	0.0631
7	299	0.3264	300	0.0849	299	0.1378	324	0.0016
8	298	0.0564	293	0.0000	293	0.2656	312	0.0074
9	288	0.0012	291	0.3720	291	0.0000	295	0.0107
10	282	0.0862	277	0.1029	282	0.1710	294	0.0000

Table 9.4: First ten singlet excitations of PtLF$^{1-4}$Cl, calculated by TD-DFT in DCM.

Excited state	MeCN		DCM		THF		Chloroform		Toluene		CTC	
	λ /nm	f	λ /nm	f	λ /nm	f	λ /nm	f	λ /nm	f	λ /nm	f
1	375	0.0004	378	0.0006	379	0.0006	382	0.0008	389	0.0014	390	0.0015
2	371	0.1798	376	0.1885	377	0.1857	380	0.1889	389	0.1889	389	0.1840
3	339	0.0106	343	0.0109	343	0.0106	345	0.0106	349	0.0102	349	0.0098
4	336	0.0203	336	0.0253	336	0.0258	336	0.0287	337	0.0331	338	0.0000
5	324	0.0000	328	0.0000	329	0.0000	331	0.0000	337	0.0000	337	0.0325
6	314	0.0000	318	0.0000	320	0.0000	324	0.0000	334	0.0000	335	0.0000
7	307	0.0957	309	0.0982	309	0.0949	310	0.0952	323	0.0000	325	0.0000
8	302	0.0000	305	0.0000	305	0.0000	309	0.0000	321	0.0887	322	0.0843
9	298	0.0329	303	0.0142	304	0.0105	307	0.0044	313	0.0001	313	0.0000
10	296	0.3449	298	0.3582	299	0.3506	302	0.3435	312	0.2757	313	0.2527

Table 9.5: First ten singlet excitations of PtL^3Cl, calculated by TD-DFT. Calculations performed in vacuum for the geometry optimisation and the indicated solvent for the TD-DFT.

Excited state	MeCN		DCM		THF		Chloroform		Toluene		CTC	
	λ /nm	f	λ /nm	f	λ /nm	f	λ /nm	f	λ /nm	f	λ /nm	f
1	364	0.0004	367	0.0006	368	0.0006	370	0.0031	376	0.0017	377	0.0018
2	353	0.1423	355	0.1566	356	0.1553	358	0.0972	364	0.1670	365	0.1629
3	341	0.0244	341	0.0203	342	0.0108	343	0.0000	345	0.0107	345	0.0103
4	339	0.0106	341	0.0110	341	0.0190	342	0.0059	342	0.0127	342	0.0120
5	314	0.0000	317	0.0000	317	0.0000	321	0.0037	332	0.0000	333	0.0000
6	310	0.0000	314	0.0000	314	0.0000	316	0.0000	319	0.0000	319	0.0000
7	300	0.1233	301	0.1297	301	0.1262	302	0.0000	307	0.0000	307	0.0000
8	293	0.2906	298	0.2712	299	0.2568	299	0.0001	306	0.1289	307	0.1233
9	292	0.0000	294	0.0000	294	0.0000	296	0.0568	303	0.1159	303	0.0938
10	287	0.1369	291	0.1557	292	0.1603	295	0.1006	297	0.2866	297	0.2963

Table 9.6: First ten singlet excitations of $PtLF^3Cl$, calculated by TD-DFT. Calculations performed in vacuum for the geometry optimisation and the indicated solvent for the TD-DFT.

Excited state	Crystal structure geometry		MeCN		CTC	
	λ /nm	f	λ /nm	f	λ /nm	f
PtL^{3}Cl						
1	404	0.0060	374	0.0004	389	0.0015
2	394	0.0869	370	0.1817	389	0.1845
3	363	0.0003	342	0.0106	350	0.0098
4	350	0.0061	336	0.0106	338	0.0000
5	341	0.0001	326	0.0000	337	0.0298
6	335	0.0000	312	0.0000	336	0.0000
7	330	0.0600	307	0.0966	325	0.0000
8	322	0.0010	304	0.0000	322	0.0850
9	307	0.0236	298	0.0512	313	0.0001
10	294	0.0020	296	0.3393	312	0.2493
PtLF^{3}Cl						
1	391	0.0059	363	0.0003	376	0.0018
2	374	0.0669	351	0.1398	364	0.1630
3	362	0.0000	342	0.0106	346	0.0103
4	347	0.0066	341	0.0260	342	0.0108
5	337	0.0461	315	0.0000	333	0.0000
6	331	0.0001	310	0.0000	320	0.0000
7	322	0.0000	309	0.1175	308	0.0000
8	318	0.0016	300	0.2965	305	0.1265
9	314	0.0278	297	0.0000	303	0.1106
10	306	0.0008	296	0.1191	297	0.2828

Table 9.7: First ten singlet excitations of PtL^{3}Cl (top) and PtLF^{3}Cl (bottom), calculated by TD-DFT. The indicated solvent was modelled for both the geometry optimisation and TD-DFT.

Excited state	6-31G		6-31G[a]		cc-pVDZ		cc-pVTZ		cc-pVTZ[a]		aug-cc-pVDZ	
	λ /nm	f	λ /nm	f	λ /nm	f	λ /nm	f	λ /nm	f	λ /nm	f
1	401	0.0025	403	0.0025	406	0.0025	410	0.0021	408	0.0028	413	0.0024
2	397	0.1060	397	0.0973	406	0.1091	408	0.1112	405	0.1087	410	0.1121
3	357	0.0000	360	0.0000	365	0.0000	367	0.0000	366	0.0000	366	0.0000
4	352	0.0065	357	0.0063	352	0.0050	358	0.0046	355	0.0046	363	0.0043
5	340	0.0000	343	0.0000	349	0.0005	350	0.0000	348	0.0000	350	0.0000
6	339	0.0000	342	0.0000	341	0.0000	347	0.0000	343	0.0000	349	0.0000
7	335	0.0416	340	0.0468	337	0.0183	343	0.0261	341	0.0291	347	0.0309
8	325	0.0016	316	0.0025	331	0.0007	334	0.0002	326	0.0001	332	0.0001
9	317	0.0318	315	0.0376	323	0.0410	328	0.0401	318	0.0425	323	0.0428
10	316	0.0056	299	0.0064	316	0.0168	322	0.0006	298	0.0001	302	0.0003

Table 9.8: First ten singlet excitations of PtL^{3}Cl, calculated by TD-DFT. The ground state geometry was first optimised using the cc-pVDZ basis set (with the acknowledged exceptions), then the excitation energies obtained using TD-DFT with the indicated basis set. [a] denotes that the geometry was calculated in the indicated basis set.

Excited state	6-31G		6-31G[a]		cc-pVDZ		cc-pVTZ		cc-pVTZ[a]		aug-cc-pVDZ	
	λ /nm	f	λ /nm	f	λ /nm	f	λ /nm	f	λ /nm	f	λ /nm	f
1	386	0.0036	387	0.0037	392	0.0031	395	0.0024	393	0.0026	398	0.0027
2	376	0.0919	379	0.0844	379	0.0972	381	0.0986	378	0.0961	382	0.0978
3	352	0.0000	355	0.0000	359	0.0000	360	0.0000	359	0.0000	359	0.0000
4	345	0.0069	349	0.0068	345	0.0059	351	0.0050	348	0.0050	355	0.0046
5	336	0.2060	339	0.0301	342	0.0037	347	0.0096	345	0.0119	349	0.0149
6	328	0.0000	332	0.0000	331	0.0000	331	0.0000	329	0.0000	329	0.0000
7	325	0.0000	330	0.0000	325	0.0000	329	0.0000	323	0.0000	329	0.0000
8	319	0.0402	307	0.0450	322	0.0001	326	0.0000	309	0.0000	313	0.0000
9	315	0.0000	300	0.0002	320	0.0568	311	0.0568	306	0.0575	310	0.0523
10	303	0.1072	291	0.0081	307	0.1006	309	0.1706	292	0.2008	296	0.2121

Table 9.9: First ten singlet excitations of $PtLF^3Cl$, calculated by TD-DFT. The ground state geometry was first optimised using the cc-pVDZ basis set (except for the acknowledged exceptions), then the excitation energies obtained using TD-DFT with the indicated basis set. [a] denotes that the geometry was calculated in the indicated basis set.

Excited state	6-31G		cc-pVDZ		cc-pVTZ	
	λ /nm	f	λ /nm	f	λ /nm	f
PtL^{3}Cl						
1	403	0.0025	349	0.1755	352	0.0021
2	397	0.0973	349	0.0005	351	0.1662
3	360	0.0000	308	0.0096	313	0.0081
4	357	0.0063	302	0.0000	304	0.0365
5	343	0.0000	300	0.0348	304	0.0121
6	342	0.0000	290	0.0000	292	0.0000
7	340	0.0468	280	0.0001	281	0.0794
8	316	0.0025	279	0.0769	280	0.0003
9	315	0.0376	275	0.0147	278	0.0177
10	299	0.0064	273	0.0000	265	0.0001
PtLF^{3}Cl						
1	334	0.0007	339	0.0002	341	0.0003
2	326	0.1290	328	0.1583	329	0.1429
3	309	0.0114	305	0.0100	308	0.0085
4	301	0.0815	302	0.0294	305	0.0532
5	296	0.0000	298	0.0000	300	0.0000
6	282	0.0000	275	0.0001	277	0.0000
7	275	0.0350	275	0.0660	273	0.1003
8	273	0.0001	275	0.0000	272	0.1004
9	266	0.0000	270	0.1040	269	0.0000
10	264	0.1074	266	0.0000	264	0.0000

Table 9.10: First ten singlet excitations of PtL^{3}Cl (top) and PtLF^{3}Cl (bottom), calculated by TD-DFT using CAM-B3LYP. The basis set used for all atoms except Pt (both for geometry optimisation and TD-DFT) is indicated in the table.

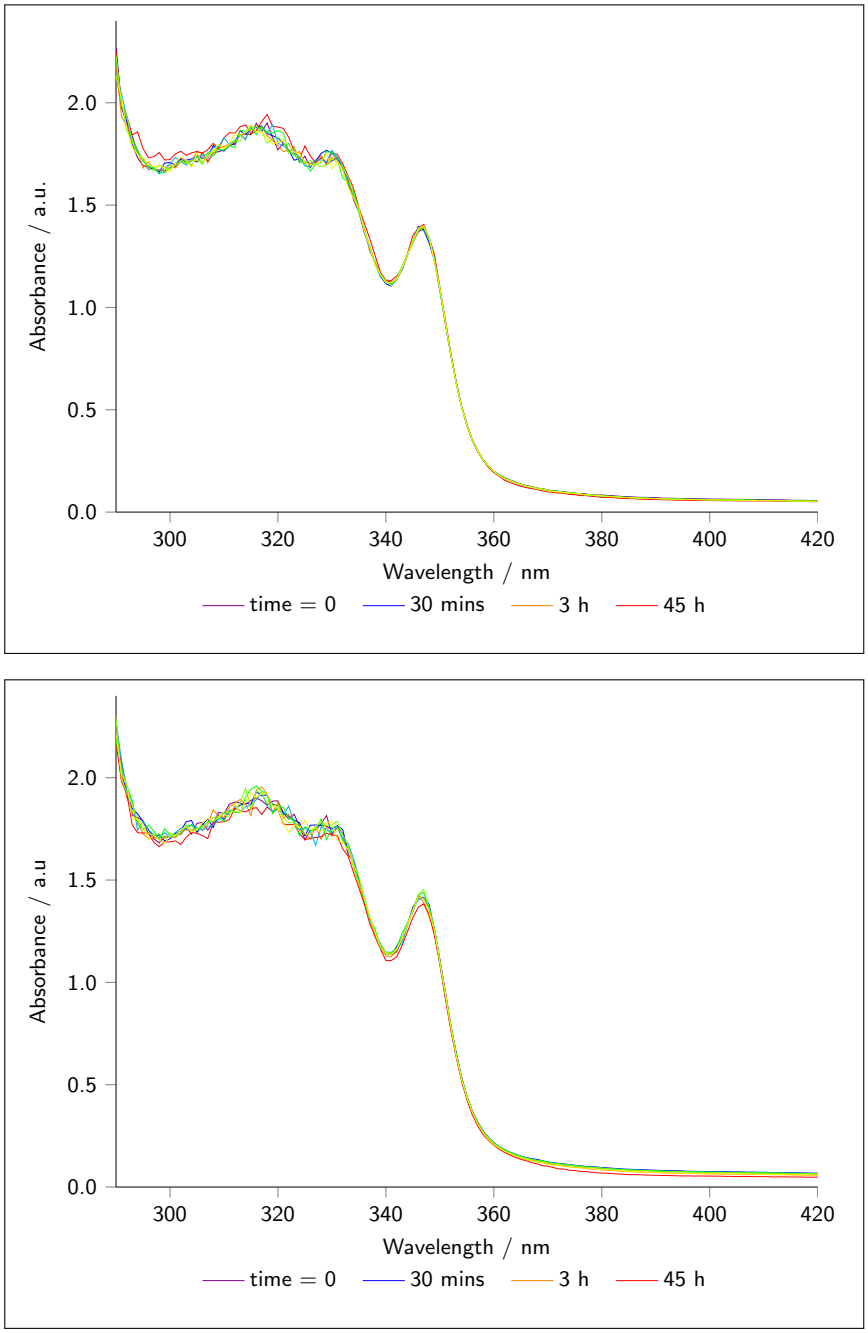

Figure 9.2: UV-vis absorption spectra of PtL^5Cl_3 kept in solution, in ambient conditions (top) and in the dark (bottom) between measurements. Measurements were taken every 30 minutes up to 3 hours, then one spectrum is shown after 45 h. The progress of the decomposition can be seen as you move from purple plots to red.

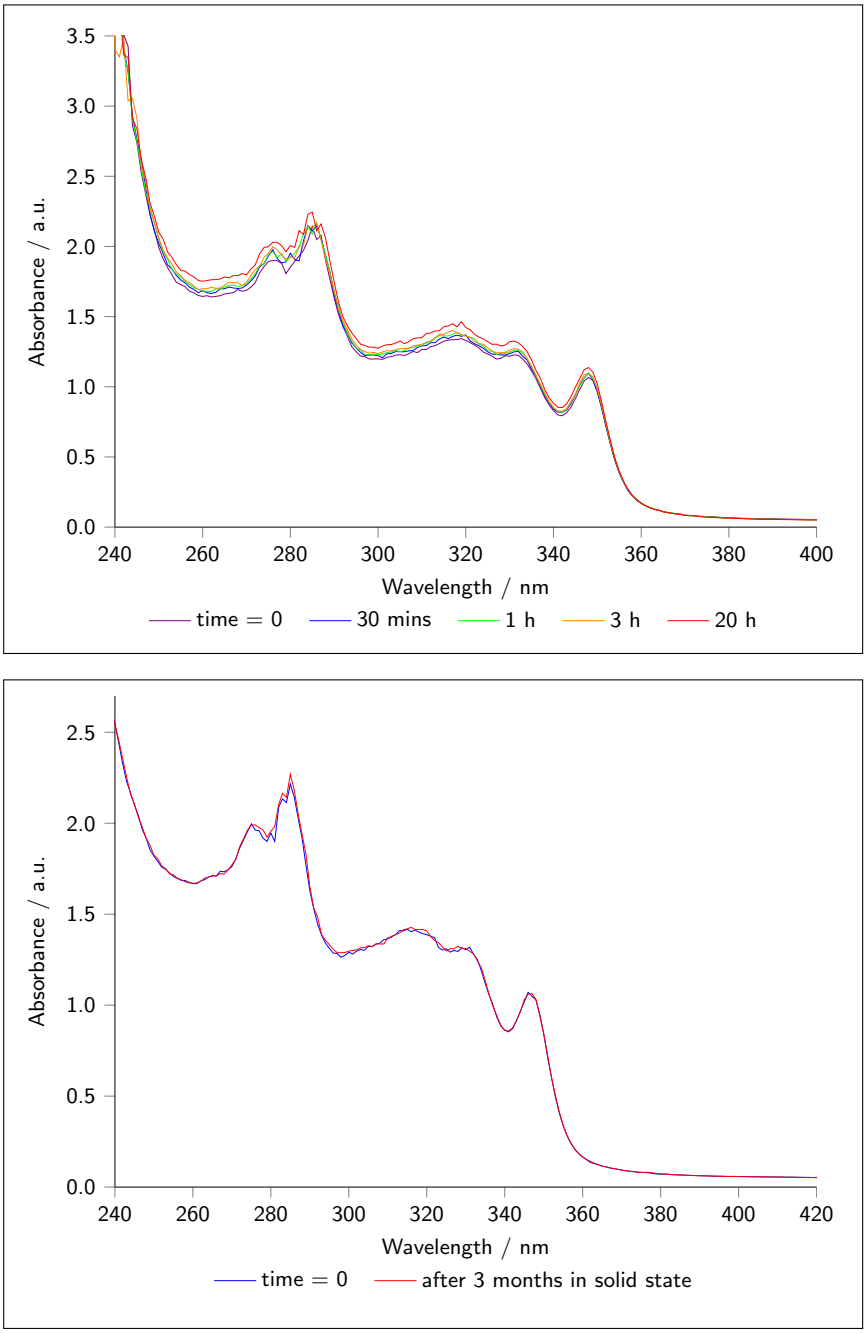

Figure 9.3: UV-vis absorption spectra of PtL^5Cl_3.
Top: sample in chloroform, heated at reflux, with exclusion of light for various time points up to 20 h.
Bottom: sample kept in ambient conditions in the solid state and compared to the absorption spectrum of a newly made sample.

Excited state	$\mathbf{PtL^5Cl}$		$\mathbf{PtL^5Cl_3}$		$\mathbf{PtL^5Br}$		$\mathbf{PtL^5Br_3}$	
	λ /nm	f	λ /nm	f	λ /nm	f	λ /nm	f
1	377	0.1576	419	0.0006	380	0.0071	484	0.0021
2	377	0.0036	395	0.0000	378	0.1489	439	0.0011
3	343	0.0107	385	0.0002	343	0.0097	437	0.0000
4	331	0.0236	381	0.0020	333	0.0000	435	0.0002
5	330	0.0007	357	0.0000	331	0.0179	415	0.0069
6	320	0.0000	354	0.0071	330	0.0000	380	0.0207
7	306	0.0234	348	0.0132	319	0.0000	377	0.0000
8	306	0.0468	318	0.1175	306	0.0767	361	0.0013
9	299	0.0062	311	0.0353	300	0.0033	337	0.0509
10	285	0.3238	302	0.0072	287	0.1527	326	0.0006

Table 9.11: First ten singlet excitations of PtL^5Cl, PtL^5Cl_3, PtL^5Br and PtL^5Br_3, calculated by TD-DFT in DCM.

9.7 Chapter 3

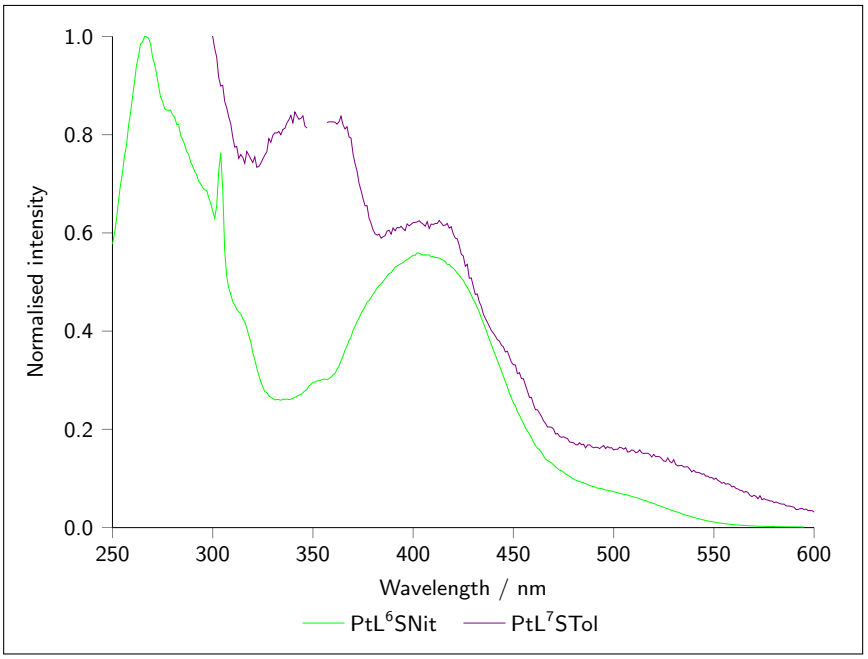

Figure 9.4: Normalised excitation spectra of PtL^{6}SNit and PtL^{7}STol in DCM at 298 K.

9.8 Chapter 4

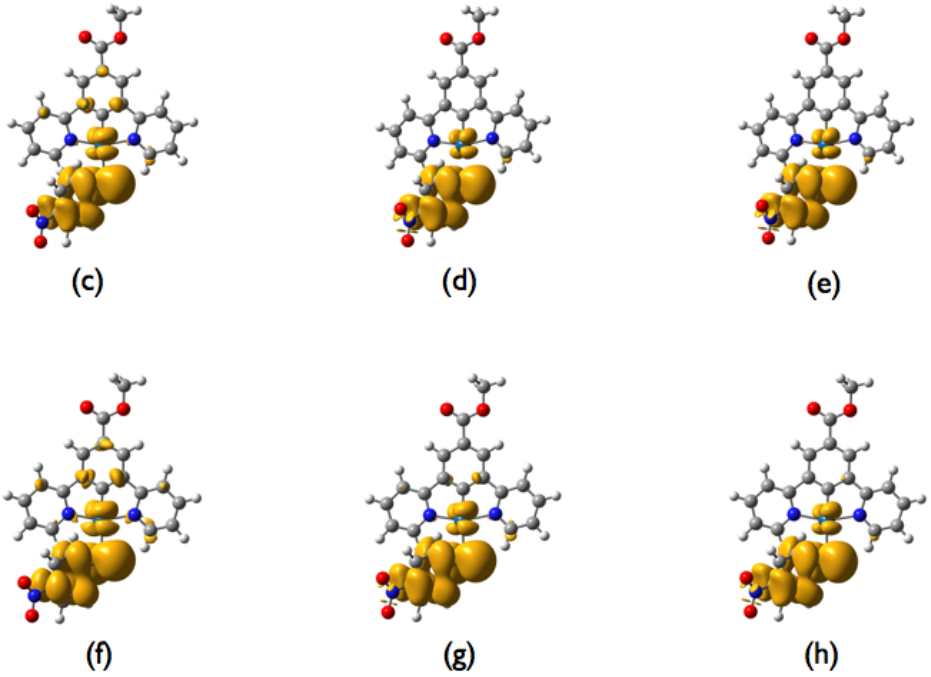

Figure 9.5: Density difference plots for $S_0 \rightarrow T_1$ excitation at the T_1 geometry of PtL^{8}SNit. Plots show electron depletion. (c) geometry calculated in vacuum, TD-DFT in DCM, (d) geometry in DCM, TD-DFT in vacuum, (e) geometry and TD-DFT both in DCM, (f) geometry calculated in vacuum, TD-DFT in hexane, (g) geometry in hexane, TD-DFT in vacuum, (h) geometry and TD-DFT both in hexane.

Excited state	**PtL^{8}SMe**		**PtL^{8}SPh**		**PtL^{8}STol**		**PtL^{8}SAni**		**PtL^{8}SNit**	
	λ /nm	f	λ /nm	f	λ /nm	f	λ /nm	f	λ / nm	f
1	520	0.0062	512	0.0267	520	0.0351	542	0.0371	455	0.0241
2	485	0.0064	481	0.0136	491	0.0157	513	0.0151	423	0.0066
3	382	0.0088	367	0.0015	373	0.0017	386	0.0033	385	0.5602
4	371	0.0023	358	0.0177	362	0.0149	367	0.0062	352	0.0043
5	369	0.0458	351	0.0895	355	0.0777	364	0.0522	348	0.1152
6	352	0.0122	348	0.0356	353	0.0482	359	0.0737	344	0.0168
7	351	0.0030	345	0.0088	346	0.0075	346	0.0060	333	0.0136
8	347	0.0486	333	0.0088	336	0.0056	346	0.0084	332	0.0110
9	345	0.0114	331	0.0061	334	0.0016	335	0.0026	326	0.0025
10	335	0.0562	330	0.0261	331	0.0295	332	0.0094	318	0.0040

Table 9.12: First ten singlet excitations of the PtL^{8}SR series of complexes in DCM calculated by TD-DFT.

Excited state	**PtL^{5}SMe**		**PtL^{5}SPh**		**PtL^{5}STol**		**PtL^{5}SAni**		**PtL^{5}SNit**	
	λ /nm	f	λ /nm	f	λ /nm	f	λ /nm	f	λ / nm	f
1	511	0.0031	501	0.0192	511	0.0236	531	0.0252	445	0.0336
2	478	0.0065	473	0.0179	485	0.0187	505	0.0182	417	0.0145
3	382	0.0045	367	0.0017	374	0.0021	385	0.0028	388	0.5021
4	373	0.0766	361	0.0068	364	0.0068	369	0.0052	358	0.0040
5	371	0.0004	356	0.1126	358	0.1040	363	0.0957	352	0.1322
6	355	0.0010	345	0.0046	348	0.0105	357	0.0183	342	0.0145
7	350	0.0455	341	0.0165	345	0.0134	345	0.0086	333	0.0164
8	347	0.0028	334	0.0035	335	0.0004	335	0.0016	332	0.0046
9	343	0.0115	331	0.0310	332	0.0318	332	0.0253	327	0.0034
10	335	0.0506	328	0.0075	330	0.0120	330	0.0181	323	0.0221

Table 9.13: First ten singlet excitations of the PtL^{5}SR series of complexes in DCM calculated by TD-DFT.

Excited state	**PtL^{8}SMe**		**PtL^{8}SPh**		**PtL^{8}STol**		**PtL^{8}SAni**		**PtL^{8}SNit**	
	λ /nm	f	λ /nm	f	λ /nm	f	λ /nm	f	λ / nm	f
1	386	0.0085	383	0.0387	390	0.0415	400	0.0419	356	0.1336
2	346	0.0541	349	0.0767	354	0.0680	363	0.0586	336	0.5342
3	326	0.0159	316	0.0142	317	0.0158	318	0.0152	324	0.1304
4	318	0.1026	309	0.0727	311	0.0821	312	0.0944	317	0.0038
5	313	0.0087	307	0.0131	307	0.0123	307	0.0116	306	0.0371
6	300	0.0652	298	0.0629	298	0.0640	299	0.0586	305	0.0268
7	298	0.0115	291	0.0239	293	0.0232	297	0.0080	304	0.0007
8	290	0.0052	283	0.0094	287	0.0230	293	0.0481	298	0.0525
9	289	0.0138	283	0.0276	284	0.0149	287	0.0050	277	0.0014
10	283	0.0092	280	0.0069	281	0.0047	282	0.0603	276	0.0138

Table 9.14: First ten singlet excitations of the PtL^{8}SR series of complexes in DCM calculated by TD-DFT with CAM-B3LYP.

Excited state	**PtL^{5}SMe**		**PtL^{5}SPh**		**PtL^{5}STol**		**PtL^{5}SAni**		**PtL^{5}SNit**	
	λ /nm	f	λ /nm	f	λ /nm	f	λ /nm	f	λ / nm	f
1	381	0.0046	380	0.0204	385	0.0279	394	0.0276	353	0.1807
2	345	0.0876	348	0.0995	354	0.0975	361	0.0817	337	0.4484
3	329	0.0017	319	0.0026	318	0.0024	320	0.0018	327	0.1836
4	321	0.1020	313	0.0885	313	0.0870	315	0.1056	319	0.0038
5	310	0.0103	304	0.0164	304	0.0174	304	0.0176	305	0.0203
6	299	0.0669	296	0.0678	296	0.0741	298	0.0497	304	0.0002
7	295	0.0176	289	0.0144	293	0.0123	295	0.0141	301	0.0269
8	291	0.0150	284	0.0161	288	0.0263	293	0.0430	296	0.0573
9	287	0.0063	281	0.0049	282	0.0188	284	0.0095	277	0.0005
10	283	0.0122	280	0.0415	282	0.0214	282	0.0124	277	0.0208

Table 9.15: First ten singlet excitations of the PtL^{5}SR series of complexes in DCM calculated by TD-DFT with CAM-B3LYP.

Excited state	THF		DCM		MeCN	
	λ /nm	f	λ /nm	f	λ /nm	f
PtL^{8}SNit						
1	457	0.0227	455	0.0241	444	0.0285
2	426	0.0063	423	0.0066	413	0.0071
3	384	0.5579	385	0.5602	385	0.5455
4	353	0.0042	352	0.0043	350	0.0040
5	348	0.1138	348	0.1152	346	0.1061
6	344	0.0164	344	0.0168	343	0.0169
7	334	0.0032	333	0.0136	332	0.0226
8	332	0.0213	332	0.0110	326	0.0005
9	326	0.0028	326	0.0025	325	0.0015
10	320	0.0027	318	0.0040	318	0.0113
PtL^{8}SPh						
1	515	0.0264	512	0.0267	497	0.0265
2	484	0.0132	481	0.0136	466	0.0143
3	369	0.0016	367	0.0015	358	0.0010
4	359	0.0171	358	0.0177	354	0.0183
5	352	0.0851	351	0.0895	348	0.0882
6	349	0.0389	348	0.0356	344	0.0086
7	346	0.0069	345	0.0088	340	0.0327
8	333	0.0052	333	0.0088	332	0.0173
9	332	0.0048	331	0.0061	328	0.0122
10	331	0.0299	330	0.0261	325	0.0048

Table 9.16: First ten singlet excitations of PtL^{8}SNit (top) and PtLF^{8}SPh (bottom) calculated by TD-DFT in the indicated solvent for both geometry optimisation and TD-DFT.

Excited state	**Cl**		**STol**		**SNit**	
	λ /nm	f	λ /nm	f	λ /nm	f
PtL^{6}R						
1	409	0.0025	589	0.0243	509	0.0102
2	394	0.1470	531	0.0237	454	0.0088
3	369	0.0078	416	0.0021	390	0.1624
4	349	0.0407	398	0.0026	380	0.3409
5	346	0.0000	377	0.0773	368	0.0159
6	344	0.0000	372	0.0031	368	0.1104
7	321	0.0002	369	0.0213	367	0.0326
8	321	0.0000	359	0.0090	350	0.0448
9	312	0.0661	353	0.0030	342	0.0057
10	297	0.3784	347	0.0434	341	0.0038
PtL^{9}R						
1	369	0.0664	503	0.0376	460	0.0686
2	367	0.0032	493	0.0130	437	0.0078
3	355	0.0219	373	0.0072	392	0.4710
4	353	0.0091	366	0.0236	360	0.0027
5	342	0.0000	356	0.0025	359	0.0045
6	338	0.0028	354	0.0053	352	0.0122
7	332	0.0146	343	0.0197	347	0.0542
8	307	0.1893	329	0.0403	338	0.0222
9	273	0.0199	323	0.0328	322	0.0249
10	268	0.0213	316	0.1399	316	0.0381

Table 9.17: First ten singlet excitations of PtL^{6}STol, PtL^{6}SNit, PtL^{6}Cl, PtL^{9}STol, PtL^{9}SNit and PtL^{9}Cl at the ground state geometry, calculated by TD-DFT in DCM.

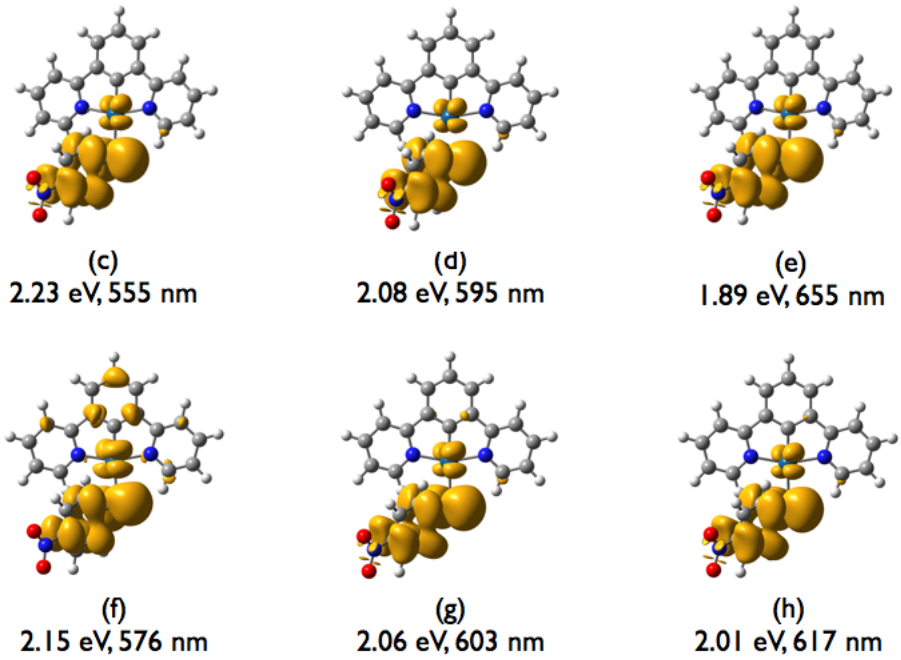

Figure 9.6: Density difference plots for $S_0 \rightarrow T_1$ excitation at the T_1 geometry of PtL^{5}SNit. Plots show electron depletion. (c) geometry calculated in vacuum, TD-DFT in DCM, (d) geometry in DCM, TD-DFT in vacuum, (e) geometry and TD-DFT both in DCM, (f) geometry calculated in vacuum, TD-DFT in hexane, (g) geometry in hexane, TD-DFT in vacuum, (h) geometry and TD-DFT both in hexane.

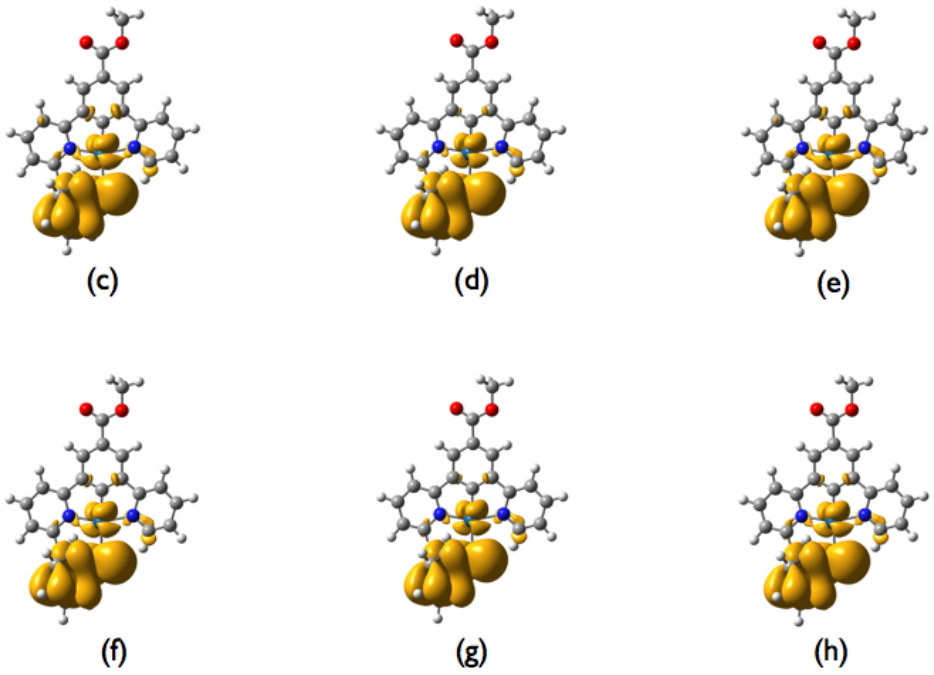

Figure 9.7: Density difference plots for $S_0 \rightarrow T_1$ excitation at the T_1 geometry of PtL^{8}SPh. Plots show electron depletion. (c) geometry calculated in vacuum, TD-DFT in DCM, (d) geometry in DCM, TD-DFT in vacuum, (e) geometry and TD-DFT both in DCM, (f) geometry calculated in vacuum, TD-DFT in hexane, (g) geometry in hexane, TD-DFT in vacuum, (h) geometry and TD-DFT both in hexane.

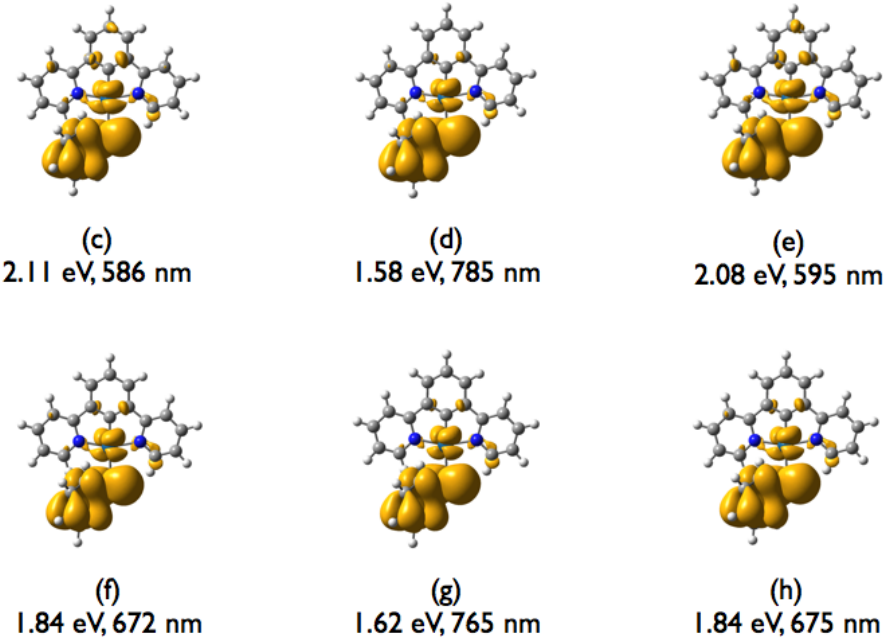

Figure 9.8: Density difference plots for $S_0 \rightarrow T_1$ excitation at the T_1 geometry of PtL^5SPh. Plots show electron depletion. (c) geometry calculated in vacuum, TD-DFT in DCM, (d) geometry in DCM, TD-DFT in vacuum, (e) geometry and TD-DFT both in DCM, (f) geometry calculated in vacuum, TD-DFT in hexane, (g) geometry in hexane, TD-DFT in vacuum, (h) geometry and TD-DFT both in hexane.

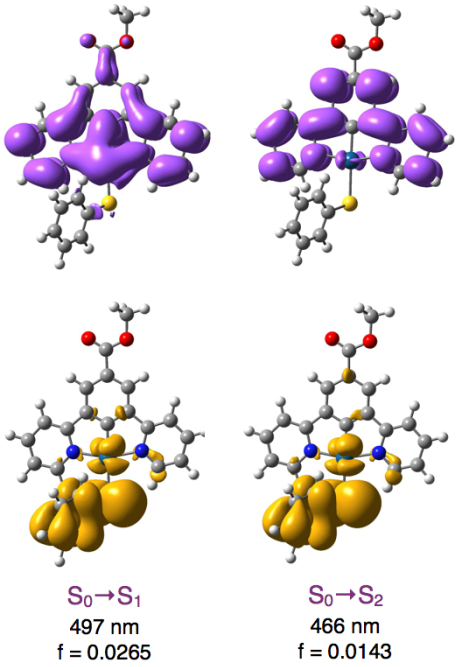

Figure 9.9: Density difference plots for the first two excitations of PtL^{8}SPh, at the ground state geometry, in MeCN, showing the oscillator strength for each transition (f).

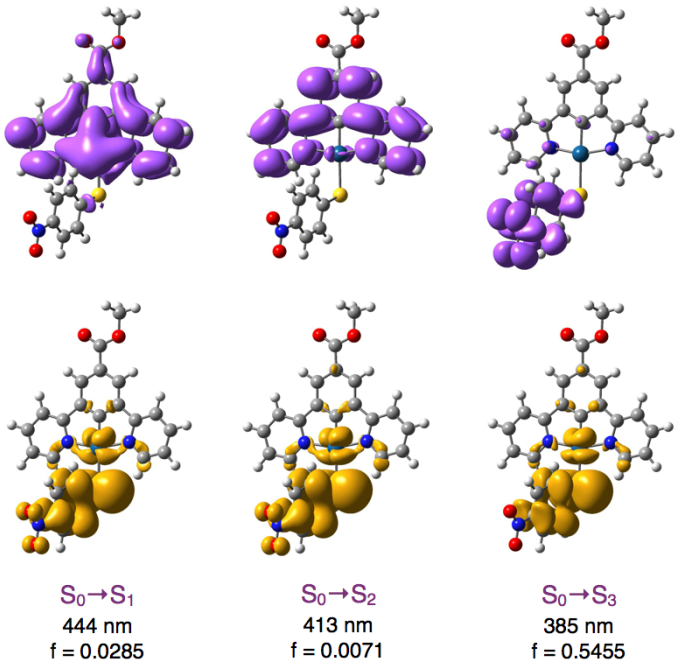

Figure 9.10: Density difference plots for the first three excitations of PtL^{8}SNit, at the ground state geometry, in MeCN, showing the oscillator strength for each transition (f).

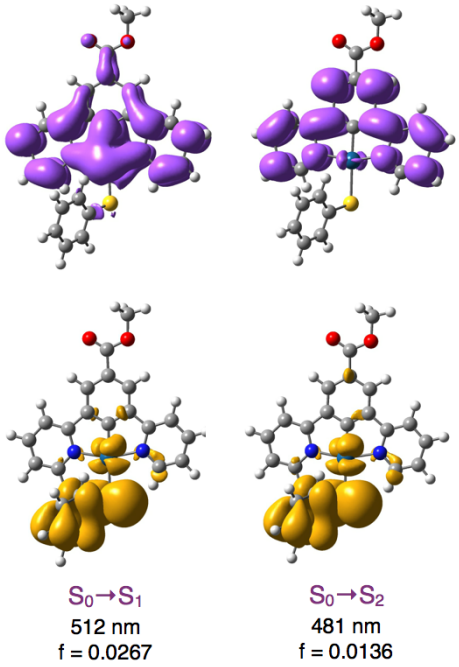

Figure 9.11: Density difference plots for the first two excitations of PtL^{8}SPh, at the ground state geometry, in DCM, showing the oscillator strength for each transition (f).

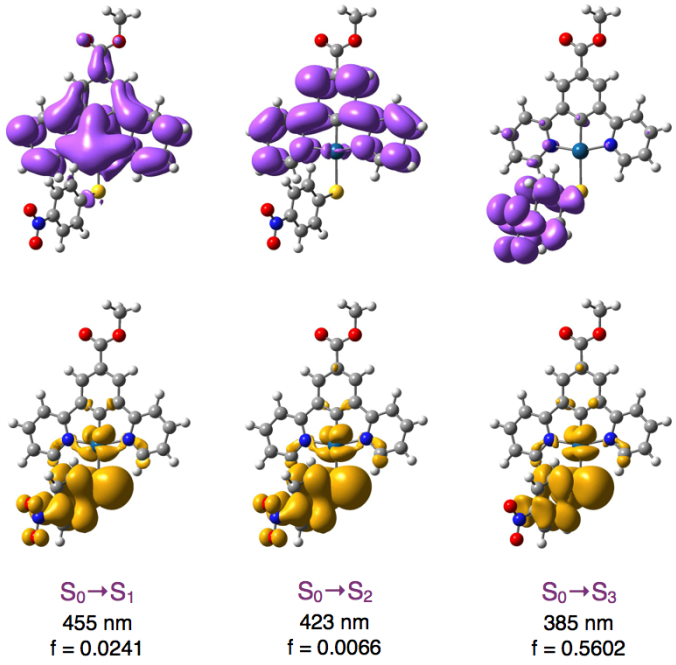

Figure 9.12: Density difference plots for the first three excitations of PtL^{8}SNit, at the ground state geometry, in DCM, showing the oscillator strength for each transition (f).

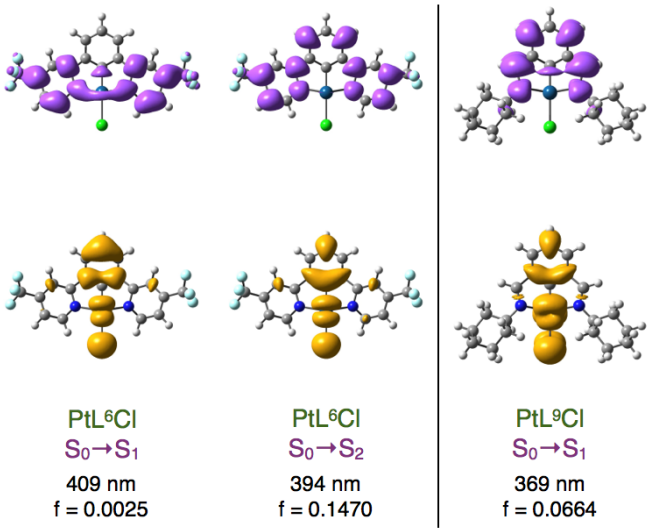

Figure 9.13: Density difference plots for the first excitation of PtL^{9}Cl and the first two excitations of PtL^{6}Cl, at the ground state geometry, in DCM, showing the oscillator strength for each transition (f).

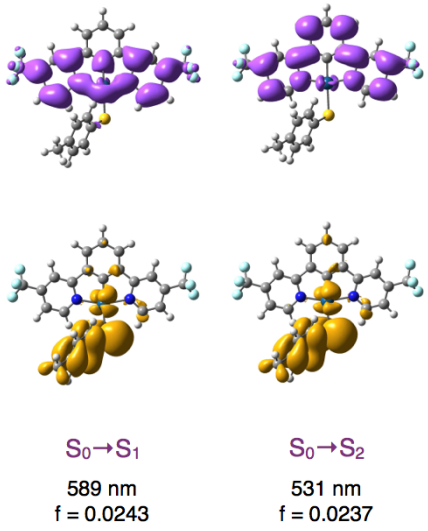

Figure 9.14: Density difference plots for the first two excitations of PtL^{6}STol, at the ground state geometry, in DCM, showing the oscillator strength for each transition (f).

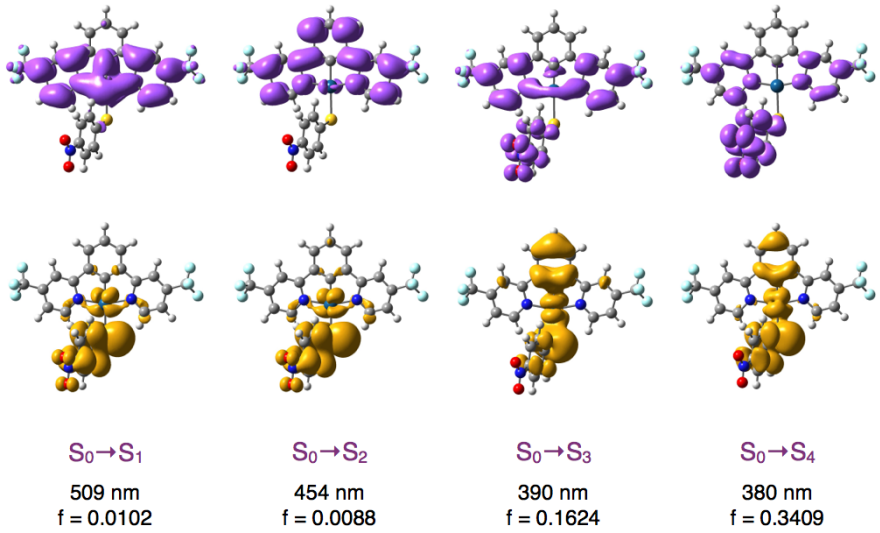

Figure 9.15: Density difference plots for the first three excitations of PtL^{6}SNit, at the ground state geometry, in DCM, showing the oscillator strength for each transition (f).

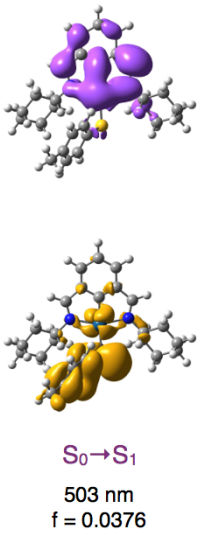

Figure 9.16: Density difference plots for the first excitation of PtL^{9}STol, at the ground state geometry, in DCM, showing the oscillator strength for each transition (f).

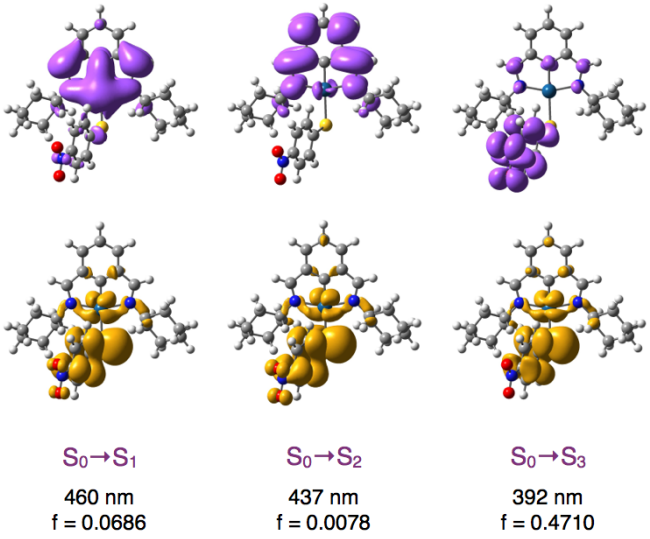

Figure 9.17: Density difference plots for the first three excitations of PtL^{9}SNit, at the ground state geometry, in DCM, showing the oscillator strength for each transition (f).

Excited state	Cl		STol		SNit	
	λ /nm	f	λ /nm	f	λ /nm	f
PtL^{6}R						
1	353	0.0001	425	0.0232	380	0.0042
2	345	0.2177	379	0.0788	343	0.1419
3	320	0.0140	337	0.0018	337	0.1139
4	307	0.0732	327	0.0883	334	0.4534
5	291	0.0000	322	0.0117	330	0.0934
6	287	0.0000	313	0.0103	320	0.0357
7	280	0.0570	306	0.0881	307	0.0917
8	279	0.0941	302	0.0101	304	0.0000
9	276	0.0000	298	0.0414	290	0.0005
10	269	0.0931	294	0.0148	287	0.0183
PtL^{9}R						
1	338	0.0020	392	0.0483	373	0.1517
2	337	0.0794	367	0.0370	342	0.1434
3	324	0.0144	330	0.0105	339	0.3946
4	321	0.0432	328	0.0009	328	0.0023
5	302	0.0002	322	0.0048	326	0.0155
6	295	0.0006	312	0.0570	322	0.0051
7	282	0.1217	301	0.0065	308	0.0678
8	276	0.0216	299	0.0625	304	0.0009
9	269	0.0642	293	0.0547	296	0.0018
10	267	0.1042	281	0.0846	283	0.0548

Table 9.18: First ten singlet excitations of PtL^{6}STol, PtL^{6}SNit, PtL^{6}Cl, PtL^{9}STol, PtL^{9}SNit and PtL^{9}Cl in DCM. Calculated by TD-DFT with CAM-B3LYP at the ground state geometry.

9.9 Chapter 5

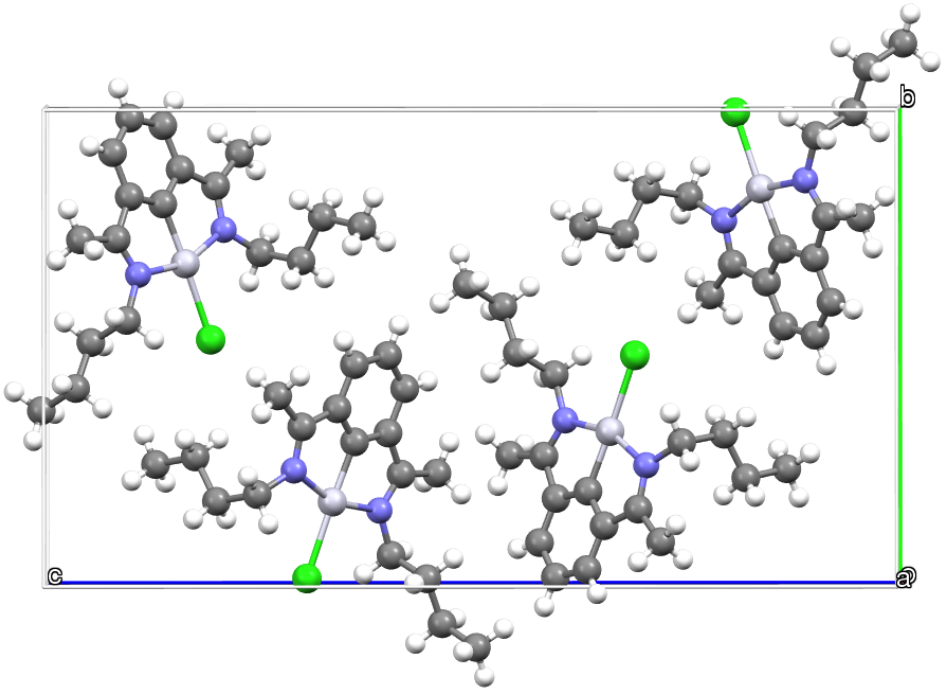

Figure 9.18: Crystal packing of $PtL^{Ket^nBu}Cl$.

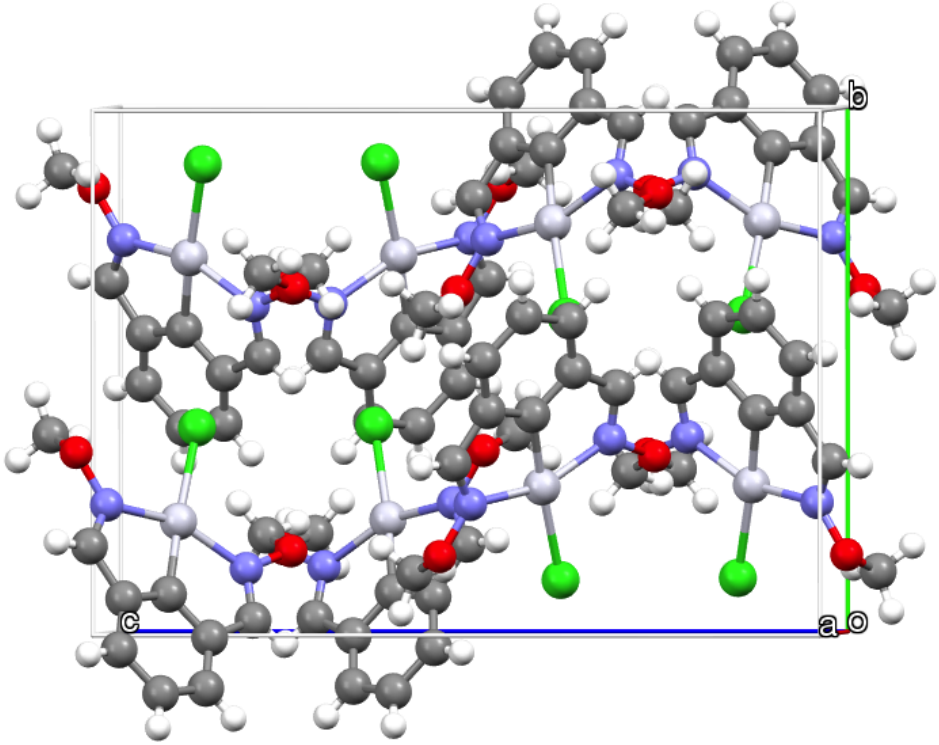

Figure 9.19: Crystal packing of $PtL^{OxIm}Cl$.

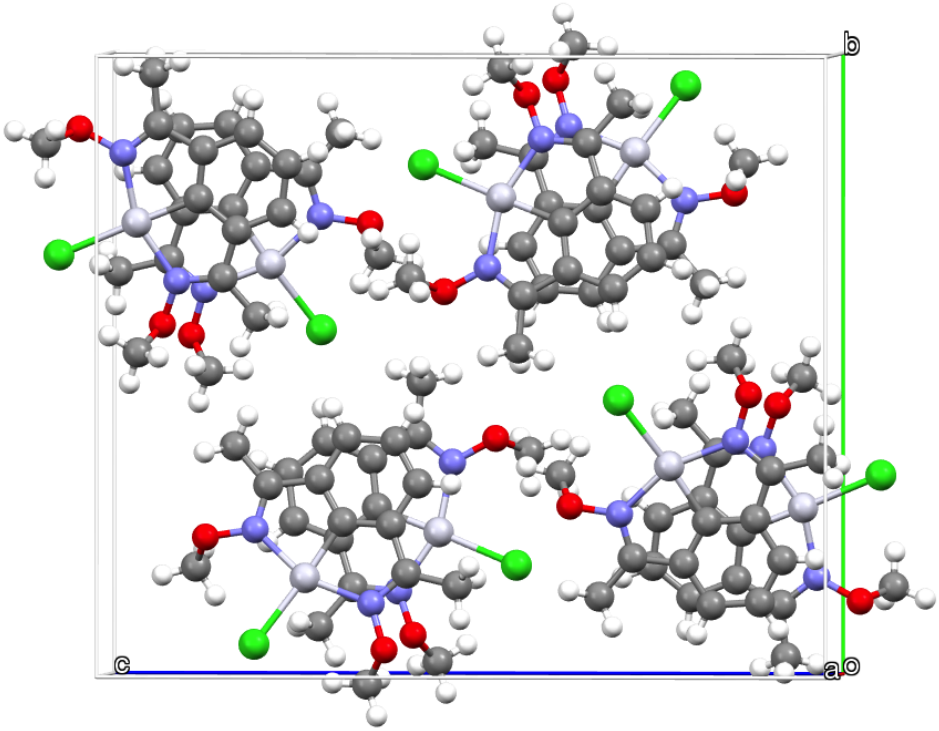

Figure 9.20: Crystal packing of $PtL^{OxKet}Cl$.

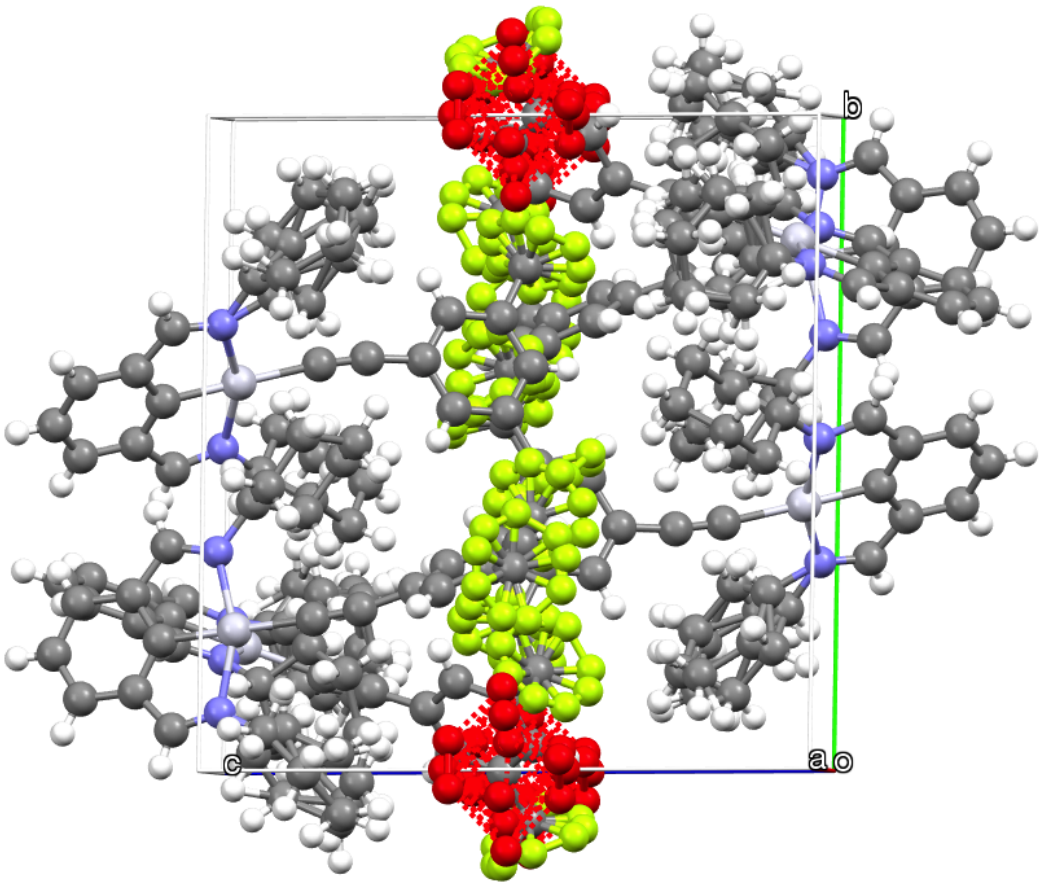

Figure 9.21: Crystal packing of $PtL^{ImCy}C_2Ar$.

Excited state	$\mathbf{PtL^{ImCy}Cl}$		$\mathbf{PtL^{KetCy}Cl}$		$\mathbf{PtL^{OxKet}Cl}$		$\mathbf{PtL^{ImPhCF_3}Cl}$	
	λ /nm	f	λ /nm	f	λ /nm	f	λ /nm	f
1	369	0.0664	369	0.0763	363	0.0529	408	0.1503
2	367	0.0032	360	0.0009	356	0.0015	397	0.0018
3	355	0.0219	344	0.0111	342	0.0181	385	0.0067
4	353	0.0091	344	0.0362	336	0.0129	378	0.0021
5	342	0.0000	344	0.0000	332	0.0035	375	0.0015
6	338	0.0028	328	0.0000	330	0.0000	371	0.0006
7	332	0.0146	325	0.0007	327	0.0133	366	0.0092
8	307	0.1893	313	0.1776	305	0.1973	337	0.2372
9	273	0.0199	269	0.0164	271	0.0087	315	0.1202
10	268	0.0213	266	0.0003	267	0.0012	302	0.1428

Table 9.19: First ten singlet excitations of $PtL^{ImCy}Cl$, $PtL^{KetCy}Cl$, $PtL^{OxKet}Cl$ and $PtL^{ImPhCF_3}Cl$ calculated by TD-DFT.

Excited state	$\mathbf{PtL^{Im^tBu}Cl}$		$\mathbf{PtL^{Im^nBu}Cl}$		$\mathbf{PtL^{Ket^nBu}Cl}$		$\mathbf{PtL^{OxIm}Cl}$	
	λ /nm	f	λ /nm	f	λ /nm	f	λ /nm	f
1	363	0.0719	370	0.0541	369	0.0456	363	0.0099
2	359	0.0028	370	0.0039	364	0.0028	353	0.0368
3	352	0.0109	358	0.0247	355	0.0539	350	0.0646
4	345	0.0090	356	0.0095	349	0.0108	340	0.0139
5	343	0.0000	345	0.0001	341	0.0001	332	0.0000
6	338	0.0000	340	0.0021	336	0.0017	317	0.0000
7	331	0.0000	333	0.0093	329	0.0107	310	0.0000
8	306	0.1770	308	0.2085	312	0.1831	297	0.2206
9	287	0.0000	274	0.0198	270	0.0141	276	0.0510
10	282	0.0116	270	0.0322	264	0.0448	275	0.0000

Table 9.20: First ten singlet excitations of $PtL^{Im^tBu}Cl$, $PtL^{Im^nBu}Cl$, $PtL^{Ket^nBu}Cl$ and $PtL^{OxIm}Cl$ calculated by TD-DFT.

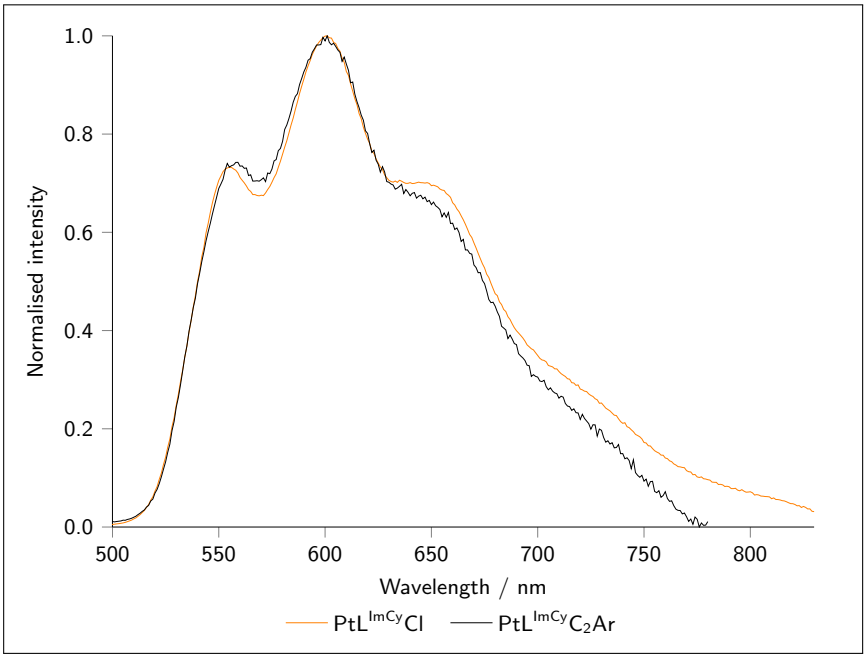

Figure 9.22: Normalised emission spectra of $PtL^{ImCy}Cl$ and $PtL^{ImCy}C_2Ar$ in degassed DCM at 298 K.

Excited state	λ /nm	f
1	390.62	0.0894
2	376.40	0.0477
3	372.60	0.0176
4	358.58	0.0042
5	354.09	0.0197
6	350.42	0.0132
7	337.11	0.0004
8	310.31	0.4899
9	300.01	0.0202
10	299.81	0.0268

Table 9.21: First ten singlet excitations of $PtL^{ImCy}C_2Ar$, calculated by TD-DFT.

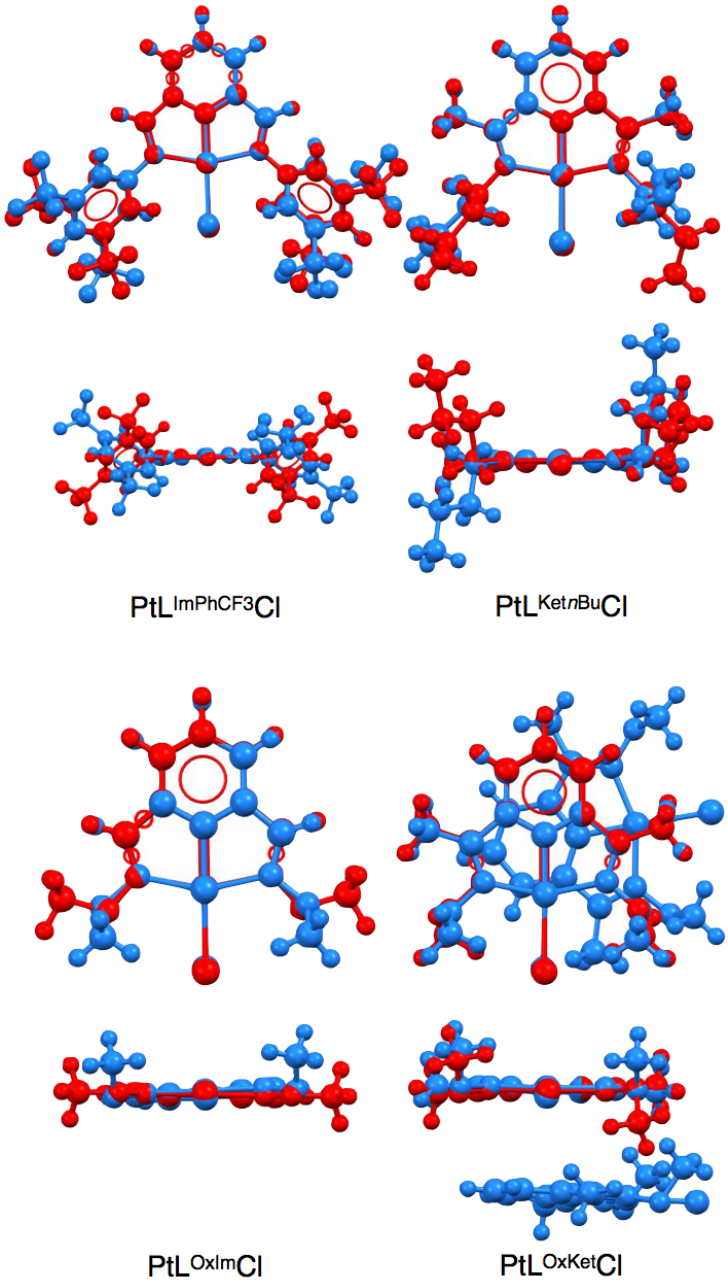

Figure 9.23: Overlay of crystal structure (blue) and S_0 DFT (red) geometries of $PtL^{ImPhCF_3}Cl$, $PtL^{KetnBu}Cl$, $PtL^{OxIm}Cl$ and $PtL^{OxKet}Cl$. DFT calculations performed with PBE0, in DCM.

9.10 Chapter 6

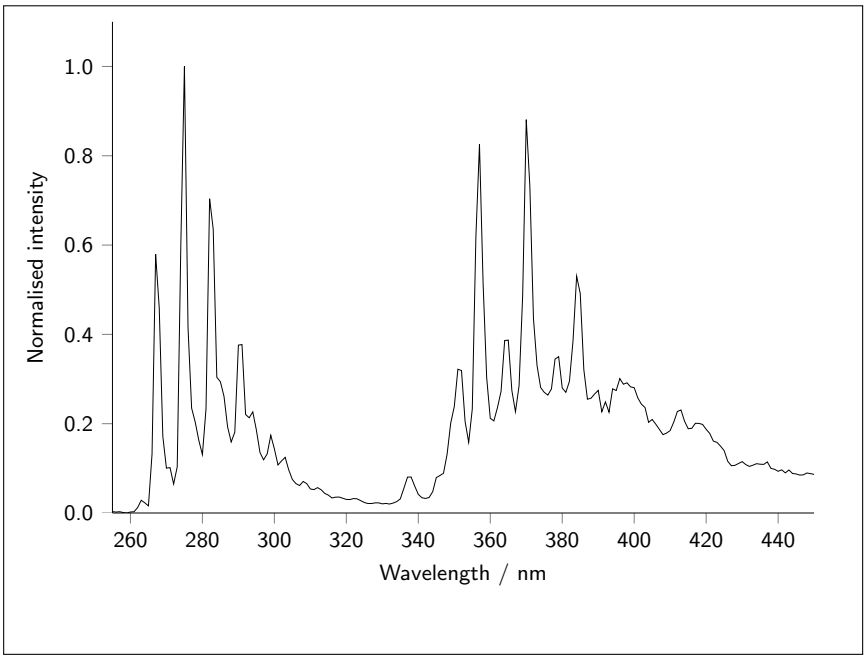

Figure 9.24: Emission spectrum of ArH, at 77 K, in an MP glass.

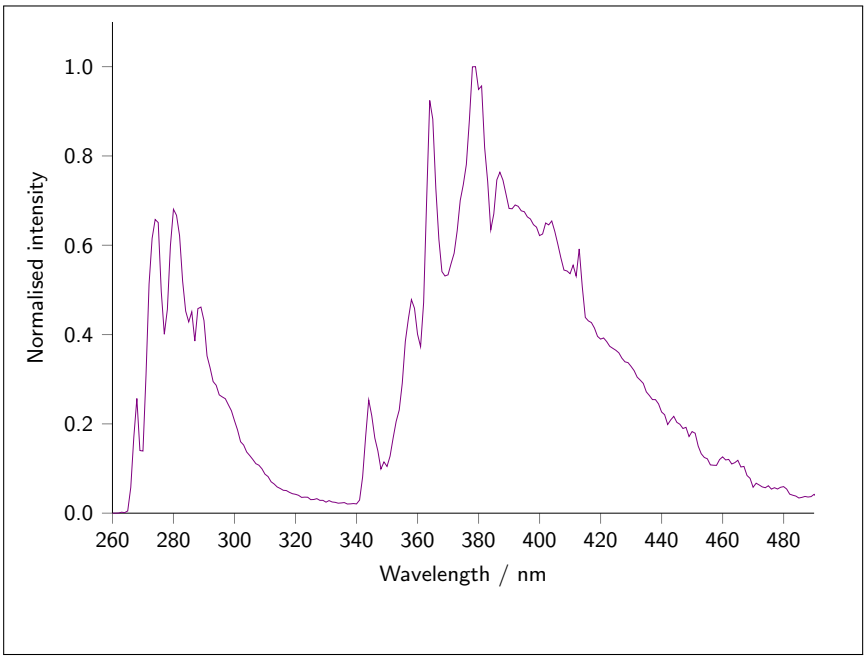

Figure 9.25: Emission spectrum of ArMe, at 77 K, in MP glass.

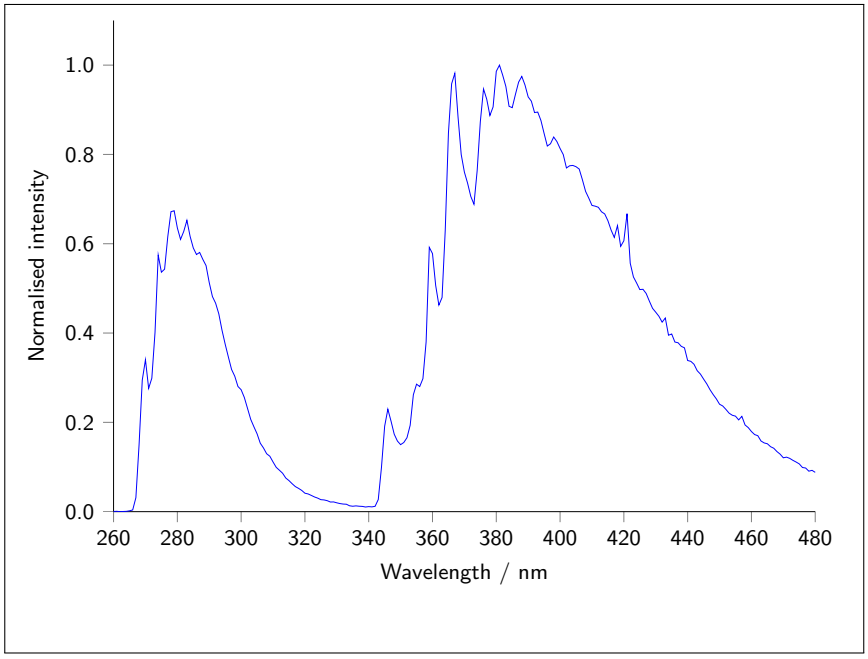

Figure 9.26: Emission spectrum of ArMe2, at 77 K, in MP glass.

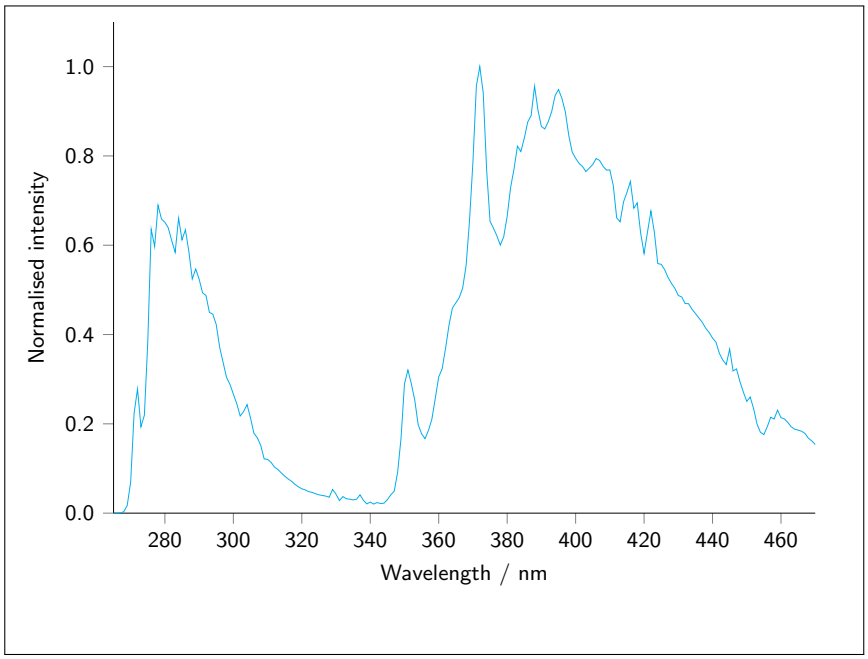

Figure 9.27: Emission spectrum of ArMe2a, at 77 K, in MP glass.

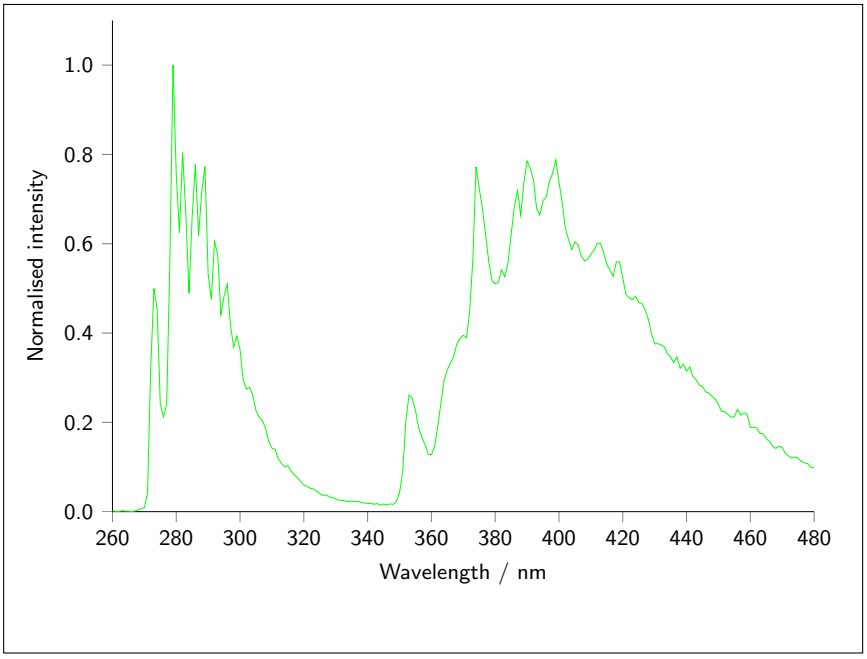

Figure 9.28: Emission spectrum of ArMe2b, at 77 K, in MP glass.

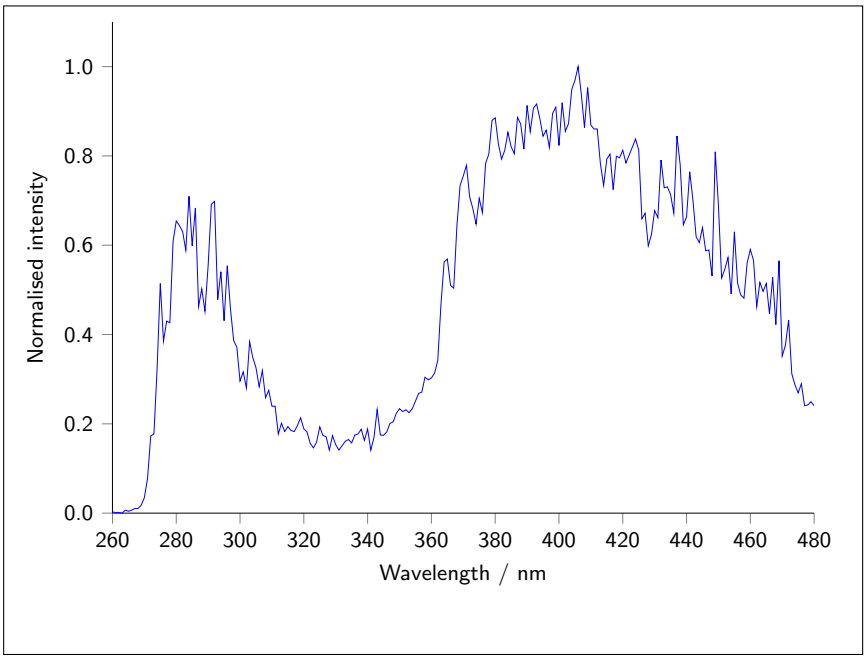

Figure 9.29: Emission spectrum of ArMe3, at 77 K, in MP glass.

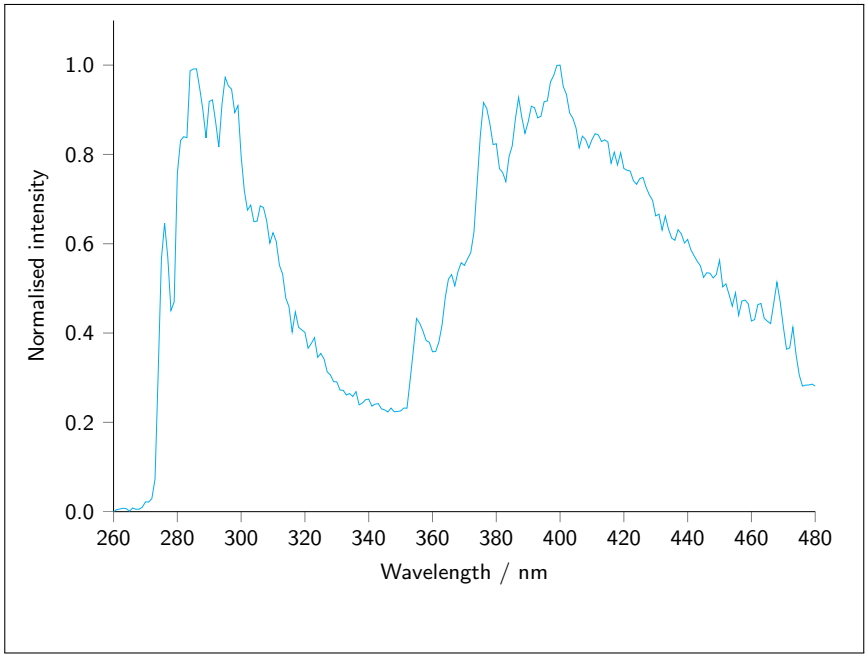

Figure 9.30: Emission spectrum of ArMe3a, at 77 K, in MP glass.

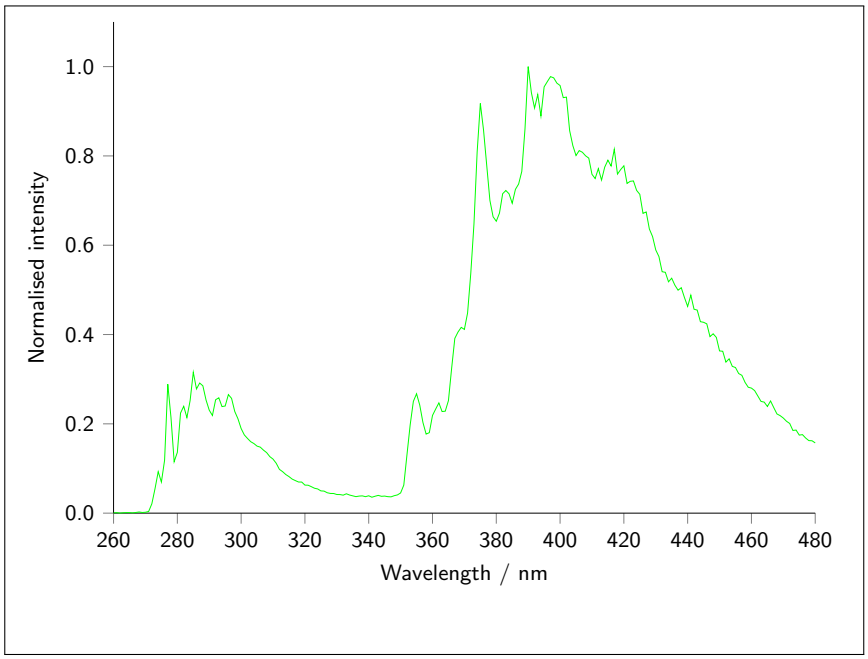

Figure 9.31: Emission spectrum of ArMe3b, at 77 K, in MP glass.

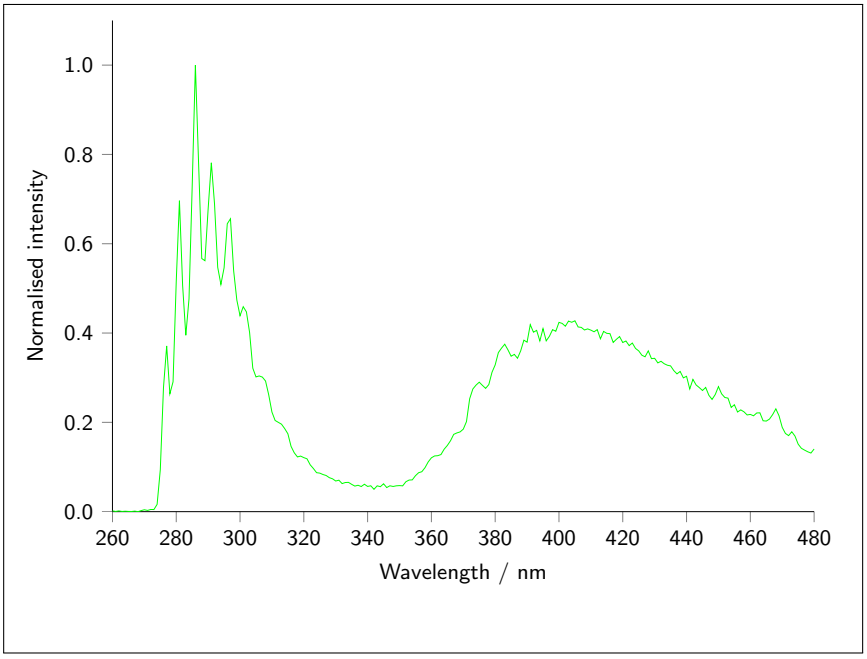

Figure 9.32: Emission spectrum of ArMe4, at 77 K, in MP glass.

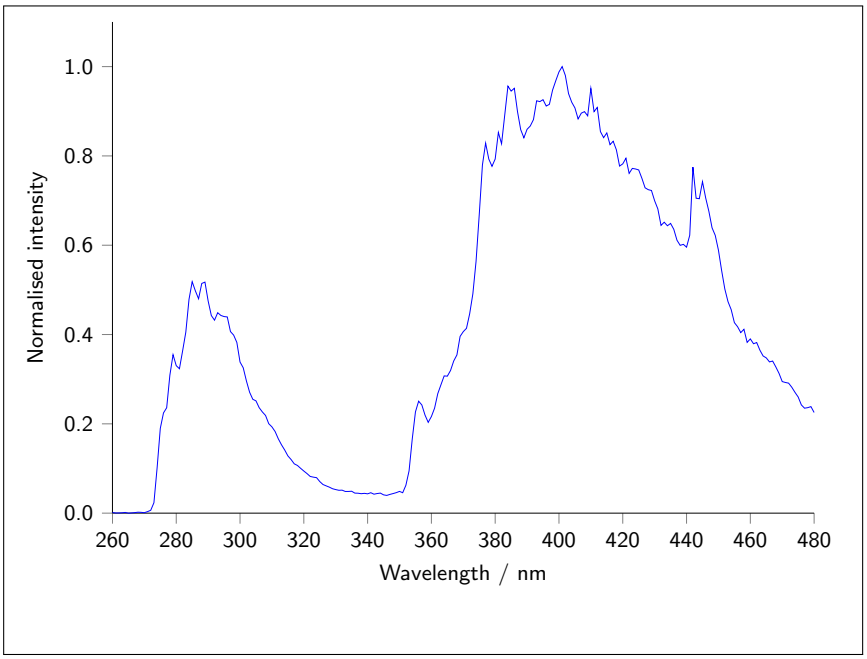

Figure 9.33: Emission spectrum of ArMe4a, at 77 K, in MP glass.

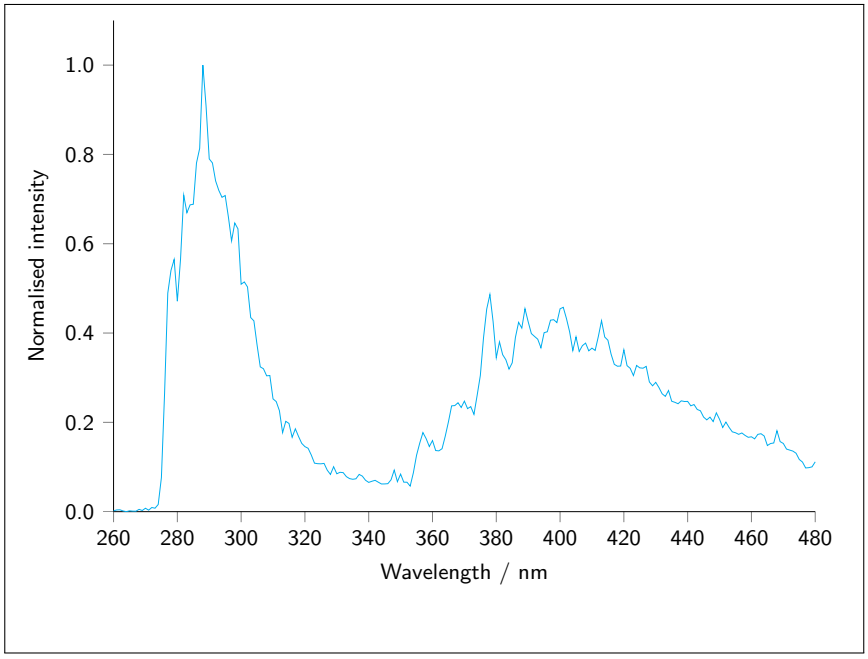

Figure 9.34: Emission spectrum of ArMe4b, at 77 K, in MP glass.

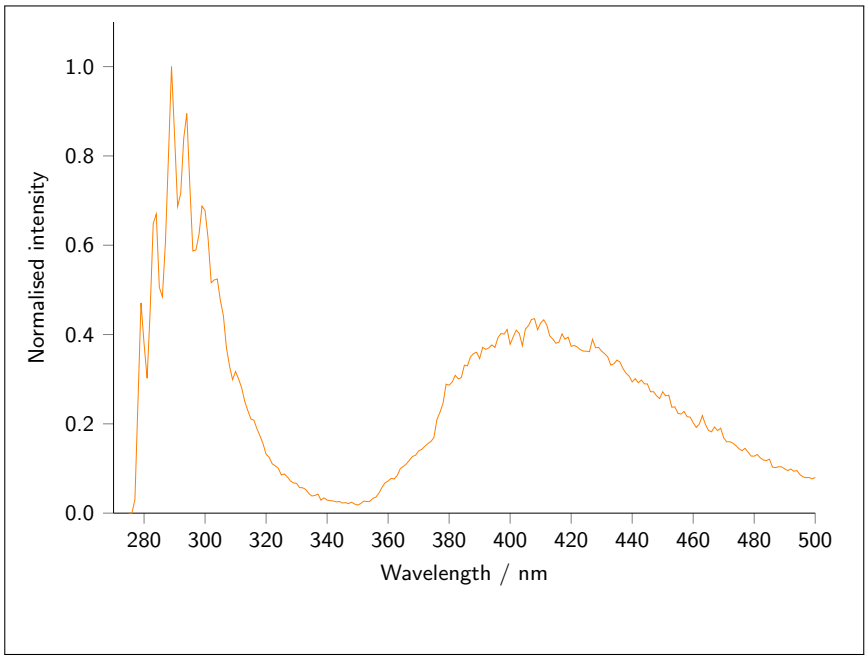

Figure 9.35: Emission spectrum of ArMe5, at 77 K, in MP glass.

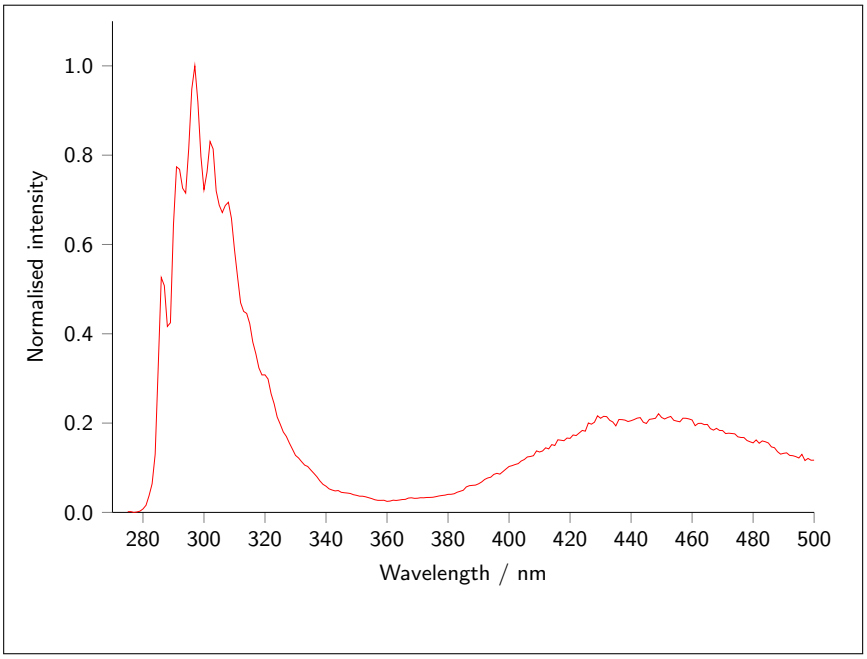

Figure 9.36: Emission spectrum of ArMe6, at 77 K, in MP glass.

9.11 Chapter 7

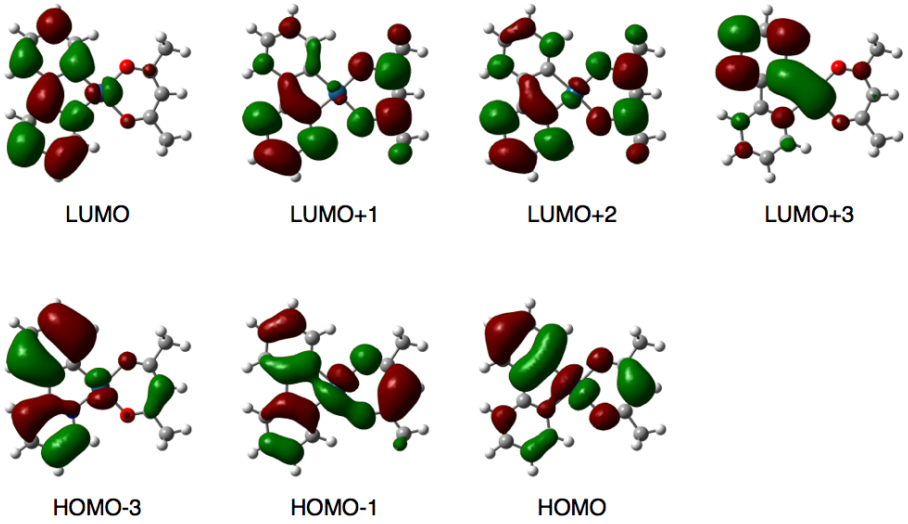

Figure 9.37: Orbital plots for the first triplet excitation of [Pt(ppy)(acac)] in DCM at the ground state geometry. Calculations performed with PBE0, cc-pVDZ and LANL2DZ.

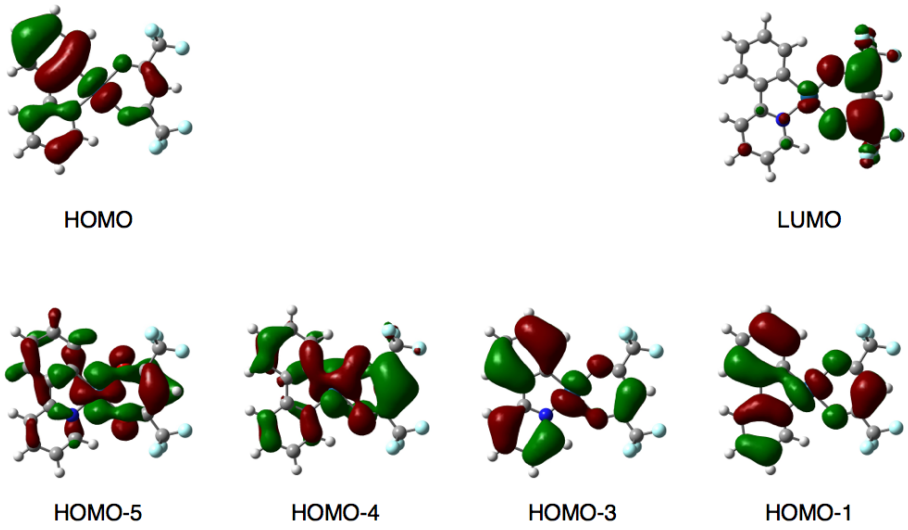

Figure 9.38: Orbital plots for the first triplet excitation of [Pt(ppy)(hfac)] at the optimised ground state geometry.

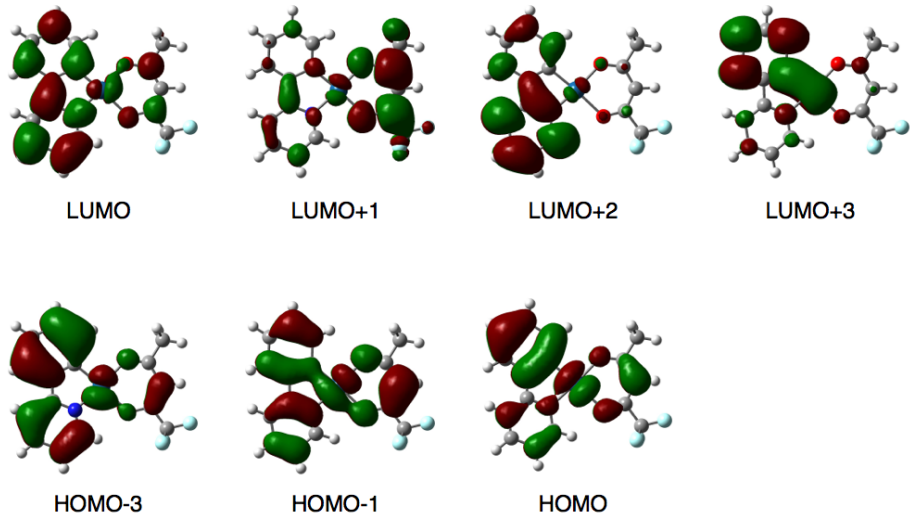

Figure 9.39: Orbital plots for the first triplet excitation of cis-[Pt(ppy)(tfac)], in DCM, at the optimised ground state geometry.

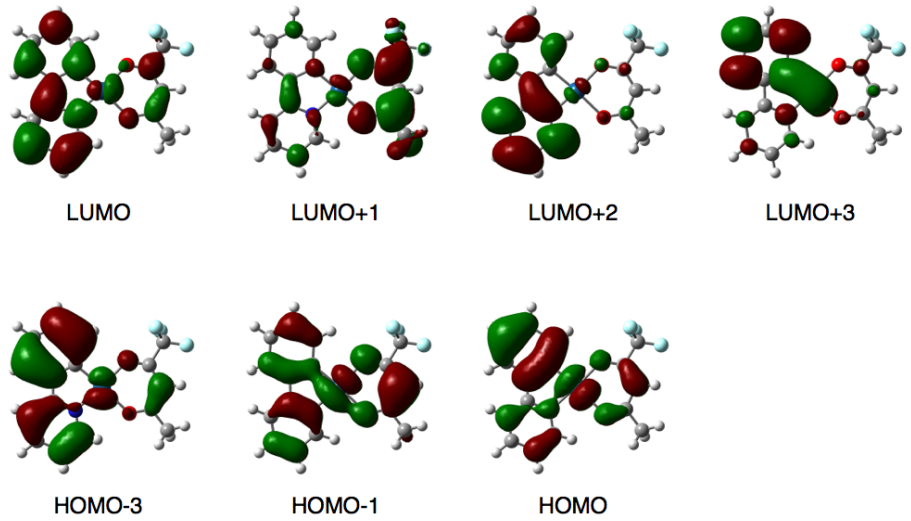

Figure 9.40: Orbital plots for the first triplet excitation of trans-[Pt(ppy)(tfac)], in DCM, at the optimised ground state geometry.

Transition			Contribution
[Pt(ppy)(acac)]			
HOMO−3	→	LUMO	0.222
HOMO−3	→	LUMO+1	0.109
HOMO−3	→	LUMO+2	0.104
HOMO−1	→	LUMO	0.397
HOMO	→	LUMO	0.457
HOMO	→	LUMO+3	0.113
[Pt(ppy)(hfac)]			
HOMO−5	→	LUMO	0.153
HOMO−4	→	LUMO	−0.275
HOMO−3	→	LUMO	−0.242
HOMO−1	→	LUMO	0.448
HOMO	→	LUMO	0.369
***cis*-[Pt(ppy)(tfac)]**			
HOMO−3	→	LUMO	−0.154
HOMO−3	→	LUMO+2	−0.149
HOMO−1	→	LUMO	0.357
HOMO	→	LUMO	0.453
HOMO	→	LUMO+1	−0.226
HOMO	→	LUMO+3	0.118
***trans*-[Pt(ppy)(tfac)]**			
HOMO−3	→	LUMO	−0.190
HOMO−3	→	LUMO+2	−0.153
HOMO−1	→	LUMO	−0.338
HOMO	→	LUMO	0.469
HOMO	→	LUMO+1	−0.193
HOMO	→	LUMO+3	0.118

Table 9.22: Dominant orbital contributions for excitation of [Pt(ppy)(acac)], [Pt(ppy)(hfac)], cis-[Pt(ppy)(tfac)] and trans-[Pt(ppy)(tfac)] from S_0 to T_1 at the optimised S_0 geometry.

Excited state	$\mathbf{PtL^{10-cis}Cl}$		$\mathbf{PtL^{10-trans}Cl}$	
	λ /nm	f	λ /nm	f
1	444	0.0282	458	0.1896
2	437	0.0822	448	0.1750
3	379	0.3570	394	1.2780
4	378	0.0231	369	0.0907
5	369	0.4518	363	0.0771
6	343	0.0102	345	0.0100
7	334	0.0082	341	0.0040
8	331	0.0039	332	0.0136
9	328	0.0000	330	0.0001
10	322	0.0434	326	0.0389

Table 9.23: First ten singlet excitations of $PtL^{10-cis}Cl$ and $PtL^{10-trans}Cl$, calculated by TD-DFT at the optimised S_0 geometry.

Bibliography

[1] B. Zhang, L. Zhang, C. Liu, Y. Zhu, M. Tang, C. Du and M. Song, *Dalton Trans.*, 2014, **43**, 7704.

[2] Y. L. Chang, S. Gong, X. Wang, R. White, C. Yang, S. Wang and Z. H. Lu, *Appl. Phys. Lett.*, 2014, **104**, 173303.

[3] L. Zhang, L. Tian, M. Li, R. He and W. Shen, *Dalton Trans.*, 2014, **43**, 6500.

[4] F. Nisic, A. Colombo, C. Dragonetti, D. Roberto, A. Valore, J. M. Malicka, M. Cocchi, G. R. Freeman and J. A. G. Williams, *J. Mater. Chem. C*, 2014, **2**, 1791.

[5] J. G. Williams, S. Develay, D. L. Rochester and L. Murphy, *Coord. Chem. Rev.*, 2008, **252**, 2596.

[6] G. Li, T. Fleetham and J. Li, *Adv. Mater.*, 2014, **26**, 2931.

[7] L.-M. Huang, G.-M. Tu, Y. Chi, W.-Y. Hung, Y.-C. Song, M.-R. Tseng, P.-T. Chou, G.-H. Lee, K.-T. Wong, S.-H. Cheng and W.-S. Tsai, *J. Mater. Chem. C*, 2013, **1**, 7582.

[8] S. W. Botchway, M. Charnley, J. W. Haycock, A. W. Parker, D. L. Rochester, J. A. Weinstein and J. A. G. Williams, *PNAS*, 2008, **105**, 16071.

[9] K. Cheng, S.-R. Kothapalli, H. Liu, A. L. Koh, J. V. Jokerst, H. Jiang, M. Yang, J. Li, J. Levi, J. C. Wu, S. S. Gambhir and Z. Cheng, *J. Am. Chem. Soc.*, 2014, **136**, 3560.

[10] W. A. Tarran, G. R. Freeman, L. Murphy, A. M. Benham, R. Kataky and J. A. G. Williams, *Inorg. Chem.*, 2014, **53**, 5738.

[11] Y. Dai, H. Xiao, J. Liu, Q. Yuan, P. Ma, D. Yang, C. Li, Z. Cheng, Z. Hou, P. Yang and J. Lin, *J. Am. Chem. Soc.*, 2013, **135**, 18920.

[12] Q.-Z. Yang, L.-Z. Wu, H. Zhang, B. Chen, Z.-X. Wu, L.-P. Zhang and C.-H. Tung, *Inorg. Chem.*, 2004, **43**, 5195.

[13] A. Dorazco-Gonzalez, *Organometallics*, 2014, **33**, 868.

[14] L. Chen, Y. Zhang, S. Ren, D. Huang, C. Zhou, Y. Chi and G. Chen, *Analyst*, 2013, **138**, 7006.

[15] J. Ni, Y.-G. Wang, J.-Y. Wang, Y.-Q. Zhao, Y.-Z. Pan, H.-H. Wang, X. Zhang, J.-J. Zhang and Z.-N. Chen, *Dalton Trans.*, 2013, **42**, 13092.

[16] J.-L. Fillaut, H. Akdas-Kilig, E. Dean, C. Latouche and A. Boucekkine, *Inorg. Chem.*, 2013, **52**, 4890.

[17] S. J. Farley, D. L. Rochester, A. L. Thompson, J. A. K. Howard and J. A. G. Williams, *Inorg. Chem.*, 2005, **44**, 9690.

[18] A. Beeby, S. W. Botchway, I. M. Clarkson, S. Faulkner, A. W. Parker, D. Parker and J. Williams, *J. Photochem. Photobiol., B*, 2000, **57**, 83.

[19] R. C. Evans, P. Douglas, J. A. G. Williams and D. L. Rochester, *J. Fluoresc.*, 2006, **16**, 201.

[20] R. C. Evans and P. Douglas, *ACS Appl. Mater. Interfaces*, 2009, **1**, 1023.

[21] C. Liu, X. Song, X. Rao, Y. Xing, Z. Wang, J. Zhao and J. Qiu, *Dyes Pigm.*, 2014, **101**, 85.

[22] A. Martínez-Olmos, J. Fernández-Salmerón, N. Lopez-Ruiz, A. Rivadeneyra Torres, L. F. Capitan-Vallvey and A. J. Palma, *Anal. Chem.*, 2013, **85**, 11098.

[23] J. F. Michalec, S. A. Bejune and D. R. McMillin, *Inorg. Chem.*, 2000, **39**, 2708.

[24] G. T. Morgan and F. H. Burstall, *J. Chem. Soc.*, 1934, 1498.

[25] S. J. Lippard, *Acc. Chem. Res.*, 1978, **11**, 211.

[26] H.-K. Yip, L.-K. Cheng, K.-K. Cheung and C.-M. Che, *J. Chem. Soc., Dalton Trans.*, 1993, 2933.

[27] D. R. McMillin and J. J. Moore, *Coord. Chem. Rev.*, 2002, **229**, 113.

[28] K. L. Garner, L. F. Parkes, J. D. Piper and J. A. G. Williams, *Inorg. Chem.*, 2010, **49**, 476.

[29] M. Maestri, N. Armaroli, V. Balzani, E. C. Constable and A. M. W. C. Thompson, *Inorg. Chem.*, 1995, **34**, 2759.

[30] J. S. Field, L. P. Ledwaba, O. Q. Munro and D. R. McMillin, *CrystEngComm*, 2008, **10**, 740.

[31] M. H. Wilson, L. P. Ledwaba, J. S. Field and D. R. McMillin, *Dalton Trans.*, 2005, 2754.

[32] R. Mureinik and M. Bidani, *Inorg. Nucl. Chem. Letters*, 1977, **13**, 625.

[33] Z. Ji, A. Azenkeng, M. Hoffmann and W. Sun, *Dalton Trans.*, 2009, 7725.

[34] E. C. Constable, R. P. G. Henney, T. A. Leese and D. A. Tocher, *J. Chem. Soc., Chem. Commun.*, 1990, 513.

[35] E. C. Constable, R. P. G. Henney, T. A. Leese and D. A. Tocher, *J. Chem. Soc., Dalton Trans.*, 1990, 443.

[36] T.-C. Cheung, K.-K. Cheung, S.-M. Peng and C.-M. Che, *J. Chem. Soc., Dalton Trans.*, 1996, 1645.

[37] J. H. K. Yip, Suwarno and J. J. Vittal, *Inorg. Chem.*, 2000, **39**, 3537.

[38] W. Lu, B.-X. Mi, M. C. W. Chan, Z. Hui, C.-M. Che, N. Zhu and S.-T. Lee, *J. Am. Chem. Soc.*, 2004, **126**, 4958.

[39] C. F. Harris, D. A. K. Vezzu, L. Bartolotti, P. D. Boyle and S. Huo, *Inorg. Chem.*, 2013, **52**, 11711.

[40] C. Deuschel-Cornioley, R. Lüönd and A. von Zelewsky, *Helv. Chim. Acta*, 1989, **72**, 377.

[41] G. W. V. Cave, F. P. Fanizzi, R. J. Deeth, W. Errington and J. P. Rourke, *Organometallics*, 2000, **19**, 1355.

[42] W. Lu, M. C. W. Chan, K.-K. Cheung and C.-M. Che, *Organometallics*, 2001, **20**, 2477.

[43] H. B. Lu, G. Q. Lv, J. L. Zuo and J. X. Yang, *Acta Crystallogr., Sect. E: Struct. Rep. Online*, 2008, **64**, m1013.

[44] S. Diring, P. Retailleau and R. Ziessel, *Tetrahedron Lett.*, 2007, **48**, 8069.

[45] S. Fuertes, S. K. Brayshaw, P. R. Raithby, S. Schiffers and M. R. Warren, *Organometallics*, 2012, **31**, 105.

[46] J. R. Berenguer, E. Lalinde and J. Torroba, *Inorg. Chem.*, 2007, **46**, 9919.

[47] C. P. Newman, G. W. V. Cave, M. Wong, W. Errington, N. W. Alcock and J. P. Rourke, *J. Chem. Soc., Dalton Trans.*, 2001, 2678.

[48] G. W. V. Cave, N. W. Alcock and J. P. Rourke, *Organometallics*, 1999, **18**, 1801.

[49] S. C. F. Kui, S. S.-Y. Chui, C.-M. Che and N. Zhu, *J. Am. Chem. Soc.*, 2006, **128**, 8297.

[50] M. Maestri, C. Deuschel-Cornioley and A. von Zelewsky, *Coord. Chem. Rev.*, 1991, **111**, 117.

[51] D. J. Cárdenas, A. M. Echavarren and M. C. Ramírez de Arellano, *Organometallics*, 1999, **18**, 3337.

[52] J. A. G. Williams, A. Beeby, E. S. Davies, J. A. Weinstein and C. Wilson, *Inorg. Chem.*, 2003, **42**, 8609.

[53] D. L. Rochester, S. Develay, S. Zalis and J. A. G. Williams, *Dalton Trans.*, 2009, 1728.

[54] M. Cocchi, J. Kalinowski, V. Fattori, J. A. G. Williams and L. Murphy, *Appl. Phys. Lett.*, 2009, **94**, 073309.

[55] K. Yoshida, S. Yamaguchi, A. Osuka and H. Shinokubo, *Organometallics*, 2010, **29**, 3997.

[56] L. F. Parkes, *Ph.D. thesis*, Durham University, 2012.

[57] D. A. K. Vezzu, D. Ravindranathan, A. W. Garner, L. Bartolotti, M. E. Smith, P. D. Boyle and S. Huo, *Inorg. Chem.*, 2011, **50**, 8261.

[58] E. Rossi, A. Colombo, C. Dragonetti, D. Roberto, F. Demartin, M. Cocchi, P. Brulatti, V. Fattori and J. A. G. Williams, *Chem. Commun.*, 2012, **48**, 3182.

[59] E. Rossi, A. Colombo, C. Dragonetti, D. Roberto, R. Ugo, A. Valore, L. Falciola, P. Brulatti, M. Cocchi and J. A. G. Williams, *J. Mater. Chem.*, 2012, **22**, 10650.

[60] C. Baik, W.-S. Han, Y. Kang, S. O. Kang and J. Ko, *J. Organomet. Chem.*, 2006, **691**, 5900.

[61] J. Terheijden, G. Van Koten, W. P. Mul, D. J. Stufkens, F. Muller and C. H. Stam, *Organometallics*, 1986, **5**, 519.

[62] M. Albrecht, R. A. Gossage, M. Lutz, A. L. Spek and G. van Koten, *Chem. Eur. J.*, 2000, **6**, 1431.

[63] M. Albrecht and G. van Koten, *Adv. Mater.*, 1999, **11**, 171.

[64] L. Murphy and J. A. G. Williams, *Top. Organomet. Chem.*, 2010, **28**, 75.

[65] H. Jude, J. A. Krause Bauer and W. B. Connick, *Inorg. Chem.*, 2002, **41**, 2275.

[66] H. Jude, J. A. Krause Bauer and W. B. Connick, *Inorg. Chem.*, 2004, **43**, 725.

[67] H. Jude, J. A. Krause Bauer and W. B. Connick, *Inorg. Chem.*, 2005, **44**, 1211.

[68] W. B. Connick, V. M. Miskowski, V. H. Houlding and H. B. Gray, *Inorg. Chem.*, 2000, **39**, 2585.

[69] G. D. Batema, M. Lutz, A. L. Spek, C. A. van Walree, C. d. M. Donegá, A. Meijerink, R. W. A. Havenith, J. Pérez-Moreno, K. Clays, M. Büchel, A. v. Dijken, D. L. Bryce, G. P. M. van Klink and G. v. Koten, *Organometallics*, 2008, **27**, 1690.

[70] X.-Q. Hao, J.-F. Gong, C.-X. Du, L.-Y. Wu, Y.-J. Wu and M.-P. Song, *Tetrahedron Lett.*, 2006, **47**, 5033.

[71] Z. Wang, Z. Sun, X.-Q. Hao, J.-L. Niu, D. Wei, T. Tu, J.-F. Gong and M.-P. Song, *Organometallics*, 2014, **33**, 1563.

[72] A. Colombo, C. Dragonetti, D. Marinotto, S. Righetto, D. Roberto, S. Tavazzi, M. Escadeillas, V. Guerchais, H. Le Bozec, A. Boucekkine and C. Latouche, *Organometallics*, 2013, **32**, 3890.

[73] J. Brooks, Y. Babayan, S. Lamansky, P. I. Djurovich, I. Tsyba, R. Bau and M. E. Thompson, *Inorg. Chem.*, 2002, **41**, 3055.

[74] P. I. Djurovich, D. Murphy, M. E. Thompson, B. Hernandez, R. Gao, P. L. Hunt and M. Selke, *Dalton Trans.*, 2007, 3763.

[75] X. Yang, Z. Huang, J. Dang, C.-L. Ho, G. Zhou and W.-Y. Wong, *Chem. Commun.*, 2013, **49**, 4406.

[76] S. Fernandez, J. Fornies, B. Gil, J. Gomez and E. Lalinde, *Dalton Trans.*, 2003, 822.

[77] J. Fornies, S. Fuertes, A. Martin, V. Sicilia, B. Gil and E. Lalinde, *Dalton Trans.*, 2009, 2224.

[78] J. R. Berenguer, Á. Díez, A. García, E. Lalinde, M. T. Moreno, S. Sánchez and J. Torroba, *Organometallics*, 2011, **30**, 1646.

[79] H. Uesugi, T. Tsukuda, K. Takao and T. Tsubomura, *Dalton Trans.*, 2013, **42**, 7396.

[80] T. Zou, C.-N. Lok, Y. M. E. Fung and C.-M. Che, *Chem. Commun.*, 2013, **49**, 5423.

[81] X. Li, Y. Liu, J. Luo, Z. Zhang, D. Shi, Q. Chen, Y. Wang, J. He, J. Li, G. Lei and W. Zhu, *Dalton Trans.*, 2012, **41**, 2972.

[82] S.-B. Ko, J.-S. Lu, Y. Kang and S. Wang, *Organometallics*, 2013, **32**, 599.

[83] N. M. Shavaleev, H. Adams, J. Best, R. Edge, S. Navaratnam and J. A. Weinstein, *Inorg. Chem.*, 2006, **45**, 9410.

[84] N. M. Shavaleev, H. Adams, J. Best, R. Edge, S. Navaratnam and J. A. Weinstein, *Inorg. Chem.*, 2006, **45**, 9410.

[85] F. Niedermair, O. Kwon, K. Zojer, S. Kappaun, G. Trimmel, K. Mereiter and C. Slugovc, *Dalton Trans.*, 2008, 4006.

[86] M. M. Mdleleni, J. S. Bridgewater, R. J. Watts and P. C. Ford, *Inorg. Chem.*, 1995, **34**, 2334.

[87] J. A. G. Williams, *Top. Curr. Chem.*, 2007, **281**, 205.

[88] L. J. Andrews, *J. Phys. Chem.*, 1979, **83**, 3203.

[89] C.-M. Che, C.-C. Kwok, S.-W. Lai, A. Rausch, W. Finkenzeller, N. Zhu and H. Yersin, *Chem. Eur. J.*, 2010, **16**, 233.

[90] Y.-Y. Lin, S.-C. Chan, M. C. W. Chan, Y.-J. Hou, N. Zhu, C.-M. Che, Y. Liu and Y. Wang, *Chem. Eur. J.*, 2003, **9**, 1521.

[91] K. Feng, C. Zuniga, Y.-D. Zhang, D. Kim, S. Barlow, S. R. Marder, J. L. Brédas and M. Weck, *Macromolecules*, 2009, **42**, 6855.

[92] A. F. Rausch, L. Murphy, J. A. G. Williams and H. Yersin, *Inorg. Chem.*, 2012, **51**, 312.

[93] M. Maestri, D. Sandrini, V. Balzani, L. Chassot, P. Jolliet and A. von Zelewsky, *Chem. Phys. Lett.*, 1985, **122**, 375.

[94] D. A. K. Vezzu, J. C. Deaton, J. S. Jones, L. Bartolotti, C. F. Harris, A. P. Marchetti, M. Kondakova, R. D. Pike and S. Huo, *Inorg. Chem.*, 2010, **49**, 5107.

[95] E. Turner, N. Bakken and J. Li, *Inorg. Chem.*, 2013, **52**, 7344.

[96] P. Hohenberg and W. Kohn, *Phys. Rev.*, 1964, **136**, B864.

[97] W. Kohn and L. J. Sham, *Phys. Rev.*, 1965, **140**, A1133.

[98] M. Levy, *PNAS*, 1979, **76**, 6062.

[99] E. Runge and E. K. U. Gross, *Phys. Rev. Lett.*, 1984, **52**, 997.

[100] C. Adamo and D. Jacquemin, *Chem. Soc. Rev.*, 2013, **42**, 845.

[101] D. Jacquemin, A. Planchat, C. Adamo and B. Mennucci, *J. Chem. Theory Comput.*, 2012, **8**, 2359.

[102] P. Kadjane, C. Platas-Iglesias, R. Ziessel and L. J. Charbonniere, *Dalton Trans.*, 2009, 5688.

[103] K. Gagnon, S. Mohammed Aly, A. Brisach-Wittmeyer, D. Bellows, J.-F. Bérubé, L. Caron, A. S. Abd-El-Aziz, D. Fortin and P. D. Harvey, *Organometallics*, 2008, **27**, 2201.

[104] H. Zhan, S. Lamare, A. Ng, T. Kenny, H. Guernon, W.-K. Chan, A. B. Djurišić, P. D. Harvey and W.-Y. Wong, *Macromolecules*, 2011, **44**, 5155.

[105] W. Wu, W. Wu, S. Ji, H. Guo, X. Wang and J. Zhao, *Dyes Pigm.*, 2011, **89**, 199.

[106] W. Wu, W. Wu, S. Ji, H. Guo and J. Zhao, *Dalton Trans.*, 2011, **40**, 5953.

[107] W. Wu, W. Wu, S. Ji, H. Guo, P. Song, K. Han, L. Chi, J. Shao and J. Zhao, *J. Mater. Chem.*, 2010, **20**, 9775.

[108] Y. Kataoka, Y. Kitagawa, T. Kawakami and M. Okumura, *J. Organomet. Chem.*, 2013, **743**, 163.

[109] R. Starosta, A. Bykowska, M. Barys, A. K. Wieliczko, Z. Staroniewicz and M. Jeżowska-Bojczuk, *Polyhedron*, 2011, **30**, 2914.

[110] R. Zhang, Z. Liang, A. Han, H. Wu, P. Du, W. Lai and R. Cao, *CrystEngComm*, 2014, **16**, 5531.

[111] S. Y.-L. Leung, W. H. Lam, N. Zhu and V. W.-W. Yam, *Organometallics*, 2010, **29**, 5558.

[112] S. Y.-L. Leung, W. H. Lam, N. Zhu and V. W.-W. Yam, *Organometallics*, 2010, **29**, 5558.

[113] R. Seeger and J. A. Pople, *J. Chem. Phys.*, 1977, **66**, 3045.

[114] A. M. Lee and N. C. Handy, *J. Chem. Soc., Faraday Trans.*, 1993, **89**, 3999.

[115] R. Bauernschmitt and R. Ahlrichs, *Chem. Phys. Lett.*, 1996, **256**, 454.

[116] S. Hirata and M. Head-Gordon, *Chem. Phys. Lett.*, 1999, **314**, 291.

[117] M. J. G. Peach, M. J. Williamson and D. J. Tozer, *J. Chem. Theory Comput.*, 2011, **7**, 3578.

[118] Y. Kaya, C. Icsel, V. T. Yilmaz and O. Buyukgungor, *J. Organomet. Chem.*, 2014, **752**, 83.

[119] M. Zhang, Y. Li, Z.-S. Li and J.-Z. Sun, *Int. J. Quantum Chem.*, 2010, **110**, 1142.

[120] B.-Z. Yang, X. Zhou, T. Liu, G.-J. Zhao and H.-X. Zhang, *Inorg. Chim. Acta*, 2009, **362**, 1209.

[121] F.-Q. Bai, X. Zhou, T. Liu, G.-J. Zhao, J.-P. Zhang and H.-X. Zhang, *Int. J. Quantum Chem.*, 2009, **109**, 308.

[122] S. Yamaguchi, T. Katoh, H. Shinokubo and A. Osuka, *J. Am. Chem. Soc.*, 2008, **130**, 14440.

[123] X.-Y. Hu, X.-J. Liu and J.-K. Feng, *Chin. J. Chem.*, 2007, **25**, 1370.

[124] X. Zhou, Q.-J. Pan, B.-H. Xia, M.-X. Li, H.-X. Zhang and A.-C. Tung, *J. Phys. Chem. A*, 2007, **111**, 5465.

[125] K. Glusac, M. E. Köse, H. Jiang and K. S. Schanze, *J. Phys. Chem. B*, 2007, **111**, 929.

[126] T. Liu, B.-H. Xia, X. Zhou, H.-X. Zhang, Q.-J. Pan and J.-S. Gao, *Organometallics*, 2007, **26**, 143.

[127] Y. Xu, W.-K. Chen, M.-J. Cao, S.-H. Liu, J.-Q. Li, A. I. Philippopoulos and P. Falaras, *Chem. Phys.*, 2006, **330**, 204.

[128] A. D. Becke, *J. Chem. Phys.*, 1993, **98**, 5648.

[129] A. D. Becke, *Phys. Rev. A*, 1988, **38**, 3098.

[130] C. Lee, W. Yang and R. G. Parr, *Phys. Rev. B*, 1988, **37**, 785.

[131] C. Adamo and V. Barone, *J. Chem. Phys.*, 1999, **110**, 6158.

[132] J. P. Perdew, K. Burke and M. Ernzerhof, *Phys. Rev. Lett.*, 1996, **77**, 3865.

[133] J. P. Perdew, K. Burke and M. Ernzerhof, *Phys. Rev. Lett.*, 1997, **78**, 1396.

[134] T. Yanai, D. P. Tew and N. C. Handy, *Chem. Phys. Lett.*, 2004, **393**, 51.

[135] P. M. W. Gill, R. D. Adamson and J. A. Pople, *Mol. Phys.*, 1996, **88**, 1005.

[136] R. Baer and D. Neuhauser, *Phys. Rev. Lett.*, 2005, **94**, 043002.

[137] J.-D. Chai and M. Head-Gordon, *J. Chem. Phys.*, 2008, **128**, 084106.

[138] M. A. Rohrdanz and J. M. Herbert, *J. Chem. Phys.*, 2008, **129**, 034107.

[139] M. J. Peach, N. Warner and D. J. Tozer, *Mol. Phys.*, 2013, **111**, 1271.

[140] R. Bauernschmitt and R. Ahlrichs, *J. Chem. Phys.*, 1996, **104**, 9047.

[141] A. Dreuw and M. Head-Gordon, *Chem. Rev.*, 2005, **105**, 4009.

[142] M. J. G. Peach and D. J. Tozer, *J. Phys. Chem. A*, 2012, **116**, 9783.

[143] M. R. Silva-Junior, M. Schreiber, S. P. A. Sauer and W. Thiel, *J. Chem. Phys.*, 2010, **133**, 174318.

[144] J. Franck and E. G. Dymond, *Trans. Faraday Soc.*, 1926, **21**, 536.

[145] E. Condon, *Phys. Rev.*, 1926, **28**, 1182.

[146] G. Herzberg and E. Teller, *Z. Phys. Chem.*, 1933, **B21**, 410.

[147] H. Mustroph and S. Ernst, *Chem. unserer Zeit*, 2011, **45**, 256.

[148] P. Shao, Y. Li, A. Azenkeng, M. R. Hoffmann and W. Sun, *Inorg. Chem.*, 2009, **48**, 2407.

[149] D. Fortin, S. Clément, K. Gagnon, J.-F. Bérubé, M. P. Stewart, W. E. Geiger and P. D. Harvey, *Inorg. Chem.*, 2009, **48**, 446.

[150] Z. Li, E. Badaeva, A. Ugrinov, S. Kilina and W. Sun, *Inorg. Chem.*, 2013, **52**, 7578.

[151] D. P. Rillema, A. J. Cruz, C. Moore, K. Siam, A. Jehan, D. Base, T. Nguyen and W. Huang, *Inorg. Chem.*, 2013, **52**, 596.

[152] N. M. O'Boyle, A. L. Tenderhold and K. M. Langner, *J. Comput. Chem.*, 2008, **29**, 839.

[153] M. Rudolph and J. Autschback, *J. Phys. Chem. A*, 2011, **115**, 2635.

[154] G.-M. Tong and C.-M. Che, *Chem. Eur. J.*, 2009, **15**, 7225.

[155] V. Barone, M. Cossi and J. Tomasi, *J. Comput. Chem.*, 1998, **19**, 404.

[156] A. J. Bridgeman, *Inorg. Chem.*, 2008, **47**, 4817.

[157] A. J. Bridgeman, B. Courcot and T. Nguyen, *Dalton Trans.*, 2012, **41**, 5362.

[158] R. Borrelli, A. Capobianco and A. Peluso, *Can. J. Chem.*, 2013, **91**, 495.

[159] I. Alata, R. Omidyan, M. Broquier, C. Dedonder and C. Jouvet, *Chem. Phys.*, 2012, **399**, 224.

[160] I. Alata, R. Omidyan, C. Dedonder-Lardeux, M. Broquier and C. Jouvet, *Phys. Chem. Chem. Phys.*, 2009, **11**, 11479.

[161] C.-H. Chang, G. Lopez, T. J. Sears and P. M. Johnson, *J. Phys. Chem. A*, 2010, **114**, 8262.

[162] I. Conti, E. Di Donato, F. Negri and G. Orlandi, *J. Phys. Chem. A*, 2009, **113**, 15265.

[163] C. W. Muller, J. J. Newby, C.-P. Liu, C. P. Rodrigo and T. S. Zwier, *Phys. Chem. Chem. Phys.*, 2010, **12**, 2331.

[164] I. Pugliesi and K. Müller-Dethlefs, *J. Phys. Chem. A*, 2006, **110**, 13045.

[165] L. Jose, M. Seth and T. Ziegler, *J. Phys. Chem. A*, 2012, **116**, 1864.

[166] V. Barone, J. Bloino, S. Monti, A. Pedone and G. Prampolini, *Phys. Chem. Chem. Phys.*, 2011, **13**, 2160.

[167] J. Tomasi, B. Mennucci and R. Cammi, *Chem. Rev.*, 2005, **105**, 2999.

[168] S. Kui, I. Sham, C. Cheung, C.-W. Ma, B. Yan, N. Zhu, C.-M. Che and W.-F. Fu, *Chem. Eur. J.*, 2007, **13**, 417.

[169] S.-W. Lai, M. C.-W. Chan, T.-C. Cheung, S.-M. Peng and C.-M. Che, *Inorg. Chem.*, 1999, **38**, 4046.

[170] C.-K. Koo, B. Lam, S.-K. Leung, M. H.-W. Lam and W.-Y. Wong, *J. Am. Chem. Soc.*, 2006, **128**, 16434.

[171] C.-K. Koo, Y.-M. Ho, C.-F. Chow, M. H.-W. Lam, T.-C. Lau and W.-Y. Wong, *Inorg. Chem.*, 2007, **46**, 3603.

[172] C.-K. Koo, K.-L. Wong, C. W.-Y. Man, Y.-W. Lam, L. K.-Y. So, H.-L. Tam, S.-W. Tsao, K.-W. Cheah, K.-C. Lau, Y.-Y. Yang, J.-C. Chen and M. H.-W. Lam, *Inorg. Chem.*, 2009, **48**, 872.

[173] S. U. Pandya, K. C. Moss, M. R. Bryce, A. S. Batsanov, M. A. Fox, V. Jankus, H. A. Al Attar and A. P. Monkman, *Eur. J. Inorg. Chem.*, 2010, **2010**, 1963.

[174] M. J. G. Peach, P. Benfield, T. Helgaker and D. J. Tozer, *J. Chem. Phys.*, 2008, **128**, 044118.

[175] D. Jacquemin, E. A. Perpète, I. Ciofini and C. Adamo, *J. Chem. Theory Comput.*, 2010, **6**, 1532.

[176] M. R. Silva-Junior, M. Schreiber, S. P. A. Sauer and W. Thiel, *J. Chem. Phys.*, 2008, **129**, 104103.

[177] D. Jacquemin, V. Wathelet, E. A. Perpète and C. Adamo, *J. Chem. Theory Comput.*, 2009, **5**, 2420.

[178] D. J. Tozer, R. D. Amos, N. C. Handy, B. O. Roos and L. Serrano-Andrés, *Mol. Phys.*, 1999, **97**, 859.

[179] C. Jamorski, M. E. Casida and D. R. Salahub, *J. Chem. Phys.*, 1996, **104**, 5134.

[180] L. Murphy, *Ph.D. thesis*, Durham University, 2010.

[181] U. S. Schubert, C. Eschbaumer and M. Heller, *Org. Lett.*, 2000, **2**, 3373.

[182] T. Kaminski, P. Gros and Y. Fort, *Eur. J. Org. Chem.*, 2003, **2003**, 3855.

[183] Z. Wang, E. Turner, V. Mahoney, S. Madakuni, T. Groy and J. Li, *Inorg. Chem.*, 2010, **49**, 11276.

[184] D. R. Weinberg, J. A. Labinger and J. E. Bercaw, *Organometallics*, 2007, **26**, 167.

[185] A. von Zelewsky, A. P. Suckling and H. Stoeckli-Evans, *Inorg. Chem.*, 1993, **32**, 4585.

[186] C. P. Newman, K. Casey-Green, G. J. Clarkson, G. W. V. Cave, W. Errington and J. P. Rourke, *Dalton Trans.*, 2007, 3170.

[187] D. M. Jenkins and S. Bernhard, *Inorg. Chem.*, 2010, **49**, 11297.

[188] A. J. Wilkinson, H. Puschmann, J. A. K. Howard, C. E. Foster and J. A. G. Williams, *Inorg. Chem.*, 2006, **45**, 8685.

[189] P. Brulatti, R. J. Gildea, J. A. K. Howard, V. Fattori, M. Cocchi and J. A. G. Williams, *Inorg. Chem.*, 2012, **51**, 3813.

[190] W. Sotoyama, T. Satoh, H. Sato, A. Matsuura and N. Sawatari, *J. Phys. Chem. A*, 2005, **109**, 9760.

[191] D. L. Rochester, S. Develay, S. Zalis and J. A. G. Williams, *Dalton Trans.*, 2009, 1728.

[192] J. Preat, C. Michaux, A. Lewalle, E. A. Perpète and D. Jacquemin, *Chem. Phys. Lett.*, 2008, **451**, 37.

[193] R. H. Hill and R. J. Puddephatt, *J. Am. Chem. Soc.*, 1985, **107**, 1218.

[194] L. Chassot, A. Von Zelewsky, D. Sandrini, M. Maestri and V. Balzani, *J. Am. Chem. Soc.*, 1986, **108**, 6084.

[195] H. Kunkely and A. Vogler, *Coord. Chem. Rev.*, 1991, **111**, 15.

[196] W. Tarran, *Ph.D. thesis*, Durham University, 2011.

[197] J. A. Zuleta, C. A. Chesta and R. Eisenberg, *J. Am. Chem. Soc.*, 1989, **111**, 8916.

[198] J. A. Zuleta, J. M. Bevilacqua, D. M. Proserpio, P. D. Harvey and R. Eisenberg, *Inorg. Chem.*, 1992, **31**, 2396.

[199] S. D. Cummings and R. Eisenberg, *Inorg. Chem.*, 1995, **34**, 2007.

[200] S. D. Cummings and R. Eisenberg, *J. Am. Chem. Soc.*, 1996, **118**, 1949.

[201] J. A. Weinstein, N. N. Zheligovskaya, M. Ya. Mel'nikov and F. Hartl, *J. Chem. Soc., Dalton Trans.*, 1998, 2459.

[202] J. A. Weinstein, A. J. Blake, E. S. Davies, A. L. Davis, M. W. George, D. C. Grills, I. V. Lileev, A. M. Maksimov, P. Matousek, M. Y. Mel'nikov, A. W. Parker, V. E. Platonov, M. Towrie, C. Wilson and N. N. Zheligovskaya, *Inorg. Chem.*, 2003, **42**, 7077.

[203] J. A. Weinstein, M. T. Tierney, E. S. Davies, K. Base, A. A. Robeiro and M. W. Grinstaff, *Inorg. Chem.*, 2006, **45**, 4544.

[204] C. J. Adams, N. Fey, M. Parfitt, S. J. A. Pope and J. A. Weinstein, *Dalton Trans.*, 2007, 4446.

[205] R. D. Rakhimov, Y. A. Weinstein, E. V. Lileeva, N. N. Zheligovskaya, M. Y. Mel'nikov and K. P. Butin, *Russ. Chem. Bull.*, 2003, **52**, 1150.

[206] T. R. Miller and I. G. Dance, *J. Am. Chem. Soc.*, 1973, **95**, 6970.

[207] C.-H. Li, S. C. F. Kui, I. H. T. Sham, S. S.-Y. Chui and C.-M. Che, *Eur. J. Inorg. Chem.*, 2008, **2008**, 2421.

[208] E. Rossi, L. Murphy, P. L. Brothwood, A. Colombo, C. Dragonetti, D. Roberto, R. Ugo, M. Cocchi and J. A. G. Williams, *J. Mater. Chem.*, 2011, **21**, 15501.

[209] M. J. G. Peach, T. Helgaker, P. Salek, T. W. Keal, O. B. Lutnaes, D. J. Tozer and N. C. Handy, *Phys. Chem. Chem. Phys.*, 2006, **8**, 558.

[210] M. J. G. Peach, A. J. Cohen and D. J. Tozer, *Phys. Chem. Chem. Phys.*, 2006, **8**, 4543.

[211] M. Cocchi, D. Virgili, V. Fattori, J. A. G. Williams and J. Kalinowski, *Appl. Phys. Lett.*, 2007, **90**, 023506.

[212] J. S. Fossey and C. J. Richards, *Organometallics*, 2002, **21**, 5259.

[213] H. Schiff, *Ann. Chem. Pharm.*, 1864, **131**, 118.

[214] C. D. Meyer, C. S. Joiner and J. F. Stoddart, *Chem. Soc. Rev.*, 2007, **36**, 1705.

[215] C. Godoy-Alcántar, A. K. Yatsimirsky and J.-M. Lehn, *J. Phys. Org. Chem.*, 2005, **18**, 979.

[216] E. H. Cordes and W. P. Jencks, *J. Am. Chem. Soc.*, 1963, **85**, 2843.

[217] M. D. Wessel and P. C. Jurs, *J. Chem. Inf. Comput. Sci.*, 1995, **35**, 841.

[218] A. V. Malkov, K. Vranková, S. Stončius and P. Kočovský, *J. Org. Chem.*, 2009, **74**, 5839.

[219] H. Shao, M. M. Crnogorac, T. Kong, S.-Y. Chen, J. M. Williams, J. M. Tack, V. Gueriguian, E. N. Cagle, M. Carnevali, D. Tumelty, X. Paliard, L. P. Miranda, J. A. Bradburne and G. G. Kochendoerfer, *J. Am. Chem. Soc.*, 2005, **127**, 1350.

[220] W. P. Jencks, *J. Am. Chem. Soc.*, 1959, **81**, 475.

[221] E. Godineau, C. Schäfer and Y. Landais, *Org. Lett.*, 2006, **8**, 4871.

[222] A. S. Ionkin, W. J. Marshall and Y. Wang, *Organometallics*, 2005, **24**, 619.

[223] O. A. Blackburn, B. J. Coe, M. Helliwell and J. Raftery, *Organometallics*, 2012, **31**, 5307.

[224] M. Cocchi, J. Kalinowski, D. Virgili, V. Fattori, S. Develay and J. A. G. Williams, *Appl. Phys. Lett.*, 2007, **90**, 163508.

[225] O. Nuyken, S. Jungermann, V. Wiederhirn, E. Backer and K. Meerholz, *Monatsh. Chem.*, 2006, **137**, 811.

[226] J. Jido, H. Shionoya and K. Nagai, *Science*, 1995, **267**, 1332.

[227] H. Shizuka, Y. Ueki, T. Iizuka and N. Kanamaru, *J. Phys. Chem.*, 1982, **86**, 3327.

[228] H. Sponer and Y. Kanda, *J. Chem. Phys.*, 1964, **40**, 778.

[229] Y. Kanda and R. Shimada, *Spectrochim. Acta*, 1961, **17**, 279.

[230] J. Demaison, H. D. Rudolph and A. G. Császár, *Mol. Phys.*, 2013, **111**, 1539.

[231] N. C. Handy and D. J. Tozer, *J. Comput. Chem.*, 1999, **20**, 106.

[232] M. de Groot and J. van der Waals, *Mol. Phys.*, 1963, **6**, 545.

[233] M. de Groot, I. Hesselmann and J. van der Waals, *Mol. Phys.*, 1965, **10**, 91.

[234] A. D. Liehr, *Z. Naturforsch*, 1961, **a16**, 641.

[235] J. W. Rabalais, H. J. Maria and S. P. McGlynn, *J. Chem. Phys.*, 1969, **51**, 2259.

[236] W. Moffitt and A. D. Liehr, *Phys. Rev.*, 1957, **106**, 1195.

[237] W. J. Buma, J. H. Van der Waals and M. C. Van Hemert, *J. Am. Chem. Soc.*, 1989, **111**, 86.

[238] W. E. Donath, *J. Chem. Phys.*, 1965, **42**, 118.

[239] S. R. Langhoff, E. R. Davidson and C. W. Kern, *J. Chem. Phys.*, 1975, **63**, 4800.

[240] R. K. Chaudhuri, S. Chattopadhyay, U. S. Mahapatra and K. F. Freed, *J. Chem. Phys.*, 2010, **132**, 034105.

[241] M. Spencer, A. Santoro, G. R. Freeman, A. Diez, P. R. Murray, J. Torroba, A. C. Whitwood, L. J. Yellowlees, J. A. G. Williams and D. W. Bruce, *Dalton Trans.*, 2012, **41**, 14244.

[242] M. Ghedini, T. Pugliese, M. La Deda, N. Godbert, I. Aiello, M. Amati, S. Belviso, F. Lelj, G. Accorsi and F. Barigelletti, *Dalton Trans.*, 2008, 4303.

[243] J. Saltiel, G.-E. Khalil and K. Schanze, *Chem. Phys. Lett.*, 1980, **70**, 233.

[244] J. Moussa, T. Cheminel, G. R. Freeman, L.-M. Chamoreau, J. A. G. Williams and H. Amouri, *Dalton Trans.*, 2014, **43**, 8162.

[245] B. Schmid, L. M. Venanzi, A. Albinati and F. Mathey, *Inorg. Chem.*, 1991, **30**, 4693.

[246] M. Shiotsuka, T. Tanamachi and Y. Matsuda, *Chem. Lett.*, 1995, **24**, 531.

[247] L. E. E. Broeckx, W. Delaunay, C. Latouche, M. Lutz, A. Boucekkine, M. Hissler and C. Müller, *Inorg. Chem.*, 2013, **52**, 10738.

[248] D. K. Crites, C. T. Cunningham and D. R. McMillin, *Inorg. Chim. Acta*, 1998, **273**, 346.

[249] J. A. Bailey, M. G. Hill, R. E. Marsh, V. M. Miskowski, W. P. Schaefer and H. B. Gray, *Inorg. Chem.*, 1995, **34**, 4591.

[250] J. V. Caspar and T. J. Meyer, *Inorg. Chem.*, 1983, **22**, 2444.

[251] A. Juris, V. Balzani, F. Barigelletti, S. Campagna, P. Belser and A. von Zelewsky, *Coord. Chem. Rev.*, 1988, **84**, 85.

[252] E. A. Medlycott and G. S. Hanan, *Chem. Soc. Rev.*, 2005, **34**, 133.

[253] K. Lashgari, M. Kritikos, R. Norrestam and T. Norrby, *Acta Crystallogr., Sect. C: Cryst. Struct. Commun.*, 1999, **55**, 64.

[254] K. Nakamaru, *Bull. Chem. Soc. Jpn.*, 1982, **55**, 2697.

[255] Y.-Z. Hu, M. H. Wilson, R. Zong, C. Bonnefous, D. R. McMillin and R. P. Thummel, *Dalton Trans.*, 2005, 354.

[256] W. K. Pek, *M.Sc. thesis*, Durham University, 2011.

[257] Y. Surace, *M.Sc. thesis*, Durham University, 2012.

[258] A. Henwood, *M.Sc. thesis*, Durham University, 2013.

[259] M. J. Frisch, G. W. Trucks, H. B. Schlegel, G. E. Scuseria, M. A. Robb, J. R. Cheeseman, G. Scalmani, V. Barone, B. Mennucci, G. A. Petersson, H. Nakatsuji, M. Caricato, X. Li, H. P. Hratchian, A. F. Izmaylov, J. Bloino, G. Zheng, J. L. Sonnenberg, M. Hada, M. Ehara, K. Toyota, R. Fukuda, J. Hasegawa, M. Ishida, T. Nakajima, Y. Honda, O. Kitao, H. Nakai, T. Vreven, J. A. Montgomery, Jr., J. E. Peralta, F. Ogliaro, M. Bearpark, J. J. Heyd, E. Brothers, K. N. Kudin, V. N. Staroverov, R. Kobayashi, J. Normand, K. Raghavachari, A. Rendell, J. C. Burant, S. S. Iyengar, J. Tomasi, M. Cossi, N. Rega, J. M. Millam, M. Klene, J. E. Knox, J. B. Cross, V. Bakken, C. Adamo, J. Jaramillo, R. Gomperts, R. E. Stratmann, O. Yazyev, A. J. Austin, R. Cammi, C. Pomelli, J. W. Ochterski, R. L. Martin, K. Morokuma, V. G. Zakrzewski, G. A. Voth, P. Salvador, J. J. Dannenberg, S. Dapprich, A. D. Daniels, Ö. Farkas, J. B. Foresman, J. V. Ortiz, J. Cioslowski and D. J. Fox, *Gaussian 09 Revision D.01*.

[260] *Dalton, a molecular electronic structure program, Release Dalton2011*, 2011.

[261] Y. Shao, L. F. Molnar, Y. Jung, J. Kussmann, C. Ochsenfeld, S. T. Brown, A. T. Gilbert, L. V. Slipchenko, S. V. Levchenko, D. P. O'Neill, R. A. DiStasio Jr, R. C. Lochan, T. Wang, G. J. Beran, N. A. Besley, J. M. Herbert, C. Yeh Lin, T. Van Voorhis, S. Hung Chien, A. Sodt, R. P. Steele, V. A. Rassolov, P. E. Maslen, P. P. Korambath, R. D. Adamson, B. Austin, J. Baker, E. F. C. Byrd, H. Dachsel, R. J. Doerksen, A. Dreuw, B. D. Dunietz, A. D. Dutoi, T. R. Furlani, S. R. Gwaltney, A. Heyden, S. Hirata, C.-P. Hsu, G. Kedziora, R. Z. Khaliullin, P. Klunzinger, A. M. Lee, M. S. Lee, W. Liang, I. Lotan, N. Nair, B. Peters, E. I. Proynov, P. A. Pieniazek, Y. Min Rhee, J. Ritchie, E. Rosta, C. David Sherrill, A. C. Simmonett, J. E. Subotnik, H. Lee Woodcock III, W. Zhang, A. T. Bell, A. K. Chakraborty, D. M. Chipman, F. J. Keil, A. Warshel, W. J. Hehre, H. F. Schaefer III, J. Kong,

A. I. Krylov, P. M. W. Gill and M. Head-Gordon, *Phys. Chem. Chem. Phys.*, 2006, **8**, 3172.

[262] D. J. Cárdenas, A. M. Echavarren and M. C. Ramírez de Arellano, *Organometallics*, 1999, **18**, 3337.